Ejecta erosion, hydrological, and chemical lake evolution in the Ries impact basin (Miocene, Germany)

Dissertation
zur Erlangung des mathematisch-naturwissenschaftlichen Doktorgrades
"Doctor rerum naturalium"
der Georg-August-Universität Göttingen

im Promotionsprogramm Geowissenschaften / Geographie
der Georg-August University School of Science (GAUSS)

vorgelegt von

Lingqi Zeng

aus Leshan, China

Göttingen 2022

"The natural scientist must know that his work is nothing else but climbing from one error to another, but, with the realization that getting closer and closer to the truth, similar to one who climbs from crag to crag and, even if he does not reach the summit, he sees the landscape open up before his eyes in ever more majestic sceneries."
Eduard Suess (1831-1914)

Preface

The present cumulative thesis comprises two published articles and two prepared manuscripts, bridged by an introductory chapter and a summary chapter delineating the main outcomes.

Below is a list of the published peer-review journal papers and prepared manuscripts, loaded as chapters to form a part of this thesis:

Zeng, L., Gätjen, J., Reimer, A., Karius, V., Thiel, V., Arp, G. (submitted) Temporary sulfate depletion and extremely ^{13}C-enriched dolomite formation in a Miocene impact crater lake: successive ejecta erosion controls lacustrine biogeochemical processes.

Arp, G., Dunkl, I., Jung, D., Karius, V., Lukács, R., **Zeng, L.**, Reimer, A. and Head III, J.W. (2021) A Volcanic Ash Layer in the Nördlinger Ries Impact Structure (Miocene, Germany): Indication of Crater Fill Geometry and Origins of Long-Term Crater Floor Sagging. **Journal of Geophysical Research: Planets** 126, e2020JE006764.

Zeng, L., Hölzl, S., Reimer, A., Karius, V., Arp, G. (prepared manuscript) Self-readjusted chemical and hydrological evolution of impact crater lake.

Zeng, L., Ruge, D.B., Berger, G., Heck, K., Hölzl, S., Reimer, A., Jung, D. and Arp, G. (2021) Sedimentological and carbonate isotope signatures to identify fluvial processes and catchment changes in a supposed impact ejecta-dammed lake (Miocene, Germany). **Sedimentology** 68, 2965-2995.

Please note that lingual correctness is not perfect in the prepared and submitted manuscripts, as they will be improved prior to submission and during the review processes.

Abstract

To inspect past environmental changes and potential habitability, the growing interests for the ancient Martian crater lakes call for better understandings of palaeolimnological evolution of impact crater lakes. Particularly, their hydrological and chemical lake histories are poorly understood because the impact processes partly recreate and complicate the limnological settings. On the other hand, lacustrine deposits are known as sensitive archives of climate changes, superimposed on the limnological processes of the impact crater catchment. The Nördlinger Ries impact structure (Miocene, Germany) hence provides unique and handy insights for similar palaeolimnological processes of the mid-sized impact craters not only on Earth, as well as on the remote, hardly ventured Martian surface.

The 14.9 Ma Ries impact event produced an eventually 24 km-wide crater by penetrating a water-saturated, bedded sedimentary cover above the crystalline basement. Well-preserved impact ejecta formations, comprising the suevite (impact melt-bearing breccia), the Bunte Breccia (primary ejecta blanket) and parautochthonous megablocks were present in the catchment and subject to erosion. Lacustrine sedimentation started on top of the crater suevite and over 300-meter-thick post-impact, mixed siliciclastic-carbonate sediments were deposited within ca. 1-2 Ma immediately after the impact.

Previous investigations, largely benefited from Sr, C and O isotope of the carbonates, have suggested that the lacustrine succession in the Ries crater may record the successive weathering in the crater lake catchment under hydrologically closed conditions. The two ejecta layers with an inverted stratigraphy (the suevite on top of the Bunte Breccia) lead to chemically distinct weathering products, resulting in different influxes to the lake water and discernible chemical lake stages. However, the throughout and general chemical lake evolution is still poorly constrained. Based on this assumption, it also remains unknown whether the biogeochemical processes, specifically microbial respirations, follow and correspond to the evolving chemical lake stages. Beyond that, due to the difficulty in sedimentary architecture by post-depositional erosion, the hydrological balance between surface runoffs and groundwater along the lake history remains unknown. The Ries lacustrine succession might have also intercepted a climate change event from the warm Miocene Climatic Optimum (MCO) to the long-term cooling during mid-Miocene Climate Transition. Thereby the Ries lacustrine deposits are of great potential to examine how the hydrology and hydrochemistry of an impact crater lake react to possible climate changes.

This thesis contains a series of sedimentological, mineralogical, geochemical and isotopic investigations, with most of the focus on a drill core from the central Ries crater (NR1003), aiming at i) reconstructing hydrological, chemical and biogeochemical lake histories of the Ries crater; ii) clarifying the importance of extrinsic changes (i.e. climate change) versus intrinsic change (catchment change and internal tectonics) on the hydrological and chemical crater lake evolutions.

The first study shows a systematic trend in biogeochemical processes following the successive erosion of the ejecta formations and hydrological changes, using stable oxygen and carbon isotopes in conjunction with biomarkers. An early sulfidic lake stage with extensive sulfate reduction is characterized by abundant thiophenes as well as biomarkers for sulfate reducing bacteria. The next stage is poor in evidence of sulfate reduction whereas pronouncedly ^{13}C-enriched dolomites are associated with an archaea-derived lipid biomarker, archaeol, demonstrating a methanogenic lake bottom. A subsequent decline in both $\delta^{13}C_{carb}$ and archaeol follows a decreasing lake level with signatures of subaerial exposure events, supporting aerobic methanotrophy as indicated by the observation of 3-methyl-hopanoids.

The second study describes the discovery of a volcanic ash layer throughout the crater basin. The observed deeply bowl-shaped geometry of this layer cannot be reconciled by calculations of sediment compaction based on sediment load and burial alone. Additional sagging would have been attributed to the subsidence of the crater floor substrate and closure of the dilatant macro-porosity, closely related to the deep, in-situ impact fractures.

In the third study, to simulate the ejecta erosion processes, a series of leaching experiments were conducted to the pre-impact target formations as well as the ejecta formations. The process from ejecta erosion to lacustrine carbonate precipitation were traced by Sr isotope to inspect the detailed hydrological and chemical lake evolutions. In conjunction with sedimentological evidence and hydrochemical modelling tests, different mixing scenarios of fluid endmember, from leachate or field waters, were tested and reconciled for each lake stage. A systematic provenance change is evident from crystalline basement and suevite, to Bunte Breccia and finally Lower/Middle Jurassic formations. This trend suggests an expanse of the catchment from central crater towards outside the crater, similar to the pre-impact hydrological condition. In addition, the sedimentary structures of the lacustrine deposits reflect a cooling and stabilizing crater floor due to long-term sagging and sediment loading, significantly changed the groundwater discharge balance via the closure of the mega-porosity. Therefore, the unique self-readjusted hydrological and hydrochemical evolutions are independent from climate change but rather controlled by the ejecta erosion and porosity change, both representing the intrinsic limnological processes of an impact crater lake.

In the fourth study, as a side topic, the deposits from a supposed impact ejecta-dammed lake, known as "Rezat-Altmühl-Lake", were investigated because it might be the only known case on Earth. However, no pebbles from impact ejecta have been detected as well as the key criteria for lacustrine lithofacies. Instead, the succession is characterized by less diagnostic floodplain fines with palaeosols, palustrine limestones with root voids and intercalated thin sandstone beds. Low, invariant $\delta^{18}O_{carb}$ reflects a short water residence time and highly variable $\delta^{13}C_{carb}$ indicates a variable degree of pedogenesis, substantiating the interpretation of a fluvial setting. The trend in $^{87}Sr/^{86}Sr$ in the carbonate and bulk carbonate content argue for increasing weathering products from the topographically low Triassics, to Jurassics at higher level.

Contents

List of Figures

List of Tables

Chapter 1.   Introduction

Lake deposits are valuable past-environmental archives (Cohen, 2003), in the sense of seasonality (Hollander and McKenzie, 1991), photosynthesis effect (Thompson et al., 1997), lake productivity (Teranes et al., 1999). Particularly lacustrine carbonates, either authigenically precipitating from the water column (Talbot, 1990), or facilitated by microbial processes (e.g. Arp, 1995), are a group of chemical deposits in balance with the ambient lake settings, thereby reflecting the chemistry of lake water (e.g. Müller et al., 1972). Studying the textures and facies of lacustrine carbonates, in conjunction with different isotope systems hence greatly unfolds a suite of hydrological and hydrochemical information. Among them, the palaeohydrology studies of fossil lakes, including investigation of the existence of hydrological closure by stable carbon and oxygen isotopes (Talbot, 1990), reconstruction of catchment history as well as fluid provenances by strontium isotopes (Gierlowski-Kordesch et al., 2008; Doebbert et al., 2014), and lake-filling style related to evaporation/precipitation and base level change according to facies associations (Carroll and Bohacs, 1999), appear to be most fundamental questions for palaeolimnological studies. Beyond that, from the lacustrine carbonates, the stable carbon and oxygen isotopes are helpful to understand the lake water salinity (Liu et al., 2009) and biogeochemical processes, e.g., photosynthesis (Thompson et al., 1997), sulfate reduction and methanogenesis (Zeng et al., submitted); the recently developed triple oxygen isotope method as quantitative approach for evaluating lake evaporation (Passey and Ji, 2019); nitrogen isotope as a pH approach (Stüeken et al., 2020), and so on.

Asteroid impact craters take the advantage for being natural underfilled basins. When the ambient precipitation is higher than ambient evaporation, a crater lake rises and forms an excellent environmental archive (e.g. the Quaternary or present-day Lake El'gygytgyn, Melles et al., 2012; Lake Bosumtwi, Talbot and Johannessen, 1992), among these many cases, the impact timing can be determined without tremendous efforts. The older, pre-Quaternary impact crater lakes on Earth are even more interesting as their sedimentary successions provide handy insights for the remote, ancient Martian crater lake counterparts, on which extensively on-going discussions exist.

The knowledge of the exotic, Earth-like planet Mars has been inspected remotely via a number of orbiter missioners (Mars Reconnaissance and MAVEN Orbiters by NASA; Mars Express by ESA, Tianwen 1 by CNSA and many others) and the serving Martian surface rovers (Curiosity and Perseverance by NASA and Zhurong by CNSA) as well as several retired models. The milestone evidence of liquified water existence by the Viking mission (Carr, 1987) has encouraged scientists to further investigate and examine any contemporary or past habitability for life forms of the red planet up to now. Much focus has been paid to the Martian craters (e.g. Gale Crater and Jezero Crater), where a number of fluvial-lacustrine facies is involved. A critical evaluation for the habitability of the ancient Mars is the information of past hydrological condition hidden in the solid rocks (Grotzinger et al., 2015). Despite of growing success and attention on these Martian crater deposits, challenges still are encountered with respect to a number of important questions, exactly related to hydrology of these impact crater lakes: To what extent had the groundwater and surface river runoffs affected the crater lake hydrology as well as the morphology (Carr, 1995; Fasset and Head, 2008; Harrison and Grimm, 2005; Wray et al., 2011; Goudge et al., 2016)? How extensive was the groundwater systems on Mars—e.g. was there a regionally connected groundwater network (Salese et al., 2019; Roseborough et al., 2021)? Parallelly to the interior crater lake hydrology, questions on the hydrochemistry of the Martian crater lakes arise as well as the past climate, closely related to habitability on Mars: What was the climate on early Mars in front of a faint young Sun (Sagan and Chyba, 1997) and how did the liquefied water survive? How did the hydrological system and sedimentation react to the extrinsic, climate-induced evaporation and precipitation (Moore et al., 2003; Andrews-Hanna

et al., 2010; Baum and Wordsworth, 2020; Roseborough et al., 2021), and to the intrinsic factors, .e.g., hydrothermal activities (Ojha et al., 2020); groundwater upwelling and the following flooding (Wang et al., 2005) and erosion (Harrison and Grimm, 2005)? Where was the most possible habitable zone on the early Mars (Michalski et al., 2013; Rivera-Valentín et al., 2020; Ojha et al., 2020)?

While most of the above-mentioned research has been made based on limited mineralogical, geochemical data and modelling, all questions and interpretations have to meet and be reconciled with a realistic geological scenario. The Miocene Nördlinger Ries (Germany) is one of the most well-investigated impact craters on Earth (Pohl, 1977; von Engelhardt, 1990; Wünnemann et al., 2005; Stöffler et al., 2013) since its evidence of asteroid impact was confirmed by Shoemaker and Chao (1961). The ca 14.9 Ma (Rocholl et al., 2018; Schwarz et al., 2020) Ries impact structure was formed by a 1.1-1.5 km sized stony meteorite with the impact velocity of 15-18 km/s (Artemieva et al., 2013). The target area is characterized by a water-saturated, over 600 m thick bedded sedimentary cover comprising the Miocene unsolidated siliciclastics, marine Jurassic formations and terrestrial Triassic formations, on top of a Hercynian crystalline basement (Pohl, 1977). The morphology of impact structure has been extraordinarily well-preserved, with the proximal ejecta formations comprising: i) the continuous ejecta blanket (so-called Bunte Breccia); ii) the melt-rich breccia (known as suevite); iii) the polymictic crystalline breccia. Minor amount of distal breccia, including iv) the upper Jurassic limestone fragments (so-called Reuter Blocks, up to 150 km from the impact center and v) the moldavite/tektite, forming a strew-like field in the Czech Republic, East Germany, and North-West Austria up to a distance of 450 km from the point of impact (Stöffler et al., 2013 and the references therein).

In central crater (i.e. within the rim of inner ring), thick lacustrine sedimentation of the Ries lake, at maximum over 300 m in thickness, starts to accumulate on top of the crater suevite (Füchtbauer et al., 1977; Jankowski, 1981): a) a siliciclastic-rich **basal member**; b) a **laminite member**, composing the main lake stage with thick laminated bituminous marlstone, showing authigenic zeolites and a paucity in bioturbation; c) a **marl member** with features of bioturbation, subaerial exposure and fade in the laminite facies; d) a **clay member,** highly distinct in lithology as the previous members, dominated by unstratified carbonaceous clay with intercalated lignite seams, as well as pedogenic signatures. Intercalated marly carbonate beds are present throughout the lacustrine succession. At the margin of the crater basin, several units of carbonate mounds, representing different hydrochemical conditions and lake stages, are also present (Arp, 1995; Arp et al., 2013ab). These widespread carbonates thereby contain valuable information of hydrological, biogeochemical and hydrochemical lake evolutions, with the following important limnological setups:

1) An overall hydrological closure of the lake basin (Talbot, 1990);
2) A quickly transgressed saline (Barakat and Rullkötter, 1997; Rothe and Hoefs, 1977), soda lake, in which the pH peaks in analcime smbr. then successively decline (Arp et al., 2013a; Stüeken et al., 2020);
3) The ion-ratios of the long-term lake hydrochemistry were dependent on the successive erosion of the ejecta blanket (Arp et al., 2013a);
4) Hydrothermal influence from the hot crater floor beneath the suevite, despite of unclear duration (Rothe and Hoefs, 1977; Osinski, 2005; Arp et al., 2013b)
5) Some other unique internal or external geological processes related to the post-impact stage, for instance, i) the impact pre-processing (Arp et al., 2019), possibly facilitating leaching processes during the erosion and in turn, enhanced salinity in the lake water; ii) crater floor sagging leading to change of mega-porosity underneath (Arp et al., 2021).

Despite of these findings, a number of questions still remain in discussion, open and require detailed investigation:

1) An earlier supposed, declining salinity trend is not in accordance with the occurrences of gypsum pseudomorphs in the clay member (Füchtbauer et al., 1977; Jankowski, 1981; Arp et al., 2017). However, is there a more intricated salinity change within the main lake stage, during the deposition of laminite member? In general, the hydrochemical lake evolution is poorly understood. Moreover, as the famous microbiologic tenet goes: "*everything is everywhere, but, the environment selects*" (Baas Becking, 1934), does this change in lake hydrochemistry post any selections on the microbial realm?

2) Lacustrine processes and depositions are a complex interaction, balanced between climate and tectonic process (Carroll and Bohacs, 1999). The timing of Ries impact event (ca. 14.9 Ma) falls into the transition between the warm Miocene Climatic Optimum (MCO) and long-term cooling mid-Miocene Climate Transition (MCT, Flower and Kennett, 1994). Was the Ries lacustrine succession controlled by the extrinsic climate change, or by the intrinsic changes related to the crater lake watershed? How do the extrinsic climate factor, and the intrinsic crater tectonic and catchment change the hydrological balance and hydrochemical evolution?

3) The temperature evolution of the crater floor remains poorly constrained. Pohl (1977) calculated that the cooling of the 200 m thick melt-rich suevite layer from initially 800 °C to 100 °C took several thousands of years. However, the stratigraphic position of hot spring travertines of the Erbisberg suggests that the impact-generated hydrothermal activity in the Ries crater was much longer than that, i.e., about 250.000 a (Arp et al. 2013b).

4) In some impact basins with bedded target rocks, an overturned stratigraphy is observed (e.g. overturned Kaibab Fm. and Moenkopi Fm. in Barringer crater, Osinski et al., 2013, their Fig. 4.5). Can this overturned stratigraphy be observed in the whole ejecta blanket?

5) Asteroid impact events might have changed the regional hydrology via damming the local drainage system (Irwin III and Howard, 2002). However, this process so far was only observed for Martian craters due to their better preservation. The Miocene Georgensgmünd Formation in southern Germany, have previously been considered as lake deposits (Dorn, 1939) that formed as a result of damming of an ancient river by ejecta from the Ries asteroid impact (Birzer, 1969). It would be, to our knowledge, the only supposed impact ejecta-dammed lake on Earth reported in literature. The sedimentological details, as well as the provenance of this Georgensgmünd Formation therefore appears highly interesting to check, as potential impact-ejecta-dammed lake analogue on Earth.

To answer these main questions, a drill core from the central crater (NR1003, Exxon Mobil) was investigated in detail. The main objectives and goals of this thesis are:

1) to investigate the biogeochemical processes and evolution in the Ries lake when exposed to the observed hydrochemical and hydrological changes due to successive ejecta erosion and lake filling. On top of the sedimentological investigation, the stable carbon and oxygen isotopes, detailed mineralogy as well as high-precision in-situ geochemistry of the Ries carbonate phases were studied. Biomarker analysis was included to provide decisive evidence to identify the specific chemo-heterotrophs.

2) to reconstruct detailed hydrological and hydrochemical evolutions of the Ries crater lake by the different isotope systems, as well as bridging the pre-impact target formations and lacustrine deposits by a series of leaching experiments. Isotope-based mass-balance calculation between different ejecta formations and lacustrine carbonates were tested, then supplemented by hydrochemical modelling from the target leachates or field water/groundwater samples;

3) clarifying the effect of tectonic control vs climate control on the crater lake sedimentation, discussing to what extent do the tectonic and climate changes influence the hydrological balance and hydrochemistry in the Ries crater lake.

The topic 1) is present in **Chapter 2** as a submitted manuscript (research data included as **Appendix A**). **Chapter 3** presents a published paper of a volcanic ash layer, where the post-impact internal tectonics provide important clues for hydrological change. The conceptual hydrological and hydrochemical evolution are finally described in **Chapter 4**, including topics 2) and 3) as a prepared manuscript (research data comes in **Appendix B**).

Materials from another drill core (Pleinfeld, Geoloical Survey of Bavaria), as well as a number of field outcrop samples, were also collected to investigate as the side topic to discern and identify the possible Miocene impact ejecta-dammed lake. This study is present in the form of a published journal paper as **Chapter 5**.

The summarizing **Chapter 6** finally outlines all the outcomes of the work in this thesis.

References

Andrews-Hanna, J.C., Zuber, M.T., Arvidson, R.E. and Wiseman, S.M. (2010) Early Mars hydrology: Meridiani playa deposits and the sedimentary record of Arabia Terra. Journal of Geophysical Research: Planets 115.

Arp, G. (1995) Lacustrine bioherms, spring mounds, and marginal carbonates of the Ries-impact-crater (Miocene, southern Germany). Facies 33, 35-89.

Arp, G., Blumenberg, M., Hansen, B.T., Jung, D., Kolepka, C., Lenz, O., Nolte, N., Poschlod, K., Reimer, A. and Thiel, V. (2013a) Chemical and ecological evolution of the Miocene Ries impact crater lake, Germany: A reinterpretation based on the Enkingen (SUBO 18) drill core. Bulletin 125, 1125-1145.

Arp, G., Dunkl, I., Jung, D., Karius, V., Lukács, R., Zeng, L., Reimer, A. and Head III, J.W. (2021) A Volcanic Ash Layer in the Nördlinger Ries Impact Structure (Miocene, Germany): Indication of Crater Fill Geometry and Origins of Long-Term Crater Floor Sagging. Journal of Geophysical Research: Planets 126, e2020JE006764.

Arp, G., Hansen, B.T., Pack, A., Reimer, A., Schmidt, B.C., Simon, K. and Jung, D. (2017) The soda lake—mesosaline halite lake transition in the Ries impact crater basin (drilling Löpsingen 2012, Miocene, southern Germany). Facies 63, 1-20.

Arp, G., Kolepka, C., Simon, K., Karius, V., Nolte, N. and Hansen, B.T. (2013b) New evidence for persistent impact‐generated hydrothermal activity in the Miocene Ries impact structure, Germany. Meteoritics & Planetary Science 48, 2491-2516.

Arp, G., Schultz, S., Karius, V. and Head, J.W. (2019) Ries impact crater sedimentary conglomerates: Sedimentary particle 'impact pre-processing', transport distances and provenance, and implications for Gale crater conglomerates, Mars. Icarus 321, 531-549.

Artemieva, N., Wünnemann, K., Krien, F., Reimold, W. and Stöffler, D. (2013) Ries crater and suevite revisited—Observations and modeling Part II: Modeling. Meteoritics & Planetary Science 48, 590-627.

Barakat, A.O. and Rullkötter, J. (1997) A Comparative Study of Molecular Paleosalinity Indicators: Chromans, Tocopherols and C20 Isoprenoid Thiophenes in Miocene Lake Sediments (Nördlinger Ries, Southern Germany). Aquatic Geochemistry 3, 169-190.

Baum, M. and Wordsworth, R. (2020) Groundwater Flow to Gale Crater in an Episodically Warm Climate. Journal of Geophysical Research: Planets 125, e2020JE006397.

Birzer, F. (1969) Molasse und Ries-Schutt im westlichen Teil der südlichen Frankenalb. Geologische Blätter für Nordost-Bayern 19, 1-28.

Carr, M.H. (1987) Water on Mars. Nature 326, 30-35.

Carr, M.H. (1995) The Martian drainage system and the origin of valley networks and fretted channels. Journal of Geophysical Research: Planets 100, 7479-7507.

Carroll, A.R. and Bohacs, K.M. (1999) Stratigraphic classification of ancient lakes: Balancing tectonic and climatic controls. Geology 27, 99-102.

Cohen, A.S. (2003) Palaeolimnology: the history and evolution of lake systems. Oxford University Press.

Doebbert, A.C., Johnson, C.M., Carroll, A.R., Beard, B.L., Pietras, J.T., Carson, M.R., Norsted, B. and Throckmorton, L.A. (2014) Controls on Sr isotopic evolution in lacustrine systems: Eocene green river formation, Wyoming. Chemical Geology 380, 172-189.

Dorn, C. (1939) Die Ablagerungen der obermiocänen Süßwasserkalke bei Pleinfeld und Georgsgemünd in Mittelfranken. Jahresberichte und Mitteilungen des Oberrheinischen Geologischen Vereins, 67-98.

Füchtbauer, H., Von Der Brelie, G., Dehm, R., Förstner, U., Gall, H., Höfling, R., Hoefs, J., Hollerbach, H., Hufnagel, B., Jankowski, B., Jung, W., Malz, H., Mertes, H., Rothe, P., Salger, M., Wehner, H. and Wolf, M. (1977) Tertiary lake Sediments of die Ries, research borehole Nördlingen 1973 - a summary. Geologica Bavarica 75, 13-20.

Fassett, C.I. and Head, J.W. (2008) The timing of martian valley network activity: Constraints from buffered crater counting. Icarus 195, 61-89.

Flower, B.P. and Kennett, J.P. (1994) The middle Miocene climatic transition: East Antarctic ice sheet development, deep ocean circulation and global carbon cycling. Palaeogeography, Palaeoclimatology, Palaeoecology 108, 537-555.

Gierlowski-Kordesch, E., Jacobson, A., Blum, J. and Valero Garćes, B.L. (2008) Watershed reconstruction of a Paleocene–Eocene lake basin using Sr isotopes in carbonate rocks. Geological Society of America Bulletin 120, 85-95.

Goudge, T.A., Fassett, C.I., Head, J.W., Mustard, J.F. and Aureli, K.L. (2016) Insights into surface runoff on early Mars from paleolake basin morphology and stratigraphy. Geology 44, 419-422.

Grotzinger, J.P., Crisp, J.A., Vasavada, A.R. and Team, M.S.L.S. (2015) Curiosity's Mission of Exploration at Gale Crater, Mars. Elements 11, 19-26.

Harrison, K.P. and Grimm, R.E. (2005) Groundwater-controlled valley networks and the decline of surface runoff on early Mars. Journal of Geophysical Research: Planets 110.

Hollander, D.J. and McKenzie, J.A. (1991) CO2 control on carbon-isotope fractionation during aqueous photosynthesis: A paleo-pCO2 barometer. Geology 19, 929-932.

Irwin III, R.P. and Howard, A.D. (2002) Drainage basin evolution in Noachian Terra Cimmeria, Mars. Journal of Geophysical Research: Planets 107, 10-11-10-23.

Jankowski, B. (1981) Die Geschichte der Sedimentation im Nördlinger Ries und Randecker Maar. Inst. für Geologie, Ruhr-Univ.

Liu, W., Li, X., Zhang, L., An, Z. and Xu, L. (2009) Evaluation of oxygen isotopes in carbonate as an indicator of lake evolution in arid areas: The modern Qinghai Lake, Qinghai–Tibet Plateau. Chemical Geology 268, 126-136.

Müller, G., Irion, G. and Förstner, U. (1972) Formation and diagenesis of inorganic Ca− Mg carbonates in the lacustrine environment. Naturwissenschaften 59, 158-164.

Melles, M., Brigham-Grette, J., Minyuk Pavel, S., Nowaczyk Norbert, R., Wennrich, V., DeConto Robert, M., Anderson Patricia, M., Andreev Andrei, A., Coletti, A., Cook Timothy, L., Haltia-Hovi, E., Kukkonen, M., Lozhkin Anatoli, V., Rosén, P., Tarasov,

P., Vogel, H. and Wagner, B. (2012) 2.8 Million Years of Arctic Climate Change from Lake El'gygytgyn, NE Russia. Science 337, 315-320.

Michalski, J.R., Cuadros, J., Niles, P.B., Parnell, J., Deanne Rogers, A. and Wright, S.P. (2013) Groundwater activity on Mars and implications for a deep biosphere. Nature Geoscience 6, 133-138.

Moore, J.M., Howard, A.D., Dietrich, W.E. and Schenk, P.M. (2003) Martian Layered Fluvial Deposits: Implications for Noachian Climate Scenarios. Geophysical Research Letters 30.

Ojha, L., Buffo, J., Karunatillake, S. and Siegler, M. Groundwater production from geothermal heating on early Mars and implication for early martian habitability. Science Advances 6, eabb1669.

Osinski, G. (2005) Hydrothermal activity associated with the Ries impact event, Germany. Geofluids 5, 202-220.

Osinski, G.R., Grieve, R.A.F. and Tornabene, L.L. (2013) Excavation and Impact Ejecta Emplacement, in: Osinski, G.R., Pierrazzo, E. (Eds.), Impact Cratering. Wiley-Blackwell, Chicester, pp. 43-59.

Passey, B.H. and Ji, H. (2019) Triple oxygen isotope signatures of evaporation in lake waters and carbonates: A case study from the western United States. Earth and Planetary Science Letters 518, 1-12.

Pohl, J., Stoeffler, D., Gall, H.v. and Ernstson, K. (1977) The Ries impact crater, Impact and explosion cratering: Planetary and terrestrial implications, pp. 343-404.

Rivera-Valentín, E.G., Chevrier, V.F., Soto, A. and Martínez, G. (2020) Distribution and habitability of (meta)stable brines on present-day Mars. Nature Astronomy 4, 756-761.

Rocholl, A., Böhme, M., Gilg, H.A., Pohl, J., Schaltegger, U. and Wijbrans, J. (2018) Comment on "A high-precision 40Ar/39Ar age for the Nördlinger Ries impact crater, Germany, and implications for the accurate dating of terrestrial impact events" by Schmieder et al.(Geochimica et Cosmochimica Acta 220 (2018) 146–157). Geochimica et Cosmochimica Acta 238, 599-601.

Roseborough, V., Horvath, D.G. and Palucis, M.C. (2021) Was Gale Crater (Mars) Connected to a Regionally Extensive Groundwater System? Geophysical Research Letters 48, e2020GL092107.

Rothe, P. and Hoefs, J. (1977) Isotopen-geochemische Untersuchungen an Kabonaten der Ries-See-Sedimente der Forschungsbohrung Nördlingen 1973. Geologica Bavarica 75, 59-66.

Sagan, C. and Chyba, C. (1997) The Early Faint Sun Paradox: Organic Shielding of Ultraviolet-Labile Greenhouse Gases. Science 276, 1217-1221.

Salese, F., Pondrelli, M., Neeseman, A., Schmidt, G. and Ori, G.G. (2019) Geological Evidence of Planet-Wide Groundwater System on Mars. Journal of Geophysical Research: Planets 124, 374-395.

Schwarz, W.H., Hanel, M. and Trieloff, M. (2020) U-Pb dating of zircons from an impact melt of the Nördlinger Ries crater. Meteoritics & Planetary Science 55, 312-325.

Shoemaker, E.M. and Chao, E.C. (1961) New evidence for the impact origin of the Ries Basin, Bavaria, Germany. Journal of Geophysical Research 66, 3371-3378.

Stüeken, E.E., Tino, C., Arp, G., Jung, D. and Lyons, T.W. (2020) Nitrogen isotope ratios trace high-pH conditions in a terrestrial Mars analog site. Science Advances 6, eaay3440.

Stöffler, D., Artemieva, N.A., Wünnemann, K., Reimold, W.U., Jacob, J., Hansen, B.K. and Summerson, I.A. (2013) Ries crater and suevite revisited—Observations and modeling Part I: Observations. Meteoritics & Planetary Science 48, 515-589.

Talbot, M. (1990) A review of the palaeohydrological interpretation of carbon and oxygen isotopic ratios in primary lacustrine carbonates. Chemical Geology: Isotope Geoscience Section 80, 261-279.

Talbot, M.R. and Johannessen, T. (1992) A high resolution palaeoclimatic record for the last 27,500 years in tropical West Africa from the carbon and nitrogen isotopic composition of lacustrine organic matter. Earth and Planetary Science Letters 110, 23-37.

Teranes, J.L., McKenzie, J.A., Lotter, A.F. and Sturm, M. (1999) Stable isotope response to lake eutrophication: Calibration of a high‐resolution lacustrine sequence from Baldeggersee, Switzerland. Limnology and Oceanography 44, 320-333.

Thompson, J.B., Schultze-Lam, S., Beveridge, T.J. and Des Marais, D.J. (1997) Whiting events: Biogenic origin due to the photosynthetic activity of cyanobacterial picoplankton. Limnology and Oceanography 42, 133-141.

von Engelhardt, W. (1990) Distribution, petrography and shock metamorphism of the ejecta of the Ries crater in Germany—A review. Tectonophysics 171, 259-273.

Wang, C.-y., Manga, M. and Wong, A. (2005) Floods on Mars released from groundwater by impact. Icarus 175, 551-555.

Wray, J.J., Milliken, R.E., Dundas, C.M., Swayze, G.A., Andrews-Hanna, J.C., Baldridge, A.M., Chojnacki, M., Bishop, J.L., Ehlmann, B.L., Murchie, S.L., Clark, R.N., Seelos, F.P., Tornabene, L.L. and Squyres, S.W. (2011) Columbus crater and other possible groundwater-fed paleolakes of Terra Sirenum, Mars. Journal of Geophysical Research: Planets 116.

Wünnemann, K., Morgan, J.V., Jödicke, H., Kenkmann, T., Hörz, F. and Deutsch, A. (2005) Is Ries crater typical for its size? An analysis based upon old and new geophysical data and numerical modeling, in: Kenkmann, T., Hörz, F., Deutsch, A. (Eds.), Large Meteorite Impacts III. Geological Society of America, p. 0.

Zeng, L., Gätjen, J., Reimer, A., Karius, V., Thiel, V. and Arp, G. (submitted) Temporary sulfate depletion and extremely 13C-enriched dolomite formation in a Miocene impact crater lake: successive ejecta erosion controls lacustrine biogeochemical processes. Geochimica et Cosmochimica Acta.

Chapter 2. Temporary sulfate depletion and extremely ^{13}C-enriched dolomite formation in a Miocene impact crater lake: successive ejecta erosion controls lacustrine biogeochemical processes

Lingqi Zeng[a*], Jochen Gätjen[a], Andreas Reimer[a], Volker Karius[a], Volker Thiel[a], Gernot Arp[a]
[a]Geoscience Center, University of Göttingen, 37075, Göttingen, Germany

Corresponding author: Lingqi Zeng (lzeng@gwdg.de)
Submitted to **Geochemica et Cosmochimica Acta**

Abstract

The chemical evolution of saline lakes reflects external, climatic factors as well as processes within the lake basin such as changes in ion influx and mineral precipitation. This is especially true for impact crater lakes, whose water chemistry is dictated by the ionic composition of solutes from different ejecta lithologies and autochthonous rocks in the catchment area.

Using stable oxygen and carbon isotopes in conjunction with biomarkers, the sequence of geochemical processes was studied in carbonates from a drill core of the Nördlinger Ries impact crater basin, which falls in the range of the mid-Miocene Climate Transition. These investigations revealed an early sulfidic interval with thiophenes and Ca-rich dolomites with low to intermediate $\delta^{13}C_{carb}$. This period was followed by a distinctive interval with extremely ^{13}C-enriched, early diagenetic ferroan dolomite ($\delta^{13}C_{carb}$ up to +20.93‰ V-PDB). The isotopically heavy dolomite is low in total sulphur but high in an archaea-derived lipid biomarker, archaeol, thus suggesting extensive methanogenesis in sulfate-depleted lake porewater. Such sulfate depletion in the course of the crater lake evolution is explained by a change from the sulfur-rich suevite and crystalline source rocks to sulfur-poor rocks of the Bunte Breccia. A subsequent decline in both $\delta^{13}C_{carb}$ and archaeol is indicative of a decreasing lake level with intermittent subaerial exposure events, as further indicated by bioturbation and mud cracks. The concomitant lake oxygenation is well supported by increasing Pr/Ph ratios as well as lipids derived from aerobic methanotrophs (3-methyl-hopanoids).

In the youngest preserved sediments of the crater basin, high total sulphur contents and thiophenes recur, in addition to allochthonous lignites, biomarkers from terrestrial sources, and further decreasing, though scattering, stable isotope ratios. These observations suggest another major change in the provenance of inflowing solutes, with increasing influx from weathered pyrite-bearing Jurassic claystones instead of Bunte Breccia ejecta.

Our results show that the climatic record accessible from stable carbon and oxygen isotopes of the Ries carbonates is strongly overprinted by the successive ejecta erosion and catchment changes. Such an intrinsic control of lacustrine biogeochemical processes is also expected for other hydrologically closed impact crater lake basins, where catchment rocks with distinctively different lithologies are present.

Keywords: ferroan dolomite, methanogenesis, sulfate depletion, biogeochemistry, impact crater

1 Introduction

Stable carbon isotope ratios of carbonates provide information on seasonality (Hollander and McKenzie, 1991), photosynthesis effect (Thompson et al., 1997) and productivity (Teranes et al., 1999). In conjunction with $\delta^{18}O$, hydrological conditions (open or closed basins) can be inferred from lacustrine carbonates (Talbot, 1990; Talbot and Kelts, 1990; Li and Ku, 1997; Leng and Marshall, 2004). Together, these two, most common stable isotopes of the carbonate form an important tool for the climate, ecological and hydrological reconstructions of lacustrine systems (Cohen, 2003). However, mixed mineralogical composition of carbonates and diagenetic effects in lake environments need to be carefully considered when interpreting lacustrine stable isotope records (McCormack et al., 2019).

Most carbonates formed in lakes show a $\delta^{13}C$ range from -10 to +10‰ (e.g. Hudson, 1977; Fontes et al., 1985; Gasse et al., 1987; Talbot and Kelts, 1990; Platt, 1992; Calvo et al., 1995; Arenas et al., 1997; Li and Ku, 1997; Leng and Marshall, 2004; Della Porta, 2015; Arp et al., 2017a). Nonetheless, notable exceptions with $\delta^{13}C$ up to +27‰ have been reported in various settings associated with extensive evaporation (Valero-Garcés et al., 1999) and early diagenesis (Talbot and Kelts, 1986; Mazzullo, 2000; Meister et al., 2011; Birgel et al., 2015) in both freshwater and marine environments.

The Miocene Nördlinger Ries is an asteroid impact structure, hosting a hydrologically closed lake basin (Talbot, 1990), with deposits mainly comprising carbonate-rich marlstone to claystone (Jankowski, 1981) and well-preserved bituminous shales (Barakat and Rullkötter, 1997). Contrary to smaller sized craters (simple impact craters), the mid-sized Ries exhibits a complex shallow structure (complex impact craters), a deeply fractured basement, highly erodible impact ejecta formations in the catchment and significant post-impact hydrothermal activity (Osinski, 2005; Arp et al., 2019). These factors add up to provenance changes of tributary waters due to the successive erosion from the melt-bearing impact breccia (suevite) to the ejecta blankets (Bunte Breccia), leading to an initial peak in lake water pH, followed by a successive pH decline (Arp et al., 2013a; Stüeken et al., 2020). The special hydrochemistry setups potentially put forward the Ries sediments to an excellent archive for past biogeochemical processes, such as primary production and microbial respiration when exposed to long-term changes, as yet a fairly new field and poorly understood (e.g. Logares et al., 2013).

Earlier studies reported $\delta^{13}C$ values of Ries carbonates falling within a normal range (-7.8 to +3.8‰, Arp et al. 2013a, 2017a). A scientific research drilling (Nördlingen 1973) revealed $\delta^{13}C$ values between -11.5 and +8.1‰, with three positive outliers (+9.5 to +11.1‰, Rothe and Hoefs, 1977). The more recent drill core Nördlinger Ries 1003 (NR1003, operated on 1981) intersected a previously undescribed high-$\delta^{13}C$-dolomite interval (up to +20.9‰). Based on this drill core, our study aims at elucidating the nature of the pronounced ^{13}C-enrichment in these dolomites. Using biomarkers, trace element data, stable oxygen isotopes, and sedimentary features, we identified lake stages reflecting different hydrological conditions, hydrochemistry and major microbial processes. Recently reported U-Pb dating data from a volcanic ash layer (ca. 14.2 Ma) in the Ries basin (Arp et al., 2021), as well as from marginal carbonate mound and bioherms (Montano et al. 2021), provides an approximate age constraint and enables comparison with regional palaeoclimate studies (e.g. Methner et al., 2020). Our results provide important insights into successive erosion of the impact ejecta formations and discern the role of climate changes versus local catchment effects on the biogeochemical and limnological evolution of the ancient crater lake.

2 Study area and geological overview

Located between the karstic areas of Swabian Alb and Franconian Alb in southern Germany, the 24 km-wide Nördlinger Ries was formed by a 1.2 to 1.5 km-sized asteroid, impacting into a water-saturated landscape at 14.808 ± 0.038 Ma (Schmieder et al. 2018a,b; for discussion of age see Rocholl et al. 2018a,b). The impact penetrated over 600 m of horizontally stratified sediments of early Permian to Miocene age, covering Hercynian crystalline

basement rocks below (Pohl et al., 1977). From the center to the outer rim, the impact structure is subdivided into i) a central crater, ii) the inner ring, and iii) the marginal megablock zone. Two ejecta layers, known as Bunte Breccia (successive ejecta blanket) and outer suevite (melt-bearing impact breccia), were formed (Pohl et al., 1977; Stöffler et al., 2013).

In the central crater basin, lake sedimentation starts on top of the crater suevite filling. Four lithostratigraphic units named after their sedimentary features have been established based on the research drilling Nördlingen 1973 (Füchtbauer et al., 1977; Jankowski, 1981): i) the basal member (alluvial fan, cyclic debrite deposits from reworked suevite material, with minor carbonate laminites); ii) the laminite member (laminated marls and bituminous shales); iii) the marl member (poorly stratified dolomite marls), and iv) the clay member (clays with intercalated lignites, diatomites, and carbonates). The investigated drill core NR1003 is located about 10 km NE of the Nördlingen town at 429 m above sea level (**Figure 2.1**).
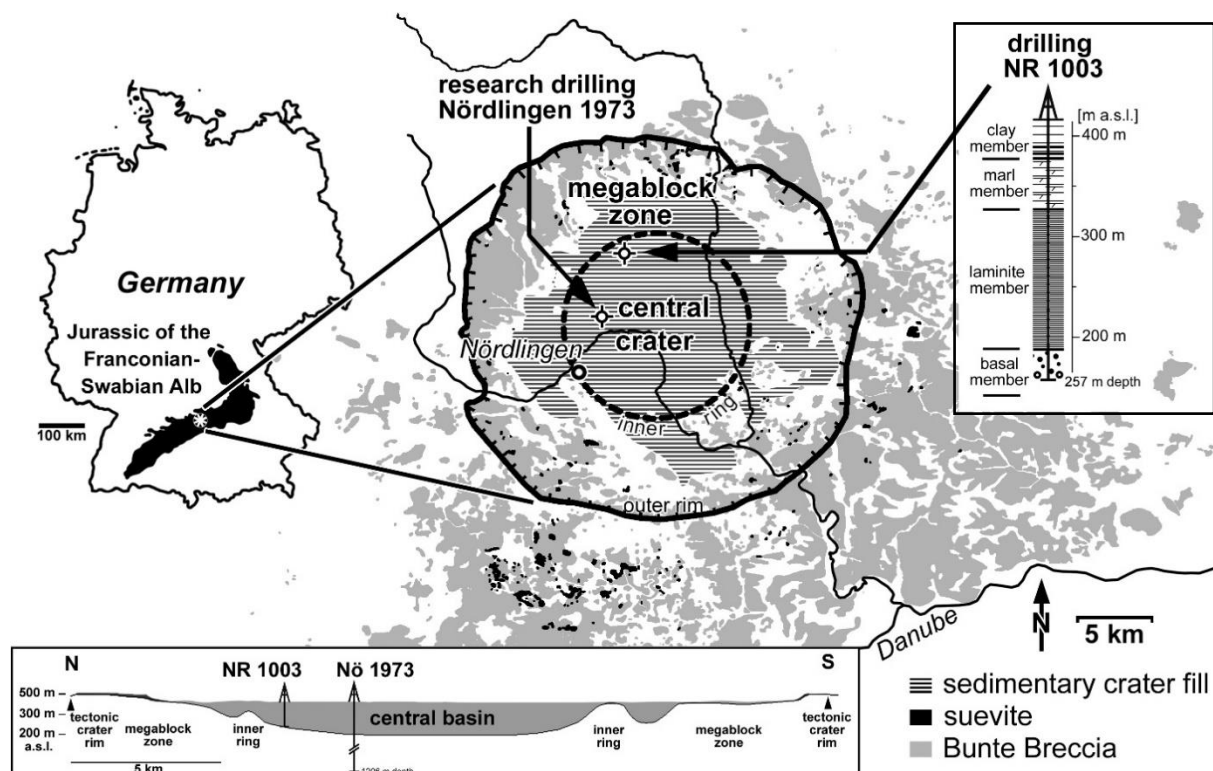
Figure 2.1 Geographical and geological overview of the Ries impact structure (based on Ernstson, 1974; Pohl et al., 1977; Hüttner and Schmidt-Kaler, 1999) and location of the drilling sites Nördlinger Ries 1003 (NR1003) and Nördlingen 1973. Lithostratigraphic subdivision of the sedimentary crater fill based on Jankowski (1981).

3 Material and Methods

3.1 Drilling and sampling overview
The NR1003 drill core is 253.6 m long and 10 cm in diameter, with a core recovery rate of 98.6%. The drilling was performed in 1981 by the Brigitta und Elwerath Betriebsforschungsgesellschaft mbH (BEB) for the exploration of bituminous shales. It is now hosted at the core facility of ExxonMobil Production Germany GmbH in Nienhagen near Celle, Germany. Sampling campaigns were performed on 11/30/2015-12/01/2015, 05/11/2016- 05/13/2016, and 11/20/2018-11/22/2018 (**Table A.1, A.2 and A.3**), including a thorough photographic documentation of the core materials.

3.2 Carbon and sulfur content, X-ray diffraction (XRD), stable carbon and oxygen isotopes

237 carbonate-rich core samples were analysed for their organic carbon (C_{org}), carbonate carbon (C_{carb}) and sulfur contents (**Table A.3**). Organic and inorganic carbon contents were determined by a LECO RC612 stepwise-heating multi-phase carbon analyzer (Leco, St Joseph, MI, USA). LECO carbon standards (1.00 wt% C, 4.98 wt % C, and 12.00 wt% C) were applied for calibration. Total carbon, and sulphur were analysed with a Euro EA 3000 Elemental Analyzer (Hekatech, Wegberg, Germany) applying BBOT (2.5-Bis [5-tert-benzoxazol-2-yl] thiophene) and atropine sulfate monohydrate (IVA Analysetechnik, Meerbusch, Germany) as reference materials. Based on C_{carb}, the bulk carbonate content is calculated as $CaCO_3$ or $CaMg(CO_3)_2$ (**Table A.3**).

The mineralogical composition was investigated by powder X-ray diffraction using a Philips PW 1800 diffractometer with monochromated Cu-Kα radiation, operating at 45 kV and 40 mA. The range 4°–70°2θ was scanned with a step width of 0.02°2θ. The counting time was 3 s per step. Mineral identification was carried out using the X'Pert High-Score Plus software (PANalytical). Identification and quantifications of calcite, magnesian calcite, aragonite and dolomite were calculated by the relative intensity ratios of the respective reflection peaks (*hkl* 104) and their d-spacing values, measured by XRD (semi-quantitative) in combination with C_{carb} results (**Table A.4**). Composition of common, non-carbonate minerals was estimated by semi-quantitation method from X'Pert High-Score Plus software (**Table A.5**)

204 among these samples were further analysed for stable carbon and oxygen isotope ratios (**Table 2.1**). Materials for carbon and oxygen stable isotope measurements of carbonates were hand-picked from cut core slabs and hand specimens using a steel needle to sample separate textures, under a Zeiss Stemi 2000-C binocular microscope. Carbonate powders were reacted with 100% phosphoric acid (density >1.95 g/cm^3) at 70 °C using a Thermo Kiel IV carbonate preparation line connected to a Finnigan Delta plus mass spectrometer (Thermo Fisher Scientific, Waltham, MA, USA). All values are reported as the mean of duplicate measurements, in per mil relative to V-PDB by assigning a δ^{13}C value of +1.95‰ and a δ^{18}O value of -2.20‰ to the NBS 19 standard. Reproducibility was checked by replicate analysis analyses of laboratory standards and is better than ±0.05‰ (1σ). Standard deviations of the stable isotope measurements, if not specifically noted, are 0.05 ‰ for δ^{13}C and 0.07 ‰ for δ^{18}O (see caption of **Table 2.1**). The oxygen isotope ratios of dolomites were corrected using an acid fractionation factor α=1.00993 at 70 °C (Rosenbaum and Sheppard, 1986), with relative calcite-dolomite mole percentages determined by the forementioned, combinative quantification of carbonate phases (**Table A.6**).

3.3 Electron microprobe analyses (EMPA)

The d-spacing values of *hkl* 104 peak (d_{104}) are effective approaches to identify dolomites and calculate their stoichiometric composition, e.g., stoichiometric dolomites (Ca:Mg =1:1) have d_{104} values of 2.886 (Füchtbauer et al., 1977). However, the incorporation of both Fe and/or excess Ca into dolomite lattice would increase the d_{104} values. As a result, it appears less likely to identify ferroan dolomite and Ca-rich dolomite solely based on the d_{104} values of bulk samples (Füchtbauer et al., 1977; Bojanowski, 2014). For this reason, 9 polished thin sections were coated with carbon for EMPA using the JEOL JXA 8900RL instrument at the Göttingen Laboratory for Correlative Light and Electron Microscopy (GoeLEM).

For imaging, both secondary electron images (SE) and backscattered electron images (BSE) were performed at 10 keV and 0.2 nA using a focused beam. For elemental analysis, due to the microcrystalline grain size of the samples (generally < 4 microns), the beam was set to diameters from 5 down to 1 micron depending on the target grains. However, carbonate minerals are known to be sensitive to element drift under a strong focused electron beam. To reduce this effect, higher beam current or measurement times were avoided intentionally despite slight decrease in the detection limit of the minor/trace elements. Therefore, accelerating voltage for elemental analysis was set to 15 keV with a beam current of 12 nA. Counting times of the wavelength dispersive spectrometry (WDS) were set to 15/5 s for

peak/background of the major carbonate elements (Ca, Mg) and to 30/15 s for trace elements (Sr, Mn, Fe).

Furthermore, the small grain size – especially such grains in the range of the excited volume of the electron beam – could cause mixed measurements with other grains including silicate minerals. Thus, major elements of silicates (Si, K) were included in the program for identification in the data. In addition, to minimize any mixed analyses between silicate and carbonate in the first place, the measurements were preferentially performed at large, pure carbonate grain or areas. Likewise, adjacency to pyrites was avoided.

Reference materials for calibration were dolomite (Mg, Ca), rhodonite (Mn), hematite (Fe), and strontianite (Sr). All standards were measured before and after every analytical session. ZAF corrections (Armstrong, 1995) were applied to all analysed samples. Relative Standard Deviations from counting statistic were < 1 % for the major elements (Mg, Ca). In total, 426 point-measurements (**Table A.7**) were assigned to where the carbonate crystals are clearly recognizable.

3.4 Biomarkers

Selected diagnostic biomarkers (**Table 2.2**) were analysed in twelve carbonate rich rock pieces ($CaCO_3$> 50 wt%, 3 g). External surfaces were removed before the samples were crushed and pulverized using a ball mill. The powdered samples were extracted three times with distilled dichloromethane (DCM)/methanol (3:1), DCM, and *n*-hexane using an ultrasonic bath (20 min, RT). After subsequent centrifugation, extracts were dried in a stream of N_2. Biomarkers were then extracted with *n*-hexane and separated by column chromatography using silica gel 60 as the stationary phase. Hydrocarbons were eluted with 7 column dead volumes of *n*-hexane, alcohols with 7 column dead volumes of DCM/acetone (9:1, v/v), and a polar fraction with 7 dead volumes of DCM/methanol (3:1, v/v). Before analyses by gas chromatography–mass spectrometry (GC-MS; see below), elemental sulfur in the hydrocarbon fraction was removed by addition of activated elemental copper. Alcohols were silylated with BSTFA (N,O-bis[trimethylsilyl]trifluoroacetamide) for 1 h at 40°C. Fatty acid methyl esters were prepared from the polar fractions by transesterification with a trimethylchlorosilane(TMCS) / methanol mixture (1:9, v:v) for 1.5 h at 80°C.

All fractions were analysed by coupled gas chromatography/mass spectrometry (GC-MS) using a Thermo trace 1300 GC coupled to a Thermo TSQ Quantum Ultra triple quadrupole MS. The GC was equipped with a fused silica capillary column (Phenomenex Zebron ZB-5MS, 30 m, 0.25 µm film thickness, 0.32 mm inner diameter). Helium was used as the carrier gas at a flow rate of 1.5 mL/min. The temperature program was 80 °C (held 5 min) and 6 °C/min to 310 °C (held 30 min). The MS ion source was operated at 240 °C at 70 eV ionization energy.

3.5 Hydrochemistry analysis

Two surface runoff water samples (**Table A.12**) in the field (Otting quary near Ottingen) were collected for hydrochemistry analysis. The pH and temperature of suevite derived surface waters was measured in the field with a portable pH meter (WTW pH330, Xylem, NY, USA) equipped with a N62 pH-electrode (Schott, Germany). Calibration was performed against standard pH buffers 7.010 and 10.010 (HI6007, HI6010, Hanna Instruments, RI, USA). Total alkalinity (TA, given as mg L^{-1} HCO3$^-$) was determined by acid-base titration within 5 h from sampling using a hand-held titration device and 1.6 N H_2SO_4 cartridges as titrant (Hach Lange GmbH, Düsseldorf, Germany). Concentrations of main cations and anions were analysed by ion chromatography with non-suppressed and suppressed conductivity detection, respectively (Metrohm 820 IC, Metrohm, Switzerland). Concentrations of Fe, Mn, and Sr were analysed by inductively coupled plasma optical emission spectrometry (ICP-OES; Optima 3300 DV, Perkin-Elmer).

4 Results

4.1 Lithostratigraphic overview of the drill core

The sedimentary profile of the NR1003 core succession is illustrated in **Figure 2.1**. Lithostratigraphic subdivision of the NR1003 drilling is adopted from that of the Nördlingen 1973 drill core (for a core and sample description, see **Table A.2 and A.3;** for lithofacies and fossils, see **Figure A.1 and A.2**), following the definitions by Jankowski (1981):

The **basal member**, from 257 m (end-of-hole) to 226 m (> 31 m thick), is composed of cyclic fining-upwards coarse to fine grained siliciclastics from conglomerate, sandstone to siltstone, sometimes with laminated carbonate beds or reworked suevite and crystalline basement materials (**Figure A.1A**). Traces of pyrites (<2.5 wt%) are detected by XRD and visible in several cut slabs (**Table A.5**). Except one thin section from a carbonate-rich sample that contains a few fecal pellets, no fossils are found.

The **laminite member** is transected from 226 m to 87.3 m depth (138.7 m in thickness) and comprises clay to silt sized, unbioturbated, siliciclastic dominated laminites and bituminous shales, with intercalated carbonate-rich laminites. Four submembers (smbr.) are identified: i) the clinoptilolite smbr. (215 m to 226 m depth, 11 m thick), based on the detection of clinoptilolite (Jankowski 1981); ii) the analcime smbr. (169.5 to 215 m depth, 45.5 m thick) characterized by the occurrence and high portion of analcime and fade of clinoptilolite in samples, generally low carbonate content (rarely over 50%); iii) the bituminous smbr. (124 to 169.5 m depth, 45.5 m thick), as it is the most organic-rich section; iv) the diatom smbr. (87.3 to 124 m depth, 36.7 m thick) with abundantly preserved diatoms (Schauderna, 1983). Pyrite peaks are absent in XRD patterns throughout the laminite member, despite the rare framboidal pyrites (<1-2 wt%) observed in thin sections. Several fish bones and fragmented scales are found (e.g. 187.4, 194.4 and 216.6 m depth, **Figure A.1F and Figure A.2E**). Besides, fecal pellets are found in several depths within the intercalated thin clay/marl beds (e.g. 102.8 m, 199.2 m, 214.8, 216.6 and 224.9 m depth, **Figure 2.2 and Figure A.2F**). Except an unclear disturbance in sediments possibly related to bioturbation at the top part of diatom smbr, no signs of bioturbation can be identified in laminite member. At 107.8 m, some carbonaceous plant debris is evident.

The **marl member**, according to Jankowski (1981), refers to an unstratified, dolomitic marl-dominated section, and is located between 87.3 m to 38.7 m depth (48.6 m in thickness). In this study, two smbrs are further distinguished: i) a varicolored marl smbr (73.6 m depth to 87.3 m depth) partially inherits characteristics from the laminite member, as it is composed of stratified to laminated dolomite-marlstones and laminated bituminous shales/clays, with common bioturbation and mud cracks (**Figure A.2C**); ii) a dolomite marl smbr (38.7 to 73.6 m depth) that is composed of poorly stratified and unstratified, commonly bioturbated dolostone-marlstones (**Figure A.2D**). In several samples, minor pyrites (2.5 – 7.5 wt%) are detected by XRD. Fecal pellet beds occur in the varicolored marl smbr, at 71.59, 74 to 76 and 79.4 m depth. Sporadic, well-preserved ostracods and shell debris are found in the dolomite marl smbr at 46.31 m depth and 63.05 m depth, respectively.

The **clay member** (38.7 m to 0 m depth, > 38.7 m thickness) is composed of massive dark to medium grey clay and marl, with allochthonous lignite seams (**Figure A.1E**). The clays and marls are frequently bioturbated or show features of subaerial exposure (**Figure A.2A**). On the other hand, pedogenic slickensides are common in the unstratified clays (**Figure A.2B**). Several gastropod-bearing beds are found (**Figure A.1G, A.1H and A.2A**): *Hydrobia* (35.08 m depth), *Gyraulus* (30.38 m depth) and *Planorbarius* (32.06 m depth). Additionally, well-preserved ostracod shells are observed in several darkgrey clay beds. Pyrites are frequently detected by XRD (up to 25 wt%) and visible as framboidal pyrites in thin sections.
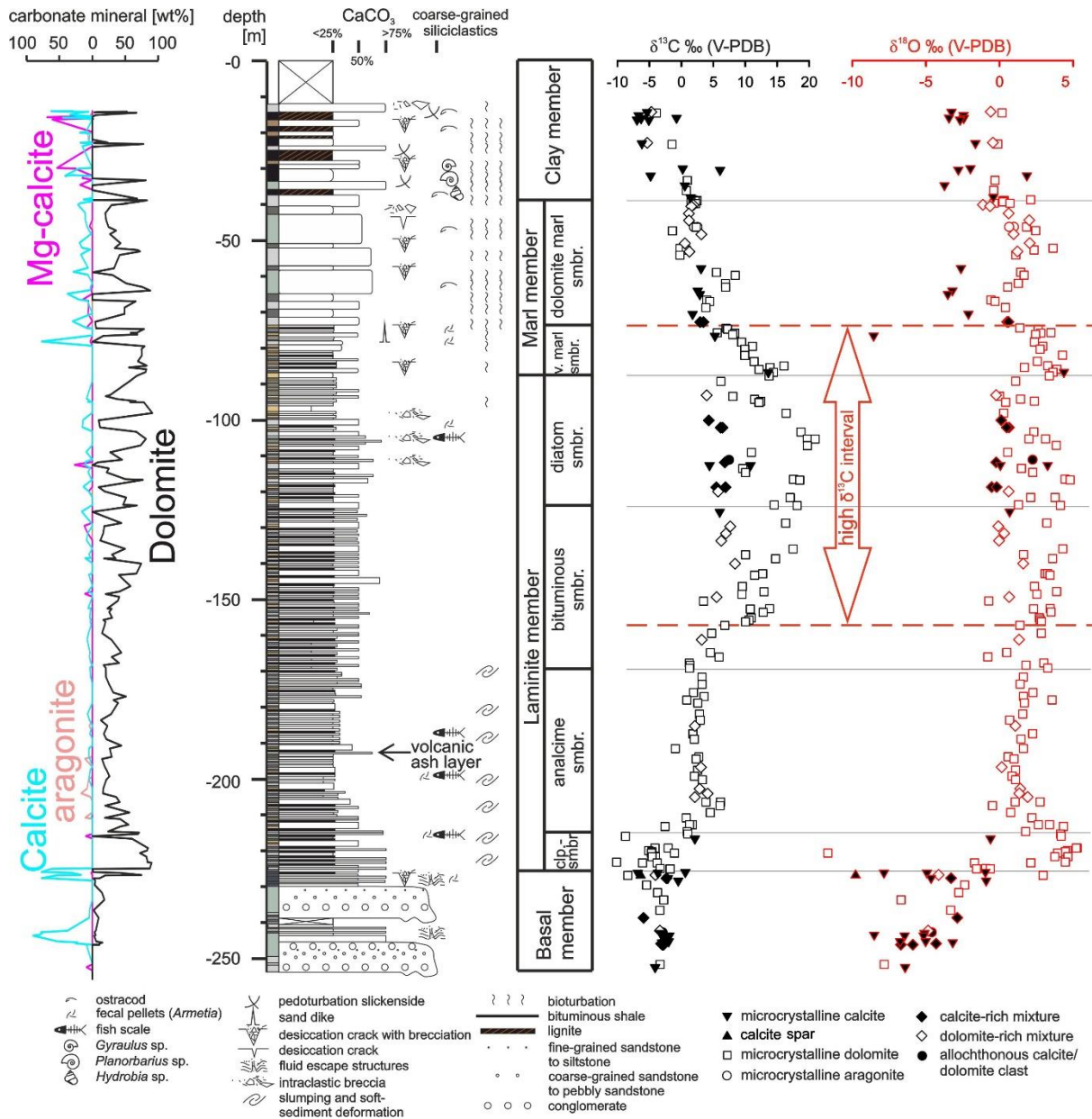
Figure 2.2 Sedimentary profile of the NR1003 drill core and profiles of carbonate contents in different phases (left), stable carbon and oxygen isotopes.
Clay, marl (or dolomite marl) and limestone (or dolostone) are defined by <25% CaCO$_3$, 25 -75% CaCO$_3$, >75% CaCO$_3$ (or equivalent CaMg(CO$_3$)$_2$). Likewise, the microcrystalline calcite, calcite-rich mixture, dolomite-rich mixture and microcrystalline dolomite are defined by >75 mol% calcite, 50 -75 mol % calcite, 50 -75 mol % dolomite and >75 mol % dolomite. See Table A.3 for detailed C$_{carb}$ and Table A.4 and A.5 for XRD data, Table 2.1 for stable isotope data. Note that the dolomite in the left column refers to the calculated dolomite content, on basis of C$_{carb}$ and relative intensity of dolomite peak (*hkl* 104) in XRD patterns (Table A.4). Only general dolomite (i.e. no subdivision between ferroan and Ca-rich dolomite) is shown here (see 3.3).

4.2 Stable isotopes, biomarker and trace elements

4.2.1 Stable isotopes of carbonate beds

Among all samples, δ^{13}C$_{carb}$ (abbreviated as δ^{13}C) shows a wide range of values from -10.13 to +20.93 ‰ V-PDB and δ^{18}O$_{carb}$ (abbreviated as δ^{18}O) from -11.67 to +5.28 ‰ V-PDB

(**Table A.8**). When calcite and calcite-rich samples from basal member to the top of the marl member (i.e., excluding the clay member) are considered, a strong positive covariation is evident between $\delta^{13}C$ and $\delta^{18}O$ (**Figure 2.3B**). Samples from basal member, dolomite-marl smbr and clay member do not show high $\delta^{13}C$ values (**Table A.4**). Low $\delta^{18}O$ (-8.52 to -0.91‰) and $\delta^{13}C$ (-2.92 to -0.48‰) are found in samples from basal member. From dolomite-marl smbr to clay member, low and scattered $\delta^{13}C$ (-5.37 to 6.05‰) and $\delta^{18}O$ (-3.26 to 3.64‰) are observed. In the laminated marlstone section, i.e. from analcime smbr to varicolored marl smbr (226 to 87.3 m core depth), the most prominent $\delta^{13}C$ shift is shown. Based on the occurrences of dolomite with elevated $\delta^{13}C$ values (*ca.* >10‰), the addressed laminate marlstone section is subdivided as:

i) Lower laminite member, i.e., from clinoptilolite to the lower part of bituminous smbr. (226 to ca. 159.4 m depth). $\delta^{13}C$ of dolomite and dolomite dominated samples (almost no calcites) range from -10.13 to +6.12‰, and $\delta^{18}O$ values from -11.67 to +5.28‰, respectively. No systematic $\delta^{13}C$- $\delta^{18}O$ covariation can be observed.

ii) A high $\delta^{13}C$ interval corresponds to the upper part of the bituminous smbr to the varicolored marl smbr (157.2 to 74.4 m depth), where. $\delta^{13}C$ and $\delta^{18}O$ of calcite and calcite dominated samples range from +4.28 to +13.62‰, and -8.55 to +4.38‰, respectively. The calcites and calcite dominated samples show a strong positive covariance (r = 0.93; n = 10 and NR1003-128 excluded as an outlier, p = 0.00). On the other hand, $\delta^{13}C$ and $\delta^{18}O$ of dolomite and dolomite dominated samples range from +3.47 to +20.93‰, and -0.73 to +4.80‰, respectively.

When calcite and calcite dominated mixture samples from the whole laminite member and varicolored smbr are considered, a clear $\delta^{13}C$-$\delta^{18}O$ covariation trend still exists (r = 0.89, n=17, p =0.00, NR1003-128 excluded as an outlier, **Figure 2.3 A**). The $\delta^{13}C$ and $\delta^{18}O$ of the samples from lower laminite member mainly rest below this covariation trend line, whereas those from the high $\delta^{13}C$ interval are generally above the covariation line (**Figure 2.3 A**).
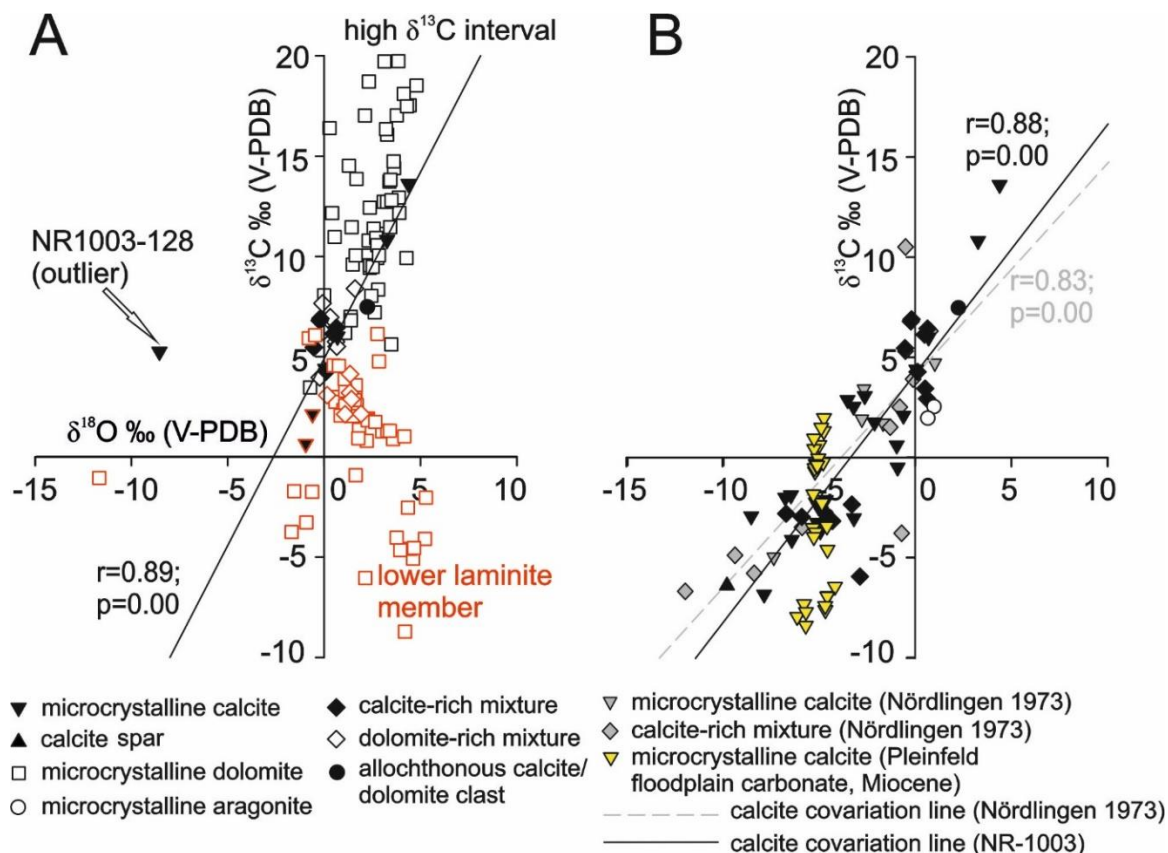
Figure 2.3 Stable carbon-oxygen covariation plots of the samples from the laminated marlstone section (226 to 87.3 m core depth).
A: samples from the high $\delta^{13}C$ interval (upper laminite member and varicolored smbr,

symbols with black outlines) and lower laminite member (red-outlined symbols); note that most of the samples are dolomites. The covariation trend line is calculated based on calcite and calcite-rich mixture samples from clinoptilolite to varicolored-marl smbr. B: Calcite and calcite-rich samples from NR1003 (black symbols) and Nördlingen 1973 (grey-filled symbols, Rothe and Hoefs, 1977); Miocene (pre-impact) floodplain carbonate (yellow-filled symbols) at Pleinfeld locality, ca. 30 km away from the Ries crater (Zeng et al., 2021).

4.2.2 Biomarkers of carbonate beds

Selected lipid biomarkers, indicative for biological sources and as indicators for the lake environment, were analysed and quantified with respect to total organic carbon (TOC) of the carbonate-free rock fraction (**Figure 2.4; Table 2.2 and 2.3**, see **Figure A.3** for chemical structures).

Pristane (Pr) and phytane (Ph), derived from chlorophyll a, were observed in most samples but are below detection limit from basal member to clinoptilolite smbr. Pr/Ph ratios are low (0.04 to 0.07) from analcime to diatom smbr. From the top part of the high $\delta^{13}C$ interval (varicolored marl smbr) to clay member, Pr/Ph ratios show a major increase (0.11 to 0.82). Among the fatty acids, the sum of the terminally methylated $C_{15:0}$ iso- and $C_{15:0}$ anteiso-tetradecanoic acids (i/ai-$C_{15:0}$, abundant compounds in sulfate-reducing bacteria) shows an increase from the analcime smbr and reaches a maximum (43.8 µg/g TOC) immediately below the base of the high $\delta^{13}C$ interval. From the base to top of the high $\delta^{13}C$ interval, i/ai-$C_{15:0}$ shows a unidirectional decreasing trend (23.7 to 0.7 µg/g TOC). Samples in dolomite-marl smbr and clay member exhibit low i/ai-$C_{15:0}$ concentrations (0.4 to 1.2 µg/g TOC).

The concentrations of C_{20}-C_{31} *n*-alkyl and isoprenoid thiophenes, diagenetically formed under high-sulfide conditions, show a remarkable spike at the base of analcime smbr (45.6 µg/g TOC). In other lithostratigraphic units, these compounds remain low and scattered in abundance (0 to 6.3 µg/g TOC). A remarkable exception is one sample (NR1003-15) from the upper part of clay member, showing a high thiophene concentration of 165.4 µg/g TOC, however, with a potentially major analytical error due to very lean TOC (0.1 to 0.2 wt%). The same effect applies to other biomarkers in this sample but does not change the general trend and interpretations.

Archaeol (ArOH), a biomarker for archaea including methanogens, is not detected below the high $\delta^{13}C$ interval, but its abundance quickly increases and reaches a peak concentration (149.6 µg/g TOC) in the diatom smbr. Towards the top of the high $\delta^{13}C$ interval (varicolored marl smbr), and above, ArOH decreases to <20 µg/g TOC. Again, however, very high concentrations are observed for sample (NR1003-15) from the upper part of clay member (137.4 µg/g TOC).

3-methyl- and 2-methyl C_{32} ββ-hopanoic acids (3-me-C_{32} ββ-HA and 2-me-C_{32} ββ-HA), derived from distinctive bacterial lipids, do not occur below varicolored marl smbr. Then, 3-me-C_{32} ββ-HA ranges from 0.8 to 2.4±1.1 µg/g TOC without showing any clear trend. 2-me-C_{32} ββ-HA, on the other hand, reveals a steady increase from dolomite-marl smbr to clay member (1.6 to 20.3 µg/g TOC).
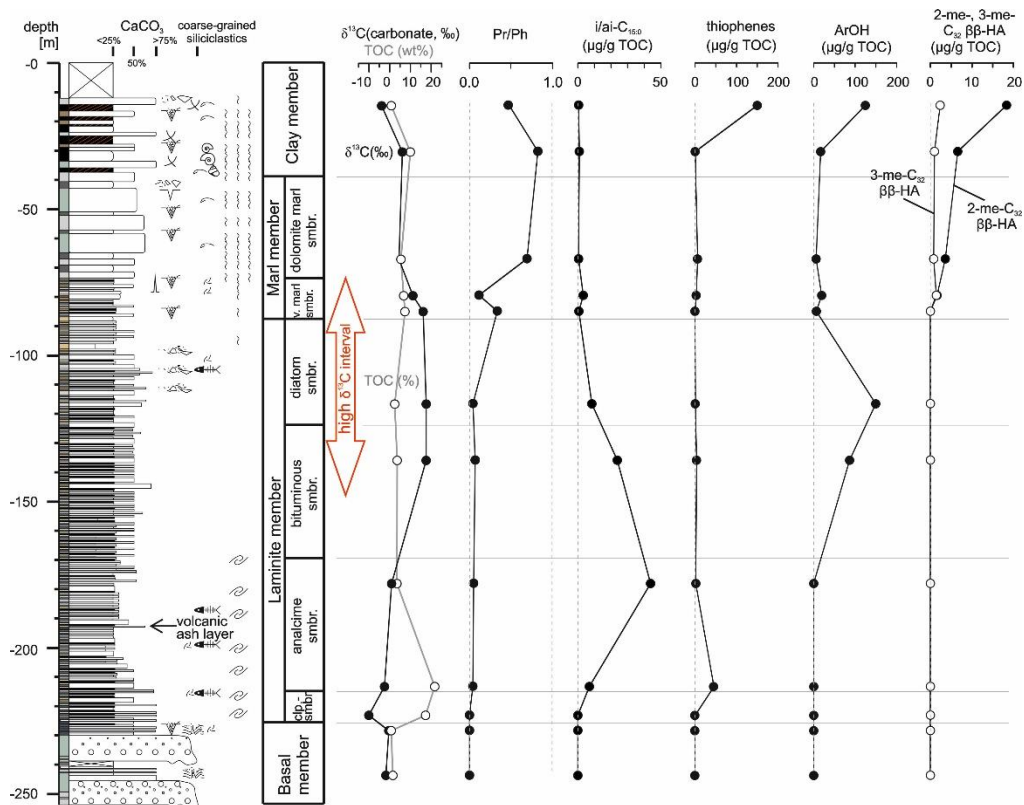
Figure 2.4 Columnar section showing total organic carbon (TOC), δ¹³C (carbonate), pristane/phytane ratios (Pr/Ph), and abundances of selected biomarkers in µg/g TOC (carbonate-free fraction).
For detailed results and abbreviations please see also 4.2.2 and Table 2.3, see Figure A.3 for chemical structures.

Table 2.1 Summaries of stable carbon and oxygen (corrected) isotope results of the carbonate beds from NR1003 drill core. The microcrystalline calcite, calcite-rich mixture, dolomite-rich mixture and microcrystalline dolomite are defined by >75 mol% calcite, 50 -75 mol % calcite, 50 -75 mol % dolomite and >75 mol % dolomite, respectively. Standard deviations of the stable isotope measurements, if not otherwise noted, are 0.05 ‰ for $\delta^{13}C$ and 0.07 ‰ for $\delta^{18}O$. For samples marked with star symbols (*), the standard deviations are 0.08‰ for $\delta^{13}C$ and 0.11‰ for $\delta^{18}O$. See Table A.6 for the calculation of $\delta^{18}O$ correction applied to dolomites.

Sample	Depth [m]	Lithostratigraphic unit	Lithology	Material mineralogy (from XRD)	$\delta^{13}C$ [‰ V-PDB]	$\delta^{18}O$ (corrected) [‰ V-PDB]
NR1003-13	14.2	clay member	yellow grey (light greenish) micrite	dolomite-rich mixture	-4.70	-0.60
NR1003-1	14.3	clay member	white grey micrite	microcrystalline calcite	-5.37	-3.26
NR1003-15	14.5	clay member	yellowish grey marly micrite	microcrystalline dolomite	-3.94	0.17
NR1003-18	15.2	clay member	light white-grey micrite	microcrystalline calcite	-6.68	-2.45
NR1003-20	15.9	clay member	white grey micrite	microcrystalline calcite	-0.75	-3.43
NR1003-21	16	clay member	medium grey micrite	microcrystalline calcite	-6.29	-2.43
NR1003-22	16.4	clay member	medium grey micrite	microcrystalline calcite	-6.95	-2.68
NR1003-23	16.5	clay member	light white grey micrite	microcrystalline calcite	-5.09	-2.68
NR1003-33	22.8	clay member	light grey micrite	dolomite-rich mixture	-5.34	-0.45
NR1003-35	23	clay member	medium grey micrite	microcrystalline calcite	-6.17	-1.64
NR1003-36	23.2	clay member	white grey micrite	microcrystalline dolomite	-1.45	-0.12
NR1003-45	30	clay member	medium grey marly micrite	microcrystalline calcite	0.21	-1.98
NR1003-47	30.4	clay member	medium grey marly micrite	microcrystalline calcite	6.05	-2.80
NR1003-56	32	clay member	medium grey marly micrite	microcrystalline calcite	-4.82	1.86
NR1003-59	33.3	clay member	light grey micrite	microcrystalline dolomite	0.94	-0.30
NR1003-62	34.7	clay member	medium grey marly micrite	microcrystalline calcite	0.55	-3.74
NR1003-69	36.1	clay member	yellowish-light grey marly micrite	microcrystalline dolomite	0.78	-0.39
NR1003-74	38	clay member	grey micrite	microcrystalline calcite	1.44	-0.42
NR1003-101	38.7	clay member	white grey marly micrite, homogeneous	microcrystalline dolomite	1.79	2.12
NR1003-75	38.9	dolomite marl smbr.	white grey micrite	microcrystalline dolomite	2.46	0.32
NR1003-76	39	dolomite marl smbr.	medium grey micrite	microcrystalline dolomite	2.18	0.22
NR1003-78	39.3	dolomite marl smbr.	light medium grey micrite	microcrystalline dolomite	1.52	0.25
NR1003-102	39.7	dolomite marl smbr.	white grey marly micrite, homogeneous	microcrystalline dolomite	1.83	0.71
NR1003-79	39.7	dolomite marl smbr.	white grey marly micrite	microcrystalline dolomite	2.25	-0.37
NR1003-80	40.1	dolomite marl smbr.	white grey marly micrite	dolomite-rich mixture	1.88	-1.13
NR1003-81	40.5	dolomite marl smbr.	white grey marly micrite	dolomite-rich mixture	1.55	-0.64
NR1003-103	42.5	dolomite marl smbr.	white grey marly micrite, homogeneous	dolomite-rich mixture	1.18	0.62
NR1003-104	44.4	dolomite marl smbr.	white grey marly micrite, homogeneous	dolomite-rich mixture	1.19	2.02
NR1003-105-1*	46.3	dolomite marl smbr.	white aragonitic ostracod shell	microcrystalline aragonite	2.54	0.98
NR1003-105-2	46.3	dolomite marl smbr.	black ostracod shell	microcrystalline aragonite	1.97	0.66

Sample	Depth	Member	Description	Mineralogy	δ13C	δ18O
NR1003-105-3	46.3	dolomite marl smbr.	white grey marly micrite, homogeneous	microcrystalline dolomite	2.33	1.84
NR1003-106	47.3	dolomite marl smbr.	white grey marly micrite, homogeneous	microcrystalline dolomite	-1.41	2.46
NR1003-107	48.3	dolomite marl smbr.	white grey marly micrite, homogeneous	dolomite-rich mixture	3.13	0.96
NR1003-108	50.8	dolomite marl smbr.	white grey marly micrite, homogeneous	dolomite-rich mixture	0.55	2.05
NR1003-2	52.2	dolomite marl smbr.	white grey marly micrite, homogeneous	microcrystalline dolomite	-0.20	3.64
NR1003-109	52.7	dolomite marl smbr.	white grey marly micrite, homogeneous	microcrystalline dolomite	0.78	2.35
NR1003-110	53.1	dolomite marl smbr.	white grey marly micrite, homogeneous	dolomite-rich mixture	1.27	1.22
NR1003-111	54.1	dolomite marl smbr.	white grey marly micrite, homogeneous	microcrystalline dolomite	-0.22	1.11
NR1003-112	57.8	dolomite marl smbr.	white grey marly micrite, homogeneous	microcrystalline calcite	3.08	-2.62
NR1003-113	58.9	dolomite marl smbr.	white grey marly micrite, homogeneous	microcrystalline dolomite	5.49	1.44
NR1003-114	59.7	dolomite marl smbr.	white grey marly micrite, homogeneous	microcrystalline dolomite	8.43	1.67
NR1003-115	62	dolomite marl smbr.	white grey marly micrite, homogeneous	microcrystalline dolomite	6.90	1.28
NR1003-116	63	dolomite marl smbr.	white grey marly micrite, homogeneous	microcrystalline dolomite	6.94	0.55
NR1003-117	64	dolomite marl smbr.	white grey marly micrite, homogeneous	microcrystalline calcite	2.55	-3.20
NR1003-118	65	dolomite marl smbr.	white grey marly micrite, homogeneous	microcrystalline calcite	2.89	-3.51
NR1003-119	66.6	dolomite marl smbr.	white grey marly micrite, homogeneous	microcrystalline dolomite	3.99	-0.58
NR1003-120	67	dolomite marl smbr.	white grey marly micrite, homogeneous	microcrystalline dolomite	4.44	-0.30
NR1003-121	68.7	dolomite marl smbr.	medium grey marly micrite, homogeneous	microcrystalline dolomite	3.84	0.40
NR1003-122	70.5	dolomite marl smbr.	medium grey marly micrite, homogeneous	microcrystalline calcite	1.76	-2.11
NR1003-123-1	72.7	dolomite marl smbr.	white grey marly micrite in yellowish beds	calcite-rich mixture	3.45	0.52
NR1003-123-2	72.7	dolomite marl smbr.	pinkish micrite, from layer below white grey layer	calcite-rich mixture	2.95	0.61
NR1003-3	74.4	varicolored smbr.	yellow grey marly micrite	microcrystalline dolomite	6.99	1.38
NR1003-124	74.7	varicolored smbr.	matrix micrite from white-yellowish fecal pellet bed	microcrystalline dolomite	7.22	2.63
NR1003-125	75.7	varicolored smbr.	white grey marly micrite, homogeneous	microcrystalline dolomite	5.61	3.49
NR1003-126	75.8	varicolored smbr.	white grey marly micrite, homogeneous	microcrystalline dolomite	8.35	2.81
NR1003-127	76.2	varicolored smbr.	white grey marly micrite, homogeneous	microcrystalline dolomite	8.04	2.45
NR1003-128	76.6	varicolored smbr.	white grey marly micrite, homogeneous	microcrystalline calcite	5.25	-8.55
NR1003-129	78.3	varicolored smbr.	white grey marly micrite, homogeneous	microcrystalline dolomite	9.43	2.37
NR1003-130	79.5	varicolored smbr.	micrite in white grey fecal pellet bed	microcrystalline dolomite	11.13	2.94
NR1003-131	80.3	varicolored smbr.	white grey marly micrite, homogeneous	microcrystalline dolomite	9.92	2.76
NR1003-132	82	varicolored smbr.	white grey marly micrite, homogeneous	microcrystalline dolomite	9.92	4.28
NR1003-133	83.7	varicolored smbr.	white grey marly micrite, homogeneous	microcrystalline dolomite	11.39	2.57
NR1003-134	84.9	varicolored smbr.	white grey marly micrite, homogeneous	microcrystalline dolomite	16.07	3.28
NR1003-4	85.4	varicolored smbr.	white grey marly micrite, homogeneous	microcrystalline dolomite	13.87	1.69
NR1003-135	85.9	varicolored smbr.	white grey marly micrite, homogeneous	microcrystalline dolomite	12.17	3.90
NR1003-136	86.7	varicolored smbr.	white grey marly micrite, homogeneous	microcrystalline dolomite	14.41	3.63
NR1003-136-2	86.7	varicoloured smbr.	ostracod shell debris	microcrystalline calcite	13.62	4.38

NR1003-137	87.7	diatom smbr.	white grey marly micrite, homogeneous	microcrystalline dolomite	13.74	3.39
NR1003-138	89.2	diatom smbr.	white grey marly micrite, homogeneous	microcrystalline dolomite	6.19	1.10
NR1003-139	93.1	diatom smbr.	white grey marly micrite, homogeneous	dolomite-rich mixture	3.97	-0.23
NR1003-140	93.4	diatom smbr.	white grey marly micrite, homogeneous	microcrystalline dolomite	8.06	0.00
NR1003-141	94.2	diatom smbr.	white grey marly micrite, homogeneous	microcrystalline dolomite	11.46	1.43
NR1003-142	94.8	diatom smbr.	white grey marly micrite, homogeneous	microcrystalline dolomite	12.43	2.37
NR1003-143	95.1	diatom smbr.	white grey marly micrite, homogeneous	microcrystalline dolomite	12.16	0.42
NR1003-5	98.1	diatom smbr.	light grey micrite	microcrystalline dolomite	16.40	0.28
NR1003-144	100.1	diatom smbr.	medium grey marly micrite, well laminated	calcite-rich mixture	4.28	0.12
NR1003-145-1*	102.1	diatom smbr.	micrite from dark grey fecal pellet bed	calcite-rich mixture	6.44	0.64
NR1003-145-2	102.1	diatom smbr.	micrite from white grey layer	calcite-rich mixture	6.14	0.49
NR1003-146	103.3	diatom smbr.	white grey marly micrite, homogeneous	microcrystalline dolomite	18.72	2.33
NR1003-147	105.3	diatom smbr.	white grey marly micrite, homogeneous	microcrystalline dolomite	19.72	3.13
NR1003-6	105.3	diatom smbr.	yellow grey, light yellowish micrite	microcrystalline dolomite	20.93	2.00
NR1003-148	107.1	diatom smbr.	white grey marly micrite, homogeneous	microcrystalline dolomite	19.74	3.86
NR1003-149	109	diatom smbr.	white grey marly micrite, homogeneous	microcrystalline dolomite	10.97	0.55
NR1003-150	111.1	diatom smbr.	carbonate pebble micrite	allochtounous calcite/dolomite clast	7.47	2.25
NR1003-151	111.8	diatom smbr.	medium grey marly micrite, homogeneous	calcite-rich mixture	6.80	-0.23
NR1003-152-1*	112.6	diatom smbr.	medium grey layer, micrite, homogeneous	microcrystalline calcite	4.40	0.06
NR1003-152-2	112.6	diatom smbr.	pinkish white grey layer, micrite, homogeneous	microcrystalline calcite	10.82	3.27
NR1003-153	113.5	diatom smbr.	medium grey marly micrite, homogeneous	microcrystalline dolomite	9.60	1.49
NR1003-154	114.6	diatom smbr.	medium grey marly micrite, homogeneous	microcrystalline dolomite	10.05	2.26
NR1003-155	116.5	diatom smbr.	white grey marly micrite, homogeneous	microcrystalline dolomite	17.54	4.45
NR1003-156	116.7	diatom smbr.	white grey marly micrite, homogeneous	microcrystalline dolomite	18.52	4.80
NR1003-157-1	118.7	diatom smbr.	medium grey marly micrite, homogeneous	calcite-rich mixture	5.47	-0.53
NR1003-157-2	118.7	diatom smbr.	pinkish white grey marly micrite	calcite-rich mixture	6.91	-0.19
NR1003-158	119.9	diatom smbr.	white grey marly micrite, homogeneous	dolomite-rich mixture	5.75	0.62
NR1003-159	121.6	diatom smbr.	white grey marly micrite, homogeneous	microcrystalline dolomite	17.04	3.78
NR1003-8	121.6	diatom smbr.	white grey, light yellowish marly micrite	microcrystalline dolomite	17.03	2.12
NR1003-9	123.6	diatom smbr.	white grey, light yellowish marly micrite	microcrystalline dolomite	14.52	1.29
NR1003-160	123.8	diatom smbr.	white grey marly micrite, homogeneous	microcrystalline dolomite	18.11	4.14
NR1003-161	125.6	bituminous smbr.	medium grey marly micrite, homogeneous	microcrystalline calcite	6.01	0.69
NR1003-162	128.7	bituminous smbr.	white grey marly micrite, homogeneous	microcrystalline dolomite	16.34	3.21
NR1003-163	129.6	bituminous smbr.	medium grey marly micrite, homogeneous	dolomite-rich mixture	7.66	-0.08
NR1003-164	131.6	bituminous smbr.	white grey marly micrite, homogeneous	dolomite-rich mixture	6.97	0.32
NR1003-165	133.6	bituminous smbr.	medium grey marly micrite, homogeneous	dolomite-rich mixture	6.25	-0.04
NR1003-166	135.9	bituminous smbr.	white grey marly micrite, homogeneous	microcrystalline dolomite	17.49	4.30

NR1003-167	137.5	bituminous smbr.	white grey marly micrite, homogeneous	microcrystalline dolomite	10.05	1.64
NR1003-168	138.6	bituminous smbr.	white grey marly micrite, homogeneous	microcrystalline dolomite	14.74	3.61
NR1003-169	140	bituminous smbr.	medium grey marly micrite, homogeneous	dolomite-rich mixture	8.40	1.61
NR1003-170-1	142.8	bituminous smbr.	white grey marly micrite, homogeneous	microcrystalline dolomite	12.73	3.10
NR1003-170-2	142.8	bituminous smbr.	white grey marly micrite, homogeneous	microcrystalline dolomite	12.73	3.27
NR1003-171	143.2	bituminous smbr.	white grey marly micrite, homogeneous	microcrystalline dolomite	11.46	3.43
NR1003-172	146.3	bituminous smbr.	white grey marly micrite, homogeneous	microcrystalline dolomite	9.56	2.38
NR1003-173	147.8	bituminous smbr.	white grey marly micrite, homogeneous	microcrystalline dolomite	12.94	3.88
NR1003-174	148.5	bituminous smbr.	white grey marly micrite, homogeneous	microcrystalline dolomite	9.49	2.53
NR1003-175	149.3	bituminous smbr.	medium grey marly micrite, homogeneous	dolomite-rich mixture	5.51	0.66
NR1003-176	150.4	bituminous smbr.	medium grey marly micrite, homogeneous	microcrystalline dolomite	3.47	-0.73
NR1003-177	152.5	bituminous smbr.	white grey marly micrite, homogeneous	microcrystalline dolomite	13.82	3.45
NR1003-178	152.6	bituminous smbr.	medium grey marly micrite, homogeneous	microcrystalline dolomite	10.79	2.31
NR1003-179	153.5	bituminous smbr.	yellowish white grey marly micrite	microcrystalline dolomite	12.80	3.50
NR1003-180	155.1	bituminous smbr.	medium grey marly micrite	microcrystalline dolomite	10.93	2.71
NR1003-181	155.7	bituminous smbr.	white grey marly micrite, homogeneous	microcrystalline dolomite	10.57	2.76
NR1003-182	156.2	bituminous smbr.	yellowish grey marly micrite	microcrystalline dolomite	10.05	2.85
NR1003-183	157.2	bituminous smbr.	yellowish white grey marly micrite	microcrystalline dolomite	6.81	1.39
NR1003-184	159.4	bituminous smbr.	yellowish white grey marly micrite	microcrystalline dolomite	4.75	2.84
NR1003-185	161.2	bituminous smbr.	white grey marly micrite, homogeneous	dolomite-rich mixture	3.18	1.33
NR1003-186	164.8	bituminous smbr.	white grey marly micrite, homogeneous	microcrystalline dolomite	4.55	0.49
NR1003-187	166	bituminous smbr.	white grey marly micrite, homogeneous	microcrystalline dolomite	5.90	-0.80
NR1003-188	167.7	bituminous smbr.	white grey marly micrite, homogeneous	microcrystalline dolomite	1.24	3.01
NR1003-189	168.3	bituminous smbr.	white grey marly micrite, homogeneous	microcrystalline dolomite	1.34	1.80
NR1003-190	169.1	bituminous smbr.	white grey argillaceous marl, homogeneous	microcrystalline dolomite	1.28	3.28
NR1003-191	171.6	analcime smbr.	white grey laminae, marly micrite, homogeneous	microcrystalline dolomite	3.22	1.62
NR1003-192	173.6	analcime smbr.	white grey laminae, marly micrite, homogeneous	microcrystalline dolomite	3.24	1.40
NR1003-193	175.9	analcime smbr.	medium grey marly micrite	microcrystalline dolomite	1.89	2.27
NR1003-194	177	analcime smbr.	white grey marly micrite	microcrystalline dolomite	3.56	1.63
NR1003-195	178	analcime smbr.	white grey marly micrite	microcrystalline dolomite	0.86	3.57
NR1003-196	178.8	analcime smbr.	yellowish white grey marly micrite	microcrystalline dolomite	2.58	1.69
NR1003-197	181.9	analcime smbr.	white grey lamina, micrite, homogeneous	microcrystalline dolomite	2.82	1.58
NR1003-198	183.6	analcime smbr.	white grey micrite, homogeneous	microcrystalline dolomite	2.96	0.69
NR1003-199	185.2	analcime smbr.	white grey micrite, homogeneous	dolomite-rich mixture	2.11	1.08
NR1003-200*	187.4	analcime smbr.	pinkish white grey marly micrite, homogeneous	microcrystalline dolomite	1.80	2.25
NR1003-201	188.9	analcime smbr.	medium grey marly micrite	microcrystalline dolomite	2.02	1.46

NR1003-203	191.5	analcime smbr.	white grey marly micrite	microcrystalline dolomite	-0.94	1.63
NR1003-204	193.8	analcime smbr.	medium grey marly micrite	microcrystalline dolomite	2.73	0.58
NR1003-205	194.4	analcime smbr.	white grey marly micrite	microcrystalline dolomite	2.31	0.99
NR1003-206	196.7	analcime smbr.	medium grey marly micrite	dolomite-rich mixture	3.06	0.15
NR1003-207	197.5	analcime smbr.	medium grey marly micrite	microcrystalline dolomite	2.54	1.09
NR1003-208	199.2	analcime smbr.	white grey marly micrite	microcrystalline dolomite	2.04	0.85
NR1003-209	200.2	analcime smbr.	white grey marly micrite	microcrystalline dolomite	3.28	1.09
NR1003-210	202.7	analcime smbr.	white grey marly micrite	dolomite-rich mixture	2.86	1.41
NR1003-211	204	analcime smbr.	medium grey marly micrite	dolomite-rich mixture	4.11	1.34
NR1003-212	205	analcime smbr.	medium grey marly micrite	dolomite-rich mixture	2.12	1.91
NR1003-213-1	206.4	analcime smbr.	white grey marly micrite, homogeneous	microcrystalline dolomite	6.12	2.76
NR1003-213-2	206.4	analcime smbr.	medium grey marly micrite, homogeneous	microcrystalline dolomite	3.86	1.06
NR1003-214	207.4	analcime smbr.	white grey marly micrite, homogeneous	microcrystalline dolomite	6.05	-0.48
NR1003-215	209.3	analcime smbr.	medium grey marly micrite	microcrystalline dolomite	4.52	0.76
NR1003-216	210.8	analcime smbr.	yellowish grey marly micrite	microcrystalline dolomite	0.77	2.20
NR1003-218-1	212.7	analcime smbr.	white grey marly micrite, homogeneous	microcrystalline dolomite	1.72	2.64
NR1003-218-2	212.7	analcime smbr.	pinkish white grey marly micrite	microcrystalline dolomite	1.28	3.40
NR1003-219	213.2	analcime smbr.	yellowish grey marly micrite	microcrystalline dolomite	-2.56	4.34
NR1003-220	214.6	analcime smbr.	medium grey marly micrite, homogeneous	microcrystalline dolomite	0.90	1.77
NR1003-222	215.3	clinoptilolite smbr.	white grey marly micrite, homogeneous	microcrystalline dolomite	0.99	4.15
NR1003-223	215.9	clinoptilolite smbr.	weathered material, white grey and medium grey micrite	microcrystalline dolomite	-8.75	4.19
NR1003-224	216.6	clinoptilolite smbr.	white grey marly micrite	microcrystalline calcite	2.11	-0.61
NR1003-225-1	219.2	clinoptilolite smbr.	matrix from yellowish white grey argillaceous marl	microcrystalline dolomite	-2.07	5.28
NR1003-225-2	219.2	clinoptilolite smbr.	matrix from yellowish grey argillaceous marl	microcrystalline dolomite	-4.12	5.22
NR1003-226*	219.9	clinoptilolite smbr.	white grey marly micrite	microcrystalline dolomite	-5.11	4.61
NR1003-227	220.2	clinoptilolite smbr.	white grey marly micrite	microcrystalline dolomite	-4.62	4.47
NR1003-228-1	220.6	clinoptilolite smbr.	white grey marly micrite	microcrystalline dolomite	-4.69	3.95
NR1003-228-2	220.6	clinoptilolite smbr.	dark grey marly micrite	microcrystalline dolomite	-1.08	-11.67
NR1003-229-1	221.6	clinoptilolite smbr.	dark grey lamina, micrite	microcrystalline dolomite	-4.06	3.76
NR1003-229-2	221.6	clinoptilolite smbr.	white grey lamina, micrite	microcrystalline dolomite	-4.58	4.65
NR1003-230	223.1	clinoptilolite smbr.	dark grey lamina, micrite	microcrystalline dolomite	-10.13	4.47
NR1003-231-1	223.3	clinoptilolite smbr.	dark grey lamina, micrite, mix?	microcrystalline dolomite	-3.78	-1.70
NR1003-231-2	223.3	clinoptilolite smbr.	white grey lamina, micrite, homogeneous	microcrystalline dolomite	-6.08	2.13
NR1003-232	224.9	clinoptilolite smbr.	medium grey argillaceous micrite	microcrystalline dolomite	-3.30	-0.93
NR1003-233-1	225	clinoptilolite smbr.	white grey lamina, micrite, homogeneous	microcrystalline dolomite	-1.78	-0.63
NR1003-233-2	225	clinoptilolite smbr.	pinkish white grey marly micrite	microcrystalline dolomite	-1.74	-1.56

NR1003-234	225.9	clinoptilolite smbr.	white grey micrite	microcrystalline calcite	0.62	-0.96
NR1003-235-1	226.1	basal member	white grey micrite	microcrystalline calcite	-3.67	-4.93
NR1003-235-2	226.1	basal member	"black irregular pebble": reworked pedogenic carbonate	microcrystalline calcite	-6.82	-7.85
NR1003-236	226.7	basal member	white grey micrite	dolomite-rich mixture	-4.06	-4.14
NR1003-237-1	226.8	basal member	calcite spar	calcite spar	-6.39	-9.78
NR1003-237-2	226.8	basal member	white grey micrite, homogeneous	microcrystalline dolomite	-8.38	2.96
NR1003-238B	227.6	basal member	dark grey lamina, micrite	microcrystalline calcite	-2.11	-4.65
NR1003-238W	227.6	basal member	white grey lamina, micrite, homogeneous	calcite-rich mixture	-2.34	-3.29
NR1003-239*	228.3	basal member	white grey marly micrite	microcrystalline calcite	-0.48	-0.91
NR1003-240*	229.5	basal member	calcareous silt matrix	microcrystalline dolomite	-5.45	-2.37
NR1003-241	231.6	basal member	calcareous silt matrix	microcrystalline dolomite	-3.74	-2.77
NR1003-242*	233.6	basal member	calcareous sand matrix	microcrystalline dolomite	-2.77	-6.69
NR1003-243	236.5	basal member	calcareous silt matrix	microcrystalline dolomite	-3.36	-3.31
NR1003-244	238.6	basal member	calcareous sand matrix	calcite-rich mixture	-5.93	-2.87
NR1003-245*	242.2	basal member	calcareous sand	dolomite-rich mixture	-3.36	-4.85
NR1003-246	242.7	basal member	white micrite lens, homogeneous	allochtounous calcite/dolomite clast	-2.91	-4.60
NR1003-247*	242.9	basal member	white grey micrite, homogeneous	microcrystalline calcite	-3.25	-5.10
NR1003-10	243.4	basal member	white grey to light grey micrite	microcrystalline calcite	-2.92	-8.52
NR1003-248-1	243.6	basal member	white grey lamina, micrite, homogeneous	microcrystalline calcite	-1.88	-6.45
NR1003-248-2	243.6	basal member	yellowish white grey lamina, micrite, homogeneous	microcrystalline calcite	-2.23	-5.16
NR1003-249-1	245.2	basal member	medium grey lamina, argillaceous marl	microcrystalline calcite	-1.99	-6.75
NR1003-249-2	245.2	basal member	medium grey lamina, micrite	microcrystalline calcite	-2.46	-5.02
NR1003-250*	245.5	basal member	white grey marly micrite, homogeneous	microcrystalline calcite	-3.02	-3.18
NR1003-251	245.8	basal member	white grey marly micrite, homogeneous	calcite-rich mixture	-3.16	-4.31
NR1003-252-1	246.1	basal member	white grey marly micrite, homogeneous	calcite-rich mixture	-2.96	-5.89
NR1003-252-2	246.1	basal member	matrix from argillaceous marl with black material	calcite-rich mixture	-2.80	-6.70
NR1003-254*	251.6	basal member	calcareous sand	microcrystalline dolomite	-3.33	-7.84
NR1003-255	252.4	basal member	calcareous sand	microcrystalline calcite	-4.10	-6.41

Table 2.2 Selected biomarkers, their biological sources and environmental indications

trivial name of the compound (abbreviation)	chemical name	putative source/environmental indication	diagnostic fragment m/z	reference
Pristane (Pr)	2,6,10,14-Tetramethylpentadecane		57, 71	Rontani and Volkman, 2003

Phytane (Ph)	2,6,10,14-Tetramethylhexadecane	chlorophyll a side chain and indicators for the redox environment	57, 71	Rontani and Volkman, 2003
Terminally $C_{15:0}$ iso- and anteiso- tetradecanoic acid (i/ai-$C_{15:0}$)	13- and 12-Methyltetradecanoic acid	sulfate reducing bacteria	74, 57	Taylor and Parkes, 1983; Parkes and Taylor, 1983
C_{20}-C_{31} n-alkyl and isoprenoid thiophenes (thiophenes)	-	early diagenetic products in sulfidic condition	97+14n	Sinninghe Damsté et al., 1986
Archaeol (ArOH)	1-Propanol, 2,3-bis[(3,7,11,15-tetramethylhexadecyl)oxy]-di-O-phytanylglycerol	archaea, including methanogenic archaea	130, 131, 278, 426	Koga et al., 1998
3-methyl-hopanoic acids (3-me-C_{32} ββ-HA)	3-methyl-C_{32} 17β(H),21β(H)-hopanoic acid	methanotrophic bacteria	205, 263, 383	Birgel and Peckmann, 2008
2-methyl-hopanoic acid (2-me-C_{32} ββ-HA)	2-methyl-C_{32} 17β(H),21β(H)-hopanoic acid	various bacteria including cyanobacteria	205, 263, 383	Welander et al., 2010

Table 2.3 Concentrations of selected biomarkers [µg/g TOC].
Note that 'TOC' refers to C_{org} (wt%) relative to silicate fractions (i.e. after decarbonation).

sample	XRD mineralogy	core depth	lithostratigraphic unit	$\delta^{13}C_{carb}$	C_{org}	TOC	Pr	Ph	Pr/Ph	i-$C_{15:0}$	ai-$C_{15:0}$	i/ai-$C_{15:0}$	C_{20-31} thiophene	2-me-$C_{32}\beta\beta$-HA	3-me-$C_{32}\beta\beta$-HA	ArOH
		[m bsf]		[‰ V-PDB]	[wt%]	[wt%]	[µg/g TOC]	[µg/g TOC]	[µg/g TOC]	[µg/g TOC]	[µg/g TOC]	[µg/g TOC]	[µg/g TOC]	[µg/g TOC]	[µg/g TOC]	[µg/g TOC]
NR1003-15	microcrystalline dolomite	14.5	clay member	-3.9	0.1	0.7	0.26	0.54	0.48	0.6	0.6	1.2	165.4	20.3	3.5	137.4
NR1003-47	microcrystalline calcite	30.2	clay member	6.0	4.7	9.9	0.002	0.002	0.82	0.4	0.4	0.9	0.6	6.6	1.0	16.9
NR1003-120	microcrystalline dolomite	67	dolomite marl smbr	4.4	1.9	5.3	0.02	0.03	0.69	0.2	0.2	0.4	6.3	3.6	0.8	5.9
NR1003-130	microcrystalline dolomite	79.5	varicolored marl smbr	11.1	1.2	6.7	0.01	0.08	0.11	2.8	0.5	3.3	3.2	1.6	1.4	19.4
NR1003-134	microcrystalline dolomite	84.9	varicoloured marl smbr	16.1	2.6	7.3	0.00	0.001	0.33	0.3	0.3	0.7	0.0	0.0	0.0	6.5
NR1003-155	microcrystalline dolomite	116.5	diatom smbr	17.5	1.0	2.4	0.03	0.61	0.04	5.1	3.3	8.4	1.0	0.0	0.0	149.6
NR1003-166	microcrystalline dolomite	135.9	bituminous smbr	17.5	1.6	3.5	0.02	0.33	0.07	13.9	9.9	23.7	3.8	0.0	0.0	86.6
NR1003-195	microcrystalline dolomite	178	analcime smbr	0.9	1.5	3.4	0.06	1.24	0.05	29.2	14.6	43.8	2.0	0.0	0.0	0.0
NR1003-219	microcrystalline dolomite	213.2	analcime smbr	-2.6	8.7	21.6	0.16	4.09	0.04	5.2	1.8	6.9	45.6	0.0	0.0	0.0
NR1003-230	microcrystalline dolomite	223.1	clinoptilolite smbr	-10.1	1.8	17.2	0.00	0.00	0.00	0.0	0.0	0.0	0.0	0.0	0.0	0.0
NR1003-239	microcrystalline calcite	228.3	basal member	-0.5	0.2	0.7	0.00	0.00	0.00	0.0	0.0	0.0	0.0	0.0	0.0	0.0

4.2.3 EMPA Geochemistry

Based on C_{carb} content, nine thin sections of the carbonate-rich samples from the whole drilling profile, including four from the high $\delta^{13}C$ interval, were investigated by electron microprobe (**Table A.7** and **Table 2.4**). All nine samples show microcrystalline-sized carbonate (**Figure 2.5**). Samples from the high $\delta^{13}C$ interval show SiO_2 contents generally below 5 wt%. Carbonate measurement points with $SiO_2 > 5$ wt% are considered as mix measurements (**Table A.7**) and will not be discussed. The iron contents are correlated with SiO_2 in NR1003-1, 2, 8 and 230, but not in NR1003-5, 6, and 129 (**Figure A.4, A.5 and A.6**). When no such correlation is evident, iron is considered to be at least partially incorporated into the dolomite lattice and was included for calculation of stoichiometric composition (**Table A.7**). NR1003-216 does not show a clear FeO-SiO_2 correlation but the Fe is below 2 mol%. Based on EMPA backscattered electron images and stoichiometric composition, different carbonate phases were distinguished (**Figure A.4, A.5, A.6** and **Table 2.4**), especially for Ca-/Fe-rich dolomite, ferroan dolomite and stoichiometric dolomite.

5 Discussion

5.1 Depositional environment

The general setting of the Ries lake is a hydrologically closed basin with high diameter to depth ratio (**Figure 2.1**, Bolten et al., 1976: p. 91; Füchtbauer et al., 1977; Pohl et al., 1977; Wolf, 1977; Jankowski 1981: p. 258; Arp 1995, 2006), and a deeply impact-fractured basement (Bauberger et al., 1974; Pohl et al., 1977; Stöffler et al., 2013). Floral and mammal fossil assemblages suggest that lacustrine deposition took place under a semi-arid climate (Bolten et al., 1976; Dehm et al., 1977, Füchtbauer et al., 1977; Jankowski, 1981; Heizmann and Fahlbusch, 1983).

Similar as in other impact structures, surface tributaries initiated from the crater wall, with a later extension of watershed during successive erosion of ejecta (Arp et al., 2019a). In parallel to surface tributaries, groundwater influx occurred via brecciated crystalline rocks at the inner ring and megablocks (Bolten, 1977; Pache et al., 2001; Arp et al., 2019b). Although under discussion, there is currently no clear indication of a late hydrological change to open-basin conditions, i.e., no evidence of an outflow (Füchtbauer et al., 1977; Jankowski 1981; Arp et al., 2017b). Indeed, the positive $\delta^{13}C$-$\delta^{18}O$ covariation of the calcite samples (between basal and marl member) from NR1003 is very similar to that of Nördlingen 1973 (**Figure 2.3 B**), confirms a hydrologically-closed lake condition (Rothe and Hoefs, 1977; Talbot, 1990; Li and Ku, 1997).

The NR1003 drill core only incompletely transects the basal member and therefore, only a partial interpretation on the early evolution of the lake can be made. The two fining-upwards cycles in the basal member represent a recurrent development from an alluvial fan to a playa lake and finally a shallow alkaline lake with carbonate precipitation, like that described from the Nördlingen 1973 drill core (Jankowski, 1981). Gneiss and granite pebbles from crystalline basement rocks are found in coarse-grained lithofacies (conglomerate, pebbly sandstone) and some siltstones, reflecting a reworking from suevites and/or crystalline rocks of the inner ring. Sporadic fine-grained pyrite in the sediments indicate sulfidic pore water conditions with dissolved iron supply.

The laminated, bituminous clay- to marlstones of the laminite member, most of which devoid of bioturbation, are considered as profundal deposits of a stratified lake. Except rare fish bones and scales, fecal pellets resembling that of the present-day brine shrimp *Artemia* are the only fossil remnants in laminite member (**Figure A.2F**). The brine shrimp *Artemia* is known from a variety of saline lakes, including highly alkaline soda lakes such as Mono Lake (e.g. Jellison et al., 1993). Therefore, most parts of the laminite member represent deposits in a permanent lake with anaerobic, saline bottom waters (Jankowski 1981).

Following the diatom smbr, sediments of the varicolored marl smbr show clear bioturbation in a number of poorly stratified marl beds. The occurrences of mud cracks and *in-situ* brecciation further indicate temporary subaerial exposure and the termination of the permanent stratification in the lake. However, laminated intercalations are still present, suggesting a transitional phase between a permanent and a temporary shallow lake setting. On top of the varicolored marl smbr, more intense bioturbation is evident in the dolomite-marl smbr, whereas lamination is totally absent. Instead, mud cracks and *in-situ* brecciation are more common, suggesting a playa lake environment.

The clay member is the most heterogenic unit with respect to lithofacies, changing from carbonaceous clay or diatomite via dark-grey marly clay to white–grey argillaceous carbonates (Jankowski 1981, Arp et al., 2017a) and thus represent several flooding-evaporation cycles, typical for a shallow lake. The white–grey argillaceous marlstones commonly show mud cracks and *in-situ* brecciation, suggesting enhanced evaporation during carbonate formation. On the other hand, several unstratified clay beds show extensive features of soil formation (pedogenic slickensides and mottling), pointing to a silting-up under less saline conditions. The clay member, in contrast to other units of the section, exhibits several intercalated fossil beds, with the halotolerant gastropod *Hydrobia*, or the freshwater gastropods *Gyraulus* and *Planorbarius*, and reworked green algal tubes from lake margin bioherms (Dehm et al., 1977; Arp et al., 2017a).

5.2 Microbial processes and chemical lake evolution

5.2.1 Establishment of a sulfate-rich lake

Fluctuating hydrological conditions with rapidly changing water volume changes during the early lake evolution are evident from the cyclic lithological changes from conglomeratic sandstones to laminated limestones, with intercalated mud cracks (NR1003: 243.15 m; Nördlingen 1973: 272.55m, Jankowski, 1981, his Figure 12). Indeed, the unstable lake volume is supported by the low and changing $\delta^{18}O$ values (**Figure 2.2**) in NR1003 carbonates of the basal member as well, consistent with the values reported by Rothe and Hoefs (1977), and similar to trends observed in other closed lakes (Li and Ku, 1997; Leng and Marshall, 2004). With respect to hydrochemistry, the presence of gypsum pseudomorphs in carbonates from basal member (Nördlingen 1973, Jankowski, 1981) indicates that sulfate has been abundant in the lake water during the early lake history. Likewise, the detected pyrites in the Basal member (NR1003) indicate that sulfate reduction was active and sulfate was available in the lake.

Carbonates of the clinoptilolite smbr show the largest $\delta^{18}O$ variations in the succession (-11.67 to +5.28‰). Whereas the dolomite with the lowest $\delta^{18}O$ value (-11.67‰) is possibly related to persistent crater floor heat emission (Arp et al., 2013b), markedly positive $\delta^{18}O$ values (ca. +5‰) observed in most dolomite samples of this smbr support a highly evaporative and saline, most likely shallow environment. For comparison, the Miocene freshwater carbonates from the surroundings of the Ries basin show $\delta^{18}O$ of about only -5 ‰ (e.g. Zeng et al., 2021, **Figure 2.3 B** and **Table A.9**). Indeed, increased salinities during the deposition of the clinoptilolite smbr are also supported by low values of the C_{20} isoprenoid thiophene paleosalinity parameter (ITR), as shown by Barakat and Rullkötter (1997). The steep increase in $\delta^{15}N$ reported from the clinoptilolite smbr of the Nördlinger 1973 drill core indicates a simultaneous increase in lake water pH (Stüeken et al., 2020).

The nearly stoichiometric dolomites in clinoptilolite smbr, determined by d_{104} values in XRD results, are confirmed by electron microprobe data of NR1003-230 (**Table 2.4 and A.7**). Iron contents of these dolomites are extremely low and whole rock Fe contents shows a positive covariance with SiO_2 (**Figure A.5**), suggesting that Fe is not incorporated into dolomite lattices.

Table 2.4 Electron microprobe results of major and trace element contents and calculated mole percentage of $CaCO_3$, $MgCO_3$ and $FeCO_3$.
"n" denotes the number of measurement points. For results of detailed, individual point measurement, the readers are referred to Table A.7.

Sample	Llithostratigraphic member	Depth [m.b.s.]	EMPA mineralogy	n	CaO wt %	MgO wt %	FeO wt %	MnO wt %	SiO$_2$ wt %	K$_2$O wt %	Sr ppm	CaCO$_3$ mol%	MgCO$_3$ mol%	FeCO$_3$ mol%
NR1003-1	clay member	14.3	low Mg calcite	21	52.2	1.0	0.46	0.22	2.0	0.2	1114	96.4	2.6	0.7
			high Mg calcite	4	47.6	2.3	0.56	0.32	3.4	0.4	828	92.5	6.1	0.9
			Ca-rich dolomite	12	34.7	17.0	0.34	0.38	2.6	0.3	530	59.0	40.0	0.5
			mix measurement	17	39.3	2.4	1.41	0.23	9.1	0.9	764	-	-	-
NR1003-2	dolomite marl smbr	52.2	high Mg calcite	1	45.6	10.4	0.46	0.08	1.0	0.1	2254	75.4	23.9	0.6
			Ca-rich dolomite	38	33.2	16.9	0.80	0.12	1.1	0.1	2194	57.7	41.0	1.1
NR1003-129	varicolored marl smbr	78.3	iron-bearing dolomite	25	31.2	20.6	0.99	0.11	0.7	0.1	1654	51.4	47.2	1.3
			ferroan dolomite	26	31.4	18.5	1.90	0.17	0.8	0.1	1581	53.4	43.9	2.5
NR1003-2	diatom smbr	98.1	Ca-rich dolomite	2	28.6	17.3	1.24	0.11	2.3	0.1	1192	53.3	44.7	1.8
			ferroan dolomite	9	30.0	18.8	1.88	0.09	1.7	0.1	1136	52.0	45.3	2.5
			iron-bearing dolomite	34	29.6	21.5	1.22	0.08	1.1	0.1	1017	49.0	49.4	1.6
			dolomite (nearly stoichiometric)	1	31.1	22.0	0.04	0.00	0.0	0.0	0	50.4	49.6	0.1
			mix measurement	2	26.1	18.9	0.96	0.07	15.6	0.0	1566	-	-	-
NR1003-6	diatom smbr	105.3	iron-bearing dolomite	4	30.9	19.5	1.33	0.09	1.0	0.1	1180	52.3	45.8	1.8
			ferroan dolomite	49	29.6	18.8	2.15	0.09	1.8	0.1	893	51.5	45.5	2.9
			mix measurement	2	27.3	17.2	2.18	0.06	5.1	0.3	999	-	-	-
NR1003-8	diatom smbr	121.6	low Mg calcite	1	54.0	1.6	0.45	0.04	0.2	0.1	0	95.5	3.8	0.6
			high Mg calcite	3	35.3	15.4	1.61	0.18	1.8	0.2	1978	60.7	36.9	2.2
			Ca-rich dolomite	27	31.0	18.6	1.57	0.13	1.7	0.2	1470	53.2	44.4	2.1
			mix measurement	3	24.3	14.0	3.29	0.10	9.5	0.6	1033	-	-	-
NR1003-187	bitumen smbr	166	low Mg calcite	1	55.8	0.0	0.18	0.00	0.2	0.1	1224	99.7	0.0	0.2
			high Mg calcite	2	46.6	3.5	1.40	0.09	2.1	0.3	1200	88.6	9.2	2.1
			Ca-rich dolomite	17	32.7	17.8	1.16	0.17	1.3	0.2	2100	55.9	42.3	1.6
			ferroan dolomite	10	31.2	15.1	4.22	0.15	2.2	0.3	1925	56.2	37.6	5.9
			ankerite?	15	29.9	11.0	11.17	0.10	1.2	0.1	1543	55.3	28.4	16.1
			mix measurement	2	30.2	13.3	3.05	0.15	6.3	0.4	2168	-	-	-
NR1003-216	analcime smbr	210.8	Ca-rich dolomite	42	33.5	17.4	0.50	0.09	1.2	0.2	1601	57.7	41.5	0.7
			mix measurement	1	22.9	12.1	0.31	0.02	20.1	3.2	2288	-	-	-

| NR1003-230 | clinoptilolite smbr | 223 | dolomite (nearly stoichiometric) | 51 | 29.5 | 21.6 | 0.15 | 0.04 | 0.9 | 0.1 | 1927 | 49.4 | 50.4 | 0.2 |
| | | | mix measurement | 1 | 26.7 | 20.4 | 0.32 | 0.00 | 5.2 | 0.7 | 1684 | - | - | - |

Table 2.5 Hydrochemistry data of the average water composition in the Ries area, including surface runoff, springs and groundwater wells.
For detailed original data, the readers are referred to Table A.12.

Source of data	Region	Aquifer	T	pH	Na^+	K^+	Ca^{2+}	Mg^{2+}	Sr^{2+}	Fe^{2+}/Fe^{3+}	Mn^{2+}/Mn^{4+}	Cl^-	SO_4^{2-}	NO_3^-	HCO_3^-
			°C		mg/L	mg/L	mg/L	mg/L	mg/L	mg/L	µg/L	mg/L	mg/L	mg/L	mg/L
Winkler 1972	Ries margin	Braunjura (mean)	8.6	7.2	2.9	1.6	81.3	3.8	0.1	0.1	2.8	16.4	22.3	13.3	203
Winkler 1972	Ries margin	Schwarzjura(mean)	7.4	7.3	5.4	1.2	142.2	6.8	0.2	0.0	3.4	27.1	87.0	44.4	284
Winkler 1972	Ries margin	Keuper (mean)	6.4	6.6	9.3	3.5	38.0	9.7	0.6	n.a.	n.a.	6.1	34.0	2.9	142
Winkler 1972	Ries margin	Bunte breccia (mean)	9.2	7.3	4.9	2.8	115.0	12.0	0.7	0.1	52.8	16.4	36.3	26.9	331
This study	Ejecta blanket	suevite (mean)	12.6	7.6	6.2	3.3	79.8	9.3	0.2	0.0	60.4	14.6	7.6	5.5	270
Winkler 1972	Crystalline ring well	Crystalline rock (mean)	14.8	7.6	79.3	9.8	148.4	59.0	0.3	0.5	56.0	60.6	335.3	35.7	404
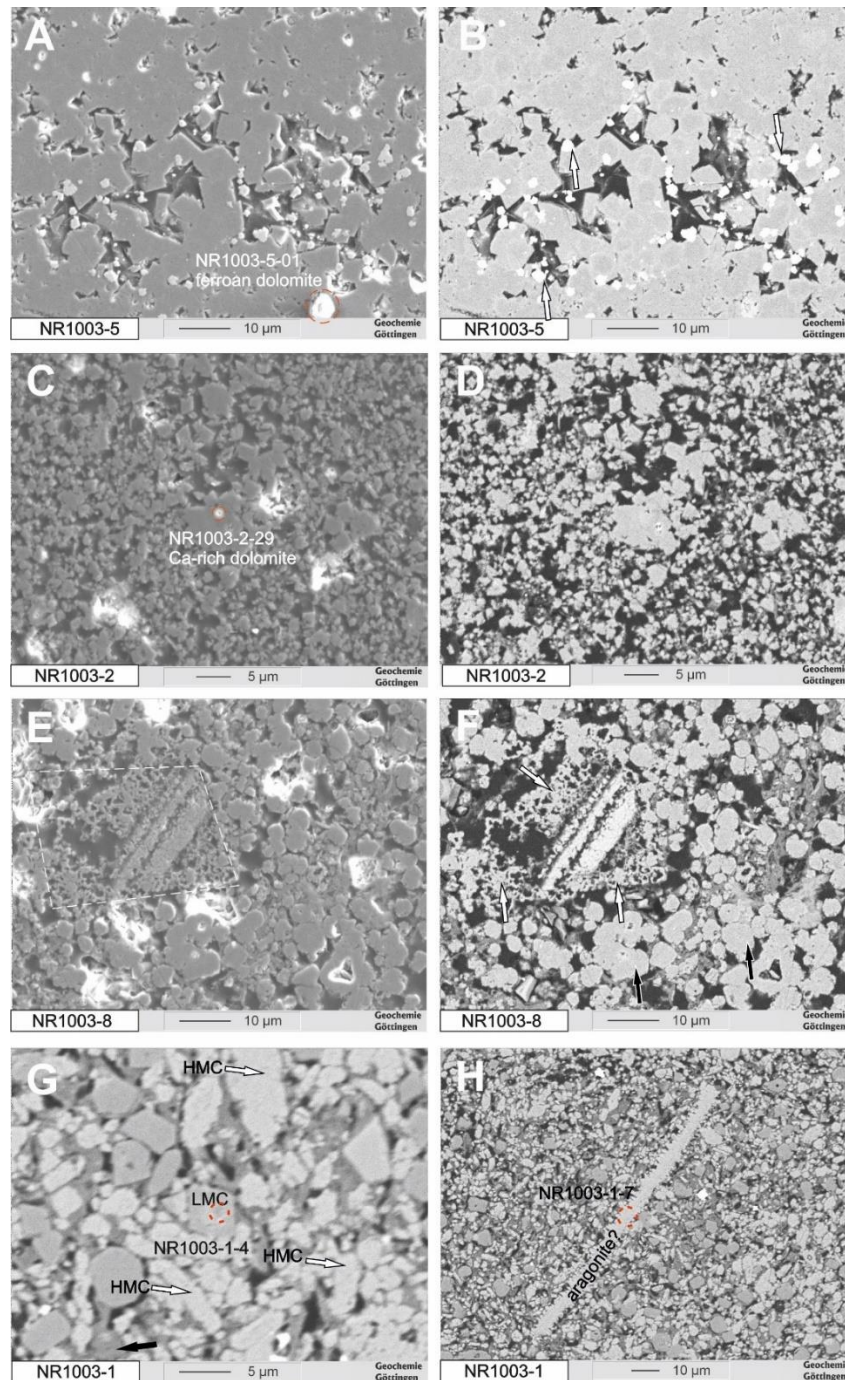
Figure 2.5 Secondary electron micrograph (SE) and backscattered electron images (BSE) of the NR1003 carbonates.
A, B: SE and BSE images of NR-1003-5 (high $\delta^{13}C$ interval, $\delta^{13}C$ = 16.4‰, see NR1003-5-01 in Table A.7 for element compositions) showing rhomboidal dolomites and pyrites (arrows). C, D: SE and BSE images of NR1003-2 (dolomite-marl smbr, $\delta^{13}C$ = -0.2‰, see NR1003-2-29 in Table A.12 for element compositions) microcrystalline Ca-rich dolomites (white-grey color in SE). E, F: SE and BSE images of NR1003-8 (high $\delta^{13}C$ interval, $\delta^{13}C$ = 17.03‰) showing dolomite aggregates (black arrow), an altered silicate (dashed outline in C, possibly an alkali feldspar) and nanocrystalline-sized dolomite replacements at its rim (white arrow). G, H: BSE images of NR1003-1 (clay member, $\delta^{13}C$ = -5.37‰, see NR1003-1-4 and NR1003-1-7 in Table A.7 for element compositions). Note that i) the different colors of low magnesium calcite (LMC) and high magnesium calcite (HMC) in BSE images; ii) the $\delta^{13}C$ values are not exactly for

the analysed electron microprobe points here.

Subsequently, in the following lower part of the analcime smbr, a remarkable decrease in $\delta^{18}O$ (from 5.28‰ at 219.2 m to -0.48‰ at 207.4 m) is evident. This decrease in $\delta^{18}O$ values is interpreted to reflect large and constant freshwater influxes into the lake, resulting in a large, stable lake volume with reduced salinities. At that time, the lake water pH reached its maximum (>10, Stüeken et al., 2020). This decreased salinity is consistent with the limited carbonate formation (generally <50 wt% $CaCO_3$, **Table A.3**) observed in the analcime smbr. Most $\delta^{13}C$ values of the dolomite in this smbr, on the other hand, are more depleted than calcite at similar $\delta^{18}O$ (**Figure 2.3A**). Such low $\delta^{13}C$ values of early diagenetic dolomites, especially in organic rich sediments, may reflect CO_2 contributions to the porewater inorganic carbon pool from anaerobic respiratory processes, particularly sulfate reduction (Talbot and Kelts, 1990; Mazzullo, 2000).

A major activity of sulfate reducing bacteria in the analcime smbr is well supported by peak concentrations of thiophenes and i/ai-$C_{15:0}$ fatty acids, which are low in the basal member and clinoptilolite smbr due to poor biomarker preservation. i/ai-$C_{15:0}$ fatty acids are abundant in the lipids of many sulfate reducing bacteria (Parkes and Taylor, 1983; Taylor and Parkes, 1983). The thiophenes form in sulfidic environments in the absence of ferrous iron (Sinninghe Damsté et al., 1986). Likewise, the dolomites in analcime smbr, with d_{104} values from 2.900 to 2.913, are probably Ca-rich, rather than iron-bearing or ferroan dolomites. Indeed, one EMPA thin section (NR1003-216, <2 mol% Fe) suggests low Fe or no Fe incorporation into the dolomite, pointing to Ca-rich dolomites. Despite trace amounts of framboidal pyrite (<1%) observed with EMPA, pyrite is below the detection limit of XRD (approximately 1%) in the investigated samples throughout the laminite member. Therefore, mineralogy, isotope and biomarker evidence all point to sufficient sulfate input from the influxes, to support major microbial sulfate reduction and a sulfidic lake bottom during sedimentation of the analcime smbr.

5.2.2 Sulfate-depleted lake interval and ^{13}C-enriched dolomite formation
5.2.2.1 Methanogenesis and geochemical constraints in the crater lake

Rothe and Hoefs (1977) already noticed the moderately high $\delta^{13}C$ in single dolomite beds (+10.5 ‰ and +11.1‰ at 171.64 and 90.4 m core depth, respectively, **Table A.10**) in the research drilling Nördlingen 1973. Their two samples were taken from the bituminous and the varicolored marl smbr, roughly falling in the range of the high $\delta^{13}C$ interval described here (**Figure 2.2**). Two possible explanations for the two ^{13}C- enriched samples were suggested (Rothe and Hoefs, 1977; Jankowski, 1981): i) long-term evaporation under a semi-arid, warm climate leads to high salinity and corresponding high $\delta^{13}C$- $\delta^{18}O$ of the lake water, and/or ii) strong photosynthesis and high primary productivity at the time when the laminated member was deposited.

However, in our view, both possibilities do not sufficiently explain the observed high $\delta^{13}C$ values. The enrichment of ^{13}C in the dissolved inorganic carbon (DIC) by photosynthesis in lakes is usually less than 5‰ (Hollander and McKenzie, 1991; Thompson et al., 1997). Evaporation can certainly lead to large ^{13}C enrichment in carbonate (>10‰, e.g., Valero-Garcés et al., 1999) and may explain the positive covariance of $\delta^{13}C$- $\delta^{18}O$ of the calcite samples in the bituminous and the varicolored marl smbr (r =0.93, **Table A.8**). However, the dolomite samples in this interval (**Figure 2.3 A**) do not follow the calcite $\delta^{13}C$- $\delta^{18}O$ covariance trend (**Figure 2.3 B**, see **5.2.1**) but show extremely high $\delta^{13}C$ values at a similar $\delta^{18}O$ as the calcite samples. Therefore, in a hydrologically closed lake, such ^{13}C enrichment cannot be explained by evaporation alone.

Similar cases of ^{13}C enrichment in dolomites from organic-rich successions are associated with methanogenesis at low sulfate concentrations (Nissenbaum et al., 1972; Talbot and Kelts, 1986; Mazzullo, 2000; Teichert et al., 2014; Birgel et al., 2015). The two principal pathways of microbial methanogenesis comprise reduction of CO_2 by H_2 (Claypool and Kaplan, 1974) and acetate fermentation (Friedman and Murata, 1979). A third, less common pathway is methylotrophic methanogenesis (see review by Conrad 2020). After its formation,

[12]C-enriched methane (Claypool and Kaplan, 1974) may be i) consumed by anaerobic oxidation within the sediment (e.g., with SO_4^{2-} as oxidant), ii) consumed by aerobic oxidation upon efflux to the oxic water column, or (iii) lost to the atmosphere by ebullition (Reeburgh, 1980; Conrad et al., 1995). Microbial methane ebullition leads to a drastic loss of ^{12}C and enrichment of ^{13}C in the remaining DIC pool and, eventually, high $\delta^{13}C$ in carbonates upon precipitation. One example, the sulfate-depleted anoxic Lake Untersee (Antarctica), shows that methane emission indeed leads to an extremely high $\delta^{13}C_{DIC}$ value in the hypolimnion of up to >30‰ (Wand et al., 2006).

Biomarker evidence further supports a methanogenic impact on the $\delta^{13}C$ of the dolomites. Archaeol (ArOH), one of the important biomarkers for archaea, including methanogenic archaea (Koga et al., 1998), is not detected in early parts of the succession but shows a peak abundance in the diatom smbr, i.e., within the high $\delta^{13}C$ interval (**Figure 2.3**). The increase in ArOH in this interval is concurrent with the increase in $\delta^{13}C$ of the dolomites (**Figure 2.2**).

Concomitantly, the relative decrease of total thiophenes, i-/ai-$C_{15:0}$ fatty acids suggest a major decline of sulfate reduction in the high $\delta^{13}C$ interval. Abundant sulfate in the water column, or pore water, would significantly suppress methanogenesis, because sulfate-reducing bacteria outcompete methanogens for electron donors such as acetate or hydrogen (McCartney and Oleszkiewicz, 1993). In addition to sulfate, specific salt ions, e.g., high sodium and chloride concentrations in the water may also inhibit methanogenesis (Liu and Boone, 1991). However, a moderate negative correlation between $\delta^{13}C$ and total sulfur content (r=-0.56) in the samples from the high $\delta^{13}C$ interval supports sulfate concentration as the most likely control on methanogenesis and thus, the observed isotopic traits (**Figure A.7**).

In addition to the negative correlation between $\delta^{13}C$ and total sulfur content, positive correlation between $\delta^{13}C$ and carbonate contents (r=0.71), as well as positive $\delta^{13}C$ -$\delta^{18}O$ correlation (r=0.69), is observed in the dolomite samples from the diatom smbr (87.7 to 123.8 m depth, although less evident in the entire high $\delta^{13}C$ interval, **Table A.11, Figure A.8 and A.9**). These correlations suggest that methanogenesis is favored during the time of low detrital inputs and decreased freshwater influxes, i.e., a low-stand with less lake water mixing (leading to high $\delta^{18}O$). Indeed, a well-stratified, anoxic bottom lake that constantly accumulates organics and ions would favor anaerobic respiration. On the other hand, increasing freshwater runoff, besides delivering poorly soluble detrital silicates to the lake, also may simultaneously provide sporadically abundant dissolved sulfate due to weathering of specific minerals in the catchment, such as pyrites. Consequently, isotope and biomarker signatures of methanogenesis appear weak during periods of higher freshwater inputs. As the high $\delta^{13}C$ values are already explained, the simultaneously high carbonate content in our samples suggest that methanogenesis may be linked with dolomite formation. However, it appears at first glance, contradictory that because methanogenesis may produce CO_2 to increase carbonate dissolution.

Dependent on the available substrates, acetoclastic, hydrogenotrophic and methylotrophic methanogenesis may have produced or consumed CO_2, leading to the re-equilibrium of carbonate system. However, hydrochemical modelling calculation by Arp et al. (2013a) and nitrogen isotope data by Stüeken et al. (2020) suggest that, although a slight drop, high pH condition (9-10), as well as alkalinity, persisted from the analcime smbr to diatom smbr. As a result, the high DIC of the Ries soda lake water is sufficient to buffer the CO_2 changes, if any, during the methanogenesis. Exceptionally, other buffering effects can compensate the drop in pH when CO_2 is produced during methanogenesis, namely (i) anaerobic oxidation of methane (AOM) in a deep zone, (ii) calcite dissolution leading to increasing dolomite saturation index (Meister et al., 2011), and (iii) silicate weathering in the anaerobic zone (Torres et al., 2020).

As yet no clear biomarker indications of AOM (e.g. Thiel, 2020) were observed throughout the core profile, and only one dolomite sample from clinoptilolite smbr shows a depleted $\delta^{13}C$ value (NR1003-230, -10.13‰) which is considered insufficient evidence of AOM (e.g. Ussler and Paull, 2008; Teichert et al., 2014). Further, in a soda lake like the Ries lake (Arp et al.,

2013a), a low Ca^{2+} concentration is certainly maintained due to immediate precipitation of carbonates. Therefore, carbonate dissolution is also not likely to happen and to increase the dolomite saturation index. Thirdly, only rare petrographic evidence pointing to silicate dissolution is observed at high magnifications: **Figure 2.5 E** and **F** show an outline of an altered silicate, with traces of dolomite forming at the altered rim. It is, however, unclear whether this process had been triggered by methanogenesis. In general, how exactly silicate dissolution works in non-marine environments is poorly understood and requires further investigation.

Despite the generally positive $\delta^{13}C$-$\delta^{18}O$ covariation in the high $\delta^{13}C$ interval, some of the ferroan dolomite with highest $\delta^{13}C$ values, nonetheless, show less-enriched $\delta^{18}O$ values (e.g. NR1003-5 and -6). This $\delta^{18}O$ deviation implies that, unlike the evaporation-controlled calcites (with strongly positive $\delta^{13}C$-$\delta^{18}O$ covariation), sporadic salinity decrease did not affect methanogenesis within the anoxic, sulfate-depleted porewater, where the ferroan dolomite formed.

5.2.2.2 Effects of salinity changes on ^{13}C-enriched dolomite formation

$\delta^{18}O$ values of lacustrine carbonates may record the water temperature, meteoric precipitation/evaporation ratios, and residence time in lakes, independent from biogeochemical processes (Talbot, 1990; Li and Ku, 1997; Leng and Marshall, 2004). Based on that, salinity changes in a closed-lake can be estimated from $\delta^{13}C$-$\delta^{18}O$ covariance and $\delta^{18}O$ values of the lacustrine carbonates. Likewise, different mineral phases of primary carbonates reflect the Mg/Ca ratios in lacustrine water bodies during evaporation and chemical evolution (Müller et al., 1972; Talbot and Kelts, 1990; Machel, 2004). However, most ^{13}C-enriched dolomites associated with methanogenesis have been considered as early diagenetic products, i.e. porewater precipitates or alteration products (e.g. Talbot and Kelts, 1986; Meister et al., 2011; Teichert et al., 2014; Birgel et al., 2015).

With respect to the microcrystalline carbonates of the investigated drill core NR1003, a number of samples is still in line with the general calcite $\delta^{13}C$-$\delta^{18}O$ covariance trend line (**Figure 2.3 A**). This may point to a primary origin and/or less diagenetic alteration of these calcites and dolomites, thereby approximating salinity trends of the primary lake water, while the $\delta^{18}O$ of samples deviating from the covariation reflect (all of them dolomites) pore water salinity.

Based on this interpretation, the high $\delta^{18}O$ values of the stoichiometric dolomite in the clinoptilolite smbr point to a salinity maximum, with possibly hypersaline conditions in the porewater (see also 5.2.1). The calcite samples (at the base and top of clinoptilolite smbr) are in line with the evaporation trend of the basal member.

During the deposition of the (comparatively carbonate-poor) analcime to lowermost bituminous smbr (**Figure 2.6 A**), i.e. prior to the high $\delta^{13}C$ interval, Ca-rich dolomites show less high $\delta^{18}O$ values, at $\delta^{13}C$ values below the $\delta^{13}C$-$\delta^{18}O$ covariation line (**Figure 2.2 and Figure 2.3 A**). This suggests decreased porewater salinities, consistent with a lake level rise and high-stand, i.e. increased freshwater influx and sulfate supply. The $\delta^{13}C$ values of the samples are affected by ^{12}C from anaerobic respiration (such as sulfate reduction) in the porewater (**Figure 2.6 A**).

Finally, during the high $\delta^{13}C$ interval, a "bifurcated trend" of $\delta^{13}C$ values, $\delta^{18}O$ values and carbonate mineral phases is evident (**Figure 2.2**), indicative of more intensive short-term variations:

a) A "depleted arm" of the trend with low carbonate content, calcite-rich mixture and Ca-rich dolomite, low $\delta^{18}O$ values suggesting low salinity, possibly due to increasing freshwater influx. Methanogenesis is weak, possibly due to temporary sulfate increase from the freshwater (**Figure 2.6 B, high-stand**);

b) An "enriched arm" with high carbonate content, ferroan dolomite (also rare stoichiometric dolomite) and high $\delta^{18}O$ values implying short-term evaporation and temporarily high salinity. The occurrence of ferroan dolomites is associated with increased Fe^{2+} levels that prevailed when a methanogenic zone developed within anoxic bottom waters

at low sulfate conditions. The δ¹³C of primary carbonates were diagenetically shifted to higher values due to methanogenesis (**Figure 2.6 B, low-stand**).

Hence, contrary to an increased long-term salinity along the laminite member as suggested by Rothe and Hoefs (1977) and Arp et al. (2013a), we suggest a salinity maximum in the lowermost laminite member, followed by a lake level rise and stabilization at marine-like salinities during later parts of this member. With respect to mineralogy, the calcite to Ca-rich dolomite to stoichiometric dolomite trend appears salinity/evaporation controlled, while the change to ferroan dolomite is microbially controlled, reflecting low sulfate and methanogenesis.
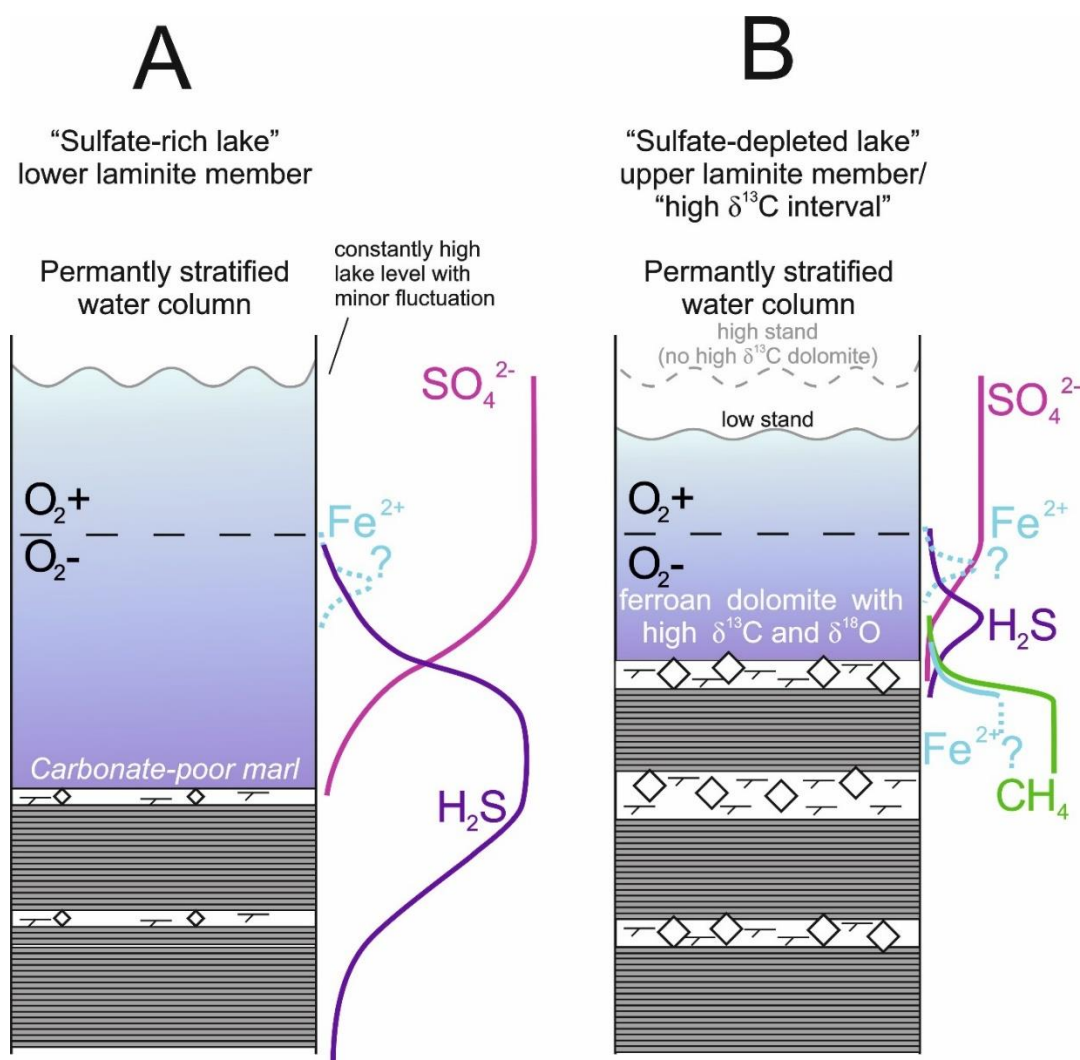
Figure 2.6 Depositional models of the Ries dolomites and related biogeochemical processes

A). Model of the Ries lake during the sulfate-rich early evolution, with decreased salinity and a stable lake volume during the formation of the analcime smbr. Sulfate is abundant and sulfate reduction is prevailing in anoxic pore water. Only sedimentation with low-carbonate content (<50 wt%) is possible (illustrated as thin carbonate beds). No evidence of methanogenesis can be derived. Fe²⁺ with a question mark in 6A refers that iron reduction may still occur in the water column to form sporadic pyrites (5.2.1). B) During the subsequent high δ¹³C interval, most sulfate has been removed. Methanogenesis and methane ebullition result in extreme ¹³C enrichment in the dolomites. Most ferroan dolomite with high δ¹³C values forms during the low stands within the interval, with simultaneous high carbonate content (illustrated as thicker carbonate beds). It is uncertain whether a maximum Fe²⁺ is reached or an infinite

increase in Fe²⁺ downwards (lower question mark). During the high stands, the carbonate formation is less intensive with both low δ¹³C and δ¹⁸O. Hypothetic porewater profiles are adopted from Jørgensen and Kasten (2006) and Roland et al. (2018).

5.2.3 Oxygenation of the lake floor and onset of methanotrophy

A successive decline in $\delta^{13}C$ of the dolomites (from 15 to 5 ‰) is already evident at the end of the varicolored smbr (i.e., 73.6 to 87.3 m depth, **Figure 2.2**). At this time, while bioturbation and mud cracks clearly point to low lake level and oxygenation of bottom water, ArOH is low in concentration but still present, suggesting declining methanogenesis (**Figure 2.3**). In the subsequent dolomite marl smbr, none of the dolomite samples shows very high $\delta^{13}C$ (> 10‰) anymore.

Further indication for a successive oxygenation of the lake bottom comes from biomarker analysis: In accordance with the more frequent subaerial exposure features in the sediments, the Pr/Ph ratio (Rontani and Volkman, 2003) shows an increase from the diatom smbr to the dolomite marl smbr. In addition, instead of typical ferroan dolomites in the high $\delta^{13}C$ interval, the electron microprobe results demonstrate that dolomites in the dolomite marls smbr (sample NR1003-2) are Ca-rich dolomites and high-Mg calcites low in Fe, indicating increasing oxidation potentials in the pore water. Strikingly, the presence of 3-me-C_{32} ββ-HA, a biomarker for aerobic methanotrophic bacteria (Birgel and Peckmann, 2008), fully corresponds to the decline of $\delta^{13}C$ in dolomites. Likewise, 2-me-C_{32} ββ-HA, indicating bacterial contributions from both soil and terrestrial aquatic environments (including cyanobacteria, Welander et al., 2010), also shows an increase with the progressive oxygenation. Similar to all earlier parts of the lake succession, no AOM is evident and all arguments thus point to a shallowing and mixing, without evidence of a significant increase in sulfate.

5.2.4 Late sulfate increase due to hydrological change

The larger size of pyrite aggregates in the clay member (up to 20 µm) is also very distinct from the underlying dolomite-marl smbr (generally <2 µm, **Figure 2.5 A**). The fact that Fe is bound as pyrites, instead of being incorporated into ferroan dolomite, again suggests increasing sulfate in the lake (see 5.2.2.2). Likewise, the occurrence of gypsum pseudomorphs in a micrite bed within the clay member clearly indicates high sulfate concentrations in the lake water (Arp et al., 2017a). Similar to the section from basal member to analcime smbr, sedimentary pyrites and organic sulfur compounds (thiophenes) in clay member reveal evidence for sulfate reduction and thus, sufficient input of sulfate from the catchment. The increase in sulfate is also evident from the bulk total sulfur contents (**Table A.3**).

During the deposition of the clay member, the lake most likely received an increased freshwater influx, as indicated by decreasing $\delta^{18}O$ values and intercalated allochthonous lignite seams. Most likely, increased sulfate contributions in the lake resulted from new tributaries that had cut through pyrite-bearing formations, specifically that of the Schwarzjura and Braunjura Group.

Furthermore, although no extremely enriched ¹³C signals from carbonates are evident, abundant 3-me-C_{32}ββ-HA (**Figure 2.4**) suggests considerable biological methane consumption and, in turn, methanogenesis. Due to the presence of sulfate and sulfate reducers in lake, methanogenesis most likely arises from the deeper sediment layers when AOM is missing. Indeed, below the sample NR1003-15, a lignite-bearing carbonaceous clay bed (14.6 to 14.8 m at least 0.2 m thick due to core loss) potentially provides methanogenic substrate. Alternatively, the methanogenic substrate could be a non-competitive one, e.g. methanol or trimethylamine (TMA, see review by Conrad 2020), instead of CO_2 or acetate.

5.3 Successive impact ejecta erosion and changes in biogeochemical processes

The above discussions demonstrate clear trends in the prevalence of certain biogeochemical processes in the Ries crater lake during its evolution, which include sulfate reduction,

methanogenesis, aerobic methanotrophy and respiration (**Figure 2.7**). Although these processes can be well distinguished spatially in modern lakes (e.g. Ingvorsen and Brock, 1982; Wand et al., 2006), a specific description on change of microbial community exposed to sulfate depletion of a fossil lake or along a long time-span have, to our knowledge, not been reported before.

Particularly the proposed variations in the prevalence of sulfate reduction versus methanogenesis require a change in hydrochemical conditions: sufficient sulfate supply acted as substrate and supported sulfate reduction, followed by methanogenesis under subsequent sulfate-depleted conditions. To support this hypothesis, it is necessary to examine potential sources of sulfate from the different catchment bedrocks of the lake, in this case, ejecta formations of the Ries crater. The hydrochemistry data from groundwater wells and surrounding areas (Winkler 1972; **Table 2.5**) show that groundwaters from Variscan basement rock aquifers have the highest sulfate concentrations (mean: 335.3 mg/L). Waters from Schwarzjura Group are also rich in sulfate (mean= 87 mg/L). On the other hand, waters derived from the Bunte Breccia and suevite are poor in sulfate (mean: 36.3 and 7.6 mg/L, respectively).

As pointed out in 5.1, the initial lake water was largely supplied by weathering solutions from suevite and groundwaters from brecciated crystalline rocks of the inner ring and megablocks. Indeed, the initial high sulfate condition would be better explained by waters mixed from both sources, while the siliciclastic sediment components of the basal member, as demonstrated by Salger (1977), came from the suevite alone (i.e., groundwater discharge does not provide siliciclastics, only water). After that, during deposition of the younger lithostratigraphic units, a decrease of $^{87}Sr/^{86}Sr$ ratios in the carbonate (0.71185 to 0.71125) suggest an increasing contribution of waters from the Bunte Breccia (low in radiogenic Sr) relative to Variscan crystalline rock and suevites (rich in radiogenic Sr, Arp et al., 2013a). However, the previous hydrochemical model for the Ries crater lake evolution suggested stepwise increasing sulfate concentrations along the lake history, with maximum values during deposition of the clay member (Arp et al., 2013a). Our present study reveals that sulfate concentrations must have been initially high during the early evolution of the lake (i.e., basal member to analcime smbr). Subsequently, a depletion of sulfate is revealed in the bituminous to dolomite marl smbr, before a final increase occurred during the deposition of clay member.

The sulfate depletion caused by increasing Bunte breccia influxes is, indeed, consistent with the provenance of siliciclastics, based on the clay mineral associations in the Nördlingen 1973 drill core (Salger, 1977; **Figure 2.7**).
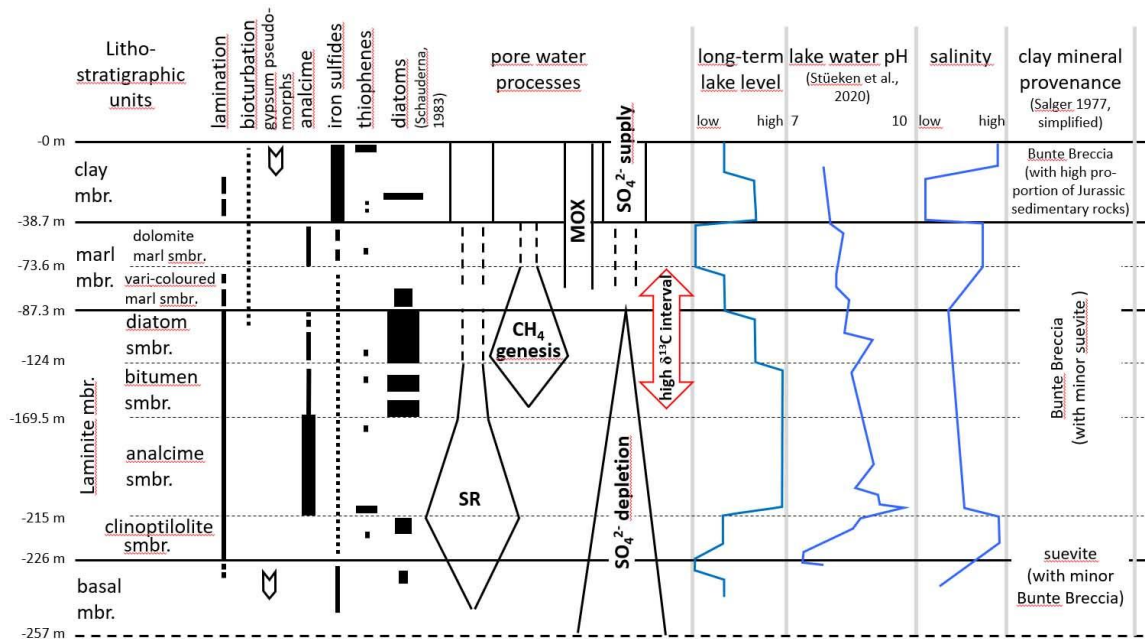
Figure 2.7 Interpretations of pore water biogeochemical processes, lake physiochemistry and solute provenance of the Ries crater lake based on observations from this study.
SR: sulfate reduction; MOX: aerobic methane oxidation. The gypsum pseudomorphs in the clay member were reported by Arp et al. (2017) and in basal member by Jankowski (1981); thiophenes in clinoptilolite smbr by Barakat and Rullkötter (1997); occurrences of diatoms by (Schauderna, 1983). The estimated lake level curve is based on sedimentological observations (e.g. lamination, bioturbation, slumping, mud cracks, *in-situ* brecciation) and diatom associations (Schauderna, 1983). The estimated salinity was derived from indicative minerals (gypsum) or organic compounds (ITR ratios by Barakat and Rullkötter, 1997), indicative diatoms (Schauderna 1983), and δ^{18}O of the carbonates.

Similarly, the late increase in sulfate supply in clay member is most plausibly explained by an increase in influxes from pyrite-bearing Jurassic marine claystones (Schwarzjura/Braunjura), either from allochtonous blocks within the Bunte Breccia, the megablock zone, or from the northern surroundings outside of the tectonic crater rim.

Taken together, our observations are in line with the following scenario of the hydrological lake evolution

i) basal member to analcime smbr: groundwater influxes of the early lake (Bolten, 1977; Pache et al., 2001; Arp et al., 2019b) mostly came from the sulfide-rich crystalline basement rocks, with additional contribution from suevites. Oxidation of the sulfides resulted in high-sulfate conditions, which successively declined during the analcime smbr due to bacterial sulfate reduction.
ii) bituminous smbr to varicolored marl smbr ("high δ^{13}C interval"): the sulfate levels in the closed lake further declined due to bacterial sulfate reduction and limited sulfate influx from the Bunte Breccia, finally permitting methanogenesis at the lake bottom. During this soda lake phase (Arp et al., 2013; Stüken et al., 2020), as sulfate dropped to low concentration, the salinity is most likely decreased if compared to the previous interval by carbonate precipitation, authigenic silicate formation (e.g. clinoptilolite and analcime) and removal via sediment porewater (see e.g. Gudden, 1974; Salger, 1977). However, short-term lake level change can lead to temporary salinity fluctuations (see 5.2.2).

iii) dolomite marl smbr: progressive silting-up of the lake and temporary subaerial exposure promoted the onset of methanotrophy and aerobic conditions at the lake bottom. The major influxes to the lake, however, still came from the Bunte Breccia, as there are no indications of increasing sulfate levels.

iv) clay member: a hydrological change in the catchment with tributaries supplying solutions from Jurassic pyrite-bearing clay formations (Schwarzjura/Braunjura) resulted in a significant increase in lake water sulfate.

In addition to the prominent intrinsic effects, i.e., successive impact ejecta weathering in the catchment, climate fluctuations also affected the sedimentation of the Ries lake. This is indicated by the temporary desiccation of the lake at the end of high $\delta^{13}C$ interval, the flooding-evaporation cycles in the clay member (Jankowski, 1981; Arp et al., 2017a), and the large $\delta^{18}O$ variation between the calcite and the dolomite laminae (NR1003-152, see 5.2.2). As discussed in 5.2.1, there was probably a rapid rise in lake level at the base of analcime smbr. While few age constraints for the NR1003 section exists, the volcanic ash layer (ca. 14.2 Ma at 192.6 m depth, **Figure 2.2**) reported by Arp et al. (2021) provides a proxy to investigate whether that lake level rise is related to regional climate events. The period between the impact event (14.808 ± 0.038 Ma, Schmieder et al., 2018a,b; see Rocholl et al., 2018a,b for discussion) and the deposition of the volcanic ash layer falls into the mid-Miocene climate transition (MMCT, 16 to 12.9 Ma, Flower and Kennett, 1994). Only a few studies, with limited sampling, are available on the MMCT of Central Europe, but they suggest that no strong changes in seasonality or precipitation occurred around the depositional time of the volcanic ash layer (e.g. Mosbrugger et al., 2005; Böhme et al., 2008; Methner et al., 2020). Based on this consideration, the inferred increase in volume of the Ries lake (water depth) may be related to either i) extrinsic factors: e.g. increasing precipitation due to climate change or ii) intrinsic factors: e.g. cooling of the crater floor (decreasing evaporation); subsidence of the crater floor and lateral expansion of the crater rim (increasing accommodation space).

Indeed, the abovementioned intrinsic factors may also trigger the large $\delta^{18}O$ shift at analcime smbr. In any case, our study suggests that climate changes caused only modifications of the major patterns of lake sedimentation and chemical evolution in the Ries crater lake, consistent with Arp et al. (2013a). For example, climate-induced evaporation can certainly increase lake sulfate concentrations during the high $\delta^{13}C$ interval, however, the evidence of high sulfate or sulfate reduction is missing. Instead, the influxes with their ion ratios determined by successive weathering of distinctive ejecta formations, essentially influenced the biogeochemical processes of the Ries crater lake. This suggests that unlike other regular lacustrine environments (Talbot, 1990; Leng and Marshall, 2004), the climate information recorded by stable isotopes of the carbonate in Ries crater lake was overprinted by the intrinsic factors during the crater lake evolution. Similar biogeochemical evolution may apply to other complex impact craters, where, due to the discernible target lithologies, the resulting successive ejecta erosions can lead to solutions with distinct ion compositions.

6 Conclusions

i) The chemical evolution of the Ries impact crater lake exhibits considerable changes in sulfate concentrations which were driven by the successive weathering of rock formations in the catchment area. Initially, high sulfate concentrations in the lake were attained by influxes from crystalline basement rock. This was followed by low-sulfate conditions during influxes from sedimentary ejecta (Bunte Breccia). Eventually, weathering solutions from Jurassic pyrite-bearing claystone formations returned the lake to high sulfate levels.

ii) High-$\delta^{13}C$ dolomites (up to + 20.9‰) in the central basin of the Ries crater correspond to a specific interval of the lake evolution with low sulfate concentrations and extensive methanogenesis at the permanently anoxic lake bottom.

iii) High-$\delta^{13}C$ dolomites terminate after a stepwise re-oxygenation of the lake, encompassing temporary subaerial exposure events and the onset of major aerobic methanotrophy.

iv) Although short-term climate fluctuation around the mid-Miocene Climate Transition (MMCT) might be more important than previously suggested, changes in ejecta erosion and hydrology in the catchment area were the most important driver of the biogeochemical processes in this hydrologically closed impact crater lake basin. The climatic information, expected by stable carbon and oxygen isotopes, behind the lacustrine carbonates in the Ries basin was obscured by the intrinsic factors.

Acknowledgements

References

Arenas, C., Casanova, J. and Pardo, G. (1997) Stable-isotope characterization of the Miocene lacustrine systems of Los Monegros (Ebro Basin, Spain): palaeogeographic and palaeoclimatic implications. *Palaeogeogr. Palaeoclimatol. Palaeoecol.*, **128,** 133-155.

Argun, M.E. (2008) Use of clinoptilolite for the removal of nickel ions from water: kinetics and thermodynamics. *J. Hazard. Mater.*, **150,** 587-595.

Armstrong, J. T. (1995) Citzaf-a package of correction programs for the quantitative Electron Microbeam X-Ray-Analysis of thick polished materials, thin-films, and particles. *Microbeam Analysis*, **4**, 177-200.

Arp, G. (1995) Lacustrine bioherms, spring mounds, and marginal carbonates of the Ries-impact-crater (Miocene, southern Germany). *Facies*, **33**, 35-89.

Arp, G. (2006) Sediments of the Ries Crater Lake (Miocene, Southern Germany). *Schriftenreihe der deutschen Gesellschaft für Geowissenschaften*, **45**, 213-236.

Arp, G., Blumenberg, M., Hansen, B.T., Jung, D., Kolepka, C., Lenz, O., Nolte, N., Poschlod, K., Reimer, A. and Thiel, V. (2013a) Chemical and ecological evolution of the Miocene Ries impact crater lake, Germany: A reinterpretation based on the Enkingen (SUBO 18) drill core. *Geol. Soc. Am. Bull.*, **125,** 1125-1145.

Arp, G., Kolepka, C., Simon, K., Karius, V., Nolte, N. and Hansen, B.T. (2013b) New evidence for persistent impact-generated hydrothermal activity in the Miocene Ries impact structure, Germany. *Meteorit. Planet. Sci.*, **48,** 2491-2516.

Arp, G., Hansen, B.T., Pack, A., Reimer, A., Schmidt, B.C., Simon, K. and Jung, D. (2017a) The soda lake—mesosaline halite lake transition in the Ries impact crater basin (drilling Löpsingen 2012, Miocene, southern Germany). *Facies*, **63,** 1-20.

Arp, G., Ulbrich, P., Reimer, A., Hartmann, G. & Jung, D. (2017b): Süßwassermergel der Kraterrandhöhen des Nördlinger Rieses (Miozän): Relikte einer Aussüßungsphase des Riessees? *Geologische Blätter für Nordost-Bayern,* **67**, 19-34.

Arp, G., Schultz, S., Karius, V. and Head, J.W. (2019a) Ries impact crater sedimentary

conglomerates: Sedimentary particle 'impact pre-processing', transport distances and provenance, and implications for Gale crater conglomerates, Mars. *Icarus*, **321,** 531-549.

Arp, G., Reimer, A., Simon, K., Sturm, S., Wilk, J., Kruppa, C., Hecht, L., Hansen, B.T., Pohl, J., Reimold, W.U., Kenkmann, T. and Jung, D. (2019b) The Erbisberg drilling 2011: Implications for the structure and postimpact evolution of the inner ring of the Ries impact crater. *Meteorit. Planet. Sci.* **54**, 2448-2482.

Arp, G., Dunkl, I., Jung, D., Karius, V., Lukács, R., Zeng, L., Reimer, A. and Head III, J.W. (2021) A Volcanic Ash Layer in the Nördlinger Ries Impact Structure (Miocene, Germany): Indication of Crater Fill Geometry and Origins of Long-Term Crater Floor Sagging. *J. Geophys. Res.* Planets **126**, e2020JE006764. https://doi.org/10.1029/2020JE006764

Böhme, M., Bruch, A.A. and Selmeier, A. (2007) The reconstruction of Early and Middle Miocene climate and vegetation in Southern Germany as determined from the fossil wood flora. *Palaeogeogr. Palaeoclimatol. Palaeoecol.*, **253**, 91-114.

Barakat, A.O. and Rullkötter, J. (1997) A Comparative Study of Molecular Paleosalinity Indicators: Chromans, Tocopherols and C20 Isoprenoid Thiophenes in Miocene Lake Sediments (Nördlinger Ries, Southern Germany). *Aquat. Geochem.*, **3,** 169-190.

Bauberger, W., Mielke, H., Schmeer, D. and Stettner, G. (1974) Petrographische Profildarstellung der Forschungsbohrung Nördlingen 1973. *Geologica Bavarica*, **72**, 33-34.

Birgel, D. and Peckmann, J. (2008) Aerobic methanotrophy at ancient marine methane seeps: A synthesis. *Org. Geochem.*, **39,** 1659-1667.Birgel, D., Meister, P., Lundberg, R., Horath, T., Bontognali, T.R., Bahniuk, A.M., de Rezende, C.E., Vásconcelos, C. and McKenzie, J.A. (2015) Methanogenesis produces strong 13C enrichment in stromatolites of Lagoa Salgada, Brazil: a modern analogue for Palaeo-/Neoproterozoic stromatolites? *Geobiology*, **13,** 245-266.

Bojanowski, M.J. (2014) Authigenic dolomites in the Eocene–Oligocene organic carbon-rich shales from the Polish Outer Carpathians: evidence of past gas production and possible gas hydrate formation in the Silesian basin. *Mar. Petrol. Geol.*, **51,** 117-135.

Bolten, R., Gall, H. and Jung, W. (1976) Die obermiozäne (sarmatische) Fossil-Lagerstätte Wemding im Nördlinger Ries (Bayern). Ein Beitrag zur Charakterisierung des Riessee-Biotops. *Geol. Bl. NO-Bayern*, **26**, 75-94.

Bolten, R. (1977) *Die Karbonatischen Ablagerungen des obermiozänen Kratersees im Nördlinger Ries*. Ph. D. thesis, Ludwig-Maximilians-Univ, München.

Calvert, S. and Pedersen, T. (1993) Geochemistry of recent oxic and anoxic marine sediments: implications for the geological record. *Mar. Geol.*, **113,** 67-88.

Calvo, J.P., Jones, B.F., Bustillo, M., Fort González, R., Alonso-Zarza, A.M. and Kendall, C. (1995) Sedimentology and geochemistry of carbonates from lacustrine sequences in the Madrid Basin, central Spain. *Chem. Geol.*, **123,** 173-191.

Claypool, G.E. and Kaplan, I.R. (1974) The Origin and Distribution of Methane in Marine Sediments. In *Natural Gases in Marine Sediments* (ed I.R. Kaplan). Springer US, Boston, MA. pp. 99-139.

Cohen, A.S. (2003) *Palaeolimnology: the history and evolution of lake systems*. Oxford University Press, Oxford.

Conrad, R., Frenzel, P. and Cohen, Y. (1995) Methane emission from hypersaline microbial mats: lack of aerobic methane oxidation activity. *FEMS Microbiol. Ecol.*, **16,** 297-305.

Della Porta, G. (2015) Carbonate build-ups in lacustrine, hydrothermal and fluvial settings: comparing depositional geometry, fabric types and geochemical signature. *Geol. Soc. Spec. Publ.*, **418,** 17-68.

Dehm, R., Gall, H., Hoefling, R., Jung, U. and Malz, H. (1977) Die Tier- und Pflanzenreste aus den Riessee-Ablagerungen. *Geologica Bavarica*, **75**, 91-109.

Ernstson, K. (1974) The structure of the Ries crater from geoelectric depth soundings. *J. Geophys. Res.*, **40,** 639-659.

Füchtbauer, H., Von Der Brelie, G., Dehm, R., Förstner, U., Gall, H., Höfling, R., Hoefs, J., Hollerbach, H., Hufnagel, B., Jankowski, B., Jung, W., Malz, H., Mertes, H., Rothe, P., Salger, M., Wehner, H. and Wolf, M. (1977) Tertiary lake Sediments of die Ries, research borehole Nördlingen 1973 - a summary. *Geologica Bavarica*, **75,** 13-20.

Flower, B.P. and Kennett, J.P. (1994) The middle Miocene climatic transition: East Antarctic ice sheet development, deep ocean circulation and global carbon cycling. *Palaeogeogr. Palaeoclimatol. Palaeoecol.*, **108**, 537-555.

Fontes, J.C., Gasse, F., Callot, Y., Plaziat, J.C., Carbonel, P., Dupeuble, P. and Kaczmarska, I. (1985) Freshwater to marine-like environments from Holocene lakes in northern Sahara. *Nature*, **317,** 608-610.

Friedman, I. and Murata, K. (1979) Origin of dolomite in Miocene Monterey Shale and related formations in the Temblor Range, California. *Geochim. Cosmochim. Acta*, **43,** 1357-1365.

Fussmann, D., von Hoyningen-Huene, A.J.E., Reimer, A., Schneider, D., Babková, H., Peticzka, R., Maier, A., Arp, G., Daniel, R. and Meister, P. (2020) Authigenic formation of Ca–Mg carbonates in the shallow alkaline Lake Neusiedl, Austria. *Biogeosciences,* **17,** 2085-2106.

Gasse, F., Fontes, J.-C., Plaziat, J., Carbonel, P., Kaczmarska, I., De Deckker, P., Soulié-Marsche, I., Callot, Y. and Dupeuble, P. (1987) Biological remains, geochemistry and stable isotopes for the reconstruction of environmental and hydrological changes in the Holocene lakes from North Sahara. *Palaeogeogr. Palaeoclimatol. Palaeoecol.*, **60,** 1-46.

Gudden, v. H. (1974) Die Forschungsbohrung Nördlingen 1973 Durchführung und erste Befunde, *Geologica Bavarica*, **72,** 11-31.

Heizmann, E.J. and Fahlbusch, V. (1983) Die mittelmiozäne Wirbeltierfauna vom Steinberg (Nördlinger Ries). Eine Übersicht. *Mitteilungen der Bayerischen Staatssammlung für Paläontologie und historische Geologie*, **23**, 83-93.

Hüttner R. and Schmidt-Kaler H. (1999) *Die Geologische Karte des Rieses 1:50000: Erläuterungen zu Erdgeschichte, Bau und Entstehung des Kraters sowie zu den Impaktgesteinen.* Bayerisches Geologisches Landesamt, Munich.

Hollander, D.J. and McKenzie, J.A. (1991) CO_2 control on carbon-isotope fractionation during aqueous photosynthesis: A paleo-pCO_2 barometer. *Geology*, **19,** 929-932.

Hudson, J. (1977) Stable isotopes and limestone lithification. *J. Geol. Soc.*, **133,** 637-660.

Ingvorsen, K. and Brock, T.D. (1982) Electron flow via sulfate reduction and methanogenesis in the anaerobic hypolimnion of Lake Mendota. *Limnol. Oceanogr.*, **27,** 559-564.

Jankowski, B. (1981) *Die Geschichte der Sedimentation im Nördlinger Ries und Randecker Maar.* Ph. D. thesis, Ruhr Univ.

Jellison, R., Miller, L.G., Melack, J.M. and Dana, G.L. (1993) Meromixis in hypersaline Mono Lake, California. 2. Nitrogen fluxes. *Limnol. Oceanogr.*, **38,** 1020-1039.

Koga, Y., MorII, H., Akagawa-Matsushita, M. and OHGA, M. (1998) Correlation of polar lipid

composition with 16S rRNA phylogeny in methanogens. Further analysis of lipid component parts. *Biosci. Biotechnol. Biochem.*, **62,** 230-236.

Logares, R., Lindström, E.S., Langenheder, S., Logue, J.B., Paterson, H., Laybourn-Parry, J., Rengefors, K., Tranvik, L. and Bertilsson, S. (2013) Biogeography of bacterial communities exposed to progressive long-term environmental change. *ISME J.,* **7**, 937-948.

Leng, M.J. and Marshall, J.D. (2004) Palaeoclimate interpretation of stable isotope data from lake sediment archives. *Quatern. Sci. Rev.*, **23,** 811-831.

Lewan, M. and Maynard, J. (1982) Factors controlling enrichment of vanadium and nickel in the bitumen of organic sedimentary rocks. *Geochim. Cosmochim. Acta*, **46,** 2547-2560.

Li, H.-C. and Ku, T.-L. (1997) δ13C–δ18C covariance as a paleohydrological indicator for closed-basin lakes. *Palaeogeogr. Palaeoclimatol. Palaeoecol.*, **133,** 69-80.

Liu, Y. and Boone, D.R. (1991) Effects of salinity on methanogenic decomposition. *Bioresour. Technol.*, **35,** 271-273.

Machel, H.G. (2004) Concepts and models of dolomitization: a critical reappraisal, in: C.J.R. Braithwaite, G. Rizzi, Darke, G. (Eds.), The Geometry and Petrogenesis of Dolomite Hydrocarbon Reservoirs. *Geol. Soc. Spec. Publ.*, **235,** 7-63.Mazzullo, S.J. (2000) Organogenic Dolomitization in Peritidal to Deep-Sea Sediments. *J. Sed. Res.*, **70,** 10-23.

McCartney, D.M. and Oleszkiewicz, J.A. (1993) Competition between methanogens and sulfate reducers: effect of COD: sulfate ratio and acclimation. *Water Environ. Res.*, **65,** 655-664.

McCormack, J., Nehrke, G., Jöns, N., Immenhauser, A. and Kwiecien, O. (2019) Refining the interpretation of lacustrine carbonate isotope records: Implications of a mineralogy-specific Lake Van case study. *Chem. Geol.*, **513,** 167-183.

Meister, P., Gutjahr, M., Frank, M., Bernasconi, S.M., Vasconcelos, C. and McKenzie, J.A. (2011) Dolomite formation within the methanogenic zone induced by tectonically driven fluids in the Peru accretionary prism. *Geology*, **39,** 563-566.

Methner, K., Campani, M., Fiebig, J., Löffler, N., Kempf, O. and Mulch, A. (2020) Middle Miocene long-term continental temperature change in and out of pace with marine climate records. *Sci. Rep.*, **10**, 7989.

Moffett, A., Poppe, L.J. and Lewis, R.S. (1994) *Trace metal concentrations in sediments from eastern Long Island Sound*. US Department of the Interior, US Geological Survey.

Montano D., Gasparrini M., Gerdes A., Della Porta G. & Albert R. (2021) *In-situ* U-Pb dating of Ries Crater lacustrine carbonates (Miocene, South-West Germany): implications for continental carbonate chronostratigraphy. *Earth Planet. Sci. Lett.*, **568**, 117011.

Mosbrugger, V., Utescher, T. and Dilcher, D.L. (2005) Cenozoic continental climatic evolution of Central Europe. *Proc. Natl. Acad. Sci. U.S.A.*, **102**, 14964.

Nissenbaum, A., Presley, B.J. and Kaplan, I.R. (1972) Early diagenesis in a reducing fjord, Saanich Inlet, British Columbia—I. chemical and isotopic changes in major components of interstitial water. *Geochim. Cosmochim. Acta*, **36,** 1007-1027.

Osinski, G. (2005) Hydrothermal activity associated with the Ries impact event, Germany. *Geofluids*, **5,** 202-220.

Parkes, R.J. and Taylor, J. (1983) The relationship between fatty acid distributions and bacterial respiratory types in contemporary marine sediments. *Estuar. Coast. Shelf Sci.*, **16,** 173-189.

Platt, N.H. (1992) Fresh-water carbonates from the Lower Freshwater Molasse (Oligocene, western Switzerland): sedimentology and stable isotopes. *Sed. Geol.*, **78,** 81-99.

Pohl, J., Stoeffler, D., Gall, H.v. and Ernstson, K. (1977) The Ries impact crater. In: *Impact and explosion cratering: Planetary and terrestrial implications* (eds. Roddy, D. J., Pepin, R. P. & Merrill, R. B.). Pergamon, New York. pp. 343-404.

Reeburgh, W.S. (1980) Anaerobic methane oxidation: rate depth distributions in Skan Bay sediments. *Earth Planet. Sci. Lett.*, **47,** 345-352.

Rocholl, A., Böhme, M., Gilg, H.A., Pohl, J., Schaltegger, U. and Wijbrans, J. (2018a) Comment on "A high-precision 40Ar/39Ar age for the Nördlinger Ries impact crater, Germany, and implications for the accurate dating of terrestrial impact events" by Schmieder et al.(Geochim. Cosmochim. Acta 220 (2018) 146–157). *Geochim. Cosmochim. Acta*, **238,** 599-601.

Rocholl, A., Schaltegger, U., Gilg, H.A., Wijbrans, J. and Böhme, M. (2018b) The age of volcanic tuffs from the Upper Freshwater Molasse (North Alpine Foreland Basin) and their possible use for tephrostratigraphic correlations across Europe for the Middle Miocene. *Int. J. Earth Sci*, **107,** 387-407.

Roland, F.A.E., Morana, C., Darchambeau, F., Crowe, S.A., Thamdrup, B., Descy, J.-P. and Borges, A.V. (2018) Anaerobic methane oxidation and aerobic methane production in an east African great lake (Lake Kivu). *J. Great Lakes Res.*, **44,** 1183-1193.

Rontani, J.-F. and Volkman, J.K. (2003) Phytol degradation products as biogeochemical tracers in aquatic environments. *Org. Geochem.*, **34,** 1-35.

Rosenbaum, J. and Sheppard, S.M.F. (1986) An isotopic study of siderites, dolomites and ankerites at high temperatures. *Geochim. Cosmochim. Acta*, **50,** 1147-1150.

Rothe, P. and Hoefs, J. (1977) Isotopen-geochemische Untersuchungen an Kabonaten der Ries-See-Sedimente der Forschungsbohrung Nördlingen 1973. *Geologica Bavarica*, **75,** 59-66.

Salger, M. (1977) Die tonminerale der forschungsbohrung Nördlingen 1973. *Geologica Bavarica*, **75,** 67-73.

Schaller, T., Moor, H.C. and Wehrli, B. (1997) Sedimentary profiles of Fe, Mn, V, Cr, As and Mo as indicators of benthic redox conditions in Baldeggersee. *Aquat. Sci.*, **59,** 345-361.

Schauderna, H. (1983) Die Diatomeenflora aus den miozänen Seeablagerungen im Nördlinger Ries. *Palaeontographica Abteilung B,* 83-193.

Schmieder, M., Kennedy, T., Jourdan, F., Buchner, E. and Reimold, W.U. (2018a) A high-precision 40Ar/39Ar age for the Nördlinger Ries impact crater, Germany, and implications for the accurate dating of terrestrial impact events. *Geochim. Cosmochim. Acta*, **220,** 146-157.

Schmieder, M., Kennedy, T., Jourdan, F., Buchner, E. and Reimold, W.U. (2018b) Response to comment on "A high-precision 40Ar/39Ar age for the Nördlinger Ries impact crater, Germany, and implications for the accurate dating of terrestrial impact events" by Schmieder et al. (Geochim. Cosmochim. Acta 220 (2018) 146–157). *Geochim. Cosmochim. Acta*, **238,** 602-605.

Jørgensen, B. and Kasten, S. (2006) Sulfur cycling and methane oxidation. In *Marine geochemistry* (eds H.D. Schulz and M. Zabel). Springer, Berlin, Heidelberg. pp. 271-309.

Shimp, N.F., Leland, H.V. and White, W.A. (1970) Distribution of major, minor, and trace constituents in unconsolidated sediments from southern Lake Michigan.

Environmental geology notes. **032**.

Sinninghe Damsté, J., Ten Haven, H., De Leeuw, J. and Schenck, P. (1986) Organic geochemical studies of a Messinian evaporitic basin, northern Apennines (Italy)—II Isoprenoid and n-alkyl thiophenes and thiolanes. *Org. Geochem.*, **10,** 791-805.

Stüeken, E.E., Tino, C., Arp, G., Jung, D. and Lyons, T.W. (2020) Nitrogen isotope ratios trace high-pH conditions in a terrestrial Mars analog site. *Sci. Adv.*, **6,** eaay3440.

Stöffler, D., Artemieva, N.A., Wünnemann, K., Reimold, W.U., Jacob, J., Hansen, B.K. and Summerson, I.A. (2013) Ries crater and suevite revisited—Observations and modeling Part I: Observations. *Meteorit. Planet. Sci.*, **48,** 515-589.

Talbot, M. (1990) A review of the palaeohydrological interpretation of carbon and oxygen isotopic ratios in primary lacustrine carbonates. *Chem. Geol.: Isotope Geoscience Section*, **80,** 261-279.

Talbot, M. and Kelts, K. (1986) Primary and diagenetic carbonates in the anoxic sediments of Lake Bosumtwi, Ghana. *Geology*, **14,** 912-916.

Talbot, M. and Kelts, K. (1990) Paleolimnological signatures from carbon and oxygen isotopic ratios in carbonates, from organic carbon-rich lacustrine sediments. In *AAPG Memoir 50: Lacustrine Basin Exploration: Case Studies and Modern Analogs* (ed. Katz, B.J.). The American Association of Petroleum Geologists, Tulsa. pp. 99-112.

Taylor, J. and Parkes, R.J. (1983) The cellular fatty acids of the sulphate-reducing bacteria, Desulfobacter sp., Desulfobulbus sp. and Desulfovibrio desulfuricans. *Microbiology*, **129,** 3303-3309.

Teichert, B.M.A., Johnson, J.E., Solomon, E.A., Giosan, L., Rose, K., Kocherla, M., Connolly, E.C. and Torres, M.E. (2014) Composition and origin of authigenic carbonates in the Krishna–Godavari and Mahanadi Basins, eastern continental margin of India. *Mar. Petrol. Geol.*, **58,** 438-460.

Teranes, J.L., McKenzie, J.A., Lotter, A.F. and Sturm, M. (1999) Stable isotope response to lake eutrophication: Calibration of a high-resolution lacustrine sequence from Baldeggersee, Switzerland. *Limnol. Oceanogr.*, **44,** 320-333.

Thiel, V. (2020) Methane Carbon Cycling in the Past: Insights from Hydrocarbon and Lipid Biomarkers. In: *Hydrocarbons, Oils and Lipids: Diversity, Origin, Chemistry and Fate* (Ed H. Wilkes), pp. 781-810. Springer International Publishing, Cham.

Thompson, J.B., Schultze-Lam, S., Beveridge, T.J. and Des Marais, D.J. (1997) Whiting events: Biogenic origin due to the photosynthetic activity of cyanobacterial picoplankton. *Limnol. Oceanogr.*, **42,** 133-141.

Torres, M.E., Hong, W.-L., Solomon, E.A., Milliken, K., Kim, J.-H., Sample, J.C., Teichert, B.M.A. and Wallmann, K. (2020) Silicate weathering in anoxic marine sediment as a requirement for authigenic carbonate burial. *Earth-Sci. Rev.*, **200,** 102960.

Valero-Garcés, B.L., Delgado-Huertas, A., Ratto, N. and Navas, A. (1999) Large 13C enrichment in primary carbonates from Andean Altiplano lakes, northwest Argentina. *Earth Planet. Sci. Lett.*, **171,** 253-266.

Wand, U., Samarkin, V.A., Nitzsche, H.-M. and Hubberten, H.-W. (2006) Biogeochemistry of methane in the permanently ice-covered Lake Untersee, central Dronning Maud Land, East Antarctica. *Limnol. Oceanogr.*, **51,** 1180-1194.

Welander, P.V., Coleman, M.L., Sessions, A.L., Summons, R.E. and Newman, D.K. (2010) Identification of a methylase required for 2-methylhopanoid production and implications for the interpretation of sedimentary hopanes. *Proc. Natl. Acad. Sci. U.S.A.*, **107,** 8537-8542.

Zeng, L., Ruge, D.B., Berger, G., Heck, K., Hölzl, S., Reimer, A., Jung, D. and Arp, G. (2021) Sedimentological and carbonate isotope signatures to identify fluvial processes and catchment changes in a supposed impact ejecta-dammed lake (Miocene, Germany). Sedimentology, *in-press*. https://doi.org/10.1111/sed.12888

Chapter 3. A volcanic ash layer in the Nördlinger Ries impact structure (Miocene, Germany): Indication of crater fill geometry and origins of long-term crater floor sagging

Gernot Arp[1], István Dunkl[1], Dietmar Jung[2], Volker Karius[1], Réka Lukács[3], Lingqi Zeng[1], Andreas Reimer[1], and James W. Head III[4]
[1]Geoscience Center, Georg-August-University, Göttingen, Germany.
[2]Geological Survey, Bavarian Environment Agency, Hof/Saale, Germany.
[3]MTA-ELTE Volcanology Research Group, Budapest, Hungary.
[4]Department of Earth, Environmental and Planetary Sciences, Brown University, Providence, RI, USA 02912

Corresponding author: Gernot Arp (garp@gwdg.de)

Abstract

Since its recognition as an impact structure 60 years ago, no volcanics were anticipated in the circular depression of the 14.8 Ma old Nördlinger Ries. Here, we describe for the first time a volcanic ash-derived clinoptilolite-heulandite-buddingtonite bed within the 330 m thick Miocene lacustrine crater fill. Zircon U-Pb ages of 14.20 ± 0.08 Ma point to the source of the volcanic ash in the Pannonian Basin, 760 km east of the Ries. The diagenetically derived zeolite-feldspar bed occurs in laminated claystones of the Ries soda-lake stage and represents the first unequivocal stratigraphic marker bed in this basin, traceable from marginal surface outcrops to 218 m below surface in the crater center. These relationships demonstrate a deeply bowl-shaped geometry of crater fill sediments, not explainable by sediment compaction and corresponding stratigraphic backstripping alone. Since most of the claystones formed at shallow water depths, the bowl-shaped geometry must reflect 134 +23/-49 m of sagging of the crater floor. We attribute the sagging to compaction and closure of the dilatant macro-porosity of the deeply fractured and brecciated crater floor during basin sedimentation and loading, a process that lasted for more than 0.6 Myr. As a result, the outcrop pattern of the lithostratigraphic crater-fill units in its present erosional plane forms a concentric pattern. Recognition of this volcanic ash stratigraphic marker in the Ries crater provides insights into the temporal and stratigraphic relationships of crater formation and subsidence that have implications for impact-hosted lakes on Earth and Mars.

Plain Language Summary

We describe for the first time a volcanic ash layer from the lake sediment fill of the 15 million year old asteroid impact crater Nördlinger Ries. Radiometric age and trace element characteristics of this ash layer are identical to that of a volcanic field in Hungary, so that the ash reflects a volcanic eruption 760 km east of the Ries basin. Recognition of this ash layer enables its use as a marker bed. The ash layer can be traced from surface outcrops to 218 m depth in drillings. This indicates that the strata are significantly inclined toward the crater center. Calculations of sediment compaction by further sediment load and burial only partially explain the observed deeply bowl-shaped geometry. We attribute the additional sagging to the subsidence of the crater floor substrate, formed of rocks highly shattered by the impact event. Both effects cause a concentric pattern of outcropping strata in the partially

eroded crater fill. The presence of the ash layer and its use to help disentangle the source and timing of subsidence (due to compaction of lake sediments, and closure of deeper, impact-induced fractures), has important implications for lakes formed in impact craters on Earth and Mars.

1 Introduction

The stratigraphy and sedimentary environments of impact crater interior sedimentary fill form valuable climate archives on Earth, in particular those in young impact structures such as Bosumtwi and El'gygytgyn. Only a few terrestrial impact structures with preserved sedimentary fill are known. These are primarily present-day crater lakes such as Pingualuit, Bosumtwi, El'gygytgyn, and Tswaing (Talbot and Johannessen, 1992; Partridge et al., 1993; Shanahan et al., 2009; Guyard et al., 2011; Melles et al., 2012). These crater fill deposits precisely record Quaternary climate changes, such as aridification or glacial cycles, as revealed by geochemistry, stable isotopes, and palynomorphs (Talbot and Johannessen, 1992; Shanahan et al., 2009; Melles et al., 2012). Fossil examples, however, are commonly buried (Boltysh: Gurov et al., 2006; Chesapeake Bay: Gohn et al., 2008) or significantly eroded (Steinheim: Reiff, 1977; Haughton: Osinski et al., 2005). In a similar manner, lacustrine crater fill deposits on Mars potentially form archives of the climatic development throughout Mars history, and particularly during the Noachian-Hesperian climate transition, when Mars changed from at least episodically warm to the current extremely cold and arid conditions (for review see e.g. Craddock and Howard, 2002; Irwin et al., 2005; Fassett and Head, 2008ab; Carr and Head, 2010ab; Milliken et al., 2010; Grotzinger and Milliken, 2012; Goudge et al., 2015, 2016). We report here on the discovery and documentation of a volcanic-ash derived marker bed in the Nördlinger Ries impact structure that we use to outline the nature of the subsidence history of the crater lake floor, and the origin and timing of the observed bowl-shaped crater fill geometry with significantly inclined strata. We explore some implications for the history of other crater lakes on Earth and Mars.

2 The Nördlinger Ries Structure and Stratigraphy

The Nördlinger Ries is a 14.808 ± 0.038 Ma old (Middle Miocene) (Schmieder et al., 2018a; for discussion see Rocholl et al., 2018ab and Schmieder et al., 2018b), partially exhumed impact crater, structurally subdivided into a central crater, an inner ring, and a marginal block zone delineated by the tectonic crater rim (**Figure 3.1**; Pohl et al. 1977). The impact occurred in volatile-rich target rocks (Osinski, 2004, 2006; Artemieva et al., 2013). Two ejecta blankets are distinguished: 1) the Bunte Breccia (showing a rampart structure; Sturm et al., 2013) and 2) the overlying impact-melt bearing suevite (Hüttner, 1969; von Engelhardt, 1997; Stöffler et al., 2013; Siegert et al., 2017, Siegert and Hecht, 2019). By the end of the Miocene (~5.33 Ma), the Ries crater was completely covered by sediments (Schröder and Dehm, 1950), and subsequently, Plio- to Pleistocene erosion removed about 100 m of sediment within the crater as well as parts of the ejecta blankets (Hüttner, 1969; Wolf, 1977). The sedimentary fill preserved today consists of four lithostratigraphic units (Jankowski, 1977a, 1981):

(i) The basal member: Consists of conglomerates and sandstones derived from suevite and crystalline basement rocks, with intercalated playa deposits.

(ii) The laminite member: Comprised of laminated marls and bituminous shales, with authigenic silicates (analcime, clinoptilolite) and abundant slumping structures.

(iii) The marl member: Characterized by stratified calcareous claystones and poorly bedded dolomitic marls. These are partially bioturbated and contain analcime only sporadically.

(iv) The clay member: The youngest preserved unit consists of an alternation of clays, marls and limestones, with intercalated carbonaceous clays, lignites, and gypsum-pseudomorph-bearing limestones.

While these units can be recognized in drill cores of the central crater basin, sections in marginal positions (short drill cores, rotary drillings, temporary exposures) are more difficult

to assign to specific units. Therefore, the surface outcrop pattern of these units, the basin-center to basin-margin correlations, and consequently, the crater fill geometry, has remained poorly constrained and a matter of controversy in the literature (Wolff and Füchtbauer, 1976; Jankowski, 1981; Schauderna, 1983; Arp et al., 2013a). The volcanic-ash derived marker bed that we describe here was discovered in a temporary exposure during the construction of a state road B 25 underpass in the western Ries basin near Wallerstein (**Figure 3.1**; Supporting Information Text S1). Subsequently, the same bed was found in a percussion drill core at northern Ries basin margin (Ehingen-SE), and in three drill cores from the basin center (**Figure 3.1**; Supporting Information Text S1). We outline the characteristics and distribution of this volcanic-ash-deposited marker bed and use these data to help constrain the filling and subsidence history of the Nördlinger Ries crater lake.
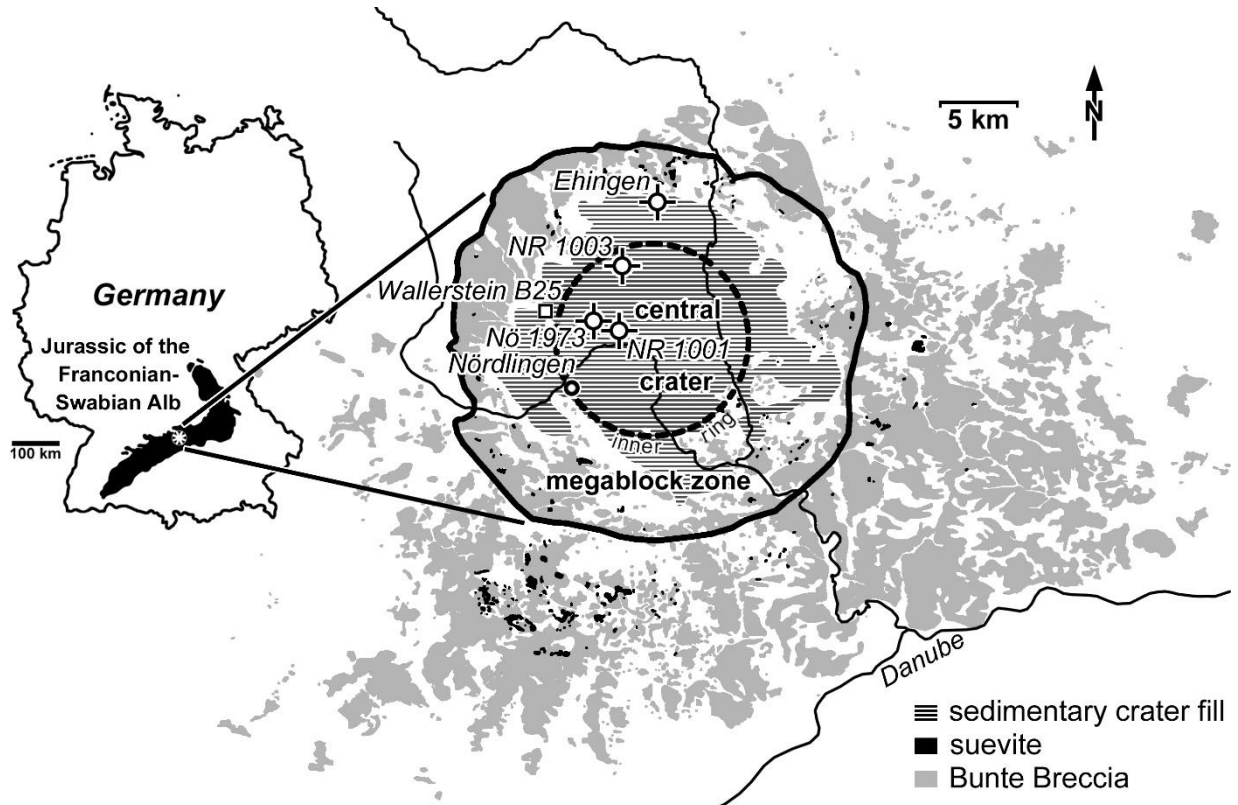
Figure 3.1 Location of the outcrop Wallerstein B25, the investigated drillings NR 1001, NR 1003, Nö 1973, Ehingen, and major structural elements of the Ries impact structure
(based on Pohl et al., 1977; Ernstson, 1974; Hüttner and Schmidt-Kaler, 1999).

3 Materials and Methods

Five samples of the outcrop Wallerstein B25, three samples of the drill cores Nördlinger Ries 1001, 1003 and Nördlingen 1973, 22 samples of percussion drill core Ehingen-SE, one sample from Ehinger Bach (**Figure 3.1**), and five reference samples from the Northern Alpine Foreland Basin and the Leinetal Graben have been investigated (Supporting Information Text S2 and Dataset S1).

The mineralogical composition (Supporting Information Text S2) was analyzed by powder X-ray diffraction using a Philips PW 1800 diffractometer operating at 45 kV and 40 mA with monochromated Cu Kα radiation. The range 4–70 °2θ was scanned with a step width of 0.02 °2θ. The counting time was 3 s per step. Mineral identification was carried out using the X'Pert High-Score Plus software (PANalytical). Quantification of mineral phases was performed by Rietveld calculations using the program AutoQuant.

The elemental composition of the samples (Supporting Information Dataset S1) was determined by X-ray fluorescence analysis (PANalytical Axios Advanced XRF spectrometer fitted with a 4 kW Rh anode SSTmAx X-ray tube) on glass fusion disks. Samples with high S and C_{org} contents were previously heated at 650 °C for 3 h in a furnace. Total carbon, nitrogen, and sulfur were analyzed with a Euro EA 3000 Elemental Analyser (Hekatech, Wegberg, Germany) applying BBOT (2.5-Bis (5-tert-benzoxazol-2-yl) thiophene) and atropine sulfate monohydrate (IVA Analysetechnik, Meerbusch, Germany) as reference materials. Organic and inorganic carbon content was separated using a gradual heating method on a LECO RC612 multi-phase carbon analyzer (Leco, St Joseph, MI, USA), calibrated against LECO carbon standards (1.00, 4.98, and 12.00 % C).

Laser ablation ICP-MS U-Pb dating of the volcanogenic zircon crystals was performed in the GÖochron Laboratories of University of Göttingen. The details of the laboratory procedure is in the Supporting Information Text S3 and Dataset S2.

Modelling of compaction and stratigraphic backstripping (Supporting Information Dataset S3 and S4) was calculated on basis of the Athy equation (Athy, 1930; Sclater and Christie, 1980), modified by Maillart (1989):

$$\phi_z = \phi_{res} + (\phi_0 - \phi_{res})e^{-\alpha z^\beta}$$

with ϕ_0 = porosity at time of deposition, ϕ_z = porosity at burial depth z [m], ϕ_{res} = residual porosity, and α and β empirical compaction coefficients. The reason for using the modified equation is that the Maillart equation introduces a "residual porosity" f_{res} to account for remaining porosities at greater depths (see e.g. Einsele, 2000; Revil et al., 2002), and an additional coefficient b, which is required for a fitting to measured porosities at near surface depth (specifically during early dewatering of laminites). The curve for pelitic sediments (**Figure 3.2**) was aligned to measured porosities in laminites of the drill core Nördlingen 1973 (Jankowski, 1977a) and porosities in surface sediments of Lake Van (Supporting Information Dataset S3; Landmann et al., 1996 and Reimer et al., 2009) by modifying the empirical compaction coefficients α and β. The varved Lake Van sediments (Landmann et al., 1996; Stockhecke et al., 2014) are similar to the laminites of the Ries (Weber, 1941; Bolten et al., 1976; Jankowski, 1981) with respect to carbonate contents and lamination (alternation of light carbonate-rich, and dark C_{org}- and clay-rich laminae; similar laminae thickness). As a measure for uncertainty, the compaction was also calculated for ±10% initial porosity (at z = 0). The compaction curve for sandstones (**Figure 3.2**) was calculated in the same way, with an initial porosity of 0.60, i.e., intermediate between 0.45 for pure sand (Beard & Weyl 1973) and the very high value of 0.75 as used e.g. in Kominz and Pekar (2001). The ratio of present-day ϕ_z and ϕ_z at the time of zeolite bed deposition was used for stratigraphic backstripping of the sediment column below the zeolite bed, subdivided in 1 m thick intervals. The surface distribution pattern of lithofacies units was compiled from percussion corings, diploma thesis mapping, unpublished and published drilling reports, and data from the drill database BIS Bayern (Supporting Information Dataset S5).
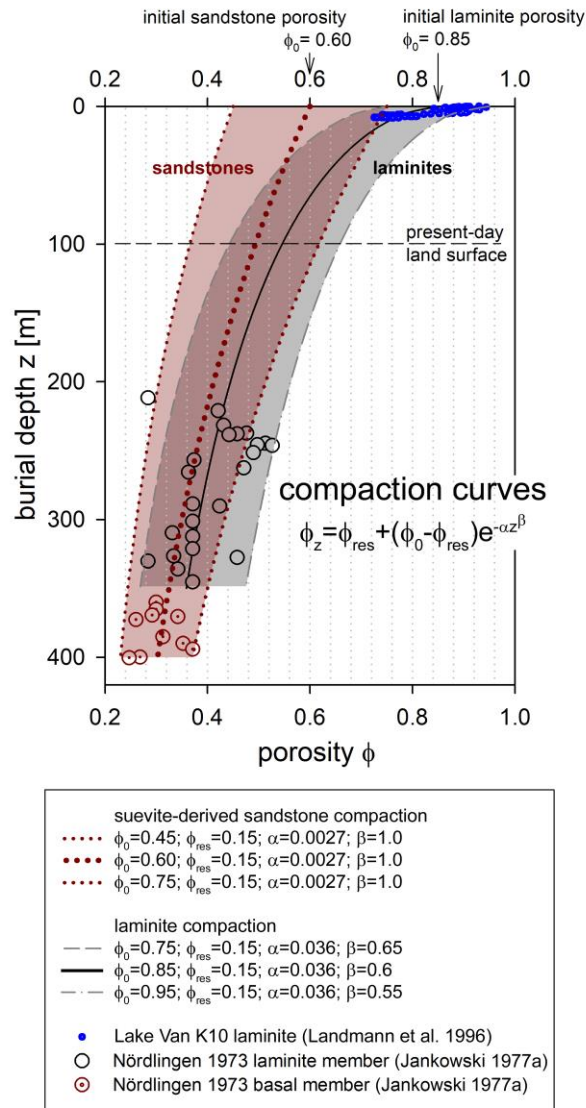
Figure 3.2 Compaction curves used in this study for back-stripping the position of the volcanic-ash-derived zeolite-feldspar bed in the Ries Crater Lake.
For calibration, porosity data of Jankowski (1977a) and Landmann et al. (1996) were used. For details of calculations see Supporting Information Dataset S3.

4 Results

4.1 Composition, age and source of the volcanic ash

Construction of the Wallerstein B25 state road underpass in the western Ries basin (**Figure 3.1**) exposed, at 440 m a.s.l., a 14 cm thick white porous and light zeolite bed intercalated between aragonite-bearing laminites. Quantitative XRD analyses demonstrate that the zeolite bed largely consists of clinoptilolite (63 wt%) and heulandite (34 wt%), with only traces of other minerals (quartz). The zeolite bed shows a 2 cm thick graded basal layer, with clinoptilolite (45 wt%), heulandite (29 wt%), smectite (8 wt%), plagioclase, quartz, muscovite and biotite. Allanite and zircon were found in the heavy mineral fraction. The black, idiomorphic biotite crystals display a grain-size gradation within the basal layer (**Figure 3.3**): the majority of the bed is massive with only a faint stratification at its top. Geochemically, the zeolite bed is very rich in SiO_2 and shows high Ba contents (**Table 3.1**). The same zeolite bed has been detected by percussion coring at the northern margin of the central basin, SE of Ehingen (**Figure 3.1**). A clinoptilolite-heulandite bed was previously mentioned at this locality from material excavated in a construction pit (**Wolff, 1974**). Our re-

investigation at this locality revealed the presence of a 15 cm thick clinoptilolite-heulandite bed at 4 m depth, i.e. at 424 m a.s.l., intercalated between aragonite-bearing laminites. Here, the aragonitic component could be identified as being formed by elongated fecal pellets (80-90 μm diameter; 400-650 μm length), probably produced by the brine shrimp *Artemia* (Jankowski, 1981). The mineralogical and geochemical composition of the bed, including a graded base with biotite crystals, is identical to the clinoptilolite-heulandite bed at the Wallerstein B25 underpass (**Table 3.1**).

Pink, euhedral, intact zircon crystals of 125 to 275 μm in size, extracted from the zeolite bed at Wallerstein B 25, revealed a 14.20 ± 0.08 Ma concordant U-Pb age (**Table 3.2**). This age is undistinguishable from that of the Harsány ignimbrite, a rhyolithic tuff of the Bükkalja Volcanic Field in Hungary (Lukács et al., 2015, 2018) and a bentonite bed located 53 km southeast of the Ries crater in the North Alpine Foreland Basin (**Table 3.2**; Supporting Information Text S3 and Dataset S2). In contrast, all other Cenozoic volcanic fields in Europe (Hegau and Urach, Kaiserstuhl, Eifel, Eger Rift, Vogelsberg and Hessian Depression, Massif Central) differ in chemistry and age (e.g., Wörner et al., 1986; Wedepohl, 2000; for review see Lustrino and Wilson, 2007) from the investigated samples. Therefore, the Ries zeolite bed is interpreted to be a distal volcanic ash from the Bükkalja Volcanic Field in the Pannonian Basin, 760 km east of the Nördlinger Ries crater, and equivalent to one of the bentonite horizons in the Northern Alpine Foreland Basin (NAFB), specifically that of Unterzell (**Table 3.1**).

Previous geochemical analysis by Unger et al. (1990) suggested that volcanism in the Pannonian Basin was the source of the NAFB bentonites, and also recently Lukács et al. (2018) suggested a correlation with the Bükkalja Volcanic Field pyroclastics based on U-Pb zircon data. However, none of the recently dated NAFB bentonites (U-Pb dating by CA-ID-TIMS; Rocholl et al., 2017) revealed an identical age to the Unterzell bentonite investigated in this paper (U-Pb dating by LA-ICP-MS; **Table 3.2**), certainly reflecting the higher accuracy of the chemical abrasion (CA-ID-TIMS) method.
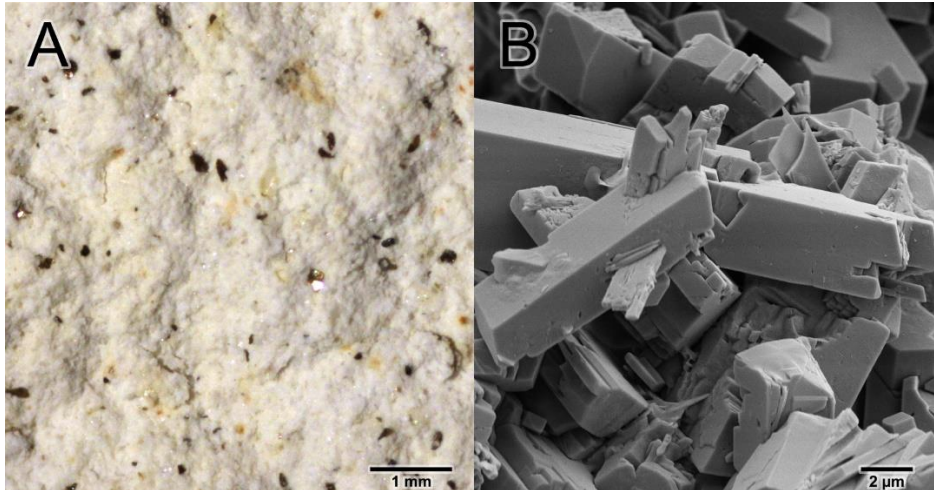
Figure 3.3 Microscopic and SEM-backscattered images of the zeolites.
(A) Basal part of the volcanic-ash derived zeolite bed at Wallerstein B 25, showing
black biotite crystals within a zeolite matrix. (B) SEM view of the same sample
showing monoclinic clinoptilolite-heulandite crystals.

Figure 3.4 Volcanic-ash derived buddingtonite bed (arrow) in the laminite member at
192.61-192.66 m core depth, drilling NR 1003.

Table 3.1 Mineralogical and geochemical composition of the volcanic-ash-derived zeolite-feldspar bed in the Miocene Ries crater lake sediments and reference samples. n.a.: not analyzed, b.d.l.: below detection limit. * average bulk composition of pumice clasts, data published in Lukács et al. (2007, 2015). **mineral name abbreviations according to Whitney & Evans (2010), except for Buddingtonite (Bud)

location	sample number	depth [m bs]	altitude [m asl]	mineral phases ** XRD [semiquant. wt%]	C_{org} [wt%]	C_{carb} [wt%]	N_{tot} [wt%]	S_{tot} [wt%]	LOI [wt%]	sum oxides [wt%]	SiO_2 [wt%]	TiO_2 [wt%]	Al_2O_3 [wt%]	MnO [wt%]	MgO [wt%]	CaO [wt%]	Na_2O [wt%]	K_2O [wt%]	P_2O_5 [wt%]	Fe_2O_3 [wt%]	Ba (ppm)	Sr (ppm)
Wallerstein B25 underpass 2015	Wal-B25 C	0.83	439.2	Cpt (52), Hul (43), Mag (3), Qz (2)	0.02	<0.003	0.011	0.002	16.0	82.8	63.6	0.14	12.84	0.00	1.22	3.65	0.47	0.56	0.01	0.35	9164	2475
Wallerstein B25 underpass 2015	Wal-B25 B	0.84	439.2	Cpt (57), Hul (38), Mag (3), Qz (1)	0.02	<0.003	0.010	0.002	15.9	82.9	63.9	0.17	12.71	0.00	1.18	3.56	0.44	0.69	0.01	0.22	10272	2033
Wallerstein B25 underpass 2015	Wal-B25 A	0.94	439.1	Cpt (45), Hul (29), Pl (9), Sme (8), Bt (2)	0.03	<0.003	0.009	0.256	15.8	83.1	60.4	0.20	14.14	0.01	1.23	3.48	0.91	0.78	0.02	2.01	7246	2968
Ehingen-SE percussion drill core 2015	Eh 11	4.01	424.0	Cpt (54), Hul (20), Gth (16), Ilt (6)	0.09	0.007	0.010	0.028	29.4	69.7	44.4	0.20	10.89	0.02	0.78	2.23	0.17	1.11	0.03	9.83	6972	1755
Ehingen-SE percussion drill core 2015	Eh 12	4.08	423.9	Cpt (57), Hul (30), Gth (4), Ilt (4)	0.03	0.007	0.009	0.008	14.8	84.2	61.4	0.20	14.96	0.01	1.14	3.2	0.34	1.48	0.03	1.44	6743	2778
Ehingen-SE percussion drill core 2015	Eh 13	4.14	423.9	Cpt (31), Hul (17), Ilt (16), Sme (14)	0.32	0.65	0.034	0.260	16.3	82.1	51.9	0.63	16.11	0.04	1.47	4.93	0.49	1.84	0.06	4.66	13733	1835
Ehingen-SE percussion drill core 2015	Eh 14	4.15	423.9	n.a.	0.03	0.01	0.008	0.463	15.6	80.0	53.5	1.11	18.99	0.01	0.73	2.41	0.76	1.30	0.03	1.19	41605	2675
Ehinger Bach 1969 (sample Wolff)	EhB	0.0	424.0	Cpt (60), Hul (35), Mag (3), Qz (2)	0.10	0.16	0.024	0.005	17.3	81.6	59.9	0.15	13.44	0.00	1.06	3.91	0.36	1.50	0.03	1.29	8803	1906
drill core Nördlingen 1973	Noe1973-71	218.5	208.6	Bud, Kfs, Ab, Qz	1.57	0.06	2.642	0.040	10.4	89.5	60.3	0.03	17.38	0.02	0.80	0.84	0.53	5.75	0.28	3.65	135	372
drill core Nördlinger Ries 1001	Noe1001-1	206.7	213.4	Bud, Kfs, Ab, Qz	1.57	<0.003	1.970	0.139	8.7	91.3	60.2	0.03	17.19	0.02	0.87	0.73	0.44	7.85	0.35	3.64	144	464
drill core Nördlinger Ries 1003	Noe1003-82	192.7	236.4	Bud, Kfs, Ab	0.37	<0.003	2.460	0.211	25.1	74.8	51.5	0.01	14.77	0.02	0.10	0.13	0.23	6.69	0.14	1.24	160	42
bentonite Ammersberg, Northern Alpine Foreland Basin	AM2	8.0	485	n.a.	0.01	0.01	0.008	<0.002	18.9	81.1	50.9	0.29	19.60	0.02	2.72	1.48	0.17	0.98	0.05	4.87	168	43
bentonite Unterzell, Northern Alpine Foreland Basin	UZ1	7.0	499	n.a.	0.01	0.01	0.011	<0.002	17.6	82.4	56.0	0.31	15.84	0.03	3.55	1.56	0.15	1.34	0.05	3.56	201	60
bentonite Unterzell, Northern Alpine Foreland Basin	UZ2	7.0	499	n.a.	0.01	0.02	0.007	<0.002	19.9	80.0	53.0	0.21	16.98	0.02	3.11	1.43	0.1	0.73	0.03	4.44	150	48
Laacher See Tuff, Bringberg, 14 km S of Göttingen	LST	0.0	193	Qz (47), Clc (27), Bt (19), Mag (6)	0.27	<0.003	0.027	0.008	13.1	86.8	50.6	0.30	21.76	0.47	0.49	1.02	5.47	3.75	0.05	2.85	1353	88
Tibolddaróc, Harsány Ignimbrit Unit, layer A *	Td-A=DX 46			n.a.	n.a.	n.a.	n.a.	n.a.	3.6	97.5	73.8	0.15	12.99	0.04	0.15	1.35	2.72	4.75	0.04	1.48	901	98

Table 3.2 Single zircon U-Pb ages of Ries crater volcanic-ash-derived zeolite bed, its

equivalent in the Northern Alpine Foreland Basin, and its source area in the Pannonian Basin.
* passing outlier tests; without pre-Miocene xenocrystals; ** data with less than 5% discordance.

locality	Ries Crater	Northern Alpine Foreland Basin	Pannonian Basin
	Wallerstein B25	Unterzell	Harsány ignimbrite
sample ID	DX-73	DX-74	DX-46
n_{total}	65	36	120
n_{OLT}*	62	27	115
$n_{conc95-105}$**	45	13	39
Concordance age [Ma]	14.20	14.16	14.27
± 2s	0.08	0.13	0.09
MSWD	1.3	1.4	1.2

4.2 Stratigraphic correlation from surface to depth

A re-inspection of drill cores NR 1001, NR 1003 and Nördlingen 1973 revealed a volcanic ash-derived bed at 192-218 m core depth, within the deeper part of the laminite member (**Figure 3.4**). Similar to its equivalents in the surface outcrops, the bed is intercalated within laminated organic-rich calcareous mudstones characterized by abundant aragonitic brine shrimp fecal pellets, typical of the analcime submember (Jankowski, 1981). However, in the drill samples the bed consists of K-NH$_4$-feldspar (buddingtonite; **Table 3.1**), a diagenetic successor derived from zeolites during burial and microbial ammonification in organic-rich sediments (Ramseyer et al., 1993). Geochemically, the bed is SiO$_2$-rich, as is the zeolite precursor, but contains K$^+$ and NH$_4^+$ instead of Ba^{2+} (**Table 3.1**). Based on the correlation of this volcanic-ash-derived silicate bed from marginal surface outcrops at 440 – 424 m a.s.l. to basin center drillings at 236 – 206 m a.s.l., a bowl-shaped crater fill geometry becomes evident (**Figure 3.5**), with the laminite member cropping out at the central basin margin, and younger crater fill units confined to drilling samples from the middle of the central basin.
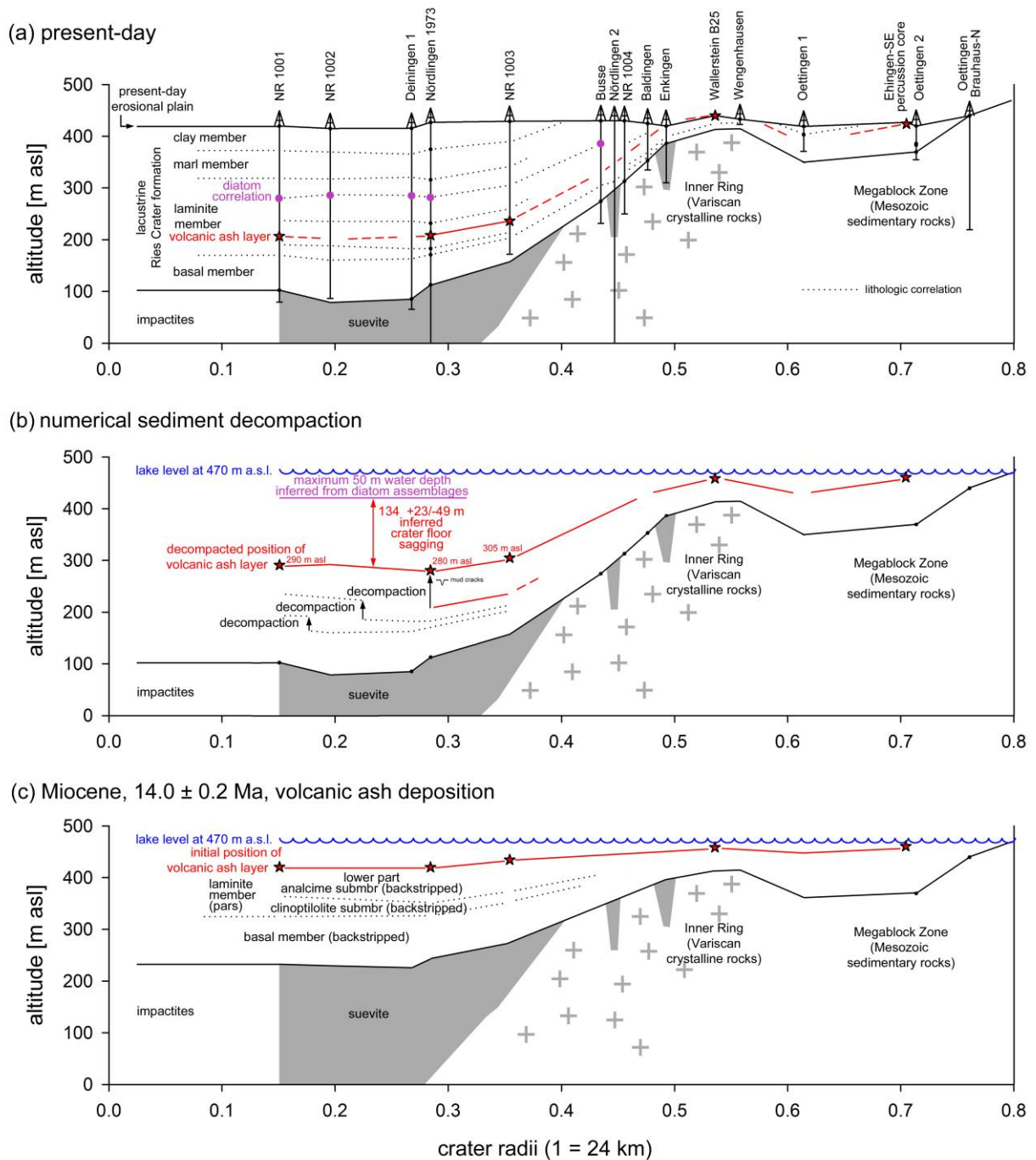
Figure 3.5 Schematic section through the Ries impact basin, with drilling locations arranged according to distance from crater center.

4.3 Concentric outcrop pattern

The compilation and interpretation of drill data and exposures demonstrate that the surface outcrop of sedimentary crater fill members can be traced in a concentric pattern (**Figure 3.6**, Supporting Information Dataset S5):

(i) The basal member is readily identifiable in drilling samples, although the temporal relation to basin margin conglomerates and sandstones remains unclear. However, the latter commonly predate bioherms and travertines of later lake stages, and are slightly inclined towards the basin center. Therefore, they largely correspond to an early phase of basin development.

(ii) The laminite member crops out in a broad fringe at the periphery of the central basin and in subbasins of the megablock zone. Temporary surface exposures show a 3-10° inclination toward the basin center, with only one slump-related exception (**Figure 3.6**, Supporting Information Dataset S5). Bituminous shales intercalated in the basal parts of this member (i.e., at more than 245 m core depth in the basin center), crop out at the outermost margin of the central Ries plain (localities Wengenhausen, Nördlingen-Freibad, Goldberg, Ehingen). Basin-margin equivalents of the laminite member consist of early algal bioherms, and tufa mounds ("travertines"), which formed predominantly subaqueously in a soda lake environment, as determined from the characteristic sickle-cell-like shrinkage void fabric (Arp et al., 1998; Arp et al., 2010). Similarly, specific biogenic components in the tufa mounds, such as brine shrimp fecal pellets and dragon fly larvae, are known only from intervals of the laminite member (Dehm et al., 1977).

 (iii) The marl member shows only a limited number of unequivocal surface outcrops (Hollaus, 1969) located at northern-central Ries. However, drillings demonstrate that this member can be traced as an approximately 500 m-wide circular strip in the central basin. Some of the basin-margin algal bioherms (e.g. at Adlersberg; Arp et al. 2013) may be equivalent to this unit.

(iv) Drilling samples and temporary exposures demonstrate that the clay member is restricted to the inner part of central Ries plain (Deffner and Fraas, 1877; Kranz, 1952). Basin margin equivalents are probably late algal bioherms (e.g. at Hainsfarth; Arp et al. 2013) and relict occurrences of oolites and freshwater limestones at hills near the crater rim.
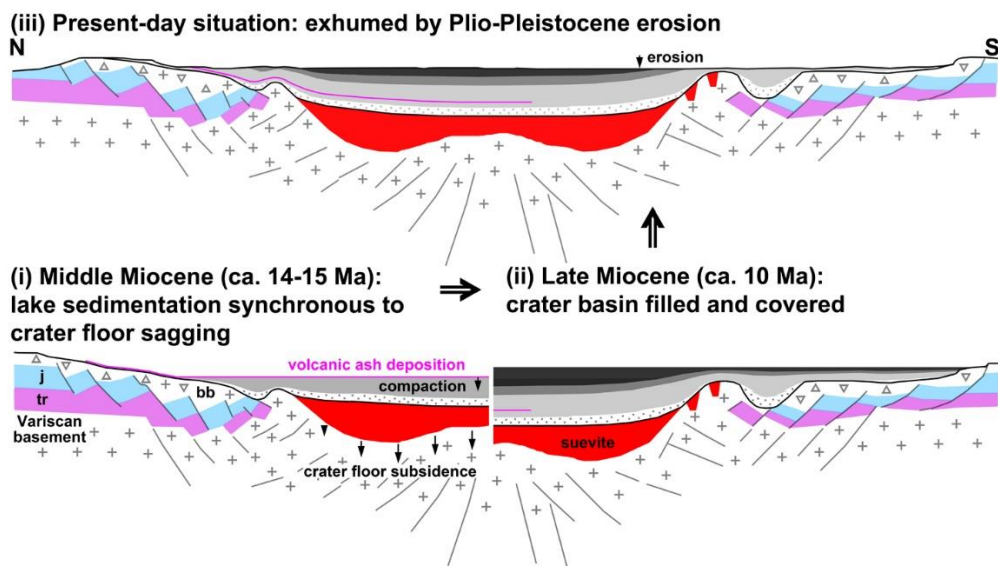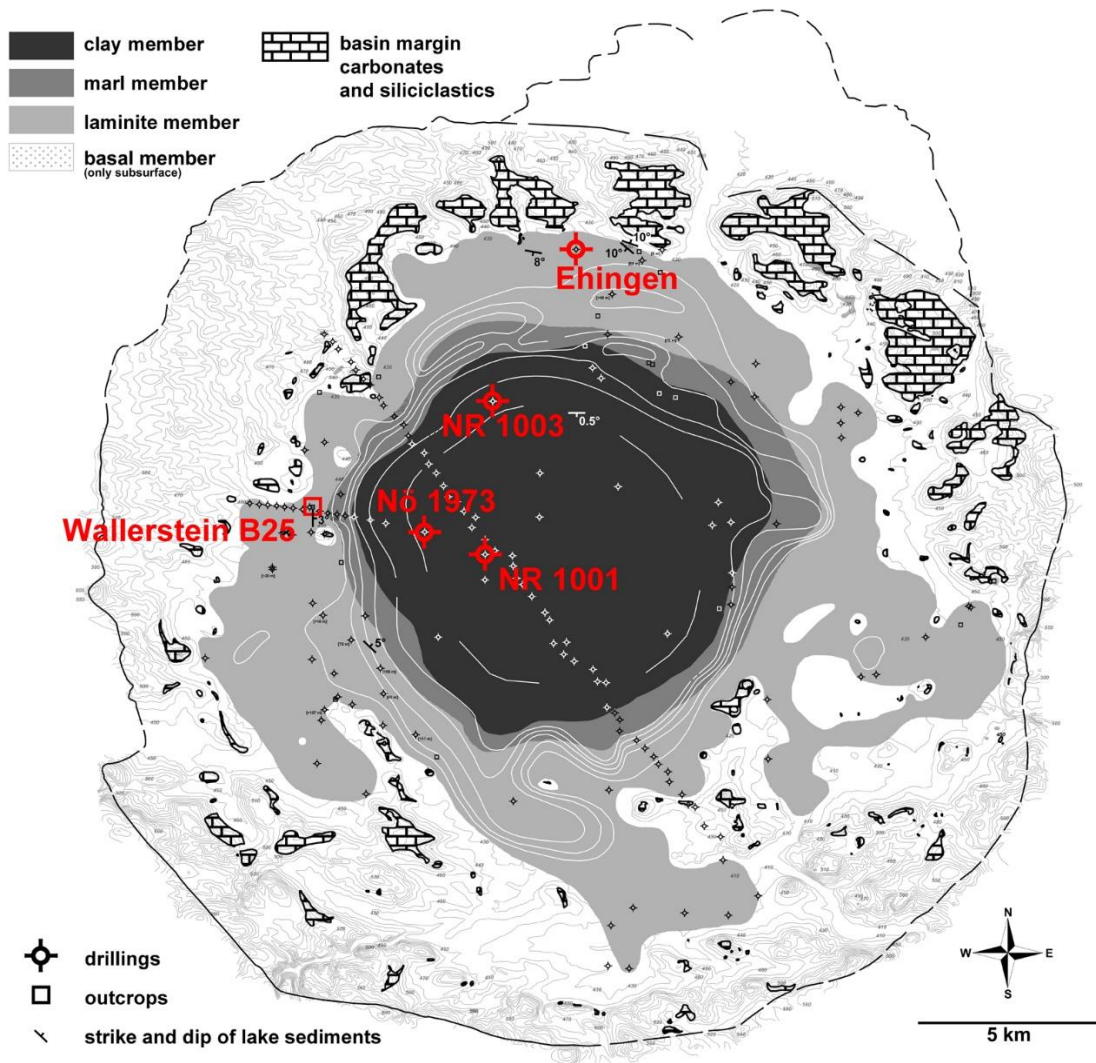
Figure 3.6 Geological map of the Ries impact crater fill showing the concentric outcrop of major lithofacies units and reconstruction of the evolution of the crater fill geometry.
Miocene sediment thickness contour lines according to Ernstson (1974), with modifications according to drill data. tr: Triassic, j: Jurassic, bb: Bunte breccia.

5 Discussion

5.1. Water depth, compaction and crater floor sagging

Using the volcanic ash layer as an unequivocal temporal marker bed, the brine-shrimp-pellet-rich lower parts of the laminite member can be traced from 177-227 m a.s.l. (i.e., 200-250 m core depth) to the surface outcrop Wallerstein B 25 at 440 m a.s.l. without any lateral change in facies. A further correlation with the soda lake stage tufa mounds at the crystalline ring (Wallerstein mound with *Artemia*-pellet-rich interval at 465-470 m a.s.l.) results in a present-day height difference of 248-293 m.

However, the calculated compaction of coarse-grained siliciclastics (suevite-derived sandstones) and laminites below the ash layer can only account for 73 +49/-23 m subsidence. Corresponding stratigraphic backstripping of the ash layer (from today 209 m a.s.l. to initially 282 +49/-23 m a.s.l.) would result in a water depth of 184 +23/-49 m, i.e. the difference between the littoral equivalents (here: Wallerstein mound basal beds at 465 m a.s.l.) and the decompacted position of the buddingtonite bed (281 +49/-23 m a.s.l.) (**Figure 3.5**; Supporting Information Dataset S3). This high water depth, however, is inconsistent with previous sedimentological and paleontological interpretations suggesting a continuously shallow Ries lake of less than 10 m (Weber, 1941: p. 145; von der Brelie, 1977; Gall and Jung, 1979). Only for the uppermost laminite/lowermost marl member Schauderna (1983: p.164) inferred intermittent maximum depths greater than 50 m. A re-evaluation of arguments indeed points to water depths generally shallower than 50 m for the volcanic-ash-containing laminate unit, as follows:

(i) Mud cracks were observed at the top of the basal member (272.55 m core depth: Jankowski, 1981: p. 56) and within the laminite member (233.1 m and 136.8 m core depth: Gall et al., 1974). These observations were interpreted as evidence for temporary subaerial exposure, and therefore shallow water depths. Our own observations in the NR 1003 core, however, revealed mud cracks only within the basal member (at 243.15, 242.95 and 242.7 m depth), and subaerial exposure with associated brecciation not until deposition of the marl member (less than 87 m core depth), suggesting a permanent water body at the time of the volcanic ash deposition.

(ii) Based on diatom associations, Schauderna (1983) suggested shallow water depths for most parts of the Nördlingen 1973 drill core. A closer look at the data of the volcanic-ash-containing analcime submember, however, shows that only few diatom assemblages are present, and all of them are dominated by planktonic species (samples at 205.4 and 218.4 m core depth with 95-97% *Stephanodiscus binderanus*). While Schauderna (1983) considers the diatom-poor laminites as shallow water deposits emplaced during periods of increased salinity, the intercalated planktonic assemblages are interpreted to represent temporary highstands, with low-salinity waters of possibly 50 m depths.

(iii) Stable isotope analysis point to successive evaporation of the initial freshwater lake to a salt lake, with a salinity maximum during the laminite member (Rothe and Hoefs, 1977; Füchtbauer et al., 1977; Jankowski, 1981).

(iv) Likewise, the biomarker palaeosalinity proxies MTTC and ITR suggest that the volcanic ash bearing laminite sequence was deposited under mesohaline to hypersaline conditions (Barakat and Rullkötter, 1997).

While the data from points (i) and (ii) indicate a permanent water body with maximum depths of about 50 m, the high salinities inferred from points (iii) isotopes, and (iv) biomarkers, exclude higher water depths (of 180-190 m). Hence, we conclude that the observed bowl-shaped geometry of the sedimentary deposit fill can only be explained by an additional, significant subsidence of the crater floor, i.e., a longer-term crater-floor sagging and subsidence.

Notably, prior to the identification of the Nördlinger Ries as an impact structure by Shoemaker and Chao (1961), several authors speculated on the possibility of syn- to post-sedimentary crater floor subsidence (Koken, 1902; Weber, 1941; Dorn, 1940, 1942a, b, c, 1943; and finally, including, Walter Kranz (Kranz, 1952: "settling of blasting debris"), i.e. the

advocate of the phreatomagmatic "blast theory" for the Ries formation; Kranz, 1911, 1912). In a similar manner, significant crater floor subsidence has been suggested for the 22 Ma Haughton impact structure, based on a 3° to 3.5° inward dip of post-impact lacustrine strata (Hickey et al., 1988).

With respect to the duration of the crater floor sagging, an estimate can be made on the basis of the alternation of normal and reverse polarity sediment intervals measured at the Nördlingen 1973 drill core (Pohl, 1977): The volcanic ash layer (14.20 ± 0.08 Ma) corresponds to magnetochron C5ADn (14.609-14.163 Ma; ATNTS 2012: Gradstein et al., 2012). Given that, the following laminated sediments between 180 and 130 m core depth, with reverse polarity, correspond to C5ACr (14.163-14.070 Ma), while top parts of laminite member (between 130 and 111 m), the marl (111-52 m) and the clay member (52-0 m) correspond to C5ACn (14.070-13.739 Ma) and possibly even younger magnetochrons. Geologic evidence indicates that the clay member (i.e.,the most recent lake sediments) accumulated on an almost stabilized crater floor, with its position and geometry explainable solely by conventional sediment compaction alone (exemplified for the *Cypridopsis* bed of the clay member: see Supporting Information Dataset 3). This implies that that the crater floor sagging did not stop until several 100 ka after the volcanic ash deposition.

5.2 Synthesis of evidence for timing and magnitude of Nördlinger Ries crater sedimentary floor filling, sagging and subsidence

In the case of the Ries crater, the impact occurred ~14.8 Ma ago, in the Middle Miocene, in a water-saturated landscape with water-containing target rocks and moist ambient atmospheric conditions. Interior crater sedimentation began with the immediate collapse of the impact vapor cloud, inducing catastrophic sedimentation in the crater interior and formation of the graded unit (Füchtbauer et al., 1977; Jankowski, 1977b; Stöffler et al., 2013). This was followed by a longer-term stepwise flooding due to 1) groundwater seepage (travertines and tufa mounds), and 2) fluvial tributaries from the rim and walls of the crater, together leading to a period of sedimentation lasting 1-2 Ma. At ~14.2 Ma, during the period of laminite unit deposition, the 14 cm thick volcanic ash layer was emplaced when the crater lake water depth was less than ~50 meters (**Figure 3.5**).

Taken together, the comparison of 1) the water depth at the time of ash emplacement, 2) the thickness of sub-ash lake sediments, 3) the estimated amount of lake sediment compaction, and 4) post-ash emplacement subsidence, show that a significant amount of non-sediment-compaction-related basin subsidence occurred during an approximately 0.6 Myr-long period following crater formation and continued for several 100 kyr after the ash emplacement (**Figures 5, 6**). We now turn to an examination of the causative factors that might be responsible for the documented 134 +23/-49 meter crater floor subsidence unaccounted for by sediment compaction.

5.3 Causes of impact crater post-formation floor subsidence and implications for Ries Crater

Detailed analysis of Earth and planetary impact craters and modeling of crater formation and evolution (Gault and Heitowitz, 1963; Gault et al.,1968; Melosh, 1989; Stöffler et al., 2006) have shown that there are several sources of positive and negative volume changes in the crater interior that can lead to vertical modification of the crater floor elevation (e.g., sagging, subsidence and uplift). In the very short-term modification-stage of the cratering event, the transient crater cavity undergoes collapse; in smaller craters, rim crest/crater wall landsliding and floor uplift occur, and in larger craters, listric faulting, wall terracing, central peak formation, and general crater floor uplift and flattening are seen (see, e.g., Kenkmann et al., 2013). Additional contributions to crater floor shallowing include impact ejecta fallback and flow of impact melt down the crater wall and terraces, ponding on the crater floor (Hawke & Head, 1977; Melosh, 1989). Following this initial *rapid modification stage of the cratering event* itself, there are five types of processes that can cause additional changes in crater floor elevation.

1) *Thermal contraction processes*: Heat is imparted to the crater interior through the transfer of the kinetic energy of the impactor to the materials of the substrate, causing an array of effects ranging from mineral deformation to bulk impact melting. The magnitude of these processes scale with the velocity and mass of the projectile. Basin-scale impacts on the Moon such as ~930-km-diameter Orientale basin are characterized by huge, kilometers-deep impact melt seas in basin interiors. Their cooling and solidification can involve ~10% contraction, and extend for many hundreds of thousands of years, and cause many hundreds of meters of floor subsidence (e.g., Vaughan et al., 2013; Vaughan and Head, 2014).

The relatively small size of the Ries crater and the dispersal of impact melted material in the suevite deposit, suggest that subsidence due to thermal contraction of impact melt is negligible. A second source of thermal contraction is the conductive and radiative cooling of heat a) broadly distributed in the shocked and ejected material, and b) brought to the near-surface environment by the uplifting of deeper geotherms by the removal of cooler, near-surface material from the cavity and collapse of the transient cavity during the rapid modification stage. The magnitudes of these processes are scale- and substrate-dependent. For basin-scale events such as the Orientale Basin, these effects can contribute to thermal contraction and minor changes in basin topography lasting several tens of millions of years (e.g., Bratt et al., 1985a,b). The relatively small size of the Ries crater and the shallower geothermal gradient of the cooler continental lithosphere target substrate indicate that these processes produced negligible changes in floor topography.

2) *Viscous relaxation processes*: Lateral variations in geothermal gradient and lithospheric thickness, and temporal variations related to planetary thermal evolution, have been shown to be important in the evolution of impact basin topography on the Moon due to viscous relaxation processes over millions of years (e.g., Solomon et al., 1982). The small size of the Ries and the continental thermal structure of its substrate indicate that viscous relaxation processes were negligible.

3) *Closure of impact-induced fractures, faults, and mega-porosity induced by dilatancy*: During an impact event, the radial shock and attendant rarefaction waves cause significant downward and outward movement and displacement of the substrate, major shear deformation, and injection of impact melt and breccia dikes into the basement rock. Broadly referred to as *dilatancy* (inelastic volume increase due to intense deformation), such processes result in the near-instantaneous increase of the porosity of the autochthonous mega-breccias in the substrate below the crater interior and in the allochthonous breccia lenses deposited on the crater floor. Numerical simulations of impact-induced dilatancy point to significant subcrater porosities, decreasing with depth from more than 16 % to less than 0.1 % depending on crater size, structure, and hard rock quality (Collins, 2014). For example, Gohn et al. (2008) noted changes in post-impact marine sediment accommodation due to differential compaction of impact-generated materials in Chesapeake impact structure. Recent high-resolution lunar gravity data have further demonstrated its importance for the Moon (e.g., Soderblom et al., 2015). Although also scale-dependent, production of substrate porosity by impact-induced dilatancy, and its subsequent loss, is likely to be an important part of the topographic evolution of all crater interiors, including the Ries.

4) *Longer-term geologic modification processes*: Impact crater landforms are produced instantaneously in geologic time, are out-of-equilibrium with the ambient environment, and undergo modification by a range of geologic processes that influence the topography of the basin interior. On the Moon, magmatic processes involve volcanic flooding of crater interiors, (e.g., Whitten and Head, 2013) and intrusion of sills in the breccia lens below the crater floor causing uplift (e.g. Jozwiak, et al., 2015; Wilson and Head, 2018), both processes resulting in crater floor shallowing. Explosive volcanic eruptions on Mars are known to produce widely dispersed tephra (e.g., Kerber et al., 2012) and potentially significant deposits on crater floors (e.g., Le Deit et al., 2013). With the exception of the deposition of the distal ash layer, magmatic processes are not known to have influenced the evolution of the Ries crater.

Sedimentary infilling processes, however, have been significant in shallowing of the Ries crater floor. Numerous studies have demonstrated the role of fluvial, lacustrine and biological processes in the production, transport and deposition of sediment onto the crater floor. Conglomerates and stream deposits at the basin margins testify to the role of fluvial processes operating to modify the crater rim and walls, and to transport suspended sediment to the basin interior. Lacustrine deposits and sedimentary facies in the crater interior demonstrate that shallowing took place by infilling with lake sediments, aided by groundwater-related tufa deposition and local algal bioherm growth. No evidence for extensive eolian deposition (e.g. subaerial cross-bedding, etc.) has been documented. Thus, fluvial and lacustrine sedimentary infilling appear to be the dominant processes in crater floor shallowing of the Ries.

5) *Loading, flexure, compaction, and floor subsidence*: A potentially important factor in crater floor subsidence is the loading of the crater interior and the changes in topography induced by these loads and their effects. At very large impact basin scales, loading of the basin interior by dense volcanic lavas has been shown to induce flexure and significant subsidence in lunar basins (e.g., Solomon and Head, 1980), a factor that appears negligible at smaller crater scales.

In the case of the Ries crater, sediments deposited in the lacustrine environment will undergo internal volume changes related to compaction, dewatering and diagenesis, factors discussed in Section 5.1 (Supporting Information Dataset 3). Indeed, sediment load causing compaction is known to modify impact craters (Tsikalas et al., 1998; Tsikalas and Faleide, 2007; Gohn et al., 2008).

In addition, the combination of the increasing sediment load and the oscillating water load (changes in depth with time) can exert pressure on the deeper substrate below the crater floor, and contribute to the closing of the dilatancy-induced mega-porosity in the underlying brecciated substrate.

In summary, of the range of processes operating to alter the interior topography of impact craters, the three most likely to be operating in the Ries crater are: 1) crater lake sedimentary infilling to reduce the depth of the floor, 2) dewatering and diagenesis of these lake sediments to increase the depth of the floor and 3) compaction of the dilatancy-induced mega-porosity in the breccia lens below the crater floor, to increase the depth of the floor. The deposition of the volcanic ash layer provides the opportunity to assess the magnitude and temporal relationships of these processes.

While a major part of the sagging in the Ries structure is to be assumed for the more than 4 km deep impact brecciated crystalline basement, crater floor sagging should also be evident by a convex surface of the 300 m thick suevite, which itself largely retained its high initial porosity (Förstner et al., 1967: 28%; Stöffler et al., 2013: 25-30%; Popov et al., 2014: high-temperature suevite 27.9 ± 3.7 %, and low-temperature suevite 21.4 ± 4.2 %) due to its early lithification. Indeed, the few drillings available at the central crater inner slope are consistent with a convex shape of the suvite layer, although more drill cores are required for a final proof. As a consequence of the bowl-shaped crater fill geometry, Plio-Pleistocene exhumation and erosion lead to a circular outcrop pattern of the subsided lithostratigraphic units of the Ries impact crater fill, with bituminous shales and laminites at the margin, massive marlstones following farther inside, and a central area with lignite-bearing clays (**Figure 3.6**).

5.4 Estimation of Ries subcrater compaction

On the basis of the available data described here, our reconstruction indicates that the 134 +23/-49 meter floor subsidence unaccounted for by lake sediment compaction is most plausibly attributable to early sediment-water loading and closure of sub-crater floor macro-porosity initially induced by impact-generated dilatancy. The exact initial geometry of the subcrater dilatant zone is unknown, but on the basis of the inferred geometry of the transient cavity, Stöffler et al. (2013) estimated a depth of ~4 km for impact-induced fractures. Unlike on the Moon, impact structures on Earth generally show a negative Bouguer gravity anomaly and reduced seismic velocities of the target basement, indicating an increased

porosity relative to the unaffected surroundings (Pilkington and Grieve, 1992; Milbury et al., 2015). This also applies to the Ries impact structure, with a present negative Bouguer gravity anomaly (0-18 mgal in the crater interior: Kahle, 1969; Pohl et al., 1977) reflecting both the lower density sedimentary fill and residual porosity in the sub-crater brecciated rocks.

Initial porosities of subcrater megabreccias (i.e., porosities shortly after an impact event) are, to our knowledge, unknown. Polymict crystalline rock breccias of the inner ring of the Ries, which underwent lateral transport and retained their initial porosity due to early carbonate cementation, show macroporosities of up to 30% (Supplementary Information 4). While this value is probably higher than for monomictic breccias and fractured blocks of the subcrater, it may represent an upper limit for initial porosity estimates f_0. Direct measurements of present-day subcrater porosities, in turn, are known from few deep drilling sites, specifically at the Puchezh-Katunki, the Chesapeake, and the Ries (Popov et al., 1998, 2003, 2014). Further data are available e.g., from the peak ring of the Chicxulub crater, whose fractured granitoids, however, were subject to lateral transport (Elbra & Pesonen, 2011; Christeson et al, 2018; Rae et al. 2019).

For the Ries impact structure, the 600 m cored subcrater lithologies consist of crystalline rocks (gneiss and granites, with additional amphibolites in upper part) with intercalated breccia dikes show highly variable porosities (0.0 - 37.9 %; Popov et al., 2003: their Tab. 3), even within the same target lithology. However, most core intervals show porosities ranging between ca. 5 and 18 % (Popov et al., 2003: their Fig. 11), providing a rough calibration for the 700-1300 m depth interval (i.e. 100 m eroded sediment added) of a subcrater compaction curve (**Figure 3.7**). For greater depth, porosity information of impact affected crystalline basement rocks is available from the 5374 m deep borehole Vorotilovo of the Puchezh-Katunki impact structure: Porosities decrease from about 10-20 % at 600 m depth, to 5-10% at 2000 m depth, and finally about 2-4% at 5000 m depth (Popov et al., 1998, 2014). This 80-km-sized impact structure, however, is larger than the Ries, with brecciation and fracturing ranging deeper into the target basement rocks. We therefore assume low porosities of 2-4% already at 2.5-3.5 km depth for the Ries subcrater rocks.

Based on these assumptions, a decompaction with an initial porosity f_0 of 25 % at z = 0 m, f_z = 11 % for z = 1000 m, and f_z = 3 % for z = 3000 m, would be consistent with 153 m long-term crater floor sagging (+37/-34 m for f_0 = 20-30%) (**Figure 3.7**; Supplementary Information 4). While these calculations are preliminary and vary dependent on the assumptions made, they demonstrate that a mechanical compaction of brecciated subcrater crystalline rocks is in the range of the inferred 134 +23/-59 m crater floor subsidence. In any case, a further investigation of subcrater porosity evolution and potential other mechanisms of crater floor subsidence is required. Likewise the microporosity of impact-affected rocks (e.g., Huber et al. 2021) is not taken into account in the present considerations.

fractured basement initial porosity
$\phi_0 = 0.25$

burial depth z [m]

exponential compaction curves
$\phi_z = \phi_{min} + (\phi_0 - \phi_{min})e^{-\alpha z^\beta}$

residual porosity
$\phi_{res} = 0.01$

porosity ϕ

subcrater megabreccia compaction
...... $\phi_0 = 0.20$; $\phi_{res} = 0.01$; $\alpha = 0.00086$; $\beta = 1.0$
●●●● $\phi_0 = 0.25$; $\phi_{res} = 0.01$; $\alpha = 0.00086$; $\beta = 1.0$
...... $\phi_0 = 0.30$; $\phi_{res} = 0.01$; $\alpha = 0.00086$; $\beta = 1.0$

—— Ries subcrater basement (Popov et al. 2003)
· Puchezh-Katunki subcrater basement (Popov et al. 1998)
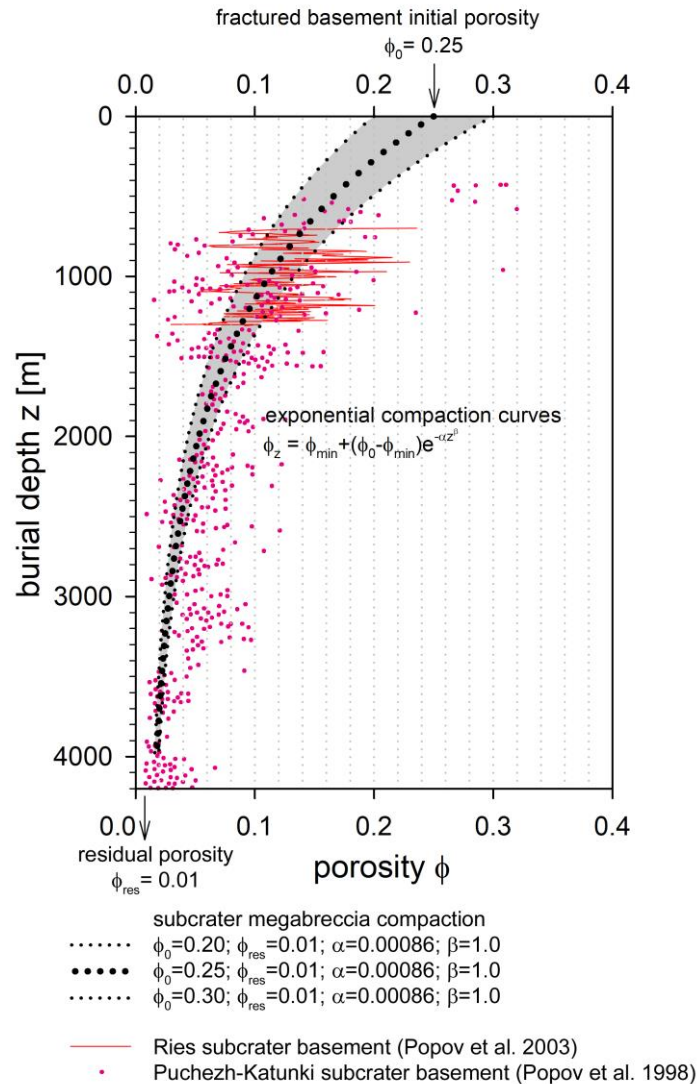
Figure 3.7 Model compaction curves of the subcrater crystalline rock breccias to demonstrate the plausibility of 134 +23/-49 m crater floor subsidence in the Ries impact structure.

5.5 Implications for craters on Earth and other planetary bodies

Clearly, initial dilatancy-related sub-crater porosity will vary as a function of a wide range of factors: impact event scale; substrate composition and structure; angle of impact; planetary gravity; presence nature and ambient state of an atmosphere and hydrosphere (e.g., Collins, 2014). Detailed documentation of the timing and likely origins of crater subsidence in the Ries crater provide a baseline for comparison to other craters on Earth and other planetary bodies.

For other craters on Earth, the relationship between crater interior subsidence and the application of loads from lake water and sediments should be assessed in detail. Does subsidence require the application of these loads, or are there examples of significant subsidence occurring prior to lake formation and sedimentary infilling? On the Earth's Moon, low gravity and overburden pressure favor development of more significant dilatancy–related porosity and the lack of an atmosphere and hydrosphere precludes loading by lake water and lacustrine sediments; thus, the Moon is an excellent laboratory for the exploration of the variable parameter space in dilatancy-related porosity formation (e.g., Soderblom et al.,

2015) and its long-term behavior. On Venus, crater floor subsidence has only been described for bright-floored (volcanism-free, lacking sedimentary infill) large impact craters, where a subsidence of 100-300 m is interpreted to reflect thermal subsidence of an insufficiently rigid, thin lithosphere (Brown and Grimm, 1996).

Mars, on the other hand, retains abundant impact craters, and was characterized early in its history by a thicker atmosphere and evidence for pluvial, fluvial and lacustrine activity and environments. An increasing number of Martian craters are known to contain sedimentary deposits (e.g., Eberswalde, Gale, Holden, Jezero: Malin and Edgett, 2000; Ehlmann et al., 2008; Schon et al., 2012; Tikhonravov, Antoniadi, Cassini: Fassett and Head, 2008). Specifically, more than 400 open and closed crater lake basins of the Noachian and Hesperian era contain post-impact sediments of deltaic or lacustrine origin (Goudge et al., 2016), when Mars was at least intermittently warm and wet (Carr and Head, 2000ab). In addition, a number of areas in the northern lowlands (e.g., Utopia Planitia) show evidence of circular deformation and subsidence features that have been interpreted to represent impact craters that have been filled with sediment that underwent compaction and caused some related faulting (e.g., McGill and Hills, 1992; Buczkowski and McGill, 2002; Buczkowski and Cooke 2002; Buczkowski et al., 2005).

There are currently no examples known of Martian craters that unequivocally show lacustrine strata inclined to the crater center. Rather, the evident and likely sedimentary crater fills are flat lying or inclined in various directions reflecting foreset beds (e.g., Terby: Wilson et al., 2007; Ansan et al., 2011) or possibly eolian, anticompensational deposition (Kite et al., 2016). At central mound in Gale Crater, strata dip gently (1.7° - 4.5°) away from the central peak (Kite et al., 2013, 2016) toward a ring moat, explained by compaction due to later sediment load (Grotzinger et al., 2015). However, the low density of the sediments exposed at the current erosional crater bottom suggest that the 5 km deep crater was never filled completely with sediments, with a maximum sediment overburden of less than 1800 m (+600/-500 m) (Lewis et al., 2019). Likewise, modelling demonstrates that the observed sediment layer orientations in Gale could only be explained by a >3 km thick donut-shaped past overburden, whose formation appears difficult to explain by known sedimentary processes (Gabasova and Kite, 2018). In any case, wherever clear concentric outcrop pattern of layered deposits in Martian craters were observed (e.g. unnamed crater within Schiaparelli basin: PSP_005897_1790; Beyer et al. 2012; unnamed crater in West Arabia Terra: MOC M14-01647; Malin and Edgett, 2000; Crommelin Crater: Lewis et al., 2008), these layered deposits are rather regional deposits (possibly duststones) draping over various, partially eroded craters (Lewis et al., 2008; Grotzinger and Milliken, 2012). On the other hand, Buczkowski and Cooke (2002) and Buczkowski et al. (2005) mapped circular graben in Utopia Planitia, and concluded that graben spacing supported the fill and compaction of wet sediment of up to 1-2 km thickness (assuming that the underlying basement was rigid and that all the compaction was in the sediment infill). In a more recent analysis, Gabasova and Kite (2018) updated approaches to the analyses of sediment compaction, but also assumed that the basement underwent no compaction. Unfortunately, details of the subsurface sediment bed orientation, the presence of any temporal marker beds, and the duration of the modification process are unknown for most of these studies.

The apparent absence of crater floor sagging of exposed beds on Mars may reflect either a lack of observations, or the possibility that many Martian impacts might have occurred during cold and dry phases (no rainfall, fluvial erosion or lacustrine environments), no significant groundwater influx, and volatile-rich but frozen icy regolith). In this case, flooding and sedimentation occur a significant time after crater formation, perhaps during intermittent wet phases. Such a scenario might be consistent with the proposed short intermittent formation time of deltaic systems in Martian crater basins (de Villiers et al., 2013). For Gale crater, the inclination of present-day surface beds may not necessarily reflect compaction of hidden strata beneath (with an estimated thickness of 1-2 km; Grotzinger et al., 2015), but may partially result from sagging in the impact-fractured subsurface. On the other hand, Buczkowski et al. (2005) and Gabasova and Kite (2018) have shown evidence for sediment filled craters that have undergone differential compaction, under the assumption that the

sub-sediment basement was rigid and non-porous. On the basis of the Ries crater example documented here, future analysis and exploration should investigate the temporal relationships between initial crater formation and the role of subsequent flooding and water-sediment flooding on crater floor subsidence.

6 Conclusions

(i) The clinoptilolite-heulandite-buddingtonite bed in the lacustrine succession of Ries impact crater is a distal volcanic ash of the contemporaneous, intensive volcanism in the Pannonian Basin, 760 km east of the Ries.

(ii) This volcanic ash bed can be traced from surface outcrops at the basin margin to 220 m depth within the basin center, thereby demonstrating a deeply bowl-shaped geometry and concentric outcrop pattern of the sedimentary crater fill.

(iii) The compaction of sedimentary units alone is insufficient to explain this geometry which we thus attribute to water-sediment loading and closure of dilatancy-induced mega-porosity in the underlying breccia lens.

(iv) These results have important implications for understanding the nature and history of impact craters on the Earth and other planetary bodies, particularly Mars.

Data Availability Statement

All data used in this publication are stored on Göttingen Research Online Data repository.

References

Ansan, V., Loizeau, D., Mangold, N., Le Mouelic, S., Carter, J., Poulet, F., Dromart, G., Lucas, A., Bibring, J.-P., Gendrin, A., Gondet, B., Langevin, Y., Masson, P., Murchie, S., Mustard, J.F., and Neukum, G. (2011), Stratigraphy, mineralogy, and origin of layered deposits inside Terby crater, Mars. *Icarus*, 211(1), 273–304. doi:10.1016/j.icarus.2010.09.011

Arp, G., Hofmann, J., and Reitner, J. (1998), Microbial fabric formation in spring mounds ("microbialites") of alkaline salt lakes in the Badain Jaran Sand Sea, PR China. *Palaios*, 13(6), 581-592. doi:10.2307/3515349

Arp, G., Bissett, A., Brinkmann, N., Cousin, S., de Beer, D., Friedl, T., Mohr, K.I., Neu, T.R., Reimer, A., Shiraishi, F., Stackebrandt, E., and Zippel, B. (2010), Tufa-forming biofilms of German karstwater streams: Microorganisms, exopolymers, hydrochemistry and calcification. - *Geological Society, London, Special Publications*, 336, 83-118. doi:10.1144/SP336.6

Arp, G., Blumenberg, M., Hansen, B.T., Jung, D., Kolepka, C., Lenz, O., Nolte, N., Poschlod, K., Reimer, A., and Thiel, V. (2013), Chemical and ecological evolution of the Miocene Ries impact crater lake, Germany: a re-interpretation based on the Enkingen (SUBO 18) drill core. *Geological Society of America Bulletin*, 125(7-8), 1125-1145. doi:10.1130/B30731.1

Artemieva, N.A., Wünnemann, K., Krien, F., Reimold, W.U., and Stöffler, D. (2013), Ries crater and suevite revisited - Observations and modeling, Part II: Modeling. *Meteoritics & Planetary Science*, 48(4), 590–627. doi:10.1111/maps.12085

Athy, L.F. (1930), Density, porosity, and compaction of sedimentary rocks. American *Association of Petroleum Geologists Bulletin*, 14(1), 1-24.

Barakat, A.O., and Rullkötter, J. (1997), A comparative study of molecular paleosalinity indicators: chromans, tocopherols and C_{20} isoprenoid thiophenes in Miocene lake sediments (Nördlinger Ries, Southern Germany). *Aquatic Geochemistry*, 3(2), 169–190. doi:10.1023/A:1009645510876

Beard, D.C., and Weyl, P.K. (1973), Influence of texture on porosity and permeability of unconsolidated sand. *American Association of Petroleum Geologists Bulletin*, 57, 349–369. doi: 10.1306/819A4272-16C5-11D7-8645000102C1865D

Beyer, R.R., Stack, K.M., Griffes, J.L., Milliken, R.E., Herkenhoff, K.E., Byrne, S., Holt, J.W., and Grotzinger, J.P. (2012), An Atlas of Mars Sedimentary Rocks as seen by HIRISE. In J.P. Grotzinger, and R.E. Milliken (Eds.), Sedimentary Geology of Mars. *SEPM Special Publication 102* (pp. 49-95). Tulsa, OK: SEPM

Bolten, R., Gall, H., and Jung, W. (1976), Die obermiozäne (sarmatische) Fossil-Lagerstätte Wemding im Nördlinger Ries (Bayern). Ein Beitrag zur Charakterisierung des Riessee-Biotops. *Geologische Blätter für Nordost-Bayern*, 26, 75-94.

Bratt, S.R., Solomon, S.C., and Head, J.W. (1985a), The evolution of impact basins: Cooling, subsidence and thermal stress. *Journal of Geophysical Research*, 90, 12415–12433.

Bratt, S.R., Solomon, S.C., Head, J.W., and Thurber, C.H. (1985b), The deep structure of lunar basins: Implications for basin formation and modification. *Journal of Geophysical Research*, 90, 3049–3064.

Brown, C.D., and Grimm, R.E. (1996), Floor subsidence and rebound of large Venus craters. *Journal of Geophysical Research*, 101, E11, 26057-26067. doi:10.1029/96JE02706

Buczkowski, D.L., and McGill G.E. (2002), Topography within circular grabens: Implications for polygon origin, Utopia Planitia, Mars. *Geophys. Res. Lett.*, 29, 1155, doi:10.1029/2001GL014100.

Buczkowski, D.L., and Cooke, M.L. (2004), Formation of double-ring circular grabens due to volumetric compaction over buried impact craters: Implications for thickness and nature of cover material in Utopia Planitia, Mars. *Journal of Geophysical Research Planets*, 109, E2, E02006. doi: 10.1029/2003JE002144

Buczkowski, D.L., Frey, H.V., Roark, J.H., and McGill, G.E. (2005), Buried impact craters: A topographic analysis of quasi-circular depressions, Utopia Basin, Mars. *J. Geophys. Res.*, 110, E03007. doi:10.1029/2004JE002324

Cabrol, N.A., and Grin, E.A. (1999), Distribution, Classification, and Ages of Martian Impact Crater Lakes. *Icarus*, 142(1), 160–172. doi:10.1006/icar.1999.6191

Cabrol, N.A., and Grin, E.A. (2005), Ancient and recent lakes on mars. In T. Tokano (Ed.), *Water on Mars and Life* (pp. 235–259). Berlin: Springer.

Carr, M.H. and Head, J.W. III (2010a), Acquisition and history of water on Mars. In N.A. Cabrol and E.A. Grin (Eds.), *Lakes on Mars* (pp. 31-67). Amsterdam: Elsevier.

Carr, M.H., and Head, J.W. III (2010b), Geologic history of Mars. *Earth and Planetary Science Letters*, 294(3-4), 185-203. doi:10.1016/j.epsl.2009.06.042.

Carr, M.H., and Clow G. (1981), Martian channels and valleys: their characteristics, distribution, and age. *Icarus*, 48(1), 91-117. doi:10.1016/0019-1035(81)90156-1

Christeson, G.L., Gulick, S.P.S., Morgan, J.V., Gebhardt, C., Kring, D.A., Le Ber, E., Lofi, J., Nixon, C., Poelchau, M., Rae, A.S.P., Rebolledo-Vieyra, M., Riller, U., Schmitt, D.R., Wittmann, A., Bralower, T.J., Chenot, E., Claeys, P., Cockell, C.S., Coolen, M.J.L., Ferrière, L., Green, S., Goto, K., Jones, H., Lowery, C.M., Mellett, C., Ocampo-Torres, R., Perez-Cruz, L., Pickersgill, A.E., Rasmussen, C., Sato, H., Smit, J., Tikoo, S.M., Tomioka, N., Urrutia-Fucugauchi, J., Whalen, M.T., Xiao, L., and Yamaguchi, K.E. (2018), Extraordinary rocks from the peak ring of the Chicxulub impact crater: P-wave velocity, density, and porosity measurements from IODP/ICDP Expedition 364. Earth and Planetary Science Letters, 495, 1–11. doi: 10.1016/j.epsl.2018.05.013

Collins, G.S. (2014), Numerical simulations of impact crater formation with dilatancy. *Journal of Geophysical Research Planets*, 119(12), 2600–2619, doi:10.1002/2014JE004708

de Villiers, G., Kleinhans, M.G., and Postma, G. (2013), Experimental delta formation in crater lakes and implications for interpretation of Martian deltas. *Journal of Geophysical Research Planets*, 118(4), 651-670. doi:10.1002/jgre.20069

Deffner, C., and Fraas, O. (1877), *Begleitworte zur geognostischen Spezialkarte von Württemberg. Atlasblätter Bopfingen und Ellenberg (Explanatory notes on the geognostic special map of Wuerttemberg. Sheets Bopfingen and Ellenberg; in German)*. 36 pp., Stuttgart: Kohlhammer.

Dehm, R., Gall, H., Höfling, R., Jung, W., and Malz, H. (1977), Die Tier- und Pflanzenreste aus den obermiozänen Riessee-Ablagerungen in der Forschungsbohrung Nördlingen 1973 (Animal and plant remains from the Upper Miocene Rieslake deposits of the research drilling Nördlingen 1973; in German). *Geologica Bavarica*, 75, 91–109.

Dorn, C. (1940), Beiträge zur Kenntnis der tertiären Ablagerungen des östlichen Vorrieses im Monheimer Gebiet (Contributions to the knowledge of the Tertiary deposits of the eastern Ries periphery in the Monheim area; in German). *Neues Jahrbuch für Mineralogie, Geologie und Paläontologie Beilage-Band*, 84 (Abt. B), 129-176.

Dorn, C. (1942a), Beiträge zur Geologie des Rieses I (Contributions to the geology of the Ries I; in German). *Zentralblatt für Mineralogie, Geologie und Paläontologie, Abt. B Geologie und Paläontologie*, 1942, 105–116, 145–159, 161–187, Stuttgart.

Dorn, C. (1942b), Beiträge zur Geologie des Rieses II (Contributions to the geology of the Ries II; in German). *Zentralblatt für Mineralogie, Geologie und Paläontologie, Abt. B Geologie und Paläontologie*, 1942, 311–348.

Dorn, C. (1942c), Beiträge zur Geologie des Rieses (Contributions to the geology of the Ries; in German). *Neues Jahrbuch für Mineralogie, Geologie und Paläontologie Beilage-Band*, 86 (Abt. B), 390–449.

Dorn, C. (1943), Beiträge zur Geologie des Rieses (Contributions to the geology of the Ries; in German). *Neues Jahrbuch für Mineralogie, Geologie und Paläontologie Monatshefte*, 1943 (Abt. B), 299–312.

Einsele, G. (2000): Mechanical and Chemical Diagenesis. In G. Einsele (Ed.), Sedimentary Basins. Evolution, Facies, and Sediment Budget. 2nd ed. (647-705). Berlin: Springer.

Elbra, T., and Pesonen, L.J. (2011), Physical properties of the Yaxcopoil-1 deep drill core, Chicxulub impact structure, Mexico. *Meteoritics & Planetary Science*, 46(11), 1640–1652. doi:10.1111/j.1945-5100.2011.01253.x

Ehlmann, B.L., Mustard, J.F., Fassett, C.I., Schon, S.C., Head, J.W., Des Marais, D.J., Grant, J.A., Murchie, S.L., and CRISM team (2008), Clay minerals in delta deposits and organic preservation potential on Mars. *Nature Geosciences*, 1, 355–358. doi:10.1038/ngeo207.

Ernstson, K. (1974), The structure of the Ries crater from geoelectric depth soundings. *Journal of Geophysics*, 40, 639–659.

Fassett, C. I., and Head III J.W. (2005), Fluvial sedimentary deposits on Mars: Ancient deltas in a crater lake in the Nili Fossae region. *Geophysical Research Letters*, 32, L14201. doi:10.1029/2005GL023456

Fassett, C.I., and Head, J.W. (2008), Valley network-fed, open-basin lakes on Mars: distribution and implications for Noachian surface and subsurface hydrology. *Icarus*, 198, 37–56. doi:10.1016/j.icarus.2008.06.016

Förstner, U. (1967), Petrographische Untersuchungen des Suevit aus den Bohrungen Deiningen und Wörnitzostheim im Ries von Nördlingen. *Contributions to Mineralogy and Petrology*, 15, 281–308. doi: 10.1007/BF00404198

Füchtbauer, H., von der Brelie, G., Dehm, R., Förstner, U., Gall, H., Höfling, R., Hoefs, J., Hollerbach, H., Jankowski, B., Jung, W., Malz, H., Mertes, H., Rothe, P., Salger, M., Wehner, H., and Wolf, M. (1977), Tertiary lake sediments of the Ries, research borehole Nördlingen 1973 - a summary. *Geologica Bavarica*, 75, 13–19.

Gabasova, L.R., and Kite, E.S. (2018) Compaction and sedimentary basin analysis on Mars. *Planetary and Space Science*, 152, 86–106. doi:10.1016/j.pss.2017.12.021

Gall, H., and Jung, W. (1979), Zur Genese der jungtertiären Fossil-Lagerstätte Wemding im Nördlinger Ries (Bayern) (On the genesis of the Late Tertiary Lagerstätte Wemding in the Nördlinger Ries (Bavaria); in German). *Geologische Blätter für Nordost-Bayern*, 29, 12–25.

Gall, H., Jung, W., and Dehm, R. (1974), Vorbericht über die Tier- und Pflanzenreste aus den obermiozänen Riessee-Ablagerungen in der Forschungsbohrung Nördlingen 1973 (Preliminary report on the animal and plant remains from the Upper Miocene Rieslake deposits of the research drilling Nördlingen 1973; in German). *Geologica Bavarica*, 72, 53–57.

Gault, D.E., and Heitowitz, B.D. (1963), The partition of energy for hypervelocity impact craters formed in rock. - Proceedings of the sixth Hypervelocity Impact Symposium, 2, 419–456.

Gault, D.E., Quaide, W.L., and Oberbeck, V.R. (1968), Impact cratering mechanics and structures. In French, B.M., and Short, N.M. (Eds.), *Shock Metamorphism in Natural Materials* (pp. 87–99), Mono Book Corp., Baltimore, MD,.

Gendrin, A., Mangold, N., Bibring, J.P., Langevin, Y., Gondet, B., Poulet, F., Bonello, G., Quantin, C., Mustard, J., Arvidson, R., and LeMouélic, S. (2005), Sulfates in Martian Layered Terrains: The OMEGA/Mars Express View. *Science*, 307, 1587–1591. doi:10.1126/science.1109087

Gohn, G.S., Koeberl, C., Miller, K.G., Reimold, W.U., Browning, J.V., Cockell, C.S., Horton, J.W. Jr., Kenkmann, T., Kulpecz, A.A., Powars, D.S., Sanford, W.E., and Voytek, M.A. (2008), Deep Drilling into the Chesapeake Bay Impact Structure. *Science*, 320(5884), 1740–1745. doi:10.1126/science.1158708

Goudge, T.A., Aureli, K.L., Head III, J.W., Fassett, C.I., and Mustard, J.F. (2015), Classification and analysis of candidate impact crater-hosted closed-basin lakes on Mars. *Icarus*, 260, 346-367. doi:10.1016/j.icarus.2015.07.026.

Goudge, T.A., Fassett, C.I., Head, J.W., Mustard, J.F., and Aureli, K.L. (2016), Insights into surface runoff on early Mars from paleolake basin morphology and stratigraphy. *Geology*, 44(6), 419–422. doi:10.1130/G37734.1

Gradstein F.M., Ogg J.G., Schmitz M.D., and Ogg G.M. (2012), *The Geologic Time Scale 2012*. Elsevier, Amsterdam, pp. 1144.

Grotzinger J.P., and Milliken R.E. (2012), The sedimentary rock record of Mars: distribution, origins and global stratigraphy. In J.P. Grotzinger, and R.E. Milliken (Eds.), *Sedimentary Geology of Mars. SEPM Special Publication 102* (pp. 1-48). Tulsa, OK: SEPM

Grotzinger, J.P., Gupta, S., Malin, M.C., Rubin, D.M., Schieber, J., Siebach, K., Sumner, D.Y., Stack, K.M., Vasavada, A.R., Arvidson, R.E., Calef, III F., Edgar, L., Fischer, W.F., Grant, J.A., Griffes, J., Kah, L.C., Lamb, M.P., Lewis, K.W., Mangold, N., Minitti, M.E., Palucis, M., Rice, M., Williams, R.M.E., Yingst, R.A., Blake, D., Blaney, D., Conrad, P., Crisp, J., Dietrich, W.E., Dromart, G., Edgett, K.S., Ewing, R.C., Gellert, R., Hurowitz, J.A., Kocurek, G., Mahaffy, P., McBride, M.J., McLennan, S.M., Mischna, M., Ming, D., Milliken, R., Newsom, H., Oehler, D., Parker, T.J., Vaniman, D., Wiens, R.C., Wilson, S.A. (2015), Deposition, exhumation, and paleoclimate of an ancient lake deposit, Gale crater, Mars. *Science*, 350(6257), aac7575-1–12. doi:10.1126/science.aac7575

Grotzinger, J.P., Hayes, A.G., Lamb, M.P., and McLennan, S.M. (2013), Sedimentary Processes on Earth, Mars, Titan, and Venus. In S.J. Mackwell, A.A Simon-Miller., J.W.Harder, and M.A. Bullock (Eds.), *Comparative Climatology of Terrestrial Planets* (pp. 439–472). Tucson: The University of Arizona Press

Gurov, E.P., Kelley, S.P., Koeberl, C., and Dykan, N.I. (2006), Sediments and impact rocks filling the Boltysh impact crater. In C.S. Cockell, C. Koeberl, and I. Gilmour (Eds.), *Biological processes associated with impact events. Impact Studies 8* (pp. 335–358). Heidelberg: Springer.

Guyard, H., St-Onge, G., Pienitz, R., Francus, P., Zolitschka, B., Clarke, G.K.C., Hausmann, S., Salonen, V.P., Lajeunesse, P., Ledoux, G., and Lamothe, M. (2011), New insights into Late Pleistocene glacial and postglacial history of northernmost Ungava (Canada) from Pingualuit Crater Lake sediments. *Quaternary Science Reviews*, 30, 3892–3907. doi:10.1016/j.quascirev.2011.10.002

Hawke, B.R., Head, J.W., 1977. Impact melt in lunar crater interiors. In: Roddy, D.J., Pepin, R.O., Merrill, R.B. (Eds.), *Impact and Explosion Cratering*. Pergamon Press, New York, NY, p. 815.

Hickey, L.J., Johnson, K.R., and Dawson, M.R. (1988), The Stratigraphy, Sedimentology, and Fossils of the Haughton Formation: A Post-Impact Crater-Fill, Devon Island, N.W.T., Canada. *Meteoritics & Planetary Science*, 23(3), 221–231. doi:10.1111/j.1945-5100.1988.tb01284.x

Huber, M.S., Gulick, S.P.S., Tisato, N., Kovaleva, E., Clark, M., and Fourie, F. (2021), Preliminary results of geophysical properties of granites taken from a transect through the Vredefort impact structure. 52nd Lunar and Planetary Science Conference, Lunar and Planetary Institute, The Woodlands, Texas, abstract #1188 (LPI Contrib. No. 2548).

Hüttner, R. (1969), Bunte Trümmermassen und Suevit (Varicolored sedimentary ejecta and suevite). *Geologica Bavarica*, 61, 142-200.

Hüttner, R., and Schmidt-Kaler, H. (1999), Die Geologische Karte des Rieses 1:50 000 (2., überarbeitete Auflage). Erläuterungen zu Erdgeschichte, Bau und Entstehung des Kraters sowie zu den Impaktgesteinen (Geological map of the Ries 1:50 000 (2nd revised edition). Explanations of earth history, structure and formation of the crater and the impact rocks; in German). *Geologica Bavarica*, 104, 7–76.

Hynek, B.M., Osterloo, M.K., and Kierein-Young, K.S. (2015), Late-stage formation of Martian chloride salts through ponding and evaporation. *Geology*, 43(9), 787–790. doi:10.1130/G36895.1

Jankowski, B. (1977a), Die Postimpakt-Sedimente in der Forschungsbohrung Nördlingen 1973 (The post-impact sediments in the research drilling Nördlingen 1973; in German). *Geologica Bavarica*, 75, 21–36.

Jankowski, B. (1977b), The graded unit on top of the suevite layer in the borehole Nördlingen 1973. *Geologica Bavarica*, 75, 155–162.

Jankowski, B. (1981), Die Geschichte der Sedimentation im Nördlinger Ries und Randecker Maar (The sedimentary history of the Nördlinger Ries and Randecker Maar; in German). *Bochumer geologische und geotechnische Arbeiten*, 6, 1–315.

Jozwiak, L.M., Head III, J.W., and Wilson, L. (2015), Lunar floor-fractured craters as magmatic intrusions: Geometry, modes of emplacement, associated tectonic and volcanic features, and implications for gravity anomalies. *Icarus*, 248, 424–447. doi:10.1016/j.icarus.2014.10.052.

Kahle, H.G. (1969), Abschätzung der Störungsmasse im Nördlinger Ries (Estimation of the disrupted mass in the Nördlinger Ries; in German). *Zeitschrift für Geophysik*, 35, S. 317–345.

Kenkmann, T., Collins, G.S., and Wünnemann, K. (2013), The modification stage of crater formation. In G.R. Osinski, and E. Pierazzo (Eds.), *Impact cratering: Processes and products* (pp. 60–75), Oxford: Wiley-Blackwell.

Kerber, L.A., Head III, J.W., Madeleine, J.B., Forget, F., and Wilson, L. (2012), The dispersal of pyroclasts from ancient explosive volcanoes on Mars: Implications for the friable layered deposits. *Icarus*, 219, 358-381. doi:10.1016/j.icarus.2012.03.016.

Kite, E.S., Lewis, K.W., Lamb, M.P., Newman, C.E., and Richardson, M.I. (2013), Growth and form of the mound in Gale Crater, Mars: Slope wind enhanced erosion and transport. *Geology*, 41(5), 543–546. doi:10.1130/G33909.1

Kite E.S., Sneed J., Mayer D.P., Lewis K.W., Michaels T.I., Hore A., and Rafkin S. C. R. (2016), Evolution of major sedimentary mounds on Mars: Buildup via

anticompensational stacking modulated by climate change. *Journal of Geophysical Research Planets*, 121(11), 2282–2324. doi:10.1002/2016JE005135.

Koken, E. (1902), Geologische Studien im fränkischen Ries. Zweite Folge (Geological studies in the Franconian Ries. Second episode; in German). *Neues Jahrbuch für Mineralogie, Geologie und Paläontologie Beilage-Band*, 15, 422–472.

Kominz, M.A., and Pekar, S.F. (2001), Oligocene eustasy from two-dimensional sequence stratigraphic backstripping. Geological Society of America Bulletin, 113(3), 291–304. doi: 10.1130/0016-7606(2001)113<0291:OEFTDS>2.0.CO;2

Kranz, W. (1911), Das Nördlinger Riesproblem (The problem of the Nördlinger Ries; in German). *Jahresberichte und Mitteilungen des Oberrheinischen Geologischen Vereins, Neue Folge*, 1, 32–35.

Kranz, W. (1912), Das Nördlinger Riesproblem II (The problem of the Nördlinger Ries II; in German. *Jahresberichte und Mitteilungen des Oberrheinischen Geologischen Vereins, Neue Folge*, 2, 54–65

Kranz, W. (1952), Die Braunkohlen im Nördlinger Riesbecken (Lignites in the Nördlinger Ries basin; in German. *Geologisches Jahrbuch*, 66, 81–117.

Landmann, G., Reimer, A., Lemcke, G., and Kempe, S. (1996), Dating late glacial abrupt climate changes in the 14,570 yr long continuous varve record of Lake Van, Turkey. *Palaeogeography Palaeoclimatology Palaeoecology*, 122, 107–118..

Le Deit, L., Hauber, E., Fueten, F., Pondrelli, M., Rossi, A.P., and Jaumann, R. (2013), Sequence of infilling events in Gale Crater, Mars: Results from morphology, stratigraphy, and mineralogy. *Journal of Geophysical Research – Planets*, 118, 2439–2473, doi:10.1002/2012JE004322, 2013.

Lewis, K.W., Aharonson, O., Grotzinger, J.P., Kirk, R.L., McEwen, A.S., and Suer, T.A. (2008), Quasi-periodic bedding in the sedimentary rock record of Mars. *Science*, 322(5907), 1532–1535. doi:10.1126/science.1161870

Lewis, K.W., Peters, S., Gonter, K., Morrison, S., Schmerr, N., Vasavada, A.R., and Gabriel, T. (2019), A surface gravity traverse on Mars indicates low bedrock density at Gale crater. *Science*, 363(6426), 535-537. doi: 10.1126/science.aat0738.

Lukács R., Harangi S., Ntaflos T., Koller F., and Pécskay Z. (2007), A Bükkalján megjelenő felső riolittufaszint vizsgálati eredményei: a harsányi ignimbrit egység [The characteristics of the Upper Rhyolite Tuff Horizon in the Bükkalja Volcanic Field: The Harsány ignimbrite unit]. Földtani Közlöny 137(4), 487-514.

Lukács, R., Harangi, S., Bachmann, O., Guillong, M., Danišík, M., Buret, Y., von Quadt, A., Dunkl, I., Fodor, L., Sliwinski, J., Soós, I., and Szepesi, J. (2015), Zircon geochronology and geochemistry to constrain the youngest eruption events and magma evolution of the Mid-Miocene ignimbrite flare-up in the Pannonian Basin, eastern central Europe. *Contributions to Mineralogy and Petrology*, 170: 52. doi:10.1007/s00410-015-1206-8

Lukács, R., Harangi, S., Guillong, M., Bachmann, O., Fodor, L., Buret, Y., Dunkl, I., Sliwinski, J., von Quadt, A., Peytcheva, I., and Zimmerer, M. (2018), Early to Mid-Miocene syn-extensional massive silicic volcanism in the Pannonian Basin (East-Central Europe): Eruption chronology, correlation potential and geodynamic implications. *Earth-Science Reviews*, 179, 1-19. doi:10.1016/j.earscirev.2018.02.005.

Lustrino, M., and Wilson, M. (2007), The Circum-Mediterranean anorogenic Cenozoic Igneous Province. *Earth-Science Reviews*, 81(1-2), 1–65. doi:10.1016/j.earscirev.2006.09.002

Maillart, J. (1989), *Differenciation entre tectonique synsedimentaire et compaction differentielle*. 193 pp., Thèse l'Ecole Nationale Superieure des Mines, Paris.

Malin, M.C., and Edgett, K.S. (2000), Sedimentary rocks of early Mars. *Science*, 290(5498), 1927-1937. doi:10.1126/science.290.5498.1927

McGill, G. E., and L. S. Hills (1992), Origin of giant Martian polygons. *J. Geophys. Res.*, 97, 2633–2647.

Melles, M., Brigham-Grette, J., Minyuk, P.S., Nowaczyk, N.R., Wennrich, V., DeConto, R.M., Anderson, P.M., Andreev, A.A., Coletti, A., Cook, T.L., Haltia-Hovi, E., Kukkonen, M., Lozhkin, A.V., Rosen, P., Tarasov, P., Vogel, H., and Wagner, B. (2012), 2.8 Million years of arctic climate change from lake El'gygytgyn, NE Russia. *Science*, 337(6092), 315–320. doi:10.1126/science.1222135

Melosh, H.J. (1989), Impact cratering: A geologic process. *Oxford Monographs on Geology and Geophysics Series*, 11, 245 p.

Milbury, C., Johnson, B.C., Melosh, H.J., Collins, G.S., Blair, D.M., Soderblom, J.M., Nimmo, F., Bierson, C.J., Phillips, R.J., and Zuber, M.T. (2015), Preimpact porosity controls the gravity signature of lunar craters. *Geophysical Research Letters*, 42, 9711–9716. doi: 10.1002/2015GL066198

Milliken, R., Grotzinger, J., and Thomson, B. (2010), Paleoclimate of Mars as captured by the stratigraphic record in Gale Crater. *Geophysical Research Letters*, 37, L04201. doi:10.1029/2009GL041870.

Murchie, S.L., Mustard, J.F., Ehlmann, B.L., Milliken, R.E., Bishop, J.L., McKeown, N.K., Noe Dobrea, E.Z., Seelos, F.P., Buczkowski, D.L., Wiseman, S.M., Arvidson, R.E., Wray, J.J., Swayze, G., Clark, R.N., Des Marais, D. J., McEwen, A.S., and Bibring, J.P. (2009), A synthesis of Martian aqueous mineralogy after 1 Mars year of observations from the Mars Reconnaissance Orbiter. *Journal of Geophysical Research Planets*, 114, E00D06, doi:10.1029/2009JE003342.

Osinski, G.R. (2004), Impact melt rocks from the Ries structure, Germany: An origin as impact melt flow. *Earth and Planetary Science Letters*, 226(3-4), 529–543. doi:10.1016/j.epsl.2004.08.012

Osinski, G.R. (2006), Effect of volatiles and target lithology on the generation and emplacement of impact crater fill and ejecta deposits on Mars. *Meteoritics & Planetary Science*, 41(10), 1571–1586. doi:10.1111/j.1945-5100.2006.tb00436.x

Osinski G.R., Lee P., Spray J.G., Parnell J, Lim D.S.S., Bunch T.E., Cockell C.S., and Glass B. (2005), Geological overview and cratering model for the Haughton impact structure, Devon Island, Canadian High Arctic. *Meteoritics & Planetary Science*, 40(12), 1759–1776. doi:10.1111/j.1945-5100.2005.tb00145.x

Partridge, T.C., Kerr, S.J., Metcalfe, S.E., Scott, L., Talma, A.S., and Vogel, J.C. (1993), The Pretoria Saltpan: a 200,000 year Southern African lacustrine sequence. *Palaeogeography, Palaeoclimatology, Palaeoecology*, 101(3-4), 317-337. doi:10.1016/0031-0182(93)90022-B

Phillips, R. J., Zuber, M.T., Solomon, S.C., Golombek, M.P., Jakosky, B.M., Banerdt, W.B., Smith, D.E., Williams, R.M.E., Hynek, B.M., Aharonson, O., and Hauck, II S.A. (2001), Ancient geodynamics and global-scale hydrology on Mars. *Science*, 291(5513), 2587–2591. doi:10.1126/science.1058701

Pilkington, M., and Grieve R.A.F. (1992), The geophysical signature of terrestrial impact craters. *Reviews of Geophysics*, 30, 161–181. doi:10.1029/92RG00192.

Pohl J. (1977), Paläomagnetische und gesteinsmagnetische Untersuchungen an den Kernen der Forschungsbohrung Nördlingen 1973. *Geologica Bavarica*, 75, 329–348.

Pohl, J., Stöffler, D., Gall, H., and Ernstson, K. (1977), The Ries impact crater. In D.J. Roddy, R.G. Pepin, and R.B. Merril (Eds.), *Impact and Explosion Cratering* (pp. 343–458), New York: Pergamon Press.

Popov Y.A., Pimenov V.P., Pevzner L.A., Romushkevich R.A., and Popov E.Y. (1998), Geothermal characteristics of the Vorotilovo deep borehole drilled into the Puchezh-Katunk impact structure. *Tectonophysics*, 291, 205–223. doi: 10.1016/S0040-1951(98)00041-9

Popov Y., Pohl J., Romushkevich R., Tertychnyi V., and Soffel H. (2003), Geothermal characteristics of the Ries impact structure. *Geophysical Journal International*, 154, 355–378. doi: 10.1046/j.1365-246X.2003.01925.x

Popov Y., Mayr S., Romushkevich R., Burkhardt H., and Wilhelm H. (2014), Comparison of petrophysical properties of impactites for four meteoritic impact structures. *Meteoritics & Planetary Science*, 49, 896–920. doi: 10.1111/maps.12299

Rae, A.S.P., Collins, G.S., Morgan, J.V., Leung, J., Salge, T., Lofi, J., Christeson, G.L., Gulick, S.P.S., Poelchau, M., Riller, U., Gebhardt, C., Grieve, R.A.F., Osinski, G.R., and IODP-ICDP Expedition 364 Scientists (2019): Impact-induced Porosity and Fracturing at the Chicxulub Impact Structure. *Journal of Geophysical Research Planets*, 124, 1960–1978. doi: 10.1029/2019JE005929

Ramseyer, K., Diamond, L.W., and Boles J.R. (1993), Autigenic K-NH4-feldspar in sandstones: a fingerprint of the diagenesis of organic matter. *Journal of Sedimentary Petrology*, 63(6), 1092-1099. doi:10.1306/D4267CAD-2B26-11D7-8648000102C1865D

Reiff, W. (1977), The Steinheim Basin – an impact structure. In D.J. Roddy, R.G. Pepin, and R.B. Merril (Eds.), *Impact and Explosion Cratering* (pp. 309–320), New York: Pergamon Press.

Reimer, A., Landmann, G., and Kempe, S. (2009), Lake Van, Eastern Anatolia, Hydrochemistry and History. *Aquatic Geochemistry*, 15, 195–222. doi: 10.1007/s10498-008-9049-9

Revil, A., Grauls, D., and Brévart, O. (2002), Mechanical compaction of sand/clay mixtures. *Journal of Geophysical Reseach*, 107(B11), 2293, doi:10.1029/2001JB000318

Rocholl, A., Schaltegger, U., Gilg, H.A., Wijbrans, J., and Böhme, M. (2018a), The age of volcanic tuffs from the Upper Freshwater Molasse (North Alpine Foreland Basin) and their possible use for tephrostratigraphic correlations across Europe for the Middle Miocene. *International Journal of Earth Sciences*, 107(2), 387–407. doi:10.1007/s00531-017-1499-0

Rocholl, A., Böhme, M., Gilg, H.A., Pohl, J., Schaltegger, U., and Wijbrans, J. (2018b), Comment on "A high-precision ^{40}Ar/^{39}Ar age for the Nördlinger Ries impact crater, Germany, and implications for the accurate dating of terrestrial impact events" by Schmieder et al. (Geochimica et Cosmochimica Acta 220 (2018) 146–157). *Geochimica et Cosmochimica Acta*, 238, 599-601. doi:10.1016/j.gca.2018.05.018

Rothe, P., and Hoefs, J. (1977), Isotopen-geochemische Untersuchungen an Karbonaten der Ries-See-Sedimente der Forschungbohrung Nördlingen 1973 (Isotope-geochemical investigation of carbonates of the Ries-lake-sediments of the research drilling Nördlingen 1973; in German). *Geologica Bavarica*, 75, 59-66.

Schauderna, H. (1983), Die Diatomeenflora aus den miozänen Seeablagerungen im Nördlinger Ries (The diatom flora of the Miocene lake deposits of the Nördlinger Ries; in German). *Palaeontographica*, B 188, 83–193.

Schmieder, M., Kennedy, T., Jourdan, F., Buchner, E., and Reimold, W.U. (2018a), A high-precision $^{40}Ar/^{39}Ar$ age for the Nördlinger Ries impact crater, Germany, and implications for the accurate dating of terrestrial impact events. *Geochimica et Cosmochimica Acta* 220: 146-157. doi:10.1016/j.gca.2017.09.036

Schmieder, M., Kennedy, T., Jourdan, F., Buchner, E., and Reimold, W.U. (2018b), Response to Comment on "A high-precision $^{40}Ar/^{39}Ar$ age for the Nördlinger Ries impact crater, Germany, and implications for the accurate dating of terrestrial impact events" by Schmieder et al. (Geochimica et Cosmochimica Acta 220 (2018) 146–157). *Geochimica et Cosmochimica Acta*, 238, 602-605. doi:10.1016/j.gca.2018.07.025

Schon, S.C., Head, J.W., and Fassett, C.I. (2012), An overfilled lacustrine system and progradational delta in Jezero crater, Mars: Implications for Noachian climate. *Planetary and Space Science*, 67, 28–45. doi:10.1016/j.pss.2012.02.003

Schröder, J., and Dehm, R. (1950), Geologische Untersuchungen im Ries. Das Gebiet des Blattes Harburg (Geological research in the Ries. The area of the sheet Harburg). *Abhandlungen des Naturwissenschaftlichen Vereins für Schwaben e.V. in Augsburg*, 5, 1-147.

Sclater, J.G., and Christie, P.A.F. (1980), Continental stretching: an explanation of the post-mid-Cretaceous subsidence of the central North Sea Basin. *Journal of Geophysical Research*, 85, B7, 3711-3739. doi: 10.1029/JB085iB07p03711Shanahan, T.M., Overpeck, J.T., Anchukaitis, K.J., Beck, J.W., Cole, J.E., Dettman, D.L., Peck, J.A., Scholz, C.A., and King, J.W. (2009), Atlantic Forcing of Persistent Drought in West Africa. *Science*, 324(5925), 377–380. doi:10.1126/science.1166352

Shoemaker, E.M., and Chao, E.C.T. (1961), New evidence for the impact origin of the Ries basin, Bavaria, Germany. *Journal of Geophysical Research*, 66(10), 3371-3378. doi:10.1029/JZ066i010p03371

Siegert, S., Branney, M.J., and Hecht L. (2017), Density current origin of a melt-bearing impact ejecta blanket (Ries suevite, Germany). *Geology*, 45(9), 855–858. doi:10.1130/G39198.1

Siegert, S., and Hecht, L. (2019), Heterogeneity of melts in impact deposits and implications for their origin (Ries suevite, Germany). *Meteoritics & Planetary Science*, 54(10), 2409–2447. doi:10.1111/maps.13210

Soderblom, J.M., Evans, A.J., Johnson, B.C., Melosh, H.J., Miljkovic, K., Phillips, R.J., Andrews-Hanna, J.C., Bierson, C.J., Head III, J.W., Milbury, C., Neumann, G.A., Nimmo, F., Smith, D.E., Solomon, S.C., Sori, M.M., Wieczorek, M.A., and Zuber, M.T. (2015), The fractured Moon: Production and saturation of porosity in the lunar highlands from impact cratering. *Geophysical Research Letters*, 42, 6939–6944. doi:10.1002/2015GL065022

Solomon, S.C., and Head, J.W. (1980): Lunar mascon basins: Lava filling, tectonics and evolution of the lithosphere. *Reviews of Geophysics and Space Physics*, 18, 107–141.

Solomon, S. C., Comer, R.P., and Head, J.W. (1982), The evolution of impact basins: Viscous relaxation of topographic relief. *Journal of Geophysical Research*, 87, 3975–3992.

Squyres, S.W., Grotzinger, J.P., Arvidson, R.E., Bell, J.F. III, Calvin, W., Christensen, P.R., Clark, B.C., Crisp, J.A., Farrand, W.H., Herkenhoff, K.E., Johnson, J.R., Klingelhofer, G., Knoll, A.H., McLennan, S.M., McSween, H.Y. Jr., Morris, R.V., Rice, J.W. Jr., Rieder, R., and Soderblom, L.A. (2004), *In situ* evidence for an ancient aqueous

environment at Meridiani Planum, Mars. *Science,* 306(5702), 1709–1714. doi:10.1126/science.1104559

Stöffler, D., Ryder, G., Ivanov, B.A., Artemieva, N.A., Cintala, M.J., and Grieve, R.A.F. (2006), Cratering History and Lunar Chronology. *Reviews in Mineralogy and Geochemistry,* 60(1), 519–596. doi:10.2138/rmg.2006.60.05

Stöffler, D., Artemieva, N.A., Wünnemann, K., Reimold, U., Jacob, J., Hansen, B.K., and Summerson, I.A.T. (2013), Ries crater and suevite revisited - Observations and modeling Part I: Observations. *Meteoritics & Planetary Science,* 48, 515–589. doi:10.1111/maps.12086

Sturm, S., Wulf, G., Jung, D., and Kenkmann, T. (2013), The Ries impact, a double-layer rampart crater on Earth. *Geology,* 41(5), 531-534. doi.org/10.1130/G33934.1

Talbot, M.R., and Johannessen, T. (1992), A high resolution palaeoclimatic record for the last 27,500 years in tropical West Africa from the carbon and nitrogen isotopic composition of lacustrine organic matter. *Earth and Planetary Science Letters,* 110(1-4), 23–37. doi:10.1016/0012-821X(92)90036-U

Tsikalas, F., and Faleide, J.I.(2007), Post-impact structural crater modification due to sediment loading: An overlooked process. *Meteoritics & Planetary Science,* 42(11), 2013–2029. doi: 10.1111/j.1945-5100.2007.tb00557.x

Tsikalas, F., Gudlaugsson, S.T., and Faleide, J.I. (1998), Collapse, infilling, and post-impact deformation at the Mjølnir impact structure, Barents Sea. *Geological Society of America Bulletin,* 110(5), 537–552. doi:10.1130/0016-7606(1998)110<0537:CIAPDA>2.3.CO;2

Unger, H.J., Fiest, W., and Niemeyer A. (1990), Die Bentonite der ostbayerischen Molasse und ihre Beziehungen zu den Vulkaniten des Pannonischen Beckens (The bentonite of the East-Bavarian Molasse and their relation to the volcanic rocks of the Pannonian Basin; in German). *Geologisches Jahrbuch* D 96: 67–112.

Vaughan, W. M., and Head III, J.W. (2014), Impact melt differentiation in the South Pole-Aitken basin: Some observations and speculations. *Planetary and Space Science,* 91, 101–106. doi: 10.1016/j.pss.2013.11.010.

Vaughan, W. M., Head III, J.W., Wilson, L., and Hess, P.C. (2013), Geology and petrology of enormous volumes of impact melt on the Moon: A case study of the Orientale basin impact melt sea. *Icarus,* 223, 749–765, doi: 10.1016/j.icarus.2013.01.017.

von der Brelie, G. (1977), Die Pollenflora der See-Sedimente in der Forschungsbohrung Nördlingen 1973 (The pollen flora of the lake sediments of the research drilling Nördlingen 1973; in German). *Geologica Bavarica,* 75, 111–125.

von Engelhardt, W. (1997), Suevite breccia of the Ries impact crater, Germany: Petrography, chemistry, and shock metamorphism of crystalline clasts. *Meteoritics & Planetary Science,* 32, 545–554. doi:10.1111/j.1945-5100.1997.tb01299.x

Weber, E. (1941), Geologische Untersuchungen im Ries. Das Gebiet des Blattes Wemding (Geological research in the Ries. The area of the sheet Wemding; in German). *Abhandlungen des Naturkunde- und Tiergartenvereins für Schwaben e.V.,* 3 (geol.-paläont. Reihe, 2. Heft), 1–248.

Wedepohl, K.H. (2000), The composition and formation of Miocene tholeiites in the central European Cenozoic plume volcanism (CECV). *Contributions to Mineralogy and Petrology,* 140(2), 180–189. doi:10.1007/s004100000184

Whitten, J.L., and Head III, J.W. (2013), Detecting volcanic resurfacing of heavily cratered terrain: Flooding simulations on the Moon using Lunar Orbiter Laser Altimeter (LOLA) data. *Planetary and Space Science,* 85, 24–37. doi: 10.1016/j.pss.2013.05.013.

Wilson, L., and Head III, J.W. (2018), Lunar floor-fractured craters: Modes of dike and sill emplacement and implications of gas production and intrusion cooling on surface morphology and structure. *Icarus*, 305, 105-122. doi:10.1016/j.icarus.2017.12.030.

Wilson, S.A., Howard, A.D., Moore, J.M., and Grant, J.A. (2007), Geomorphic and stratigraphic analysis of Crater Terby and layered deposits north of Hellas Basin, Mars. *Journal of Geophysical Research Planets*, 112(8), E08009. doi:10.1029/2006JE002830

Wolf, M. (1977), Kohlenpetrographische Untersuchung der See-Sedimente der Forschungsbohrung Nördlingen 1973 und Vergleich mit anderen Untersuchungsergebnissen aus dem Ries (Coal petrological investigation of the lake sediments of the research drilling Nördlingen 1973; in German). *Geologica Bavarica*, 75, 127-138.

Wolff, M. (1974), *Limnische Kalke und Dolomite im Nördlinger Ries und Steinheimer Becken (Limnic limestones and dolomites of the Nördlinger Ries and Steinheim Basin)*. 116 + 28 pp., doctoral thesis Ruhr-University Bochum.

Wolff, M., and Füchtbauer, H. (1976), Die karbonatische Randfazies der tertiären Süßwasserseen des Nördlinger Ries und des Steinheimer Beckens (The calcareous marginal facies of the Tertiary freshwater lakes of the Nördlinger Ries and Steinheim Basin; in German). *Geologisches Jahrbuch*, D 14, 3–53.

Wörner, G., Zindler, A., Staudigel, H., Schmincke, H.U., (1986), Sr, Nd and Pb isotope geochemistry of Tertiary and Quaternary volcanics from West Germany. *Earth and Planetary Science Letters*, 79(1-2), 107–119. doi:10.1016/0012-821X(86)90044-0

Supporting Information

(available online: https://doi.org/10.1029/2020JE006764)
Text S1. Documentation of outcrops and drillings.

Text S2. XRD analysis of volcanic-ash derived zeolite bed of the Miocene Ries impact crater and reference material.

Text S3. Laser ablation zircon U-Pb geochronology.

Data Set S1. RFA and CNS data. [Type or paste caption here (upload your dataset(s) to AGU's journal submission site and select "Supporting Information (SI)" as the file type. Following naming convention: ds01.]

Data Set S2. Numerical results of the LA-ICP-MS U-Pb geochronology of zircons

Data Set S3. Model calculations of the sediment compaction.

Data Set S4. Model calculations of the subcrater compaction.

Data Set S5. Compilation of drillings and outcrops in the Miocene Ries impact crater basin. (A) Drillings. (B) Outcrops. (C) Strata dip. (D) Geological map of the Ries impact crater fill showing the concentric outcrop of major lithofacies units.

References From the Supporting Information

Arp, G., Reimer, A., Simon, K., Sturm, S., Wilk, J., Kruppa, C., Hecht, L., Hansen, B.T., Pohl, J., Reimold W.U., Kenkmann, T., and Jung, D. (2019), The Erbisberg drilling 2011: Implications for the structure and post-impact evolution of the inner ring of the Ries

impact crater. *Meteoritics & Planetary Science*, 54(10), 2448–2482. doi: 10.1111/maps.13293

Dunkl, I., Mikes, T., Simon, K., and von Eynatten, H. (2008), Brief introduction to the Windows program Pepita: data visualization, and reduction, outlier rejection, calculation of trace element ratios and concentrations from LA-ICP-MS data. In*: Laser ablation ICP-MS in the Earth Sciences: Current practices and outstanding issues. Mineralogical Association of Canada, Short Course (Ed. by Sylvester, P.)*, 40, 334-340.

Frei, D. and Gerdes, A. (2009), Precise and accurate in situ U-Pb dating of zircon with high sample throughput by automated LA-SF-ICP-MS. *Chemical Geology* 261, 261-270.

Jackson, S., Pearson, N., Griffin, W. and Belousova, E. (2004), The application of laser ablation inductively coupled plasma-mass spectrometry to in situ U-Pb zircon geochronology. *Chemical Geology,* 211, 47-69.

Ludwig, K.R. (2012), User's manual for Isoplot 3.75: A geochronological Toolkit for Microsoft Excel. *Berkeley Geochronology Center Special Publication*, no. 4, p. 70.

Lukács, R., Harangi, Sz., Bachmann, O., Guillong, M., Danišík, M., Buret, Y., von Quadt, A., Dunkl, I. Fodor, L., Sliwinski, J., Soós, I. and Szepesi, J. (2015), Zircon geochronology and geochemistry to constrain the youngest eruption events and magma evolution of the Mid-Miocene ignimbrite flare-up in the Pannonian Basin, eastern central Europe. *Contrib. Mineral Petrol.*, 170:52, DOI 10.1007/s00410-015-1206-8.

Marillo-Sialer, E., Woodhead, J., Hergt, J., Greig, A., Guillong, M., Gleadow, A., Evans, N., and Paton, C. (2014), The zircon 'matrix effect': evidence for an ablation rate control on the accuracy of U-Pb age determinations by LA-ICP-MS. *J. Anal. At. Spectrom.*, 29 (6), 981-989.

Paces, J.B. and Miller, J.D. (1993), Precise U–Pb ages of Duluth Complex and related mafic intrusions, northeastern Minnesota: geochronological insights into physical,petrogenetic, paleomagnetic and tectonomagmatic processes associated with the 1.1 Ga midcontinent rift system. *Journal of Geophysical Research*, 98, 13997-14013.

Pupin, J.P. (1980), Zircon and granite petrology. *Contributions to Mineralogy and Petrology*, 73, 207-220.

Sliwinski, J.T., Guillong, M., Liebske, C., Dunkl, I., von Quadt, A. and Bachmann O. (2017), Improved accuracy of LA-ICP-MS U-Pb ages of Cenozoic zircons by alpha dose correction. *Chemical Geology*, 472, 8–21.

Vermeesch, P. (2018), IsoplotR: a free and open toolbox for geochronology. *Geoscience Frontiers*, 9, 1479-1493, doi: 10.1016/j.gsf.2018.04.001.

Wiedenbeck, M., Allé, P., Corfu, F., Griffin, W.L., Meier, M., Oberli, F., von Quadt, A., Roddick, J.C. and Spiegel, W. (1995), Three natural zircon standards for U–Th–Pb, Lu–Hf, trace element and REE analyses. *Geostandards Newsletters*, 19, 1-23.

Wotzlaw, J-F., Schaltegger, U., Frick, D.A., Dungan, M.A., Gerdes, A. and Günther, D. (2013), Tracking the evolution of large-volume silicic magma reservoirs from assembly to supereruption. *Geology*, 41, 867-870.

Chapter 4. A self-readjusted chemical and hydrological evolution of a terrestrial impact crater lake

Lingqi Zeng[a*], Stefan Hölzl[b], Andreas Reimer[a], Volker Karius[a], Dietmar Jung[c], Gernot Arp[a]

[a]Georg-August-Universität Göttingen, Geowissenschaftliches Zentrum, Goldschmidtstrasse 3, 37077 Göttingen, Germany,

[b]Staatliche Naturwissenschaftliche Sammlungen Bayerns - RiesKraterMuseum Nördlingen, Eugene-Shoemaker-Platz 1, 86720 Nördlingen, Germany

[c]Bayerisches Landesamt für Umwelt, Geologischer Dienst, Hans-Högn-Straße 12, 95030 Hof/Saale

Corresponding author: Lingqi Zeng (lzeng@gwdg.de)

Abstract

Lacustrine deposits contain important information on the hydrological and hydrochemical evolution of impact crater lakes on Earth and other planets. The present study combines $^{87}Sr/^{86}Sr$ of lacustrine carbonates and hydrochemical data of leachates from pre-impact target rocks, to reconstruct fluid provenance, hydrochemical and hydrological changes of a terrestrial, mid-sized complex impact crater. In conjunction with sedimentological evidence and hydrochemical modelling, different mixing scenarios of fluid endmembers were tested for each lake stage. The initial high carbonate $^{87}Sr/^{86}Sr$ signatures suggest a groundwater upwelling from the crystalline basement and melt-bearing breccias (suevite), driven by impact-generated heat, within the crater rim-restricted catchment at a low groundwater table. Thick, laminated sediments of the main crater lake stage, with low and constant carbonate $^{87}Sr/^{86}Sr$, indicate a readjustment of groundwater table to shallower depth to leach the proximal impact ejecta blanket (Bunte Breccia). A final minor increase in $^{87}Sr/^{86}Sr$ reflects a further expansion of the catchment, with riverine influx from outside the morphological crater rim and re-establishment of a swampy and pedogenic depositional environment, similar to the pre-impact hydrological situation. While heat-driven groundwater influx dominated the early impact basin, crater floor temperature decline, sealing of subcrater porosity, and ejecta erosion led to a dominance of surface influx over time, with a final expansion of the catchment beyond the crater rim. Mid- or larger-sized impact craters with sufficient impact-heat release, therefore, have an unique self-readjusted hydrological and hydrochemical evolution that is independent from climate change but rather controlled by the sedimentation and crater floor sagging, leading to the increasing crater floor stability.

1 Introduction

The hydrological conditions and evolution are key aspects in the investigation of past climate and habitability of extraplanetary settings, with a contemporary focus on Martian impact craters. Studies related to hydrology of ancient Martian crater lakes continue to grow in number recently—e.g., how does the groundwater system influence crater lake hydrology (Fasset and Head, 2008) and lacustrine deposits (Andrews-Hanna et al., 2010)? To what extent did climate play the role in the hydrological changes (Roseborough et al., 2021)? Despite the huge progress that has been made by the numerous orbiters and the surface rovers, an analogous terrestrial impact crater lake may provide important insights to understand the above questions. The ca. 14.9 Ma (Rocholl et al., 2018; Schwarz et al.,

2020) Miocene Nördlinger Ries in Germany (**Figure 1**) is one of the best-investigated impact structures on Earth, with extraordinarily well-preserved ejecta formations, specifically the impact melt-bearing breccia, known as suevite (Artemieva et al., 2013; Siegert et al., 2017; Stöffler et al., 2013) on top of the primary ejecta blanket, i.e. the Bunte breccia (Hörz et al., 1983). Beyond that, the over 300-meter-thick post-impact crater lake sediments, deposited within ca. 1-2 Ma immediately after the impact event (Jankowski, 1981; Montano et al., 2021), allow the study of crater lake hydrology (Jankowski, 1981; Talbot, 1990; Arp et al., 2017; 2019a), pH and saline lake water evolution (e.g. Arp et al., 2013a; 2017; Stüeken et al., 2020) and biogeochemistry histories inside the lake (Zeng et al., submitted). The lacustrine sedimentation in the central crater starts on top of the crater suevite and four major lithostratigraphic members are recognized (Jankowski, 1981): 1) the **basal member**, comprising several cycles of coarse- to fine-grained siliciclastics and finally laminated marl to limestones (alluvial to playa lake facies), with features of subaerial exposure and percolating hydrothermal fluids (Zeng et al., submitted); 2) the **laminite member** (Jankowski, 1981), including four submembers (smbr) of laminated marlstones, with intercalated bituminous shales, authigenic zeolites and carbonate-rich beds (profundal lake facies); 3) the **marl member** (fluctuating between profundal and shallow lake facies), comprising a lower **varicolored-marl smbr** with transitional features between the laminated facies and thicker marlstones (occasionally with mud cracks and *in-situ* brecciation), and an upper **dolomite-marl smbr** exhibiting more frequent bioturbation and subaerial exposures (Zeng et al., submitted); 4) the **clay member**, rich in unstratified, carbonaceous claystone with intercalated marlstone beds formed in a variety of settings from flooded, deep to shallow lake and pedogenic environments (Arp et al., 2017; Zeng et al., submitted). At the lake margin, several carbonate mound units with distinct features are also recognized (Reis, 1926; Wolf and Füchtbauer, 1976; Bolten, 1977; Riding, 1979; Arp, 1995; Arp et al., 2013a,b).
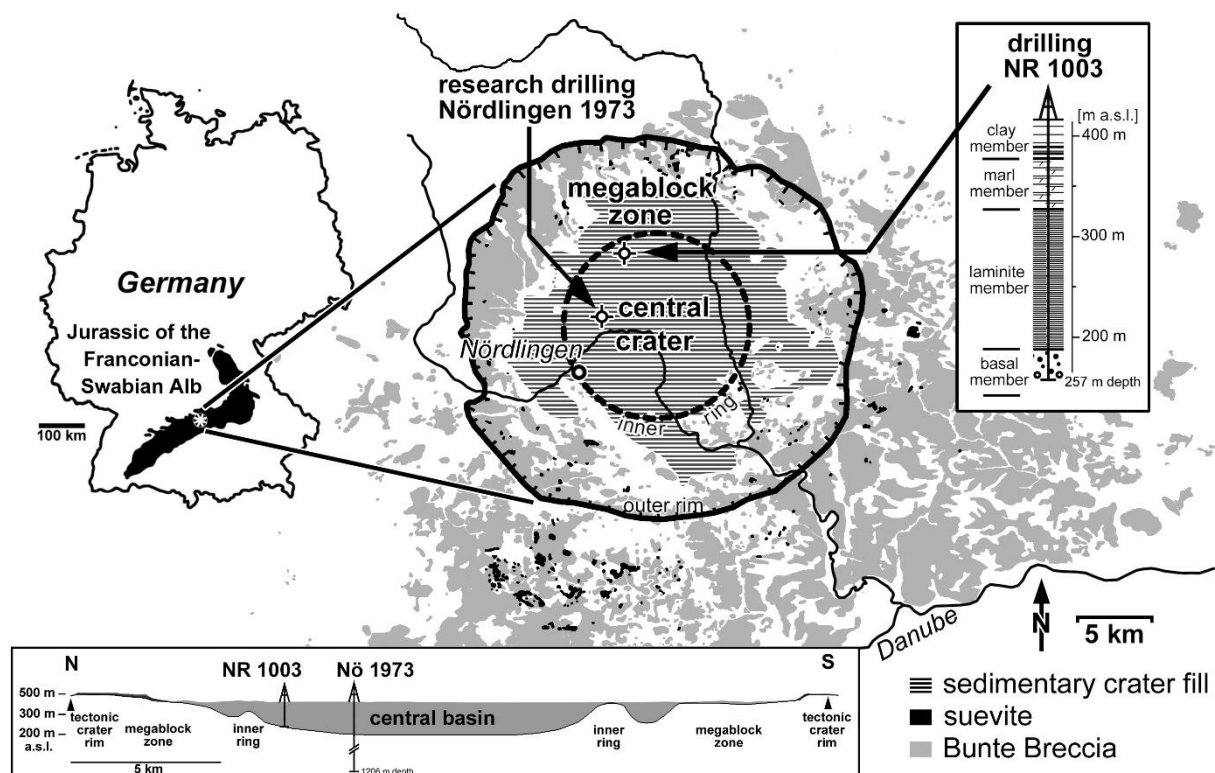
Figure 4.1 Location and geological context of the Miocene Nördlinger Ries Crater ,including the distribution of the ejecta formations (suevite and Bunte Breccia), and the location of the studied drill core (NR1003).

The Ries lacustrine sediments were deposited under hydrologically closed conditions (Talbot, 1990; Zeng et al., submitted) and a semi-arid climate (Arp et al., 2013a; Füchtbauer et al., 1977). However, many details on the impact- and post-impact processes are still under discussion, for instance, the extent of the overturned strata at the primary crater margin (Arp et al., 2019a); the biogeochemical processes following the successive ejecta erosion and crater lake filling, especially processes affecting sulfate concentrations along lake history (Arp et al., 2013a; Zeng et al., submitted); the timespan and extent of the hydrothermal activities (Arp et al., 2013b; Caudill et al., 2021)— these questions entail the hydrological history of the Ries and potentially other impact crater lakes. In addition, recent radiometric dating (Arp et al., 2021; Montano et al., 2021) confirm that the time range of the Ries lacustrine sediments falls within the mid-Miocene Climate Transition (Flower and Kennett, 1994). The Ries, therefore, appears well-suited for the study of hydrology and hydrochemistry of an impact crater lake, reacting to possible climate changes.

One excellent tracer for the provenance of solutes and corresponding catchment changes are Sr isotopes, well documented in the lacustrine carbonates (Doebbert et al., 2014; Gierlowski-Kordesch et al., 2008). So far, significant fractionation of Sr isotopes is not known either during the impact processes (e.g. the formation of impactites), or during the limnological processes when lacustrine carbonate forms. This allow us to use Sr isotopes of pre-impact target formation and lacustrine carbonates to reconstruct both impact and limnological processes. As authigenic calcium carbonates reflect chemical condition at the time of precipitation from lake water column or pore water, the ubiquitous carbonate beds throughout the lacustrine succession in the Ries basin provide opportunities for reconstruction of long-term chemical lake conditions (Arp et al., 2013a; Stüeken et al., 2020). To trace and reconstruct the hydrological evolution of the crater lake and its catchment, we conducted a series of leaching experiments to simulate weathering solutions from specific target rock and ejecta formations or discharges from groundwater aquifers. The leaching experiments cover all major pre-impact target rocks, from the Variscan crystalline basement to every sedimentary Triassic and Jurassic formation. $^{87}Sr/^{86}Sr$ of the carbonate beds along the whole post-impact lacustrine succession (drill core NR1003) was analysed as well as that of the leachates, to identify different sources of Sr. We then studied the provenance of the authigenic lacustrine carbonates to disentangle influx sources and sedimentary structures to understand the post-impact crater internal movements as well as the hydrological evolution. The chemical composition of leachates and representative field waters were also analyzed, as a basis for hydrochemical modelling of different crater lake stages.

2 Sr isotope of calculated leachates to discern ejecta formations

$^{87}Sr/^{86}Sr$ values and Sr concentrations of leachate from each single formation are shown in **Figure 2**. The Upper Jurassic limestone and dolostone formations have the lowest $^{87}Sr/^{86}Sr$ values (0.7075-0.7084), in accordance with their marine origins (Veizer et al., 1999). Middle and Lower Jurassic marlstone and claystones have higher $^{87}Sr/^{86}Sr$ values (0.7080-0.7110), except one sample from Angulatensandstein Fm. has higher $^{87}Sr/^{86}Sr$ of 0.7164. The Triassic (mainly Keuper Group) terrestrial sandstone- and claystone-leachates have systematically higher $^{87}Sr/^{86}Sr$, owing to the Sr release from the silicate minerals provenanced to older massifs (e.g. Paul et al., 2008).

In addition to the leachate samples, the $^{87}Sr/^{86}Sr$ data range of **crystalline basement** was supplemented by the reported bulk $^{87}Sr/^{86}Sr$ and Sr concentration results. According to the average composition of crystalline basement in the Ries basin (0.18 mafic, 0.42 granite and 0.38 gneiss, Graup 1978; Siegert et al., 2019), the mean $^{87}Sr/^{86}Sr$ of crystalline basement rocks is estimated to be 0.7141 (Horn et al., 1985; Schnetzler et al., 1969).

$^{87}Sr/^{86}Sr$ of the **suevite leachates** range from 0.7118-0.7120. Our **calculated** average $^{87}Sr/^{86}Sr$ of suevite leachate is 0.7129, based on mass-balance and simple mixing of the individual melted formation. The bulk rock (silicate fraction) $^{87}Sr/^{86}Sr$ of **suevite** is 0.7125

(Arp et al., 2019a; Schnetzler et al., 1969), between the ^{87}Sr/^{86}Sr ratios of our calculated suevite leachate and sample from leaching experiments. The slight deviation between the bulk suevite and suevite leachate is considered acceptable since a spatial heterogeneity is suggested recently. According to Siegert et al. (2017), suevite originated and migrated radically from the melt center in a similar manner to pyroclastic density flows, involving in the uneven, underlying crystalline basement. The ^{87}Sr/^{86}Sr ratio of the suevite leachate (0.7118) was used in ^{87}Sr/^{86}Sr during modelling. In any case, the ^{87}Sr/^{86}Sr endmember of suevite leachate falls between the crystalline basement and Bunte Breccia, which will be discussed next.

Likewise, spatial heterogeneity and compositional complexity exist in the Bunte Breccia (Hörz et al., 1983) and representative sample from either field or drill cores is thereby difficult. It is, however, possible to calculate the average ^{87}Sr/^{86}Sr of **Bunte breccia** (0.7101) based on mass-balance using the method described in the supplementary material.
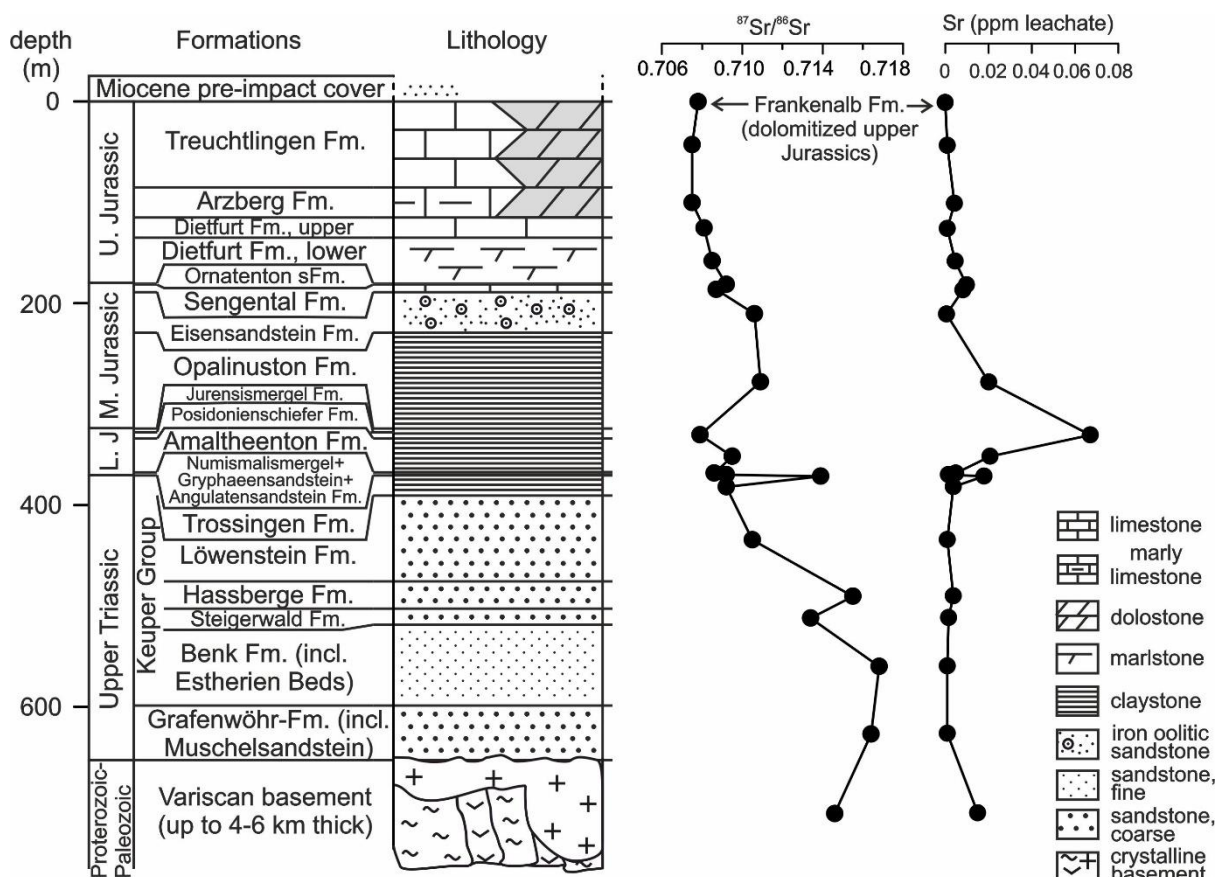
Figure 4.2 Lithologic log of the pre-impact sedimentary formations and crystalline basement (left), ^{87}Sr/^{86}Sr and Sr concentration of the leachates from them. L. J.: Lower Jurassic.

3 Lacustrine sediments mirrors ejecta erosion and catchment history

Within the proximal crater catchment, i.e., inside the crater rim, three impact ejecta formations are clear immediately after the impact event: the **crystalline breccia** (high-degree shocked allochthonous crystalline rocks), the **suevite** (impact-melt bearing breccia) and the **Bunte Breccia** (largely unshocked, allochthonous breccia containing sedimentary components). If an overturned stratigraphy of the whole impact ejecta resulting from the impact exists (e.g. overturned Kaibab Fm. and Moenkopi Fm. in Barringer crater, Osinski et al., 2013, his Fig. 4.5), then a reverse ^{87}Sr/^{86}Sr time series of the lacustrine sediments should match the trend of the pre-impact target sequences upon weathering and lake filling.

Under this assumption, the $^{87}Sr/^{86}Sr$ trend of lacustrine carbonate from base to top corresponds to the $^{87}Sr/^{86}Sr$ in the order of crystalline basement, suevite, lower to upper Triassics, and finally lower to upper Jurassics (**Figure 2**).

The $^{87}Sr/^{86}Sr$ ratios of lacustrine carbonate range from 0.7103 to 0.7138 (**Figure 3**). Values higher than 0.7110 are almost exclusively observed from the basal member to the clinoptilolite smbr. Strikingly, only four phases neither mirroring the whole pre-impact sequence, or corresponded to lithostratigraphic members, are recognized by $^{87}Sr/^{86}Sr$ trend of the lacustrine carbonates: 1) high and largely variable $^{87}Sr/^{86}Sr$ at basal member (0.7138 to 0.7126); 2) steep decreasing $^{87}Sr/^{86}Sr$ at clinoptilolite smbr (0.7125 to 0.7111); 3) low and nearly invariant $^{87}Sr/^{86}Sr$ from top part of analcime smbr to dolomite-marl smbr (0.7105); 4) minor increasing $^{87}Sr/^{86}Sr$ at clay member (to 0.7108).

Instead, the $^{87}Sr/^{86}Sr$ intervals of the lacustrine carbonate can be explained by endmember mixing with the calculated $^{87}Sr/^{86}Sr$ leachate ratios of the crystalline, suevite and Bunte Breccia components. The observed $^{87}Sr/^{86}Sr$ trend does not reflect the trend of an "entirely overturned stratigraphy".

Alternatively, to reach a $^{87}Sr/^{86}Sr$ range similar to the basal member, assuming discharges from the Triassic aquifers are the major water source for the earliest lake stage, would lead to inconsistence with the alkaline lake condition upon hydrochemical modelling test (Arp et al., 2013a; Stüeken et al., 2020). However, field mapping suggests within the crater rim, outcrops of Triassic Keuper Group are indeed exposed right adjacent to the allochthonous crystalline blocks (Hüttner and Schmidt-Kaler, 2005), thereby the high $^{87}Sr/^{86}Sr$ during the earliest lake stage cannot rule out minor Triassic influxes. This possible "partly overturned stratigraphy" (**Figure 4C**), nonetheless, agrees with the modelling prediction that the ejection velocity increases with target depth (Oberbeck, 1975).
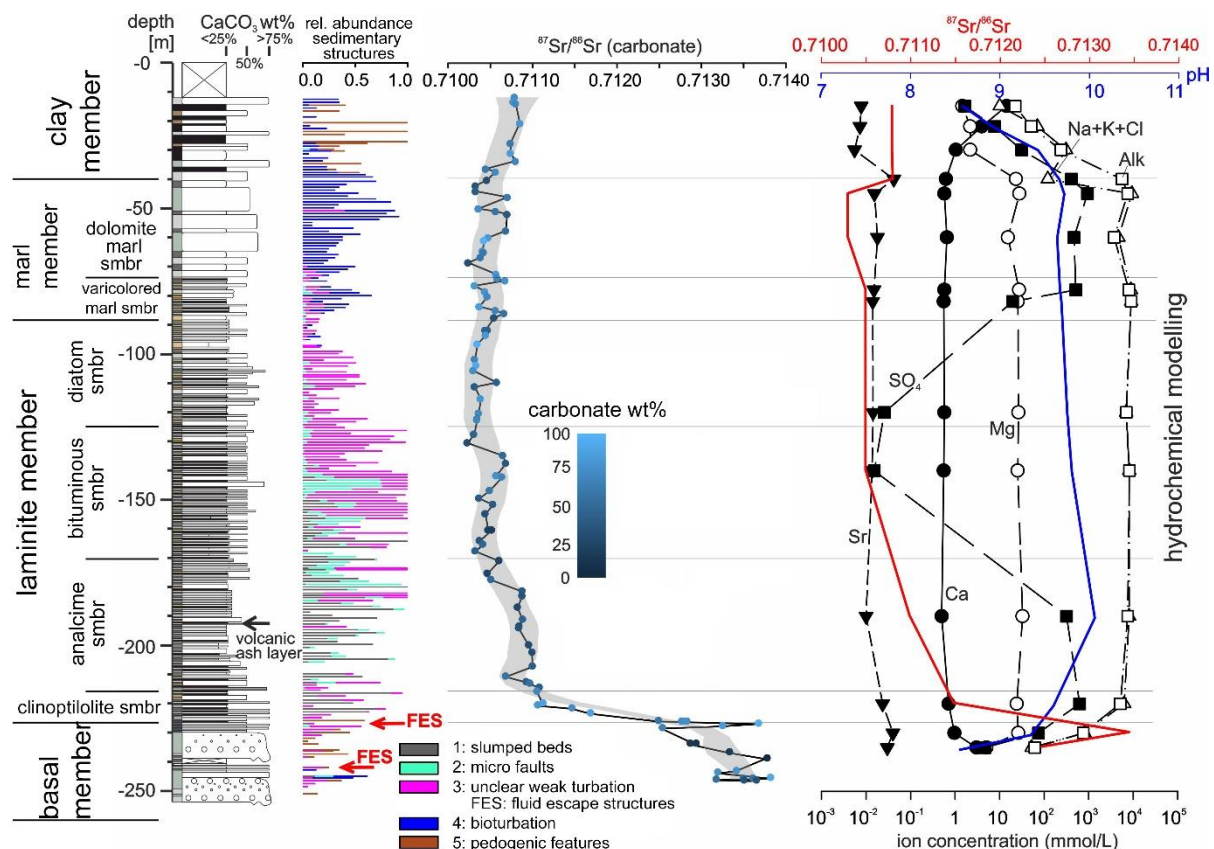
Figure 4.3 Lithological log, relative abundance of sedimentary structure and carbonate $^{87}Sr/^{86}Sr$ of the Miocene Ries lacustrine deposits transected from NR1003. The relative abundance of sedimentary structures related to syn-sedimentary turbation was noted in 5 categories for every meter of the core (Table B.1). The

carbonate content (wt %) is a calculated dolomite weight percentage. Hydrochemical modelling results by PHREEQC program were shown for each lake stage, at the right side.

Whereas in another scenario, assuming incoming waters only from crystalline basement and Jurassic limestone/dolomite, a common groundwater aquifer in the area (Winkler, 1972), are mixed to introduce a numerically similar Sr isotope range of the basal member, is not consistent with the occurrence of a diagnostic clay mineral, the 660 °C montmorillonite, produced by suevite alteration (Salger, 1977). Likewise, successively increasing karstic waters from the Jurassic aquifer relative to crystalline basement waters may also explain a decline in lake water pH at the clinoptilolite smbr (Arp et al., 2013a; Stüeken et al., 2020) and thereby cannot be ruled out. The discernment of endmember mixing during each lake stage (**Figure 3**), according to $^{87}Sr/^{86}Sr$ and Sr concentration of solutions, as well as hydrochemical modelling tests, therefore needs to be consistent with other geochemical and geological constraints. Detailed modelling constraints for each stage are provided in **Appendix B**. The $^{87}Sr/^{86}Sr$ of lacustrine carbonates rather suggests homogeneous erosion processes of the Bunte Breccia and suevite than from individual sedimentary formation.

4 Implication for hydrological evolution of terrestrial and Martian impact crater lakes

Unlike the Martian craters, the post-depositional modifications (e.g. late glacial erosion, vegetation and anthropogenic activities) of the post-Miocene Ries landscape severely bewildered some important palaeohydrological indications at the Ries region. Post-impact coarse-grained siliciclastics at the crater margin resembling channel and delta facies do exist, however, most of them currently are poorly investigated and cannot be assigned to corresponding lithostratigraphic members with confidence. An exception is the conglomerates at Ulrichsberg, with the intercalated laminites correlated to the laminite member, also equivalent as the Adlersberg bioherm (Arp et al., 2013a; Arp et al., 2019b). Without precise sedimentary architecture, the relative amount and importance of surface runoff in the hydrological system are hard to determine. However, either by groundwater sapping or surface runoff, or both, could lead to the erosion of the ejecta formations in watershed. The pre-impact swamp facies at the margin suggests that the groundwater table is very close to the ground surface (e.g. Stöffler et al., 2013, see **Figure 4A**). Considering the highly fractured crystalline basement and porous ejecta formations soon after the impact (Arp et al., 2021; Tsikalas and Faleide, 2007), groundwater flows should be pervasive at the earliest lake stages, when the weak compaction by the thin sediment loadings does not seal the pathways. Indeed, two horizons of fluid escape structures, indicating groundwater seepage, were only shown in the earliest lake stage, i.e. the basal member (**Figure 3**). Later when the crater lake quickly transgressed to a deep lake with a stable volume, the observed sedimentary structures are dominated by slumping, most extensive in the analcime smbr, as well as other high degree of soft sedimentary deformations (**Figure 3**). Above the analcime smbr, slumpings faded in occurrence and were replaced by increasing abundance in brittle deformation (syn-sedimentary microfaults) and even gentler, weakly contorted deformations in bituminous and diatom smbr. Upon sedimentary filling and evaporation, increasing mixing (Zeng et al. submitted), reoxygenation of the lake bottom (bioturbation) and even subaerial exposure finally follow the lake level drops (diatom smbr to dolomite-marl smbr). This change to a more arid setting at marl member, indeed reflects silt-up of a lake basin (Zeng et al. submitted), sufficiently explained by decreasing groundwater discharges and does not require a climate-induced warming and/or decrease in precipitation.

The trend of this change in sedimentary structures indicate: 1) increasing crater floor stability when subjected to crater floor sagging as well as sedimentation and compaction (Arp et al., 2021; Tsikalas and Faleide, 2007) and 2) from a water-saturated, adhesive syn-sedimentary setting with soft sediment deformation to a less hydrated syn-sedimentary setting with even

brittle deformation. The latter could be explained by the decreasing groundwater upwelling, following the loss of mega porosity resulting from increasing crater floor stabilities. Indeed, an external, deep earthquake event may produce heavy shockwaves propagated to the deep part of laminite member and relatively less deformed upper laminite member during the deposition of laminite member—however, the long-term crater floor sagging due to its instability (Arp et al., 2021) and the reactivation of the *in situ* fractures (Tsikalas and Faleide, 2007) convincingly suggest external triggers are not necessary for the trend of syn-sedimentary deformations. Moreover, any post-impact earthquake events are not surprising for the early unsettled crater floor and the crater stability will increase with time in any case. In fact, similar trends in sedimentary structures are also observed in other impact crater lakes (Ebinghaus et al., 2017; Sauerbrey et al., 2013), despite of little attentions on their hydrological implications.

Based on mainly sedimentologic and isotopic approaches, we suggest a new hydrological history for the Ries crater lake:

1) The drainage system, surprisingly, did not leach entire catchment significantly (especially the Bunte Breccia) at the early lake stage (basal member). This is most possibly due to a deep groundwater table caused by the heated crater floor, resulting in the utterly higher evaporation rate than the precipitation(discharging) rates (**Figure 4B**). The precipitation/evaporation (P/E) ratio is lowest.

2) Due to the cooling of the warm crater floor, decreased evaporation rate led to a groundwater table rise. At the time equivalent to the top of clinoptilolite smbr, groundwater table rose high enough to leach the Bunte Breccias (**Figure 4C**). The P/E ratio slightly increases.

3) When the crater floor totally cooled down, the maximum P/E ratio was encountered and a maximum lake level at analcime smbr is evident (**Figure 4D**).

4) Ongoing sedimentation led to greater compaction and waived the loose fractures/mega porosities in the crater floor. As the consumption of accommodation spaces and rise of base level (bituminous smbr to diatom smbr, **Figure 4E**), sporadic surface runoffs stood out for lake discharging, since the pathways of groundwater upwelling were largely sealed. At a significantly shallower lake level, discharge by surface runoffs undoubtably disturb the lake stratification, as well as the biogeochemical processes (episodically sulfate-increase within the extensive methanogenic interval, Zeng et al., submitted). P/E ratio decreased again to highly evaporative setting (marl member, **Figure 4F**).

5) When the lake was completely silted-up (clay member, **Figure 4G**), new tributaries started at the outside of crater margin and leached the specific formations (e.g. the Lower/Middle Jurassic pyrite-rich claystones, especially Opalinuston Fm.).
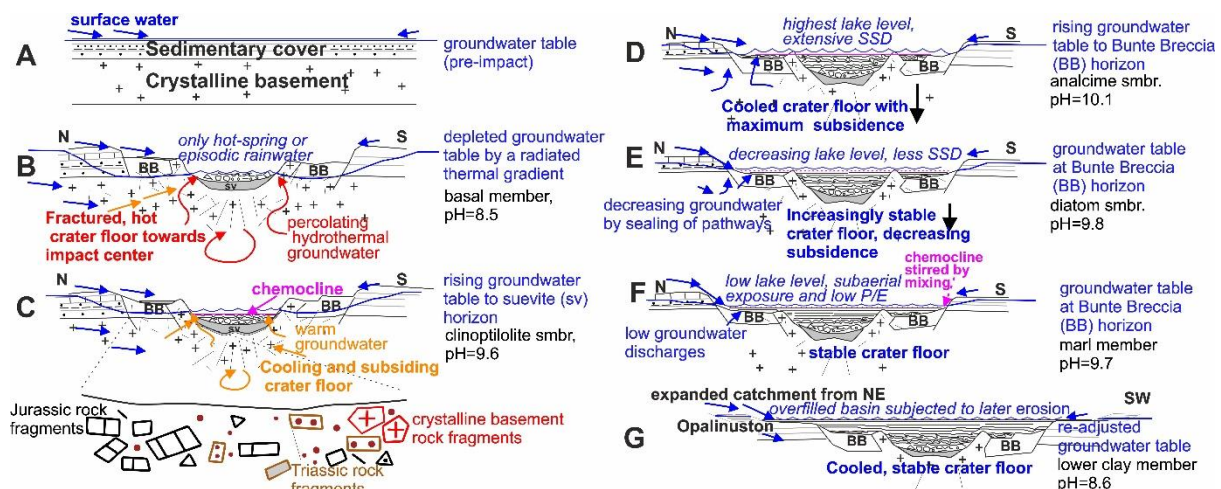
Figure 4.4 Hydrological evolution of the Ries impact crater lake.
An ambient groundwater table close to the surface is assumed (A) and then shoved downwards due to the immense heat of the hot crater floor by impact event (B). The

readjustment of the groundwater table soon started to successively leach crystalline basement rock, suevite then Bunte Breccia (B to C). Maximum groundwater discharge was marked at analcime smbr (D), then the sediment loading and compaction lead to seal of groundwater pathway and standing out of surface runoffs. SSD: soft sediment deformation. The low groundwater discharge leads to standing-out of the surface water and higher evaporation towards marl member (decreasing P/E ratios), which do not require a change to a warmer climate (E,F). When the crater was completely filled, the re-adjustment is finished, and new tributaries occurred at new catchment area (G).

The abovementioned evolution of crater lake hydrology describes a catchment expansion from i) initially restricted catchment within inner ring to ii) between inner ring and crater rim to iii) finally expanding over the crater rim. These changes, however, do not necessarily require a change in climate, especially increasing precipitation. Assuming a climate-induced ambient P/E ratio similar to the pre-impact condition persisted throughout the lake history, the observed hydrology of the initial lake stage convincingly shows that the impact-released heat significantly changed the P/E ratio only at the beginning. Indeed, the timing of Ries impact event (ca. 14.9 Ma) falls into the transition between the warm Miocene Climatic Optimum (MCO) and long-term cooling mid-Miocene Climate Transition (MCT, Flower and Kennett, 1994). The current discussions on this climate change are still greatly disputed due to limited data, e.g., while Mosbrugger et al. (2005) points a rather pure cooling and less change in mean annual precipitation (MAT) by studying the flora records, Methner et al. (2020) suggests a drier and decrease in MAT towards MCT. In any case, it is unlikely that a climate-induced warming leads to the decreased P/E ratio and enhanced evaporation at the beginning (basal member). Instead, the initial hot crater floor with a low P/E would readjust to ambient P/E ratio when the crater floor cooled down again. The presence of increasing precipitation events, if any, would only lead to a faster readjustment rate of the described post-impact hydrological system.

Impact craters take the advantage of impact-created accommodation spaces to be natural underfilled basins. Whereas the Miocene Ries surrounding area was characterized by low relief and accommodation spaces as well as slow sedimentation (e.g. Zeng et al., 2021), the hydrological readjustment leads to similar sedimentary settings during the deposition of the clay member. A prerequisite for this self-readjusted trend is the ambient P/E ratio ≈ 1. If P<<E, nor bedload transportation or sedimentation take place, instead as a constant evaporative setting. As deposition consumes accommodation spaces in the crater and base level rises, successive erosion of the vertically stacked ejecta formations thereby leads to influxes with distinct hydrochemical compositions (Arp et al., 2013a; Zeng et al., submitted). The lacustrine biogeochemical processes, e.g. anaerobic sulfate reduction, methanogenesis and aerobic methanotrphy, finally follow this hydrological and hydrochemical trend (Zeng et al., submitted). The present study elucidated a self-readjusted hydrological and hydrochemical system of an impact crater lake, providing valuable insights to other terrestrial and extra-terrestrial impact crater lake system, particularly for the ongoing discussions on the Martian craters.

References

Andrews-Hanna, J.C., Zuber, M.T., Arvidson, R.E. and Wiseman, S.M. (2010) Early Mars hydrology: Meridiani playa deposits and the sedimentary record of Arabia Terra. Journal of Geophysical Research: Planets 115.

Appelo, C.A.J. and Postma, D. (2005) Geochemistry, groundwater and pollution. CRC press, London.

Arp, G. (1995) Lacustrine bioherms, spring mounds, and marginal carbonates of the Ries-impact-crater (Miocene, southern Germany). Facies 33, 35-89.

Arp, G., Blumenberg, M., Hansen, B.T., Jung, D., Kolepka, C., Lenz, O., Nolte, N., Poschlod, K., Reimer, A. and Thiel, V. (2013a) Chemical and ecological evolution of the Miocene Ries impact crater lake, Germany: A reinterpretation based on the Enkingen (SUBO 18) drill core. GSA Bulletin 125, 1125-1145.

Arp, G., Kolepka, C., Simon, K., Karius, V., Nolte, N. and Hansen, B.T. (2013b) New evidence for persistent impact-generated hydrothermal activity in the Miocene Ries impact structure, Germany. Meteoritics & Planetary Science 48, 2491-2516.

Arp, G., Dunkl, I., Jung, D., Karius, V., Lukács, R., Zeng, L., Reimer, A. and Head III, J.W. (2021) A Volcanic Ash Layer in the Nördlinger Ries Impact Structure (Miocene, Germany): Indication of Crater Fill Geometry and Origins of Long-Term Crater Floor Sagging. Journal of Geophysical Research: Planets 126, e2020JE006764.

Arp, G., Hansen, B.T., Pack, A., Reimer, A., Schmidt, B.C., Simon, K. and Jung, D. (2017) The soda lake—mesosaline halite lake transition in the Ries impact crater basin (drilling Löpsingen 2012, Miocene, southern Germany). Facies 63, 1-20.

Arp, G., Reimer, A. and Reitner, J. (2003) Microbialite Formation in Seawater of Increased Alkalinity, Satonda Crater Lake, Indonesia. Journal of Sedimentary Research 73, 105-127.

Arp, G., Reimer, A., Simon, K., Sturm, S., Wilk, J., Kruppa, C., Hecht, L., Hansen, B.T., Pohl, J., Reimold, W.U., Kenkmann, T. and Jung, D. (2019a) The Erbisberg drilling 2011: Implications for the structure and postimpact evolution of the inner ring of the Ries impact crater. Meteoritics & Planetary Science 54, 2448-2482.

Arp, G., Schultz, S., Karius, V. and Head, J.W. (2019b) Ries impact crater sedimentary conglomerates: Sedimentary particle 'impact pre-processing', transport distances and provenance, and implications for Gale crater conglomerates, Mars. Icarus 321, 531-549.

Artemieva, N., Wünnemann, K., Krien, F., Reimold, W. and Stöffler, D. (2013) Ries crater and suevite revisited—Observations and modeling Part II: Modeling. Meteoritics & Planetary Science 48, 590-627.

Barakat, A.O. and Rullkötter, J. (1997) A Comparative Study of Molecular Paleosalinity Indicators: Chromans, Tocopherols and C20 Isoprenoid Thiophenes in Miocene Lake Sediments (Nördlinger Ries, Southern Germany). Aquatic Geochemistry 3, 169-190.

Birck, J.L. (1986) Precision K-Rb-Sr isotopic analysis: application to Rb-Sr chronology. Chemical geology 56, 73-83.

Bolten R.H . (1977): Die karbonatischen Ablagerungen des obermiozänen Kratersees im Nördiinger Ries. Ludwig-Maximilians-Universität, München.

Caudill, C., Osinski, G.R., Greenberger, R.N., Tornabene, L.L., Longstaffe, F.J., Flemming, R.L. and Ehlmann, B.L. (2021) Origin of the degassing pipes at the Ries impact structure and implications for impact-induced alteration on Mars and other planetary bodies. Meteoritics & Planetary Science 56, 404-422.

Doebbert, A.C., Johnson, C.M., Carroll, A.R., Beard, B.L., Pietras, J.T., Carson, M.R., Norsted, B. and Throckmorton, L.A. (2014) Controls on Sr isotopic evolution in lacustrine systems: Eocene green river formation, Wyoming. Chemical Geology 380, 172-189.

Ebinghaus, A., Jolley, D.W., Andrews, S.D. and Kemp, D.B. (2017) Lake sedimentological and ecological response to hyperthermals: Boltysh impact crater, Ukraine. Sedimentology 64, 1465-1487.

Füchtbauer, H., Von Der Brelie, G., Dehm, R., Förstner, U., Gall, H., Höfling, R., Hoefs, J., Hollerbach, H., Hufnagel, B., Jankowski, B., Jung, W., Malz, H., Mertes, H., Rothe,

P., Salger, M., Wehner, H. and Wolf, M. (1977) Tertiary lake Sediments of die Ries, research borehole Nördlingen 1973 - a summary. Geologica Bavarica 75, 13-20.

Fassett, C.I. and Head, J.W. (2008) The timing of martian valley network activity: Constraints from buffered crater counting. Icarus 195, 61-89.

Flower, B.P. and Kennett, J.P. (1994) The middle Miocene climatic transition: East Antarctic ice sheet development, deep ocean circulation and global carbon cycling. Palaeogeography, Palaeoclimatology, Palaeoecology 108, 537-555.

Freudenberger, W., Linhardt, E. and Wrobel, J.P. (2000) Geologie, Hydrogeologie und Geochemie der Thermalwasserbohrung Treuchtlingen 2 (T2). Geologica Bavarica 105, 97-121.

Gierlowski-Kordesch, E., Jacobson, A., Blum, J. and Valero Garćes, B.L. (2008) Watershed reconstruction of a Paleocene–Eocene lake basin using Sr isotopes in carbonate rocks. Geological Society of America Bulletin 120, 85-95.

Graup, G. (1978) Das Kristallin im Nördlinger Ries: Petrographische Zusammensetzung und Auswurfmechanismus der kristallinen Trümmermassen, Struktur des kristallinen Untergrundes und Beziehungen zum Moldanubikum. Enke Verlag. , Stuttgart, Germany.

Groiss, J. T., Haunschild, H. and Zeiss, A. (2000) Das Ries und sein Vorland. Sammlung Geologischer Führer 92, 1-271.

Hörz, F., Ostertag, R. and Rainey, D. (1983) Bunte Breccia of the Ries: Continuous deposits of large impact craters. Reviews of Geophysics 21, 1667-1725.

Hüttner, R. and Schmidt-Kaler, H. (1999) Wanderungen in die Erdgeschichte: Meteoritenkrater Nördlinger Ries. Verlag Dr. Friedrich Pfeil, München.

Horn, P., Müller-Sohnius, D., Köhler, H. and Graup, G. (1985) Rb-Sr systematics of rocks related to the Ries Crater, Germany. Earth and Planetary Science Letters 75, 384-392.

Huber, G., Huber, R., Jones, B.E., Lauerer, G., Neuner, A., Segerer, A., Stetter, K.O. and Degens, E.T. (1991) Hyperthermophilic Archaea and Bacteria Occurring within Indonesian Hydrothermal Areas. Systematic and Applied Microbiology 14, 397-404.

Iturrino, G.J., Christensen, N.I., Kirby, S.H. and Salisbury, M.H. (1991) Seismic velocities and elastic properties of oceanic gabbroic rocks from Hole 735B. Proceedings of the Ocean Drilling Program, Scientific Results 118, 227-244.

Jankowski, B. (1981) Die Geschichte der Sedimentation im Nördlinger Ries und Randecker Maar. Inst. für Geologie, Ruhr-Univ.

Johnson, G.R. and Olhoeft, G.R. (1984) Density of rocks and minerals, in: R.S., C. (Ed.), Handbook of physical properties of rocks, Volume III. CRC Press, Boca Raton, pp. 1-38.

Kempe, S. and Kazmierczak, J. (1994) The role of alkalinity in the evolution of ocean chemistry, organization of living systems, and biocalcification processes. Bulletin de la Institut Océanographique (Monaco) 13, 61-117.

Lindemann, S., Moran, J., Stegen, J., Renslow, R., Hutchison, J., Cole, J., Dohnalkova, A., Tremblay, J., Singh, K., Malfatti, S., Chen, F., Tringe, S., Beyenal, H. and Fredrickson, J. (2013) The epsomitic phototrophic microbial mat of Hot Lake, Washington: community structural responses to seasonal cycling. Frontiers in Microbiology 4.

Müller, D. (1969) Ein neues Profil vom Mittelkeuper bis zum Unterdogger bei Harburg nahe dem Nördlinger Ries. Mitteilungen der Bayerischen Staatssammlung für Paläontologie und historische Geologie 9, 73-92.

Müller, G., Irion, G. and Förstner, U. (1972) Formation and diagenesis of inorganic Ca− Mg carbonates in the lacustrine environment. Naturwissenschaften 59, 158-164.

Manger, G.E. (1963) Porosity and bulk density of sedimentary rocks, in: Udall, S.L., Nolan, T.B. (Eds.), Contributions to Geochemistry, Washington.

Methner, K., Campani, M., Fiebig, J., Löffler, N., Kempf, O. and Mulch, A. (2020) Middle Miocene long-term continental temperature change in and out of pace with marine climate records. Scientific Reports 10, 7989.

Montano, D., Gasparrini, M., Gerdes, A., Della Porta, G. and Albert, R. (2021) In-situ U-Pb dating of Ries Crater lacustrine carbonates (Miocene, South-West Germany): Implications for continental carbonate chronostratigraphy. Earth and Planetary Science Letters 568, 117011.

Mosbrugger, V., Utescher, T. and Dilcher, D.L. (2005) Cenozoic continental climatic evolution of Central Europe. Proceedings of the National Academy of Sciences 102, 14964-14969.

Oberbeck, V.R. (1975) The role of ballistic erosion and sedimentation in lunar stratigraphy. Reviews of Geophysics 13, 337-362.

Osinski, G.R., Grieve, R.A.F. and Tornabene, L.L. (2013) Excavation and Impact Ejecta Emplacement, in: Osinski, G.R., Pierrazzo, E. (Eds.), Impact Cratering. Wiley-Blackwell, Chicester, pp. 43-59.

Owen, R.B., Renaut, R.W. and Jones, B. (2008) Geothermal diatoms: a comparative study of floras in hot spring systems of Iceland, New Zealand, and Kenya. Hydrobiologia 610, 175-192.

Paul, J., Wemmer, K. and Ahrendt, H. (2008) Provenance of siliciclastic sediments (Permian to Jurassic) in the Central European Basin. Zeitschrift der Deutschen Gesellschaft für Geowissenschaften 159, 641-650.

Reimer, A., Landmann, G. and Kempe, S. (2009) Lake Van, Eastern Anatolia, Hydrochemistry and History. Aquatic Geochemistry 15, 195-222.

Reis, O. M. (1926) Zusammenfassung über die im Ries südlich von Nördlingen auftretenden Süßwasserkalke und ihre Entstehung. Jahresberichtc und Mitteilungen des oberrheinischen geologischen Vereins, Neue Folge, 14 (1925), 176-190, Stuttgart

Renaut, R., Tiercelin, J. and Owen, R. (1986) Mineral precipitation and diagenesis in the sediments of the Lake Bogoria basin, Kenya Rift Valley. Geological Society, London, Special Publications 25, 159-175.

Renaut, R.W. and Tiercelin, J.-J. (1993) Lake Bogoria, Kenya: soda, hot springs and about a million flamingoes. Geology Today 9, 56-61.

Riding, R. (1979): Origin and diagenesis of lacustrine algal bioherms at the margin of the Ries crater, Upper Miocene, southern Germany. Sedimentology, 26, 645 -680.

Rocholl, A., Böhme, M., Gilg, H.A., Pohl, J., Schaltegger, U. and Wijbrans, J. (2018) Comment on "A high-precision 40Ar/39Ar age for the Nördlinger Ries impact crater, Germany, and implications for the accurate dating of terrestrial impact events" by Schmieder et al.(Geochimica et Cosmochimica Acta 220 (2018) 146–157). Geochimica et Cosmochimica Acta 238, 599-601.

Roseborough, V., Horvath, D.G. and Palucis, M.C. (2021) Was Gale Crater (Mars) Connected to a Regionally Extensive Groundwater System? Geophysical Research Letters 48, e2020GL092107.

Rothe, P. and Hoefs, J. (1977) Isotopen-geochemische Untersuchungen an Kabonaten der Ries-See-Sedimente der Forschungsbohrung Nördlingen 1973. Geologica Bavarica 75, 59-66.

Rullkötter, J., Littke, R. and Schaefer, R.G. (1990) Characterization of Organic Matter in Sulfur-Rich Lacustrine Sediments of Miocene Age (Nördlinger Ries, Southern Germany), Geochemistry of Sulfur in Fossil Fuels. American Chemical Society, pp. 149-169.

Salger, M. (1977) Die tonminerale der forschungsbohrung Nördlingen 1973. Geologica Bavarica 75, 67-73.

Sauerbrey, M.A., Juschus, O., Gebhardt, A.C., Wennrich, V., Nowaczyk, N.R. and Melles, M. (2013) Mass movement deposits in the 3.6 Ma sediment record of Lake El'gygytgyn, Far East Russian Arctic. Climate of the Past 9, 1949-1967.

Schauderna, H. (1983) Die Diatomeenflora aus den miozänen Seeablagerungen im Nördlinger Ries. Palaeontographica Abteilung B, 83-193.

Schnetzler, C., Philpotts, J.A. and Pinson Jr, W. (1969) Rubidium-strontium correlation study of moldavites and Ries crater material. Geochimica et Cosmochimica Acta 33, 1015-1021.

Schwarz, W.H., Hanel, M. and Trieloff, M. (2020) U-Pb dating of zircons from an impact melt of the Nördlinger Ries crater. Meteoritics & Planetary Science 55, 312-325.

Siegert, S., Branney, M.J. and Hecht, L. (2017) Density current origin of a melt-bearing impact ejecta blanket (Ries suevite, Germany). Geology 45, 855-858.

Siegert, S. and Hecht, L. (2019) Heterogeneity of melts in impact deposits and implications for their origin (Ries suevite, Germany). Meteoritics & Planetary Science 54, 2409-2447.

Stüeken, E.E., Tino, C., Arp, G., Jung, D. and Lyons, T.W. (2020) Nitrogen isotope ratios trace high-pH conditions in a terrestrial Mars analog site. Science Advances 6, eaay3440.

Stöffler, D., Artemieva, N.A., Wünnemann, K., Reimold, W.U., Jacob, J., Hansen, B.K. and Summerson, I.A. (2013) Ries crater and suevite revisited—Observations and modeling Part I: Observations. Meteoritics & Planetary Science 48, 515-589.

Talbot, M. (1990) A review of the palaeohydrological interpretation of carbon and oxygen isotopic ratios in primary lacustrine carbonates. Chemical Geology: Isotope Geoscience Section 80, 261-279.

Tsikalas, F. and Faleide, J.I. (2007) Post-impact structural crater modification due to sediment loading: An overlooked process. Meteoritics & Planetary Science 42, 2013-2029.

Veizer, J., Ala, D., Azmy, K., Bruckschen, P., Buhl, D., Bruhn, F., Carden, G.A., Diener, A., Ebneth, S. and Godderis, Y. (1999) 87Sr/86Sr, δ13C and δ18O evolution of Phanerozoic seawater. Chemical geology 161, 59-88.

Wand, U., Samarkin, V.A., Nitzsche, H.-M. and Hubberten, H.-W. (2006) Biogeochemistry of methane in the permanently ice-covered Lake Untersee, central Dronning Maud Land, East Antarctica. Limnology and Oceanography 51, 1180-1194.

Wand, U., Schwarz, G., Brüggemann, E. and Bräuer, K. (1997) Evidence for physical and chemical stratification in Lake Untersee (central Dronning Maud Land, East Antarctica). Antarctic Science 9, 43-45.

Winkler, H.A.G. (1972) Das Grundwasser im Nörlinger Ries unter Berücksichtigung der hydrologischen und hydrochemischen Seziehungen zum Speichergestein. Technische Universität München.

Wolff, M. and Füchtbauer, H. (1976) Die karbonatische Randfazies der tertiären Süßwasserseen des Nördlinger Ries und des Steinheimer Beckens. Geologisches Jahrbuch Reihe D, Band D 14.

Wünnemann, K., Morgan, J.V. and Jödicke, H. (2005) Is Ries crater typical for its size? An analysis based upon old and new geophysical data and numerical modeling, in: Kenkmann, T., Hörz, F., Deutsch, A. (Eds.), Large Meteorite Impacts III. Geological Society of America, p. 0.

Zeng, L., Gätjen, J., Reimer, A., Karius, V., Thiel, V. and Arp, G. (submitted) Temporary sulfate depletion and extremely 13C-enriched dolomite formation in a Miocene impact crater lake: successive ejecta erosion controls lacustrine biogeochemical processes. Geochimica et Cosmochimica Acta.

Zeng, L., Ruge, D.B., Berger, G., Heck, K., Hölzl, S., Reimer, A., Jung, D. and Arp, G. (2021) Sedimentological and carbonate isotope signatures to identify fluvial processes and catchment changes in a supposed impact ejecta-dammed lake (Miocene, Germany). Sedimentology 68, 2965-2995.

Chapter 5.   Sedimentological and carbonate isotope signatures to identify fluvial processes and catchment changes in a supposed impact ejecta-dammed lake (Miocene, Germany)

LINGQI ZENG*, DAG B. RUGE*, GÜNTHER BERGER†, KARIN HECK‡, STEFAN HÖLZL‡, ANDREAS REIMER*, DIETMAR JUNG§ and GERNOT ARP*
*Georg-August-Universität Göttingen, Geowissenschaftliches Zentrum, Goldschmidtstrasse 3, 37077 Göttingen, Germany,
†Sudetenstraße 6, Pleinfeld, Germany
‡Staatliche Naturwissenschaftliche Sammlungen Bayerns - RiesKraterMuseum Nördlingen, Eugene-Shoemaker-Platz 1, 86720 Nördlingen, Germany
§Bayerisches Landesamt für Umwelt, Geologischer Dienst, Hans-Högn-Straße 12, 95030 Hof/Saale

Correspondence author: LINGQI ZENG (email: lzeng@gwdg.de)
Associate Editor – Concha Arenas
Short title – Identification of fluvial processes and catchment changes
Published on *Sedimentology*

Abstract

The identification and distinction of fluvial from lacustrine deposits and the recognition of catchment changes are crucial for the reconstruction of climate changes in terrestrial environments. The investigated drill core succession shows a general evolution from red-brown claystones to white-grey marlstones and microcrystalline limestones, which all have previously been considered as relict deposits of an impact ejecta-dammed lake, falling within the mid-Miocene Climate Transition. However, recent mammal biostratigraphic dating, suggests a likely pre-impact age. Indeed, no pebbles from impact ejecta have been detected, only local clasts of Mesozoic formations, in addition to rare Palaeozoic lydites from outside of the study area. Lithofacies analysis demonstrates only the absence of lacustrine criteria, except for one charophyte-bearing mudstone. Instead, the succession is characterized by less diagnostic floodplain fines with palaeosols, palustrine limestones with root voids and intercalated thin sandstone beds. Carbonate isotope signatures of the mottled marlstones, palustrine limestones and mud-supported conglomerates substantiate the interpretation of a fluvial setting: Low, invariant $\delta^{18}O_{carb}$ reflects a short water residence time and highly variable $\delta^{13}C_{carb}$ indicates a variable degree of pedogenesis. Carbonate $^{87}Sr/^{86}Sr$ ratios of the entire succession show a unidirectional trend from 0.7103 to 0.7112, indicating a change of the source of solutes from Triassic to Jurassic rocks, identical to the provenance trend from extraclasts. The increase in carbonate along the succession is therefore independent from climate changes but reflects a base-level rise from the level of the siliciclastic Upper Triassic to the carbonate-bearing Lower to Middle Jurassic bedrocks. This study demonstrates that, when information on sedimentary architecture is limited, a combination of facies criteria (i.e., presence or absence of specific sedimentary structures and diagnostic organisms), component provenance, and stable and radiogenic isotopes is required to unequivocally distinguish between lacustrine and fluvial sediments, and to disentangle regional geological effects in the catchment and climate influences.

1 Introduction

Non-marine sediments, when constituting long lasting stratigraphic records, form valuable climate archives for the reconstruction of past terrestrial environments. Specifically, lacustrine series provide high-resolution records of temperatures, precipitation and orbital forcing (e.g., Olsen, 1986; Cohen, 2003; Leng & Marshall, 2004; Andrews, 2006). Likewise, climate trends can be deduced from fluvial series and palaeosols, although at a lower time resolution (e.g., Demko *et al.*, 2004, Allen *et al.*, 2014, Opluštil *et al.*, 2015). In any case, a proper identification of the depositional setting as well as local effects of tectonics and catchment changes is required. The distinction between a lacustrine and a fluvial setting for sediments such as fine-grained sandstones, floodplain fines, palustrine limestones and oncolitic tufa, however, is still challenging when surface exposures are limited, only few or isolated drillings are available, or occurrences are relict. Then, the geometry of sedimentary bodies (e.g., Miall 1985, 1996) cannot be determined, and interpretations rely on sedimentological and palaeontological evidence (e.g., Rust, 1982; Selley 1992; Reading 1996; Flügel, 2004).

However, stable and radiogenic isotope signatures of carbonate rocks can provide crucial information with respect to hydrology and catchment, and also help to distinguish between fluvial and lacustrine settings. Strontium isotopes form a useful tool in tracing the provenance of fluids and catchment reconstruction (Faure, 1986). Examples are catchment changes during expansion-contraction lake cycles (Rhodes *et al.*, 2002, Doebbert *et al.*, 2014), differentiation of sub-basins with different catchments (Gierlowski-Kordesch *et al.*, 2008) and changes in the chemical composition of lake tributaries upon erosion of different lithological units (Jin *et al.*, 2009; Pietzsch *et al.*, 2018) or impact ejecta (Arp *et al.*, 2013) in the catchment area. In turn, carbonate $\delta^{13}C$ and $\delta^{18}O$ data sets from continental series are commonly used for reconstructions of palaeoclimate (e.g., Ekart *et al.*, 1999; Leng & Marshall 2004; Andrews 2006), but also help to constrain hydrological conditions (e.g., Talbot, 1990; Li & Ku, 1997), biological activity (e.g., Thompson *et al.*, 1997), palaeoaltimetry (e.g., Cyr *et al.*, 2005; Rowley, 2007) and diagenetic alterations (e.g., Swart, 2015).

The present isotopic and sedimentological study focuses on the example of the Miocene Georgensgmünd Formation in southern Germany. These deposits have previously been considered as lake deposits (Dorn, 1939) that formed as a result of damming of an ancient river by ejecta from the Ries asteroid impact (Birzer, 1969), immediately north of the Northern Alpine Foreland Basin (**Figure 5.1**). It would be, to the knowledge of the authors, the only supposed impact ejecta-dammed lake on Earth reported in literature.

Dependent on different stratigraphic interpretations (Birzer, 1969; Berger, 2010; Schirmer, 2014), the Georgensgmünd Formation falls into the time range of the pre-Ries-impact Miocene Climatic Optimum (MCO, *ca.* 17 to 15 Ma; Zachos *et al.*, 2001) or the following post-Ries-impact mid-Miocene Climate Transition (MMCT, *ca.* 15 to 13 Ma; e.g., Methner *et al.*, 2020). However, the pre-impact age of deposits, as indicated by mammal fossils (early MN5, Berger 2010; see **Figure 5.2**), has been questioned (Schirmer, 2014), and later publications (e.g., Sturm *et al.*, 2015) still assume the existence of an impact ejecta-dammed lake. Hence, the effect of the asteroid impact on the fluvial system in this region is still under debate.

The aim of the study is to clarify the lacustrine versus fluvial nature of these deposits, and their relation to the asteroid impact event. The study investigates how sedimentological criteria can be supplemented by stable and radiogenic isotope data to trace provenance of sediments and fluids (from local and distant bedrocks) and disentangle regional factors (base-level changes/tectonics and headwater erosion) and climatic factors controlling sedimentation, when information on sedimentary architecture is limited.

2 Geographic and geological overview

The study area is located in the South German Scarplands (Peterek & Schröder, 2010; and references therein), approximately 100 km NNW of Munich (Figure 5.1). In this area, high-grade metamorphics and plutonites of the Variscan basement are covered by a 300 to 600 m thick Permomesozoic sediment series: local volcanics and coarse siliciclastics of the Permian Rotliegend Group (up to 300 m), and Triassic arkoses, sandstones and claystones of the Buntsandstein (*ca.* 50 m), Muschelkalk (*ca.* 50 m) and Keuper Group (225 m) (Haunschild, 1992; Freudenberger, 1996). The latter is overlain by marine deposits of the Jurassic, which comprise dark grey claystones and shales of the Schwarzjura Group (35 m), brown sandstones, iron oolites and claystones of the Braunjura Group (100 m), and white grey limestones and dolomites of the Weißjura Group (>115 m) (Berger, 1971, 1982). Since the Cretaceous, the study area has been subject to subaerial exposure and karstification. During the Cenozoic, intense erosion led to the present-day landscape (Wagner, 1960; Knetsch, 1963; Hofbauer, 2001; Peterek & Schröder, 2010), however, with an initially southward directed drainage system (i.e., the Moenodanuvius and Paleonaab) (**Figure 5.1**; Peterek & Schröder, 2010; Schirmer, 2014). At 15 Ma, a double asteroid impact event caused the formation of the Ries and Steinheim crater basins, burial of its vicinity by a decametre to 120 m thick ejecta blanket, and subsequent formation of crater lakes (Shoemaker & Chao, 1961; Pohl *et al.,* 1977; for discussion of impact age see Schmieder *et al.* 2018a,b; Rocholl *et al.* 2018a,b). Miocene relict deposits of a supposed impact ejecta-dammed lake NE of the Ries crater basin are the subject of the present study (**Figure 5.1**), because recent biostratigraphic dating points to a likely age older than the impact, consequently leading to questioning of the lacustrine nature of the deposits (Berger, 2010). Herein, the lithostratigraphic name of these Miocene relict deposits is defined as the Georgensgmünd Formation, of which the type locality is a hill ("Bühl") near Georgensgmünd, subject to quarrying at least since the 16th century (coordinates: 49°11'49.93" N, 11°0'2.79" E; von Meyer, 1834; Berger, 2010). The region was subject to an epirogenic uplift from 16.5 Ma at near sea-level to the latest Pliocene, leading to present-day altitudes of 360 to 600 metres above sea-level (m a.s.l.) (Gall, 1974; Hoffmann & Friedrich, 2017; Sant *et al.*, 2017). As a result of the Palaeogene-Neogene erosion, the escarpment of the Franconian Alb, i.e., the Upper Jurassic limestone plateau, is located approximately 8.5 km SE of the drill site. Top elevations of hills in the vicinity of Pleinfeld still show Lower to Middle Jurassic to marine claystone covers, while slopes and valley floors expose siliciclastics of the Triassic Keuper Group (Berger, 1971).

3 Material and methods

The site of the investigated drill core (coordinates: 49°6'58.44" N, 10°58'35.10" E; Berger, 1971) is located about 1.3 km NW of the town Pleinfeld at 412.6 m a.s.l. and lies ~42 m above the water level of the present-day river Rezat (Figure 5.1). The obtained drill core is 63 m in length and 5 cm in diameter. The core recovery is 87%, with losses mainly in the lowermost part of the section. The drilling was performed in 1968 by the Bavarian Building Authority for geological site investigation and groundwater observation concerning the establishment of a water reservoir. It is now hosted at the core facility of the Geological Survey at the Bavarian Environmental Agency in Hof a.d. Saale.

Macroscopic documentation of drill core lithofacies types was carried out using a Sony SLT-A99V camera (Sony Corporation, Tokyo, Japan). For microfacies analysis of carbonates, 7 thin sections (10 x 7.5 cm in size) from the Pleinfeld drill core and 12 thin sections from reference location Bühl near Georgensgmünd were used, with a thickness of 80 μm. The microscopic documentation was carried out by a Zeiss Stemi 2000-C binocular (Carl Zeiss AG, Oberkochen, Germany) equipped with a Canon EOS 500 D camera (Canon Inc., Tokyo, Japan).

Thirty-nine samples were analysed with respect to their organic (C_{org}) and carbonate carbon (C_{carb}) contents, and stable carbon and oxygen isotope ratios of the carbonate fraction [$\delta^{13}C$ and $\delta^{18}O$; and reported in per mil relative to Vienna Pee dee belemnite (V-PDB)]. From the

same samples, carbonate for carbon and oxygen stable isotope measurements was obtained under a Zeiss Stemi 2000-C binocular microscope from cut core slabs and hand specimens using a steel needle to sample separate textures. Carbonate powders were reacted with 100% phosphoric acid (density >1.95 g/cm^3) at 70 °C using a Thermo Kiel IV carbonate preparation line connected to a Finnigan Delta plus mass spectrometer (Thermo Fisher Scientific, Waltham, MA, USA). All values are reported in per mil relative to V-PDB by assigning a δ^{13}C value of +1.95‰ and a δ^{18}O value of -2.20‰ to the NBS 19 standard. Reproducibility was checked by replicate analyses of laboratory standards and is better than ±0.05‰ (1σ). Standard deviations of the stable isotope measurements, if not specifically noted, are 0.05 ‰ for δ^{13}C and 0.07 ‰ for δ^{18}O.
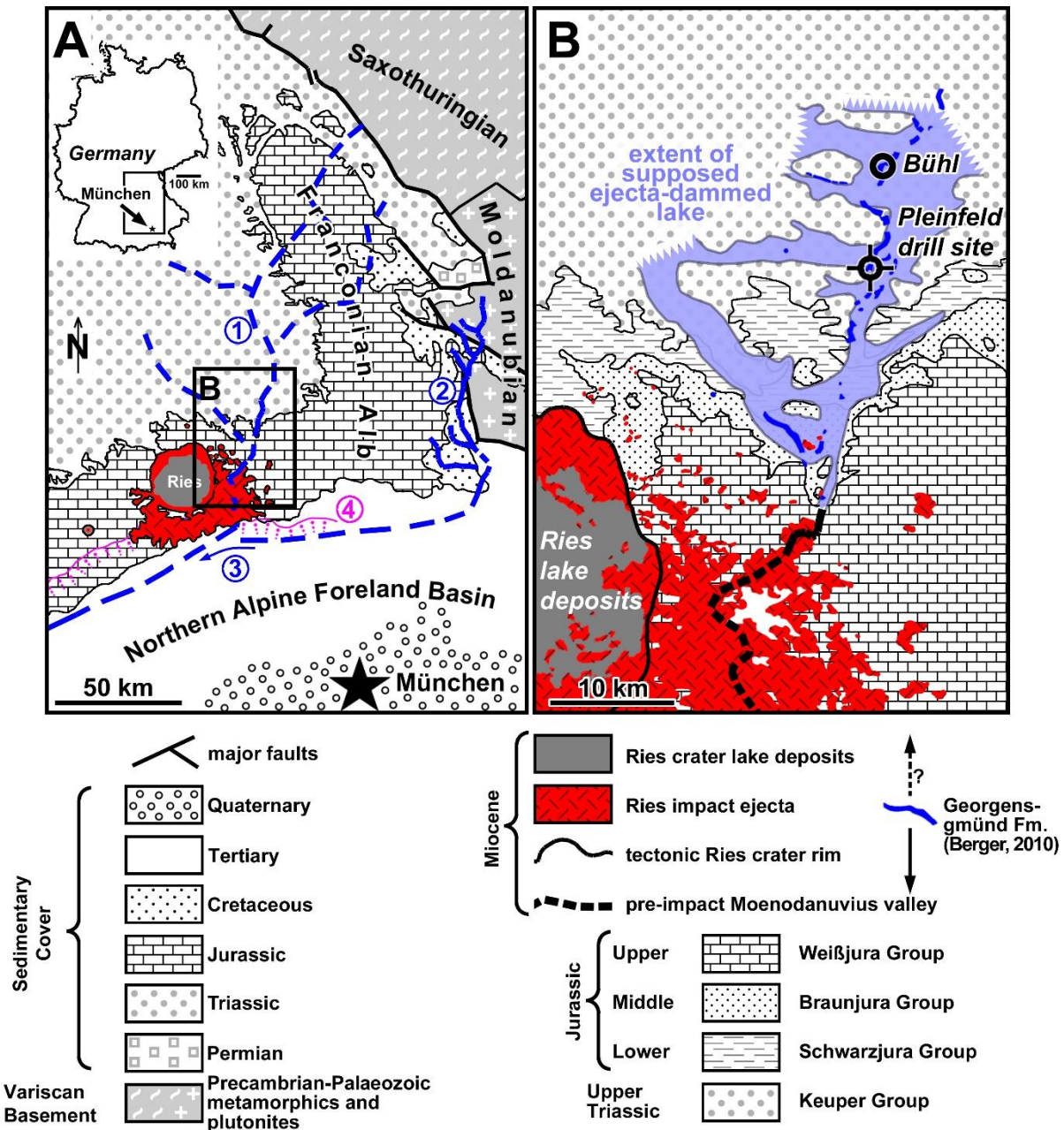
Figure 5.1 Geographical and geological overview of the study area (based on Freudenberger *et al*. 1996).
(A) South German Scarplands, with the Ries impact structure and adjacent Northern Alpine Foreland Basin (NAFB). Blue dashed lines indicate the early to middle Miocene south-directed drainage system. Both, the "Moenodanuvius" (1) (Schirmer, 2014) and

the "Paleonaab" (2) (Bader *et al.*, 2000), discharge into the "Graupensand river" (3) (Doppler *et al.*, 2002, Pippèrr & Reichenbacher, 2017), which drains farther west (finally ending in the westernmost NAFB). The magenta line and dots (4) indicate the cliff line of the early Miocene Upper Marine Molasse (early Ottnangian), which is used as a reference for late tectonic tilting (Gall, 1974; Freudenberger *et al.*, 1996; Doppler *et al.*, 2002). Note the Variscan basement high (Saxothuringian domain and Moldanubian domain) in the NE. (B) Detail showing the outline of the supposed Rezat-Altmühl Lake according to Schmidt-Kaler (1999) and Peterek & Schröder (2010), distribution of the actual sediment relicts of the Georgensgmünd Formation (Berger, 2010) and their geographic relationship to Ries impact ejecta.
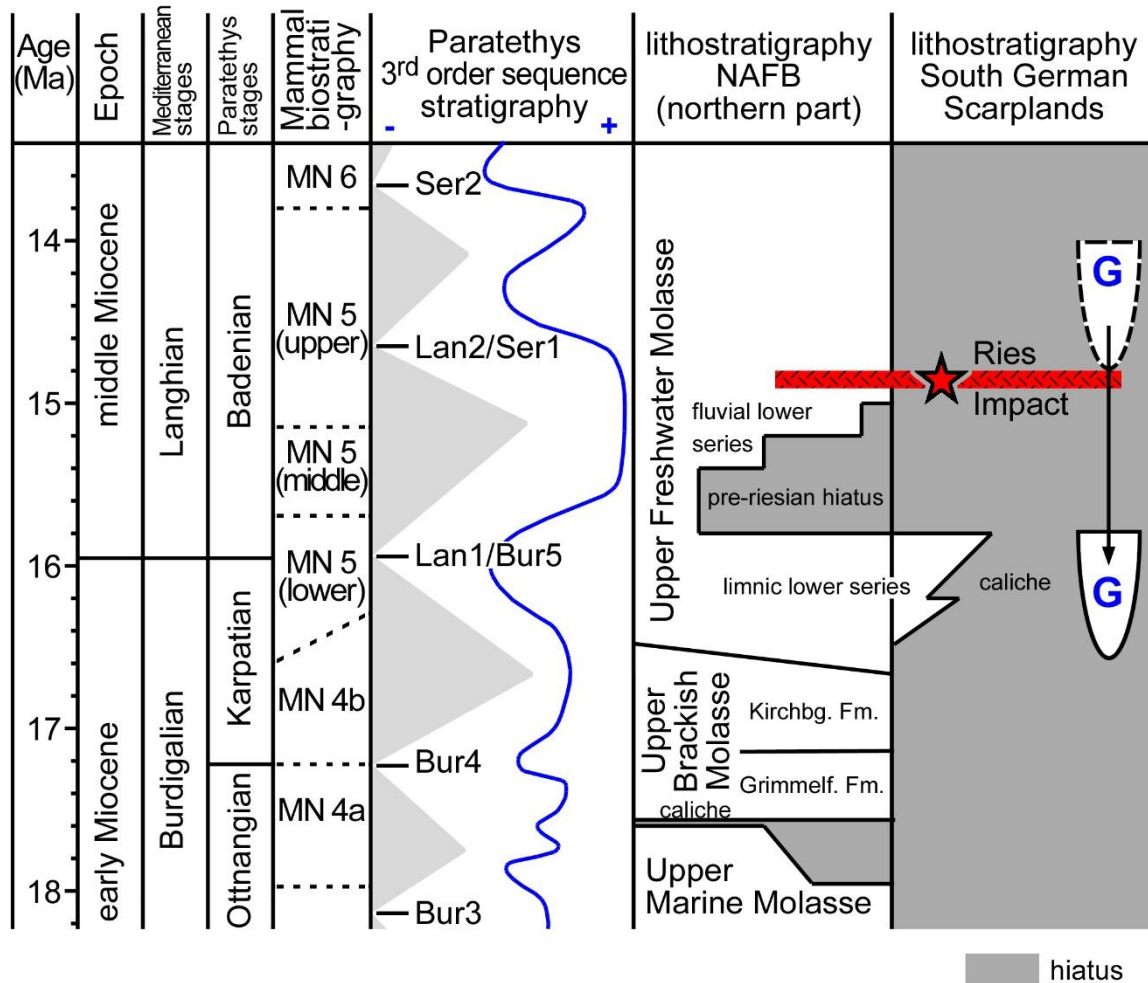
Figure 5.2 Chronostratigraphy, biostratigraphy and sequence stratigraphy of the Miocene sediment series discussed in this paper.
Lithostratigraphy of the NAFB and the adjacent part of the South German Scarplands according to Doppler *et al.* (2002), Reichenbacher *et al.* (2013) and Pippèrr and Reichenbacher (2017). Paratethys sequence stratigraphy and eustatic sea-level curve after Piller *et al.* (2007) and Hardenbol *et al.* (1998), respectively. "G" indicates the stratigraphic position of the Georgensgmünd Formation suggested by Berger (2013) (solid outline) and previous studies (dashed outline), respectively.

Strontium isotope analyses of 26 samples were carried out at the ZERIN, RiesKraterMuseum, Nördlingen, Germany. To specifically dissolve the calcium carbonate fraction, 1 ml of 6N HCl was added to 10 mg of finely ground samples in Teflon beakers and

mixed. After 30 s the reactant was pipetted into 1.5 ml containers and centrifuged. While sequential carbonate leaching (Liu *et al.,* 2013; Bellefroid *et al.,* 2018) is required for high-accuracy studies in the context of, for example, recording primary seawater $^{87}Sr/^{86}Sr$ values from bulk samples, the present study aims at resolving trends in a sedimentary setting with weathering solutions from source materials with highly different $^{87}Sr/^{86}Sr$ ratios (i.e., marine Jurassic carbonate, siliciclastics from Variscan basement), and calcite as the sole carbonate mineral phase in the samples. Nonetheless, despite of the single-leaching procedure applied here, no correlation between siliciclastic content and $^{87}Sr/^{86}Sr$ ratios was found, neither for 6N HCl leaching nor acetic acid leaching (**Table S1**), indicating that the $^{87}Sr/^{86}Sr$ variations (0.00091) within the calcite phase between the different samples is much higher than the potential contamination by Sr from the silicate fraction. Indeed, Bailey *et al.* (2000) demonstrated that the application of different methods of dissolution (i.e., water wash, acetic acid, mixed 6N HCl and 6N HNO₃) resulted in errors of up to ± 0.000076 in $^{87}Sr/^{86}Sr$ in marly chalks. Furthermore, the 6N HCl protocol applied here resulted in systematically lower, not higher, $^{87}Sr/^{86}Sr$ values (by 0.00002 to 0.00036), if compared to results from acetic acid leaching, indicating that these values show the lowest potential contamination by Sr from silicates (with high radiogenic values).

The supernatants of the centrifuged samples were dried and lead to purification and accumulation of Sr, which was achieved using a strontium-specific crown-ether resin (Sr-Spec ®; recipe modified from Horwitz *et al.*, 1992 and Pin & Basin, 1992). Strontium was loaded in a mixture of TaCl₅, HF, HNO₃, H₃PO₄ and H₂O (Birck, 1986) on single-band tungsten filaments. Strontium isotope ratios were measured in static mode by a thermal ionization mass spectrometer [Thermo Finnigan MAT 261 (Thermo Fisher Scientific, Waltham, MA, USA) modified by Spectromat GmbH (Bremen, Germany)]. Measured isotope values were normalized for mass fractionation using the naturally invariant value for $^{88}Sr/^{86}Sr$ of 8.37521 and the exponential fractionation law. Accuracy and precision of the mass spectrometer runs were controlled by analysing reference material SrCO₃ NIST SRM 987. During the period of analysis, the measured $^{87}Sr/^{86}Sr$ value was 0.710218 ± 0.000014 (1 SD, n = 7). Based on replicate analyses of natural samples the accuracy for the $^{87}Sr/^{86}Sr$ including the complete laboratory procedure is assumed to be better than ± 0.0050% (1 SD). For more details see Koester *et al.* (2018).

Comparing the results of HCl-aliquots and acetic acid-aliquots, equal or lower radiogenic $^{87}Sr/^{86}Sr$ values in the HCl-leachates were found within uncertainties (**Table S1**). This finding is interpreted as clear indication that fast HCl-treatment did not mobilize significant amounts of silicate-derived strontium which are expected to be more radiogenic than the carbonate phase. Thus, it is assumed that the short HCl-leach gives a good approximation of the easily soluble carbonate fraction.

4 Results

Overview of lithofacies succession

The investigated drill core comprises three lithostratigraphic units (**Figure 5.3**). The topmost 1.7 m recovered unconsolidated Quaternary fluvial sands. Between 1.70 m and 48.95 m depth, mixed carbonate-siliciclastic deposits of the Miocene Georgensgmünd Formation were transected. These rocks show a general increase in carbonate content from base to top, associated with change from red brown to white-grey colours. The base of the Miocene has been positioned at the first occurrence of pebbles derived from the Mesozoic (i.e., a subrounded Jurassic limonite pebble of 2.5 cm diameter at 48.70 m depth). The basal 14 m of the drill core are composed of sandstones and siltstones of the Middle Keuper Group (Carnian-Norian).

Lithofacies types

Based on carbonate and siliciclastic components, fabric and colour, 10 lithofacies types (LFT) are identified in deposits of the Georgensgmünd Formation from the Pleinfeld drill core and Bühl locality (**Figure 5.4 and 5.5; Table 5.1**). Organic carbon content of all analysed

lithofacies types is very low (0.04 to 0.09 wt. %), with highest values in LFTs 5 and 7c (0.10 to 0.12 wt. %). Classic lithofacies codes of Miall (1985, 1996) are listed in the table as far as they are equivalent to LFTs from the present study. However, rooted floodplain fines (Fr) of the investigated deposits show a broader spectrum in lithology and fabric so that a more specific denomination by LFTs 7a to 9c is used in this paper.

Generally, the transected sedimentary succession is poor in fossils. Only in LFTs 8 and 9, poorly preserved pulmonate gastropod moulds were found at several depths. One fragment of a long bone at -25.30 m depth (**Figure 5.6E**) is the only vertebrate remain found in the Pleinfeld core. Carbonaceous plant debris was detected in fine-grained sandstones (LFT 4) at -3.55 m depth, and in calcareous marlstone with root voids (LFT 8) at -33.10 m depth.

Pebble lithofacies

In addition to palustrine limestone pebbles, which have been reworked within the formation (intraclasts), several extraclasts were detected within the drill core succession (see **Figure 5.6**). These extraclasts included:

1 Five to 10 cm thick intercalations of white grey, pebbly arkose with angular quartz grains and kaolinized feldspars near the basis of the Miocene section (48.90 to 48.95 m and 47.60 to 47.70 m; **Figure 5.6A**) representing a lithology identical to that of the underlaying formation. A similar, less coarse-grained arkose clast, about 4 cm in diameter at 39.10 m depth (within LFT 7) belongs to this pebble group, too.

2 Subrounded pebbles, 2 to 5 cm in size, consisting of carbonate-cemented, gravelly, coarse-grained quartz sandstones were found within LFT 7 at 20.05 m, 32.18 m and 39.08 m core depth (**Figure 5.6B**).

3 Subangular to subrounded, white-grey limestone pebbles, 1.5 to 8 cm in size, that occur at 32.30 m, 35.86 m, 37.08 m, 39.04 m and 39.40 m within LFT 7 (**Figure 5.6B**). In thin section, pisoid fragments, coarsely laminated crusts and root voids within a clotted microcrystalline matrix are evident (**Figure 5.6C**).

4 Several subrounded limonite and siderite clasts between 1.5 and 2.5 cm in size were detected in the section at 29.25 m, 38.42 m and 48.60 m depth (**Figure 5.6D**). In addition, a limonite-cemented fine-grained sandstone pebble, 3.5 cm in size, showing a bivalve imprint, was found at 5.10 to 5.20 m depth.

5 One angular lydite pebble was observed at 46.4 m depth. The 0.5 cm sized pebble is composed of black chert and white quartz fissures.

Stable carbon and oxygen isotopes

All analysed carbonates of the investigated drill core and reference samples are calcitic. In general, Miocene carbonates of the Pleinfeld core show a wide range in $\delta^{13}C$ from -7.38 to +2.27 ‰, at a rather limited range in $\delta^{18}O$ from -5.48 to -4.16 ‰ (**Figure 5.7; Table 5.2**). Indeed, $\delta^{18}O$ values neither differ significantly between lithofacies types nor along the core depth (mean value $\delta^{18}O$ = -4.94 ± 0.31 ‰). On the other hand, $\delta^{13}C$ values of microcrystalline matrix and nodules in the different lithofacies types (LFTs 4, 7, 8, 9a) show a significant trend (**Figure 5.7**).

Lowest $\delta^{13}C$ average values ($\delta^{13}C$ = -6.93 ± 0.30 ‰) were obtained from a reworked caliche pebble in LFT 7. The carbonate matrix and nodules in LFT 7 revealed a wide range in $\delta^{13}C$ but show the lowest value (-7.38 ‰) and average ratios (-1.99 ± 2.91 ‰). Reworked material of this lithofacies type in LFT 6 have a similar wide range (-2.75 ± 2.96 ‰). Increasing $\delta^{13}C$ values were obtained from LFT 8 (mean: -0.55 ± 1.47 ‰) and highest $\delta^{13}C$ values were found in palustrine limestone LFT 9a (mean: +0.77 ± 0.65‰).

Further single measurements fit into this framework: One value obtained from microcrystalline carbonate in the LFT 4 sandstone ($\delta^{13}C$ = -1.89 ‰) is close to values in LFT 7. One gastropod shell in LFT 9a shows a $\delta^{13}C$ of +0.96 ‰, i.e., within range of host rock LFT 9a. The bone remains in LFT 7 exhibit a $\delta^{13}C$ of -3.71 ‰, again within range of host

rock. The diagenetic calcite spar vein ($\delta^{13}C = +2.27‰,$) in LFT 7 is close to the maximum values in its host rock.
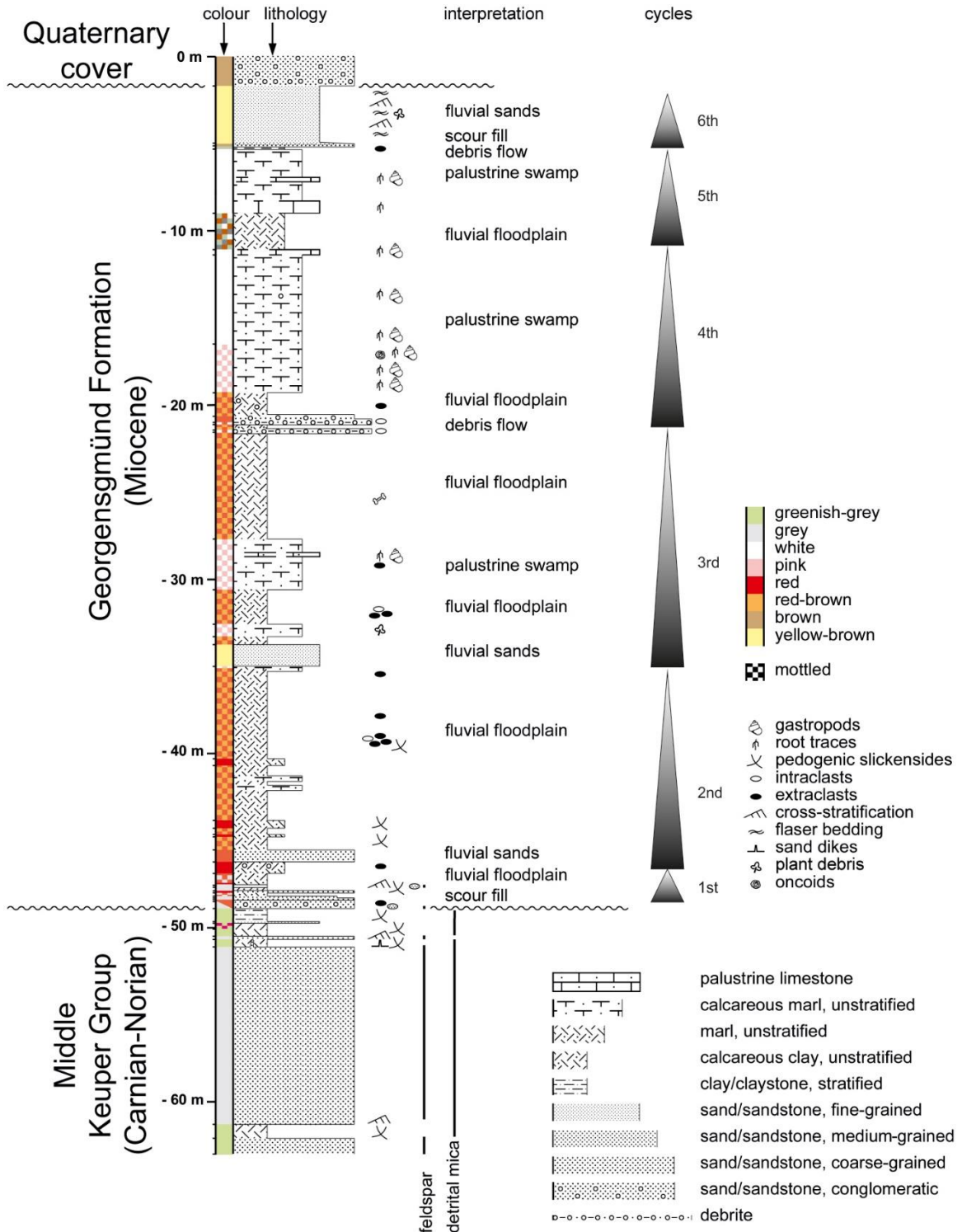
Figure 5.3 Log of the Miocene Georgensgmünd Formation, underlying Upper Triassic Keuper Group and overlying Quaternary cover deposits of the Pleinfeld drill core.
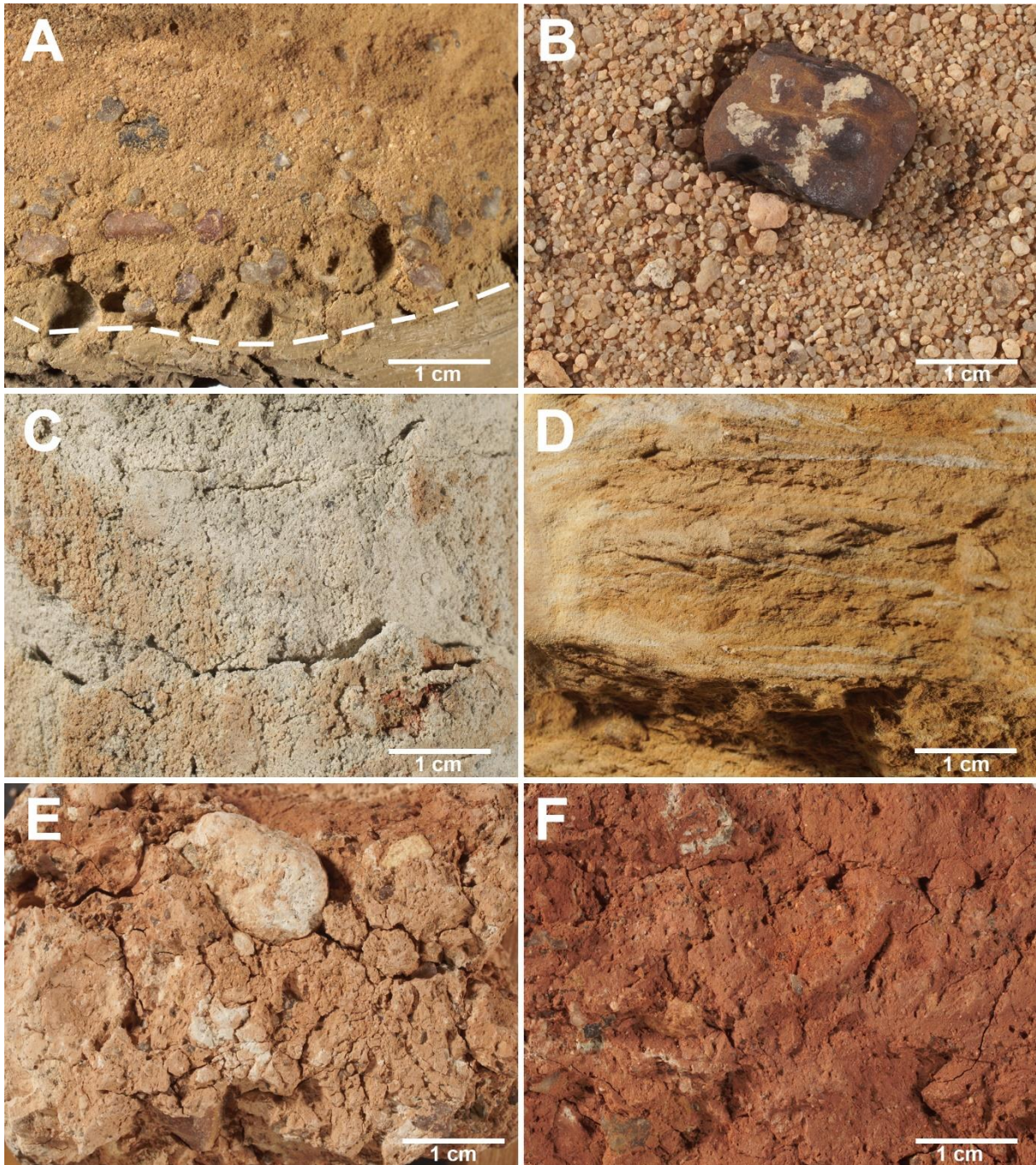
Figure 5.4 Lithofacies types of the Georgensgmünd Formation.
(A) Brown sandy conglomerate/LFT 1 overlaying olive grey claystone/LFT 5 (below the dash line) at 5.10 m core depth. (B) Brown pebbly coarse-grained quartz sand/LFT 2 at 48.64 m core depth, with limonite pebble. (C) Greenish-grey medium-grained quartz sandstone/LFT 3 at 48.25 m core depth. (D) Yellow-brown fine-grained quartz sandstone/LFT4 at 2.30 m, with low-angle cross-stratification. (E) Varicoloured mud-supported conglomerate LFT 6 at 21.10 m core depth. The white grey pebble is a reworked palustrine limestone. (F) Intense red-brown mottled mudstone LFT 7a at 46.50 m core depth. Note mm-sized subangular quartz grains reworked from Keuper arkoses.
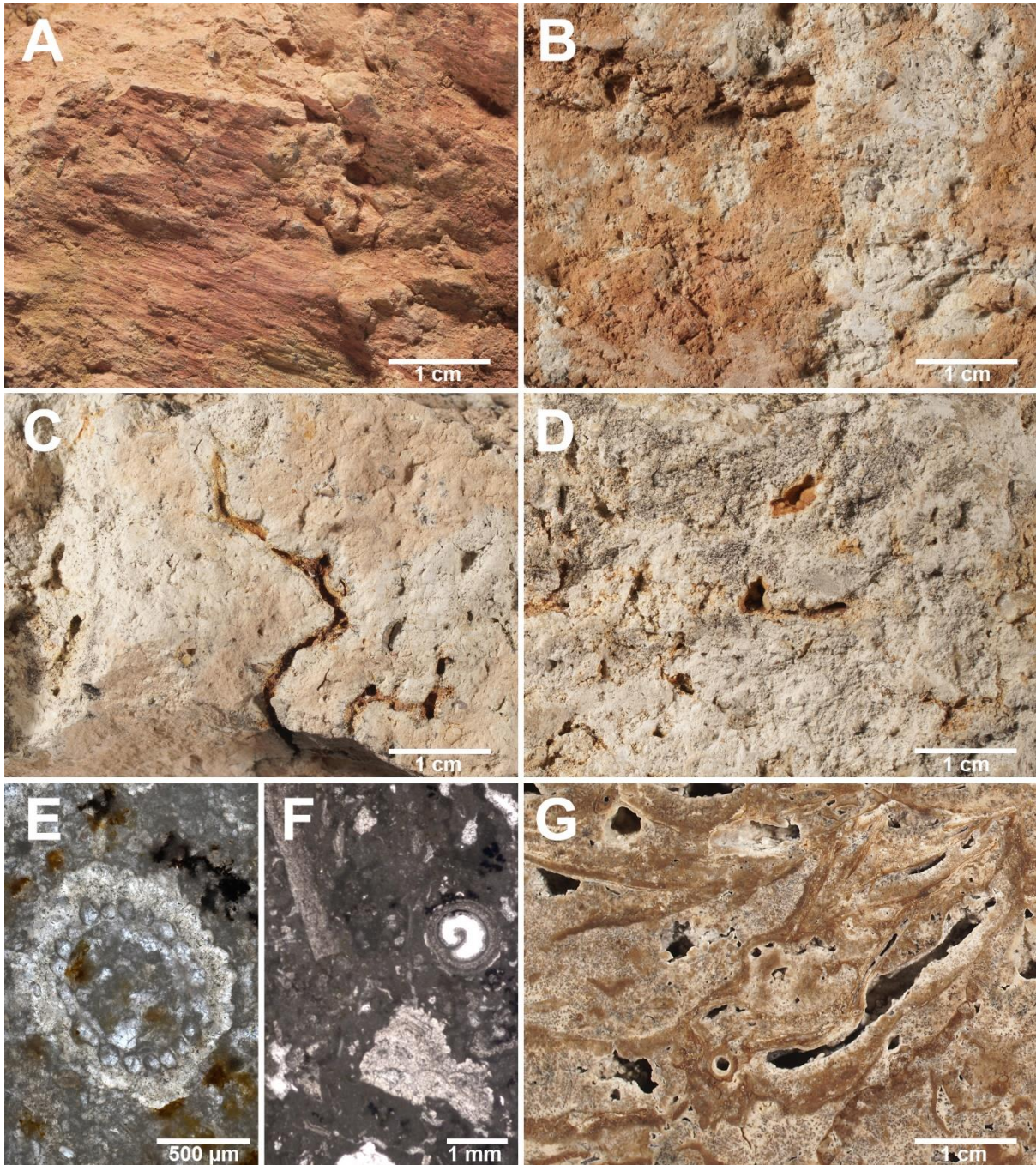
Figure 5.5 Lithofacies types of the Georgensgmünd Formation.
(A) Pedogenic slickensides in intense red-brown mottled mudstone LFT 7a at 39.10 m
core depth. (B) Light red-brown mottled mudstone LFT 7b at 22.10 m core depth, with
white-grey carbonate patches. (C) Pink-white grey calcareous marlstone LFT 8 with
root voids at 17.40 m core depth. (D) White grey limestone with root voids LFT 9 at
8.40 m core depth. (E) Thin section microphotograph (transmitted light) of white grey
limestone with charophyte remains LFT9b, at Bühl near Georgensgmünd. Sample
GGM 3. (F) Thin section microphotograph (transmitted light) of white grey limestone
with angular tufa fragments LFT 9c and one cement-encrusted hydrobiid gastropod,
at Bühl near Georgensgmünd, Sample GGM 4. (G) Polished slab of vacuolar tufa LFT
10, at Bühl near Georgensgmünd, Sample GGM 1.
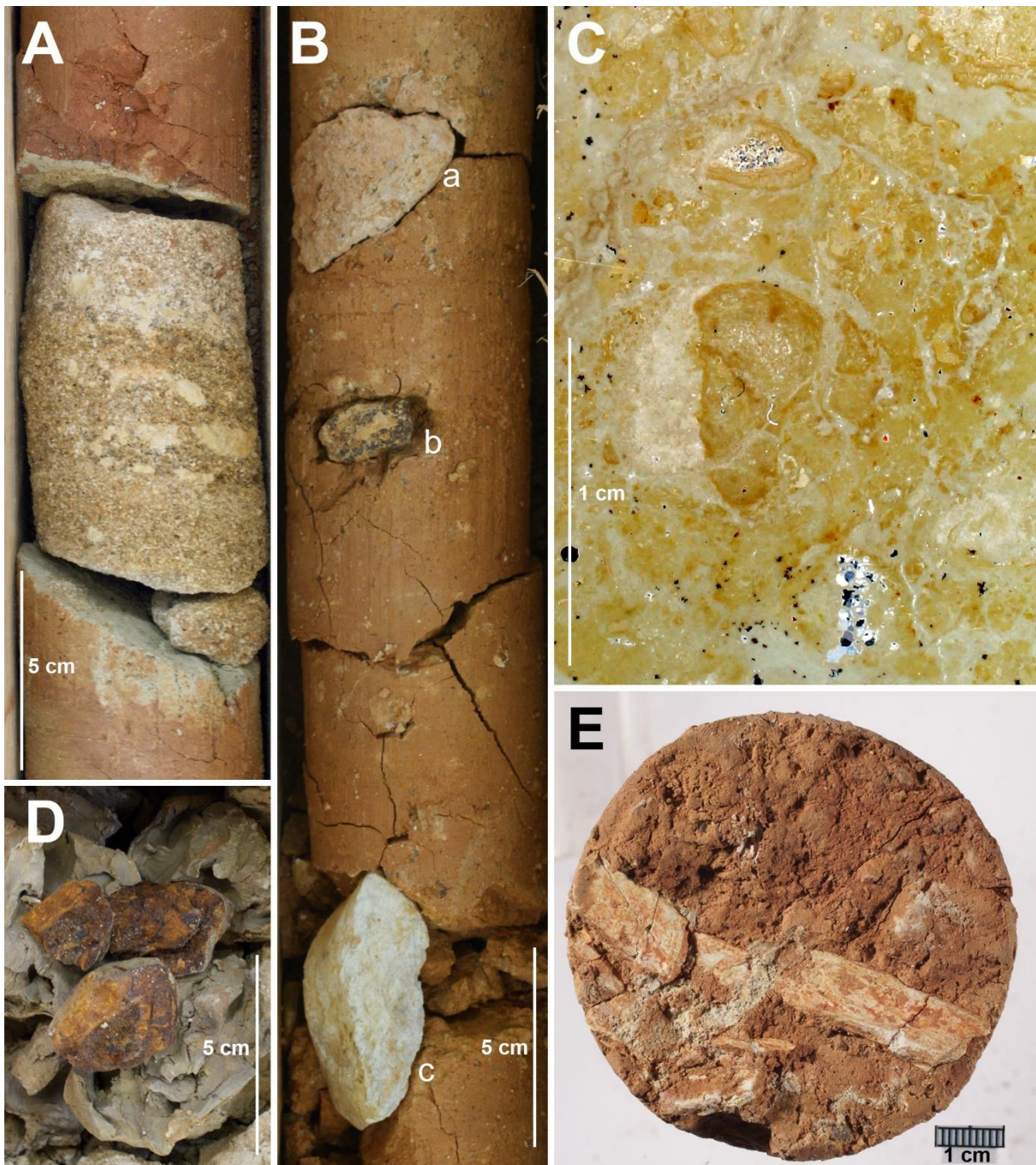
Figure 5.6 Pebble facies of the Georgensgmünd Formation.
(A) Pleinfeld drill core at 47.55 to 47.75 m depth showing a 10 cm arkose intercalation (i.e., a cobble) of Upper Triassic origin, between Miocene mottled mudstones. (B) Drill core at 32.05 to 32.35 m depth showing a pink-white grey limestone pebble (a: 32.10 m), a sub-angular manganese-oxide-stained Arietensandstein pebble (b: 32.18 m) and a subrounded caliche pebble reminiscent of Upper Jurassic marine limestone (c: 32.30 m). (C) Thin section microphotograph (transmitted light) of the caliche pebble at 32.30 m core depth, showing laminar crusts and *in situ* cracked components. (D) Limonitic sandstone pebble (fragmented) in olive grey claystones of LFT 5 at 5.15 m core depth. (E) Fragmented long bone within light red brown mottled mudstone of LFT 7b at 25.40 m core depth.

Table 5.1 Lithofacies types of sediments present in the Miocene Georgensgmünd Formation from the Pleinfeld drill core and samples from Bühl.

LFT	lithofacies	description	interpretation	facies code (Miall 1985, 2006)	carbonate content (wt %)	thickness (m)
1	sandy conglomerate	The light-brown conglomerate is composed of well-rounded quartz pebbles up to 1 cm Ø, embedded within fine- to coarse-grained quartz sand. Grain size distribution is fining-upwards (**Figure 5.4A**). Quartz pebbles are subangular to poorly rounded.	fluvial sands	Ss	0	0.05
2	pebbly coarse-grained sand	This brown-coloured, coarse-grained sand shows quartz pebbles up to 5 mm diameter (**Figure 5.4B**). Due to disintegration by the drilling process, no information on sedimentary structures are available.	fluvial sands	St, Sr, Ss	0	0.4
3	medium-grained sandstone	Grain size is dominated by medium quartz sand, with a minor argillaceous as well as coarse-grained component. Colour is commonly greenish-grey, but reddish-brown colours occur as well (**Figure 5.4C**). Similar to the LFTs mentioned above, no carbonate has been detected.	fluvial sands	St, Sr	0	0.1-0.7
4	fine-grained sandstone	This fine-grained, yellow-brown sandstone is poorly consolidated, rich in silt (**Figure 5.4D**), and locally contains carbonaceous plant debris (e.g., at 3.55 m depth). $CaCO_3$ content is low, except at the contact to overlying marlstones. Two varieties were recognized: LFT 4a is characterized by a low-angle cross-stratification. LFT 4b shows discontinuous clay laminae reminiscent of flaser bedding.	fluvial sands	Sr, Sl	<0.1	1.25-3.35
5	clay with pebbles	The olivgrey clay (**Figure 5.4A**) exhibits cm-sized limonite sandstone pebbles derived from the Jurassic (Eisensandstein-Formation). Scattered quartz pebbles are floating in the clay matrix. No stratification is evident.	debris flow	Gmm	0.2	0.1-0.15

6	mud-supported conglomerate	Major components (**Figure 5.4E**) are subrounded quartz (up to 9 mm diameter) and palustrine limestone pebbles (up to 4 cm diameter). These pebbles float in a redbrown-whitegrey mottled, argillaceous to arenaceous matrix.	debris flow	Gmm	34-44	0.07-0.1
7a	mottled mudstone	Intense red-brown, massive mudstone with pedogenic slickensides (**Figure 5.4F and 5.5A**) and mm-sized quartz pebbles.	floodplain	Fm	0.1-6.5	0.15-5.3
7b	mottled mudstone	light red-brown mottled mudstone, with mm-sized quartz pebbles and white-grey carbonate nodules (**Figure 5.5B**)	floodplain with pedogenic carbonate precipitation	Fm	0-63	0.10-6.25
7c	mottled mudstone	vari-coloured (white-brown-grey) mottled mudstone with mm-sized quartz pebbles.	floodplain with pedogenic carbonate precipitation	Fm	17-56	0.17-2.1
8	calcareous marlstone	This lithofacies has a whitegrey to pale-pink colour. Abundant yellowish root voids (**Figure 5.5C**) are preserved as well as shell fragments of pulmonate gastropods. Dispersed quartz grains up to 5mm diameter are also common; locally, the isolated and rounded quartz pebbles have a size up to 1 cm diameter. Except rare intercalated light-olivegrey clay layers, no evident stratifications are shown. $CaCO_3$ content varies between 54 and 74 wt%, with lower content upon olivegrey clay intercalations (31 wt%).	Palustrine swamp	Fr	54-74	0.7-5.1
9a	limestone	whitegrey microcrystalline limestone with abundant root voids (**Figure 5.5D**), mud-supported fabric	palustrine swamp	Fr	85-93	0.3-3.8
9b	limestone	whitegrey microcrystalline limestone with charophytes, poor in root voids (**Figure 5.5E**), mud-supported fabric	pond	Fr	85-93	0.3-3.8
9c	limestone	whitegrey limestone with oncoid fragments, poor in root voids, mud- to grain-supported fabric	marginal pond	Fr	85-93	0.3-3.8

| 10 | vacuolar tufa | This lithofacies represents a mixture of grey phytoclastic and framestone tufa (Manzo et al. 2012, **Figure 5.5G)**. The tufa is a porous but solid-framed limestone composed of undulating horizontal 5-mm-thick calcite sheets (probably encrusted leaves), peloidal fabric and laminoid fenestrae. Pulmonate gastropods were locally observed. $CaCO_3$ content can be high (not analysed). | freshwater spring or small tufa barrage | [n.a.] | [n.a.] | [n.a.] |

Table 5.2 Carbonate stable oxygen and carbon isotope ratios, and carbonate content of the Pleinfeld drill core (PF) and Bühl (GGM) samples from the Miocene Georgensgmünd Formation.
Standard deviations of the stable isotope measurements, if not specifically noted, are 0.05 ‰ for $\delta^{13}C$ and 0.07 ‰ for $\delta^{18}O$.

sample number	depth (m)	lithofacies description	lithofacies type	analysed material	$\delta^{13}C$ (‰ V-PDB)	$\delta^{18}O$ (‰ V-PDB)	$CaCO_3$ (wt %)
PF10	5.7	whitegrey limestone with root voids	9	microcrystalline matrix (calcite)	0.65	-4.97	53.72
PF10	5.7	whitegrey limestone with root voids	9	microcrystalline matrix (calcite)	0.45	-5.24	53.72
PF12	6.7	whitegrey calcareous marlstone with root voids	8	microcrystalline matrix (calcite)	1.34	-4.74	31.27
PF12	6.7	whitegrey calcareous marlstone with root voids	8	microcrystalline matrix (calcite)	1.51	-4.87	31.27
PF15	7.5	whitegrey limestone with root voids	9	microcrystalline matrix (calcite)	1.99	-4.73	84.51
PF15	7.5	whitegrey limestone with root voids	9	algal carbonate tube (calcite)	1.56	-4.9	84.51
PF16	8.0	whitegrey limestone with root voids	9	microcrystalline matrix (calcite)	0.97	-5.25	54.67
PF17	8.4	whitegrey limestone with root voids	9	microcrystalline matrix (calcite)	1.47	-4.98	92.53
PF21	9.0	whitegrey limestone with root voids	9	microcrystalline matrix (calcite)	0.9	-5.15	91.01
PF21	9.0	whitegrey limestone with root voids	9	gastropod shell fragment (calcite)	0.96	-4.77	91.01
PF22	9.3	varicoloured mottled marlstone	7c	microcrystalline matrix (calcite)	2.13	-4.8	16.64
PF22	9.3	varicoloured mottled marlstone	7c	microcrystalline matrix (calcite)	1.79	-4.73	16.64
PF23*	10.3	whitegrey limestone with root voids	9	microcrystalline matrix (calcite)	-0.31	-4.72	55.68
PF23	10.3	whitegrey limestone with root voids	9	microcrystalline matrix (calcite)	0.5	-4.52	55.68
PF24	11.3	whitegrey limestone with root voids	9	microcrystalline matrix (calcite)	1.78	-5.25	92.52

PF25	12.4	whitegrey calcareous marlstone with root voids	8	microcrystalline matrix (calcite)	-0.48	-5.06	67.32
PF27	14.5	whitegrey calcareous marlstone with root voids	8	microcrystalline matrix (calcite)	-2.25	-4.84	58.12
PF28	15.5	whitegrey limestone with root voids	9	microcrystalline matrix (calcite)	0.17	-4.87	73.99
PF29*	16.8	whitegrey calcareous marlstone with root voids	8	microcrystalline matrix (calcite)	-0.29	-4.92	73.03
PF29*	16.8	whitegrey calcareous marlstone with root voids	8	microcrystalline matrix (calcite)	0.39	-5.07	73.03
PF33*	17.8	light-pink limestone with root voids	9	microcrystalline matrix (calcite)	0.47	-5.03	72.58
PF33	17.8	light-pink limestone with root voids	9	microcrystalline matrix (calcite)	0.47	-5.04	72.58
PF35	19.0	light-pink limestone with root voids	9	microcrystalline matrix (calcite)	0.53	-4.86	72.35
PF37	20.1	redbrown mottled marlstone	7b	microcrystalline nodule (calcite)	-0.68	-5.19	34.18
PF37	20.1	redbrown mottled marlstone	7b	microcrystalline nodule (calcite)	-0.51	-5.22	34.18
PF38*	21.1	varicolored mud-supported conglomerate	6	microcrystalline matrix (calcite)	-5.72	-4.39	44.31
PF38	21.1	varicolored mud-supported conglomerate	6	microcrystalline nodule (calcite)	-0.09	-5	44.31
PF39	21.5	varicolored mud-supported conglomerate	6	microcrystalline nodule (calcite)	-0.33	-4.97	34.32
PF39	21.5	varicolored mud-supported conglomerate	6	microcrystalline matrix (calcite)	-4.87	-5.41	34.32
PF40	22.1	redbrown mottled marlstone	7b	microcrystalline carbonate streak (calcite)	-1.81	-5.28	43.5
PF41	23.3	redbrown mottled marlstone	7b	microcrystalline matrix (calcite)	-3.5	-5.31	35.59
PF43*	25.3	redbrown mottled marlstone	7b	microcrystalline matrix (calcite)	-4.58	-4.55	31.52
PF43	25.3	redbrown mottled marlstone	7b	calcified bone remains (calcite)	-3.71	-5.16	31.52
PF45	27.2	redbrown mottled marlstone	7b	microcrystalline nodule (calcite)	-3.94	-5.26	30
PF46	28.4	light-pink calcareous marlstone with root voids	8	microcrystalline matrix (calcite)	-2.63	-5.39	68.63
PF49*	30.2	light-pink calcareous marlstone with root voids	8	microcrystalline matrix (calcite)	-1.56	-5.04	59.02
PF49	30.2	light-pink calcareous marlstone with root voids	8	microcrystalline matrix (calcite)	-1.02	-5.18	59.02
PF52	32.2	redbrown mottled marlstone	7b	microcrystalline nodule (calcite)	-6.42	-4.16	25.72
PF53	32.3	caliche pebble (found within LFT 7b)	7b	clotted microcrystalline matrix (calcite)	-6.51	-4.59	n.a.
PF53	32.3	caliche pebble (found within LFT 7b)	7b	clotted microcrystalline matrix (calcite)	-7.12	-4.67	n.a.

PF53	32.3	caliche pebble (found within LFT 7b)	7b	clotted microcrystalline matrix (calcite)	-6.7	-4.58	n.a.
PF53	32.3	caliche pebble (found within LFT 7b)	7b	clotted microcrystalline matrix (calcite)	-7.14	-4.61	n.a.
PF53	32.3	caliche pebble (found within LFT 7b)	7b	clotted microcrystalline matrix (calcite)	-7.17	-4.65	n.a.
PF54	33.1	redbrown mottled marlstone	7b	microcrystalline matrix (calcite)	-0.22	-4.77	62.61
PF55	34.0	yellow-brown fine-grained sandstone	4	microcrystalline carbonate between sand grains (calcite)	-1.89	-5.2	33.55
PF56	35.1	redbrown mottled marlstone	7b	microcrystalline carbonate streak (calcite)	-0.03	-5.02	58.79
PF58	37.1	redbrown mottled marlstone	7b	microcrystalline matrix (calcite)	-3.41	-4.58	30.78
PF58	37.1	redbrown mottled marlstone	7b	microcrystalline nodule (calcite)	-6.9	-4.56	30.78
PF58	37.1	redbrown mottled marlstone	7b	microcrystalline nodule (calcite)	-7.38	-4.67	30.78
PF58	37.1	redbrown mottled marlstone	7b	microcrystalline carbonate streak (calcite)	-0.3	-5.16	30.78
PF58	37.1	redbrown mottled marlstone	7b	microcrystalline carbonate streak (calcite)	-0.37	-5.08	30.78
PF61	39.1	redbrown mottled marlstone	7b	microcrystalline matrix (calcite)	0.87	-5.48	47.9
PF63*	41.8	redbrown mottled marlstone	7b	microcrystalline matrix (calcite)	-3.36	-4.26	21.43
PF65	43.3	redbrown mottled marlstone	7b	microcrystalline carbonate streak (calcite)	0.76	-5.44	60.12
PF65	43.3	redbrown mottled marlstone	7b	calcite spar vein	2.27	-5.36	60.12
GGM1	n.a.	stromatolitic tufa	10	spar cement (calcite)	-1.87	-6.21	n.a.
GGM1	n.a.	stromatolitic tufa	10	stromatolite lamina (calcite)	3.74	-5.04	n.a.
GGM2	n.a.	whitegrey limestone with root voids	9	microcrystalline matrix (calcite)	-1.69	-4.75	n.a.
GGM2	n.a.	whitegrey limestone with root voids	9	microcrystalline matrix (calcite)	-2.4	-4.99	n.a.
GGM3	n.a.	yellow-grey limestone with charophytes	9	microcrystalline matrix (calcite)	1.57	-5.34	n.a.
GGM3	n.a.	yellow-grey limestone with charophytes	9	microcrystalline matrix (calcite)	4.04	-4.9	n.a.
GGM3	n.a.	yellow-grey limestone with charophytes	9	oncoid (calcite)	4.59	-5.14	n.a.
GGM4	n.a.	whitegrey limestone with root voids and oncoid clasts	9	microcrystalline matrix (calcite)	4.06	-5.03	n.a.
GGM4	n.a.	whitegrey limestone with root voids and oncoid clasts	9	oncoid (calcite)	5.14	-4.44	n.a.

Table 5.3 ^{87}Sr/^{86}Sr ratio of the carbonate samples from the Miocene Georgensgmünd Formation, reacted with standard 6N HCl. Note that 2σ indicates the instrumental precision of measurements.

sample number	depth (m)	sample description	facies	analysed material	^{87}Sr/^{86}Sr [6N HCl] mean	2σ
PF10	5.7	whitegrey calcareous marl with root voids	8	microcrystalline matrix	0.71121	0.00001
PF12	6.7	whitegrey calcareous marl with root voids	8	microcrystalline matrix	0.71099	0.00002
PF15	7.5	whitegrey limestone with root voids	9	microcrystalline matrix	0.71086	0.00001
PF16	7.95	whitegrey calcareous marl with root voids	8	microcrystalline matrix	0.71093	0.00002
PF17	8.4	whitegrey limestone with root voids	9	microcrystalline matrix	0.71093	0.00002
PF21	8.95	whitegrey limestone with root voids	9	microcrystalline matrix	0.71089	0.00002
PF23	10.33	varicoloured mottled mudstone	7c	microcrystalline matrix	0.71085	0.00001
PF24	11.25	whitegrey limestone with root voids	9	microcrystalline matrix	0.71094	0.00002
PF25	12.4	whitegrey calcareous marl with root voids	8	microcrystalline matrix	0.71086	0.00002
PF27	14.5	whitegrey calcareous marl with root voids	8	microcrystalline matrix	0.71066	0.00002
PF28	15.48	whitegrey calcareous marl with root voids	8	microcrystalline matrix	0.71066	0.00002
PF29	16.75	whitegrey calcareous marl with root voids	8	microcrystalline matrix	0.71074	0.00002
PF33	17.8	lightpink calcareous marl with root voids	8	microcrystalline matrix	0.71069	0.00002
PF35	18.98	light-pink calcareous marl with root voids	8	microcrystalline matrix	0.71066	0.00001
PF38	21.1	varicolored mud-supported conglomerate	6	microcrystalline matrix	0.71067	0.00001
PF40	22.1	redbrown mottled mudstone	7b	microcrystalline carbonate streak	0.71061	0.00002
PF43	25.3	redbrown mottled mudstone	7b	microcrystalline matrix	0.71044	0.00002
PF46	28.37	light-pink calcareous marl with root voids	8	microcrystalline matrix	0.71046	0.00001
PF49	30.2	light-pink calcareous marl with root voids	8	microcrystalline matrix	0.71030	0.00002
PF54	33.1	light-pink calcareous marl with root voids	8	microcrystalline matrix	0.71037	0.00001
PF55	33.95	yellow-brown fine-grained (calcareous) sandstone	4	microcrystalline carbonate between sand grains	0.71045	0.00002
PF56	35.07	redbrown mottled mudstone	7b	microcrystalline carbonate streak	0.71033	0.00001
PF61	39.1	redbrown mottled mudstone	7b	microcrystalline matrix	0.71034	0.00002
PF63	41.8	redbrown mottled mudstone	7b	microcrystalline matrix	0.71030	0.00004

| PF65 | 43.27 | redbrown mottled mudstone | 7b | microcrystalline matrix | 0.71038 | 0.00002 |
| PF67 | 45.35 | redbrown mottled mudstone | 7b | microcrystalline matrix | 0.71036 | 0.00002 |

Nine reference isotope analyses have been carried out on carbonates of the Georgensgmünd Formation from Bühl near Georgensgmünd; the $\delta^{13}C$ values of the microcrystalline matrix of palustrine limestones LFT 9a are similar to that of palustrine limestones in the Pleinfeld core. The matrix of charophyte and oncoid bearing LFT 9bc already shows increased, positive $\delta^{13}C$ values, exceeding Pleinfeld palustrine limestone LFT 9a. Very high $\delta^{13}C$ values up to +5.14 ‰ were obtained from stromatolitic and oncoid fragments (LFT 10). Likewise, the $\delta^{18}O$ of matrix and components mentioned above is within the same narrow range (mean: -4.95 ± 0.27 ‰) as the Pleinfeld carbonates. The diagenetic spar cement in LFT 10 (Figure 5.7A) is, with respect to its $\delta^{13}C$ ratio, within the range of palustrine carbonates ($\delta^{13}C$ = -1.87 ‰) but differs from all other samples by a lower $\delta^{18}O$ value ($\delta^{18}O$ = -6.21 ‰).
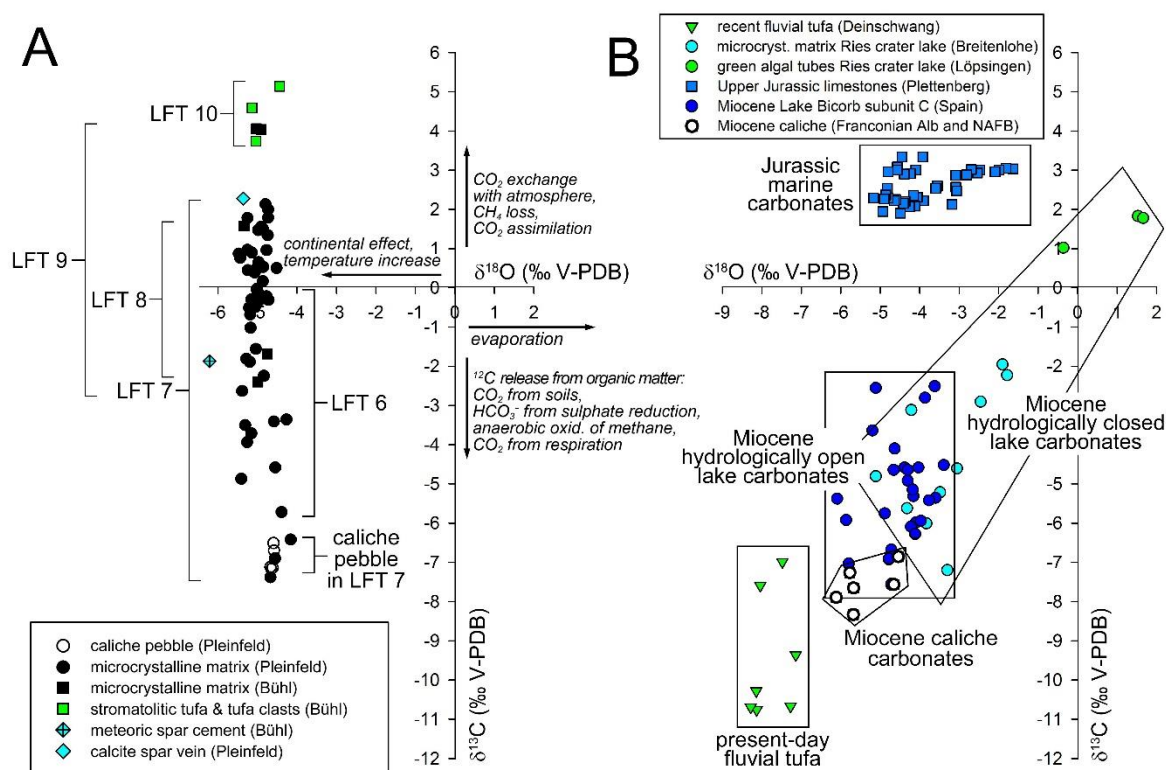
Figure 5.7 stable carbon and oxygen isotope covariation plots of the carbonate samples in Georgensgmünd Formation
(A) Covariation plot of stable carbon and oxygen isotopes of the carbonate samples in different lithofacies from Georgensgmünd Formation (drill core from Pleinfeld and outcrop from Bühl, this study). (B) Covariation plot of stable carbon and oxygen isotopes of reference material. Miocene caliche carbonates from the Franconian Alb (Hofstetten, Langenaltheim) and NAFB (Burgau), the Miocene Ries impact crater lake carbonates (Arp *et al.*, 2017a,b), the Miocene Lake Bicorb subunit C (Spain; Utrilla *et al.*, 1998), Upper Jurassic marine limestone (Southern Germany; Ruf *et al.*, 2005), and present-day fluvial tufa (Franconian Alb; Arp *et al.*, 2001).

Finally, seven reference values were obtained from early Miocene caliche carbonates (Karpatian and Ottangian) of the Frankenalb and Northern Alpine Forland Basin (NAFB). Except for one outlier, the $\delta^{13}C$ values of the caliche range from -8.36 to -6.88 ‰, with an average of -7.62 ± 0.51 ‰. These values are similar to that of the analysed caliche pebble in the Pleinfeld core. The $\delta^{18}O$ values of the caliche carbonates range from -6.12 to -4.54 ‰, with an average value of -5.41 ± 0.65 ‰.

Strontium isotopes

$^{87}Sr/^{86}Sr$ ratios of the carbonate fraction of LFTs 4 and 6 to 9 were analysed, with all samples showing carbonate content >20 wt. %. In total, the $^{87}Sr/^{86}Sr$ values range from 0.71030 to 0.71121, with a mean value of 0.71065 (**Table 5.3**). An almost unidirectional trend of increasing $^{87}Sr/^{86}Sr$ ratios from the base to the top of the section is evident (**Figure 5.8**).

Low $^{87}Sr/^{86}Sr$ values obtained from red brown mottled mudstones (LFT 7b, n = 7, 21.4 to 60.1 wt.% $CaCO_3$) range between 0.71033 and 0.71061 (mean value: 0.71039). A single sample of yellow-brown fine-grained (calcareous) sandstone (LFT 4, 33.6 wt.% $CaCO_3$) falls in the same range (0.71045), whereas the analysed sample of varicoloured mottled mudstone (LFT 7c, 55.7 wt.% $CaCO_3$) is higher in $^{87}Sr/^{86}Sr$ (0.71085). Light-pink calcareous marlstones with root voids (LFT 8, n = 12, 31.3 to 74.0 wt.% $CaCO_3$) show a wide range of $^{87}Sr/^{86}Sr$ values, ranging from 0.71030 to 0.71121 (mean value: 0.71071). White-grey limestone with root voids (LFT 9, n = 4, 84.5 to 92.5 wt.% $CaCO_3$) is characterized by high values with low standard deviation (0.71086 to 0.71094; mean value: 0.71090).

A covariation plot of silicate content and $^{87}Sr/^{86}Sr$ ratios indicates that there is no correlation between both parameters (**Fig. S1**), confirming that there is no or only insignificant leaching of Sr from silicates during sample preparation. Even within LFT 8, i.e., the lithofacies showing the most variable $^{87}Sr/^{86}Sr$, no covariance can be found between silicate content and $^{87}Sr/^{86}Sr$.
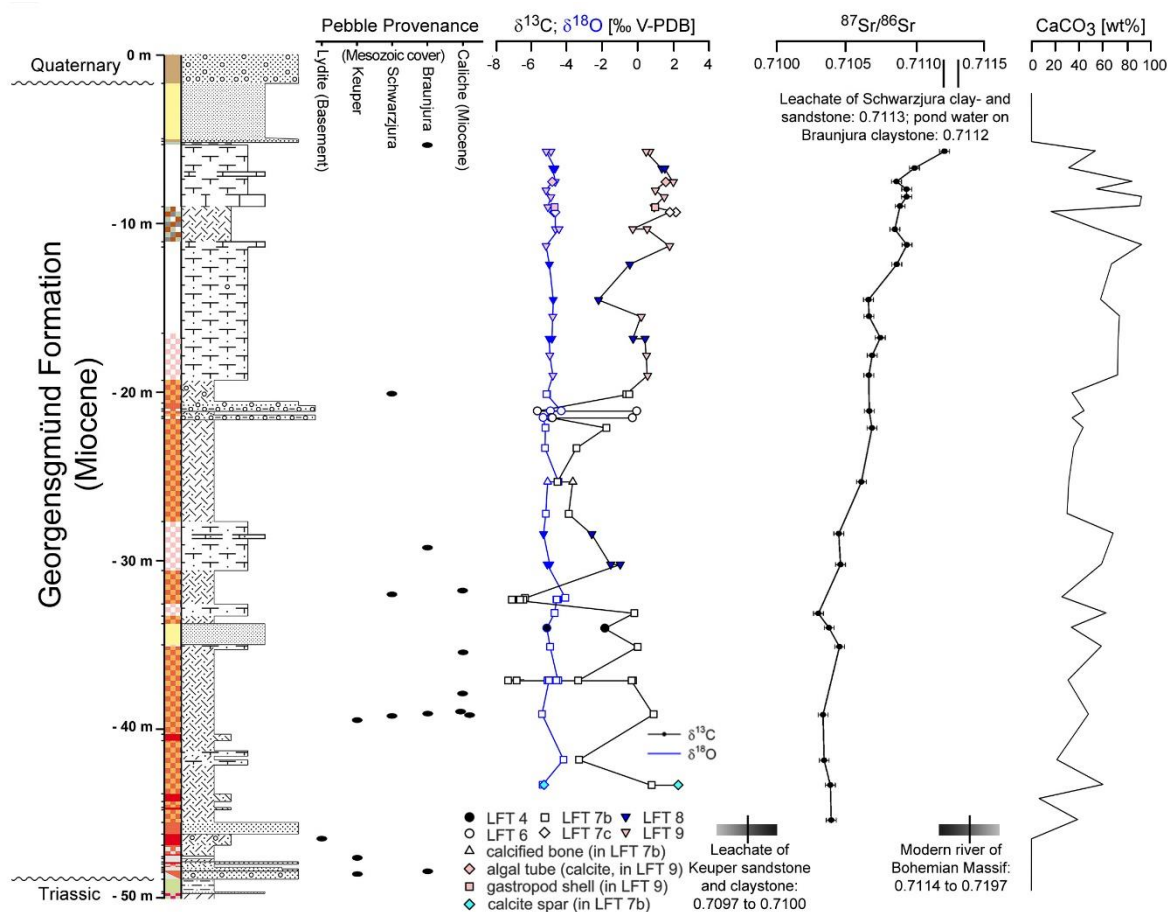
Figure 5.8 Provenance of the pebbles, trend of δ^{13}C and δ^{18}O of the carbonates and $^{87}Sr/^{86}Sr$ trend of the carbonates and carbonate contents in the investigated Pleinfeld drill section.
The general trend of the increasing $^{87}Sr/^{86}Sr$ trend is shown in comparison to $^{87}Sr/^{86}Sr$ ratios of leachates from Schwarzjura claystone and Keuper sandstone from Southern Germany (Ufrecht and Hölzl, 2006), pond water on Braunjura claystone of the Steinheim crater (Tütken *et al.,* 2006), and modern river water on Saxothuringian

bedrock (Zieliński _et al.,_ 2018).

5 Interpretation and discussion

Depositional setting: fluvial or lacustrine?

Early geologists studying the Georgensgmünd Formation were puzzled by the occurrence of Miocene limestones isolated within the siliciclastic-dominated landscape of the Keuper outcrop (Reck, 1912). Krumbeck (1926, 1927) explained the isolated limestones as karstic spring deposits, which indicated the former position of the Jurassic escarpment. Reck (1912, p. 202) and Wagner (1923), in turn, argued for a lake setting which reflected the damming of a drainage system. This view was supported by Dorn (1939, p. 82) who noted that the freshwater limestones form nodules and thin lenses embedded within claystones and argillaceous marlstones.

The lacustrine interpretation was expanded by Birzer (1969) who suggested that the Georgensgmünd Formation consisted of "deposits from a lake dammed by the Ries impact ejecta formations onto the Moenodanuvius (Paleo-Main River) in Franconian Alb area". Consequently, the supposed ejecta-dammed "Rezat-Altmühl-lake" was assigned to a post-Ries-impact age, i.e., Badenian age (Berger, 1973; Fischer, 1983). This view persisted until recent times (e.g., Hüttner & Schmidt-Kaler, 1999; Weiss _et al.,_ 2008; Peterek & Schröder, 2010; Sturm _et al.,_ 2015).

However, Berger (2010) argued that on the basis of mammal teeth fossils (specifically _Anomalomys minor Fejfar_, _Megacricetodon bourgeoisi (Schaub)_ and _Galerix exilis (Blainville)_) being present at Bühl (**Figure 5.1**), that the calcareous top parts of the Georgensgmünd Formation belongs to early MN5 (Karpatian), i.e., an age that is probably older than the radiometrically dated Ries impact event (Schmieder _et al._ 2018 a,b: 14.808 ± 0.038 Ma; Rocholl _et al._ 2018a,b: 14.93 to 15.00 Ma). Indeed, while an accurate radiometric age of the upper boundary of MN5 is available (Krijgsman _et al._ 1996, Agustí _et al._ 2001: 13.75 ± 0.03 Ma), the precise age position of its lower boundary (Krijgsman _et al._ 1996: 17.26 ± 0.01 Ma; Reichenbacher _et al._ 2013: 16.3 to 16.6 Ma) and subunits (early, middle, late MN5) are less well established. This biostratigraphic dating, therefore, leads to the question whether the deposits are related to the Ries impact, and whether they are of lacustrine origin at all.

While the distinction of lacustrine and fluvial sedimentary rocks is facilitated when the three-dimensional geometry of beds is observable, depositional interpretations of relict deposits with limited outcrops and/or isolated drill cores can be ambiguous. For instance, red brown massive mudstones, can be formed both in lacustrine setting (e.g., Clemmensen _et al.,_ 1998) as well as fluvial settings (e.g., Newell _et al.,_ 1999). The same applies to fine-grained sandstones (Cant, 1982; Fouch & Dean, 1982), palustrine limestones (Alonso-Zara 2003, Alonso-Zarza & Wright, 2010), and oncolitic tufa (e.g., Arenas _et al.,_ 2007, 2010).

In such cases, fossil assemblages are important criteria to distinguish between fluvial and lacustrine settings (Rust, 1982; Selley, 1992; Reading, 1996; Flügel, 2004). Indeed, the mollusc fauna of the Georgensgmünd Formation is dominated by terrestrial taxa of pulmonate gastropods, and only a few aquatic representatives of Lymneidae and Planorbidae occur (Berger 2010, 2013b). This fact was already noticed by Dorn (1939) who, nonetheless, argued for a lacustrine setting. A further aquatic gastropod, the prosobranch _Hydrobia trochulus_, was mentioned by Gümbel (1891), Krumbeck (1926) and Dorn (1939) from the Bühl and Pleinfeld locations. This species is common in saline aquatic settings such as the Ries crater lake (e.g., Bolten, 1977). However, a re-investigation assigns these poorly preserved moulds to the freshwater hydrobiid genus _Heleobia_ (Berger, 2013b; see also Kadolsky, 2008). The presence of the salinity-indicating taxon _Hydrobia trochulus_, as known from the saline Ries crater lake, therefore appears questionable. In any case, hydrobiid gastropods are not abundant or characteristic components of the Georgensgmünd Formation. Consistent with these previous findings, the Pleinfeld drill core did only yield pulmonate gastropod fossils, specifically in LFTs 6, 8 and 9. There is no indication of aquatic

gastropods. Likewise, other unequivocal aquatic organisms such as ostracods or bivalves are absent. The only exceptions are charophyte stem fragments in LFT 9b (**Fig. 5E**), which is a rare lithofacies type which, to date, is only known from the Bühl locality. While many charophytes occur in lakes as well as sluggish parts of rivers, the association of their fossil remains within a mud-supported fabric indicates deposition of LFT 9b in a standing water environment (floodplain pond or dammed area upstream of tufa barrages; e.g., Vázquez-Urbez *et al.*, 2012).

Indeed, sedimentological observations only provide a lack of evidence for a lacustrine origin of the formation. While clear bedding or lamination – characteristic of deposits in stagnant water bodies – is absent, the majority of the Pleinfeld deposits (e.g., LFTs 7 to 9; **Fig. 5A to F; Table 5.1**) is poorly stratified or massive, with various features of pedogenesis. Only the vacuolar tufa LFT 10 may represent a spring deposit or small tufa barrage nearby a spring (see Manzo *et al.*, 2012; Perri *et al.*, 2012), and LFT 9b may represent a pond deposit, but both LFTs are rare and only observed at the Bühl locality.

However, further support for the fluvial interpretation comes from stable carbon and oxygen isotope ratios of the carbonate fraction of the samples. The data show a very distinct pattern, with strongly varying $\delta^{13}C$ at almost constant $\delta^{18}O$ values (**Figure 5.7A**). This pattern is known from fluvial settings (e.g., freshwater fluvial tufa deposits of the same region; Arp *et al.,* 2001) as well as from paleosols (e.g., Palaeogene Bighorn Basin; Koch *et al.* 1995). There is no covariation of $\delta^{13}C$ and $\delta^{18}O$ of the carbonate fraction along the entire profile (**Figure 5.7A**, r = 0.44, p < 0.05, n = 55) except for a weak covariation trend in the floodplain-paleosol section (r = 0.77, p < 0.05, n = 22). This isotopic pattern neither fits to hydrologically closed lakes showing a clear covariation (e.g., Talbot, 1990; Li & Ku, 1997; Utrilla *et al.*, 1998; Arp *et al.* 2017a,b), nor to hydrologically open lakes, which are characterized by cloud-like $\delta^{13}C$-$\delta^{18}O$ patterns (e.g., Last *et al.*, 1994; Utrilla *et al.*, 1998; Hammarlund *et al.*, 2003; Benavente *et al.*, 2019) (**Figure 5.7B**).

The narrow range of $\delta^{18}O$ (-4.94 ± 0.31 ‰; n = 55) in the Georgensgmünd Formation therefore indicates a short residence time of water, consistent with a fluvial setting. The only example of hydrologically open lake deposits with a similar stable isotope pattern is reported from the Eocene Fenghuoshan Group (Hoh-Xil Basin), with thin palustrine and shallow lacustrine limestone beds intercalated in a series of fluvial sandstones and red-brown floodplain mudstones (Cyr, 2004; Cyr *et al.*, 2005). These deposits are reminiscent of the Georgensgmünd lithofacies association, however, with a greater thickness and lateral extension. This example may underline that a low residence time of water (as derived from invariant $\delta^{18}O$ values) is not a definitive proof on its own for a fluvial setting. However, lipid biomarker analyses indicate that the Fenghuoshan Group carbonates suffered significant thermal alteration and the measured oxygen isotope values may not reflect primary values (Polissar *et al.*, 2009; Staisch *et al.*, 2014).

Fluvial sub-environments and causes of lithofacies stacking patterns
A straight-forward assignment of LFTs to specific fluvial sub-environments of this succession is hampered by the unknown geometry of beds. This is especially true for the coarse-grained siliciclastic LFTs. Nonetheless, sedimentary structures, thickness information and stacking pattern allow a number of statements to be made.

> **1** Fluvial floodplain. Major parts of the Georgensgmünd Formation are composed of massive, mottled mudstone (LFT 7abc). They are characterized by pedogenic features such as root voids, cutans, pedogenic slickensides, nodules and *in situ* brecciated microfabrics. Light to intense red-brown mottling indicates a successive change from a deeper soil zone with increasing groundwater saturation to prolonged oxygenation and paleosol formation (Bown & Kraus, 1987; Alonso-Zarza, 2003). A weak covariation of $\delta^{13}C$ and $\delta^{18}O$ in carbonates from 22.10 to 43.27 m depth (LFTs 4, 7b and 8; PF38 to PF65, r = 0.71; p < 0.05) possibly indicates a minor evaporation effect on the floodplain (Bowen & Bloch, 2002; Leng & Marshall, 2004; Arenas *et al.*, 2010).

2 Palustrine swamp. Carbonate-rich parts (LFT 8 and LFT 9abc) of the core section show more characteristics of a water-saturated and vegetated environment, when compared to the paleosols described in the fluvial floodplain. Instead of intense red brown mottling, the palustrine lithofacies shows a predominantly light pink to white-grey colour. Pulmonate gastropod shell debris and intense rooting of the mud-supported fabric suggest a swamp environment. Stratified, greenish clay-rich intercalations within LFT 8 (and charophytes in LFT 9b at the Bühl locality) are the only features that may point to temporary ponding.

3 Debrites. Thin intercalations of mud-supported conglomerates (LFTs 5 and 6), with reworked components of the floodplain deposits and/or Mesozoic clasts, are interpreted as event deposits, reflecting heavy flooding. While a localized reworking within the floodplain sufficiently explains LFT 5, extraclasts embedded in a Jurassic-clay-derived matrix of LFT 6 point to a sediment gravity flow from the valley slope.

4 Fluvial sands. LFTs 1 to 4 are most difficult to interpret. Although bed thickness and sedimentary structures give some indication, no definitive distinction between channel, point bar, crevasse channel or crevasse splay deposits can be made from the drill core. Presumably, thin intercalations rather represent crevasse splay deposits, especially when affected by pedogenic concretionary carbonate (e.g., LFT 4 at 33.75 to 35.00 m core depth). In turn, thicker and coarse-grained sandstones could be channel, point bar, or crevasse channel deposits.

The cyclic stacking pattern and dominance of fine-grained floodplain and palustrine lithofacies, however, further constrains the depositional setting. Six cycles have been identified (**Figure 5.3**). A complete cycle starts with coarse-grained to fine-grained sandstones (LFTs 1 to 4), followed by floodplain fines, which were subjected to different extents of pedogenesis (LFT 7), and finally carbonate-rich palustrine swamp deposits (LFTs 8 and 9; **Figure 5.3**). Non-cyclically intercalated mud conglomerates LFT 5 and LFT 6, in turn, reflect episodic flooding events.

Such fining-upwards cycles are well known from various river systems (e.g., Alpine molasse deposits, Miall, 1996; Lower Old Red Sandstone of South Wales, Allen, 1965; Norian Arnstadt Formation, Beutler *et al.*, 1999; Arp *et al.*, 2005; Shukla *et al.*, 2006) and reflect autocyclic migration of a sinuous stream bed. However, typical features of braided river deposits such as amalgamating channel sandstones are absent in the investigated succession. Instead, the Georgensgmünd Formation is dominated by fine-grained floodplain deposits. Indeed, the gradient reconstruction of the ancient Moenodanuvius river by Hofbauer (2012) and Schirmer (2014) suggests a 50 m descent along the 40 km long river section at Pleinfeld, plausibly indicating a low-gradient river system (Schumm, 1985; Buffington & Montgomery, 2013). No climatic fluctuations can be derived from the cyclic lithofacies stacking pattern alone.

Provenance of pebbles
The characteristic lithology of pebbles allows the identification of different older formations in the catchment of the Georgensgmünd Formation. Several groups of pebbles, derived from different formations, are identified (see section on Pebble Lithofaices):

1 The first group of clasts is considered to be derived from the Upper Triassic Keuper Group because of their lithologic similarity (angular quartz grains, kaolinized feldspar) with the Keuper arkose in the lowermost part of the drill core.

2 Similar to group (1), pebbles from group (2) are lithologically identical to rocks of the Sinemurian Gryphaeensandstein Formation ("Arietensandstein", Lower Jurassic Schwarzjura-Group; Berger, 1971) of the region.

3 Pebbles of group (3) superficially resemble Upper Jurassic limestone clasts. However, a thin section of the pebble at 32.30 m, containing pisoid fragments with coarsely laminated crusts within a clotted and rooted matrix (**Figure 5.6C**) indicates a caliche origin. Another white-grey limestone pebble from 37.08 m depth also turned out to be of pedogenic origin.

4 Group (4) pebbles are derived from siderite concretions, which are abundant in the Lower Jurassic Amaltheenton Formation and Middle Jurassic Opalinuston Formation of the region (Berger, 1971). A limonite pebble at 48.60 m depth is possibly derived from the Middle Jurassic Eisensandstein Formation (Braunjura Group), while a 3.5 cm sized brown limonitic sandstone fragment with a bivalve mould at 5.15 m depth is clearly derived from this formation. Two 5 mm sized limonite pisoids ("pisolitic iron-ore"; Birzer, 1939) at -39.60 m depth indicate that components of Paleogene-Neogene origin are present, too.

5 For the last pebble group (5), i.e., the lydites, an origin from the Palaeozoic of the Frankenwald (north-western part of Saxothuringian in **Figure 5.1**) is evident, i.e., 120 km NNE of the working area (Berger, 2013a).

Except for the lydite, all pebbles of the investigated drill core section can be derived from formations close to the Pleinfeld drill site. Specifically, clasts from the Upper Triassic Keuper Group, Lower Jurassic Schwarzjura and Middle Jurassic Braunjura Group are present and indicate sediment influxes from these formations and groups to the Georgensgmünd Formation. Upper Jurassic Weißjura limestone clasts, however, remain without evidence. All white-grey limestone pebbles turned out to be of pedogenic origin and appear to be reworked from lower Miocene caliche deposits. Indeed, Berger (2010) already questioned an Upper Jurassic Weißjura origin of similar clasts found at the Bühl locality.
The lydite pebble is the only evidence of long-distance transport, i.e., a provenance of isolated components in the Saxothuringian, 120 km NNE of the study area (Krumbeck, 1927; Dorn, 1939). However, most of the lydites of the Georgensgmünd Formation appear to be reworked from older, pre-Karpatian gravel deposits ("high-lying gravel", Dorn, 1939; Berger & Wittmann, 1968; Berger et al., 1971; Berger, 2010), and their initial transport possibly dates back to the Early Cenozoic and Late Cretaceous (Lemcke, 1985; Berger, 2010: p. 161-163, 165; Schirmer, 2014).
An important result is that no pebbles that were possibly reworked from ejecta of the Ries impact (i.e., Variscan crystalline rocks) or Mesozoic sedimentary rocks with internal fracturing or shock features, were found. The possibility of an effect of impact ejecta on the Moenodanuvius drainage system, therefore, remains without evidence; this is consistent with the suggested pre-impact age (MN 5).

Systematic change in sediment and water provenance in the catchment
Strikingly, the Mesozoic-derived pebbles of the drill core section show a clear trend from Keuper-derived pebbles (with few Jurassic pebbles) at the base to only Schwarzjura-derived and finally Braunjura-derived pebbles near the top of the section. Since both Keuper and Braunjura pebbles occur already at the base of the section, this trend cannot be explained by simple headward catchment erosion. Furthermore, the stratigraphic trend in clast provenance matches the successive, unidirectional increasing trend in $^{87}Sr/^{86}Sr$ ratios (0.7103 to 0.7112) of the carbonates (**Figure 5.8**). This trend is independent from $\delta^{18}O$ values, suggesting that changes in water provenance occurred (e.g. Doebbert et al., 2014). With respect to the potential catchment area of the Georgensgmünd Formation/Moenodanuvius, a number of $^{87}Sr/^{86}Sr$ values from whole rock leachates are available for Triassic to Lower Jurassic formations (Ufrecht & Hölzl, 2006): Pure water leachates of Upper Triassic Keuper sandstones, arkoses and claystones show $^{87}Sr/^{86}Sr$ values ranging from 0.7086 to 0.7140, with an average of 0.7105. On the other hand,

$^{87}Sr/^{86}Sr$ values of pure water leachates from Lower Jurassic claystones and sandstones reveal higher ratios, from 0.7102 to 0.7124, with an average $^{87}Sr/^{86}Sr$ of 0.7113. A pond water sample on the Middle Jurassic Opalinuston revealed a $^{87}Sr/^{86}Sr$ ratio of 0.7112 (Tütken *et al.*, 2006).

This increase in $^{87}Sr/^{86}Sr$ of solutions probably reflects the fact that Keuper siliciclastics were largely derived from Variscan rocks (320 Ma) of the Bohemian Massif (i.e., the Saxothuringian and Moldanubian in **Figure 5.1**), while Lower and Middle Jurassic siliciclastics have a mixed source and are derived from Variscan and older basement rocks ("Caledonian" and "Cadomian"; 350 and 580 Ma, respectively) from farther north-east and east (Paul *et al.*, 2008, 2009). As ^{87}Sr is generated by radiogenic decay of ^{87}Rb, older rocks tend to have a higher $^{87}Sr/^{86}Sr$ ratio (Faure & Powell, 1972). This explains the relatively low $^{87}Sr/^{86}Sr$ values for Keuper siliciclastics and high $^{87}Sr/^{86}Sr$ values for Jurassic siliciclastics, as the latter contain mica or other Rb-rich detrital minerals older in age. Finally, Upper Jurassic groundwater shows much lower values (0.7075 to 0.7078), similar to the marine $^{87}Sr/^{86}Sr$ signal for this time interval (Tütken *et al.,* 2006).

The unidirectional trend in $^{87}Sr/^{86}Sr$ ratios in carbonates of the Pleinfeld section, therefore, perfectly mirrors the trend from Keuper-derived solutes to Schwarzjura-derived solutes and finally Braunjura-derived solutes (**Figure 5.8**). Initial $^{87}Sr/^{86}Sr$ values (0.7104) are close to the average Keuper leachate ratio (0.7105) and successively increase to $^{87}Sr/^{86}Sr$ values identical to the Opalinuston pond water ratio (0.7112). Strikingly, this trend matches the trend in pebble provenance. In turn, there is no indication of a former influx of solutes from the Upper Jurassic Weißjura to the Georgensgmünd Formation deposits at Pleinfeld. Indeed, a significant contribution of karstic waters from these marine carbonates should have led to much lower values and a decreasing trend in $^{87}Sr/^{86}Sr$, towards Upper Jurassic marine ratios (0.7068 to 0.7070; Veizer, 1989; Veizer *et al.,* 1999, Wierzbowski *et al.,* 2017).

A possible contribution of Variscan basement derived headwaters from the Frankenwald (i.e., the north-eastern part of the Saxothuringian in **Figure 5.1**), however, is more difficult to demonstrate on basis of the current data. Anthropogenically uncontaminated headwaters of modern rivers draining Saxothuringian bedrocks of the northern Bohemian Massif show $^{87}Sr/^{86}Sr$ ratios ranging from 0.7114 to 0.7197 at low Sr concentration of 64 to 117 ppb [Zieliński *et al.*, 2018 (sites Nl4, K2, Br4, Br5, B3)]. Solutes carrying this high $^{87}Sr/^{86}Sr$ signal may have contributed to the riverine waters of the working area, but dilution along the >120 km long Moenodanuvius river certainly obliterated any significant impact on the $^{87}Sr/^{86}Sr$ in the carbonates of the Pleinfeld drill core.

Major control of fluvial sedimentation: climate change versus base-level change
Continental sedimentary successions are sensitive to climatic changes as well as to base-level changes governed by upstream controls (e.g. tectonic movements) and/or downstream controls (e.g. sea-level or lake level change) (Carroll & Bohacs, 1999; Bohacs *et al.*, 2000; Cohen, 2003; Arenas *et al.*, 2010; Tanner, 2010). Many of these continental sedimentary successions comprise red brown siliciclastics ("red beds"; e.g. van Houten, 1973). Likewise, carbonate contents in terrestrial successions have been taken as a paleoclimate proxy reflecting humid or arid condition (e.g. Chen *et al.,* 1999; Yan *et al.,* 2017).

Among these deposits, red brown mottled mudstones are common floodplain sediments that reflect good drainage and temporary, well oxidized conditions (Sheldon, 2005). They commonly, though not necessarily (Sheldon, 2005; Song *et al.*, 2018), reflect semi-arid or even arid climatic conditions (Kraus, 1987; Kraus & Aslen, 1993; Mack & James, 1994). Carbonate precipitates within these mottled mudstones reflect capillary rise of groundwater at times of reduced siliciclastic influx (Semeniuk & Meagher, 1981; Wright *et al.*, 1988; Tandon & Gibling, 1994).

Palustrine limestones and marlstones, on the other hand, essentially form under semi-arid to sub-humid conditions (Platt & Wright, 1992; Alonso-Zarza, 2003; Alonso-Zarza *et al.*, 2012), with more arid phases recognizable by extensive calcretization (Djamali *et al.*, 2006) or dolomite (Abdul Aziz *et al.*, 2000). Wetter conditions are indicated by extensive rooting, specific pulmonate gastropods and the absence of evaporites (Platt & Wright, 1992).

Moreover, comparatively low $\delta^{18}O$ values in palustrine limestones have been taken as an argument for wetter conditions, if compared to contemporaneous paleosol carbonates (Bowen & Bloch, 2002).

At first glance, the observed lithofacies change within the investigated Georgensgmünd Formation (**Figure 5.3**) may therefore reflect a climatic change. The lower part of the section is dominated by red-brown carbonate-poor mottled mudstones, which may point to conditions that are more arid. In turn, parts with light-coloured palustrine limestones, which contain abundant root voids and pulmonate gastropods, could reflect a change to more humid conditions.

However, the carbonate stable oxygen isotopes of the investigated succession show a strikingly low variance at $\delta^{18}O$ = -4.94 ± 0.31 ‰ (n = 55), across all lithofacies types analysed (**Figure 5.7 and 5.8**). No systematic $\delta^{18}O$ trend is observed along the section, suggesting a hydrologically stable condition. Neither significant changes in evaporation, inflow-outflow ratio, ambient temperatures, nor changes in the continental effect during the deposition of the Georgensgmünd Formation are evident.

Likewise, no general trend in carbonate $\delta^{13}C$ is observed along the section, although (in contrast to $\delta^{18}O$) $\delta^{13}C$ values considerably vary (**Figure 5.7A**). Specifically, $\delta^{13}C$ variations coincide with changes in lithofacies, with low values in floodplain paleosol nodules (LFTs 6 and 7: $\delta^{13}C$ = -2.57 ± 2.63 ‰; n = 22) and reworked caliche pebbles (within LFT 7: $\delta^{13}C$ = -6.93 ± 0.30 ‰; n = 5), and high values in floodplain pond and spring-fed carbonates (LFTs 9b, 9c and 10: $\delta^{13}C$ = 3.04 ± 2.44 ‰; n = 7).

The latter high values probably reflect a photosynthesis-effect by cyanobacteria or eukaryotic algae within the shallow ponds and a CO_2 degassing effect at spring sites (LFTs 9b, 9c and 10), where discharging waters initially show intermediate $\delta^{13}C_{DIC}$ values reflecting a mixture of dissolved inorganic carbon (DIC) from Jurassic carbonate (**Figure 5.7B**) and soil-derived CO_2. Nonetheless, $\delta^{13}C$ values in LFT 9 and LFT 10 are higher than similar present-day and Quaternary tufa and pond deposits (e.g., Andrews et al., 1997; Mayer & Schwark 1999; Arp et al., 2001; Valero Garcés et al., 2008; Arenas et al., 2010, 2019; **Figure 5.7B**). While temporary anaerobic conditions may have occurred in floodplain pond sediments (and palustrine sediments), the lack of extremely high $\delta^{13}C$ values (see Talbot & Kelts, 1986) indicates that methanogenesis and associated CH_4 loss did not affect the DIC pool significantly. Likewise, the invariant $\delta^{18}O$ argues against an evaporation effect, which should have affected both $\delta^{13}C$ and $\delta^{18}O$ simultaneously. Instead, climatic conditions warmer than present-day (Methner et al., 2020) may have enhanced aquatic productivity, thereby causing a higher ^{12}C depletion of surface waters in this region if compared to today.

In turn, the former, low values, are characteristic of ^{13}C-depleted CO_2 from respiratory processes in soils (LFTs 6 and 7) (e.g. Stevenson, 1969; Kraus et al., 1987; Quade et al., 1989; Whiticar, 1999). Values of palustrine facies types (LFTs 8 and 9a) vary between these end members (**Figure 5.7A**). A potential, increasing admixture of DIC from marine Jurassic carbonate to the top of the section (**Figure 5.8**) appears possible, but remains unresolvable against the background of strong $\delta^{13}C$ variations within the pedogenesis-affected lithofacies types (e.g., at 37.1 m depth; **Figure 5.8**). Likewise, there is no indication of potential post-Miocene meteoric diagenetic alterations of microcrystalline carbonate $\delta^{13}C$ values in top parts of the section. None of these samples shows a decrease in $\delta^{13}C$ associated with a shift of $\delta^{18}O$ towards meteoric values as it is seen in a late diagenetic spar cement (**Figure 5.7A**) or present-day tufa carbonate of the region (**Figure 5.7B**).

No climatic trend related to possible atmospheric pCO_2 changes can be derived on the basis of these data. This would be consistent with a pre-impact age of the Georgensgmünd Formation, falling in the time range of the Miocene Climatic Optimum (MCO; e.g. Zachos et al., 2001), as opposed to the post-impact scenario and time of the mid-Miocene Climate Transition (MMCT; e.g. Methner et al., 2020).

On the other hand, a clear change in the provenance of water and sediment is evident from the change in pebble lithology and $^{87}Sr/^{86}Sr$ values of carbonates (**Figure 5.8**). Both signatures suggest a change from water and sediment predominantly derived from the Keuper Group to the Schwarzjura and Braunjura Groups. This trend of changing provenance

can be explained by a rise in base-level (Holbrook *et al.*, 2006; Catuneanu *et al.*, 2009), either by downstream controls (e.g. sea level rise) and/or upstream controls (e.g. regional subsidence or increasing rainfall). Likewise, a rise in base-level controlled by upstream factors explains, without any change in climate, the trend of increasing carbonate contents from the base to the top of the Georgensgmünd Formation: Initial waters derived from the Keuper Group are poor in carbonate (**Figure 5.9A**), while their later replacement by waters from Lower/Middle Jurassic calcareous claystones and marlstones supply sufficient calcium and carbonate to enhance the formation of palustrine limestones (**Figure 5.9B**).

Indeed, base-level changes are known from a number of studies as a major steering factor for fluvial and floodplain successions and their paleosol development (e.g. Leeder, 1975; Schumm, 1993; Leeder & Stewart, 1996; Pla-Pueyo *et al.*, 2009). Specifically, base-level changes may alter fluvial style (slope and gradient, sinuosity, channel parameters), sediment supply, accommodation spaces and groundwater table (Wright & Marriott, 1993; Miall, 1996; Ethridge *et al.*, 1999; Blum & Törnqvist, 2000; Alonso-Zarza, 2003; Pla-Pueyo *et al.*, 2009). Furthermore, the adjacent Northern Alpine Foreland Basin (NAFB), in which the Moenodanuvius drained, experienced several marine ingressions and regression (see **Figure 5.2**; Reuter, 1927; Lemcke, 1975; Doppler & Schwerd, 1996), which are considered as eustatic sea-level changes (Bachmann *et al.*, 1987; Bachmann & Müller, 1992; Jin *et al.*, 1995; Zweigel *et al.*, 1998).

A detailed comparison with the 3rd order sequences of the central Paratethys (Piller *et al.*, 2007), the marine ingressions and regressions in the NAFB (western Paratethys; Pippèrr & Reichenbacher, 2017; and references therein), however, suggests that the Georgensgmünd Formation accumulated simultaneously with sea-level fall and lowstand conditions (**Figure 5.2**). Indeed, early Upper Freshwater Molasse deposits (**Figure 5.2**) of the NAFB also progressively overstep the karstic plateau of the southern Franconian and Swabian Alb (pre-Ries-impact "limnic lower series"; Doppler *et al.*, 2002) at the same time, forming a low-relief swampy landscape (Doppler *et al.*, 2002) with local caliche development (Bolten & Müller, 1969).
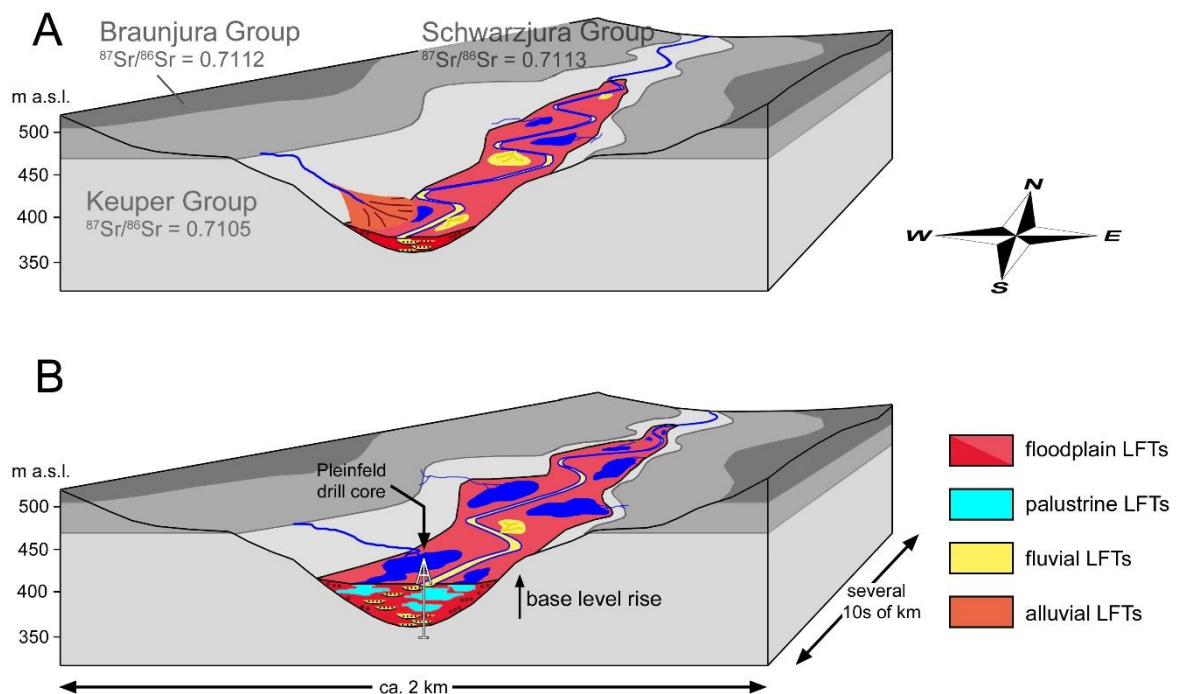
Figure 5.9 Sedimentary model of (A) lower and (B) upper Georgensgmünd Formation. See Figure 5.1 and Figure 5.2 for legends. During the early development of the formation (A), base-level was low and Triassic bedrocks are widely exposed in the Pleinfeld area. With the increasing base-level during the later development (B) Georgensgmünd Formation, Triassic Keuper bedrock was successively covered and

the proportion of influx from the carbonate-bearing Schwarzjura/Braunjura rocks increased. Weathering of Schwarzjura/Braunjura rocks derived calcium-rich solutes to the depositional area, promoted the formation of calcareous palustrine deposit. $^{87}Sr/^{86}Sr$ data represent leachates from Keuper and Schwarzjura Group rocks, and pond water on Braunjura Group rocks.

This means that the base-level rise controlled sedimentation of the Georgensgmünd Formation (**Figure 5.9**) is caused by a tectonic subsidence in this region (Bolten & Müller, 1969: p. 121; Doppler *et al.,* 2002), independent from sea-level changes. Later tectonic movement, leading to uplift and minor tilting of the whole region is indicated by tilting of the lower Miocene cliff line [**Figure 5.2**; "post-middle Miocene tilting" (Gall, 1974); "during the Pliocene" (Doppler *et al.,* 2002)].

6 Conclusions

1 Despite the fact that the impact ejecta covers the downstream fluvial section, no traces of damming and possible lake evolution are seen, because only pre-impact fluvial deposits are preserved. Instead, lithofacies associations (dominance of fine-grained lithofacies types), sedimentary structures (lack of lamination), fossils (lack of lacustrine organisms), and stable oxygen and carbon isotopes (strong variation in $\delta^{13}C$ at almost constant $\delta^{18}O$) point to a low-gradient river system with a narrow stream bed and dominant floodplains. This interpretation is consistent with a pre-Ries-impact age of the formation suggested by Berger (2010), implying that its sedimentation is unrelated to impact ejecta damming.

2 The observed trend in sediment lithofacies within the formation, from red-brown carbonate-poor siliciclastics to white-grey palustrine limestones, is unrelated to climatic changes. Constant carbonate oxygen isotope ratios throughout the section point to constant climatic conditions.

3 Instead, a unidirectional increase in $^{87}Sr/^{86}Sr$ in carbonates and a change of pebble provenance from Keuper to Schwarz and Braunjura parent rocks indicate that a base-level rise in this region controlled fluvial sedimentation and lithofacies succession. A comparison with sea-level changes in the adjacent Northern Alpine Foreland Basin suggests that this base-level rise is tectonically induced.

4 In drill core sections, where the three-dimensional geometry of beds is unknown, the distinction of lacustrine and fluviatile deposits can be made using palaeontological and lithofacies criteria (presence or absence of lacustrine organisms and laminated mudstones) in combination with carbonate stable isotope signatures (invariant $\delta^{18}O$ at highly variable $\delta^{13}C$). The provenance of extraclasts and changes in carbonate $^{87}Sr/^{86}Sr$ ratios allow the differentiation of climatic and regional geological effects such as changes in catchment area and base-level.

Acknowledgements

References

Abdul Aziz, H., Hilgen, F., Krijgsman, W., Sanz, E. and **Calvo, J.** (2000) Astronomical forcing of sedimentary cycles in the middle to late Miocene continental Calatayud Basin (NE Spain). *Earth Planet. Sci. Lett.*, **177,** 9-22.

Agustí, J., Cabrera, L., Garcés, M., Krijgsman, W., Oms, O. and **Parés, J.M.** (2001) A calibrated mammal scale for the Neogene of Western Europe. State of the art. *Earth-Science Reviews*, **52**, 247-260.

Allen, J.R.L. (1965) Fining-upwards cycles in alluvial successions. *Geological Journal*, **4,** 229-246.

Allen, J.P., Fielding, C.R., Gibling, M.R. and **Rygel, M.C.** (2014) Recognizing products of palaeoclimate fluctuation in the fluvial stratigraphic record: An example from the Pennsylvanian to Lower Permian of Cape Breton Island, Nova Scotia. *Sedimentology,.***61,** 1332-1381.

Alonso-Zarza, A.M. (2003) Palaeoenvironmental significance of palustrine carbonates and calcretes in the geological record. *Earth-Sci. Rev.*, **60,** 261-298.

Alonso-Zarza, A.M. and **Wright, V.P.** (2010) Chapter 2: Palustrine Carbonates. In: *Dev. Sedimentol.* (Eds A.M. Alonso-Zarza and L.H. Tanner), **61**, pp. 103-131. Elsevier.

Alonso-Zarza, A.M., Meléndez, A., Martín-García, R., Herrero, M.J. and **Martín-Pérez, A.** (2012) Discriminating between tectonism and climate signatures in palustrine deposits: Lessons from the Miocene of the Teruel Graben, NE Spain. *Earth-Sci. Rev.*, **113,** 141-160.

Andrews, J.E., Riding, R. and **Dennis, P.F.** (1997) The stable isotope record of environmental and climatic signals in modern terrestrial microbial carbonates from Europe. *Palaeogeogr. Palaeoclimatol. Palaeoecol.*, **129,** 171-189.

Andrews, J. (2006) Palaeoclimatic records from stable isotopes in riverine tufas: synthesis and review. *Earth-Sci. Rev.*, **75,** 85-104.

Arenas, C., Cabrera, L. and **Ramos, E.** (2007) Sedimentology of tufa facies and continental microbialites from the Palaeogene of Mallorca Island (Spain). *Sed. Geol.*, **197,** 1-27.

Arenas, C., Osácar, C., Sancho, C., Vázquez-Urbez, M., Auqué, L. and **Pardo, G.** (2010) Seasonal record from recent fluvial tufa deposits (Monasterio de Piedra, NE Spain): sedimentological and stable isotope data. *Geol. Soc. London Spec. Publ.*, **336,** 119.

Arenas, C., Vázquez-Urbez, M., Pardo-Tirapu, G. and **Sancho-Marcén, C.** (2010) Fluvial and associated carbonate deposits. *Dev. Sedimentol.* (Eds A.M. Alonso-Zarza and L.H. Tanner), **61,** 133-175.

Arenas, C., Osácar, M.C., Auqué, L. and **Sancho, C.** (2019) Coupling textural and stable-isotope variations in fluvial stromatolites: Comparison of Pleistocene and recent records in NE Spain. *Journal of Palaeogeography*, **e** 13.

Arp, G., Wedemeyer, N. and **Reitner, J.** (2001) Fluvival tufa formation in a hard-water creek (Deinschwanger Bach, Franconian Alb, Germany). *Facies*, **44,** 1-22.

Arp, G., Bielert, F., Hoffmann, V.-E. and **Löffler, T.** (2005) Palaeoenvironmental significance of lacustrine stromatolites of the Arnstadt Formation ("Steinmergelkeuper", Upper Triassic, N-Germany). *Facies*, **51,** 419-441.

Arp, G., Kolepka, C., Simon, K., Karius, V., Nolte, N., and **Hansen, B. T.** (2013) New evidence for persistent impact-generated hydrothermal activity in the Miocene Ries impact structure, Germany. *Meteoritics & Planetary Science*, **48**, 2491-2516.

Arp, G., Hansen, B.T., Pack, A., Reimer, A., Schmidt, B.C., Simon, K. and **Jung, D.** (2017a)

The soda lake—mesosaline halite lake transition in the Ries impact crater basin (drilling Löpsingen 2012, Miocene, southern Germany). *Facies*, **63,** 1.

Arp, G., Ulbrich, P., Reimer, A., Hartmann, G. and **Jung, D.** (2017b): Süßwassermergel der Kraterrandhöhen des Nördlinger Rieses (Miozän): Relikte einer Aussüßungsphase des Riessees? *Geologische Blätter für Nordost-Bayern*, 67, 19-34.

Bachmann, G.H., Müller, M. and **Weggen, K.** (1987) Evolution of the Molasse Basin (Germany, Switzerland). *Tectonophysics*, **137,** 77-92.

Bachmann, G. and **Müller, M.** (1992) Sedimentary and structural evolution of the German Molasse Basin. *Eclogae Geologicae Helvetiae*, **85,** 519-530.

Bader, K., Meyer, R.K.F. and **Brunold, H.** (2000) Graupensandrinne-Urnaabrinne, ihre Verbindung und tektonische Verstellung zwischen Donauworth und Regensburg. *Geologica Bavarica*, **105**, 243-250.

Bailey, T.R., McArthur, J.M., Prince, H. and **Thirlwall, M.F.** (2000) Dissolution methods for strontium isotope stratigraphy: whole rock analysis. *Chem. Geol.*, **167,** 313-319.

Bellefroid, E.J., Planavsky, N.J., Miller, N.R., Brand, U. and **Wang, C.** (2018) Case studies on the utility of sequential carbonate leaching for radiogenic strontium isotope analysis. *Chem. Geol.*, **497,** 88-99.

Benavente, C.A., Mancuso, A.C. and **Bohacs, K.M.** (2019) Paleohydrogeologic reconstruction of Triassic carbonate paleolakes from stable isotopes: Encompassing two lacustrine models. *J. S. Am. Earth Sci.*, **95,** 102292.

Berger, G. (2010) Die miozäne Flora und Fauna (MN5) der historischen Fossil-Lagerstätte Georgensgmünd (Mfr.): unter Berücksichtigung der Ablagerungen des Urmaintals zwischen Roth und Treuchtlingen. *Abhandlungen der Naturhistorischen Gesellschaft Nürnberg*, **46**, 1-191.

Berger, G. (2013a) Graptolithen aus Lyditgeröllen und untermiozäne Sedimente zwischen Schwabach und Roth. *Natur und Mensch*, **2011,** 107-111.

Berger, G. (2013b) Erstfunde von untermiozänen (MN 5) Säugetierüberresten bei Rittersbach (Mittelfranken). *Natur und Mensch*, **2012**, 105-118.

Berger, K. and **Wittmann, O.** (1968) *Geologische Karte von Bayern 1:25000 Erläuterungen zum Blatt Nr. 6832 Heideck*. Bayerisches Geologisches Landesamt, Munich.

Berger, K., Apel, R., Bader, K., and **Diez, T.** (1971) Geologische Karte von Bayern 1:25000 Erläuterungen zum Blatt Nr. 6831 Spalt, München, Bayerisches Geologisches Landesamt.

Berger, K. (1973) Obermiozäne Sedimente mit Süßwasserkalken im Rezat-Rednitz-Gebiet von Pleinfeld-Spalt und Georgensgmünd/Mfr. *Geologica Bavarica*, **67,** 238-248.

Berger, K., Apel, R., Bader, K., Kröger, J., Schmidt-Kaler, H., Wellnhofer, P. and **Wittmann, O.** (1982) Geologische Karte von Bayern 1:25000 Erläuterungen zum Blatt Nr. 6931 Weißenburg i. Bay. Bayerisches Geologisches Landesamt, Munich.

Beutler, G., Hauschke, N. and **Nitsch, E.** (1999) Faziesentwicklung des Keupers im Germanischen Becken. In: *Trias-Eine ganz andere Welt* (Ed V. Wilde), pp. 129-174. Pfeil Verlag, Munich.

Birck, J. L. (1986) Precision K-Rb-Sr isotopic analysis: application to Rb-Sr chronology. *Chem. Geol.*, **56**, 73-83.

Birzer, F. (1939): Verwitterung und Landschaftsgeschichte in der südlichen Frankenalb. *Zeitschrift der Deutschen Geologischen Gesellschaft,* **91**, 1-57; Berlin.

Birzer, F. (1969) Molasse und Ries-Schutt im westlichen Teil der südlichen Frankenalb.

Geologische Blätter für Nordost-Bayern, **19,** 1-28.

Blum, M.D. and **Törnqvist, T.E.** (2000) Fluvial responses to climate and sea-level change: a review and look forward. *Sedimentology*, **47**, 2-48.

Bohacs, K.M., Carroll, A.R., Neal, J.E. and **Mankiewicz, P.J.** (2000) Lake-basin type, source potential, and hydrocarbon character: an integrated sequence-stratigraphic-geochemical framework. *Lake basins through space and time: AAPG Studies in Geology*, **46,** 3-34.

Bolten, R. and **Müller, D.** (1969) Das Tertiär im Nördlinger Ries und in seiner Umgebung. *Geologica Bavarica*, **61,** 87-130.

Bolten, R.H. (1977) *Die karbonatischen Ablagerungen des obermiozänen Kratersees im Nördlinger Ries*, Ludwig-Maximilians-Universität, München, 288 + XXI pp.

Bowen, G.J. and **Bloch, J.I.** (2002) Petrography and geochemistry of floodplain limestones from the Clarks Fork Basin, Wyoming, USA: carbonate deposition and fossil accumulation on a Paleocene-Eocene floodplain. *J. Sed. Res.,* **72,** 46-58.

Bown, T.M. and **Kraus, M.J.** (1987) Integration of channel and floodplain suites; I, Developmental sequence and lateral relations of alluvial Paleosols. *J. Sed. Res.*, **57,** 587-601.

Buffington, J. and **Montgomery, D.** (2013) Geomorphic classification of rivers. In: *Treatise on Geomorphology, Fluvial Geomorphology (Eds, Shroder, J.; Wohl, E.)*, **9**. San Diego, CA: Academic Press. p. 730-767.

Cant, D.J. (1982) Fluvial facies models and their application. In: *Sandstone Depositional Environments* (Eds P.A. Scholle and D. Spearing), AAPG Memoir, **31**, 115-137.

Carroll, A.R. and **Bohacs, K.M.** (1999) Stratigraphic classification of ancient lakes: Balancing tectonic and climatic controls. *Geology*, **27,** 99-102.

Catuneanu, O., Abreu, V., Bhattacharya, J., Blum, M., Dalrymple, R., Eriksson, P., Fielding, C.R., Fisher, W., Galloway, W. and **Gibling, M.** (2009) Towards the standardization of sequence stratigraphy. *Earth-Sci. Rev*, **92**, 1-33.

Chen, F.H., Bloemendal, J., Zhang, P.Z. and **Liu, G.X.** (1999) An 800 ky proxy record of climate from lake sediments of the Zoige Basin, eastern Tibetan Plateau. *Palaeogeogr. Palaeoclimatol. Palaeoecol.*, **151**, 307-320.

Clemmensen, L.B., Kent, D.V. and **Jenkins, F.A.** (1998) A Late Triassic lake system in East Greenland: facies, depositional cycles and palaeoclimate. *Palaeogeogr. Palaeoclimatol. Palaeoecol.*, **140,** 135-159.

Cohen, A. S. (2003) Palaeolimnology: the history and evolution of lake systems, New York, Oxford University Press, 500 pp.

Cyr, A.J. (2004) Geochemical and stable isotopic evaluation of Fenghuoshan Group lacustrine carbonates, north-central Tibet: implications for the paleoaltimetry of the mid-Tertiary Tibetan Plateau (thesis), Miami University.

Cyr, A. J., Currie, B. S. and **Rowley, D. B.** (2005) Geochemical Evaluation of Fenghuoshan Group Lacustrine Carbonates, North-Central Tibet: Implications for the Paleoaltimetry of the Eocene Tibetan Plateau. *J. Geol.*, **113,** 517-533.

Demko, T.M., Currie, B.S. and **Nicoll, K.A.** (2004) Regional paleoclimatic and stratigraphic implications of paleosols and fluvial/overbank architecture in the Morrison Formation (Upper Jurassic), Western Interior, USA. *Sed. Geol.*, **167,** 115-135.

Djamali, M., Soulié-Märsche, I., Esu, D., Gliozzi, E. and **Okhravi, R.** (2006) Palaeoenvironment of a Late Quaternary lacustrine–palustrine carbonate complex:

Zarand Basin, Saveh, central Iran. *Palaeogeogr. Palaeoclimatol. Palaeoecol.*, **237,** 315-334.

Doebbert, A.C., Johnson, C.M., Carroll, A.R., Beard, B.L., Pietras, J.T., Carson, M.R., Norsted, B. and **Throckmorton, L.A.** (2014) Controls on Sr isotopic evolution in lacustrine systems: Eocene green river formation, Wyoming. *Chem. Geol.*, **380,** 172-189.

Doppler, G. and **Schwerd, K.** (1996) Gesteinsfolge des Molassebeckens und der inneralpinen Tertiärbecken. Faltenmolasse, Aufgerichtete Molasse und westliche Vorlandmolasse. - In: Freudenberger, W., Schwerd, K. (Eds.), Erläuterungen zur Geologischen Karte von Bayern 1:500000. Bayerisches Geologisches Landesamt, München, p. 150–168.

Doppler, G., Fiebig, M. and **Meyer, R.** (2002) Erläuterungen zur Geologischen Karte 1: 100.000, Geowissenschaftliche Landesaufnahme in der Planungsregion 10 Ingolstadt. *Bayerisches Geologisches Landesamt.*

Dorn, C. (1939) Die Ablagerungen der obermiocänen Süßwasserkalke bei Pleinfeld und Georgsgemünd in Mittelfranken. *Jahresberichte und Mitteilungen des Oberrheinischen Geologischen Vereins, Neue Folge*, **28**, 67-98.

Ekart, D.D., Cerling, T.E., Montanez, I.P. and **Tabor, N.J.** (1999) A 400 million year carbon isotope record of pedogenic carbonate: implications for paleoatmospheric carbon dioxide. *Am. J. Sci.*, **299,** 805-827.

El Hamdouni, R., Irigaray, C., Fernández, T., Chacón, J. and **Keller, E.** (2008) Assessment of relative active tectonics, southwest border of the Sierra Nevada (southern Spain). *Geomorphology*, **96**, 150-173.

Ethridge, F., Skelly, R. and **Bristow, C.** (1999) Avulsion and crevassing in the sandy, braided Niobrara River: complex response to base-level rise and aggradation. In: *Fluvial Sedimentology VI* (Eds N.D. Smith and J. Rogers), **28**, pp. 179-192. Int. Assoc. Sedimentol. Spec. Publ., 28.

Faure, G., and **Powell, J.** (1972) Strontium isotope geology, Berlin, Springer-Verlag, 189 pp.

Faure, G. (1986) Principles of Isotope Geology, 2nd ed.. New York, John Wiley & Sons, xv + 589 pp.

Fischer, K. (1983) Die Reliefentwicklung im Osten des Rieses. In: *Rieser Kulturtage*, pp. 564-588.

Flügel, E. (2004) *Microfacies of Carbonate Rocks: Analysis, Interpretation and Application*. Springer Science & Business Media.

Fouch, T. and **Dean, W.** (1982) Lacustrine and associated clastic depositional environments. In: *Sandstone depositional environments* (Eds P.A. Scholle and D. Spearing), **31**, pp. 87-114. AAPG Memoir.

Freudenberger, W. (1996) Erläuterungen zur geologischen Karte von Bayern 1: 500 000, Bayerisches Geologisches Landesamt.

Gümbel, C. W. (1891) Geognostische Beschreibung der Fränkischen Alb (Frankenalb) mit dem anstossenden Fränkischen Keupergebiete: Geognostische Beschreibung des Königreichs Bayern, Abtheilung 4, Kassel, Fischer, 763 pp.

Gall, H. (1974) Neue Daten zum Verlauf der Klifflinie der Oberen Meeresmolasse (Helvet) im südlichen Vorries. *Mitt. Bayer. Staatssamml. Paläont. hist. Geologie*, **14,** 81-101.

Gierlowski-Kordesch, E., Jacobson, A., Blum, J. and **Valero Garćes, B.L.** (2008) Watershed reconstruction of a Paleocene–Eocene lake basin using Sr isotopes in carbonate rocks. *Geol. Soc. Am. Bull.*, **120,** 85-95.

Hüttner, R. and **Schmidt-Kaler, H.** (1999) *Wanderungen in die Erdgeschichte: Meteoritenkrater Nördlinger Ries*. Verlag Dr. Friedrich Pfeil, München.

Hack, J.T. (1973) Stream-profile analysis and stream-gradient index. *Journal of Research of the U.S. Geological Survey*, **1**, 421-429.

Hardenbol J., Thierry J., Farley M.B., Jacquin T., Graciansky P.C. and **Vail P.R.** (1998) Mesozoic and Cenozoic Sequence Chronostratigraphic Framework of European Basins. In: *Mesozoic and Cenozoic sequence stratigraphy of European basins* (Eds, Graciansky, C.-P., Hardenbol, J., Jacquin, T. and Vail, P.R,), SEPM Spec. Publ., **60**: 3-13; Tulsa.

Hammarlund, D., Björck, S., Buchardt, B., Israelson, C. and Thomsen, C.T. (2003) Rapid hydrological changes during the Holocene revealed by stable isotope records of lacustrine carbonates from Lake Igelsjön, southern Sweden. *Quatern. Sci. Rev.*, **22,** 353-370.

Haunschild, H. (1992) Die Thermalwasser-Erschließungsbohrung Treuchtlingen 2 (T 2)-Kurzmitteilung. *Geologische Blätter für NO-Bayern*, **42,** 269-276.

Hofbauer, G. (2001) Die Diskussion um die Entstehung der Süddeutschen Schichtstufenlandschaft: Eine historischmethodologische Skizze mit einem Modell zur fluviatil gesteuerten Schichtstufen-Morphogenese. *Natur und Mensch, Jahresmitteilungen der Naturhistorischen Gesellschaft Nürnberg eV, Jubiläumsausgabe*, **200,** 85-108.

Hofbauer, G. (2012) Jungtertiäre Talverschüttung und tektonische Verstellung entlang des Regnitz-Rezat-Tals. *GDGH Berichte*, **15**, 1-16.

Hoffmann, M. and **Friedrich, A.** (2017) Erosional and tectonic overprint of the mid-Miocene marine cliff line and its applicability as a paleo-geodetic marker of regional-scale tilting, Swabian Alb, southwestern Germany. In: *Young tectonic evolution of the Northern Alpine Foreland Basin, southern Germany, based on linking geomorphology and structural geology*.

Holbrook, J. M., Scott, R. W. and **Oboh-Ikuenobe, F. E.** (2006) Base-Level Buffers and Buttresses: A Model for Upstream Versus Downstream Control on Fluvial Geometry and Architecture Within Sequences. *J. Sed. Res.*, **76**, 162–174.

Horwitz E.P., Chiarizia R., and **Dietz M.L.** (1992) A novel strontium-selective extraction chromatographic resin. *Solvent extraction and ion exchange*, **10**, 313–336.

Jin, J., Aigner, T., Luterbacher, H., Bachmann, G.H. and **Müller, M.** (1995) Sequence stratigraphy and depositional history in the south-eastern German Molasse Basin. *Mar. Petrol. Geol.*, **12,** 929-940.

Jin, Z., Yu, J., Wang, S., Zhang, F., Shi, Y. and **You, C.-F.** (2009) Constraints on water chemistry by chemical weathering in the Lake Qinghai catchment, northeastern Tibetan Plateau (China): clues from Sr and its isotopic geochemistry. *Hydrogeology Journal*, **17,** 2037-2048.

Köster, M.H., Hölzl, S. and **Gilg, H.A.** (2017) A strontium isotope and trace element geochemical study of dolomite-bearing bentonite deposits in Bavaria (Germany). *Clay Mineral.*, **52,** 161-190.

Kadolsky, D. (2008) Zur Identität und Synonymie der häufigeren „Hydrobien" der Rüssingen-Formation (Inflata-Schichten) und Wiesbaden-Formation (Hydrobien-Schichten) (Miozän, Mainzer Becken) (Gastropoda, Prosobranchia: Rissooidea). *Senckenbergiana lethaea*, **88**, 229-266.

Knetsch, G. (1963) *Geologie von Deutschland: und einigen Randgebieten*. Ferdinand Enke Verlag, Stuttgart, pp 386.

Koch, P.L., Zachos, J.C. and **Dettman, D.L.** (1995) Stable isotope stratigraphy and paleoclimatology of the Paleogene Bighorn Basin (Wyoming, USA). *Palaeogeogr. Palaeoclimatol. Palaeoecol.*, **115,** 61-89.

Kraus, M.J. (1987) Integration of channel and floodplain suites; II, Vertical relations of alluvial Paleosols. *J. Sed. Res.*, **57,** 602-612.

Kraus, M.J. and **Aslan, A.** (1993) Eocene hydromorphic Paleosols; significance for interpreting ancient floodplain processes. *J. Sed. Res.*, **63,** 453-463.

Krijgsman, M., Garcés, M., Langereis, C.G., Daams, R., van Dam, J., Meulen, A., van der Augustí, J. and **Cabrera, L.** (1996) A new chronology for the middle to late Miocene continental record in Spain. *Earth Planet. Sci. Lett.*, **142**, 367–380.

Kruiver, P.P., Krijgsman, W., Langereis, C.G. and **Dekkers, M.J.** (2002) Cyclostratigraphy and rock-magnetic investigation of the NRM signal in late Miocene palustrine-alluvial deposits of the Librilla section (SE Spain). *J. Geophys. Res.: Solid Earth*, **107,** EPM 3-1-EPM 3-18.

Krumbeck, L. (1926) Über neue und bekannte Tertiärvorkommen in Mittelfranken: Centralblatt für Mineralogie. *Geologie und Paläontologie, Abt. B*, **1926**, 33-43.

Krumbeck, L. (1927) Zur Kenntnis der alten Schotter des nordbayrischen Deckgebirges: ein Beitrag zur älteren Flußgeschichte Nordbayerns. *Geologische und Paläontologische Abhandlungen*, *Neue Folge*, **15,** 181-318.

Last, W.M., Teller, J.T. and **Forester, R.M.** (1994) Paleohydrology and paleochemistry of Lake Manitoba, Canada: the isotope and ostracode records. *Journal of Paleolimnology*, **12,** 269-282.

Leeder, M. (1975) Pedogenic carbonates and flood sediment accretion rates: a quantitative model for alluvial arid-zone lithofacies. *Geol. Mag.*, **112,** 257-270.

Leeder, M. and **Stewart, M.** (1996) Fluvial incision and sequence stratigraphy: alluvial responses to relative sea-level fall and their detection in the geological record. *Geological Society, London, Special Publications*, **103,** 25-39.

Lemcke, K. (1975) Molasse und vortertiärer Untergrund im Westteil des süddeutschen Alpenvorlandes. *Jahresberichte und Mitteilungen des Oberrheinischen Geologischen Vereins,* 87-115.

Lemcke, K. (1985) Flußfracht von Ur-Main und Ur-Naab in der Schweiz und im deutschen Molassebecken. *Bulletin der Vereinigung Schweizerischer Petroleum-Geologen und-Ingenieure*, **51,** 13-21.

Leng, M.J. and **Marshall, J.D.** (2004) Palaeoclimate interpretation of stable isotope data from lake sediment archives. *Quatern. Sci. Rev.*, **23,** 811-831.

Liu, C., Wang, Z. and **Raub, T.D.** (2013) Geochemical constraints on the origin of Marinoan cap dolostones from Nuccaleena Formation, South Australia. *Chem. Geol.*, **351,** 95-104.

Mack, G.H. and **James, W.** (1994) Paleoclimate and the global distribution of paleosols. *J. Geol.*, **102,** 360-366.

Manzo, E., Perri, E. and **Tucker, M.E** (2012) Carbonate deposition in a fluvial tufa system: processes and products (Corvino Valley – southern Italy). Sedimentology, **59**, 553–577.

Mayer, B. and **Schwark, L.** (1999) A 15,000-year stable isotope record from sediments of Lake Steisslingen, Southwest Germany. *Chem. Geol.*, **161,** 315-337.

Methner, K., Campani, M., Fiebig, J., Löffler, N., Kempf, O. and **Mulch, A.** (2020) Middle Miocene long-term continental temperature change in and out of pace with marine climate records. *Scientific Reports*, **10,** 7989.

Miall, A.D. (1985) Architectural-element analysis: A new method of facies analysis applied to fluvial deposits. *Earth-Sci. Rev.*, **22,** 261-308.

Miall, A.D. (1996) The geology of fluvial deposits: sedimentary facies, basin analysis, and petroleum geology. Springer.

Newell, A.J., Tverdokhlebov, V.P. and **Benton, M.J.** (1999) Interplay of tectonics and climate on a transverse fluvial system, Upper Permian, Southern Uralian Foreland Basin, Russia. *Sed. Geol.*, **127,** 11-29.

Olsen, P.E. (1986) A 40-million-year lake record of early Mesozoic orbital climatic forcing. *Science*, **234,** 842-848.

Opluštil, S., Lojka, R., Rosenau, N.A., Strnad, L. and **Sýkorová, I.** (2015) Middle Moscovian climate of eastern equatorial Pangea recorded in paleosols and fluvial architecture. *Palaeogeogr. Palaeoclimatol. Palaeoecol.*, **440,** 328-352.

Paul, J., Wemmer, K. and **Ahrendt, H.** (2008) Provenance of siliciclastic sediments (Permian to Jurassic) in the Central European Basin. *Zeitschrift der Deutschen Gesellschaft für Geowissenschaften*, **159,** 641-650.

Paul, J., Wemmer, K. and **Wetzel, F.** (2009) Keuper (Late Triassic) sediments in Germany– indicators of rapid uplift of Caledonian rocks in southern Norway. *Norwegian Journal of Geology/Norsk Geologisk Forening*, **89,** 193-202.

Perri, E., Manzo, E. and **Tucker, M.E.** (2012) Multi-scale study of the role of the biofilm in the formation of minerals and fabrics in calcareous tufa. *Sedimentary Geology*, **263-264**, 16-29.

Peterek, A. and **Schröder, B.** (2010) Geomorphologic evolution of the cuesta landscapes around the Northern Franconian Alb–review and synthesis. *Zeitschrift für Geomorphologie*, **54,** 305-345.

Pietzsch, R., Oliveira, D.M., Tedeschi, L.R., Queiroz Neto, J.V., Figueiredo, M.F., Vazquez, J.C. and **de Souza, R.S.** (2018) Palaeohydrology of the Lower Cretaceous pre-salt lacustrine system, from rift to post-rift phase, Santos Basin, Brazil. *Palaeogeogr. Palaeoclimatol. Palaeoecol.*, **507,** 60-80.

Pin, C. and **Bassin, C. (1992)** Evaluation of a strontium-specific extraction chromatographic method for isotopic analysis in geological materials. *Anal. Chim. Acta*, **269**, 249-255.

Pippèrr, M. and **Reichenbacher, B.** (2017) Late Early Miocene palaeoenvironmental changes in the North Alpine Foreland Basin. *Palaeogeogr. Palaeoclimatol. Palaeoecol.*, **468,** 485-502.

Pla-Pueyo, S., Gierlowski-Kordesch, E.H., Viseras, C. and **Soria, J.M.** (2009) Major controls on sedimentation during the evolution of a continental basin: Pliocene– Pleistocene of the Guadix Basin (Betic Cordillera, southern Spain). *Sed. Geol.*, **219,** 97-114.

Platt, N.H. and **Wright, V.P.** (1992) Palustrine carbonates and the Florida Everglades; towards an exposure index for the fresh-water environment? *J. Sed. Res.,* **62,** 1058-1071.

Pohl, J., Stoeffler, D., Gall, H.v. and **Ernstson, K.** (1977) The Ries impact crater. In: *Impact and explosion cratering: Planetary and terrestrial implications*, pp. 343-404.

Polissar, P.J., Freeman, K.H., Rowley, D.B., McInerney, F.A. and **Currie, B.S.** (2009) Paleoaltimetry of the Tibetan Plateau from D/H ratios of lipid biomarkers. *Earth Planet.*

Sci. Lett., **287,** 64-76.

Quade, J., Cerling, T.E. and **Bowman, J.R.** (1989) Systematic variations in the carbon and oxygen isotopic composition of pedogenic carbonate along elevation transects in the southern Great Basin, United States. *Geol. Soc. Am. Bull.*, **101,** 464-475.

Reading, H. G. (1996) *Sedimentary Environments: Processes, Facies and Stratigraphy, 3rd Edition*, 704 pp, Wiley-Blackwell.

Reck, H. (1912) Die morphologische Entwicklung der süddeutschen Schichtstufenlandschaft im Lichte der Davis' schen Cyclustheorie. *Zeitschrift der Deutschen Geologischen Gesellschaft*, 81-232.

Reichenbacher, B., Krijgsman, W., Lataster, Y., Pippèrr**, M., Van Baak, C.G., Chang, L., Kälin, D., Jost, J., Doppler, G.** and **Jung, D.** (2013) A new magnetostratigraphic framework for the lower Miocene (Burdigalian/Ottnangian, Karpatian) in the North Alpine Foreland Basin. *Swiss Journal of Geosciences*, **106,** 309-334.

Reuter, L. (1927) Geologische Darstellung des schwäbisch-fränkischen Juras, seines triadischen Vorlandes und des südlich angrenzenden Molasse-Gebietes. In: *Abriß der Geologie von Bayern r.d.Rh. in sechs Abteilungen, Abteilung IV* (Ed M. Schuster), pp. 166, Oldenbourg und Piloty & Loehle, Munich.

Rhodes, M.K., Carroll, A.R., Pietras, J.T., Beard, B.L. and **Johnson, C.M.** (2002) Strontium isotope record of paleohydrology and continental weathering, Eocene Green River Formation, Wyoming. *Geology*, **30,** 167-170.

Rocholl, A., Schaltegger, U., Gilg, H.A., Wijbrans, J. and **Böhme, M.** (2018a) The age of volcanic tuffs from the Upper Freshwater Molasse (North Alpine Foreland Basin) and their possible use for tephrostratigraphic correlations across Europe for the Middle Miocene. *Int J Earth Sci (Geol Rundsch)*, 107, 387-407.

Rocholl, A., Böhme, M., Gilg, H.A., Pohl, J., Schaltegger, U. and **Wijbrans, J.** (2018b) Comment on "A high-precision $^{40}Ar/^{39}Ar$ age for the Nördlinger Ries impact crater, Germany, and implications for the accurate dating of terrestrial impact events" by Schmieder et al.(Geochim. Cosmochim. Acta **220** (2018) 146–157). *Geochim. Cosmochim. Acta*, **238,** 599-601.

Rowley, D.B. and **Garzione, C.N.** (2007) Stable isotope-based paleoaltimetry. *Annu. Rev. Earth Planet. Sci.*, **35,** 463-508.

Ruf, M., Link, E., Pross, J. and **Aigner, T.** (2005) Integrated sequence stratigraphy: Facies, stable isotope and palynofacies analysis in a deeper epicontinental carbonate ramp (Late Jurassic, SW Germany). *Sed. Geol.*, **175**: 391-414.

Rust B.R. (1982) Sedimentation in fluvial and lacustrine environments. In: Sly P.G. (eds) Sediment/Freshwater Interaction. *Developments in Hydrobiology*, **9**, pp. 59-70, Springer, Dordrecht.

Sant, K., Kirscher, U., Reichenbacher, B., Pippèrr, M., Jung, D., Doppler, G. and **Krijgsman, W.** (2017) Late Burdigalian sea retreat from the North Alpine Foreland Basin: new magnetostratigraphic age constraints. *Global Planet. Change*, **152,** 38-50.

Schirmer, W. (2014) Moenodanuvius–Flussweg quer durch Franken. *Natur und Mensch, Jahresmitteilungen der Naturhistorischen Gesellschaft Nürnberg*, **2013,** 89-146.

Schmieder, M., Kennedy, T., Jourdan, F., Buchner, E. and **Reimold, W.U.** (2018a) A high-precision 40Ar/39Ar age for the Nördlinger Ries impact crater, Germany, and implications for the accurate dating of terrestrial impact events. *Geochim. Cosmochim. Acta*, **220,** 146-157.

Schmieder, M., Kennedy, T., Jourdan, F., Buchner, E. and **Reimold, W.U.** (2018b)

Response to comment on "A high-precision ^{40}Ar/^{39}Ar age for the Nördlinger Ries impact crater, Germany, and implications for the accurate dating of terrestrial impact events" by Schmieder et al. (Geochim. Cosmochim. Acta 220 (2018) 146–157). *Geochim. Cosmochim. Acta*, **238,** 602-605.

Schumm, S.A. (1985) Patterns of alluvial rivers. *Annu. Rev. Earth Planet. Sci.*, **13**, 5-27.

Schumm, S.A. (1993) River Response to Baselevel Change: Implications for Sequence Stratigraphy. *J. Geol.*, **101,** 279-294.

Selley, R. C. (1992). Ancient sedimentary environments and their sub-surface diagnosis. 3rd ed., repr. London: Chapman and Hall.**Semeniuk, V.** and **Meagher, T.D.** (1981) Calcrete in Quaternary coastal dunes in southwestern Australia; a capillary-rise phenomenon associated with plants. *J. Sed. Res.*, **51,** 47-68.

Sheldon, N.D. (2005) Do red beds indicate paleoclimatic conditions?: a Permian case study. *Palaeogeogr. Palaeoclimatol. Palaeoecol.*, **228,** 305-319.

Shoemaker, E.M. and **Chao, E.C.** (1961) New evidence for the impact origin of the Ries Basin, Bavaria, Germany. *J. Geophys. Res.*, **66,** 3371-3378.

Shukla, U., Bachmann, G., Beutler, G., Barnasch, J. and **Franz, M.** (2006) Extremely distal fluvial sandstone within the playa system of Arnstadt Formation (Norian, Late Triassic), Central Germany. *Facies*, **52,** 541-554.

Song, B., Zhang, K., Zhang, L., Ji, J., Hong, H., Wei, Y., Xu, Y., Algeo, T.J. and **Wang, C.** (2018) Qaidam Basin paleosols reflect climate and weathering intensity on the northeastern Tibetan Plateau during the Early Eocene Climatic Optimum. *Palaeogeogr. Palaeoclimatol. Palaeoecol.*, **512,** 6-22.

Staisch, L.M., Niemi, N.A., Hong, C., Clark, M.K., Rowley, D.B. and **Currie, B.** (2014) A Cretaceous-Eocene depositional age for the Fenghuoshan Group, Hoh Xil Basin: Implications for the tectonic evolution of the northern Tibet Plateau. *Tectonics*, **33,** 281-301.

Stevenson, F. (1969) Pedohumus: accumulation and diagenesis during the Quaternary. *Soil Sci.*, **107,** 470-479.

Sturm, S., Kenkmann, T., Willmes, M., Pösges, G. and **Hiesinger, H.** (2015) The distribution of megablocks in the Ries crater, Germany: Remote sensing, field investigation, and statistical analyses. *Meteoritics & Planetary Science*, **50,** 141-171.

Swart, P.K. (2015) The geochemistry of carbonate diagenesis: The past, present and future. *Sedimentology*, **62,** 1233-1304.

Tütken, T., Vennemann, T., Janz, H. and **Heizmann, E.** (2006) Palaeoenvironment and palaeoclimate of the Middle Miocene lake in the Steinheim basin, SW Germany: a reconstruction from C, O, and Sr isotopes of fossil remains. *Palaeogeogr. Palaeoclimatol. Palaeoecol.*, **241,** 457-491.

Talbot, M. and **Kelts, K.** (1986) Primary and diagenetic carbonates in the anoxic sediments of Lake Bosumtwi, Ghana. *Geology*, **14,** 912-916.

Talbot, M. (1990) A review of the palaeohydrological interpretation of carbon and oxygen isotopic ratios in primary lacustrine carbonates. *Chem. Geol.: Isotope Geoscience Section*, **80,** 261-279.

Tandon, S. and **Gibling, M.** (1994) Calcrete and coal in late Carboniferous cyclothems of Nova Scotia, Canada: Climate and sea-level changes linked. *Geology*, **22,** 755-758.

Tanner, L.H. (2010) Continental Carbonates as Indicators of Paleoclimate. In: *Dev. Sedimentol.* (Eds A.M. Alonso-Zarza and L.H. Tanner), **62**, pp. 179-214. Elsevier.

Thompson, J.B., Schultze-Lam, S., Beveridge, T.J. and Des Marais, D.J. (1997) Whiting

events: Biogenic origin due to the photosynthetic activity of cyanobacterial picoplankton. *Limnol. Oceanogr.*, **42,** 133-141.

Ufrecht, W. and **Hölzl, S.** (2006) Salinare Mineral-und Thermalwässer im Oberen Muschelkalk (Trias) im Großraum Stuttgart–Rückschlüsse auf Herkunft und Entstehung mit Hilfe der $^{87}Sr/^{86}Sr$-Strontium-Isotopie [Saline waters in the Upper Muschelkalk Aquifer (Triassic) in the area of Stuttgart-conclusions to origin and evolution by means of $^{87}Sr/^{86}Sr$-strontium isotopes]. *Zeitschrift der deutschen Gesellschaft für Geowissenschaften*, **157,** 299-315.

Utrilla, R., Vázquez, A. and **Anadón, P.** (1998) Paleohydrology of the Upper Miocene Bicorb Lake (eastern Spain) as inferred from stable isotopic data from inorganic carbonates. *Sed. Geol.*, **121,** 191-206.

Valero Garcés, B.L., Moreno, A., Navas, A., Mata, P., Machín, J., Delgado Huertas, A., González Sampériz, P., Schwalb, A., Morellón, M., Cheng, H. and **Edwards, R.L.** (2008) The Taravilla lake and tufa deposits (Central Iberian Range, Spain) as palaeohydrological and palaeoclimatic indicators. *Palaeogeogr. Palaeoclimatol. Palaeoecol.*, **259,** 136-156.

van Houten, F.B. (1973) Origin of Red Beds. A Review-1961-1972. *Annu. Rev. Earth Planet. Sci.*, **1,** 39-61.

Vázquez-Urbez, M., Arenas, C. and **Pardo, G.** (2012) A sedimentary facies model for stepped, fluvial tufa systems in the Iberian Range (Spain): the Quaternary Piedra and Mesa valleys. *Sedimentology*, **59,** 502-526.

Veizer, J. (1989) Strontium isotopes in seawater through time. *Palaeogeogr. Palaeoclimatol. Palaeoecol.*, **17,** 141-167.

Veizer, J., Ala, D., Azmy, K., Bruckschen, P., Buhl, D., Bruhn, F., Carden, G.A., Diener, A., Ebneth, S. and **Godderis, Y.** (1999) $^{87}Sr/^{86}Sr$, $\delta^{13}C$ and $\delta^{18}O$ evolution of Phanerozoic seawater. *Chem. Geol.*, **161,** 59-88.

von Horstig, G. (1952) Neue Graptolithen-Funde in gotlandischen Lyditen des Frankenwaldes und ihre Erhaltung in weißer Kieselsäure. *Senckenbergiana*, **33,** 345-352.

von Meyer, H. (1834) Die fossilien Zähne und Knochen und ihre Ablagerungen in der Gegend von Georgensgmünd in Bayern. *Frankfurt/Main,* pp. 1-122.

Wagner, G. (1923) Aus der Geschichte der Altmühl, Nürnberg, Fränkische Heimat-Schriften, Spindler, 116 pp.

Wagner, (1960) Einführung in die Erd-und Landschaftsgeschichte: mit besonderer Berücksichtigung Süddeutschlands, Ferdinand Rau, 622 + 176 pp.

Weiss, C., Höfling, R. and **Lorenz, H.G.** (2008) Die Fazies lakustriner und palustriner Karbonate aus dem Miozän von Langenaltheim/Südliche Frankenalb. *Jahresberichte und Mitteilungen des Oberrheinischen Geologischen Vereins*, **90,** 73-90.

Whiticar, M.J. (1999) Carbon and hydrogen isotope systematics of bacterial formation and oxidation of methane. *Chem. Geol.*, **161,** 291-314.

Wierzbowski, H., Anczkiewicz, R., Pawlak, J., Rogov, M.A. and **Kuznetsov, A.B.** (2017) Revised middle–upper Jurassic strontium isotope stratigraphy. *Chem. Geol.*, **466,** 239-255.

Wright, V.P. and **Marriott, S.B.** (1993) The sequence stratigraphy of fluvial depositional systems: the role of floodplain sediment storage. *Sed. Geol.*, **86,** 203-210.

Wright, V.P., Platt, N.H. and **Wimbledon, W.** (1988) Biogenic laminar calcretes: evidence of calcified root-mat horizons in paleosols. *Sedimentology*, **35,** 603-620.

Yan, Y., Zhou, J., He, Z., Sun, Q., Fei, J., Zhou, X., Zhao, K., Yang, L., Long, H. and **Zheng, H.** (2017) Evolution of Luyang Lake since the last 34,000 years: Climatic changes and anthropogenic impacts. *Quatern. Int.*, **440,** 90-98.

Zachos, J., Pagani, M., Sloan, L., Thomas, E. and **Billups, K.** (2001) Trends, rhythms, and aberrations in global climate 65 Ma to present. *Science*, **292,** 686-693.

Zieliński, M., Dopieralska, J., Belka, Z., Walczak, A., Siepak, M. and **Jakubowicz, M.** (2018) Strontium isotope identification of water mixing and recharge sources in a river system (Oder River, central Europe): A quantitative approach. *Hydrol. Process.*, **32,** 2597-2611.

Zweigel, J., Aigner, T. and **Luterbacher, H.** (1998) Eustatic versus tectonic controls on Alpine foreland basin fill: sequence stratigraphy and subsidence analysis in the SE German Molasse. *Geological Society, London, Special Publications*, **134,** 299.

Supplementary files (available online: https://doi.org/10.1111/sed.12888)

Fig. S1. Covariation plot of silicate content and ^{87}Sr/^{86}Sr of the carbonate samples (6N HCl) of the Miocene Georgensgmünd Formation. From LFT 4 to 9 there is a general increase in the carbonate content. However, neither the different LFTs, nor all LFTs taken together, show a correlation between silicate content and ^{87}Sr/^{86}Sr ratios, indicating that there is no significant contamination from silicate-derived Sr during sample preparation.

Table S1. Comparison of strontium isotope results of acetic acid and HCl treatments.

Table S2. Reference data for stable carbon and oxygen isotopes.

Chapter 6.   Summaries and conclusions

This thesis works in two parallel lines of direction by bridging 1) **sedimentology, paleolimnology and isotope geochemistry of terrestrial carbonate-bearing succession** and 2) **planetary science related to impact processes, particularly focusing on the post-impact stage**, towards the designated scientific questions.

1 Timeline of thesis working

The timeline of the working plan started with ***Chapter 5***, a side topic to investigate the only supposed impact ejecta-dammed lake on Earth (2018 to 2021, complete). The investigation of the volcanic ash layer (***Chapter 3***) was involved during the sampling of NR1003 drill core in 2018 and is also complete (published in 2021, complete). The major topics, i.e., hydrochemical and hydrological evolution of the Ries crater lake (***Chapter 2 and 4***), entail the extensive samples during the NR1003 sampling campaign. ***Chapter 2*** has been submitted on November 2021 and ***Chapter 4*** is now a prepared manuscript. The most important findings of the thesis work are outlined below, following the timeline.

2 Conclusions of Chapter 2

1) Considerable change in sulfate concentration exists along the chemical lake history of the Ries crater lake. Initial sulfate-rich lake water, attributed to the crystalline basement erosion, is followed by low-sulfate conditions by the erosion of sedimentary ejecta and constant sulfate-reduction in a closed-lake setting.
2) The formation of high $\delta^{13}C$ ferroan dolomite is closely related to the specific low sulfate condition, thereby granting extensive methanogenesis at the permanently stratified lake bottom.
3) Occurrences of high $\delta^{13}C$ dolomite terminate after a stepwise re-oxygenation of the lake, encompassing temporary subaerial exposure events and the onset of major aerobic methanotrophy.
4) Although short-term climate fluctuation might have been more significant than previously suggested, the changes in ejecta erosion and crater lake hydrology were the primary causes of the observed biogeochemical trend. The climate information expected by stable $\delta^{13}C$ and $\delta^{18}O$ of the lacustrine carbonate was largely obscured by the intrinsic crater lake processes.

3 Conclusions of Chapter 3

1) A diagenetically altered volcanic ash bed (clinoptilolite-heulandite-buddingtonite) exists in the Ries crater lacustrine deposits. This specific bed is traced back to the volcanic activities in 14.20 ± 0.08 Ma, 760 km away from the Pannonian Basin.
2) The basin-wide volcanic ash layer can be used as an excellent marker bed to trace the stratigraphic correlation between the marginal and central basin deposits.
3) Compaction alone cannot explain the deep bowl-shaped outline of the crater fill. Water-sediment loading and the closure of porosity, related to crater floor sagging during the post-impact lake evolution, are required to explain the geometry of this marker bed.

4 Conclusions of Chapter 4

1) $^{87}Sr/^{86}Sr$ trend from the leachates of the pre-impact target formations and lacustrine carbonates in the Ries crater convincingly supports the provenance change along the lake history. The initial lake stage is fed by influxes from crystalline basement and suevite, followed by the influxes largely from Bunte Breccia at the main lake stage, and finally to new lower/middle Jurassic waters.

2) An expanse in catchment and hydrological change are accompanied with the described influx provenance change. The early lake area is restricted within the inner ring and later expands towards the crater rim. The rise of base-level of the crater basin successively consumes available accommodation spaces by sedimentation filling. When the lower-order, regional base level remains constant, the catchment expanded outwards to seek and create new accommodation spaces for sedimentation.

3) The observed trend in sedimentary structures varies from intensive to weak soft sediment deformation, then to bioturbation and subaerial exposure, and finally pedogenesis. It supports the interpretation that intrinsic crater processes dominate the hydrological change. This trend reflects a) decreasing initial deep evaporation and rise of groundwater level due to the cooling-down of the early, hot crater floor; b) decreasing groundwater discharge to the lake due to the closure of mega-porosity and sealing groundwater pathways, indicating increasing crater floor stability by sagging and sediment loading.

4) While the hydrochemical evolution of the impact crater lakes follows the successive erosion of impact ejecta formations, their hydrological evolution shows a unique recovery towards the pre-impact hydrology and does not necessarily require a change in climate.

5 Conclusions of Chapter 5

1) No sedimentological evidence supports the impact ejecta-damming and lacustrine deposits, from the supposed "Rezat-Altmühl-Lake". Instead, lithofacies, sedimentary structures as well as stable oxygen and carbon isotopes point to a low-gradient river system with extensive floodplain setting behind these deposits, consistent with the suggested pre-impact age of the Georgensgmünd Formation.

2) The deposits reflect low energy bed-loaded process and pedogenesis, triggered by the autogenic fluvial cycles under a nearly constant climate condition.

3) The unidirectional $^{87}Sr/^{86}Sr$ increase in the carbonates and the pebble provenances indicate the change in lithofacies and carbonate contents are related to a local base level rise.

4) In the area where limited outcrops or relic deposits largely bewildering the sedimentary architecture, a combination of indicative facies criteria, component provenance, and stable and radiogenic isotopes facilitates the discernment between lacustrine and fluvial sediments, as well as disentangles regional geological effects in the catchment and climate influences.

6 A final summary

Sedimentary filling in impact crater basins, particularly crater lakes offers valuable opening to understand the how intrinsic and extrinsic changes . Indeed, a number of researches show that the impact crater fillings might have recorded some remarkable geological events, especially related to climate changes. For instance, 1) the lacustrine deposits of crater Lake El'gygytgyn provides a continuous, high-resolution global climate records from Pliocene to Quaternary (Melles et al., 2003); 2) the lacustrine deposits of Boltysh crater preserves a complete record of increasingly warming event (Dan-C2 hyperthermal event) intercalated between the above and below deposits reflecting a cooler and wetter climate (Gilmour et al., 2013).

It is not surprising that the impact basin fillings contain information of drastic past environmental changes, as the asteroid impacts themselves are destructive and catastrophic events (e.g. the Chicxulub Impact event, Pope et al., 1997). However, to trigger a significant climate change via the impact-released dust and soot into atmosphere, an impact energy ≥ est. 3 x 107 Mt TNT (associated with terrestrial impact craters with final diameters ≥ 100 km) is essentially required (Rampino, 2020). Smaller-sized impact craters up 80 km in diameter are known not fatal enough to be associated with extinction events so far (Rampino, 2020). Recent studies also show that the recovery of ecological system after the impact devastation is fairly fast (e.g. Lowery et al., 2018; Schaefer et al., 2020). Behind this ecological comeback, the crucial hydrological and hydrochemical processes essential to aquatic organisms, are poorly understood. On the other hand, a better understanding for

hydrological processes greatly provides insights for the current discussions on Martian crater deposits (see ***Chapter 1***).

The unique Ries impact structure and its lacustrine fillings demonstrate that a close association with climate change may exist but not necessarily crucial for post-impact limnological evolution of the mid-sized impact craters, many of which on Earth and on exoplanets. The crater lake evolution on other water-saturated target areas may also share similar hydrological evolution, characterized by an early groundwater upwelling, followed by basement sagging, increasing crater floor stability and closure of mega-porosities, towards the readjustment of groundwater table and recovery of hydrology (***Chapter 3 and Chapter 4***). At a layered target area, hydrochemically distinct solutions are eroded from the pre-processed ejecta formations (Arp et al., 2019) and introduced to feed the lake, resulting in discernible chemical lake stages (Arp et al., 2013). On top of chemical lake variations, environmental selection on the preferred organisms as well as biogeochemical processes might occur, especially for the microorganisms (***Chapter 2***). Climate change might pose impact on these changes, only in the senses of scale and rate, however, less critical for the final trends (***Chapter 4***). Post-impact hydrological and hydrochemical processes inside the mid-sized impact craters thereby are largely intrinsic, controlled by the unique, internal crater tectonics interacting with limnological processes. Emphasis on discerning climate change and intrinsic processes is thereby important for other analogous crater lakes. For example, the interpretation of evaporation facies needs to be carefully considered, since not all of them may reflect a warm and arid climate (***Chapter 4***).

References

Arp, G., Blumenberg, M., Hansen, B.T., Jung, D., Kolepka, C., Lenz, O., Nolte, N., Poschlod, K., Reimer, A. and Thiel, V. (2013) Chemical and ecological evolution of the Miocene Ries impact crater lake, Germany: A reinterpretation based on the Enkingen (SUBO 18) drill core. GSA Bulletin 125, 1125-1145.

Arp, G., Schultz, S., Karius, V. and Head, J.W. (2019) Ries impact crater sedimentary conglomerates: Sedimentary particle 'impact pre-processing', transport distances and provenance, and implications for Gale crater conglomerates, Mars. Icarus 321, 531-549.

Gilmour, I., Gilmour, M., Jolley, D., Kelley, S., Kemp, D., Daly, R. and Watson, J. (2013) A high-resolution nonmarine record of an early Danian hyperthermal event, Boltysh crater, Ukraine. Geology 41, 783-786.

Lowery, C.M., Bralower, T.J., Owens, J.D., Rodríguez-Tovar, F.J., Jones, H., Smit, J., Whalen, M.T., Claeys, P., Farley, K., Gulick, S.P.S., Morgan, J.V., Green, S., Chenot, E., Christeson, G.L., Cockell, C.S., Coolen, M.J.L., Ferrière, L., Gebhardt, C., Goto, K., Kring, D.A., Lofi, J., Ocampo-Torres, R., Perez-Cruz, L., Pickersgill, A.E., Poelchau, M.H., Rae, A.S.P., Rasmussen, C., Rebolledo-Vieyra, M., Riller, U., Sato, H., Tikoo, S.M., Tomioka, N., Urrutia-Fucugauchi, J., Vellekoop, J., Wittmann, A., Xiao, L., Yamaguchi, K.E. and Zylberman, W. (2018) Rapid recovery of life at ground zero of the end-Cretaceous mass extinction. Nature 558, 288-291.

Melles, M., Brigham-Grette, J., Minyuk Pavel, S., Nowaczyk Norbert, R., Wennrich, V., DeConto Robert, M., Anderson Patricia, M., Andreev Andrei, A., Coletti, A., Cook Timothy, L., Haltia-Hovi, E., Kukkonen, M., Lozhkin Anatoli, V., Rosén, P., Tarasov, P., Vogel, H. and Wagner, B. (2012) 2.8 Million Years of Arctic Climate Change from Lake El'gygytgyn, NE Russia. Science 337, 315-320.

Pope, K. O., Baines, K. H., Ocampo, A. C., and Ivanov, B. A. (1997) Energy, volatile production, and climatic effects of the Chicxulub Cretaceous/Tertiary impact. Journal Geophysical Research, 102(E9), 21645– 21664.

Rampino, M.R. (2020) Relationship between impact-crater size and severity of related extinction episodes. Earth-Science Reviews 201, 102990.

Schaefer, B., Grice, K., Coolen, M.J.L., Summons, R.E., Cui, X., Bauersachs, T., Schwark, L., Böttcher, M.E., Bralower, T.J., Lyons, S.L., Freeman, K.H., Cockell, C.S., Gulick, S.P.S., Morgan, J.V., Whalen, M.T., Lowery, C.M. and Vajda, V. (2020) Microbial life in the nascent Chicxulub crater. Geology 48, 328-332.

Appendix A

Supplementary Figures
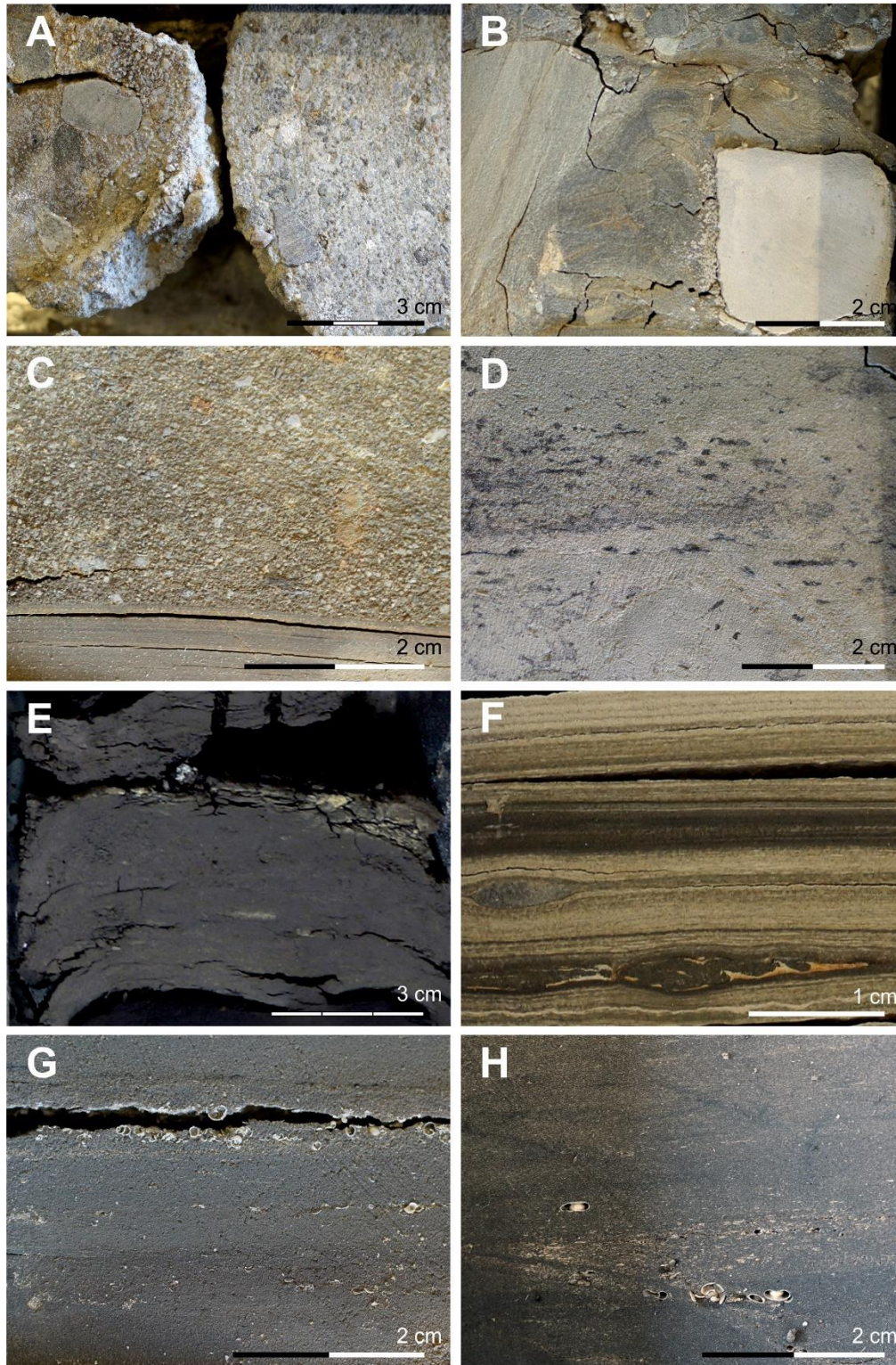
Figure A.1 Different lithofacies and fabrics from the drill core NR 1003.

Conglomerate and coarse-grained pebbly sandstone in basal member (242.0 to 242.8 m depth), containing pebbles reworked from the crystalline basement rock of the inner ring. B: Matrix-supported breccia in laminated member (98.5 to 99.3 m depth), at left side is a reworked laminite clast; at the right is a reworked unstratified marl/dolomitic marl clast. C: yellowish medium to coarse-grained lithic sandstone intercalated in laminated member (224 to 225 m depth) and laminated claystone at the base. D: olive-white grey calcareous fine-grained sandstone to siltstone containing carbonaceous debris in basal member (245.5 to 246 m depth). E: dark grey to black stratified (foliated) lignite with sulphur from oxidation. F: laminated dolomite and bituminous shale with remnants of fish scale in laminated member (217.6 to 218.6 m depth). G. Hydrobia trocholus and/or ostracod shell debris from clay member (38.4 m depth). F. Gyraulus and/or shell debris from clay member (30.26 m depth).
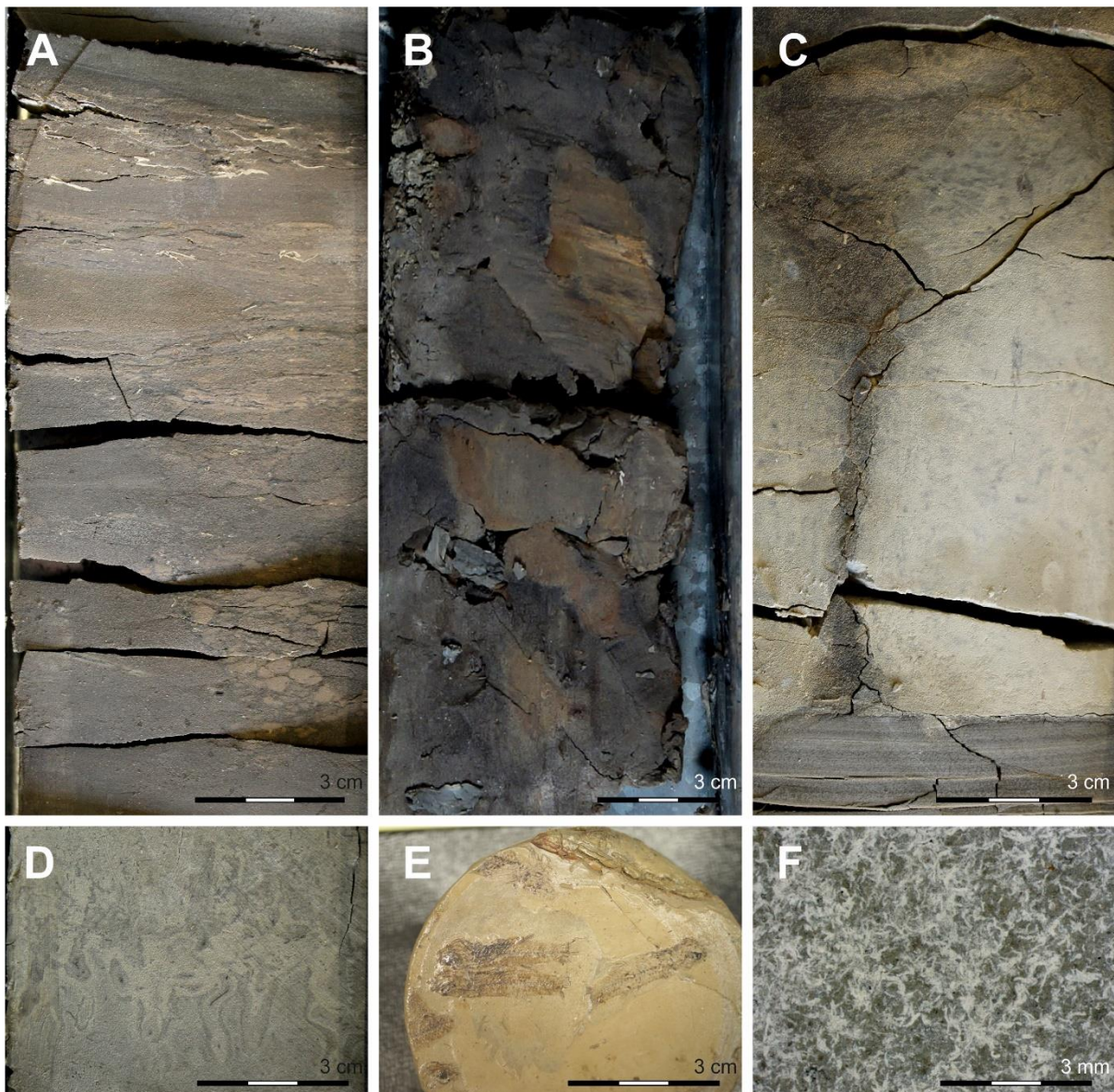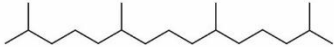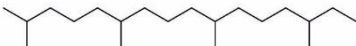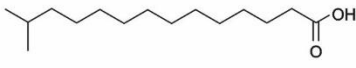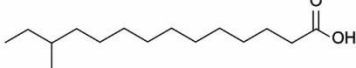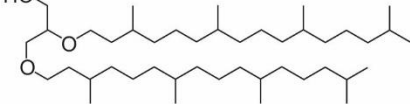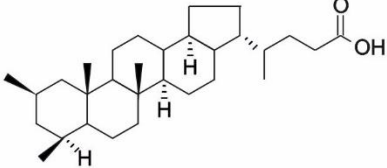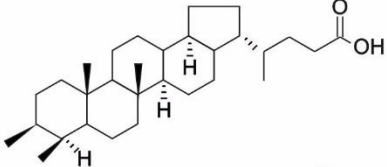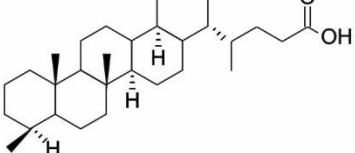
Figure A.2 Different lithographic fabrics from drill core NR 1003.
A: compressed shell debris of *Planorbarius* at the top and desiccation crack with in-situ brecciation at the base (clay member, 32.0 to 32.1 m depth). B: Pedoturbation/pedogenic slickenside in the dark grey and ochre-brown mottling carbonaceous claystone (clay member, 22.0 to 22.2 m depth). C: Sand dike structure

injected from the lower laminated clay and marl into the overlying white grey massive bioturbated argillaceous marl (marl member, 76.6 m depth). D: worm-like bioturbation in the marl member (39.7 to 40.5 m depth). E: well-preserved fish scale from laminated member (diatom subunit, 106 m depth). F: *Artemia* faecal pellets from laminated member (clinoptilolite subunit, 216.6 m depth).

Compound	Structure	Typical fragments (m/z)
Pristane(Pr)		57, 71,183
Phytane(Ph)		57, 71,183,197
13-Methyltetradecanoic acid (i-$C_{15:0}$)		74, 57, 213
12-Methyltetradecanoic acid (ai-$C_{15:0}$)		74, 57, 199
Archaeol		130, 131, 278, 426
3-methyl-C_{32} 17β(H)21β(H)-hopanoic acid (3-me-C_{32}ββ -HA)		205, 217, 263
2-methyl-C_{32} 17β(H)21β(H)-bishomohopanoic acid (2-me-C_{32}ββ-HA)		205, 217, 263
C_{32} 17β(H)21β(H)-hopanoic acid (C_{32}HA)		191, 217, 263

Figure A.3 Structures of the selected organic compounds detected from the NR1003 drill core.
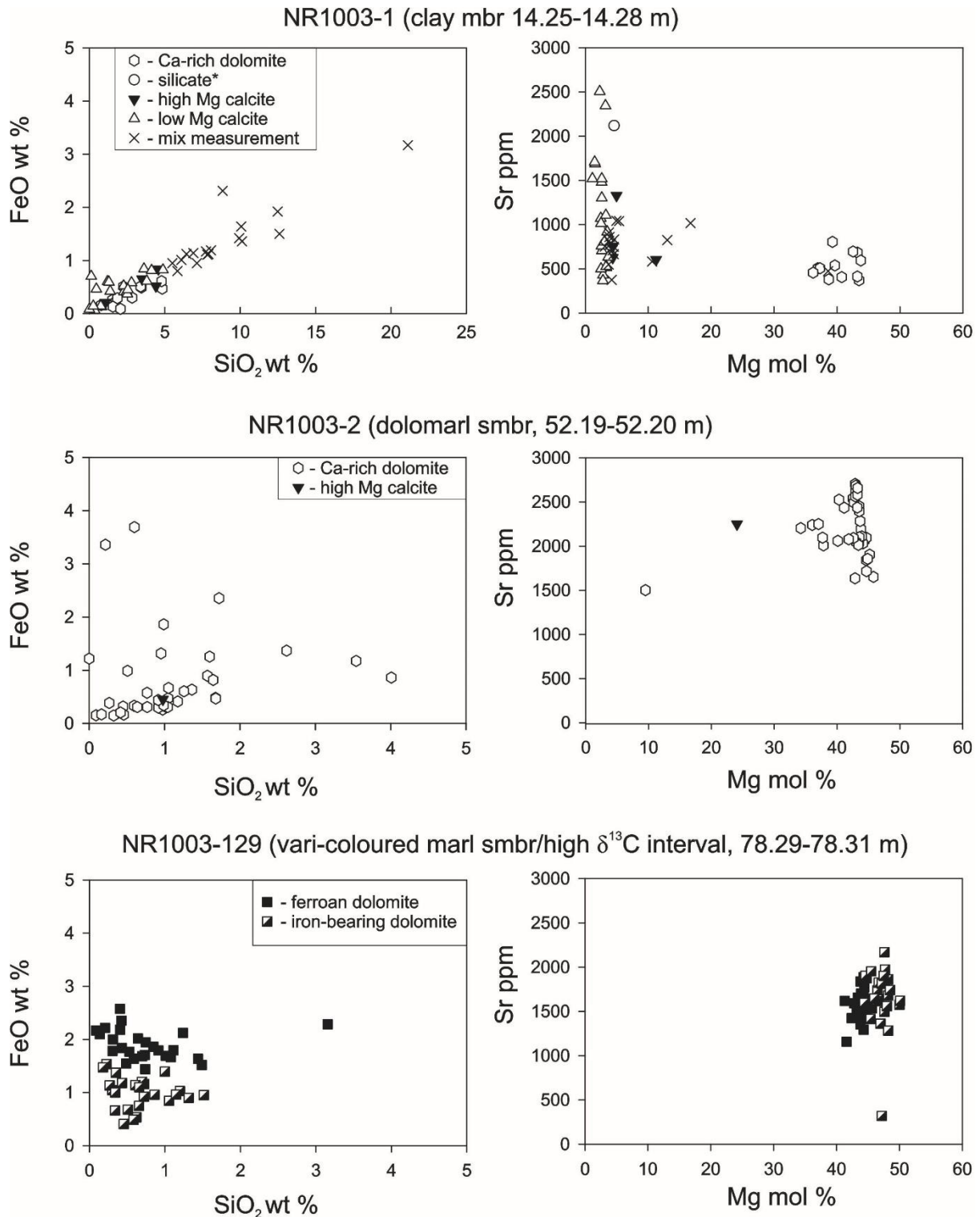
Figure A.4 FeO-SiO₂ and Sr(ppm)-Mg(mol%) correlations of the selected samples from NR1003 drill core (continued in Figure A.5) by electron microprobe analysis. When Fe and Mn do not show any correlation with Si, Fe and Mn are considered as incorporated into the carbonate lattice. Note that different carbonate phases are nicely separated into different zones in Sr(ppm)-Mg(mol%) plots.
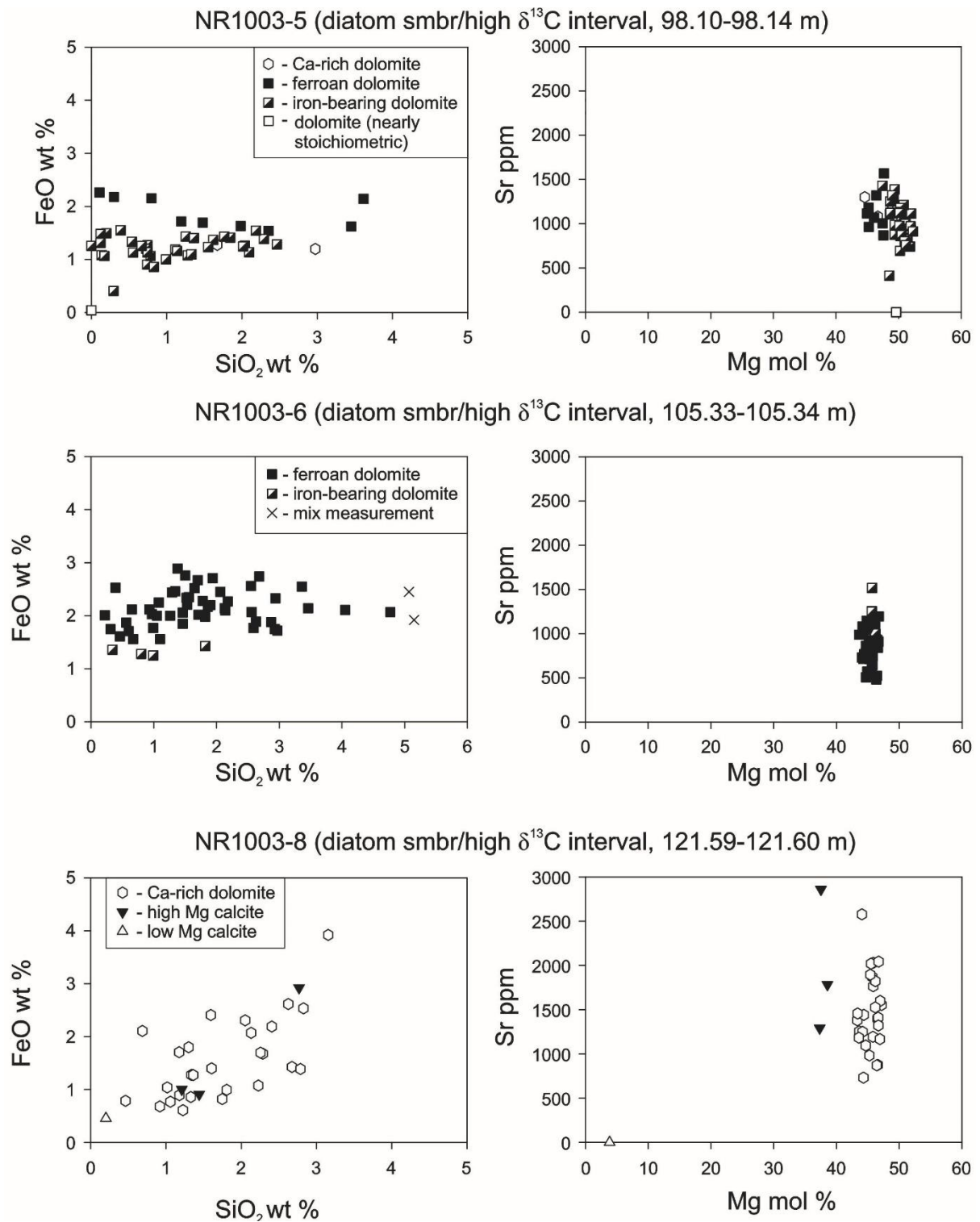
Figure A.5 FeO-SiO₂ and Sr(ppm)-Mg(mol%) correlations of the selected samples from NR1003 drill core by electron microprobe analysis (continued in Figure A.6).
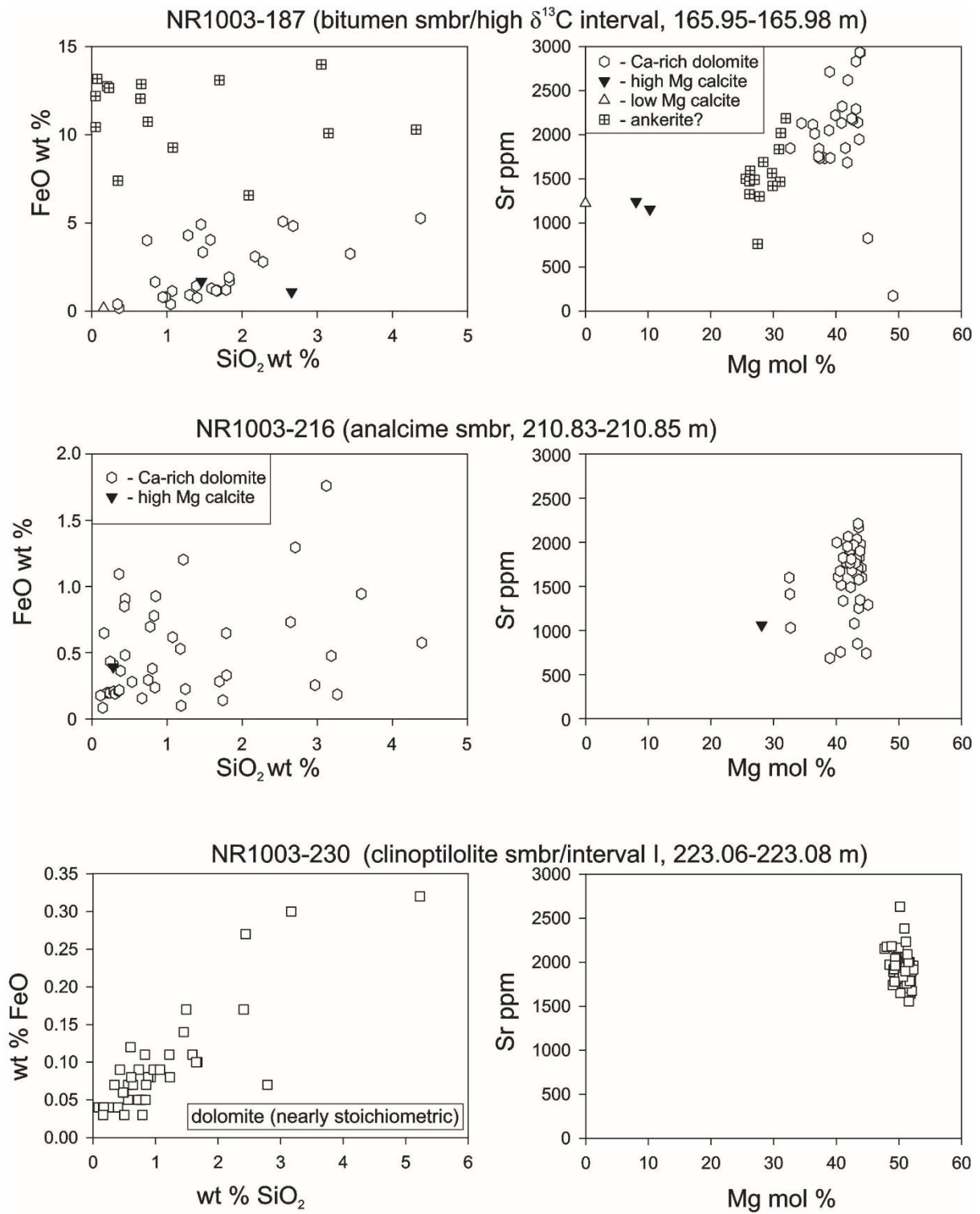
Figure A.6 FeO-SiO₂ and Sr(ppm)-Mg(mol%) correlations of the selected samples from NR1003 drill core by electron microprobe analysis.
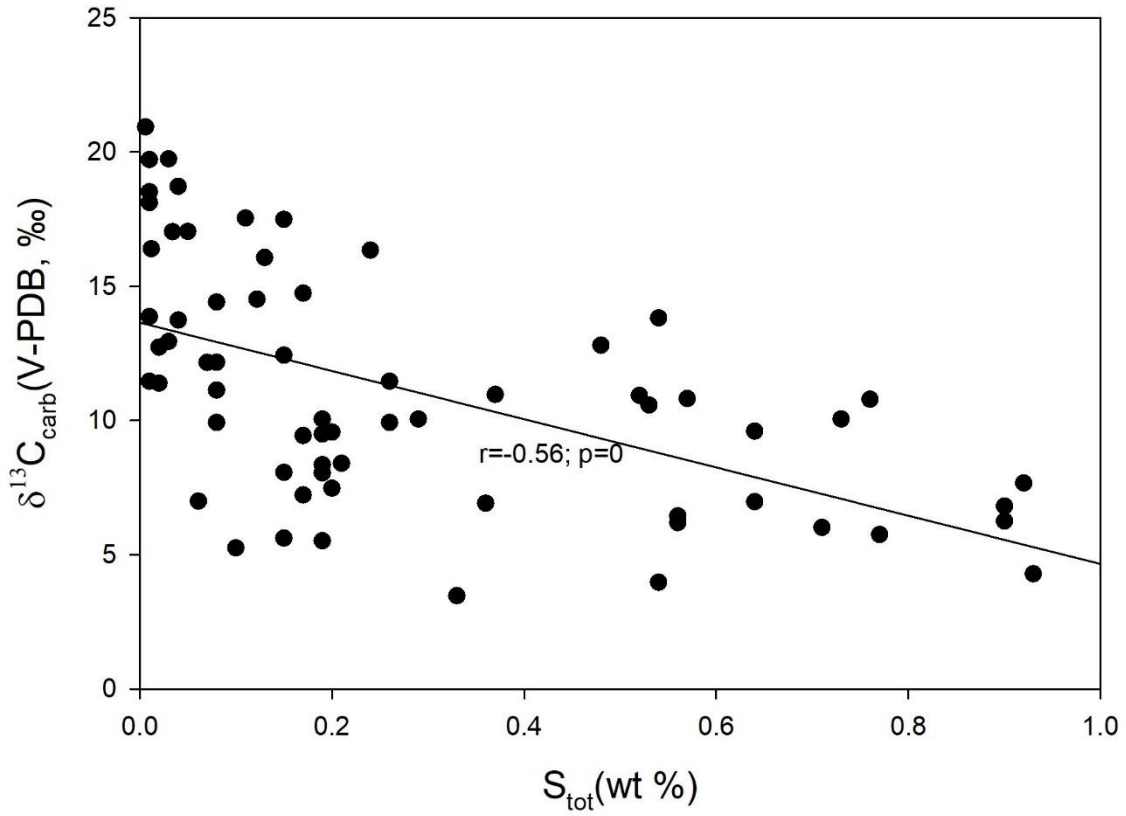
Figure A.7 Correlation plot between S$_{tot}$ and δ^{13}C of samples from the high δ^{13}C interval
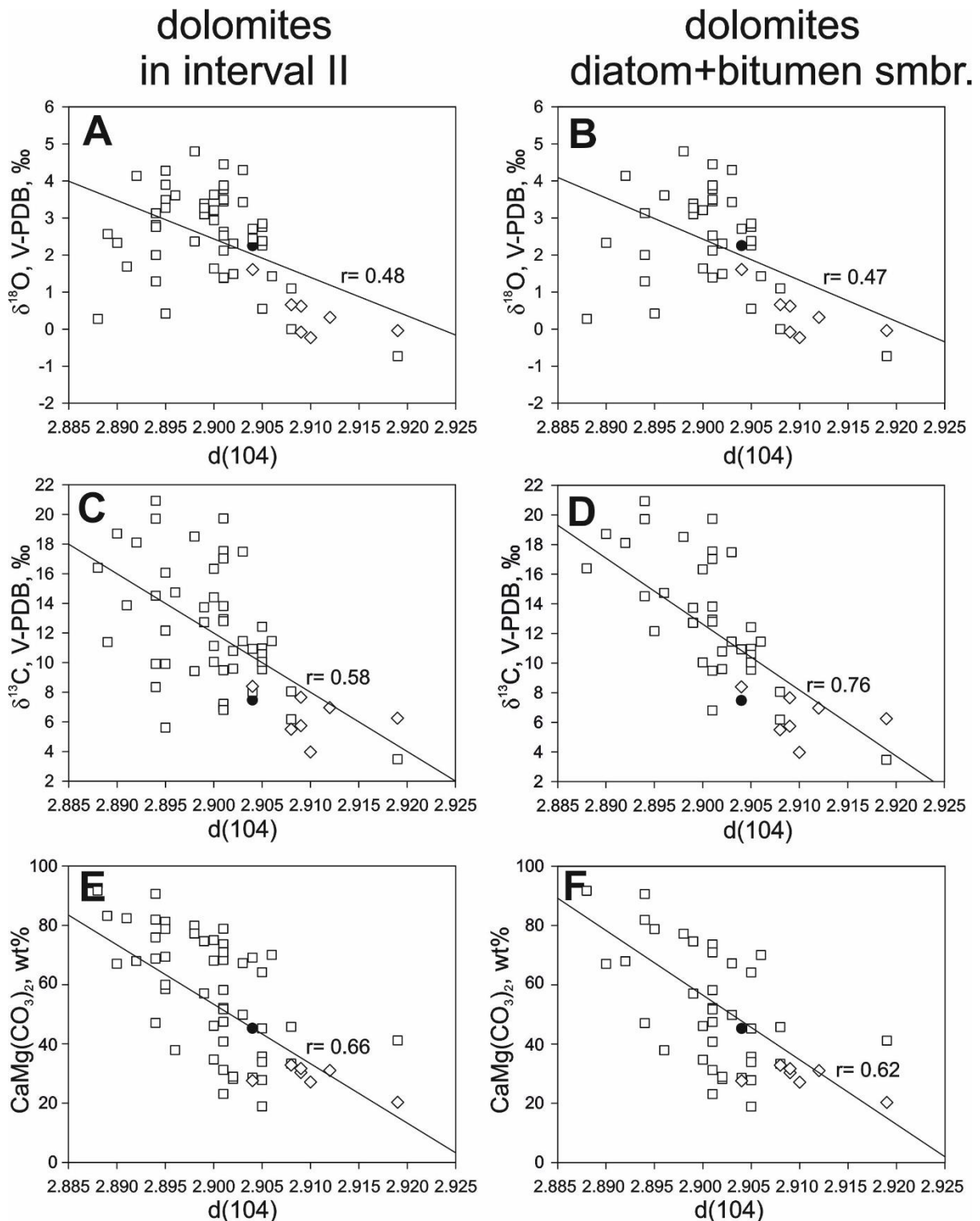
Figure A.8 Correlation plots between δ¹³C, δ¹⁸O, CaCO₃, d_{104} values and bulk iron contents (micro XRF) in dolomite and dolomite-rich samples from the high δ¹³C interval and from only diatom submember (continued in Figure A.9).
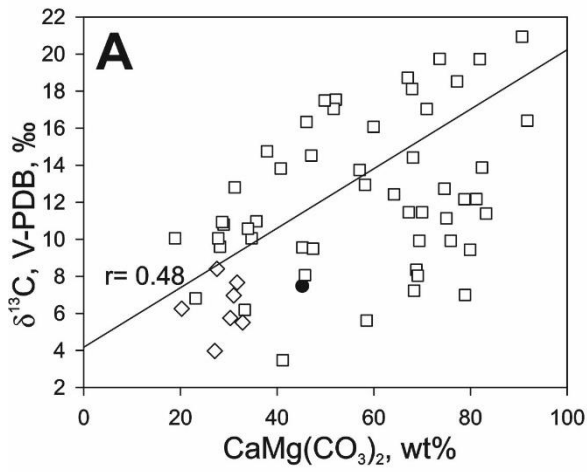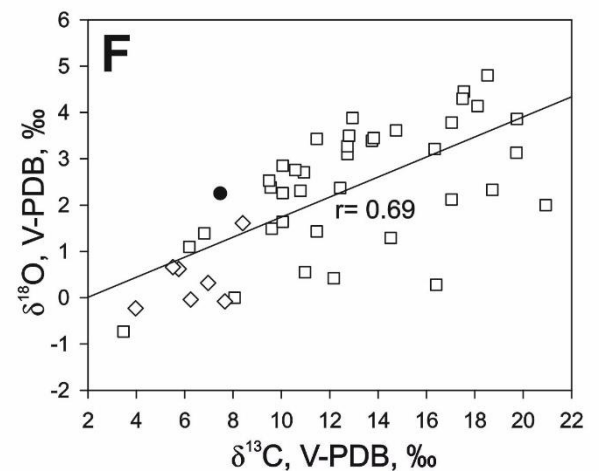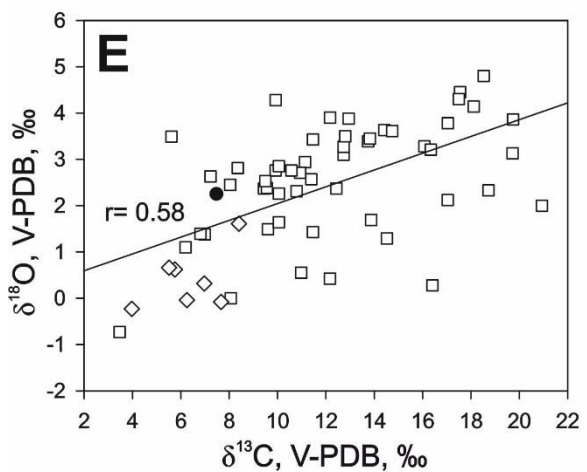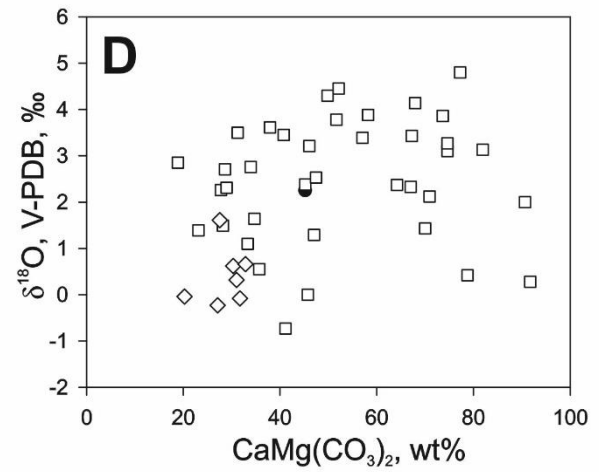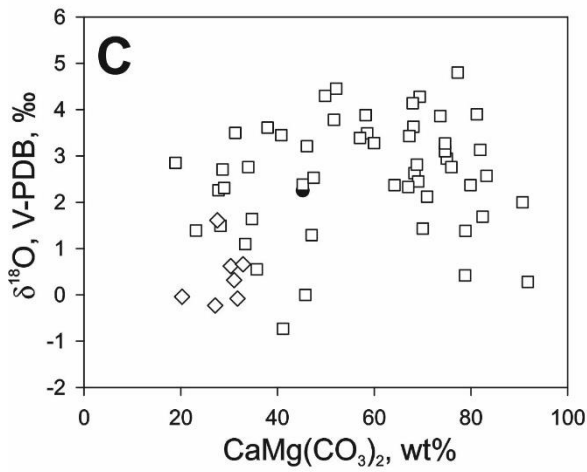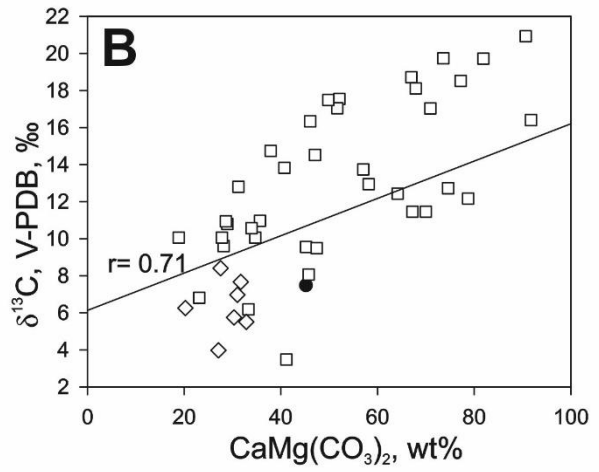
Figure A.9 Correlation plots between δ¹³C, δ¹⁸O, CaCO₃, d_{104} values in dolomite and dolomite-rich samples from the high δ¹³C interval and from only diatom submember.
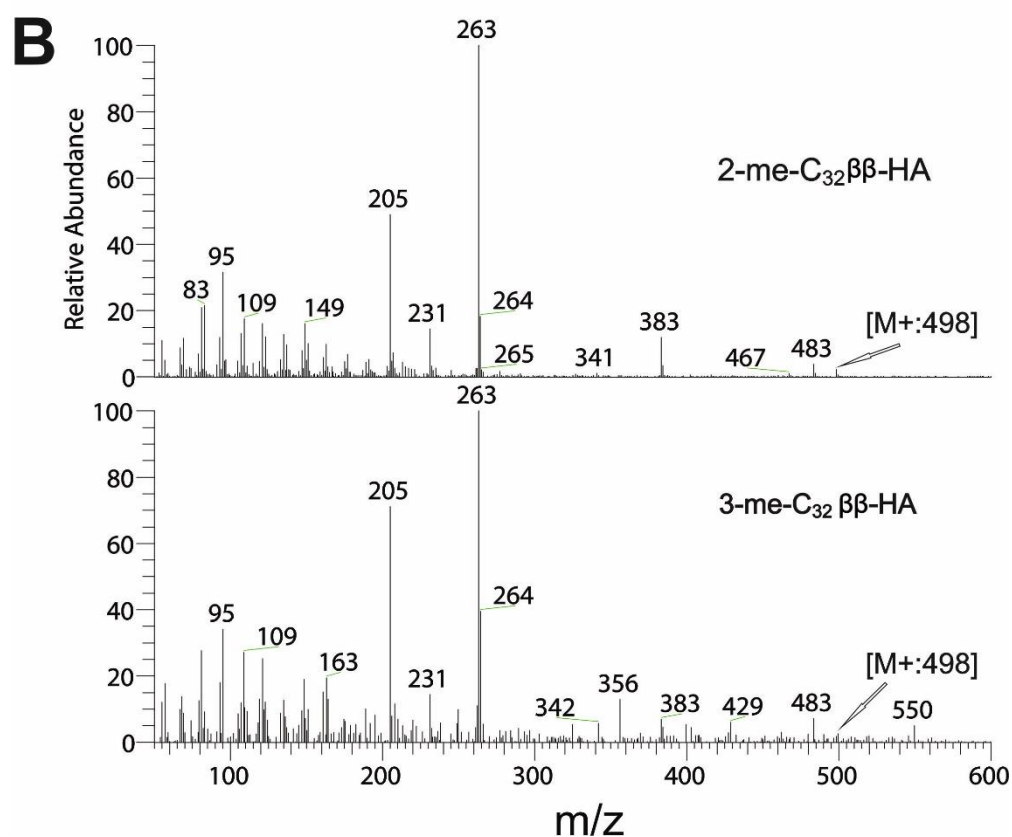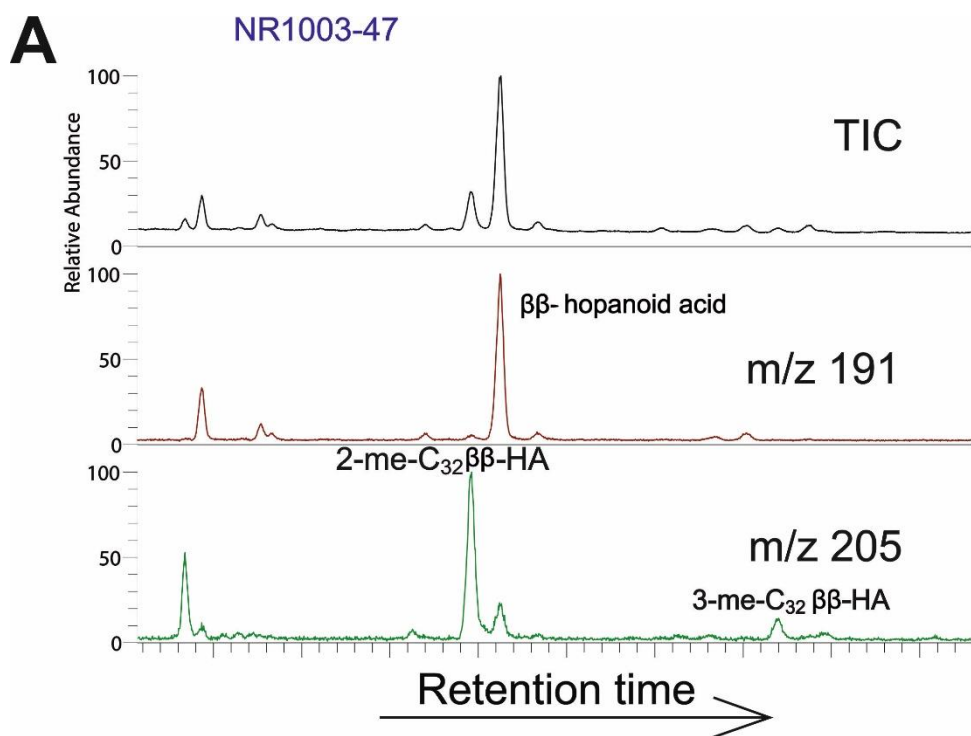
Figure A.10 Total ion current diagram, mass fraction diagram 191/205 and mass spectra diagram of the methylated hopanoids.
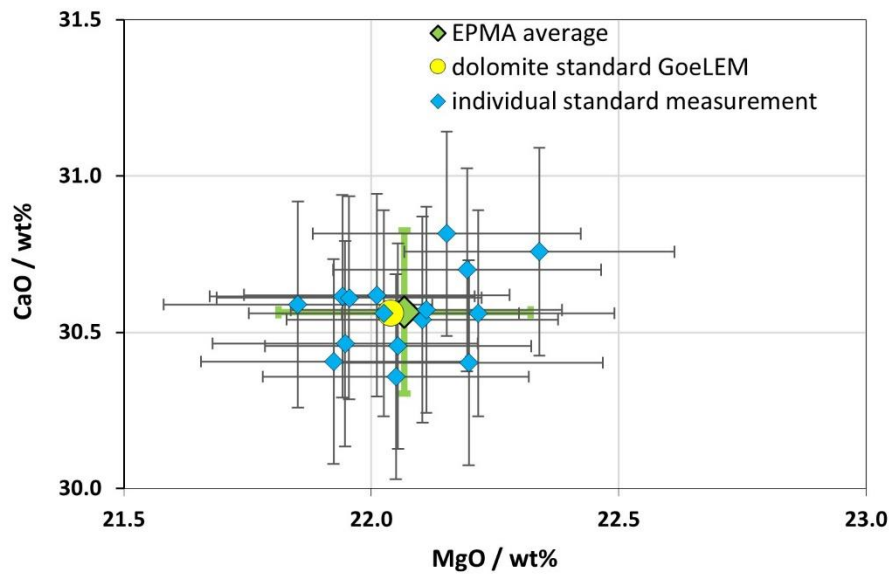
Figure A.11 Calibration of the dolomite standard during EMPA measurement and the reported results for Ca and Mg.
2SD of the standard measurements is shown as the whole error bar. The yellow point represents claimed values for the dolomite standard in the lab. The green, average standard result is in agreement with the claimed standard values.

Supplementary Tables

Table A.1 Overview of NR1003 drilling: location, performing date and lithostratigraphic member division after Jankowski (1981).

Drilling Nördlingen 1003 (NR 1003)

location:	topographic map #7029	Oettingen i.Bay.
	coordinates	r 4392810
		h 5421500
	height	429 m a.s.l.
	date	1981

end depth [m]	lithostratigraphy member	start depth [m]	lithostratigraphy submember / informal short description
-38.7	clay member	0	heterogenic in colors and lithologies but mostly dark-grey clayish, with allochthonous lignite seams, common bioturbation and mudcracks
-87.3	marl member	-73.6	dolomite-marl smbr, unstratified marl with common bioturbation and mudcracks
		-87.3	varicoloured marl smbr, laminites with occasionally intercalated, unstratified marl and horizons of bioturbation or subaerial exposure
-226.05	laminite member	-124	diatom smbr, laminites with abundantly preserved diatoms
		-169.5	bitumeninous smbr, laminites with high organic contents
		-215	analcime smbr, laminites with low carbonate and abundant analcime contents
		-226	clinoptilolite smbr, laminites with clinoptilolites
-257.0 (end core)	basal member	-242.4	cyclic, mud-rich conglomerates and sandstones, laminated carbonates with mud cracks and "water/gas escape structures"
		-245	laminated carbonates with mud cracks and brecciation
		>245	re-sedimented suevite

Table A.2 Short drill core description, sampling of carbonate beds and their corresponding carbonate contents (calculated as CaCO$_3$, see Table A.4).

sample	CaCO$_3$ [wt%]	depth [m]	lithological description
		-4.0	Quaternary cover
		-14.0	greenish-grey clay (cuttings)
Noe 1003-12	4.7	-14.2	greenish-grey slightly calcareous clay, poorly bedded, minor bioturbation; sharp lower contact
Noe 1003-13	87.1	-14.44	white-grey argillaceous limestone, massive, slightly mottled; lower part laminated; gradual lower contact
Noe 1003-14	8.5	-14.47	greenish-grey slightly calcareous clay, poorly bedded; sharp lower contact
Noe 1003-15	89.3	-14.58	white-grey argillaceous limestone, massive, slightly mottled, vertical traces of brecciation; sharp lower contact
Noe 1003-16	4.5	-14.83	dark-grey slightly calcareous clay, poorly bedded, few transparent ostracod valves; unknown lower contact due to core loss
		-15	core loss
Noe 1003-17	1.7	-15.15	dark-grey slightly clay, poorly bedded, gradual lower contact;
Noe 1003-18	41.2	-15.65	white-grey marl, massive, scattered ostracods and peloids; gradual lower contact
Noe 1003-19	3.9	-15.85	medium to dark grey clay, massive; gradual lower contact
Noe 1003-20	83.1	-15.90	white-grey argillaceous limestone, poorly bedded, minor ostracod shell debris; sharp lower contact
Noe 1003-21	48.2	-16.0	medium-grey marl, massive, with iron sulfide nodules
Noe 1003-22	14.1	-16.4	medium-grey calcareous clay, massive, with iron sulfide nodules; gradual lower contact
Noe 1003-23	73.4	-16.5	white-grey calcareous marl, massive, possible ostracods valves; sharp lower contact
Noe 1003-24	22.6	-16.9	dark-grey calcareous clay, poorly bedded, with ostracod shell debris and iron sulfide nodules; gradual lower contact
Noe 1003-25	0	-17.0	black carbonaceous clay to lignite, foliated, strongly sulfidic, with sulfur efflorescence
Noe 1003-26	0	-17.75	black lignite, foliated, strongly sulfidic, with sulfur efflorescence; gradual lower contact
Noe 1003-27	0.4	-18.0	dark-grey, at the top carbonaceous, clay, poorly bedded;
Noe 1003-28	13.7	18.7	medium-grey clay, bedded, with mm-sized carbonaceous plant debris, ostracod valves, peloids, and white-grey micrite intraclasts up to 5 mm size;
		-20.0	core loss
Noe 1003-29	9.8	-20.2	dark-grey slightly calcareous clay, bedded, with iron sulfides; gradual lower contact
Noe 1003-30	19	-20.4	light-grey calcareous clay, massive, with white-grey peloids; gradual lower contact
Noe 1003-31	11.1	-21.0	medium-grey calcareous clay, poorly bedded (bottom) to massive (top), with white-grey peloids;

		-22.0	core loss
Noe 1003-32	10.3	-22.8	medium-grey calcareous clay, massive, with iron sulfides and white-grey carbonate grains; gradual lower contact
Noe 1003-33	37.3	-22.83	light-grey marl, massive, with white-grey carbonate grains; gradual lower contact
Noe 1003-34	5.4	-22.9	medium-grey slightly calcareous clay, massive;
		-23.0	core loss
Noe 1003-35	21.7	-23.2	medium-grey calcareous clay, poorly bedded, with white-grey carbonate grains; gradual lower contact
Noe 1003-36	84.7	-23.7	white-grey argillaceous limestone, poorly bedded (bottom) to massive (top); sharp lower contact
Noe 1003-37	4.9	-24.0	dark-grey slightly calcareous clay, stratified; gradual lower contact
Noe 1003-38	15.3	-25.0	medium-grey calcareous clay, with sulfide nodules, poorly bedded; minor sulfur efflorescence; sharp lower contact
Noe 1003-39	20.2	-26.0	greenish-grey calcareous clay, laminated, iron sulfide nodules and carbonaceous plant debris; gradual lower contact
Noe 1003-40	9.9	-27.0	grey and greenish-grey slightly calcareous clay (desintegrated from drilling), some white-grey laminated marl fragments and carbonaceous plant debris; unclear lower contact
		-28.5	core loss
Noe 1003-41	3.3	-29.0	grey and greenish-grey slightly calcareous clay (desintegrated from drilling), some white-grey laminated marl fragments and carbonaceous plant debris; sharp lower contact
Noe 1003-42	4.8	-29.45	medium-grey slightly calcareous clay; no stratification evident; gradual lower contact
Noe 1003-43	0	-29.95	black lignite, strongly sulfidic, with sulfur efflorescence; wood remains; gradual lower contact
Noe 1003-44	0	-30.0	black lignite, foliated, sulfidic, composed of carbonaceous plant debris; sharp lower contact
Noe 1003-45	64.8	-30.05	medium-grey marlstone, stratified; compacted dewatering structures; sharp lower contact;
Noe 1003-46	0	-30.2	medium-grey clay, poorly bedded, with signs of pedoturbated slickensides; gradual lower contact
Noe 1003-47	52.4	-30.38	medium-grey marl, laminated, with gastropod (*Gyraulus*) shell layers at 1, 3 and 5 cm below top
Noe 1003-48	16	-31.0	dark-grey calcareous carbonaceous clay to lignite, laminated, sulfidic, with sulfur efflorescence
Noe 1003-49	21.5	-31.07	medium-grey calcareous clay, laminated, with microfaults; sharp lower contact;
Noe 1003-50	0.4	-31.08	medium-grey clay, laminated; sharp lower contact;
Noe 1003-51	41.7	-31.25	medium to dark-grey marl, laminated, with carbonaceous plant debris; gradual lower contact;
Noe 1003-52	0	-31.3	medium-grey clay, mottled, with microbrecciation;
Noe 1003-53	1.3	-31.6	black carbonaceous clay to lignite, foliated, strongly sulfidic, with sulfur efflorescence
Noe 1003-54	0	-31.88	black carbonaceous clay to lignite, foliated, strongly sulfidic, with sulfur efflorescence; gradual lower contact;
Noe 1003-55	22.7	-32	medium-grey calcareous clay, laminated; gradual lower contact;

Noe 1003-56	32	-32.06	medium-grey argillaceous marl, well stratified, with compressed gastropods (Planorbarius) at 1-2 and 4 cm below top;
Noe 1003-57	17.4	-32.6	medium to dark-grey calcareous clay, bedded, with minor shell debris; one 8-cm-deep dike-like in-situ brecciated zone from top
Noe 1003-58	18.6	-33.3	medium-grey calcareous clay, bedded, minor bioturbation; gradual lower contact
Noe 1003-59	88.7	-33.38	light-grey argillaceous dolomicrite, massive; sharp lower contact;
Noe 1003-60	0	-33.6	black lignite, foliated, sulfidic, with sulfur efflorescence;
		-34.0	core loss
Noe 1003-61	6.5	-34.7	medium-grey slightly calcareous clay, bedded; yellowish-grey layers at 13-15, 41-44 and 57-59 cm below top; gradual lower contact;
Noe 1003-62	22.7	-35.00	medium-grey calcareous clay, bedded; top 5-8 cm disrupted by *in situ* brecciated zone;
Noe 1003-63	5.4	-35.07	medium-grey slightly calcareous clay, bedded; sharp lower contact;
Noe 1003-64	0	-35.08	dark-grey to black carbonaceous clay, well stratified, with 1-2 mm sized gastopods (Hydrobia); sharp lower contact;
Noe 1003-65	0	-35.5	medium-grey clay, poorly bedded, with iron sulfide nodule at 35.3 m; gradual lower contact;
Noe 1003-66	0	-35.7	dark-grey (bottom) to medium-grey (top) clay, poorly bedded; gradual lower contact;
Noe 1003-67	0	-36.0	dark-grey to black lignite, foliated, sulfidic, with sulfur efflorescence;
Noe 1003-68	8.9	-36.05	medium-grey slightly calcareous clay, laminated; gradual lower contact;
Noe 1003-69	74.2	-36.08	yellowish-grey argillaceous dolomicrite, massive; sharp lower contact;
Noe 1003-70	0.7	-36.45	medium-grey clay, laminated, with iron sulfide nodules and carbonaceous plant debris; gradual lower contact;
Noe 1003-71	0	-36.66	dark-grey clay, laminated, with iron sulfide nodules and abundant carbonaceous plant debris; sulfur efflorescence;
Noe 1003-72	0	-37.0	dark-grey carbonaceous clay, laminated, with iron sulfide nodules and carbonaceous plant debris; sulfur efflorescence;
Noe 1003-73	9.5	-38.0	medium-grey slightly calcareous clay, bedded, minor bioturbation at 48-55 and 89-93 cm below top; carbonaceous plant debris at 36 cm below top; possible ostracod valve at 72 cm below top;
Noe 1003-74	15.6	-38.7	medium-grey calcareous clay, well bedded, with several shell layers at 34, 39, 40, 41 cm (ostracods, Hydrobia), 44 cm (Hydrobia) and 42, 43, 45.5, 50, 51 cm below top (shell debris); sharp erosive lower contact;
Noe 1003-75	90.7	-38.92	white-grey argillaceous dolomicrite, massive, with minor bioturbation; sharp lower contact;
Noe 1003-76	75.2	-39.0	medium-grey argillaceous dolomicrite, poorly bedded;
Noe 1003-77	0.6	-39.3	medium-grey clay, laminated, with iron sulfide nodules and carbonaceous plant debris; gradual lower contact;

Noe 1003-78	74.1	-39.45	alternation of light-grey argillaceous dolomicrite and medium-grey calcareous marl, bedded; gradual lower contact;
Noe 1003-79	66.2	-39.7	white-grey calcareous dolomite marl, poorly bedded, minor bioturbation;
Noe 1003-80	53.7	-40.07	white-grey calcitic-dolomitic marl, poorly bedded, minor bioturbation; gradual lower contact;
Noe 1003-81	32.3	-40.5	white-grey argillaceous dolomite marl, massive, with 1-4 mm sized vertical burrows
NR1003-103	33.6	-43.25	white-grey argillaceous dolomite marl, poorly bedded, with 1-6 mm sized vertical and irregular burrows; gradual lower contact;
		-43.85	medium-grey argillaceous dolomite marl, well bedded, minor bioturbation; sharp lower contact;
NR1003-104	39.9	-48.15	medium to dark-grey argillaceous dolomite marl, well bedded, minor bioturbation and carbonaceous debris; with dike-like brecciated zone from top; gradual lower contact;
NR1003-107	66.1	-49.0	light-grey dolomite marl, poorly bedded, minor bioturbation; gradual lower contact;
NR1003-108	52.9	-51.10	light-grey dolomite marl, massive, intensively burrowed, from 49.3-49.3 mottled (?fluidization); gradual lower contact
		-51.75	medium-grey dolomite marl, poorly bedded, minor bioturbation; gradual lower contact
NR1003-2; NR1003-109 to NR1003-111	42.4 to 86.7	-54.08	alternation of dark-grey dolomite marl and light-grey argillaceous dolomite, well bedded
		-54.56	with dike-like brecciated zone from top
		-54.95	brownish medium grey unstratified clay with in-situ breccaition and desiccation cracks, bioturbated
		-55.43	dark grey calcareous clay with carbonaceous debris, unstratified, bioturbated
NR1003-112	30.1	-58.23	orche grey poorly stratified marl, from 55.69 to 57.06 m depth disturbed by benthic invertibrates and storms, only at 56.75 m depth possible root traces; less bioturbated below 57.06 m
		-58.64	alternating greenish medium grey cm-pooly stratified marl and white grey cm-poorly stratified carlcareous limestone, strongly bioturbated by benthic invertibrates;
NR1003-113	40.6	-59.63	58.64 - 59.33 greenish medium grey poorly stratified marl and white grey poorly stratified calcareous limestone, less bioturbated, mud crack at 59.34 m
NR1003-114	56.0	-59.73	white grey unstratified marl, bioturbated, mud crack at 59.73 m
		-59.84	greenish medium grey poorly stratified marl, mud crack from 59.73 to 59.90 m
		-60	medium-light grey poorly stratified marl, bioturbated
		-60.14	greenish medium grey and dark grey poorly stratified marl, bioturbated

		-61.89	alternations from unstratified bioturbated marl (base) to pedogenetically modified marl or in-situ breccia with desiccation cracks (top): 1) from 60.14 to 60.36; 2) from 60.36 to 60.46; 3) from 60.46 to 60.61; 4) from 60.61 to 60.65; unclear cyclicity from 60.65 to 61.89 m (the stratification becomes thin as 1 cm, thus "pedogenically modified marl to unstratified clay" alternation is replaced by "bioturbated marl to clay "cycle). Mud cracks at 60.23, 60.29, 60.41, 60.44, 60.49, 60.60, 60.62?, and 60.64 m core depth;
NR1003-115	85.2	-62.1	alternations from unstratified bioturbated marl (base) to pedogenetically modified marl or in-situ breccia with desiccation cracks (top); 1) from 61.89 to 62; 2) from 62 to 62.1
NR1003-116 to 117	37.9 to 101.7	-64.1	alternations of cm-stratified bioturbated ankeritic marl (1-3 cm thick) and argillaceous clay (<1cm thick); at 63.04-63.07 m ankeritic dolomite bed, cyclicity becomes unclear from 63.85 to 64.1: almost unstratified marl
		-65	alternations of unstratified dark grey argillaceous clay (1-2cm thick) and medium grey bioturbated ankeritic argillaceous marl (2-3cm thick)
NR1003-118 to 120	38.3 to 86.1	-68.65	alternations of "cm-thick bioturbated marl to argillaceous clay" become unclear, instead, "tens-cm thick carbonate rich marl section and carbonate poor clay" alternations are shown, overlain by "cm-thick bioturbated marl to argillaceous clay" alternations. alternation 1, 65.00 to 65.70, yellowish white grey ankeritic marl (top) to dark grey argillaceous clay (bottom), bottom of ankeritic marl is bioturbated; alternation 2, 65.7 to 66.51, yellowish white grey ankeritic marl (top) to dark grey argillaceous clay (bottom), bottom of ankeritic part is composed of 1 cm thick white grey bioturbated ankeritic dolomite; alternation 3, 66.51 to 67.02, white grey argillaceous ankeritic dolomite (top) to dary grey argillaceous clay, bottom of the dolomite is bioturbated; alternation 4, 67.02 to 67.26, white grey argillaceous ankeritic dolomite (top) to dary grey argillaceous clay, bottom of the dolomite is bioturbated; alternation 5, 67.26 to 67.50; alternation 6, 67.50-67.80; alternation 7, 67.80-67.98; alternation 8, 67.98 to 68.12; alternation 9, 68.12 to 68.48; alternation 10, 68.48 to 68.65;
NR1003-121 to 122	34.5 to 61.5	-71.51	alternations of stratified bioturbated intraclastic ankeritic marl and poorly stratified argillaceous clay; the intraclastic ankeritic marls are mm-thick, composed of carbonate nodules less than 2mm in size=>flooding events??
NR1003-123	26.2	-73.61	alternation 1: laminated bioturbated marlsotne (with laminated bituminous shale?, 71.51 to 71.61 m depth), unstratified marlstone with in-situ brecciation and desiccation crack (71.61 to .76 m depth), poorly stratified marlstone with bioturbation (71.76 to 72.56 m depth); alternation 2 laminated marlstone (with laminated bituminous shale?, 72.56 to .69 m depth), unstratified marlstone with in-situ brecciation and desiccation crack (72.69 to 73.16 m depth), poorly stratified marlstone with bioturbation (73.16 to .61 m depth)

NR1003-3, NR1003-124 to 133	63.5 to 90.3	-84.4	alternation 1 bioturbated poorly stratified marlstone (73.61 to 73.75 m depth), alternating laminated marlstone and bioturbated argillaceous limestone/dolomite (73.75 to 76.26 m depth), unstratified marlstone with desiccation crack-overlying poorly stratified marlstone-bioturbated dolomite/argillaceous limestone (76.26 to .41 m depth), strongly bioturbated marlstone with desiccation cracks, root traces and in-situ brecciation (76.41 to.67 m depth); alternation 2 laminated marlstone (and bituminous shale?, 74.67 to 78.70 m depth), only 78.39 m depth 1 cm layer shows bioturbation; laminated marlstone and argillaceous limestone with soft deformation (78.70 to 79.72 m depth), bioturbated laminated marlstone (top) and deformed stratified alternating limestone and marlstone (79.72 to 80.20 m depth), laminated argillaceous marl-bituminous shale-bioturbated unstratified marl-stratified calcareous marl with desiccation cracks and in-situ brecciation (80.20-.35 m depth); fecal pellet bed at 74.96 m depth.
NR1003-4, NR1003-134 to 137	61.9 to 89.4	-87.7	alternations: upper part dark grey stratified to laminated argillaceous marl, lower part white grey bioturbated stratified to laminated dolomite/ankerite marl; the thickness ratio of dolomite:argillaceous marl increases from 87.7 to 83.4; decreases from 83.4 to 74.2 m depth
NR1003-138 to 143	26.4 to 79.0	-95.09	alternations: medium grey laminated marl with analcime? Without dolomite, only calcite and ankerite, no bioturbation! At 89.62-89.64 a strongly deformed slump structure
NR1003-5, NR1003-143	85.5 to 99.6	-98.26	alternations: pinky white grey bioturbated poorly stratified dolomitic marl (bird eye structures at 95.11 m depth) and medium grey argillaceous marl (and analcime?)
		-98.5	unstratified clay
NR1003-144 to 146	24.4 to 72.7	-103.3	from 98.50 to 98.58m depth a polymic breccia, comprised of medium grey laminted marlstone and white grey massive limestone? From 98.58 to 103.3 m, laminated to poorly laminated medium grey marl and analcime? Both brittle deformation (micro normal faults) and soft deformation (liquification of laminations, slump) occur. fecal pellet bed at 102.08 m depth.
		-103.33	pinky white grey poorly stratified dolomitic marl and brownish grey laminated analcime-bearing clay alternations (no bioturbation)
		-104.64	medium grey poorly stratified to poorly laminated argillaceous marl and brownish grey laminated analcime-bearing clay alternations with soft and brittle deformation structures
		-104.7	pinky white grey poorly stratified dolomitic marl and brownish grey laminated analcime-bearing clay alternations (no bioturbation)
		-105.26	medium grey poorly stratified to poorly laminated argillaceous marl and brownish grey laminated analcime-bearing clay alternations with soft and brittle deformation structures, at 105.00 to .10 a polymictic breccia
NR1003-147, NR1003-6	88.9 to 98.4	-105.35	pinky white grey poorly stratified dolomitic marl and brownish grey laminated analcime-bearing clay alternations (no bioturbation)
		-107.04	medium grey poorly stratified to poorly laminated argillaceous marl and brownish grey laminated analcime-bearing clay alternations with soft and brittle deformation structures, from 105.53 to 105.59 again dolomitic marl/analcime-bearing clay alternations;

		-107.09	pinky white grey poorly stratified dolomitic marl and brownish grey laminated analcime-bearing clay alternations (no bioturbation)
NR1003-148	79.9	-108.1	medium grey poorly stratified to poorly laminated argillaceous marl and brownish grey laminated analcime-bearing clay alternations with soft and brittle deformation structures
		-108.13	pinky white grey poorly stratified dolomitic marl and brownish grey laminated analcime-bearing clay alternations (no bioturbation)
NR1003-149 to 154	19.8 to 49.1	-116.52	medium grey poorly stratified to poorly laminated argillaceous marl and brownish grey laminated analcime-bearing clay alternations with soft and brittle deformation structures
NR1003-155	56.6	-116.56	pinky white grey poorly stratified dolomitic marl and brownish grey laminated analcime-bearing clay alternations (no bioturbation), with normal microfaults
		-116.7	medium grey poorly stratified to poorly laminated argillaceous marl and brownish grey laminated analcime-bearing clay alternations with soft and brittle deformation structures
NR1003-156	83.8	-116.76	white grey poorly stratified dolomitic marl and brownish grey laminated analcime-bearing clay alternations (no bioturbation), with normal microfaults
NR1003-157 to 159, NR1003-8	24.2 to 77.0	-121.6	medium grey poorly stratified to poorly laminated argillaceous marl and brownish grey laminated analcime-bearing clay alternations with soft and brittle deformation structures, 119.90-.92 cm-stratified dolomitic marl
		-121.62	pinky white grey poorly stratified dolomitic marl and brownish grey laminated analcime-bearing clay alternations (no bioturbation)
NR1003-9	51.1	-123.61	medium grey poorly stratified to poorly laminated argillaceous marl and brownish grey laminated analcime-bearing clay alternations with soft and brittle deformation structures
NR1003-160	73.7	-123.86	from 123.61 to 123.80: white grey poorly stratified dolomitic marl and medium grey argillaceous marl alternations; from 123.80 to 123.86 pinky ankeritic marl and medium grey argillaceous marl alternations
NR1003-161	16.3	-128.69	medium grey poorly stratified argillaceous ankeritic marl and laminated bituminous shale alternations
NR1003-162	50.0	-128.85	pinky white grey poorly stratified dolomitic marl and brownish-dark grey laminated bituminous shale alternations (no bioturbation)
NR1003-163 to 165	22.0 to 34.4	-135.13	medium grey poorly stratified argillaceous ankeritic marl and laminated bituminous shale alternations, occassionally with thin <5mm thick dolomitic intercalations
NR1003-166 to 170	29.9 to 81.0	-143.13	at 135.13 m depth a sharp contact with the overlying argillaceous marl (flooding event?), below are clay-marl alternations composed of ankeritic dolomite marl at top following by yellowish white grey-pinky ankeritic marl and medium grey to brown laminated analcime bearing clay beds: from 135.16 to 135.76; 135.76 to 135.85; 135.85 to 136.40; 136.40 to 137.17; 137.17 to 138.03; 138.03 to 143.13; both soft and brittle deformation structure drastically increase from this section with increasing depth
NR1003-171 to 174	49.1 to 71.0	-148.9	yellowish white grey stratified to laminated ankeritic marl and brown laminated clay, partly deformed by soft and brittle deformation

NR1003-175	35.7	-149.9	upper part of the marl-clay alternations: yellowish white grey laminated to stratified ankeritic marl and brown laminated clay; lower part of the marl-clay alternations: medium grey argillaceous marl and brown laminated clay. 148.9 to 149.2; 149.2 to 149.45; 149.45 to 149.90; partly deformed by soft and brittle deformations
NR1003-176	44.7	-152	medium grey laminated to poorly stratified marlstone and brown laminated clay alternations
NR1003-177	44.2	-152.52	yellowish white grey stratified to laminated ankeritic marl and brown laminated clay, partly deformed by soft and brittle deformation
NR1003-178 to 221	18.4 to 61.6	-215.02	yellowish white grey poorly stratified ankeritic marl and brown laminated clay alternations; at 192.62-192.66 volcanic ash layer
		-215.14	dark grey to black laminated bituminous shale
NR1003-222 to 230	65.8 to 92.2	-223.1	white grey (few yellow white grey) laminated to cm-stratified dolomitic (few ankeritic) marl and dark grey to black laminated bituminous shale alternations
NR1003-231 to 234	61.58 to 98.2	-226	medium grey laminated to poorly stratified marlstone and brown laminated clay alternations, with dolomitic intercalations at 223.32 to 223.34, 224.87-90, 225.04-225.05
NR1003-235 to 239	71.6 to 98.5	-228.74	white grey ankeritic marl and dark grey argillaceous limestone alternations, with intensive fluid escape structures
NR1003-240 to 245	3.9 to 20	-242.4	white to medium grey massive coarse grain ankeritic/calcareous (sometimes pebbly) sandstone to ankeritic/calcareous siltstone alternations: from 228.74-234.64; 234.64 to 235; 235-236.0 core loss; 236.2 to 237.1; 237.1 to 237.78; from 237.78 to 238.80; 238.8 to 242.4; some of the sand- and siltstone has been modified by fluid escape structure
NR1003-246 to 250, NR1003-10 to 11	43.3 to 93.4	-245.6	white grey and dark grey laminated marl and argillaceous limestone cycles; strongly modified by fluid escape structures
NR1003-251 to 256	0.6 to 39.1	-253.6	white grey pebbly lithic sandstone-coarse grained sandstone-calcareous sand/siltstone alternations: 245.6 to 247.25; 247.25 to 248.8; 248.8 to 251.2; 251.2 to 251.39; 251.39 to 251.7; 251.7 to 252.2; 252.2 to 252.7; 252.7 to 253.6

Table A.3 Description of the sampling carbonate beds, their lithofacies types, and CaCO₃ (calculated by C_carb), organic carbon and total sulfur contents determined by Leco and CNS analyzer.

lithostratigraphy	sample number	depth [m.b.s.]	depth (plot) [m.b.s.]	lithofacies type	lithological description	C_{org} [wt%]	S_{tot} [wt%]	C_{carb} [wt%]	$CaCO_3$ [wt%]
Clay member	NR1003-12	14.00-14.20 m	14	mottled clay	greenish-grey clay, poorly stratified, mottled fabric (bioturbation) between 14.05-14.08 m; sharp lower contact;	0.9	0.7	0.57	4.7
Clay member	NR1003-13	14.20-14.44 m	14.2	massive dolomicrite	yellowish white-grey argillaceous dolostone, unstratified, mottled fabric (possible bioturbation); at 14.34-14.35 fine-stratified marl; sharp lower contact;	0.1	0.2	10.45	87.1
Clay member	NR1003-1	14.25-14.28 m	14.3	massive micrite	whitegrey argillaceous limestone, unstratified; gradual lower contact;	0.2	0.2	9.39	78.2
Clay member	NR1003-14	14.44-14.47 m	14.4	mottled clay	greenish-grey, slightly calcareous claystone, poorly stratified, mottled fabric; sharp lower contact;	0.4	0.6	1.04	8.7
Clay member	NR1003-15	14.47-14.58 m	14.5	massive dolomicrite	yellowish white-grey argillaceous dolostone, unstratified-mottled, with vertical fine-brecciated structures; sharp lower contact;	0.1	0.1	10.72	89.3
Clay member	NR1003-16	14.58-14.83 m	14.6	weakly stratified clay	dark-grey slightly calcareous claystone, stratified to weakly stratified; with scattered thin and transparent ostracod valves;	1.5	1.5	0.54	4.5
Clay member	NR1003-17	15.00-15.15 m	15	weakly stratified clay	dark-grey claystone, stratified to weakly stratified; gradual lower contact;	1.8	1.5	0.21	1.7
Clay member	NR1003-18	15.15-15.65 m	15.2	massive marlstone	white-grey marlstone, unstratified; with scattered ostracods and peloids; gradual lower contact;	0.6	1.1	4.94	41.2
Clay member	NR1003-19	15.65-15.85 m	15.7	mottled clay	medium to dark grey claystone, unstratified-mottled; gradual lower contact;	0.5	1.7	0.47	3.9
Clay member	NR1003-20	15.85-15.90 m	15.9	massive micrite	white-grey calcareous marlstone, weakly stratified; with shell remnants (possibly ostracods); sharp lower contact;	0.3	0.3	9.97	83.1

Clay member	NR1003-21	15.90-16.00 m	16	mottled marl	medium-grey marlstone, unstratified; with iron sulfide nodules;	0.4	1.1	5.78	48.2
Clay member	NR1003-22	16.00-16.40 m	16.2	mottled clay	medium-grey marlstone, unstratified-mottled; with iron sulfide nodules; gradual lower contact	1.2	2.4	1.69	14.1
Clay member	NR1003-23	16.40-16.50 m	16.5	massive marlstone	white-grey calcareous marlstone, unstratified; fragile shell remnants (possibly ostracods); gradual lower contact;	0.3	0.4	8.81	73.4
Clay member	NR1003-24	16.50-16.90 m	16.6	weakly stratified clay	dark-grey calcareous clay, weakly stratified; fine fragments of shell remains; with iron sulfide nodules; gradual lower contact;	1.0	6.5	2.71	22.6
Clay member	NR1003-25	16.90-17.00 m	16.9	carbonaceous clay	black carbonaceous clay, stratified, strongly sulfidic, with secondary sulfur efflorescence;	1.6	7.1	0.00	0.0
Clay member	NR1003-26	17.00-17.75 m	17	**stratified lignite**	black lignite, stratified, strongly sulfidic, with secondary sulfur effluorescence; gradual lower contact;	17.3	9.8	0.00	0.0
Clay member	NR1003-27	17.75-18.00 m	17.8	carbonaceous clay	dark-grey carbonaceous clay, weakly stratified;	1.9	3.7	0.05	0.4
Clay member	NR1003-28	18.00-18.70 m	18.4	weakly stratified clay	medium-grey calcareous claystone, stratified; with mm-sized carbonaceous plant debris, ostracod shell remains, white carbonate intraclasts and peloids up to 5 mm size;	1.8	2.2	1.64	13.7
Clay member	NR1003-29	20.00-20.20 m	20.1	weakly stratified clay	dark-grey claystone, weakly stratified, with iron sulfide nodules; gradual lower contact;	1.6	3.3	1.18	9.8
Clay member	NR1003-30	20.20-20.40 m	20.2	mottled clay	light-grey calcareous claystone, unstratified-mottled; with white carbonate grains (peloids); gradual lower contact;	0.5	1.7	2.28	19.0
Clay member	NR1003-31	20.40-21.00 m	20.4	stratified clay	medium-grey calcareous claystone, stratified, with microfaults; at the top unstratified-mottled;	1.4	1.7	1.33	11.1

Clay member	NR1003-32	22.00-22.80 m	22.4	weakly stratified clay	medium-grey calcareous claystone, weakly stratified; with iron sulfides; scattered carbonate grains; gradual lower contact;	1.0	1.5	1.24	10.3
Clay member	NR1003-33	22.80-22.83 m	22.8	mottled dolomitic marl	light-grey dolomarlstone, unstratified-mottled; scattered white carbonate grains;	0.7	0.8	4.48	37.3
Clay member	NR1003-34	22.83-23.00 m	22.9	mottled clay	medium-grey slightly calcareous claystone, unstratified-mottled;	0.6	1.7	0.65	5.4
Clay member	NR1003-35	23.00-23.20 m	23	weakly stratified clay	medium-grey calcareous claystone, weakly stratified; scattered white carbonate grains; gradual lower contact;	0.4	1.6	2.60	21.7
Clay member	NR1003-36	23.20-23.70 m	23.2	massive dolomicrite	white grey argillaceous dolostone, unstratified; in the lower part two indistinct clay layers intercalated; sharp lower contact;	0.1	0.4	10.17	84.7
Clay member	NR1003-37	23.70-24.00 m	23.7	weakly stratified clay	dark-grey slightly calcareous claystone, weakly stratified;	1.8	3.1	0.59	4.9
Clay member	NR1003-38	24.00-25.00 m	24.5	weakly stratified clay	medium-grey calcareous claystone, weakly stratified; with iron sulfide concretions; from 24.50 to 24.60 m unstratified marl; at 24.90 m sulfidic with minor sulfur effluorescence;	1.7	3.0	1.84	15.3
Clay member	NR1003-39	25.00-26.00 m	25.5	weakly stratified clay	greenish to medium-grey calcareous claystone, weakly stratified; with iron sulfide concretions and carbonaceous plant debris;	1.4	2.0	2.43	20.2
Clay member	NR1003-40	26.00-27.00 m	26.5	(weakly stratified clay)	grey and greenish-grey clay, unstratified: disintegrated by drilling process; with white-grey laminated marlstone fragments and black carbonaceous plant debris;	2.0	2.5	1.19	9.9
Clay member	NR1003-41	28.50-29.00 m	28.7	(weakly stratified clay)	grey and greenish-grey clay, unstratified: disintegrated by drilling process; with white-grey laminated marlstone fragments and black carbonaceous plant debris;	1.5	2.1	0.40	3.3

Clay member	NR1003-42	29.00-29.45 m	29.2	mottled clay	medium-grey slightly calcareous claystone, unstratification-mottled; gradual lower contact;	1.4	3.0	0.58	4.8
Clay member	NR1003-43	29.45-29.95 m	29.5	**stratified lignite**	black lignite, stratified, with wood remains, strongyl sulfidic; secondary sulfur effluorescence;	27.9	7.7	0.00	0.0
Clay member	NR1003-44	29.95-30.00 m	29.95	**stratified lignite**	black-brown lignite, stratified, sulfidic; abundant carbonaceous plant debris,	11.9	5.6	0.00	0.0
Clay member	NR1003-45	30.00-30.05 m	30	stratified marl	medium-grey marlstone, stratified; compacted dewatering structures; sharp lower contact;	6.3	2.3	7.78	64.8
Clay member	NR1003-46	30.05-30.20 m	30.1	weakly stratified clay	medium-grey claystone, weakly stratified with soft deformation structures;	1.1	1.5	0.00	0.0
Clay member	NR1003-47	30.20-30.38 m	30.3	**laminated marlstone with freshwater gastropods**	medium-grey marlstone, sulfidic, laminated, with fossil shell debris (*Gyraulus*) at 30.21, 30.23, and 30.25 m; sharp lower contact;	4.7	5.9	6.29	52.4
Clay member	NR1003-48	30.38-31.00 m	30.7	**carbonaceous clay**	dark-grey carbonaceous claystone, calcareous and sulfidic, stratified, with black lignite layers and secondary sulfur effluorescence;	8.4	5.8	1.92	16.0
Clay member	NR1003-49	31.00-31.07 m	31	stratified clay	medium-grey calcareous claystone, stratified, with microfaults; sharp lower contact;	6.5	4.8	2.58	21.5
Clay member	NR1003-50	31.07-31.08 m	31.1	stratified clay	medium-grey claystone, stratified; sharp lower contact;	1.9	1.7	0.05	0.4
Clay member	NR1003-51	31.08-31.25 m	31.2	**laminated marlstone**	medium- to dark-grey marlstone, sulfidic, laminated, with carbonaceous plant debris; uneven lower contact;	9.7	6.6	5.00	41.7
Clay member	NR1003-52	31.25-31.30 m	31.3	mottled clay	medium-grey claystone, sulfidic, mottled to in situ brecciated (dewatering?)	5.6	14.8	0.00	0.0
Clay member	NR1003-53	31.30-31.60 m	31.5	**carbonaceous clay**	dark-grey carbonaceous claystone, stratified; secondary sulfur and gypsum efflorescence;	7.3	8.5	0.16	1.3

157

Clay member	NR1003-54	31.60-31.88 m	31.7	**stratified lignite**	dark-grey lignite, stratified, sulfidic; with secondary sulfur effluorescence; sharp lower contact;	18.1	10.8	0.00	0.0
Clay member	NR1003-55	31.88-32.00 m	31.9	**bituminous shale (?)**	medium-grey bituminous calcareous claystone, laminated, sharp lower contact;	20.4	6.3	2.72	22.7
Clay member	NR1003-56	32.00-32.05 m	32	**laminated marlstone with freshwater gastropods**	medium-grey stratified argillaceous marlstone, with layers of compacted gastropods (*Planorbarius,* up to 1 cm size) near top of the bed; uneven lower contact;	10.7	3.3	3.84	32.0
Clay member	NR1003-57	32.05-32.60 m	32.3	stratified clay	medium- to dark-grey calcareous claystone, stratified; with few white shell remains; top parts with in situ brecciated pockets (dewatering?).	3.7	2.8	2.09	17.4
Clay member	NR1003-58	32.60-33.30 m	32.8	stratified clay	medium-grey calcareous claystone, stratified, weak bioturbation, gradual lower contact;	1.8	2.3	2.23	18.6
Clay member	NR1003-59	33.30-33.38 m	33.3	massive dolomicrite	light-grey argillaceous dolostone, unstratified; sharp lower contact;	0.4	0.6	10.64	88.7
Clay member	NR1003-60	33.38-33.60 m	33.5	**stratified lignite**	black lignite, stratified; secondary sulfur and gypsum efflorescence;	30.5	9.6	0.00	0.0
Clay member	NR1003-61	34.00-34.70 m	34.4	stratified clay	medium-grey slightly calcareous claystone, stratified; light grey layer at 34.13-34.15 m, 34.41-34.44 m, and 34.57-34.59 m; gradual lower contact;	1.4	1.9	0.78	6.5
Clay member	NR1003-62	34.70-35.00 m	34.7	stratified clay, top: mottled	medium-grey calcareous claystone, stratified; top 8 cm formed by in situ brecciated claystone (pocket-like; dewatering?);	2.2	2.0	2.72	22.7
Clay member	NR1003-63	35.00-35.07 m	35	stratified clay	medium- to dark-grey calcareous claystone, stratified; sharp lower contact;	3.1	5.1	0.65	5.4
Clay member	NR1003-64	35.07-35.08 m	35.1	**carbonaceous clay**	dark-grey carbonaceous claystone, stratified, sulfidic; with 1-2 mm sized Hydrobia shells; sharp lower contact;	2.8	11.7	0.00	0.0

Clay member	NR1003-65	35.08-35.50 m	35.3	weakly stratified clay	medium-grey claystone, weakly stratified; with iron sulfide concretion at 35.30 m; gradual lower contact;	0.6	2.1	0.00	0.0
Clay member	NR1003-66	35.50-35.70 m	35.6	weakly stratified clay	dark-grey claystone, weakly stratified; gradual lower contact;	1.6	1.9	0.00	0.0
Clay member	NR1003-67	35.70-36.00 m	35.8	**stratified lignite**	dark-grey to black lignite, sulfidic, stratified; with secondary sulfur effluorescence;	37.2	9.1	0.00	0.0
Clay member	NR1003-68	36.00-36.05 m	36	stratified clay	medium-grey calcareous claystone, stratified; gradual lower contact;	1.7	1.8	1.07	8.9
Clay member	NR1003-69	36.05-36.08 m	36.05	massive dolomicrite	yellowish-light grey argillaceous dolomite, unstratified; sharp lower contact;	0.8	0.8	8.90	74.2
Clay member	NR1003-70	36.08-36.45 m	36.2	weakly stratified clay	medium-grey claystone, weakly stratified; with iron sulfide concretions and carbonaceous plant debris; gradual lower contact;	1.4	1.9	0.09	0.7
Clay member	NR1003-71	36.45-36.66 m	36.5	stratified clay	dark-grey claystone, stratified; with iron sulfide concretions and abundant carbonaceous plant debris; sharp lower contact;	3.4	2.1	0.00	0.0
Clay member	NR1003-72	36.66-37.00 m	36.8	stratified clay	dark-grey claystone, stratified; with abundant carbonaceous plant debris; secondary sulfur effluorescence;	2.6	3.5	0.00	0.0
Clay member	NR1003-73	37.00-38.00 m	37.5	stratified clay	medium-grey slightly calcareous claystone, stratified; bioturbation at 37.48-37.55 m and 37.89-37.93 m; carbonaceous plant remains at 37.36 m; one layer full of shell debris at 37.72 cm (ostracods?);	1.6	2.5	1.14	9.5
Clay member	NR1003-74	38.00-38.70 m	38.4	**laminated claystone with freshwater gastropods**	medium- to dark-grey calcareous claystone, laminated; with layers of *Hydrobia* (38.34 m, 38.39 m, 38.40 m, 38.41 m, 38.44 m), ostracods (38.34 m) and shell debris (38.42 m, 38.43 m, 38.45 m, 38.50 m, 38.51 m);	2.2	1.1	1.9	15.6

dolomite-marl smbr	NR1003-101	38.70-38.74 m	38.7	unstratified dolomitic marl	white-grey calcareous dolomarlstone, unstratified; gradual lower contact;	2.6	0.8	8.00	66.7
dolomite-marl smbr	NR1003-75	38.74-38.92 m	38.8	unstratified dolomicrite	white-grey dolomite, unstratified, bioturbated; gradual lower contact;	0.7	0.3	10.89	90.7
dolomite-marl smbr	NR1003-76	38.92-39.00 m	38.9	unstratified dolomicrite	medium-grey argillaceous dolomarlstone, weakly stratified;	0.7	0.6	9.03	75.2
dolomite-marl smbr	NR1003-77	39.00-39.30 m	39.2	**stratified carbonaceous clay**	medium-grey claystone, stratified; with iron sulfide concretions and carbonaceous plant debris; gradual lower contact;	1.3	1.2	0.07	0.6
dolomite-marl smbr	NR1003-78	39.30-39.45 m	39.3	stratified dolomitic marl	alternating medium-grey to white-grey dolomarlstone, stratified, with bioturbation; sharp lower contact	1.3	0.6	8.89	74.1
dolomite-marl smbr	NR1003-79	39.45-39.70 m	39.6	weakly stratified dolomitic marl	white-grey dolomarlstone, weakly stratified, with bioturbation; sharp lower contact	0.9	0.4	7.94	66.2
dolomite-marl smbr	NR1003-102	39.70-39.75 m	39.7	weakly stratified dolomicrite	white-grey dolostone, weakly stratified, with bioturbation; gradual lower contact	1.1	0.2	9.20	76.7
dolomite-marl smbr	NR1003-80	39.70-40.07 m	39.8	weakly stratified dolomitic marl	white-grey dolomarlstone, weakly stratified, with bioturbation; gradual lower contact	0.6	0.4	6.45	53.7
dolomite-marl smbr	NR1003-81	40.07-40.50 m	40.2	weakly stratified dolomitic marl	white-grey dolomarlstone, weakly stratified, with bioturbation; sharp lower contact	0.6	0.9	3.88	32.3
dolomite-marl smbr	NR1003-103	42.51-42.54 m	42.5	weakly stratified dolomitic marl	white-grey argillaceous dolomarlstone with bioturbation, unstratified; sharp lower contact	0.6	0.7	4.03	33.6

Member	Sample	Depth	Depth (m)	Lithology	Description				
dolomite-marl smbr	NR1003-104	44.41-44.43 m	44.4	weakly stratified dolomitic marl	white-grey to grey dolomarlstone, weakly stratified; with bioturbation and minor carbonaceous debris; sharp lower contact	1.4	0.5	4.79	39.9
dolomite-marl smbr	NR1003-105	46.31-46.33 m	46.3	weakly stratified dolomitic marl	white-grey dolomarlstone, weakly stratified; with bioturbation; sharp lower contact; with well preserved ostracod shells: white shell (non-altered); grey shell (possibly redeposited in sulfidic environment); locally plant debris	2.3	0.4	5.41	45.1
dolomite-marl smbr	NR1003-106	47.27-47.30 m	47.3	weakly stratified dolomitic marl	white-grey dolomarlstone, weakly stratified; with bioturbation; sharp lower contact	0.9	0.2	3.69	30.7
dolomite-marl smbr	NR1003-107	48.32-48.36 m	48.3	weakly stratified dolomitic marl	white-grey calcareous dolomarlstone, weakly stratified, with bioturbation; sharp lower contact	1.0	0.0	7.93	66.1
dolomite-marl smbr	NR1003-108	50.80-50.85 m	50.8	weakly stratified dolomitic marl	medium-grey calcareous dolomarlstone, weakly stratified, with bioturbation; sharp lower contact	1.8	0.1	6.35	52.9
dolomite-marl smbr	NR1003-2	52.19-52.20 m	52.2	stratified dolomicrite	white-grey argillaceous dolostone, stratified, with peloids and pellets (packstone, slightly compacted); sharp lower contact	2.9	0.2	9.39	78.2
dolomite-marl smbr	NR1003-109	52.73-52.75 m	52.7	weakly stratified dolomicrite	white grey slightly argillaceous dolostone, weakly stratified, with bioturbation; sharp lower contact	1.7	0.1	10.41	86.7
dolomite-marl smbr	NR1003-110	53.09-53.11 m	53.1	stratified dolomitic marl	white-grey dolomarlstone, stratified; gradual lower contact	1.9	0.1	7.52	62.7
dolomite-marl smbr	NR1003-111	54.08-54.10 m	54.1	unstratified dolomitic marl	greenish to medium-grey dolomarlstone, unstratified; sharp lower contact	0.2	0.4	5.09	42.4

dolomite-marl smbr	NR1003-112	57.84-57.86 m	57.8	stratified marl	medium-grey argillaceous marlstone, stratified; gradual lower contact	2.7	1.2	3.61	30.1
dolomite-marl smbr	NR1003-113	58.85-58.87 m	58.9	weakly stratified dolomitic marl	white-grey dolomarlstone, weakly stratified, with bioturbation; gradual lower contact	0.6	0.5	4.87	40.6
dolomite-marl smbr	NR1003-114	59.66-59.70 m	59.7	weakly stratified dolomitic marl	white-grey dolomarlstone, weakly stratified, with bioturbation; gradual lower contact	0.5	0.2	6.72	56.0
dolomite-marl smbr	NR1003-115	62.00-62.04 m	62	unstratified dolomicrite	white-grey slightly calcareous dolostone, unstratified; at base 4 cm forming in-situ brecciation	0.9	0.3	10.22	85.2
dolomite-marl smbr	NR1003-116	63.05-63.07 m	63	stratified dolomicrite	white-grey dolostone, stratified, with bioturbation, sharp lower contact; with ostracods (only debris of shells, preservation: not perfect compared to NR 105)	0.7	0.1	12.21	101.7
dolomite-marl smbr	NR1003-117	64.04-64.07 m	64	weakly stratified dolomitic marl	medium-grey dolomarlstone, weakly stratified, with bioturbation, sharp lower contact	1.9	1.2	4.55	37.9
dolomite-marl smbr	NR1003-118	65.09-65.11 m	65	weakly stratified dolomitic marl	medium-grey dolomarlstone, weakly stratified, with bioturbation, sharp lower contact	3.8	1.2	4.60	38.3
dolomite-marl smbr	NR1003-119	66.55-66.57 m	66.6	stratified dolomicrite	white-grey dolostone, stratified, with bioturbation, gradual lower contact	2.4	0.2	10.33	86.1
dolomite-marl smbr	NR1003-120	67.03-67.05 m	67	stratified dolomarlstone	white-grey dolomarlstone, stratified, with bioturbation, sharp lower contact	1.9	0.2	7.74	64.5
dolomite-marl smbr	NR1003-121	68.71-68.72 m	68.7	stratified dolomarlstone	white-grey dolomarlstone, stratified, with bioturbation, sharp lower contact	3.6	0.6	7.38	61.5

dolomite-marl smbr	NR1003-122	70.46-70.47 m	70.5	weakly stratified marl	medium-grey marlstone, weakly stratified, gradual lower contact; at 71.59 a possible fecal pellet bed	2.0	0.7	4.14	34.5
dolomite-marl smbr	NR1003-123	72.67-72.68 m	72.7	stratified marl	medium-grey marlstone, stratified, sharp lower contact	2.4	0.5	3.14	26.2
varicolored-marl smbr.	NR1003-3	74.43-74.45 m	74.4	stratified dolomicrite	yellowish white-grey dolostone, stratified, partly granular (peloids), sharp lower contact	0.4	0.1	10.27	85.6
varicolored-marl smbr.	NR1003-124	74.73-74.76 m	74.7	laminated dolomicrite	slightly pinkish, white-grey dolostone, laminated, sharp lower contact; several fecal pellet beds in reddish and yellowish-white colour beds	0.7	0.2	8.90	74.2
varicolored-marl smbr.	NR1003-125	75.67-75.69 m	75.7	stratified dolomitic marl	white-grey dolomarlstone, stratified, gradual lower contact	1.1	0.2	7.62	63.5
varicolored-marl smbr.	NR1003-126	75.84-75.85 m	75.8	stratified dolomitic marl	slightly pinkish, white-grey dolomarlstone, stratified, with bioturbation, gradual lower contact; possible reddish faecal pellet bearing beds	0.6	0.2	8.96	74.7
varicolored-marl smbr.	NR1003-127	76.27-76.29 m	76.2	stratified dolomicrite	slightly pinkish, white-grey dolostone, stratified, with bioturbation, gradual lower contact; possible medium grey faecal pellet beds	0.7	0.2	9.00	75.0
varicolored-marl smbr.	NR1003-128	76.62-76.65 m	76.6	unstratified micrite	medium-grey to white-grey limestone, unstratified, with plant debris and bioturbation, sharp lower contact	0.2	0.1	9.75	81.2
varicolored-marl smbr.	NR1003-129	78.29-78.31 m	78.3	weakly laminated dolomicrite	white-grey to pink slightly argillaceous dolostone, weakly laminated, sharp lower contact	1.3	0.2	10.41	86.7
varicolored-marl smbr.	NR1003-130	79.46-79.47 m	79.5	weakly laminated dolomicrite	white-grey to pink argillaceous dolostone, weakly laminated, sharp lower contact; white grey faecal pellet beds	1.2	0.1	9.77	81.4
varicolored-marl smbr.	NR1003-131	80.26-80.29 m	80.3	stratified dolomicrite	white-grey to pink argillaceous dolostone, stratified, with bioturbation; gradual lower contact	0.6	0.1	9.89	82.4

varicolored-marl smbr.	NR1003-132	82.06-82.08 m	82	weakly stratified dolomicrite	white-grey to pink argillaceous dolostone, weakly stratified, with bioturbation; sharp lower contact	0.6	0.3	9.04	75.3
varicolored-marl smbr.	NR1003-133	83.69-83.72 m	83.7	weakly stratified dolomicrite	white-grey slightly argillaceous dolostone, weakly stratified; sharp lower contact	0.7	0.0	10.84	90.3
varicolored-marl smbr.	NR1003-134	84.90-84.91 m	84.9	laminated dolomitic marl	white-grey calcareous dolomarlstone, laminated, with bituminous shale intercalated; gradual lower contact	2.6	0.1	7.81	65.1
varicolored-marl smbr.	NR1003-4	85.41-85.43 m	85.4	laminated dolomicrite	white-grey slightly argillaceous dolostone, thick laminated (0.5-cm thick), at base granular-porous; one fish scale	0.7	0.0	10.73	89.4
varicolored-marl smbr.	NR1003-135	85.88-85.91 m	85.9	weakly stratified dolomicrite	white-grey slightly argillaceous dolostone, weakly stratifeid, with bioturbation; gradual lower contact	0.6	0.1	10.58	88.2
varicolored-marl smbr.	NR1003-136	86.66-86.68 m	86.7	stratified calcareous dolomitic marl	white-grey calcareous dolomarlstone, stratified; sharp lower contact; with possible ostracod debris	0.6	0.1	8.9	73.9
diatom smbr	NR1003-137	87.68-87.69 m	87.7	stratified dolomitic marl	white-grey dolomarlstone, stratified, with few laminated bituminous shale at lower part; gradual lower contact; with possible ostracod debris	0.7	0.0	7.43	61.9
diatom smbr	NR1003-138	89.17-89.18 m	89.2	laminated dolomitic marl	white-grey dolomarlstone, laminated, with dark bituminous intercalations; gradual lower contact	1.5	0.6	4.34	36.2
diatom smbr	NR1003-139	91.31-91.32 m	93.1	laminated argillaceous dolomitic marl	white-grey argillaceous dolomarlstone, laminated; gradual lower contact	1.4	0.5	3.53	29.4
diatom smbr	NR1003-140	93.39-93.41 m	93.4	laminated argillaceous dolomitic marl	white-grey dolomarlstone, laminated, with dark bituminous intercalations; gradual lower contact	0.8	0.2	5.96	49.7

164

diatom smbr	NR1003-141	94.17-94.18 m	94.2	stratified dolomicrite	white-grey argillaceous dolostone, stratified; sharp lower contact; with possible ostracod debris	0.5	0.3	9.12	76.0
diatom smbr	NR1003-142	94.83-94.84 m	94.8	stratified calcareous dolomitic marl	white-grey calcareous dolomarlstone, stratified; sharp lower contact	0.6	0.2	8.36	69.7
diatom smbr	NR1003-143	95.12-95.14 m	95.1	stratified dolomicrite	yellowish to white-grey slightly argillaceous dolostone, weakly stratified; sharp lower contact; with possible ostracod debris	0.3	0.1	10.26	85.5
diatom smbr	NR1003-5	98.10-98.14 m	98.1	weakly stratified dolomicrite	medium-grey dolostone, weakly stratified, with imprint of plant debris	0.3	0.0	11.95	99.6
diatom smbr	NR1003-144	100.07-100.09 m	100.1	laminated calcareous clay	pinky white-grey calcareous claystone, laminated, with bituminous intercalations; gradual lower contact	1.7	0.9	2.93	24.4
diatom smbr	NR1003-145	102.08-102.09 m	102.1	laminated argillaceous dolomitic marl	white-grey to medium grey argillaceous marlstone, laminated, with bituminous intercalations; gradual lower contact; abundant fecal pellet on bed plain	2.4	0.6	3.37	28.1
diatom smbr	NR1003-146	103.30-103.32 m	103.3	laminated calcareous dolomitic marl	medium-grey to white-grey calcareous dolomarlstone, laminated, with bituminous intercalations; sharp lower contact; with possible ostracod debris	0.6	0.0	8.73	72.7
diatom smbr	NR1003-147	105.30-105.32 m	105.3	laminated dolomicrite	white-grey argillaceous dolostone, laminated, with bituminous intercalations; gradual lower contact	0.7	0.0	10.67	88.9
diatom smbr	NR1003-6	105.325-105.34 m	105.3	laminated dolomicrite	yellow grey, light yellowish dolomitic micrites, well stratified, with granular layers(peloids)	0.3	0.0	11.81	98.4
diatom smbr	NR1003-148	107.05-107.06 m	107.1	weakly laminated dolomicrite	white-grey argillaceous dolostone, weakly laminated (soft-sediment deformation feature); gradual lower contact; with carbonaceous plant debris	1.4	0.0	9.59	79.9

diatom smbr	NR1003-149	109.00-109.02 m	109	laminated dolomitic marl	medium-grey dolomarlstone, laminated, gradual lower contact	1.3	0.4	4.65	38.7
diatom smbr	NR1003-150	111.05 - 111.06 m	111.1	lenticular dolomicrite in massive debrite	white-grey lenticular dolomarlstone clasts (2x1 cm) in massive debrite; sharp lower contact	1.1	0.2	5.89	49.1
diatom smbr	NR1003-151	111.82-111.84 m	111.8	laminated calcareous clay	white-grey to medium-grey calcareous clay, laminated, gradual lower contact	1.5	0.9	2.38	19.8
diatom smbr	NR1003-152	112.56-112.57 m	112.6	laminated dolomitic marl	yellowish medium-grey marlstone, laminated, gradual lower contact	2.8	0.6	5.34	44.5
diatom smbr	NR1003-153	113.46-113.47 m	113.5	weakly laminated dolomitic marl	white-grey dolomarlstone, weakly laminated, sharp lower contact	1.6	0.6	3.67	30.6
diatom smbr	NR1003-7	113.67-113.675	113.65	diagenic product	yellowish-grey to brown limonite bed with secondary gypsum (oxidized iron sulfide layer; no zeolite)	1.5	10.3	0.02	0.2
diatom smbr	NR1003-154	114.58-114.60 m	114.6	laminated dolomitic marl	white-grey dolomarlstone, laminated, gradual lower contact	0.9	0.3	3.62	30.2
diatom smbr	NR1003-155	116.53-116.55 m	116.5	laminated dolomitic marl	white-grey dolomarlstone, laminated, with microfaults (possible soft-sediment deformation/seismite feature) and bituminous intercalations; gradual lower contact	1.0	0.1	6.79	56.6
diatom smbr	NR1003-156	116.74-116.75 m	116.7	stratified dolomicrite	white-grey argillaceous dolostone, stratified, with laminated bituminous intercalations; gradual lower contact	0.3	0.0	10.06	83.8
diatom smbr	NR1003-157	118.74-118.75 m	118.7	laminated calcareous clay	medium-grey calcareous claystone, laminated, gradual lower contact	1.7	0.4	2.91	24.2

diatom smbr	NR1003-158	119.91-119.93 m	119.9	laminated argillaceous dolomitic marl	white-grey to medium-grey argillaceous dolomarlstone, laminated, gradual lower contact; with possible ostracod debris	2.5	0.8	3.95	32.9
diatom smbr	NR1003-159	121.55-121.57 m	121.55	laminated dolomitic marl	white-grey to grey dolomarlstone, laminated, gradual lower contact	0.8	0.1	6.73	56.1
diatom smbr	NR1003-8	121.59-121.60 m	121.6	laminated dolomicrite	white-grey to yellowish grey dolostone, laminated, gradual lower contact	0.7	0.0	9.24	77.0
diatom smbr	NR1003-9	123.595-123.605 m	123.6	laminated dolomitic marl	white-grey to yellowish grey dolomarlstone, laminated, gradual lower contact	1.2	0.1	6.13	51.1
diatom smbr	NR1003-160	123.75-123.77 m	123.8	weakly stratified dolomitic marl	white-grey dolomarlstone, weakly stratified, with soft sediment deformation; gradual lower contact	0.6	0.0	8.85	73.7
bituminous smbr	NR1003-161	125.55-125.56 m	125.6	laminated claystone	medium-grey claystone, laminated; gradual lower contact	3.2	0.7	1.96	16.3
bituminous smbr	NR1003-162	128.73-128.76 m	128.7	laminated dolomitic marl	white-grey dolomarlstone, laminated, gradual lower contact	2.2	0.2	6.00	50.0
bituminous smbr	NR1003-163	129.56-129.57 m	129.6	weakly laminated dolomitic marl	medium-grey dolomarlstone, laminated, sharp lower contact	3.1	0.9	4.13	34.4
bituminous smbr	NR1003-164	131.64-131.66 m	131.6	weakly stratified dolomitic marl	medium-grey dolomarlstone, weakly stratified; gradual lower contact	2.6	0.6	4.04	33.7
bituminous smbr	NR1003-165	133.58-133.60 m	133.6	laminated clay	medium-grey claystone, laminated; gradual lower contact	2.2	0.9	2.64	22.0

bituminous smbr	NR1003-166	135.85-135.86 m	135.9	laminated dolomitic marl	white-grey dolomarlstone, laminated; gradual lower contact	1.6	0.2	6.49	54.1
bituminous smbr	NR1003-167	137.47-137.49 m	137.5	laminated dolomitic marl	white-grey dolomarlstone, laminated; gradual lower contact	1.1	0.2	4.52	37.7
bituminous smbr	NR1003-168	138.62-138.63 m	138.6	weakly stratified dolomitic marl	white-grey dolomarlstone, weakly stratified; sharp lower contact; with possible ostracod debris	1.2	0.2	4.94	41.2
bituminous smbr	NR1003-169	140.05-140.07 m	140	laminated dolomitic marl	white-grey dolomarlstone, laminated; with micro faults; gradual lower contact	1.2	0.2	3.59	29.9
bituminous smbr	NR1003-170	142.79-142.81 m	142.8	weakly stratified dolomicrite	white grey dolostone, weakly stratified; gradual lower contact	0.6	0.0	9.72	81.0
bituminous smbr	NR1003-171	143.17-143.19 m	143.2	weakly laminated dolomitic marl	white-grey dolomarlstone, weakly stratified; gradual lower contact	0.7	0.0	8.76	73.0
bituminous smbr	NR1003-172	146.27-146.29 m	146.3	weakly stratified marl	white-grey marlstone, weakly laminated; gradual lower contact	1.5	0.2	5.89	49.1
bituminous smbr	NR1003-173	147.77-147.80 m	147.8	weakly stratified dolomitic marl	white-grey dolomarlstone, weakly stratified, with micro faults; gradual lower contact	1.5	0.0	7.58	63.2
bituminous smbr	NR1003-174	148.45-148.46 m	148.5	unstratified dolomitic marl	white-grey dolomarlstone, unstratified, disturbed by soft sediment deformation; gradual lower contact	1.4	0.2	6.18	51.5
bituminous smbr	NR1003-175	149.31-149.34 m	149.3	weakly laminated dolomitic marl	white-grey dolomarlstone, weakly laminated, with loop bedding (top part) and microfaults; gradual lower contact	2.8	0.2	4.28	35.7

bituminous smbr	NR1003-176	150.39-150.40 m	150.4	laminated dolomitic marl	white-grey dolomarlstone, laminated; gradual lower contact	8.1	0.3	5.36	44.7
bituminous smbr	NR1003-177	152.52-152.53 m	152.5	weakly laminated dolomitic marl	white-grey dolomarlstone, weakly laminated, with micro slumps; sharp lower contact	3.6	0.5	5.31	44.2
bituminous smbr	NR1003-178	152.63-152.64 m	152.6	weakly stratified dolomitic marl	white-grey dolomarlstone, weakly stratified; with micro slumps; sharp lower contact	2.9	0.8	3.77	31.4
bituminous smbr	NR1003-179	153.46-153.47 m	153.5	weakly laminated dolomitic marl	white-grey dolomarlstone, weakly laminated; with loop bedding and microfaults; gradual lower contact	3.9	0.5	4.07	33.9
bituminous smbr	NR1003-180	155.14-155.16 m	155.1	stratified dolomitic marl	white-grey dolomarlstone, stratified; gradual lower contact	2.4	0.5	3.73	31.1
bituminous smbr	NR1003-181	155.70-155.73 m	155.7	weakly laminated dolomitic marl	white-grey dolomarlstone, weakly laminated; with micro faults; gradual lower contact	2.9	0.5	4.42	36.8
bituminous smbr	NR1003-182	156.15-156.17 m	156.2	weakly stratified clay	yellowish white-grey claystone, weakly stratified, with soft sediment deformation features; gradual lower contact	2.3	0.7	2.46	20.5
bituminous smbr	NR1003-183	157.24-157.26 m	157.2	weakly laminated dolomitic marl	yellowish white-grey dolomarlstone, weakly laminated, with bituminous intercalations; gradual lower contact	2.5	0.6	3.01	25.1
bituminous smbr	NR1003-184	159.42-159.43 m	159.4	weakly laminated clay	yellowish grey to white-grey to claystone, weakly laminated, sharp lower contact	2.7	1.1	2.64	22.0

bituminous smbr	NR1003-185	161.15-161.16 m	161.2	weakly laminated clay	yellowish grey to white-grey to claystone, weakly laminated, gradual lower contact	1.5	0.5	2.62	21.8
bituminous smbr	NR1003-186	164.75-164.76 m	164.8	weakly laminated dolomitic marl	white-grey to yellowish grey dolomarlstone, weakly laminated, sharp lower contact	2.1	0.4	4.74	39.5
bituminous smbr	NR1003-187	165.96-165.98 m	166	weakly stratified dolomitic marl	white-grey to medium-grey dolomarlstone, weakly stratified, gradual lower contact	1.3	0.3	6.22	51.8
bituminous smbr	NR1003-188	167.70-167.71 m	167.7	weakly stratified dolomitic marl	white-grey dolomarlstone and dark-grey clay, weakly stratified, with micro slumps, sharp lower contact	5.2	1.0	4.37	36.4
bituminous smbr	NR1003-189	168.32-168.34 m	168.3	weakly laminated dolomitic marl	white-grey to medium-grey dolomarlstone, weakly laminated, with bituminous intercalations, gradual lower contact	2.3	0.4	5.57	46.4
analcime smbr	NR1003-190	169.14-169.15 m	169.1	laminated clay	medium-grey and reddish claystone, laminated, sharp lower contact	2.5	0.2	2.23	18.6
analcime smbr	NR1003-191	171.64-171.66 m	171.6	weakly laminated dolomitic marl	medium-grey to white-grey dolomarlstone, weakly laminated, gradual lower contact	1.1	0.3	3.22	26.8
analcime smbr	NR1003-192	173.55-173.56 m	173.6	weakly laminated dolomitic marl	medium-grey dolomarlstone, weakly laminated, sharp lower contact	1.0	0.2	3.04	25.3
analcime smbr	NR1003-193	175.88-175.89 m	175.9	weakly laminated dolomitic marl	yellowish white-grey dolomarlstone, weakly laminated; gradual lower contact	1.9	0.3	3.30	27.5

analcime smbr	NR1003-194	176.95-176.96 m	177	laminated dolomitic marl	white-grey dolomarlstone, laminated, with bituminous intercalations, gradual lower contact	2.3	0.2	4.16	34.7
analcime smbr	NR1003-195	178.02-178.03 m	178	stratified dolomitic marl	white-grey dolomarlstone, stratified, with few laminated bituminous intercalations; gradual lower contact	1.5	0.1	6.67	55.6
analcime smbr	NR1003-196	178.77-178.78 m	178.8	weakly laminated dolomitic marl	yellowish white-grey dolomarlstone, weakly laminated, gradual lower contact	1.0	0.2	4.18	34.8
analcime smbr	NR1003-197	181.91-181.93 m	181.9	laminated dolomitic marl	white-grey dolomarlstone, laminated, gradual lower contact	1.1	0.2	5.12	42.7
analcime smbr	NR1003-198	183.55-183.57 m	183.6	weakly laminated dolomitic marl	white-grey dolomarlstone, weakly laminated, gradual lower contact	0.8	0.1	4.59	38.2
analcime smbr	NR1003-199	185.20-185.22 m	185.2	weakly laminated clay	white-grey clay, weakly laminated, with microfaults (soft sediment deformation features); gradual lower contact	1.0	0.7	2.21	18.4
analcime smbr	NR1003-200	187.41-187.42 m	187.4	weakly laminated dolomitic marl	white-grey dolomarlstone, weakly laminated in slumped bed; gradual lower contact; 0.3 cm long fish scale fossil	2.6	0.4	3.58	29.8
analcime smbr	NR1003-201	188.93-188.95 m	188.9	unstratified clay	white-grey clay, unstratified, gradual lower contact	1.7	0.6	2.73	22.7
analcime smbr	NR1003-202	190.68-190.69 m	190.7	weakly laminated clay	white-grey clay, weakly laminated, gradual lower contact	4.5	0.9	2.80	23.3
analcime smbr	NR1003-203	191.51-191.52 m	191.5	weakly laminated dolomitic marl	white-grey dolomarlstone, weakly laminated, sharp lower contact	1.7	0.3	5.78	48.2

analcime smbr	NR1003-82	192.61-192.65 m	192.6	autigenic feldspar	yellowish-whitegrey massive buddingtonite; lowermost 3 mm with lamination;	0.37	0.2	0.00	0.0
analcime smbr	NR1003-204	193.84-193.86 m	193.8	weakly stratified dolomitic marl	white-grey dolomarlstone, weakly stratified in slump beds; unclear contact	1.3	0.4	4.09	34.1
analcime smbr	NR1003-205	194.38-194.40 m	194.4	unstratified dolomitic marl	white-grey dolomarlstone, unstratified, gradual lower contact; 0.5 cm fish scale fossil	1.4	0.8	4.48	37.3
analcime smbr	NR1003-206	196.68-196.70 m	196.7	laminated marl	white-grey to medium-grey marlstone, laminated, gradual lower contact	4.5	0.3	3.72	31.0
analcime smbr	NR1003-207	197.46-196.48 m	197.5	laminated clay	white-grey clay, laminated, gradual lower contact	1.7	1.2	2.50	20.8
analcime smbr	NR1003-208	199.24-199.26 m	199.2	laminated dolomitic marl	white-grey dolomarlstone, laminated, gradual lower contact; with abundant fecal pellets	1.5	0.7	3.21	26.7
analcime smbr	NR1003-209	200.20-200.22 m	200.2	weakly laminated dolomitic marl	white-grey dolomarlstone, weakly laminated, gradual lower contact	1.7	0.6	3.94	32.8
analcime smbr	NR1003-210	202.74-202.76 m	202.7	weakly laminated marl	white-grey marlstone, weakly laminated, gradual lower contact	2.1	0.7	4.05	33.7
analcime smbr	NR1003-211	204.00-204.02 m	204	weakly laminated marl	white-grey marlstone, weakly laminated, gradual lower contact	3.8	0.7	3.13	26.1
analcime smbr	NR1003-212	205.01-205.03 m	205	weakly laminated marl	yellowish-grey to white-grey marlstone, weakly laminated, gradual lower contact	4.3	0.3	4.14	34.5
analcime smbr	NR1003-213	206.38-206.39 m	206.4	laminated dolomitic marl	medium-grey dolomarlstone, laminated, gradual lower contact	4.6	1.1	5.12	42.7

172

analcime smbr	NR1003-214	207.38-207.39 m	207.4	laminated dolomitic marl	white-grey and medium-grey dolomarlstone, laminated, gradual lower contact	1.1	0.3	5.43	45.2
analcime smbr	NR1003-215	209.30-209.75 m	209.3	laminated clay	medium-grey clay, laminated, gradual lower contact	4.4	1.7	2.56	21.3
analcime smbr	NR1003-216	210.83-210.85 m	210.8	laminated dolomitic marl	white grey dolomarlstone, laminated in slump bed, gradual lower contact	3.9	0.6	7.39	61.6
analcime smbr	NR1003-217	211.08-211.09 m	211.1	laminated marl	medium-grey marlstone, laminated in slump bed, gradual lower contact	6.6	2.1	4.05	33.7
analcime smbr	NR1003-218	212.74-212.75 m	212.7	laminated dolomitic marl	white grey dolomarlstone, laminated, gradual lower contact	3.3	0.8	5.51	45.9
analcime smbr	NR1003-219	213.24-213.25 m	213.2	laminated dolomitic marl	yellowish to white-grey dolomarlstone, weakly laminated and disturbed by soft sediment deformation, gradual lower contact	8.7	0.8	7.17	59.7
analcime smbr	NR1003-220	214.63-214.65 m	214.6	wealy laminated dolomitic marl	light-grey dolomarlstone, weakly laminated, gradual lower contact	4.7	0.7	5.6	46.3
analcime smbr	NR1003-221	214.86-214.88 m	214.9	laminated dolomitic marl	white-grey dolomarlstone, laminated, gradual lower contact; with few fecal pellets	7.6	1.6	3.1	26.1
clinoptilolite smbr	NR1003-222	215.27-215.28 m	215.3	unstratified dolomicrite	white-grey dolostone lens above a slump	3.7	0.9	9.3	77.6
clinoptilolite smbr	NR1003-223	215.89-215.90 m	215.9	weakly stratified dolomitic marl	white grey dolomarlstone, weakly stratified, gradual lower contact	5.6	0.7	9.0	75.3
clinoptilolite smbr	NR1003-224	216.64-216.65 m	216.6	laminated clay	white grey clay, laminated, gradual lower contact; 5cm fish scale fossil; at 216.60 a fecal pellet-rich bed	8.2	2.2	1.4	12.0

clinoptilolite smbr	NR1003-225	219.21-219.22 m	219.2	laminated dolomarlstone	pinkish to yellowish-grey dolomarlstone, laminated, gradual lower contact	3.1	0.8	7.9	65.8
clinoptilolite smbr	NR1003-226	219.94-219.96 m	219.9	weakly stratified dolomicrite	yellowish white-grey dolostone, weakly stratified, sharp lower contact	0.7	0.1	11.1	92.2
clinoptilolite smbr	NR1003-227	220.16-220.18 m	220.2	weakly laminated dolomicrite	white-grey dolostone, weakly laminated, gradual lower contact	0.8	0.2	10.9	90.6
clinoptilolite smbr	NR1003-228	220.56-220.57 m	220.6	laminated dolomicrite	white-grey dolostone, laminated, gradual lower contact; possible replacive structure formed by former evaporite mineral	1.6	0.4	10.2	85.0
clinoptilolite smbr	NR1003-229	221.55-221.57 m	221.6	laminated dolomicrite	white-grey dolostone, laminated, gradual lower contact	2.2	0.6	9.5	79.0
clinoptilolite smbr	NR1003-230	223.06-223.08 m	223.1	weakly stratified dolomicrite	medium-grey dolostone, weakly stratified, gradual lower contact	1.8	0.3	10.8	89.8
clinoptilolite smbr	NR1003-231	223.32-223.34 m	223.3	laminated dolomicrite	greenish-grey to white-grey dolostone, laminated, gradual lower contact	1.6	0.4	11.0	91.3
clinoptilolite smbr	NR1003-232	224.87-224.90 m	224.9	laminated dolomicrite	white-grey to medium-grey dolostone, weakly laminated, gradual lower contact; abundant fecal pellets on bed plain	1.0	0.2	11.8	98.2
clinoptilolite smbr	NR1003-233	225.04-225.05 m	225	laminated dolomicrite	white-grey dolostone, laminated, with dark grey laminated marl/bituminous shale, gradual lower contact	0.7	0.2	11.4	95.2
clinoptilolite smbr	NR1003-234	225.85-225.87 m	225.9	laminated micrite	white-grey marlstone, laminated, with dark grey laminated marl/bituminous shale, gradual lower contact	1.6	1.9	7.4	61.8
Basal member	NR1003-235	226.10-226.14 m	226.1	unstratified micrite	medium-grey to light-grey limestone, unstratified in a dike structure, with black limestone pebble, sharp lower contact	0.3	0.5	9.5	78.9
Basal member	NR1003-236	226.74-226.79 m	226.7	unstratified dolomicrite	white-grey to light-grey dolostone, unstratified, disturbed by fluid escape structure, sharp lower contact	0.1	0.1	9.7	80.7

Member	Sample	Depth range	Depth	Lithology	Description				
Basal member	NR1003-237	226.80-226.86 m	226.8	unstratified dolomicrite	white-grey to light-grey dolostone, unstratified, disturbed by fluid escape structure, sharp lower contact	0.1	0.1	11.8	98.5
Basal member	NR1003-238W	227.64-227.66 m	227.6	unstratified micrite	white-grey to light-grey limestone, unstratified, gradual lower contact	0.1	0.3	8.9	74.2
Basal member	NR1003-238B	227.64-227.66 m	227.6	laminated micrite	dark-grey limestone, laminated, gradual lower contact	0.1	0.1	10.7	89.0
Basal member	NR1003-239	228.30-228.33 m	228.3	unstratified marl	white-grey marlstone, unstratified, gradual lower contact	0.2	0.1	8.6	71.6
Basal member	NR1003-240	229.50-229.56 m	229.5	unstratified sand	greenish to medium-grey sandstone, unstratified, gradual lower contact	0.2	1.6	0.6	4.6
Basal member	NR1003-241	231.57-231.63 m	231.6	unstratified sand	greenish to medium-grey sandstone with carbonate flaser beds, unstratified, sharp lower contact	0.1	1.0	0.5	3.9
Basal member	NR1003-242	233.56-233.60 m	233.6	unstratified sand	greenish to medium-grey sandstone, unstratified, gradual lower contact	0.1	0.7	1.9	15.8
Basal member	NR1003-243	236.53-236.58 m	236.5	unstratified sand	greenish to medium-grey sandstone with carbonate flaser beds, unstratified, gradual lower contact	0.1	0.9	2.4	20.0
Basal member	NR1003-244	238.60-238.65 m	238.6	unstratified sand	light-grey to medium-grey pebbly coarse grained sandstone, unstratified, gradual lower contact	0.1	1.0	0.8	6.4
Basal member	NR1003-245	242.19-242.26 m	242.2	unstratified sand	light-grey to medium-grey coarse grained sandstone, unstratified, graded from base to top, sharp lower contact	0.1	0.9	1.8	15.0
Basal member	NR1003-246	242.66-242.69 m	242.7	unstratified micrite	light-grey to medium-grey marlstone with mm-sized white-grey limestone clasts, unstratified, sharp lower contact	0.2	1.0	5.2	43.3
Basal member	NR1003-247	242.92-242.98 m	242.9	laminated micrite	white-grey to white limestone, laminated but strongly slumped or brecciated, gradual lower contact	0.2	0.3	9.9	82.1
Basal member	NR1003-10	243.35-243.36 m	243.4	laminated micrite	white-grey to light-grey limestone, laminated, gradual lower contact	0.1	0.3	9.6	80.2

Basal member	NR1003-248	243.61-243.63 m	243.6	laminated micrite	white-grey to light-grey limestone, laminated, gradual lower contact	0.2	0.2	10.3	85.7
Basal member	NR1003-11	245.22-245.23 m	245.2	laminated micrite	white-grey to white limestone, laminated, gradual lower contact	0.1	0.2	10.6	88.4
Basal member	NR1003-249	245.20-245.22 m	245.2	laminated micrite	white-grey to white limestone, laminated, gradual lower contact	0.1	0.1	11.2	93.4
Basal member	NR1003-250	245.50-245.54 m	245.5	weakly laminated marl	white to white-grey marlstone, weakly laminated, gradual lower contact	0.1	0.7	7.2	59.9
Basal member	NR1003-251	245.83-245.87 m	245.8	unstratified marl	white to white-grey marlstone, unstratified, gradual lower contact	0.2	0.8	4.7	39.1
Basal member	NR1003-252	246.13-246.18 m	246.1	unstratified marl	white to white-grey marlstone, unstratified, gradual lower contact	0.1	0.8	4.4	36.4
Basal member	NR1003-253	247.65-247.74 m	247.7	unstratified silt	white-grey to light-grey siltstone, unstratified, gradual lower contact	0.1	0.6	1.4	11.5
Basal member	NR1003-254	251.56-251.61 m	251.6	unstratified sand	white-grey medium-grained sandstone, unstratified, gradual lower contact	0.1	0.0	0.3	2.5
Basal member	NR1003-255	252.35-252.40 m	252.4	unstratified sand	white-grey medium-grained sandstone, unstratified, gradual lower contact	0.1	0.5	1.1	9.1
Basal member	NR1003-256	253.29-253.39 m	253.3	unstratified sand	light-grey clay-rich medium-coarse grained sandstone with crystalline rock clast(1 cm sized), unstratified, sharp lower contact	0.1	0.5	0.1	0.6

Table A.4 XRD-determined, 104 peak relative intensities of different carbonate mineral phases and d104 values (high Mg calcite and dolomite), NR1003 drill core.
Combined with C$_{carb}$ and CaCO$_3$ (wt%, calculated), weight percentage of different phases are quantified.

sample number	Relative intensity of 104 peak				Relative wt% ratios of mineral phases				Calculated carbonate content in wt%					d(104) values	
	I_calcite	I_Mg calcite	I_dolomite	I_aragonite	calcite	Mg calcite	dolomite	aragonite	C$_{carb}$	calcite	Mg calcite	dolomite	aragonite	Mg calcite	dolomite
	[XRD]	[XRD]	[XRD]	[XRD]					[wt%]	[wt%]	[wt%]	[wt%]	[wt%]	d$_{104}$	d$_{104}$
NR1003-13	2189	0	4205	0	0.34	0.00	0.66	0.00	10.45	29.81	0.00	52.41	0.00	-	2.905
NR1003-1	6817	0	1657	0	0.80	0.00	0.20	0.00	9.39	62.95	0.00	14.00	0.00	-	2.904
NR1003-14	556	0	292	0	0.66	0.00	0.34	0.00	1.04	5.68	0.00	2.73	0.00	-	2.905
NR1003-15	1197	0	5456	0	0.18	0.00	0.82	0.00	10.72	16.08	0.00	67.03	0.00	-	2.906
NR1003-18	2187	0	275	185	0.83	0.00	0.10	0.07	4.94	34.02	0.00	3.91	2.88	-	2.907
NR1003-19	0	492	0	0	0.00	1.00	0.00	0.00	0.47	0.00	3.25	0.00	0.00	3.019	-
NR-1003-20	0	1	0	0	0.00	1.00	0.00	0.00	9.97	0.00	68.96	0.00	0.00	3.018	-
NR-1003-21	2762	0	0	183	0.94	0.00	0.00	0.06	5.78	45.18	0.00	0.00	2.99	-	2.911
NR1003-22	1603	0	133	0	0.92	0.00	0.08	0.00	1.69	13.00	0.00	0.99	0.00	-	2.907
NR1003-23	0	4098	0	0	0.00	1.00	0.00	0.00	8.81	0.00	60.94	0.00	0.00	3.020	-
NR-1003-29	709	0	0	0	1.00	0.00	0.00	0.00	1.18	9.83	0.00	0.00	0.00	-	-
NR-1003-30	1768	0	0	0	1.00	0.00	0.00	0.00	2.28	19.00	0.00	0.00	0.00	-	-
NR-1003-31	301	0	0	523	0.37	0.00	0.00	0.63	1.33	4.05	0.00	0.00	7.04	-	-
NR-1003-32	298	0	0	375	0.44	0.00	0.00	0.56	1.24	4.57	0.00	0.00	5.76	-	-
NR-1003-33	381	0	1514	333	0.17	0.00	0.68	0.15	4.48	6.39	0.00	23.21	5.58	-	2.910
NR-1003-34	125	0	123	0	0.50	0.00	0.50	0.00	0.65	2.73	0.00	2.46	0.00	-	2.908
NR-1003-35	1522	0	283	0	0.84	0.00	0.16	0.00	2.60	18.27	0.00	3.11	0.00	-	2.907
NR-1003-36	0	0	1	0	0.00	0.00	1.00	0.00	10.17	0.00	0.00	77.55	0.00	-	2.904
NR-1003-38	1	0	0	0	1.00	0.00	0.00	0.00	1.84	15.33	0.00	0.00	0.00	-	-
NR1003-45	0	1	0	0	0.00	1.00	0.00	0.00	7.78	0.00	53.81	0.00	0.00	3.004	-
NR-1003-47	1014	1467	0	0	0.41	0.59	0.00	0.00	6.29	21.42	25.73	0.00	0.00	2.997	-
NR-1003-51	1	0	0	0	1.00	0.00	0.00	0.00	5.00	41.67	0.00	0.00	0.00	-	-

NR-1003-56	2241	0	0	178	0.93	0.00	0.00	0.07	3.84	29.65	0.00	0.00	2.35	-	-
NR-1003-57	0	1	0	0	0.00	1.00	0.00	0.00	2.09	0.00	14.46	0.00	0.00	3.022	-
NR-1003-58	0	1	0	0	0.00	1.00	0.00	0.00	2.23	0.00	15.42	0.00	0.00	3.003	-
NR1003-59	0	0	1	0	0.00	0.00	1.00	0.00	10.64	0.00	0.00	81.13	0.00	-	2.905
NR1003-62	0	1	0	0	0.00	1.00	0.00	0.00	2.72	0.00	18.81	0.00	0.00	3.024	-
NR-1003-64	0	0	0	0	0.00	0.00	0.00	0.00	0.00	0.00	0.00	0.00	0.00	-	-
NR1003-69	0	0	1	0	0.00	0.00	1.00	0.00	8.90	0.00	0.00	67.86	0.00	-	-
NR1003-74	1711	0	239	0	0.88	0.00	0.12	0.00	1.87	13.67	0.00	1.75	0.00	-	2.900
NR 1003-101	186	0	941	0	0.17	0.00	0.83	0.00	8.00	11.02	0.00	50.91	0.00	-	2.901
NR1003-75	0	0	1	0	0.00	0.00	1.00	0.00	10.89	0.00	0.00	83.04	0.00	-	2.903
NR1003-76	0	0	1	0	0.00	0.00	1.00	0.00	9.03	0.00	0.00	68.85	0.00	-	2.904
NR1003-78	1043	0	5271	0	0.17	0.00	0.83	0.00	8.89	12.24	0.00	56.59	0.00	-	2.907
NR-1003-79	782	0	3295	0	0.19	0.00	0.81	0.00	7.94	12.69	0.00	48.93	0.00	-	2.905
NR 1003-102	355	0	1114	0	0.24	0.00	0.76	0.00	9.20	18.51	0.00	53.21	0.00	-	2.904
NR1003-80	1859	0	2687	0	0.41	0.00	0.59	0.00	6.45	21.98	0.00	29.07	0.00	-	2.904
NR1003-81	1091	0	2135	0	0.34	0.00	0.66	0.00	3.88	10.94	0.00	19.58	0.00	-	2.904
NR 1003-103	247	0	524	0	0.32	0.00	0.68	0.00	4.03	10.76	0.00	20.88	0.00	-	2.905
NR 1003-104	147	96	492	0	0.20	0.13	0.67	0.00	4.79	7.98	4.34	24.44	0.00	3.012	2.909
NR 1003-105	73	0	517	0	0.12	0.00	0.88	0.00	5.41	5.61	0.00	36.12	0.00	-	2.909
NR 1003-106	43	0	773	0	0.05	0.00	0.95	0.00	3.69	1.60	0.00	26.67	0.00	-	2.908
NR 1003-107	420	0	1005	0	0.29	0.00	0.71	0.00	7.93	19.47	0.00	42.65	0.00	-	2.905
NR 1003-108	314	0	728	0	0.30	0.00	0.70	0.00	6.35	15.95	0.00	33.83	0.00	-	2.907
NR1003-2	252	0	6337	0	0.04	0.00	0.96	0.00	9.39	2.99	0.00	68.86	0.00	-	2.9086
NR 1003-109	152	0	1541	0	0.09	0.00	0.91	0.00	10.41	7.79	0.00	72.25	0.00	-	2.905
NR 1003-110	350	0	896	0	0.28	0.00	0.72	0.00	7.52	17.60	0.00	41.24	0.00	-	2.906
NR 1003-111	135	0	740	0	0.15	0.00	0.85	0.00	5.09	6.54	0.00	32.83	0.00	-	2.907
NR 1003-112	1022	0	42	0	0.96	0.00	0.04	0.00	3.61	28.91	0.00	1.07	0.00	-	2.908
NR 1003-113	131	0	632	0	0.17	0.00	0.83	0.00	4.87	6.96	0.00	30.76	0.00	-	2.906
NR 1003-114	0	0	1158	0	0.00	0.00	1.00	0.00	6.72	0.00	0.00	51.24	0.00	-	2.904
NR 1003-115	45	0	1410	0	0.03	0.00	0.97	0.00	10.22	2.62	0.00	75.53	0.00	-	2.903
NR 1003-116	48	44	1536	0	0.03	0.03	0.94	0.00	12.21	2.98	2.27	87.88	0.00	3.006	2.904

NR 1003-117	1014	0	0	0	1.00	0.00	0.00	0.00	4.55	37.92	0.00	0.00	0.00	-	-
NR 1003-118	940	782	0	0	0.55	0.45	0.00	0.00	4.60	20.93	14.44	0.00	0.00	3.024	-
NR 1003-119	93	96	943	0	0.08	0.08	0.83	0.00	10.33	7.07	6.05	65.63	0.00	3.008	2.909
NR 1003-120	64	112	858	0	0.06	0.11	0.83	0.00	7.74	3.99	5.81	48.97	0.00	3.005	2.908
NR 1003-121	0	103	684	0	0.00	0.13	0.87	0.00	7.38	0.00	6.69	48.89	0.00	3.023	2.904
NR 1003-122	781	0	116	0	0.87	0.00	0.13	0.00	4.14	30.06	0.00	4.06	0.00	-	2.904
NR 1003-123	154	186	106	0	0.35	0.42	0.24	0.00	3.14	9.05	9.05	5.68	0.00	3.013	2.914
NR1003-3	0	0	1	0	0.00	0.00	1.00	0.00	10.27	0.00	0.00	78.31	0.00	-	2.9011
NR 1003-124	0	0	1	0	0.00	0.00	1.00	0.00	8.90	0.00	0.00	67.86	0.00	-	2.901
NR 1003-125	0	0	1	0	0.00	0.00	1.00	0.00	7.62	0.00	0.00	58.10	0.00	-	2.895
NR 1003-126	0	0	1	0	0.00	0.00	1.00	0.00	8.96	0.00	0.00	68.32	0.00	-	2.894
NR 1003-127	0	0	1	0	0.00	0.00	0.24	0.00	9.00	0.00	0.00	16.47	0.00	-	2.904
NR 1003-128	2476	226	0	0	0.95	0.05	0.00	0.00	9.75	77.19	3.37	0.00	0.00	3.017	-
NR 1003-129	0	0	1	0	0.00	0.00	1.00	0.00	10.41	0.00	0.00	79.38	0.00	-	2.898
NR 1003-130	0	0	1	0	0.00	0.00	1.00	0.00	9.77	0.00	0.00	74.50	0.00	-	2.900
NR 1003-131	0	0	1	0	0.00	0.00	1.00	0.00	9.89	0.00	0.00	75.41	0.00	-	2.894
NR 1003-132	0	0	1	0	0.00	0.00	1.00	0.00	9.04	0.00	0.00	68.93	0.00	-	2.895
NR 1003-133	0	0	1	0	0.00	0.00	1.00	0.00	10.84	0.00	0.00	82.66	0.00	-	2.889
NR 1003-134	0	0	1	0	0.00	0.00	0.93	0.00	7.81	0.00	0.00	55.38	0.00	-	2.895
NR1003-4	0	0	1	0	0.00	0.00	1.00	0.00	10.73	0.00	0.00	81.82	0.00	-	2.89087
NR 1003-135	0	0	1	0	0.00	0.00	1.00	0.00	10.58	0.00	0.00	80.67	0.00	-	2.895
NR 1003-136	0	0	0	0	0.00	0.00	1.00	0.00	8.87	0.00	0.00	67.63	0.00	-	2.900
NR 1003-137	0	0	1	0	0.00	0.00	1.00	0.00	7.43	0.00	0.00	56.65	0.00	-	2.899
NR 1003-138	125	0	530	0	0.19	0.00	0.81	0.00	4.34	6.92	0.00	26.76	0.00	-	2.908
NR 1003-139	138	0	409	0	0.25	0.00	0.75	0.00	3.53	7.44	0.00	20.11	0.00	-	2.910
NR 1003-140	155	0	722	0	0.18	0.00	0.82	0.00	5.96	8.79	0.00	37.40	0.00	-	2.908
NR 1003-141	77	0	1451	0	0.05	0.00	0.95	0.00	9.12	3.82	0.00	66.04	0.00	-	2.906
NR 1003-142	136	0	1241	0	0.10	0.00	0.90	0.00	8.36	6.90	0.00	57.43	0.00	-	2.905
NR 1003-143	0	0	2398	0	0.00	0.00	1.00	0.00	10.26	0.00	0.00	78.23	0.00	-	2.895
NR1003-5	0	0	9322	0	0.00	0.00	1.00	0.00	11.95	0.00	0.00	91.12	0.00	-	2.905, 2.888
NR 1003-144	168	0	122	0	0.58	0.00	0.42	0.00	2.93	14.16	0.00	9.39	0.00	-	2.905

NR 1003-145	109	0	90	0	0.55	0.00	0.45	0.00	3.37	15.37	0.00	11.63	0.00	-	2.921
NR 1003-146	0	0	1	0	0.00	0.00	1.00	0.00	8.73	0.00	0.00	66.57	0.00	-	2.890
NR 1003-147	0	0	1	0	0.00	0.00	1.00	0.00	10.67	0.00	0.00	81.36	0.00	-	2.894
NR 1003-148	0	0	88	0	0.00	0.00	1.00	0.00	9.59	0.00	0.00	73.12	0.00	-	2.901
NR 1003-149	121	0	375	0	0.24	0.00	0.76	0.00	4.65	9.42	0.00	26.83	0.00	-	2.905
NR 1003-150	0	0	1	0	0.00	0.00	1.00	0.00	5.89	0.00	0.00	44.91	0.00	-	2.904
NR 1003-151	54	0	46	0	0.54	0.00	0.46	0.00	2.38	10.71	0.00	8.35	0.00	-	2.906
NR 1003-152	141	397	0	0	0.26	0.74	0.00	0.00	5.34	11.64	27.27	0.00	0.00	2.991	-
NR 1003-153	58	0	474	0	0.11	0.00	0.89	0.00	3.67	3.34	0.00	24.93	0.00	-	2.902
NR 1003-154	110	0	399	0	0.22	0.00	0.78	0.00	3.62	6.53	0.00	21.63	0.00	-	2.905
NR 1003-155	44	0	1337	0	0.03	0.00	0.97	0.00	6.79	1.79	0.00	50.14	0.00	-	2.901
NR 1003-156	0	0	100	0	0.00	0.00	1.00	0.00	10.06	0.00	0.00	76.71	0.00	-	2.898
NR 1003-157	105	0	79	0	0.57	0.00	0.43	0.00	2.91	13.81	0.00	9.55	0.00	-	2.910
NR 1003-158	119	129	397	0	0.19	0.20	0.62	0.00	3.95	6.09	5.45	18.54	0.00	3.012	2.909
NR 1003-159	0	0	1	0	0.00	0.00	1.00	0.00	6.73	0.00	0.00	51.32	0.00	-	2.901
NR1003-9	0	0	1	0	0.00	0.00	1.00	0.00	6.13	0.00	0.00	46.74	0.00	-	2.894
NR 1003-160	0	0	1	0	0.00	0.00	1.00	0.00	8.85	0.00	0.00	67.48	0.00	-	2.892
NR 1003-161	1	0	0	0	1.00	0.00	0.00	0.00	1.96	16.33	0.00	0.00	0.00	-	-
NR 1003-162	39	0	940	0	0.04	0.00	0.96	0.00	6.00	1.98	0.00	43.94	0.00	-	2.900
NR 1003-163	0	117	157	0	0.00	0.43	0.57	0.00	4.13	0.00	12.20	18.04	0.00	3.005	2.909
NR 1003-164	80	102	207	0	0.21	0.26	0.53	0.00	4.04	6.93	7.34	16.38	0.00	2.995	2.912
NR 1003-165	88	0	130	0	0.40	0.00	0.60	0.00	2.64	8.90	0.00	11.99	0.00	-	2.919
NR 1003-166	0	0	1	0	0.00	0.00	1.00	0.00	6.49	0.00	0.00	49.49	0.00	-	2.903
NR 1003-167	110	0	710	0	0.13	0.00	0.87	0.00	4.52	5.07	0.00	29.83	0.00	-	2.900
NR 1003-168	44	0	614	0	0.07	0.00	0.93	0.00	4.94	2.74	0.00	35.16	0.00	-	2.896
NR 1003-169	242	0	423	0	0.36	0.00	0.64	0.00	3.59	10.88	0.00	17.42	0.00	-	2.904
NR 1003-170	0	0	1	0	0.00	0.00	1.00	0.00	9.72	0.00	0.00	74.12	0.00	-	2.899
NR 1003-171	0	0	89	0	0.00	0.00	1.00	0.00	8.76	0.00	0.00	66.80	0.00	-	2.903
NR 1003-172	103	0	844	0	0.11	0.00	0.89	0.00	5.89	5.32	0.00	40.04	0.00	-	2.905
NR 1003-173	0	0	1	0	0.00	0.00	1.00	0.00	7.58	0.00	0.00	57.80	0.00	-	2.901
NR 1003-174	98	0	690	0	0.12	0.00	0.88	0.00	6.18	6.41	0.00	41.26	0.00	-	2.901

NR 1003-175	0	144	233	0	0.00	0.38	0.62	0.00	4.28	0.00	11.28	20.20	0.00	3.007	2.908
NR 1003-176	0	0	1	0	0.00	0.00	1.00	0.00	5.36	0.00	0.00	40.87	0.00	2.979	2.919
NR 1003-177	54	0	1023	0	0.05	0.00	0.95	0.00	5.31	2.21	0.00	38.47	0.00	-	2.901
NR 1003-178	122	0	476	0	0.20	0.00	0.80	0.00	3.77	6.42	0.00	22.87	0.00	-	2.902
NR 1003-179	51	0	766	0	0.06	0.00	0.94	0.00	4.07	2.10	0.00	29.11	0.00	-	2.901
NR 1003-180	13	0	114	0	0.10	0.00	0.90	0.00	3.73	3.21	0.00	25.50	0.00	-	2.904
NR 1003-181	80	0	642	0	0.11	0.00	0.89	0.00	4.42	4.06	0.00	29.99	0.00	-	2.905
NR 1003-182	46	0	346	0	0.12	0.00	0.88	0.00	2.46	2.38	0.00	16.58	0.00	-	2.905
NR 1003-183	63	0	393	0	0.14	0.00	0.86	0.00	3.01	3.46	0.00	19.78	0.00	-	2.905
NR 1003-184	40	0	448	0	0.08	0.00	0.92	0.00	2.64	1.81	0.00	18.48	0.00	-	2.905
NR 1003-185	128	0	348	0	0.27	0.00	0.73	0.00	2.62	5.86	0.00	14.62	0.00	-	2.904
NR 1003-186	102	0	409	0	0.20	0.00	0.80	0.00	4.74	7.87	0.00	28.94	0.00	-	2.907
NR 1003-187	66	0	841	0	0.07	0.00	0.93	0.00	6.22	3.76	0.00	43.98	0.00	-	2.909
NR 1003-188	82	0	570	0	0.13	0.00	0.88	0.00	4.37	4.60	0.00	29.32	0.00	-	2.902
NR 1003-189	46	0	873	0	0.05	0.00	0.95	0.00	5.57	2.31	0.00	40.36	0.00	-	2.904
NR 1003-190	0	0	1	0	0.00	0.00	1.00	0.00	2.23	0.00	0.00	17.00	0.00	-	2.902
NR 1003-191	69	0	418	0	0.14	0.00	0.83	0.00	3.22	3.80	0.00	20.38	0.00	-	2.900
NR 1003-192	56	0	470	0	0.11	0.00	0.89	0.00	3.04	2.71	0.00	20.70	0.00	-	2.902
NR 1003-193	0	0	1	0	0.00	0.00	1.00	0.00	3.30	0.00	0.00	25.16	0.00	-	2.903
NR 1003-194	0	0	1	0	0.00	0.00	1.00	0.00	4.16	0.00	0.00	31.72	0.00	-	2.903
NR 1003-195	0	0	1411	0	0.00	0.00	1.00	0.00	6.67	0.00	0.00	50.86	0.00	-	2.904
NR 1003-196	0	0	820	0	0.00	0.00	1.00	0.00	4.18	0.00	0.00	31.87	0.00	-	2.905
NR 1003-197	0	0	761	0	0.00	0.00	1.00	0.00	5.12	0.00	0.00	39.04	0.00	-	2.904
NR 1003-198	148	0	629	0	0.19	0.00	0.81	0.00	4.59	7.29	0.00	28.33	0.00	-	2.906
NR 1003-199	122	0	363	0	0.25	0.00	0.75	0.00	2.21	4.64	0.00	12.61	0.00	-	2.905
NR 1003-200	0	0	492	93	0.00	0.00	0.84	0.16	3.58	0.00	0.00	22.96	4.74	-	2.908
NR 1003-201	84	0	410	0	0.17	0.00	0.83	0.00	2.73	3.86	0.00	17.29	0.00	-	2.906
NR 1003-202	0	0	394	0	0.00	0.00	1.00	0.00	2.80	0.00	0.00	21.35	0.00	-	2.907
NR 1003-203	0	0	978	0	0.00	0.00	1.00	0.00	5.78	0.00	0.00	44.07	0.00	-	2.906
NR 1003-204	85	0	470	0	0.15	0.00	0.85	0.00	4.09	5.23	0.00	26.40	0.00	-	2.909
NR 1003-205	78	0	466	0	0.14	0.00	0.86	0.00	4.48	5.38	0.00	29.24	0.00	-	2.907

NR 1003-206	76	0	303	217	0.13	0.00	0.51	0.36	3.72	3.95	0.00	14.42	11.29	-	2.910
NR 1003-207		0	1	0	0.00	0.00	1.00	0.00	2.50	0.00	0.00	19.06	0.00	-	2.906
NR 1003-208	66	0	486	0	0.12	0.00	0.88	0.00	3.21	3.22	0.00	21.53	0.00	-	2.908
NR 1003-209	84	0	515	0	0.14	0.00	0.86	0.00	3.94	4.61	0.00	25.82	0.00	-	2.908
NR 1003-210	98	0	447	111	0.15	0.00	0.68	0.17	4.05	5.06	0.00	21.04	5.69	-	2.909
NR 1003-211	0	0	273	124	0.00	0.00	0.69	0.31	3.13	0.00	0.00	16.40	8.16	-	2.908
NR 1003-212	0	0	314	304	0.00	0.00	0.51	0.49	4.14	0.00	0.00	16.04	16.98	-	2.912
NR 1003-213	0	0	867	67	0.00	0.00	0.93	0.07	5.12	0.00	0.00	36.24	3.06	-	2.908
NR 1003-214	0	0	903	0	0.00	0.00	1.00	0.00	5.43	0.00	0.00	41.40	0.00	-	2.907
NR 1003-215	0	0	1	0	0.00	0.00	1.00	0.00	2.56	0.00	0.00	19.52	0.00	-	2.910
NR 1003-216	0	0	1331	0	0.00	0.00	1.00	0.00	7.39	0.00	0.00	56.35	0.00	-	2.911
NR 1003-217	50	0	486	256	0.06	0.00	0.61	0.32	4.05	2.12	0.00	18.96	10.90	-	2.913
NR 1003-218	0	0	977	0	0.00	0.00	1.00	0.00	5.51	0.00	0.00	42.01	0.00	-	2.911
NR 1003-219	0	0	1	0	0.00	0.00	1.00	0.00	7.17	0.00	0.00	54.67	0.00	-	2.903
NR 1003-220	0	0	1	0	0.00	0.00	1.00	0.00	5.56	0.00	0.00	42.40	0.00	-	2.911
NR 1003-221	0	0	1	0	0.00	0.00	1.00	0.00	3.13	0.00	0.00	23.87	0.00	-	2.903
NR 1003-222	0	0	1	0	0.00	0.00	1.00	0.00	9.31	0.00	0.00	70.99	0.00	-	2.906
NR 1003-223	0	0	1	0	0.00	0.00	1.00	0.00	9.04	0.00	0.00	68.93	0.00	-	2.897
NR 1003-224	0	1	0	0	0.00	1.00	0.00	0.00	1.44	0.00	9.96	0.00	0.00	2.971	-
NR 1003-225	0	0	1	0	0.00	0.00	1.00	0.00	7.90	0.00	0.00	60.24	0.00	-	2.892
NR 1003-226	0	0	1	0	0.00	0.00	1.00	0.00	11.07	0.00	0.00	84.41	0.00	-	2.890
NR 1003-227	0	0	1	0	0.00	0.00	1.00	0.00	10.87	0.00	0.00	82.88	0.00	-	2.892
NR 1003-228	0	0	1	0	0.00	0.00	1.00	0.00	10.20	0.00	0.00	77.78	0.00	-	2.892
NR 1003-229	0	0	1	0	0.00	0.00	1.00	0.00	9.48	0.00	0.00	72.29	0.00	-	2.895
NR 1003-230	0	0	1	0	0.00	0.00	1.00	0.00	10.78	0.00	0.00	82.20	0.00	-	2.889
NR 1003-231	0	0	1	0	0.00	0.00	1.00	0.00	10.96	0.00	0.00	83.57	0.00	-	2.897
NR 1003-232	0	0	1	0	0.00	0.00	1.00	0.00	11.79	0.00	0.00	89.90	0.00	-	2.893
NR 1003-233	0	0	1	0	0.00	0.00	1.00	0.00	11.43	0.00	0.00	87.15	0.00	-	2.904
NR 1003-234	1	0	0	0	1.00	0.00	0.00	0.00	7.42	61.83	0.00	0.00	0.00	-	2.908
NR 1003-235	2501	0	45	0	0.98	0.00	0.02	0.00	9.47	77.51	0.00	1.28	0.00	-	2.904
NR 1003-236	759	60	1064	0	0.40	0.03	0.57	0.00	9.69	32.56	2.12	41.76	0.00	3.009	2.906

ID															
NR 1003-237	297	0	1422	0	0.17	0.00	0.83	0.00	11.82	17.04	0.00	74.53	0.00	-	2.904
NR 1003-238W	1360	0	551	0	0.71	0.00	0.29	0.00	8.90	52.77	0.00	19.58	0.00	-	2.907
NR 1003-238B	2166	0	325	0	0.87	0.00	0.13	0.00	10.68	77.40	0.00	10.62	0.00	-	2.909
NR 1003-239	2349	0	74	0	0.97	0.00	0.03	0.00	8.59	69.41	0.00	1.99	0.00	-	2.908
NR 1003-240	0	0	1	0	0.00	0.00	1.00	0.00	0.55	0.00	0.00	4.19	0.00	-	2.901
NR 1003-241	0	0	1	0	0.00	0.00	1.00	0.00	0.47	0.00	0.00	3.58	0.00	-	-
NR 1003-242	0	0	1	0	0.00	0.00	1.00	0.00	1.90	0.00	0.00	14.49	0.00	-	2.900
NR 1003-243	0	0	1	0	0.00	0.00	1.00	0.00	2.40	0.00	0.00	18.30	0.00	-	2.904
NR 1003-244	200	0	89	0	0.69	0.00	0.31	0.00	0.77	4.44	0.00	1.81	0.00	-	2.900
NR 1003-245	200	0	431	0	0.32	0.00	0.68	0.00	1.80	4.75	0.00	9.38	0.00	-	2.905
NR 1003-246	1428	0	214	0	0.87	0.00	0.13	0.00	5.20	37.68	0.00	5.17	0.00	-	2.903
NR 1003-247	2370	0	102	0	0.96	0.00	0.04	0.00	9.85	78.68	0.00	3.11	0.00	-	2.903
NR1003-10	9601	0	497	0	0.95	0.00	0.05	0.00	9.62	76.22	0.00	3.61	0.00	-	2.9033
NR 1003-248	2146	0	152	0	0.93	0.00	0.07	0.00	10.29	80.08	0.00	5.18	0.00	-	2.904
NR 1003-249	2673	0	84	0	0.97	0.00	0.03	0.00	11.21	90.57	0.00	2.61	0.00	-	2.903
NR 1003-250	1543	0	181	0	0.89	0.00	0.11	0.00	7.19	53.62	0.00	5.76	0.00	-	2.909
NR 1003-251	617	0	451	0	0.58	0.00	0.42	0.00	4.69	22.57	0.00	15.11	0.00	-	2.908
NR 1003-252	739	0	344	0	0.68	0.00	0.32	0.00	4.37	24.84	0.00	10.60	0.00	-	2.906
NR 1003-253	0	0	1	0	0.00	0.00	1.00	0.00	1.38	0.00	0.00	10.52	0.00	-	2.906
NR 1003-254	0	0	1	0	0.00	0.00	1.00	0.00	0.30	0.00	0.00	2.29	0.00	-	2.907
NR 1003-255	1	0	0	0	1.00	0.00	0.00	0.00	1.09	9.08	0.00	0.00	0.00	-	-
NR 1003-256	0	0	0	0	0.00	0.00	0.00	0.00	0.07	0.00	0.00	0.00	0.00	-	-

Table A.5 XRD semi-quantified results of the non-carbonate mineral phases.

lithostratigraphy	sample	depth	depth (plot)	analcime	quartz	clay minerals	iron sulfide	gypsum*	feldspar
				[semi-quantative calculation by XRD]					
	number	[m.b.s.]	[m.b.s.]	[wt%]	[wt%]	[wt%]	[wt%]	[wt%]	[wt%]
Clay member	NR1003-12	14.00-14.20 m	14	-	-	-	-	-	-
Clay member	NR1003-13	14.20-14.44 m	14.2	0	0-5	5-10	0	-	-
Clay member	NR1003-1	14.25-14.28 m	14.3	0	0-5	10-20	0	-	-
Clay member	NR1003-14	14.44-14.47 m	14.4	0	50-60	20-30	0	-	-
Clay member	NR1003-15	14.47-14.58 m	14.5	0	0-5	0-10	0	0-5	-
Clay member	NR1003-16	14.58-14.83 m	14.6	-	-	-	-	-	-
Clay member	NR1003-17	15.00-15.15 m	15	-	-	-	-	-	-
Clay member	NR1003-18	15.15-15.65 m	15.2	0	0-5	20-30	0	20-30	-
Clay member	NR1003-19	15.65-15.85 m	15.7	0	35-45	20-40	0	15-25	-
Clay member	NR1003-20	15.85-15.90 m	15.9	0	0-5	15-25	0	-	-
Clay member	NR1003-21	15.90-16.00 m	16	0	10-20	10-20	0	0-10	-
Clay member	NR1003-22	16.00-16.40 m	16.2	0	25-35	15-25	0-5	25-35	-
Clay member	NR1003-23	16.40-16.50 m	16.5	0	5-10	10-20	0	0-10	-

Clay member	NR1003-24	16.50-16.90 m	16.5	-	-	-	-	-	-
Clay member	NR1003-25	16.90-17.00 m	16.9	-	-	-	-	-	-
Clay member	NR1003-26	17.00-17.75 m	17	-	-	-	-	-	-
Clay member	NR1003-27	17.75-18.00 m	17.8	-	-	-	-	-	-
Clay member	NR1003-28	18.00-18.70 m	18	-	-	-	-	-	-
Clay member	NR1003-29	20.00-20.20 m	20	0	35-45	15-25	0	15-25	-
Clay member	NR1003-30	20.20-20.40 m	20.2	0	15-20	10-20	0	30-40	-
Clay member	NR1003-31	20.40-21.00 m	20.4	0	35-45	15-25	0	20-30	-
Clay member	NR1003-32	22.00-22.80 m	22	0	30-40	20-30	0	20-30	-
Clay member	NR1003-33	22.80-22.83 m	22.8	0	10-20	10-20	0	25-35	-
Clay member	NR1003-34	22.83-23.00 m	22.9	0	30-40	30-40	0	10-20	-
Clay member	NR1003-35	23.00-23.20 m	23	0	10-20	30-40	0	15-25	-
Clay member	NR1003-36	23.20-23.70 m	23.2	0	0-5	0-5	0	10-20	-
Clay member	NR1003-37	23.70-24.00 m	23.7	-	-	-	-	-	-
Clay member	NR1003-38	24.00-25.00 m	24	0	35-45	15-25	0-5	10-20	-
Clay member	NR1003-39	25.00-26.00 m	25	-	-	-	-	-	-

Clay member	NR1003-40	26.00-27.00 m	26	-	-	-	-	-	-
Clay member	NR1003-41	28.50-29.00 m	28.5	-	-	-	-	-	-
Clay member	NR1003-42	29.00-29.45 m	29	-	-	-	-	-	-
Clay member	NR1003-43	29.45-29.95 m	29.5	-	-	-	-	-	-
Clay member	NR1003-44	29.95-30.00 m	29.95	-	-	-	-	-	-
Clay member	NR1003-45	30.00-30.05 m	30	0	0-5	0-10	5-15	10-20	-
Clay member	NR1003-46	30.05-30.20 m	30.1	-	-	-	-	-	-
Clay member	NR1003-47	30.20-30.38 m	30.2	0	0	0	0	40-50	-
Clay member	NR1003-48	30.38-31.00 m	30.4	-	-	-	-	-	-
Clay member	NR1003-49	31.00-31.07 m	31	-	-	-	-	-	-
Clay member	NR1003-50	31.07-31.08 m	31.1	-	-	-	-	-	-
Clay member	NR1003-51	31.08-31.25 m	32.2	0	0-5	10-20	20-25	-	-
Clay member	NR1003-52	31.25-31.30 m	31.3	-	-	-	-	-	-
Clay member	NR1003-53	31.30-31.60 m	31.5	-	-	-	-	-	-
Clay member	NR1003-54	31.60-31.88 m	31.7	-	-	-	-	-	-
Clay member	NR1003-55	31.88-32.00 m	31.9	-	-	-	-	-	-

Clay member	NR1003-56	32.00-32.05 m	32	0	10-20	5-15	5-10	5-10	-
Clay member	NR1003-57	32.05-32.60 m	32.3	0	15-25	15-25	10-20	15-20	-
Clay member	NR1003-58	32.60-33.30 m	32.8	0	20-30	20-30	10-20	0-10	-
Clay member	NR1003-59	33.30-33.38 m	33.3	0	0-5	0-5	<1	0-10	-
Clay member	NR1003-60	33.38-33.60 m	33.5	-	-	-	-	-	-
Clay member	NR1003-61	34.00-34.70 m	34.4	-	-	-	-	-	-
Clay member	NR1003-62	34.70-35.00 m	34.7	0	15-25	15-25	5-10	15-25	-
Clay member	NR1003-63	35.00-35.07 m	35	-	-	-	-	-	-
Clay member	NR1003-64	35.07-35.08 m	35.1	-	-	-	-	-	-
Clay member	NR1003-65	35.08-35.50 m	35.3	-	-	-	-	-	-
Clay member	NR1003-66	35.50-35.70 m	35.6	-	-	-	-	-	-
Clay member	NR1003-67	35.70-36.00 m	35.8	-	-	-	-	-	-
Clay member	NR1003-68	36.00-36.05 m	36	-	-	-	-	-	-
Clay member	NR1003-69	36.05-36.08 m	36.05	0	5-10	5-15	<1	5-10	-
Clay member	NR1003-70	36.08-36.45 m	36.2	-	-	-	-	-	-
Clay member	NR1003-71	36.45-36.66 m	36.5	-	-	-	-	-	-

Clay member	NR1003-72	36.66-37.00 m	36.8	-	-	-	-	-	-
Clay member	NR1003-73	37.00-38.00 m	37.5	-	-	-	-	-	-
Clay member	NR1003-74	38.00-38.70 m	38.4	0	10-15	25-40	0	20-30	-
dolomite-marl smbr	NR1003-101	38.69-38.74 m	38.7	0	10-15	5-10	0	10-20	-
dolomite-marl smbr	NR1003-75	38.70-38.92 m	38.8	0	5-10	<5	0	0-10	-
dolomite-marl smbr	NR1003-76	38.92-39.00 m	38.9	0	5-15	10-20	0	-	-
dolomite-marl smbr	NR1003-77	39.00-39.30 m	39.2	-	-	-	-	-	-
dolomite-marl smbr	NR1003-78	39.30-39.45 m	39.3	0-5	10-15	5-10	0-5	-	-
dolomite-marl smbr	NR1003-79	39.45-39.70 m	39.6	0-5	10-15	10-25	0	-	-
dolomite-marl smbr	NR1003-102	39.70-39.75 m	39.7	0-5	5-10	10-25	0	-	-
dolomite-marl smbr	NR1003-80	39.70-40.07 m	39.8	5-10	10-15	15-25	0	-	-
dolomite-marl smbr	NR1003-81	40.07-40.50 m	40.2	9-15	15-20	20-30	0-5	-	-
dolomite-marl smbr	NR1003-103	42.51-42.54 m	42.5	0	15-20	20-30	5-10	-	-
dolomite-marl smbr	NR1003-104	44.41-44.43 m	44.4	0	20-30	20-30	0	-	-
dolomite-marl smbr	NR1003-105	46.31-46.33 m	46.3	0-5	25-35	10-25	0	-	-
dolomite-marl smbr	NR1003-106	47.27-47.30 m	47.3	10-15	25-35	10-25	0	5-10	-

dolomite-marl smbr	NR1003-107	48.32-48.36 m	48.3	0-5	10-15	20-30	0	-	-
dolomite-marl smbr	NR1003-108	50.80-50.85 m	50.8	0	0	35-45	0	0-5	-
dolomite-marl smbr	NR1003-2	52.19-52.20 m	52.2	0	5-10	10-15	0	-	-
dolomite-marl smbr	NR1003-109	52.73-52.75 m	52.7	0	10-15	0-5	0	-	-
dolomite-marl smbr	NR1003-110	53.09-53.11 m	53.1	0-5	15-25	25-50	0	-	-
dolomite-marl smbr	NR1003-111	54.08-54.10 m	54.1	0	25-35	5-15	0	-	-
dolomite-marl smbr	NR1003-112	57.84-57.86 m	57.8	0	25-35	10-25	5-10	-	-
dolomite-marl smbr	NR1003-113	58.85-58.87 m	58.9	0-5	35-40	10-25	0	-	-
dolomite-marl smbr	NR1003-114	59.66-59.70 m	59.7	0	30-40	5-10	0	-	-
dolomite-marl smbr	NR1003-115	62.00-62.04 m	62	0	10-15	0-5	0	-	-
dolomite-marl smbr	NR1003-116	63.05-63.07 m	63	0	0-5	0	0	-	-
dolomite-marl smbr	NR1003-117	64.04-64.07 m	64	0	10-20	10-20	0-5	-	-
dolomite-marl smbr	NR1003-118	65.09-65.11 m	65	0	10-20	10-20	0-5	-	-
dolomite-marl smbr	NR1003-119	66.55-66.57 m	66.6	0	5-10	5-10	0	-	-
dolomite-marl smbr	NR1003-120	67.03-67.05 m	67	0	20-30	5-10	0	-	-
dolomite-marl smbr	NR1003-121	68.71-68.72 m	68.7	0-5	20-25	10-25	0	-	-

dolomite-marl smbr	NR1003-122	70.46-70.47 m	70.5	0	30-35	15-25	-	-	-
dolomite-marl smbr	NR1003-123	72.67-72.68 m	72.7	0	50-65	15-25	0	-	-
varicolored-marl smbr.	NR1003-3	74.43-74.45 m	74.4	0	10-15	5-10	0	-	-
varicolored-marl smbr.	NR1003-124	74.73-74.76 m	74.7	0	20-30	0-10	0	-	-
varicolored-marl smbr.	NR1003-125	75.67-75.69 m	75.7	0	20-30	0-10	0	-	-
varicolored-marl smbr.	NR1003-126	75.84-75.85 m	75.8	0	15-20	0-10	0	-	-
varicolored-marl smbr.	NR1003-127	76.27-76.29 m	76.2	0	25-30	0-10	-	-	-
varicolored-marl smbr.	NR1003-128	76.62-76.65 m	76.6	0	5-10	5-10	0	-	-
varicolored-marl smbr.	NR1003-129	78.29-78.31 m	78.3	0	5-10	5-10	0	-	-
varicolored-marl smbr.	NR1003-130	79.46-79.47 m	79.5	0	5-15	0-5	0	0-5	-
varicolored-marl smbr.	NR1003-131	80.26-80.29 m	80.3	0	20-25	0-5	0	-	-
varicolored-marl smbr.	NR1003-132	82.06-82.08 m	82	0	25-35	0-5	0	-	-
varicolored-marl smbr.	NR1003-133	83.69-83.72 m	83.7	0	0-10	0-5	0	-	-
varicolored-marl smbr.	NR1003-134	84.90-84.91 m	84.9	0	20-25	15-20	0	-	-
varicolored-marl smbr.	NR1003-4	85.41-85.43 m	85.4	0	5-10	5-15	0	-	-
varicolored-marl smbr.	NR1003-135	85.88-85.91 m	85.9	0	10-20	0-5	0	-	-

varicolored-marl smbr.	NR1003-136	86.66-86.68 m	86.7	0	30-40	0-5	0	-	-
diatom smbr	NR1003-137	87.68-87.69 m	87.7	0	25-35	5-15	0	-	-
diatom smbr	NR1003-138	89.17-89.18 m	89.2	0-5	~50	15-25	0	-	-
diatom smbr	NR1003-139	91.31-91.32 m	93.1	0-5	45-50	15-25	0	-	-
diatom smbr	NR1003-140	93.39-93.41 m	93.4	0	20-30	5-15	0	-	-
diatom smbr	NR1003-141	94.17-94.18 m	94.2	0	15-25	0-10	0	-	-
diatom smbr	NR1003-142	94.83-94.84 m	94.8	0	10-20	10-20	0	-	-
diatom smbr	NR1003-143	95.12-95.14 m	95.1	0	10-20	10-20	0	-	-
diatom smbr	NR1003-5	98.10-98.14 m	98.1	0	0-5	0-5	0	-	-
diatom smbr	NR1003-144	100.07-100.09 m	100.1	0-5	50-55	15-25	0	-	-
diatom smbr	NR1003-145	102.08-102.09 m	102.1	0-5	40-50	20-35	0	-	-
diatom smbr	NR1003-146	103.30-103.32 m	103.3	0-5	15-20	5-10	0	-	-
diatom smbr	NR1003-147	105.30-105.32 m	105.3	0	5-15	0-10	0	-	-
diatom smbr	NR1003-6	105.325-105.34 m	105.3	-	-	-	-	-	-
diatom smbr	NR1003-148	107.05-107.06 m	107.1	0	5-15	0-10	0	-	-
diatom smbr	NR1003-149	109.00-109.02 m	109	0-5	55-60	5-10	0	-	-

diatom smbr	NR1003-150	111.05 -111.06 m	111.1	0	45-55	0-5	0	-	-
diatom smbr	NR1003-151	111.82-111.84 m	111.8	0-5	60-65	15-20	0	-	-
diatom smbr	NR1003-152	112.56-112.57 m	112.6	0-5	50-55	10-15	0	-	-
diatom smbr	NR1003-153	113.46-113.47 m	113.5	0-5	55-60	10-15	0	-	-
diatom smbr	NR1003-7	113.67-113.675	113.65					-	-
diatom smbr	NR1003-154	114.58-114.60 m	114.6	0-5	~50	15-20	0	-	-
diatom smbr	NR1003-155	116.53-116.55 m	116.5	0-5	25-30	10-15	0	-	-
diatom smbr	NR1003-156	116.74-116.75 m	116.7	0-5	15-20	0-5	0	-	-
diatom smbr	NR1003-157	118.74-118.75 m	118.7	10-15	55-60	15-20	0	-	-
diatom smbr	NR1003-158	119.91-119.93 m	119.9	~1	50-55	10-15	0	-	-
diatom smbr	NR1003-159	121.55-121.57 m	121.55	~2	35-40	10-15	0	-	-
diatom smbr	NR1003-8	121.59-121.60 m	121.6	-	-	-	-	-	-
diatom smbr	NR1003-9	123.59-123.60 m	123.6	0-5	30-40	10-20	0	-	-
diatom smbr	NR1003-160	123.75-123.77 m	123.8	0	20-30	0-10	0	-	-
bituminous smbr	NR1003-161	125.55-125.56 m	125.6	0	45-55	20-30	-	-	-
bituminous smbr	NR1003-162	128.73-128.76 m	128.7	0	40-50	10-15	0	-	-

bituminous smbr	NR1003-163	129.56-129.57 m	129.6	0	50-60	15-25	0	-	-
bituminous smbr	NR1003-164	131.64-131.66 m	131.6	0	50-65	10-20	0	-	-
bituminous smbr	NR1003-165	133.58-133.60 m	133.6	0	60-70	10-20	0	-	-
bituminous smbr	NR1003-166	135.85-135.86 m	135.9	0-5	25-30	5-10	0	-	-
bituminous smbr	NR1003-167	137.47-137.49 m	137.5	~5	40-45	10-15	0	-	-
bituminous smbr	NR1003-168	138.62-138.63 m	138.6	~2	45-50	10-15	0	-	-
bituminous smbr	NR1003-169	140.05-140.07 m	140	5-10	50-55	15-20	0	-	-
bituminous smbr	NR1003-170	142.79-142.81 m	142.8	0-5	10-25	0-5	0	-	-
bituminous smbr	NR1003-171	143.17-143.19 m	143.2	0-5	10-20	0-5	0	-	-
bituminous smbr	NR1003-172	146.27-146.29 m	146.3	~2	25-30	25-35	0	-	-
bituminous smbr	NR1003-173	147.77-147.80 m	147.8	0	20-30	10-15	0	-	-
bituminous smbr	NR1003-174	148.45-148.46 m	148.5	0	35-45	10-20	0	-	-
bituminous smbr	NR1003-175	149.31-149.34 m	149.3	0	45-55	15-25	0	-	-
bituminous smbr	NR1003-176	150.39-150.40 m	150.4	0	35-45	10-20	0	-	-
bituminous smbr	NR1003-177	152.52-152.53 m	152.5	0-5	50-55	10-15	-	-	-
bituminous smbr	NR1003-178	152.63-152.64 m	152.6	0-5	50-55	15-20	0	-	-

bituminous smbr	NR1003-179	153.46-153.47 m	153.5	0-5	45-50	15-20	0	-	-
bituminous smbr	NR1003-180	155.14-155.16 m	155.1	0-5	45-50	10-15	0	-	-
bituminous smbr	NR1003-181	155.70-155.73 m	155.7	0-5	40-45	10-15	0	-	-
bituminous smbr	NR1003-182	156.15-156.17 m	156.2	~2	60-65	10-15	0	-	-
bituminous smbr	NR1003-183	157.24-157.26 m	157.2	0-5	50-60	10-20	0	-	-
bituminous smbr	NR1003-184	159.42-159.43 m	159.4	0-5	50-55	10-20	0	-	-
bituminous smbr	NR1003-185	161.15-161.16 m	161.2	0-5	50-60	10-20	0	-	-
bituminous smbr	NR1003-186	164.75-164.76 m	164.8	5-10	45-50	10-20	0	-	-
bituminous smbr	NR1003-187	165.96-165.98 m	166	0-5	25-30	10-15	0	-	-
bituminous smbr	NR1003-188	167.70-167.71 m	167.7	~15	35-40	15-20	0	-	-
bituminous smbr	NR1003-189	168.32-168.34 m	168.3	5-10	25-35	5-10	0	-	-
analcime smbr	NR1003-190	169.14-169.15 m	169.1	0-5	55-65	10-15	0	-	0-5
analcime smbr	NR1003-191	171.64-171.66 m	171.6	5-10	65-70	10-15	0	-	0-5
analcime smbr	NR1003-192	173.55-173.56 m	173.6	5-10	55-65	10-15	0	-	-
analcime smbr	NR1003-193	175.88-175.89 m	175.9	~5	50-55	15-20	0	-	0-5
analcime smbr	NR1003-194	176.95-176.96 m	177	~5	40-45	10-20	0	-	0-5

analcime smbr	NR1003-195	178.02-178.03 m	178	0-5	25-30	10-15	0	-	0-5
analcime smbr	NR1003-196	178.77-178.78 m	178.8	~5	50-60	10-15	0	-	0-5
analcime smbr	NR1003-197	181.91-181.93 m	181.9	10-15	35-40	10-15	0	-	-
analcime smbr	NR1003-198	183.55-183.57 m	183.6	15-20	30-40	15-20	0	-	-
analcime smbr	NR1003-199	185.20-185.22 m	185.2	~15	55-60	10-20	0	-	-
analcime smbr	NR1003-200	187.41-187.42 m	187.4	~10	40-45	10-20	0	-	-
analcime smbr	NR1003-201	188.93-188.95 m	188.9	15-20	45-50	10-20	0	-	-
analcime smbr	NR1003-202	190.68-190.69 m	190.7	10-15	35-45	15-20	0	-	-
analcime smbr	NR1003-203	191.51-191.52 m	191.5	5-10	20-25	15-25	0	-	-
analcime smbr	NR1003-82	192.61-192.65 m	192.6	-	-	-	-	-	-
analcime smbr	NR1003-204	193.84-193.86 m	193.8	15-20	45-55	5-15	0	-	-
analcime smbr	NR1003-205	194.38-194.40 m	194.4	15-20	35-45	5-10	0	-	-
analcime smbr	NR1003-206	196.68-196.70 m	196.7	15-20	30-35	15-30	0	-	-
analcime smbr	NR1003-207	197.46-196.48 m	197.5	~15	40-50	5-10	0	-	-
analcime smbr	NR1003-208	199.24-199.26 m	199.2	15-20	30-40	10-20	0	-	-
analcime smbr	NR1003-209	200.20-200.22 m	200.2	15-20	50-55	5-10	0	-	-

analcime smbr	NR1003-210	202.74-202.76 m	202.7	20-25	25-35	10-20	0	-	-
analcime smbr	NR1003-211	204.00-204.02 m	204	10-15	35-40	10-20	0	-	-
analcime smbr	NR1003-212	205.01-205.03 m	205	15-20	20-30	15-25	0	-	-
analcime smbr	NR1003-213	206.38-206.39 m	206.4	10-15	25-35	10-20	0	-	-
analcime smbr	NR1003-214	207.38-207.39 m	207.4	10-15	30-35	10-20	0	-	-
analcime smbr	NR1003-215	209.30-209.75 m	209.3	10-15	35-40	15-30	0	-	-
analcime smbr	NR1003-216	210.83-210.85 m	210.8	5-10	10-20	10-30	0	-	-
analcime smbr	NR1003-217	211.08-211.09 m	211.1	15-25	25-35	10-30	0	-	-
analcime smbr	NR1003-218	212.74-212.75 m	212.7	5-10	25-30	10-20	0	-	-
analcime smbr	NR1003-219	213.24-213.25 m	213.2	25-40	10-20	5-10	0	-	-
analcime smbr	NR1003-220	214.63-214.65 m	214.6	5-10	20-40	10-30	0	-	-
analcime smbr	NR1003-221	214.86-214.88 m	214.9	10-15	15-20	10-20	0	-	-
clinoptilolite smbr	NR1003-222	215.27-215.28 m	215.3	0	0	5-10	0	0-5	-
clinoptilolite smbr	NR1003-223	215.89-215.90 m	215.9	0	0	15-25	0	-	-
clinoptilolite smbr	NR1003-224	216.64-216.65 m	216.6	0	45-55	25-30	0	15-25	-
clinoptilolite smbr	NR1003-225	219.21-219.22 m	219.2	0	0-5	0-5	0	20-25	-

clinoptilolite smbr	NR1003-226	219.94-219.96 m	219.9	0	0	0	0	-	-
clinoptilolite smbr	NR1003-227	220.16-220.18 m	220.2	0	0	0-5	0	-	-
clinoptilolite smbr	NR1003-228	220.56-220.57 m	220.6	0	0	0-5	0	-	-
clinoptilolite smbr	NR1003-229	221.55-221.57 m	221.6	0	10-15	10-15	0	-	-
clinoptilolite smbr	NR1003-230	223.06-223.08 m	223.1	0	0	0	0	-	-
clinoptilolite smbr	NR1003-231	223.32-223.34 m	223.3	0	0-5	0-5	0	0-5	-
clinoptilolite smbr	NR1003-232	224.87-224.90 m	224.9	0	0	0-10	0	-	-
clinoptilolite smbr	NR1003-233	225.04-225.05 m	225	0	0-10	0-5	0	-	-
clinoptilolite smbr	NR1003-234	225.85-225.87 m	225.9	0	5-10	10-15	0	0-10	-
Basal member	NR1003-235	226.10-226.14 m	226.1	0	10-15	5-10	0	0-5	-
Basal member	NR1003-236	226.74-226.79 m	226.7	0	10-20	10-20	0	-	-
Basal member	NR1003-237	226.80-226.86 m	226.8	0	0	0-5	0	0-5	-
Basal member	NR1003-238W	227.64-227.66 m	227.6	0	5-10	5-10	0	0-10	0-10
Basal member	NR1003-238B	227.64-227.66 m	227.6	0	0-5	0-5	0	0-5	-
Basal member	NR1003-239	228.30-228.33 m	228.3	0	10-15	10-15	0	-	-
Basal member	NR1003-240	229.50-229.56 m	229.5	0	65-70	20-30	0	-	-

Basal member	NR1003-241	231.57-231.63 m	231.6	0	70-80	15-25	0-5	0-5	0-5
Basal member	NR1003-242	233.56-233.60 m	233.6	0	70-80	5-15	0-5	0-5	0-5
Basal member	NR1003-243	236.53-236.58 m	236.5	0	60-70	10-20	0	-	0-5
Basal member	NR1003-244	238.60-238.65 m	238.6	0	65-75	10-20	~1	-	0-5
Basal member	NR1003-245	242.19-242.26 m	242.2	0	65-75	10-20	0	-	0-10
Basal member	NR1003-246	242.66-242.69 m	242.7	0	25-35	15-25	~1	-	-
Basal member	NR1003-247	242.92-242.98 m	242.9	0	~5	10-15	~1	-	-
Basal member	NR1003-10	243.35-243.36 m	243.4	0	0-5	10-20	0		-
Basal member	NR1003-248	243.61-243.63 m	243.6	0	5-10	5-10	0-2	-	-
Basal member	NR1003-11	245.22-245.23 m	245.2	-	-	-	-	-	-
Basal member	NR1003-249	245.20-245.22 m	245.2	0	0-5	0	0	-	-
Basal member	NR1003-250	245.50-245.54 m	245.5	0	10-15	15-20	0	-	10-20
Basal member	NR1003-251	245.83-245.87 m	245.8	0	20-30	30-40	~1	-	10-20
Basal member	NR1003-252	246.13-246.18 m	246.1	0	45-55	10-15	~1	-	15-25
Basal member	NR1003-253	247.65-247.74 m	246.1	0	75-85	10-15	~1	-	0-5
Basal member	NR1003-254	251.56-251.61 m	251.6	0	75-85	10-15	0	-	5-10

Basal member	NR1003-255	252.35-252.40 m	252.4	0	70-80	10-15	0	-	0-5
Basal member	NR1003-256	253.29-253.39 m	253.3	0	70-80	10-15	0	-	10-20

Table A.6 Correction of the stable oxygen isotope data.
*: CO2 produced by pure calcite during measurement; **: CO2 produced by pure dolomite during measurement.

	$\delta^{18}O$ (uncorrected) ‰, SMOW	$\delta^{13}C$ ‰, V-PDB	$\delta^{18}O$ (uncorrected) ‰, V-PDB	C_{carb} [wt%]	calcite [wt%]	Mg calcite [wt%]	dolomite [wt%]	aragonite [wt%]	calcite group relative wt %	dolomite group relative wt%	calcite group mol %	dolomite group mol %	$\delta^{18}O$ (corrected) ‰, V-PDB	$\delta^{18}O$ (test calculation) ‰, SMOW	$^{18}O/^{16}O$, CO2 *	$^{18}O/^{16}O$, CO2, corrected **	$\delta^{18}O$, as 100% dolomite ‰, SMOW	$\delta^{18}O$, as 100% dolomite ‰, V-PDB
NR1003-13	31.51	-4.70	0.57	10.45	29.8	0.0	52.4	0.0	36.3	63.7	34.4	65.6	-0.60	31.51	0.002068	0.002065	29.67	-1.22
NR1003-1	27.92	-5.37	-2.91	9.39	62.9	0.0	14.0	0.0	81.8	18.2	80.5	19.5	-3.26	27.92	0.002061	0.002057	26.08	-4.70
NR1003-15	32.60	-3.94	1.64	10.72	16.1	0.0	67.0	0.0	19.3	80.7	18.1	81.9	0.17	32.60	0.002071	0.002067	30.76	-0.15
NR1003-18	28.58	-6.68	-2.27	4.94	34.0	0.0	3.9	2.9	90.4	9.6	89.7	10.3	-2.45	28.58	0.002063	0.002059	26.74	-4.05
NR1003-20	27.38	-0.75	-3.43	9.97	0.0	69.0	0.0	0.0	100.0	0.0	100.0	0.0	-3.43	27.38	0.002060	0.002056	25.54	-5.22
NR1003-21	28.41	-6.29	-2.43	5.78	45.2	0.0	0.0	3.0	100.0	0.0	100.0	0.0	-2.43	28.41	0.002062	0.002058	26.57	-4.22
NR1003-22	28.30	-6.95	-2.54	1.69	13.0	0.0	1.0	0.0	92.9	7.1	92.4	7.6	-2.68	28.30	0.002062	0.002058	26.46	-4.33
NR1003-23	28.16	-5.09	-2.68	8.81	0.0	60.9	0.0	0.0	100.0	0.0	100.0	0.0	-2.68	28.16	0.002062	0.002058	26.32	-4.46
NR1003-33	31.71	-5.34	0.77	4.48	6.4	0.0	23.2	5.6	34.0	66.0	32.2	67.8	-0.45	31.71	0.002069	0.002065	29.86	-1.02
NR1003-35	29.51	-6.17	-1.37	2.60	18.3	0.0	3.1	0.0	85.5	14.5	84.4	15.6	-1.64	29.51	0.002064	0.002061	27.67	-3.15
NR1003-36	32.64	-1.45	1.67	10.17	0.0	0.0	77.5	0.0	0.0	100.0	0.0	100.0	-0.12	32.64	0.002071	0.002067	30.79	-0.12
NR1003-45	28.87	0.21	-1.98	7.78	0.0	53.8	0.0	0.0	100.0	0.0	100.0	0.0	-1.98	28.87	0.002063	0.002059	27.03	-3.77
NR1003-47	28.03	6.05	-2.80	6.29	21.4	25.7	0.0	0.0	100.0	0.0	100.0	0.0	-2.80	28.03	0.002061	0.002058	26.19	-4.58
NR1003-56	32.84	-4.82	1.86	3.84	29.6	0.0	0.0	2.4	100.0	0.0	100.0	0.0	1.86	32.84	0.002071	0.002067	30.99	0.07
NR1003-59	32.46	0.94	1.49	10.64	0.0	0.0	81.1	0.0	0.0	100.0	0.0	100.0	-0.30	32.46	0.002070	0.002067	30.61	-0.30
NR1003-62	27.06	0.55	-3.74	2.72	0.0	18.8	0.0	0.0	100.0	0.0	100.0	0.0	-3.74	27.06	0.002059	0.002056	25.22	-5.53
NR1003-69	32.36	0.78	1.40	8.90	0.0	0.0	67.9	0.0	0.0	100.0	0.0	100.0	-0.39	32.36	0.002070	0.002066	30.51	-0.39
NR1003-74	30.71	1.44	-0.20	1.87	13.7	0.0	1.7	0.0	88.7	11.3	87.8	12.2	-0.42	30.71	0.002067	0.002063	28.87	-1.99

ID																		
NR1003-101	34.65	1.79	3.62	8.00	11.0	0.0	50.9	0.0	17.8	82.2	16.6	83.4	2.12	34.65	0.002075	0.002071	32.80	1.82
NR1003-75	33.10	2.46	2.11	10.89	0.0	0.0	83.0	0.0	0.0	100.0	0.0	100.0	0.32	33.10	0.002072	0.002068	31.25	0.32
NR1003-76	32.99	2.18	2.01	9.03	0.0	0.0	68.9	0.0	0.0	100.0	0.0	100.0	0.22	32.99	0.002071	0.002068	31.14	0.22
NR1003-78	32.72	1.52	1.75	8.89	12.2	0.0	56.6	0.0	17.8	82.2	16.6	83.4	0.25	32.72	0.002071	0.002067	30.87	-0.05
NR1003-102	33.05	1.83	2.07	9.20	18.5	0.0	53.2	0.0	25.8	74.2	24.2	75.8	0.71	33.05	0.002071	0.002068	31.21	0.28
NR1003-79	32.03	2.25	1.08	7.94	12.7	0.0	48.9	0.0	20.6	79.4	19.3	80.7	-0.37	32.03	0.002069	0.002066	30.18	-0.71
NR1003-80	30.84	1.88	-0.08	6.45	22.0	0.0	29.1	0.0	43.1	56.9	41.0	59.0	-1.13	30.84	0.002067	0.002063	29.00	-1.87
NR1003-81	31.48	1.55	0.54	3.88	10.9	0.0	19.6	0.0	35.8	64.2	33.9	66.1	-0.64	31.48	0.002068	0.002065	29.64	-1.25
NR1003-103	32.81	1.18	1.83	4.03	10.8	0.0	20.9	0.0	34.0	66.0	32.2	67.8	0.62	32.81	0.002071	0.002067	30.96	0.04
NR1003-104	34.27	1.19	3.25	4.79	8.0	4.3	24.4	0.0	33.5	66.5	31.7	68.3	2.02	34.27	0.002074	0.002070	32.42	1.45
NR1003-105-1	33.55	2.54	2.55	5.41	5.6	0.0	36.1	0.0	13.4	86.6	12.5	87.5	0.98	33.55	0.002072	0.002069	31.70	0.76
NR1003-105-2	32.49	1.97	2.23	5.41	5.6	0.0	36.1	0.0	13.4	86.6	12.5	87.5	0.66	33.21	0.002072	0.002068	31.37	0.43
NR1003-105-3	34.44	2.33	3.41	5.41	5.6	0.0	36.1	0.0	13.4	86.6	12.5	87.5	1.84	34.44	0.002074	0.002071	32.59	1.62
NR1003-106	35.21	-1.41	4.16	3.69	1.6	0.0	26.7	0.0	5.7	94.3	5.2	94.8	2.46	35.21	0.002076	0.002072	33.36	2.37
NR1003-107	33.21	3.13	2.22	7.93	19.5	0.0	42.6	0.0	31.3	68.7	29.6	70.4	0.96	33.21	0.002072	0.002068	31.36	0.43
NR1003-108	34.33	0.55	3.31	6.35	15.9	0.0	33.8	0.0	32.0	68.0	30.3	69.7	2.05	34.33	0.002074	0.002070	32.48	1.51
NR1003-2	36.45	-0.20	5.37	9.39	3.0	0.0	68.9	0.0	4.2	95.8	3.8	96.2	3.64	36.45	0.002078	0.002075	34.60	3.57
NR1003-109	35.03	0.78	3.98	10.41	7.8	0.0	72.3	0.0	9.7	90.3	9.0	91.0	2.35	35.03	0.002075	0.002072	33.18	2.19
NR1003-110	33.50	1.27	2.51	7.52	17.6	0.0	41.2	0.0	29.9	70.1	28.2	71.8	1.22	33.50	0.002072	0.002069	31.65	0.71
NR1003-111	33.62	-0.22	2.62	5.09	6.5	0.0	32.8	0.0	16.6	83.4	15.5	84.5	1.11	33.62	0.002073	0.002069	31.77	0.83
NR1003-112	28.29	3.08	-2.55	3.61	28.9	0.0	1.1	0.0	96.4	3.6	96.1	3.9	-2.62	28.29	0.002062	0.002058	26.45	-4.34
NR1003-113	33.94	5.49	2.93	4.87	7.0	0.0	30.8	0.0	18.5	81.5	17.2	82.8	1.44	33.94	0.002073	0.002070	32.09	1.13
NR1003-114	34.49	8.43	3.46	6.72	0.0	0.0	51.2	0.0	0.0	100.0	0.0	100.0	1.67	34.49	0.002074	0.002071	32.64	1.67
NR1003-115	34.03	6.90	3.02	10.22	2.6	0.0	75.5	0.0	3.4	96.6	3.1	96.9	1.28	34.03	0.002073	0.002070	32.18	1.23
NR1003-116	33.24	6.94	2.25	12.21	3.0	2.3	87.9	0.0	5.6	94.4	5.2	94.8	0.55	33.24	0.002072	0.002068	31.39	0.46
NR1003-117	27.62	2.55	-3.20	4.55	37.9	0.0	0.0	0.0	100.0	0.0	100.0	0.0	-3.20	27.62	0.002061	0.002057	25.78	-4.98
NR1003-118	27.30	2.89	-3.51	4.60	20.9	14.4	0.0	0.0	100.0	0.0	100.0	0.0	-3.51	27.30	0.002060	0.002056	25.47	-5.29
NR1003-119	31.88	3.99	0.93	10.33	7.1	6.0	65.6	0.0	16.7	83.3	15.5	84.5	-0.58	31.88	0.002069	0.002065	30.03	-0.86

200

NR1003-120	32.17	4.44	1.22	7.74	4.0	5.8	49.0	0.0	16.7	83.3	15.5	84.5	-0.30	32.17	0.002070	0.002066	30.33	-0.58
NR1003-121	32.98	3.84	2.00	7.38	0.0	6.7	48.9	0.0	12.0	88.0	11.2	88.8	0.40	32.98	0.002071	0.002068	31.13	0.20
NR1003-122	28.98	1.76	-1.88	4.14	30.1	0.0	4.1	0.0	88.1	11.9	87.2	12.8	-2.11	28.98	0.002063	0.002060	27.14	-3.67
NR1003-123-1	32.21	3.45	1.25	3.14	9.0	0.0	5.7	0.0	61.4	38.6	59.4	40.6	0.52	32.21	0.002070	0.002066	30.36	-0.54
NR1003-123-2	32.30	2.95	1.34	3.14	9.0	0.0	5.7	0.0	61.4	38.6	59.4	40.6	0.61	32.30	0.002070	0.002066	30.46	-0.45
NR1003-3	34.19	6.99	3.18	10.27	0.0	0.0	78.3	0.0	0.0	100.0	0.0	100.0	1.38	34.19	0.002074	0.002070	32.35	1.38
NR1003-124	35.49	7.22	4.43	8.90	0.0	0.0	67.9	0.0	0.0	100.0	0.0	100.0	2.63	35.49	0.002076	0.002073	33.64	2.63
NR1003-125	36.37	5.61	5.29	7.62	0.0	0.0	58.1	0.0	0.0	100.0	0.0	100.0	3.49	36.37	0.002078	0.002074	34.52	3.49
NR1003-126	35.67	8.35	4.61	8.96	0.0	0.0	68.3	0.0	0.0	100.0	0.0	100.0	2.81	35.67	0.002077	0.002073	33.82	2.81
NR1003-127	35.29	8.04	4.24	9.00	0.0	0.0	16.5	0.0	0.0	100.0	0.0	100.0	2.45	35.29	0.002076	0.002072	33.44	2.45
NR1003-128	22.11	5.25	-8.55	9.75	77.2	3.4	0.0	0.0	100.0	0.0	100.0	0.0	-8.55	22.11	0.002050	0.002046	20.28	-10.32
NR1003-129	35.21	9.43	4.16	10.41	0.0	0.0	79.4	0.0	0.0	100.0	0.0	100.0	2.37	35.21	0.002076	0.002072	33.36	2.37
NR1003-130	35.80	11.13	4.74	9.77	0.0	0.0	74.5	0.0	0.0	100.0	0.0	100.0	2.94	35.80	0.002077	0.002073	33.95	2.94
NR1003-131	35.62	9.92	4.56	9.89	0.0	0.0	75.4	0.0	0.0	100.0	0.0	100.0	2.76	35.62	0.002077	0.002073	33.77	2.76
NR1003-132	37.18	9.92	6.07	9.04	0.0	0.0	68.9	0.0	0.0	100.0	0.0	100.0	4.28	37.18	0.002080	0.002076	35.33	4.28
NR1003-133	35.42	11.39	4.37	10.84	0.0	0.0	82.7	0.0	0.0	100.0	0.0	100.0	2.57	35.42	0.002076	0.002073	33.57	2.57
NR1003-134	36.16	16.07	5.08	7.81	0.0	0.0	55.4	0.0	0.0	100.0	0.0	100.0	3.28	36.16	0.002078	0.002074	34.30	3.28
NR1003-4	34.51	13.87	3.48	10.73	0.0	0.0	81.8	0.0	0.0	100.0	0.0	100.0	1.69	34.51	0.002074	0.002071	32.66	1.69
NR1003-135	36.07	12.17	5.70	10.58	0.0	0.0	80.7	0.0	0.0	100.0	0.0	100.0	3.90	36.79	0.002079	0.002075	34.94	3.90
NR1003-136	36.52	14.41	5.43	8.87	0.0	0.0	67.6	0.0	0.0	100.0	0.0	100.0	3.63	36.52	0.002078	0.002075	34.66	3.63
NR1003-136-2	36.57	13.62	6.18	8.87	0.0	0.0	67.6	0.0	0.0	100.0	0.0	100.0	4.38	37.29	0.002080	0.002076	35.44	4.38
NR1003-137	36.27	13.74	5.19	7.43	0.0	0.0	56.7	0.0	0.0	100.0	0.0	100.0	3.39	36.27	0.002078	0.002074	34.41	3.39
NR1003-138	33.55	6.19	2.55	4.34	6.9	0.0	26.8	0.0	20.5	79.5	19.2	80.8	1.10	33.55	0.002072	0.002069	31.70	0.76
NR1003-139	32.06	3.97	1.10	3.53	7.4	0.0	20.1	0.0	27.0	73.0	25.4	74.6	-0.23	32.06	0.002069	0.002066	30.21	-0.69
NR1003-140	32.44	8.06	1.47	5.96	8.8	0.0	37.4	0.0	19.0	81.0	17.8	82.2	0.00	32.44	0.002070	0.002067	30.59	-0.32
NR1003-141	34.15	11.46	3.14	9.12	3.8	0.0	66.0	0.0	5.5	94.5	5.1	94.9	1.43	34.15	0.002074	0.002070	32.30	1.34
NR1003-142	35.03	12.43	3.98	8.36	6.9	0.0	57.4	0.0	10.7	89.3	10.0	90.0	2.37	35.03	0.002075	0.002072	33.18	2.19
NR1003-143	33.20	12.16	2.21	10.26	0.0	0.0	78.2	0.0	0.0	100.0	0.0	100.0	0.42	33.20	0.002072	0.002068	31.35	0.42

NR1003-5	33.05	16.40	2.07	11.95	0.0	0.0	91.1	0.0	0.0	100.0	0.0	100.0	0.28	33.05	0.002071	0.002068	31.21	0.28
NR1003-144	31.82	4.28	0.87	2.93	14.2	0.0	9.4	0.0	60.1	39.9	58.1	41.9	0.12	31.82	0.002069	0.002065	29.97	-0.92
NR1003-145-1	32.42	6.44	1.45	3.37	15.4	0.0	11.6	0.0	56.9	43.1	54.9	45.1	0.64	32.42	0.002070	0.002067	30.57	-0.34
NR1003-145-2	32.26	6.14	1.30	3.37	15.4	0.0	11.6	0.0	56.9	43.1	54.9	45.1	0.49	32.26	0.002070	0.002066	30.42	-0.49
NR1003-146	35.18	18.72	4.13	8.73	0.0	0.0	66.6	0.0	0.0	100.0	0.0	100.0	2.33	35.18	0.002076	0.002072	33.33	2.33
NR1003-147	36.00	19.72	4.93	10.67	0.0	0.0	81.4	0.0	0.0	100.0	0.0	100.0	3.13	36.00	0.002077	0.002074	34.15	3.13
NR1003-6	34.83	20.93	3.80	10.67	0.0	0.0	81.4	0.0	0.0	100.0	0.0	100.0	2.00	34.83	0.002075	0.002071	32.98	2.00
NR1003-148	36.75	19.74	5.66	9.59	0.0	0.0	73.1	0.0	0.0	100.0	0.0	100.0	3.86	36.75	0.002079	0.002075	34.90	3.86
NR1003-149	32.88	10.97	1.90	4.65	9.4	0.0	26.8	0.0	26.0	74.0	24.4	75.6	0.55	32.88	0.002071	0.002067	31.04	0.11
NR1003-150	35.09	7.47	4.05	5.89	0.0	0.0	44.9	0.0	0.0	100.0	0.0	100.0	2.25	35.09	0.002076	0.002072	33.24	2.25
NR1003-151	31.53	6.80	0.59	2.38	10.7	0.0	8.3	0.0	56.2	43.8	54.1	45.9	-0.23	31.53	0.002068	0.002065	29.69	-1.19
NR1003-152-1	30.98	4.40	0.06	5.34	11.6	27.3	0.0	0.0	100.0	0.0	100.0	0.0	0.06	30.98	0.002067	0.002064	29.13	-1.73
NR1003-152-2	34.29	10.82	3.27	5.34	11.6	27.3	0.0	0.0	100.0	0.0	100.0	0.0	3.27	34.29	0.002074	0.002070	32.44	1.48
NR1003-153	34.10	9.60	3.09	3.67	3.3	0.0	24.9	0.0	11.8	88.2	11.0	89.0	1.49	34.10	0.002074	0.002070	32.25	1.29
NR1003-154	34.69	10.05	3.66	3.62	6.5	0.0	21.6	0.0	23.2	76.8	21.7	78.3	2.26	34.69	0.002075	0.002071	32.84	1.86
NR1003-155	37.30	17.54	6.19	6.79	1.8	0.0	50.1	0.0	3.4	96.6	3.2	96.8	4.45	37.30	0.002080	0.002076	35.45	4.39
NR1003-156	37.72	18.52	6.60	10.06	0.0	0.0	76.7	0.0	0.0	100.0	0.0	100.0	4.80	37.72	0.002081	0.002077	35.87	4.80
NR1003-157-1	31.17	5.47	0.24	2.91	13.8	0.0	9.6	0.0	59.1	40.9	57.1	42.9	-0.53	31.17	0.002068	0.002064	29.32	-1.55
NR1003-157-2	31.51	6.91	0.58	2.91	13.8	0.0	9.6	0.0	59.1	40.9	57.1	42.9	-0.19	31.51	0.002068	0.002065	29.67	-1.21
NR1003-158	32.73	5.75	1.76	3.95	6.1	5.4	18.5	0.0	38.4	61.6	36.4	63.6	0.62	32.73	0.002071	0.002067	30.89	-0.03
NR1003-159	36.67	17.04	5.58	6.73	0.0	0.0	51.3	0.0	0.0	100.0	0.0	100.0	3.78	36.67	0.002079	0.002075	34.81	3.78
NR1003-8	34.95	17.03	3.92	6.73	0.0	0.0	51.3	0.0	0.0	100.0	0.0	100.0	2.12	34.95	0.002075	0.002072	33.11	2.12
NR1003-9	34.10	14.52	3.08	6.13	0.0	0.0	46.7	0.0	0.0	100.0	0.0	100.0	1.29	34.10	0.002074	0.002070	32.25	1.29
NR1003-160	37.04	18.11	5.94	8.85	0.0	0.0	67.5	0.0	0.0	100.0	0.0	100.0	4.14	37.04	0.002079	0.002076	35.19	4.14
NR1003-161	31.63	6.01	0.69	1.96	16.3	0.0	0.0	0.0	100.0	0.0	100.0	0.0	0.69	31.63	0.002069	0.002065	29.78	-1.10
NR1003-162	36.01	16.34	4.94	6.00	2.0	0.0	43.9	0.0	4.3	95.7	4.0	96.0	3.21	36.01	0.002077	0.002074	34.15	3.14
NR1003-163	31.98	7.66	1.03	4.13	0.0	12.2	18.0	0.0	40.3	59.7	38.4	61.6	-0.08	31.98	0.002069	0.002066	30.13	-0.76
NR1003-164	32.28	6.97	1.32	4.04	6.9	7.3	16.4	0.0	46.5	53.5	44.5	55.5	0.32	32.28	0.002070	0.002066	30.43	-0.47

Sample																		
NR1003-165	31.97	6.25	1.02	2.64	8.9	0.0	12.0	0.0	42.6	57.4	40.6	59.4	-0.04	31.97	0.002069	0.002066	30.13	-0.77
NR1003-166	37.21	17.49	6.10	6.49	0.0	0.0	49.5	0.0	0.0	100.0	0.0	100.0	4.30	37.21	0.002080	0.002076	35.35	4.30
NR1003-167	34.21	10.05	3.19	4.52	5.1	0.0	29.8	0.0	14.5	85.5	13.5	86.5	1.64	34.21	0.002074	0.002070	32.36	1.40
NR1003-168	36.37	14.74	5.29	4.94	2.7	0.0	35.2	0.0	7.2	92.8	6.7	93.3	3.61	36.37	0.002078	0.002074	34.52	3.49
NR1003-169	33.75	8.40	2.75	3.59	10.9	0.0	17.4	0.0	38.4	61.6	36.5	63.5	1.61	33.75	0.002073	0.002069	31.90	0.95
NR1003-170-1	35.97	12.73	4.90	9.72	0.0	0.0	74.1	0.0	0.0	100.0	0.0	100.0	3.10	35.97	0.002077	0.002074	34.12	3.10
NR1003-170-2	36.15	12.73	5.07	9.72	0.0	0.0	74.1	0.0	0.0	100.0	0.0	100.0	3.27	36.15	0.002078	0.002074	34.29	3.27
NR1003-171	35.59	11.46	5.23	8.76	0.0	0.0	66.8	0.0	0.0	100.0	0.0	100.0	3.43	36.31	0.002078	0.002074	34.46	3.43
NR1003-172	35.02	9.56	3.97	5.89	5.3	0.0	40.0	0.0	11.7	88.3	10.9	89.1	2.38	35.02	0.002075	0.002072	33.17	2.18
NR1003-173	36.78	12.94	5.68	7.58	0.0	0.0	57.8	0.0	0.0	100.0	0.0	100.0	3.88	36.78	0.002079	0.002075	34.92	3.88
NR1003-174	35.15	9.49	4.11	6.18	6.4	0.0	41.3	0.0	13.4	86.6	12.5	87.5	2.53	35.15	0.002076	0.002072	33.30	2.31
NR1003-175	32.82	5.51	1.85	4.28	0.0	11.3	20.2	0.0	35.8	64.2	33.9	66.1	0.66	32.82	0.002071	0.002067	30.98	0.05
NR1003-176	32.01	3.47	1.06	5.36	0.0	0.0	40.9	0.0	0.0	100.0	0.0	100.0	-0.73	32.01	0.002069	0.002066	30.16	-0.73
NR1003-177	36.24	13.82	5.16	5.31	2.2	0.0	38.5	0.0	5.4	94.6	5.0	95.0	3.45	36.24	0.002078	0.002074	34.38	3.36
NR1003-178	34.77	10.79	3.73	3.77	6.4	0.0	22.9	0.0	21.9	78.1	20.5	79.5	2.31	34.77	0.002075	0.002071	32.92	1.94
NR1003-179	36.27	12.80	5.19	4.07	2.1	0.0	29.1	0.0	6.7	93.3	6.2	93.8	3.50	36.27	0.002078	0.002074	34.41	3.39
NR1003-180	35.38	10.93	4.32	3.73	3.2	0.0	25.5	0.0	11.2	88.8	10.4	89.6	2.71	35.38	0.002076	0.002072	33.53	2.53
NR1003-181	35.41	10.57	4.35	4.42	4.1	0.0	30.0	0.0	11.9	88.1	11.1	88.9	2.76	35.41	0.002076	0.002072	33.56	2.56
NR1003-182	35.49	10.05	4.44	2.46	2.4	0.0	16.6	0.0	12.6	87.4	11.7	88.3	2.85	35.49	0.002076	0.002073	33.64	2.64
NR1003-183	33.95	6.81	2.94	3.01	3.5	0.0	19.8	0.0	14.9	85.1	13.9	86.1	1.39	33.95	0.002073	0.002070	32.10	1.14
NR1003-184	35.54	4.75	4.48	2.64	1.8	0.0	18.5	0.0	8.9	91.1	8.3	91.7	2.84	35.54	0.002076	0.002073	33.69	2.69
NR1003-185	33.64	3.18	2.64	2.62	5.9	0.0	14.6	0.0	28.6	71.4	26.9	73.1	1.33	33.64	0.002073	0.002069	31.79	0.85
NR1003-186	32.90	4.55	1.92	4.74	7.9	0.0	28.9	0.0	21.4	78.6	20.0	80.0	0.49	32.90	0.002071	0.002067	31.06	0.13
NR1003-187	31.80	5.90	0.86	6.22	3.8	0.0	44.0	0.0	7.9	92.1	7.3	92.7	-0.80	31.80	0.002069	0.002065	29.96	-0.93
NR1003-188	35.64	1.24	4.58	4.37	4.6	0.0	29.3	0.0	13.6	86.4	12.6	87.4	3.01	35.64	0.002077	0.002073	33.79	2.78
NR1003-189	34.54	1.34	3.51	5.57	2.3	0.0	40.4	0.0	5.4	94.6	5.0	95.0	1.80	34.54	0.002074	0.002071	32.69	1.71
NR1003-190	36.15	1.28	5.08	2.23	0.0	0.0	17.0	0.0	0.0	100.0	0.0	100.0	3.28	36.15	0.002078	0.002074	34.30	3.28

NR1003-191	34.17	3.22	3.15	3.22	3.8	0.0	20.4	0.0	15.7	84.3	14.6	85.4	1.62	34.17	0.002074	0.002070	32.32	1.36
NR1003-192	34.02	3.24	3.00	3.04	2.7	0.0	20.7	0.0	11.6	88.4	10.8	89.2	1.40	34.02	0.002073	0.002070	32.17	1.21
NR1003-193	35.11	1.89	4.07	3.30	0.0	0.0	25.2	0.0	0.0	100.0	0.0	100.0	2.27	35.11	0.002076	0.002072	33.26	2.27
NR1003-194	34.45	3.56	3.42	4.16	0.0	0.0	31.7	0.0	0.0	100.0	0.0	100.0	1.63	34.45	0.002074	0.002071	32.60	1.63
NR1003-195	36.46	0.86	5.37	6.67	0.0	0.0	50.9	0.0	0.0	100.0	0.0	100.0	3.57	36.46	0.002078	0.002075	34.60	3.57
NR1003-196	34.51	2.58	3.49	4.18	0.0	0.0	31.9	0.0	0.0	100.0	0.0	100.0	1.69	34.51	0.002074	0.002071	32.66	1.69
NR1003-197	34.40	2.82	3.37	5.12	0.0	0.0	39.0	0.0	0.0	100.0	0.0	100.0	1.58	34.40	0.002074	0.002070	32.55	1.58
NR1003-198	33.12	2.96	2.14	4.59	7.3	0.0	28.3	0.0	20.5	79.5	19.1	80.9	0.69	33.12	0.002072	0.002068	31.27	0.34
NR1003-199	33.42	2.11	2.42	2.21	4.6	0.0	12.6	0.0	26.9	73.1	25.3	74.7	1.08	33.42	0.002072	0.002069	31.57	0.63
NR1003-200	34.80	1.80	3.76	3.58	0.0	0.0	23.0	4.7	17.1	82.9	16.0	84.0	2.25	34.80	0.002075	0.002071	32.95	1.97
NR1003-201	33.96	2.02	2.95	2.73	3.9	0.0	17.3	0.0	18.3	81.7	17.0	83.0	1.46	33.96	0.002073	0.002070	32.11	1.15
NR1003-203	34.45	-0.94	3.42	5.78	0.0	0.0	44.1	0.0	0.0	100.0	0.0	100.0	1.63	34.45	0.002074	0.002071	32.60	1.63
NR1003-204	33.08	2.73	2.10	4.09	5.2	0.0	26.4	0.0	16.5	83.5	15.4	84.6	0.58	33.08	0.002072	0.002068	31.23	0.31
NR1003-205	33.52	2.31	2.52	4.48	5.4	0.0	29.2	0.0	15.5	84.5	14.5	85.5	0.99	33.52	0.002072	0.002069	31.67	0.73
NR1003-206	32.01	3.06	1.06	3.72	4.0	0.0	14.4	11.3	51.4	48.6	49.3	50.7	0.15	32.01	0.002069	0.002066	30.16	-0.73
NR1003-207	33.89	2.54	2.88	2.50	0.0	0.0	19.1	0.0	0.0	100.0	0.0	100.0	1.09	33.89	0.002073	0.002069	32.04	1.09
NR1003-208	33.42	2.04	2.43	3.21	3.2	0.0	21.5	0.0	13.0	87.0	12.1	87.9	0.85	33.42	0.002072	0.002069	31.57	0.64
NR1003-209	33.63	3.28	2.63	3.94	4.6	0.0	25.8	0.0	15.1	84.9	14.1	85.9	1.09	33.63	0.002073	0.002069	31.78	0.84
NR1003-210	33.63	2.86	2.63	4.05	5.1	0.0	21.0	5.7	33.8	66.2	32.0	68.0	1.41	33.63	0.002073	0.002069	31.78	0.84
NR1003-211	33.57	4.11	2.57	3.13	0.0	0.0	16.4	8.2	33.2	66.8	31.4	68.6	1.34	33.57	0.002073	0.002069	31.72	0.78
NR1003-212	33.83	2.12	2.82	4.14	0.0	0.0	16.0	17.0	51.4	48.6	49.3	50.7	1.91	33.83	0.002073	0.002069	31.98	1.03
NR1003-213-1	35.48	6.12	4.43	5.12	0.0	0.0	36.2	3.1	7.8	92.2	7.2	92.8	2.76	35.48	0.002076	0.002073	33.63	2.63
NR1003-213-2	33.73	3.86	2.72	5.12	0.0	0.0	36.2	3.1	7.8	92.2	7.2	92.8	1.06	33.73	0.002073	0.002069	31.88	0.93
NR1003-214	32.27	6.05	1.31	5.43	0.0	0.0	41.4	0.0	0.0	100.0	0.0	100.0	-0.48	32.27	0.002070	0.002066	30.43	-0.48
NR1003-215	33.55	4.52	2.55	2.56	0.0	0.0	19.5	0.0	0.0	100.0	0.0	100.0	0.76	33.55	0.002072	0.002069	31.70	0.76
NR1003-216	35.04	0.77	3.99	7.39	0.0	0.0	56.3	0.0	0.0	100.0	0.0	100.0	2.20	35.04	0.002075	0.002072	33.19	2.20
NR1003-218-1	35.50	1.72	4.44	5.51	0.0	0.0	42.0	0.0	0.0	100.0	0.0	100.0	2.64	35.50	0.002076	0.002073	33.65	2.64

NR1003-218-2	36.28	1.28	5.20	5.51	0.0	0.0	42.0	0.0	0.0	100.0	0.0	100.0	3.40	36.28	0.002078	0.002074	34.43	3.40
NR1003-219	37.25	-2.56	6.14	7.17	0.0	0.0	54.7	0.0	0.0	100.0	0.0	100.0	4.34	37.25	0.002080	0.002076	35.40	4.34
NR1003-220	34.60	0.90	3.57	5.56	0.0	0.0	42.4	0.0	0.0	100.0	0.0	100.0	1.77	34.60	0.002075	0.002071	32.75	1.77
NR1003-222	37.06	0.99	5.95	9.31	0.0	0.0	71.0	0.0	0.0	100.0	0.0	100.0	4.15	37.06	0.002080	0.002076	35.20	4.15
NR1003-223	37.09	-8.75	5.99	9.04	0.0	0.0	68.9	0.0	0.0	100.0	0.0	100.0	4.19	37.09	0.002080	0.002076	35.24	4.19
NR1003-224	30.29	2.11	-0.61	1.44	0.0	10.0	0.0	0.0	100.0	0.0	100.0	0.0	-0.61	30.29	0.002066	0.002062	28.45	-2.40
NR1003-225-1	38.22	-2.07	7.08	7.90	0.0	0.0	60.2	0.0	0.0	100.0	0.0	100.0	5.28	38.22	0.002082	0.002078	36.37	5.28
NR1003-225-2	38.16	-4.12	7.02	7.90	0.0	0.0	60.2	0.0	0.0	100.0	0.0	100.0	5.22	38.16	0.002082	0.002078	36.30	5.22
NR1003-226	37.52	-5.11	6.40	11.07	0.0	0.0	84.4	0.0	0.0	100.0	0.0	100.0	4.61	37.52	0.002080	0.002077	35.67	4.61
NR1003-227	37.38	-4.62	6.27	10.87	0.0	0.0	82.9	0.0	0.0	100.0	0.0	100.0	4.47	37.38	0.002080	0.002076	35.53	4.47
NR1003-228-1	36.12	-4.69	5.75	10.20	0.0	0.0	77.8	0.0	0.0	100.0	0.0	100.0	3.95	36.84	0.002079	0.002075	34.99	3.95
NR1003-228-2	19.99	-1.08	-9.90	10.20	0.0	0.0	77.8	0.0	0.0	100.0	0.0	100.0	-11.67	20.71	0.002047	0.002043	18.89	-11.67
NR1003-229-1	36.65	-4.06	5.56	9.48	0.0	0.0	72.3	0.0	0.0	100.0	0.0	100.0	3.76	36.65	0.002079	0.002075	34.80	3.76
NR1003-229-2	36.84	-4.58	6.45	9.48	0.0	0.0	72.3	0.0	0.0	100.0	0.0	100.0	4.65	37.56	0.002081	0.002077	35.71	4.65
NR1003-230	37.38	-10.13	6.27	10.78	0.0	0.0	82.2	0.0	0.0	100.0	0.0	100.0	4.47	37.38	0.002080	0.002076	35.53	4.47
NR1003-231-1	31.01	-3.78	0.09	10.96	0.0	0.0	83.6	0.0	0.0	100.0	0.0	100.0	-1.70	31.01	0.002067	0.002064	29.16	-1.70
NR1003-231-2	34.24	-6.08	3.92	10.96	0.0	0.0	83.6	0.0	0.0	100.0	0.0	100.0	2.13	34.96	0.002075	0.002072	33.11	2.13
NR1003-232	31.81	-3.30	0.86	11.79	0.0	0.0	89.9	0.0	0.0	100.0	0.0	100.0	-0.93	31.81	0.002069	0.002065	29.96	-0.93
NR1003-233-1	32.11	-1.78	1.16	11.43	0.0	0.0	87.2	0.0	0.0	100.0	0.0	100.0	-0.63	32.11	0.002070	0.002066	30.27	-0.63
NR1003-233-2	31.16	-1.74	0.23	11.43	0.0	0.0	87.2	0.0	0.0	100.0	0.0	100.0	-1.56	31.16	0.002068	0.002064	29.31	-1.56
NR1003-234	29.93	0.62	-0.96	7.42	61.8	0.0	0.0	0.0	100.0	0.0	100.0	0.0	-0.96	29.93	0.002065	0.002062	28.09	-2.75
NR1003-235-1	25.87	-3.67	-4.90	9.47	77.5	0.0	1.3	0.0	98.4	1.6	98.2	1.8	-4.93	25.87	0.002057	0.002053	24.03	-6.68
NR1003-235-2	22.86	-6.82	-7.82	9.47	77.5	0.0	1.3	0.0	98.4	1.6	98.2	1.8	-7.85	22.86	0.002051	0.002047	21.03	-9.59
NR1003-236	27.69	-4.06	-3.13	9.69	32.6	2.1	41.8	0.0	45.4	54.6	43.3	56.7	-4.14	27.69	0.002061	0.002057	25.85	-4.91
NR1003-237-1	20.84	-6.39	-9.78	11.82	17.0	0.0	0.0	0.0	100.0	0.0	100.0	0.0	-9.78	20.84	0.002047	0.002043	19.01	-11.55
NR1003-237-2	35.50	-8.38	4.44	11.82	17.0	0.0	74.5	0.0	18.6	81.4	17.4	82.6	2.96	35.50	0.002076	0.002073	33.65	2.64
NR1003-238B	25.64	-2.11	-4.42	10.68	77.4	0.0	10.6	0.0	87.9	12.1	87.0	13.0	-4.65	26.36	0.002058	0.002054	24.53	-6.20

NR1003-238W	27.33	-2.34	-2.78	8.90	52.8	0.0	19.6	0.0	72.9	27.1	71.3	28.7	-3.29	28.05	0.002061	0.002058	26.22	-4.56
NR1003-239	30.04	-0.48	-0.86	8.59	69.4	0.0	2.0	0.0	97.2	2.8	97.0	3.0	-0.91	30.04	0.002065	0.002062	28.20	-2.64
NR1003-240	30.32	-5.45	-0.58	0.55	0.0	0.0	4.2	0.0	0.0	100.0	0.0	100.0	-2.37	30.32	0.002066	0.002062	28.48	-2.37
NR1003-241	29.90	-3.74	-0.99	0.47	0.0	0.0	3.6	0.0	0.0	100.0	0.0	100.0	-2.77	29.90	0.002065	0.002061	28.06	-2.77
NR1003-242	25.86	-2.77	-4.91	1.90	0.0	0.0	14.5	0.0	0.0	100.0	0.0	100.0	-6.69	25.86	0.002057	0.002053	24.03	-6.69
NR1003-243	29.35	-3.36	-1.53	2.40	0.0	0.0	18.3	0.0	0.0	100.0	0.0	100.0	-3.31	29.35	0.002064	0.002060	27.51	-3.31
NR1003-244	28.52	-5.93	-2.33	0.77	4.4	0.0	1.8	0.0	71.1	28.9	69.4	30.6	-2.87	28.52	0.002062	0.002059	26.68	-4.11
NR1003-245	27.17	-3.36	-3.64	1.80	4.8	0.0	9.4	0.0	33.6	66.4	31.8	68.2	-4.85	27.17	0.002060	0.002056	25.33	-5.42
NR1003-246	26.42	-2.91	-4.37	5.20	37.7	0.0	5.2	0.0	87.9	12.1	87.0	13.0	-4.60	26.42	0.002058	0.002054	24.58	-6.15
NR1003-247	25.74	-3.25	-5.03	9.85	78.7	0.0	3.1	0.0	96.2	3.8	95.9	4.1	-5.10	25.74	0.002057	0.002053	23.90	-6.81
NR1003-10	22.23	-2.92	-8.43	9.62	76.2	0.0	3.6	0.0	95.5	4.5	95.1	4.9	-8.52	22.23	0.002050	0.002046	20.40	-10.20
NR1003-248-1	23.67	-1.88	-6.33	10.29	80.1	0.0	5.2	0.0	93.9	6.1	93.4	6.6	-6.45	24.39	0.002054	0.002050	22.56	-8.11
NR1003-248-2	25.00	-2.23	-5.04	10.29	80.1	0.0	5.2	0.0	93.9	6.1	93.4	6.6	-5.16	25.72	0.002057	0.002053	23.89	-6.82
NR1003-249-1	24.01	-1.99	-6.70	11.21	90.6	0.0	2.6	0.0	97.2	2.8	97.0	3.0	-6.75	24.01	0.002053	0.002050	22.18	-8.48
NR1003-249-2	25.08	-2.46	-4.96	11.21	90.6	0.0	2.6	0.0	97.2	2.8	97.0	3.0	-5.02	25.80	0.002057	0.002053	23.97	-6.74
NR1003-250	27.84	-3.02	-2.99	7.19	53.6	0.0	5.8	0.0	90.3	9.7	89.6	10.4	-3.18	27.84	0.002061	0.002057	26.00	-4.77
NR1003-251	27.25	-3.16	-3.56	4.69	22.6	0.0	15.1	0.0	59.9	40.1	57.9	42.1	-4.31	27.25	0.002060	0.002056	25.41	-5.34
NR1003-252-1	24.70	-2.96	-5.33	4.37	24.8	0.0	10.6	0.0	70.1	29.9	68.3	31.7	-5.89	25.42	0.002056	0.002053	23.59	-7.11
NR1003-252-2	23.87	-2.80	-6.14	4.37	24.8	0.0	10.6	0.0	70.1	29.9	68.3	31.7	-6.70	24.59	0.002055	0.002051	22.76	-7.91
NR1003-254	24.67	-3.33	-6.06	0.30	0.0	0.0	2.3	0.0	0.0	100.0	0.0	100.0	-7.84	24.67	0.002055	0.002051	22.84	-7.84
NR1003-255	24.31	-4.10	-6.41	1.09	9.1	0.0	0.0	0.0	100.0	0.0	100.0	0.0	-6.41	24.31	0.002054	0.002050	22.48	-8.19

Table A.7 Electron microprobe results of major and trace element contents and calculated mole percentage of Fe, Ca and Mg.

probe diameter	mineralogy	Sample	lithostratigraphic member	core depth	MgO	SrO	Sr	CaO	MnO	FeO	SiO$_2$	K$_2$O	CaCO$_3$	MgCO$_3$	FeCO$_3$
(micron)	(EMPA)			[m.b.s.]	wt %	wt %	ppm	wt %	wt %	wt %	wt %	wt %	mol%	mol%	mol%
5	low Mg calcite	NR1003-1-1	Clay member	14.3	1.0	0.1	704	53.4	0.3	0.46	0.5	0.1	96.4	2.6	0.7
5	low Mg calcite	NR1003-1-2	Clay member	14.3	1.0	0.1	1071	54.1	0.1	0.13	0.8	0.1	97.2	2.4	0.2
5	low Mg calcite	NR1003-1-3	Clay member	14.3	1.1	0.1	431	53.2	0.2	0.14	0.7	0.1	96.8	2.8	0.2
5	low Mg calcite	NR1003-1-4	Clay member	14.3	0.6	0.2	1687	55.3	0.1	0.06	0.3	0.1	98.2	1.6	0.1
5	low Mg calcite	NR1003-1-5	Clay member	14.3	0.5	0.2	1519	57.0	0.1	0.08	<0.036	0.0	98.6	1.1	0.1
5	low Mg calcite	NR1003-1-6	Clay member	14.3	1.2	0.1	513	49.4	0.3	0.45	2.4	0.3	95.5	3.3	0.7
5	low Mg calcite	NR1003-1-7	Clay member	14.3	0.6	0.2	1707	55.3	0.2	0.14	0.3	0.1	98.0	1.5	0.2
5	low Mg calcite	NR1003-1-8	Clay member	14.3	1.3	0.1	917	50.1	0.2	0.58	2.8	0.3	95.4	3.5	0.9
5	Ca-rich dolomite	NR1003-1-14	Clay member	14.3	17.0	0.0	381	37.6	0.4	0.26	1.5	0.2	60.8	38.3	0.3
5	Ca-rich dolomite	NR1003-1-15	Clay member	14.3	16.2	0.1	507	38.4	0.4	0.49	3.4	0.4	62.3	36.5	0.6
5	Ca-rich dolomite	NR1003-1-16	Clay member	14.3	18.0	0.1	538	38.2	0.4	0.22	1.7	0.2	59.9	39.4	0.3
1	Ca-rich dolomite	NR1003-1-16	Clay member	14.3	18.8	0.0	370	34.0	0.4	0.13	1.6	0.1	56.1	43.2	0.2
1	low Mg calcite	NR1003-1-20	Clay member	14.3	1.3	0.1	631	49.3	0.3	0.84	3.6	0.4	94.8	3.6	1.3
1	low Mg calcite	NR1003-1-23	Clay member	14.3	0.9	0.1	499	51.6	0.3	0.41	2.3	0.3	96.5	2.5	0.6
1	low Mg calcite	NR1003-1-24	Clay member	14.3	1.0	0.2	1479	52.8	0.2	0.41	2.5	0.2	96.5	2.6	0.6

1	low Mg calcite	NR1003-1-26	Clay member	14.3	1.0	0.2	1518	51.5	0.1	0.61	3.8	0.4	96.3	2.6	0.9
1	low Mg calcite	NR1003-1-28	Clay member	14.3	1.1	0.2	1301	55.0	0.3	0.42	1.4	0.2	96.5	2.6	0.6
1	Ca-rich dolomite	NR1003-1-30	Clay member	14.3	17.1	0.0	413	31.2	0.4	0.47	4.8	0.4	56.1	42.7	0.7
1	high Mg calcite	NR1003-1-32	Clay member	14.3	4.1	0.1	604	45.4	0.3	0.65	3.5	0.4	87.4	11.1	1.0
1	high Mg calcite	NR1003-1-33	Clay member	14.3	1.6	0.1	754	48.6	0.3	0.52	4.4	0.5	94.4	4.3	0.8
1	low Mg calcite	NR1003-1-35	Clay member	14.3	1.2	0.1	1105	49.5	0.2	0.81	4.1	0.5	95.2	3.2	1.2
1	low Mg calcite	NR1003-1-38	Clay member	14.3	0.9	0.1	759	46.0	0.3	0.82	4.9	0.6	95.7	2.5	1.3
1	Ca-rich dolomite	NR1003-1-40	Clay member	14.3	14.5	0.1	507	34.0	0.4	0.61	4.8	0.5	61.8	36.8	0.9
1	Ca-rich dolomite	NR1003-1-41	Clay member	14.3	13.9	0.1	457	34.0	0.4	0.51	3.4	0.4	63.0	35.7	0.7
1	low Mg calcite	NR1003-1-42	Clay member	14.3	0.9	0.1	1013	51.1	0.2	0.60	1.2	0.2	96.4	2.5	0.9
1	Ca-rich dolomite	NR1003-1-43	Clay member	14.3	15.9	0.1	805	34.2	0.4	0.51	2.3	0.2	60.0	38.8	0.7
1	Ca-rich dolomite	NR1003-1-44	Clay member	14.3	18.8	0.1	683	34.3	0.3	0.16	0.8	0.1	56.4	43.0	0.2
1	low Mg calcite	NR1003-1-45	Clay member	14.3	0.9	0.3	2505	52.7	0.1	0.70	0.1	0.1	96.6	2.3	1.0
1	Ca-rich dolomite	NR1003-1-47	Clay member	14.3	16.9	0.1	695	31.7	0.4	0.29	1.9	0.2	56.9	42.1	0.4
1	high Mg calcite	NR1003-1-48	Clay member	14.3	1.4	0.1	627	44.0	0.3	0.84	4.6	0.6	93.8	4.3	1.4
1	Ca-rich dolomite	NR1003-1-49	Clay member	14.3	19.2	0.1	594	34.4	0.4	0.09	2.1	0.2	55.9	43.5	0.1
1	Ca-rich dolomite	NR1003-1-50	Clay member	14.3	17.1	0.0	406	34.5	0.4	0.30	2.8	0.3	58.7	40.4	0.4
1	low Mg calcite	NR1003-1-51	Clay member	14.3	1.3	0.3	2345	54.0	0.1	0.59	1.3	0.2	95.8	3.2	0.8

1	high Mg calcite	NR1003-1-52	Clay member	14.3	2.0	0.2	1329	52.4	0.3	0.21	1.1	0.2	94.4	4.9	0.3
1	low Mg calcite	NR1003-1-53	Clay member	14.3	1.2	0.1	803	53.0	0.4	0.52	2.3	0.3	95.8	3.0	0.7
1	low Mg calcite	NR1003-1-54	Clay member	14.3	1.3	0.1	527	51.5	0.4	0.37	2.5	0.3	95.7	3.3	0.5
1	low Mg calcite	NR1003-1-55	Clay member	14.3	1.1	0.0	366	51.5	0.2	0.45	2.6	0.3	96.2	2.8	0.7
1	Ca-rich dolomite	NR1003-2-1	dolomite marl smbr	52.2	18.4	0.3	2626	34.1	0.1	1.22	<0.028	<0.028	56.1	42.2	1.6
1	Ca-rich dolomite	NR1003-2-2	dolomite marl smbr	52.2	4.2	0.2	1509	55.2	0.1	0.15	0.1	<0.029	90.2	9.5	0.2
1	Ca-rich dolomite	NR1003-2-3	dolomite marl smbr	52.2	19.0	0.3	2457	34.3	0.1	0.15	0.3	0.1	56.3	43.4	0.2
1	Ca-rich dolomite	NR1003-2-4	dolomite marl smbr	52.2	16.4	0.2	1909	27.6	0.1	0.86	4.0	0.4	54.0	44.5	1.3
1	Ca-rich dolomite	NR1003-2-5	dolomite marl smbr	52.2	14.2	0.3	2244	35.0	0.1	0.35	0.9	0.2	63.5	35.9	0.5
1	Ca-rich dolomite	NR1003-2-6	dolomite marl smbr	52.2	17.8	0.2	1848	30.6	0.1	0.48	1.7	0.2	54.9	44.3	0.7
1	Ca-rich dolomite	NR1003-2-7	dolomite marl smbr	52.2	14.5	0.2	1659	23.8	0.1	0.64	1.4	0.2	53.5	45.2	1.1
1	Ca-rich dolomite	NR1003-2-8	dolomite marl smbr	52.2	15.3	0.2	2013	35.0	0.1	0.31	0.8	0.1	61.8	37.6	0.4
1	Ca-rich dolomite	NR1003-2-9	dolomite marl smbr	52.2	16.4	0.2	2065	34.0	0.1	0.26	1.0	0.1	59.6	40.0	0.4
1	Ca-rich dolomite	NR1003-2-10	dolomite marl smbr	52.2	17.0	0.3	2439	33.8	0.1	0.31	1.0	0.1	58.5	40.9	0.4
1	Ca-rich dolomite	NR1003-2-11	dolomite marl smbr	52.2	18.5	0.3	2707	34.2	0.2	0.39	0.3	0.1	56.7	42.6	0.5
1	Ca-rich dolomite	NR1003-2-12	dolomite marl smbr	52.2	18.1	0.3	2198	32.3	0.1	0.41	1.2	0.1	55.8	43.5	0.6
1	Ca-rich dolomite	NR1003-2-13	dolomite marl smbr	52.2	18.7	0.3	2543	35.2	0.2	0.47	1.0	0.1	57.0	42.2	0.6
1	Ca-rich dolomite	NR1003-2-14	dolomite marl smbr	52.2	15.0	0.3	2255	35.4	0.1	0.33	0.6	0.1	62.6	36.8	0.5

1	Ca-rich dolomite	NR1003-2-15	dolomite marl smbr	52.2	19.2	0.2	1862	32.7	0.0	0.17	0.2	0.0	55.0	44.7	0.2
1	Ca-rich dolomite	NR1003-2-16	dolomite marl smbr	52.2	17.6	0.2	2069	30.6	0.1	0.30	0.9	0.1	55.3	44.1	0.4
1	Ca-rich dolomite	NR1003-2-18	dolomite marl smbr	52.2	17.5	0.3	2289	31.4	0.2	3.69	0.6	0.1	53.4	41.4	4.9
1	Ca-rich dolomite	NR1003-2-19	dolomite marl smbr	52.2	19.0	0.2	2100	32.8	0.1	0.31	1.0	0.1	55.0	44.4	0.4
1	Ca-rich dolomite	NR1003-2-20	dolomite marl smbr	52.2	19.2	0.2	1723	33.0	0.1	0.34	1.0	0.1	55.0	44.5	0.4
1	high Mg calcite	NR1003-2-21	dolomite marl smbr	52.2	10.4	0.3	2254	45.6	0.1	0.46	1.0	0.1	75.4	23.9	0.6
1	Ca-rich dolomite	NR1003-2-22	dolomite marl smbr	52.2	18.2	0.2	2037	32.0	0.1	0.31	0.6	0.1	55.5	43.9	0.4
1	Ca-rich dolomite	NR1003-2-23	dolomite marl smbr	52.2	15.5	0.2	2101	35.7	0.1	0.32	0.4	0.1	61.9	37.5	0.4
1	Ca-rich dolomite	NR1003-2-24	dolomite marl smbr	52.2	18.0	0.3	2116	32.0	0.2	1.26	1.6	0.2	55.0	43.1	1.7
1	Ca-rich dolomite	NR1003-2-25	dolomite marl smbr	52.2	18.4	0.3	2497	34.4	0.1	1.32	1.0	0.1	56.3	41.9	1.7
1	Ca-rich dolomite	NR1003-2-26	dolomite marl smbr	52.2	16.8	0.3	2529	34.6	0.1	0.90	1.6	0.2	58.9	39.8	1.2
1	Ca-rich dolomite	NR1003-2-27	dolomite marl smbr	52.2	17.4	0.2	2042	31.5	0.2	1.86	1.0	0.1	54.9	42.3	2.5
1	Ca-rich dolomite	NR1003-2-28	dolomite marl smbr	52.2	17.5	0.3	2566	32.3	0.2	1.37	2.6	0.1	55.9	42.0	1.8
1	Ca-rich dolomite	NR1003-2-29	dolomite marl smbr	52.2	17.5	0.2	2106	31.6	0.1	0.47	1.7	0.2	56.0	43.2	0.6
1	Ca-rich dolomite	NR1003-2-30	dolomite marl smbr	52.2	18.0	0.3	2687	33.2	0.1	0.44	0.9	0.1	56.6	42.7	0.6
1	Ca-rich dolomite	NR1003-2-31	dolomite marl smbr	52.2	16.2	0.2	2051	29.8	0.1	0.82	1.6	0.2	56.2	42.5	1.2
1	Ca-rich dolomite	NR1003-2-32	dolomite marl smbr	52.2	17.7	0.2	2019	32.0	0.2	0.58	0.8	0.1	56.0	43.0	0.8
1	Ca-rich dolomite	NR1003-2-33	dolomite marl smbr	52.2	17.5	0.3	2399	31.6	0.1	0.67	1.1	0.1	55.8	43.1	0.9

1	Ca-rich dolomite	NR1003-2-34	dolomite marl smbr	52.2	17.8	0.3	2441	32.4	0.1	0.61	1.3	0.1	56.2	42.8	0.8
1	Ca-rich dolomite	NR1003-2-35	dolomite marl smbr	52.2	15.7	0.2	1643	29.1	0.2	3.36	0.2	<0.031	54.1	40.7	4.9
1	Ca-rich dolomite	NR1003-2-36	dolomite marl smbr	52.2	18.8	0.3	2585	34.4	0.1	0.17	0.5	0.1	56.5	43.1	0.2
1	Ca-rich dolomite	NR1003-2-37	dolomite marl smbr	52.2	16.9	0.2	2097	31.6	0.2	2.36	1.7	0.2	55.4	41.2	3.2
1	Ca-rich dolomite	NR1003-2-38	dolomite marl smbr	52.2	18.9	0.3	2661	34.5	0.1	0.21	0.4	0.1	56.5	43.1	0.3
1	Ca-rich dolomite	NR1003-2-39	dolomite marl smbr	52.2	15.3	0.2	2083	29.5	0.1	1.18	3.5	0.3	57.0	41.0	1.8
1	Ca-rich dolomite	NR1003-2-40	dolomite marl smbr	52.2	14.5	0.3	2209	38.8	0.2	0.99	0.5	0.1	64.8	33.7	1.3
1	iron-bearing dolomite	NR1003-129-01	varicolored marl smbr.	78.3	20.0	0.0	320	30.5	0.2	0.53	0.6	0.1	51.9	47.2	0.7
1	ferroan dolomite	NR1003-129-02	varicolored marl smbr.	78.3	19.1	0.2	1536	30.3	0.2	1.52	1.5	0.1	52.1	45.6	2.0
1	ferroan dolomite	NR1003-129-03	varicolored marl smbr.	78.3	19.2	0.2	1644	30.5	0.2	1.79	0.9	0.1	52.0	45.4	2.4
1	ferroan dolomite	NR1003-129-04	varicolored marl smbr.	78.3	18.2	0.2	1470	30.5	0.2	1.77	0.5	0.1	53.2	44.1	2.4
1	ferroan dolomite	NR1003-129-05	varicolored marl smbr.	78.3	18.8	0.2	1839	31.9	0.2	1.84	0.4	0.0	53.5	43.8	2.4
1	ferroan dolomite	NR1003-129-06	varicolored marl smbr.	78.3	18.0	0.2	1354	30.4	0.2	2.02	0.6	0.1	53.2	43.8	2.8
1	ferroan dolomite	NR1003-129-07	varicolored marl smbr.	78.3	17.5	0.2	1542	29.8	0.2	1.69	1.0	0.1	53.6	43.8	2.4
1	iron-bearing dolomite	NR1003-129-08	varicolored marl smbr.	78.3	19.8	0.2	1831	29.4	0.1	0.95	1.5	0.2	50.9	47.7	1.3
1	ferroan dolomite	NR1003-129-09	varicolored marl smbr.	78.3	18.4	0.2	1425	32.6	0.2	2.58	0.4	0.0	53.9	42.4	3.3
1	iron-bearing dolomite	NR1003-129-10	varicolored marl smbr.	78.3	20.5	0.2	1363	31.1	0.2	1.16	0.7	0.1	51.2	47.0	1.5
1	iron-bearing dolomite	NR1003-129-11	varicolored marl smbr.	78.3	19.5	0.2	1812	30.0	0.1	1.03	1.2	0.1	51.7	46.8	1.4

1	iron-bearing dolomite	NR1003-129-12	varicolored marl smbr.	78.3	20.4	0.2	1416	32.8	0.2	1.38	0.3	0.0	52.6	45.4	1.7
1	ferroan dolomite	NR1003-129-13	varicolored marl smbr.	78.3	18.1	0.2	1773	30.0	0.2	1.80	1.1	0.1	52.9	44.4	2.5
1	ferroan dolomite	NR1003-129-14	varicolored marl smbr.	78.3	18.3	0.2	1629	30.1	0.1	1.64	1.4	0.1	52.8	44.8	2.2
1	ferroan dolomite	NR1003-129-15	varicolored marl smbr.	78.3	16.5	0.2	1620	31.0	0.2	1.95	0.7	0.1	55.7	41.3	2.7
1	ferroan dolomite	NR1003-129-16	varicolored marl smbr.	78.3	17.8	0.2	1460	30.3	0.2	2.13	1.2	0.1	53.3	43.5	2.9
1	ferroan dolomite	NR1003-129-17	varicolored marl smbr.	78.3	18.9	0.2	1593	33.2	0.2	2.17	0.1	0.0	54.2	42.8	2.8
1	iron-bearing dolomite	NR1003-129-18	varicolored marl smbr.	78.3	20.3	0.2	1738	31.5	0.1	1.20	0.7	0.1	51.9	46.5	1.5
1	iron-bearing dolomite	NR1003-129-19	varicolored marl smbr.	78.3	20.6	0.2	1497	30.6	0.1	1.14	0.6	0.0	50.7	47.6	1.5
1	iron-bearing dolomite	NR1003-129-20	varicolored marl smbr.	78.3	22.2	0.2	1577	30.5	0.1	0.49	0.6	0.1	49.3	50.0	0.6
1	iron-bearing dolomite	NR1003-129-21	varicolored marl smbr.	78.3	20.9	0.2	1826	32.2	0.1	1.04	0.3	0.1	51.8	46.7	1.3
1	iron-bearing dolomite	NR1003-129-22	varicolored marl smbr.	78.3	20.4	0.2	1681	29.8	0.1	0.84	1.1	0.1	50.5	48.2	1.1
1	ferroan dolomite	NR1003-129-23	varicolored marl smbr.	78.3	19.4	0.2	1887	32.6	0.1	1.64	0.6	0.1	53.5	44.3	2.1
1	iron-bearing dolomite	NR1003-129-24	varicolored marl smbr.	78.3	19.7	0.2	1640	30.4	0.1	0.96	0.9	0.1	51.9	46.7	1.3
1	ferroan dolomite	NR1003-129-25	varicolored marl smbr.	78.3	18.2	0.1	1158	33.8	0.3	2.00	0.3	0.0	55.5	41.6	2.6
1	iron-bearing dolomite	NR1003-129-26	varicolored marl smbr.	78.3	19.7	0.2	1617	30.5	0.1	1.40	1.0	0.1	51.6	46.4	1.8
1	ferroan dolomite	NR1003-129-27	varicolored marl smbr.	78.3	18.5	0.2	1876	30.3	0.2	1.67	1.1	0.1	52.7	44.8	2.3
1	ferroan dolomite	NR1003-129-28	varicolored marl smbr.	78.3	17.7	0.2	1456	28.7	0.1	2.29	3.2	0.3	52.0	44.6	3.2
1	iron-bearing dolomite	NR1003-129-29	varicolored marl smbr.	78.3	20.9	0.2	1284	30.7	0.1	0.66	0.3	0.0	50.8	48.2	0.9

1	ferroan dolomite	NR1003-129-30	varicolored marl smbr.	78.3	19.7	0.2	1294	32.6	0.2	2.18	0.4	0.0	52.7	44.3	2.8
1	ferroan dolomite	NR1003-129-31	varicolored marl smbr.	78.3	19.3	0.2	1703	32.8	0.1	1.71	0.7	0.1	53.7	43.9	2.2
1	ferroan dolomite	NR1003-129-32	varicolored marl smbr.	78.3	18.9	0.2	1692	31.5	0.1	1.78	0.3	0.0	53.2	44.3	2.3
1	ferroan dolomite	NR1003-129-33	varicolored marl smbr.	78.3	19.0	0.2	1520	32.9	0.1	2.22	0.2	0.0	53.8	43.2	2.8
1	iron-bearing dolomite	NR1003-129-34	varicolored marl smbr.	78.3	20.1	0.2	1647	31.8	0.1	1.13	0.3	0.0	52.4	46.0	1.5
1	iron-bearing dolomite	NR1003-129-35	varicolored marl smbr.	78.3	19.8	0.2	1863	28.8	0.1	0.96	1.1	0.1	50.4	48.2	1.3
1	ferroan dolomite	NR1003-129-36	varicolored marl smbr.	78.3	17.6	0.2	1448	30.3	0.2	2.10	0.1	0.0	53.6	43.3	2.9
1	iron-bearing dolomite	NR1003-129-37	varicolored marl smbr.	78.3	20.8	0.2	1814	31.4	0.1	1.10	0.7	0.1	51.3	47.2	1.4
1	iron-bearing dolomite	NR1003-129-38	varicolored marl smbr.	78.3	19.8	0.2	1905	33.0	0.1	1.54	0.2	0.0	53.3	44.6	1.9
1	iron-bearing dolomite	NR1003-129-39	varicolored marl smbr.	78.3	22.9	0.2	1621	31.4	0.1	0.41	0.5	0.1	49.3	50.1	0.5
1	iron-bearing dolomite	NR1003-129-40	varicolored marl smbr.	78.3	21.6	0.2	1561	32.0	0.1	0.68	0.5	0.0	51.1	48.0	0.8
1	iron-bearing dolomite	NR1003-129-41	varicolored marl smbr.	78.3	21.4	0.2	1973	31.9	0.1	0.90	1.3	0.1	51.1	47.7	1.1
1	ferroan dolomite	NR1003-129-42	varicolored marl smbr.	78.3	18.5	0.2	1696	31.6	0.2	1.55	0.5	0.0	53.8	43.9	2.1
1	iron-bearing dolomite	NR1003-129-43	varicolored marl smbr.	78.3	20.6	0.2	1953	33.3	0.1	1.18	0.4	0.1	52.9	45.5	1.5
1	ferroan dolomite	NR1003-129-44	varicolored marl smbr.	78.3	17.8	0.2	1696	30.4	0.2	1.44	0.7	0.1	53.9	43.9	2.0
1	ferroan dolomite	NR1003-129-45	varicolored marl smbr.	78.3	19.8	0.2	1611	32.9	0.2	2.35	0.4	0.0	52.7	44.1	2.9
1	iron-bearing dolomite	NR1003-129-46	varicolored marl smbr.	78.3	20.6	0.3	2170	31.0	0.1	0.75	0.7	0.1	51.4	47.6	1.0
1	iron-bearing dolomite	NR1003-129-47	varicolored marl smbr.	78.3	20.9	0.2	1903	31.3	0.1	1.00	0.3	0.0	51.1	47.5	1.3

1	ferroan dolomite	NR1003-129-49	varicolored marl smbr.	78.3	18.5	0.2	1655	31.9	0.1	1.86	0.8	0.1	53.9	43.4	2.5
1	iron-bearing dolomite	NR1003-129-50	varicolored marl smbr.	78.3	21.4	0.2	1743	30.8	0.1	0.92	0.7	0.1	50.2	48.5	1.2
1	ferroan dolomite	NR1003-129-51	varicolored marl smbr.	78.3	19.6	0.2	1533	32.1	0.1	1.69	0.7	0.1	52.8	44.9	2.2
1	iron-bearing dolomite	NR1003-129-52	varicolored marl smbr.	78.3	19.7	0.2	1597	33.0	0.1	1.47	0.2	0.0	53.6	44.4	1.9
1	ferroan dolomite	NR1003-5-01	diatom smbr	98.1	20.3	0.2	1569	31.0	0.1	1.71	1.2	0.1	51.1	46.6	2.2
1	ferroan dolomite	NR1003-5-02	diatom smbr	98.1	18.1	0.1	1117	30.9	0.1	2.26	0.1	<0.026	53.3	43.5	3.0
1	iron-bearing dolomite	NR1003-5-03	diatom smbr	98.1	21.1	0.1	1162	30.6	0.1	1.26	<0.030	<0.027	50.1	48.2	1.6
1	iron-bearing dolomite	NR1003-5-1	diatom smbr	98.1	21.5	0.1	1050	29.6	0.1	1.19	1.1	0.1	48.8	49.5	1.5
1	iron-bearing dolomite	NR1003-5-2	diatom smbr	98.1	22.4	0.1	1115	28.8	0.1	0.90	0.7	0.1	47.4	51.4	1.2
1	iron-bearing dolomite	NR1003-5-3	diatom smbr	98.1	20.9	0.1	890	29.3	<0.034	1.16	1.1	0.1	49.4	49.1	1.5
1	iron-bearing dolomite	NR1003-5-4	diatom smbr	98.1	20.1	0.2	1284	29.0	0.1	1.26	2.0	0.2	49.9	48.3	1.7
1	ferroan dolomite	NR1003-5-5	diatom smbr	98.1	17.2	0.1	1183	29.0	0.1	2.14	3.6	0.3	53.0	43.7	3.1
1	ferroan dolomite	NR1003-5-7	diatom smbr	98.1	17.7	0.1	964	29.8	0.1	1.63	2.0	0.1	53.4	44.1	2.3
1	iron-bearing dolomite	NR1003-5-8	diatom smbr	98.1	22.0	0.1	1164	30.9	0.1	1.27	0.7	0.1	49.3	49.0	1.6
1	iron-bearing dolomite	NR1003-5-9	diatom smbr	98.1	19.9	0.1	874	28.4	0.1	1.38	2.3	0.2	49.6	48.3	1.9
1	iron-bearing dolomite	NR1003-5-10	diatom smbr	98.1	20.1	0.1	1107	29.5	0.1	1.00	1.0	0.1	50.7	47.9	1.3
1	ferroan dolomite	NR1003-5-11	diatom smbr	98.1	20.2	0.1	1125	29.7	0.1	1.69	1.5	0.1	50.1	47.5	2.2
1	Ca-rich dolomite	NR1003-5-12	diatom smbr	98.1	16.6	0.2	1301	28.6	0.1	1.20	3.0	0.2	54.3	43.7	1.8

1	ferroan dolomite	NR1003-5-13	diatom smbr	98.1	19.4	0.2	1322	31.0	0.1	2.15	0.8	0.1	52.0	45.1	2.8
1	iron-bearing dolomite	NR1003-5-14	diatom smbr	98.1	20.3	0.1	861	27.9	0.1	1.28	2.5	0.2	48.8	49.4	1.7
1	iron-bearing dolomite	NR1003-5-15	diatom smbr	98.1	22.5	0.1	939	29.2	0.1	1.43	1.3	0.1	47.3	50.8	1.8
1	iron-bearing dolomite	NR1003-5-17	diatom smbr	98.1	21.0	0.1	1014	29.3	0.1	1.40	1.4	0.2	49.1	49.0	1.8
1	iron-bearing dolomite	NR1003-5-18	diatom smbr	98.1	22.6	0.1	806	29.7	0.1	1.06	0.8	0.1	47.9	50.7	1.3
1	ferroan dolomite	NR1003-5-19	diatom smbr	98.1	20.5	0.1	1005	31.6	0.1	2.18	0.3	<0.030	51.1	46.1	2.7
1	iron-bearing dolomite	NR1003-5-20	diatom smbr	98.1	21.2	0.0	412	31.4	0.1	0.41	0.3	0.0	51.2	48.2	0.5
1	iron-bearing dolomite	NR1003-5-21	diatom smbr	98.1	21.0	0.1	1253	30.8	0.1	1.49	0.2	<0.026	50.3	47.7	1.9
1	iron-bearing dolomite	NR1003-5-22	diatom smbr	98.1	21.2	0.1	1213	28.6	0.1	1.08	1.3	0.1	48.4	50.0	1.4
1	iron-bearing dolomite	NR1003-5-23	diatom smbr	98.1	21.0	0.2	1389	30.0	0.1	1.14	2.1	0.1	49.8	48.6	1.5
1	iron-bearing dolomite	NR1003-5-24	diatom smbr	98.1	21.7	0.1	878	29.6	0.0	1.10	1.3	0.1	48.8	49.7	1.4
1	iron-bearing dolomite	NR1003-5-25	diatom smbr	98.1	22.1	0.1	741	28.5	0.1	1.33	0.5	0.1	47.3	50.9	1.7
1	iron-bearing dolomite	NR1003-5-26	diatom smbr	98.1	21.0	0.1	986	29.9	0.1	1.55	0.4	0.1	49.5	48.4	2.0
1	iron-bearing dolomite	NR1003-5-27	diatom smbr	98.1	21.3	0.2	1321	30.9	0.1	0.86	0.8	0.1	50.4	48.4	1.1
1	iron-bearing dolomite	NR1003-5-28	diatom smbr	98.1	20.8	0.2	1430	32.1	0.1	1.48	0.1	<0.027	51.5	46.4	1.9
1	iron-bearing dolomite	NR1003-5-29	diatom smbr	98.1	22.6	0.1	931	29.1	0.1	1.13	0.6	0.0	47.3	51.1	1.4
1	iron-bearing dolomite	NR1003-5-31	diatom smbr	98.1	22.1	0.1	693	30.5	0.1	1.08	0.1	<0.028	49.1	49.5	1.4
1	iron-bearing dolomite	NR1003-5-33	diatom smbr	98.1	20.4	0.1	1180	28.1	0.1	1.25	2.0	0.1	48.8	49.4	1.7

215

1	iron-bearing dolomite	NR1003-5-34	diatom smbr	98.1	21.0	0.1	1076	28.7	0.1	1.37	1.6	0.1	48.6	49.5	1.8
1	iron-bearing dolomite	NR1003-5-35	diatom smbr	98.1	22.2	0.1	999	29.5	0.1	1.23	1.6	0.1	48.1	50.2	1.6
1	iron-bearing dolomite	NR1003-5-36	diatom smbr	98.1	22.4	0.1	970	28.9	<0.034	1.20	0.7	0.0	47.3	51.1	1.5
1	iron-bearing dolomite	NR1003-5-37	diatom smbr	98.1	22.2	0.1	801	29.7	0.1	1.13	0.7	<0.031	48.3	50.2	1.4
1	Ca-rich dolomite	NR1003-5-38	diatom smbr	98.1	18.0	0.1	1083	28.7	0.1	1.27	1.7	0.0	52.3	45.8	1.8
1	iron-bearing dolomite	NR1003-5-39	diatom smbr	98.1	21.4	0.1	1136	29.3	0.1	1.54	2.2	0.1	48.6	49.3	2.0
1	ferroan dolomite	NR1003-5-40	diatom smbr	98.1	18.2	0.1	869	27.9	0.1	1.62	3.5	0.2	51.2	46.4	2.3
1	iron-bearing dolomite	NR1003-5-41	diatom smbr	98.1	20.1	0.1	1125	29.4	0.1	1.41	1.8	0.1	50.3	47.7	1.9
1	iron-bearing dolomite	NR1003-5-42	diatom smbr	98.1	22.4	0.1	757	29.8	0.1	1.31	0.1	<0.025	48.0	50.3	1.7
1	iron-bearing dolomite	NR1003-5-43	diatom smbr	98.1	21.1	0.1	976	29.2	0.1	1.43	1.8	0.1	48.9	49.1	1.9
1	iron-bearing dolomite	NR1003-5-44	diatom smbr	98.1	23.2	0.1	912	29.5	0.1	1.25	0.7	0.1	46.9	51.4	1.6
1	iron-bearing dolomite	NR1003-5-48	diatom smbr	98.1	22.4	0.1	1123	30.9	0.1	1.06	0.2	0.0	49.1	49.5	1.3
1	dolomite (nearly stoichiometric)	NR1003-5-49	diatom smbr	98.1	22.0	<0.024	0	31.1	<0.033	0.04	<0.028	<0.026	50.4	49.6	0.1
1	ferroan dolomite	NR1003-5-50	diatom smbr	98.1	17.7	0.1	1070	28.8	0.1	1.54	2.4	0.2	52.7	45.0	2.2
5	ferroan dolomite	NR1003-6-1	diatom smbr	105.3	19.0	0.1	968	30.6	0.1	1.77	1.0	0.1	52.4	45.2	2.4
5	ferroan dolomite	NR1003-6-2	diatom smbr	105.3	18.2	0.1	996	27.9	0.1	2.14	3.5	0.3	50.8	46.0	3.0
5	ferroan dolomite	NR1003-6-3	diatom smbr	105.3	18.6	0.1	809	29.0	0.1	2.17	1.9	0.1	51.2	45.7	3.0

5	ferroan dolomite	NR1003-6-4	diatom smbr	105.3	18.5	0.1	928	29.0	0.1	2.27	2.2	0.2	51.2	45.6	3.1
5	iron-bearing dolomite	NR1003-6-5	diatom smbr	105.3	19.0	0.1	1251	30.5	0.1	1.25	1.0	0.1	52.6	45.6	1.7
5	ferroan dolomite	NR1003-6-6	diatom smbr	105.3	19.0	0.1	1045	30.4	0.1	1.56	1.1	0.1	52.3	45.5	2.1
5	ferroan dolomite	NR1003-6-7	diatom smbr	105.3	18.8	0.1	749	29.0	0.0	2.46	1.3	0.1	50.8	45.8	3.4
5	ferroan dolomite	NR1003-6-8	diatom smbr	105.3	18.4	0.1	744	29.0	0.1	2.45	2.1	0.2	51.3	45.3	3.4
5	ferroan dolomite	NR1003-6-9	diatom smbr	105.3	18.9	0.1	1144	29.9	0.1	1.98	1.8	0.1	51.7	45.4	2.7
5	ferroan dolomite	NR1003-6-10	diatom smbr	105.3	18.9	0.1	904	29.4	0.1	2.21	1.5	0.1	51.1	45.7	3.0
2	ferroan dolomite	NR1003-6-11	diatom smbr	105.3	18.6	0.1	1086	29.0	0.1	2.06	1.5	0.1	51.3	45.7	2.8
2	iron-bearing dolomite	NR1003-6-12	diatom smbr	105.3	18.6	0.2	1518	29.7	0.1	1.43	1.8	0.2	52.3	45.7	2.0
2	ferroan dolomite	NR1003-6-13	diatom smbr	105.3	18.1	0.1	978	28.4	0.1	1.75	2.9	0.3	51.6	45.8	2.5
2	ferroan dolomite	NR1003-6-14	diatom smbr	105.3	18.8	0.1	923	29.4	0.1	2.00	1.3	0.1	51.4	45.8	2.7
2	ferroan dolomite	NR1003-6-15	diatom smbr	105.3	17.5	0.1	846	27.3	0.0	1.88	2.9	0.2	51.3	45.9	2.8
2	ferroan dolomite	NR1003-6-17	diatom smbr	105.3	15.6	0.1	989	26.4	0.1	2.11	4.0	0.4	53.0	43.6	3.3
2	ferroan dolomite	NR1003-6-18	diatom smbr	105.3	18.5	0.1	1120	28.6	<0.034	1.77	2.6	0.2	51.3	46.2	2.5
2	ferroan dolomite	NR1003-6-19	diatom smbr	105.3	19.1	0.1	644	30.0	0.1	1.87	0.6	0.0	51.6	45.7	2.5
2	ferroan dolomite	NR1003-6-20	diatom smbr	105.3	18.4	0.1	1196	27.6	0.0	1.89	2.6	0.3	50.5	46.8	2.7
2	ferroan dolomite	NR1003-6-21	diatom smbr	105.3	18.8	0.1	918	29.0	0.1	1.85	1.5	0.1	51.1	46.2	2.5
2	ferroan dolomite	NR1003-6-22	diatom smbr	105.3	18.7	0.1	983	28.6	<0.035	2.34	1.5	0.1	50.8	46.0	3.2

2	ferroan dolomite	NR1003-6-23	diatom smbr	105.3	19.3	0.1	936	29.8	0.1	1.61	0.5	<0.030	51.4	46.3	2.2
2	ferroan dolomite	NR1003-6-24	diatom smbr	105.3	18.8	0.1	906	29.3	0.1	2.25	1.1	0.1	51.1	45.7	3.1
2	ferroan dolomite	NR1003-6-25	diatom smbr	105.3	18.8	0.1	852	28.8	<0.034	2.02	1.7	0.2	50.9	46.3	2.8
2	ferroan dolomite	NR1003-6-26	diatom smbr	105.3	18.9	0.1	911	28.3	0.1	2.14	2.1	0.2	50.3	46.7	3.0
2	ferroan dolomite	NR1003-6-27	diatom smbr	105.3	19.5	0.1	842	29.5	0.2	1.71	0.6	0.1	50.8	46.6	2.3
2	ferroan dolomite	NR1003-6-28	diatom smbr	105.3	18.3	0.1	633	28.6	0.1	2.10	2.1	0.2	51.2	45.6	2.9
2	ferroan dolomite	NR1003-6-29	diatom smbr	105.3	18.6	0.1	524	27.9	0.1	2.33	2.9	0.2	50.2	46.4	3.3
2	ferroan dolomite	NR1003-6-30	diatom smbr	105.3	18.3	0.1	713	29.0	0.1	2.35	1.6	0.1	51.4	45.3	3.3
1	ferroan dolomite	NR1003-6-31	diatom smbr	105.3	18.6	0.1	766	29.9	0.1	2.56	2.5	0.2	51.7	44.7	3.5
1	ferroan dolomite	NR1003-6-32	diatom smbr	105.3	18.7	0.1	863	30.0	0.1	2.74	2.7	0.2	51.5	44.7	3.7
1	ferroan dolomite	NR1003-6-33	diatom smbr	105.3	19.4	0.1	999	29.8	0.1	2.07	2.6	0.2	50.9	46.2	2.8
1	ferroan dolomite	NR1003-6-34	diatom smbr	105.3	18.9	0.1	963	28.9	0.0	2.28	1.8	0.1	50.7	46.1	3.1
1	ferroan dolomite	NR1003-6-35	diatom smbr	105.3	18.6	0.1	826	29.7	0.1	2.71	1.9	0.2	51.4	44.8	3.7
1	ferroan dolomite	NR1003-6-37	diatom smbr	105.3	18.1	0.1	1033	29.2	0.1	2.55	3.4	0.2	51.7	44.7	3.5
1	ferroan dolomite	NR1003-6-38	diatom smbr	105.3	19.7	0.1	1000	32.0	0.1	2.01	0.2	0.0	52.4	44.9	2.6
1	ferroan dolomite	NR1003-6-39	diatom smbr	105.3	18.3	0.1	783	29.4	0.1	2.52	1.6	0.1	51.8	44.7	3.5
1	ferroan dolomite	NR1003-6-40	diatom smbr	105.3	18.9	0.1	715	31.4	0.1	2.12	0.9	0.1	52.8	44.3	2.8
1	ferroan dolomite	NR1003-6-41	diatom smbr	105.3	17.9	0.1	1145	29.0	0.1	2.07	4.8	0.1	52.2	44.8	2.9

1	ferroan dolomite	NR1003-6-42	diatom smbr	105.3	19.1	0.1	1082	31.8	0.2	2.20	1.9	0.1	52.8	44.1	2.8
1	ferroan dolomite	NR1003-6-43	diatom smbr	105.3	20.1	0.1	484	31.0	0.2	1.75	0.3	0.0	51.2	46.3	2.3
1	ferroan dolomite	NR1003-6-44	diatom smbr	105.3	19.6	0.1	1053	31.6	0.1	2.53	0.4	0.0	51.9	44.8	3.2
1	iron-bearing dolomite	NR1003-6-45	diatom smbr	105.3	20.0	0.1	946	32.0	0.1	1.28	0.8	0.1	52.5	45.8	1.6
1	ferroan dolomite	NR1003-6-46	diatom smbr	105.3	18.9	0.1	508	30.4	0.1	2.67	1.7	0.1	51.6	44.7	3.5
1	ferroan dolomite	NR1003-6-47	diatom smbr	105.3	18.9	0.1	731	31.1	0.1	2.89	1.4	0.1	52.1	44.1	3.8
1	ferroan dolomite	NR1003-6-48	diatom smbr	105.3	18.1	0.1	1110	28.6	<0.034	1.72	3.0	0.3	51.9	45.7	2.4
1	ferroan dolomite	NR1003-6-49	diatom smbr	105.3	20.1	0.1	929	31.0	0.1	1.56	0.7	0.1	51.4	46.5	2.0
1	ferroan dolomite	NR1003-6-50	diatom smbr	105.3	19.3	0.1	1256	30.4	0.0	2.00	1.1	0.1	51.6	45.6	2.7
1	ferroan dolomite	NR1003-6-51	diatom smbr	105.3	18.9	0.1	769	30.9	0.1	2.44	1.3	0.1	52.2	44.4	3.2
1	ferroan dolomite	NR1003-6-52	diatom smbr	105.3	19.7	0.1	1059	31.9	0.1	2.12	0.6	0.1	52.3	44.8	2.7
1	ferroan dolomite	NR1003-6-53	diatom smbr	105.3	19.6	0.1	573	31.8	0.1	2.03	1.0	0.1	52.3	44.9	2.6
1	iron-bearing dolomite	NR1003-6-54	diatom smbr	105.3	20.2	0.1	1004	31.6	0.1	1.36	0.3	<0.029	51.9	46.2	1.7
1	ferroan dolomite	NR1003-6-55	diatom smbr	105.3	19.1	0.1	818	30.2	0.1	2.76	1.5	0.1	51.1	45.1	3.7
1	low Mg calcite	NR1003-8-01	diatom smbr	121.6	1.6	<0.027	0	54.0	0.0	0.45	0.2	0.1	95.5	3.8	0.6
1	Ca-rich dolomite	NR1003-8-3	diatom smbr	121.6	19.0	0.2	1397	30.3	0.1	1.68	2.3	0.2	52.1	45.4	2.3
1	Ca-rich dolomite	NR1003-8-5	diatom smbr	121.6	18.4	0.1	874	29.3	0.1	2.07	2.1	0.2	51.8	45.2	2.9
1	Ca-rich dolomite	NR1003-8-8	diatom smbr	121.6	19.2	0.2	1411	30.5	0.1	1.00	1.8	0.2	52.6	46.0	1.3

1	Ca-rich dolomite	NR1003-8-9	diatom smbr	121.6	19.5	0.2	2030	32.0	0.1	0.86	1.3	0.1	53.4	45.3	1.1
1	high Mg calcite	NR1003-8-11	diatom smbr	121.6	16.3	0.2	1292	38.1	0.2	1.00	1.2	0.1	61.7	36.8	1.3
1	Ca-rich dolomite	NR1003-8-12	diatom smbr	121.6	19.1	0.1	1254	34.4	0.1	0.79	0.5	0.1	55.7	43.1	1.0
1	Ca-rich dolomite	NR1003-8-13	diatom smbr	121.6	17.4	0.2	1379	31.6	0.1	2.11	0.7	0.1	55.0	42.0	2.9
1	Ca-rich dolomite	NR1003-8-15	diatom smbr	121.6	17.5	0.1	982	29.5	0.1	2.31	2.1	0.2	52.9	43.7	3.2
1	Ca-rich dolomite	NR1003-8-18	diatom smbr	121.6	19.0	0.2	1764	31.3	0.1	1.70	2.3	0.2	52.8	44.8	2.2
1	Ca-rich dolomite	NR1003-8-19	diatom smbr	121.6	18.3	0.3	2576	32.3	0.1	1.04	1.0	0.1	55.1	43.4	1.4
1	Ca-rich dolomite	NR1003-8-20	diatom smbr	121.6	17.1	0.1	1249	30.1	0.1	2.62	2.6	0.3	53.7	42.5	3.6
1	high Mg calcite	NR1003-8-21	diatom smbr	121.6	15.3	0.3	2859	35.5	0.1	0.91	1.4	0.1	61.6	37.0	1.2
1	Ca-rich dolomite	NR1003-8-22	diatom smbr	121.6	19.0	0.1	1193	31.3	0.1	1.71	1.2	0.1	52.9	44.7	2.3
1	Ca-rich dolomite	NR1003-8-23	diatom smbr	121.6	17.1	0.1	1183	30.8	0.1	2.19	2.4	0.2	54.6	42.2	3.0
1	Ca-rich dolomite	NR1003-8-24	diatom smbr	121.6	17.0	0.2	1440	29.6	0.3	1.43	2.7	0.2	54.3	43.3	2.0
1	Ca-rich dolomite	NR1003-8-25	diatom smbr	121.6	19.8	0.2	1867	32.6	0.1	0.61	1.2	0.1	53.7	45.3	0.8
1	Ca-rich dolomite	NR1003-8-28	diatom smbr	121.6	19.7	0.1	1167	30.9	0.1	0.82	1.7	0.1	52.4	46.4	1.1
1	Ca-rich dolomite	NR1003-8-30	diatom smbr	121.6	19.2	0.2	2020	32.0	0.1	0.89	1.2	0.1	53.7	44.9	1.2
1	Ca-rich dolomite	NR1003-8-31	diatom smbr	121.6	18.9	0.2	1320	30.0	0.1	1.39	2.8	0.3	52.2	45.7	1.9
1	Ca-rich dolomite	NR1003-8-35	diatom smbr	121.6	19.4	0.2	1553	30.3	0.1	1.08	2.2	0.2	52.0	46.5	1.4
1	Ca-rich dolomite	NR1003-8-36	diatom smbr	121.6	20.1	0.2	1598	31.6	0.1	0.68	0.9	0.2	52.5	46.5	0.9

1	Ca-rich dolomite	NR1003-8-37	diatom smbr	121.6	18.0	0.1	1094	31.0	0.3	2.41	1.6	0.1	53.3	43.1	3.2
1	Ca-rich dolomite	NR1003-8-39	diatom smbr	121.6	20.0	0.2	1821	32.5	0.1	0.77	1.1	0.1	53.2	45.7	1.0
1	Ca-rich dolomite	NR1003-8-40	diatom smbr	121.6	16.9	0.1	871	27.1	0.1	2.53	2.8	0.3	51.5	44.6	3.8
1	Ca-rich dolomite	NR1003-8-41	diatom smbr	121.6	19.0	0.2	1525	30.8	0.1	1.40	1.6	0.2	52.7	45.2	1.9
1	high Mg calcite	NR1003-8-42	diatom smbr	121.6	14.6	0.2	1783	32.3	0.3	2.92	2.8	0.3	58.6	36.8	4.1
1	Ca-rich dolomite	NR1003-8-43	diatom smbr	121.6	18.5	0.2	1457	33.6	0.1	1.80	1.3	0.1	55.2	42.3	2.3
1	Ca-rich dolomite	NR1003-8-45	diatom smbr	121.6	19.9	0.2	2042	31.5	0.1	1.28	1.3	0.1	52.3	45.9	1.7
1	Ca-rich dolomite	NR1003-8-47	diatom smbr	121.6	16.4	0.1	731	28.6	0.2	3.92	3.2	0.2	52.4	41.7	5.6
1	Ca-rich dolomite	NR1003-8-50	diatom smbr	121.6	18.3	0.2	1895	30.6	0.2	1.27	1.4	0.1	53.5	44.5	1.7
1	Ca-rich dolomite	NR1003-187-01	bitumen smbr.	166	15.8	0.3	2221	31.7	0.1	1.70	1.8	0.2	57.4	39.9	2.4
1	ferroan dolomite	NR1003-187-02	bitumen smbr.	166	15.7	0.2	1734	31.3	0.1	4.91	1.5	0.2	54.9	38.2	6.7
1	high Mg calcite	NR1003-187-03	bitumen smbr.	166	3.0	0.1	1243	46.3	0.1	1.10	2.7	0.3	90.1	8.1	1.7
1	Ca-rich dolomite	NR1003-187-04	bitumen smbr.	166	21.4	0.0	174	30.7	0.0	0.17	0.4	0.1	50.7	49.1	0.2
1	Ca-rich dolomite	NR1003-187-09	bitumen smbr.	166	17.7	0.3	2292	31.1	0.1	1.66	0.8	0.1	54.4	43.2	2.3
1	Ca-rich dolomite	NR1003-187-10	bitumen smbr.	166	17.3	0.2	1850	33.2	0.1	0.92	1.3	0.2	57.1	41.5	1.2
1	ferroan dolomite	NR1003-187-11	bitumen smbr.	166	16.5	0.2	1737	32.3	0.2	4.30	1.3	0.2	54.9	39.1	5.7
1	ferroan dolomite	NR1003-187-12	bitumen smbr.	166	14.3	0.3	2116	30.8	0.1	5.08	2.5	0.3	56.3	36.3	7.2
1	Ca-rich dolomite	NR1003-187-13	bitumen smbr.	166	19.1	0.3	2932	33.7	0.0	0.40	0.3	0.1	55.5	43.9	0.5

1	ferroan dolomite	NR1003-187-16	bitumen smbr.	166	16.7	0.3	2134	31.1	0.1	3.10	2.2	0.2	54.7	40.9	4.3
1	Ca-rich dolomite	NR1003-187-17	bitumen smbr.	166	18.0	0.3	2831	32.0	0.1	1.17	1.7	0.2	55.1	43.2	1.6
1	low Mg calcite	NR1003-187-18	bitumen smbr.	166	0.0	0.1	1224	55.8	0.0	0.18	0.2	0.1	99.7	0.0	0.2
1	ferroan dolomite	NR1003-187-19	bitumen smbr.	166	12.9	0.3	2131	31.0	0.2	4.02	0.7	0.1	59.3	34.5	6.0
1	ferroan dolomite	NR1003-187-22	bitumen smbr.	166	14.3	0.2	1842	30.9	0.2	3.25	3.4	0.4	57.7	37.3	4.7
1	Ca-rich dolomite	NR1003-187-25	bitumen smbr.	166	15.1	0.3	2714	30.7	0.1	2.80	2.3	0.2	56.8	39.0	4.0
1	Ca-rich dolomite	NR1003-187-26	bitumen smbr.	166	19.2	0.3	2140	34.2	0.1	0.40	1.1	0.2	55.8	43.5	0.5
1	Ca-rich dolomite	NR1003-187-27	bitumen smbr.	166	17.6	0.3	2322	34.1	0.2	1.29	1.6	0.1	57.1	41.0	1.7
1	ferroan dolomite	NR1003-187-29	bitumen smbr.	166	14.1	0.2	2013	31.4	0.2	3.34	1.5	0.2	58.4	36.6	4.9
1	Ca-rich dolomite	NR1003-187-33	bitumen smbr.	166	18.3	0.1	827	28.7	1.1	1.92	1.8	0.3	50.7	45.1	2.7
1	Ca-rich dolomite	NR1003-187-34	bitumen smbr.	166	17.4	0.3	2170	31.2	0.2	1.43	1.4	0.2	55.1	42.7	2.0
1	Ca-rich dolomite	NR1003-187-35	bitumen smbr.	166	17.8	0.3	2185	32.8	0.1	0.77	1.4	0.2	56.4	42.5	1.0
1	ferroan dolomite	NR1003-187-36	bitumen smbr.	166	16.7	0.2	2051	33.2	0.2	4.05	1.6	0.2	55.6	38.9	5.3
1	Ca-rich dolomite	NR1003-187-39	bitumen smbr.	166	17.6	0.3	2620	32.9	0.2	1.14	1.1	0.1	56.4	41.9	1.5
1	high Mg calcite	NR1003-187-41	bitumen smbr.	166	4.0	0.1	1157	46.9	0.1	1.69	1.5	0.3	87.1	10.3	2.5
1	ferroan dolomite	NR1003-187-43	bitumen smbr.	166	13.9	0.2	1734	28.1	0.1	5.27	4.4	0.5	54.5	37.4	8.0
1	ferroan dolomite	NR1003-187-44	bitumen smbr.	166	15.3	0.2	1754	32.2	0.1	4.83	2.7	0.2	56.0	37.2	6.6
1	Ca-rich dolomite	NR1003-187-46	bitumen smbr.	166	18.4	0.2	1685	34.7	0.2	1.17	1.7	0.2	56.5	41.8	1.5

1	Ca-rich dolomite	NR1003-187-47	bitumen smbr.	166	19.9	0.2	1948	34.9	0.1	0.80	1.0	0.2	55.1	43.7	1.0
1	Ca-rich dolomite	NR1003-187-48	bitumen smbr.	166	13.5	0.2	1847	37.7	0.1	1.21	1.8	0.2	65.5	32.7	1.6
1	Ca-rich dolomite	NR1003-187-50	bitumen smbr.	166	18.5	0.3	2936	32.2	0.1	0.80	0.9	0.1	54.9	43.8	1.1
1	ankerite?	NR1003-187-37	bitumen smbr.	166	11.2	0.2	1691	30.7	0.2	10.74	0.7	0.1	56.1	28.4	15.3
1	ankerite?	NR1003-187-38	bitumen smbr.	166	10.5	0.2	1594	31.1	0.1	12.19	0.1	0.1	56.3	26.3	17.2
1	ankerite?	NR1003-187-42	bitumen smbr.	166	10.5	0.1	763	28.4	0.1	13.10	1.7	0.3	53.2	27.5	19.2
1	ankerite?	NR1003-187-45	bitumen smbr.	166	11.0	0.2	1565	27.8	0.1	10.30	4.3	0.4	54.3	29.8	15.7
1	ankerite?	NR1003-187-49	bitumen smbr.	166	11.0	0.2	1302	29.7	0.1	12.87	0.7	0.1	53.8	27.8	18.2
1	ankerite?	NR1003-187-06	bitumen smbr.	166	10.2	0.2	1501	30.5	0.1	12.76	0.2	0.1	55.7	26.0	18.2
1	ankerite?	NR1003-187-07	bitumen smbr.	166	12.4	0.2	1468	30.8	0.1	9.28	1.1	0.1	55.6	31.1	13.1
1	ankerite?	NR1003-187-14	bitumen smbr.	166	11.9	0.2	1421	30.4	0.2	10.44	0.1	0.1	55.1	29.9	14.8
1	ankerite?	NR1003-187-15	bitumen smbr.	166	10.0	0.2	1500	30.5	0.1	12.66	0.2	0.1	56.1	25.6	18.2
1	ankerite?	NR1003-187-20	bitumen smbr.	166	11.9	0.2	2021	28.7	0.1	10.09	3.2	0.4	53.9	31.2	14.8
1	ankerite?	NR1003-187-21	bitumen smbr.	166	10.2	0.2	1473	29.7	0.1	13.17	0.1	0.1	54.7	26.2	19.0
1	ankerite?	NR1003-187-24	bitumen smbr.	166	12.7	0.3	2187	31.8	0.1	7.40	0.3	0.0	57.5	32.0	10.4
1	ankerite?	NR1003-187-28	bitumen smbr.	166	10.4	0.2	1491	29.8	0.1	12.05	0.6	0.1	55.4	27.0	17.5
1	ankerite?	NR1003-187-31	bitumen smbr.	166	12.0	0.2	1836	31.9	0.1	6.57	2.1	0.1	59.4	30.9	9.5
1	ankerite?	NR1003-187-32	bitumen smbr.	166	9.7	0.2	1328	27.0	0.1	13.99	3.1	0.1	52.5	26.2	21.2
1	Ca-rich dolomite	NR1003-216-01	analcime smbr	210.8	18.9	0.2	1826	33.6	0.0	0.23	1.2	0.2	55.9	43.7	0.3
1	Ca-rich dolomite	NR1003-216-02	analcime smbr	210.8	18.8	0.2	1901	35.8	0.1	0.20	0.2	0.1	57.6	42.1	0.2
1	Ca-rich dolomite	NR1003-216-04	analcime smbr	210.8	18.1	0.2	1707	31.9	0.0	0.29	0.7	0.2	55.5	44.0	0.4
1	Ca-rich dolomite	NR1003-216-05	analcime smbr	210.8	18.9	0.2	1290	31.9	0.0	0.10	1.2	0.2	54.7	45.1	0.1
1	Ca-rich dolomite	NR1003-216-07	analcime smbr	210.8	19.2	0.1	1251	34.1	0.2	0.36	0.4	0.1	55.7	43.6	0.5
1	Ca-rich dolomite	NR1003-216-08	analcime smbr	210.8	19.1	0.3	2169	34.2	0.0	0.20	0.2	0.1	56.1	43.6	0.3

1	Ca-rich dolomite	NR1003-216-09	analcime smbr	210.8	16.4	0.2	1515	32.5	0.2	0.73	2.6	0.3	58.0	40.8	1.0
1	Ca-rich dolomite	NR1003-216-10	analcime smbr	210.8	17.1	0.2	1909	31.9	0.1	0.78	0.8	0.1	56.6	42.2	1.1
1	Ca-rich dolomite	NR1003-216-11	analcime smbr	210.8	12.7	0.1	1030	35.4	0.1	1.20	1.2	0.2	65.4	32.7	1.7
1	Ca-rich dolomite	NR1003-216-12	analcime smbr	210.8	20.1	0.1	740	34.2	0.1	0.21	0.3	0.1	54.8	44.8	0.3
1	Ca-rich dolomite	NR1003-216-13	analcime smbr	210.8	18.1	0.2	1975	33.5	0.0	0.41	0.3	0.1	56.7	42.7	0.5
1	Ca-rich dolomite	NR1003-216-14	analcime smbr	210.8	16.5	0.2	1769	31.5	0.1	0.91	0.4	0.1	57.0	41.6	1.3
1	Ca-rich dolomite	NR1003-216-15	analcime smbr	210.8	17.8	0.2	1996	36.8	0.1	0.19	0.3	0.1	59.6	40.1	0.2
1	Ca-rich dolomite	NR1003-216-16	analcime smbr	210.8	17.7	0.1	1078	32.1	0.2	0.65	0.2	0.1	55.9	42.9	0.9
1	Ca-rich dolomite	NR1003-216-19	analcime smbr	210.8	18.6	0.2	1815	33.9	0.0	0.15	0.7	0.2	56.5	43.3	0.2
1	Ca-rich dolomite	NR1003-216-22	analcime smbr	210.8	11.4	0.1	1061	40.1	0.1	0.39	0.3	0.0	71.2	28.1	0.5
1	Ca-rich dolomite	NR1003-216-24	analcime smbr	210.8	14.1	0.2	1412	40.2	0.2	0.28	1.7	0.3	66.8	32.6	0.4
1	Ca-rich dolomite	NR1003-216-25	analcime smbr	210.8	17.5	0.2	2063	33.4	0.1	0.38	0.8	0.1	57.6	41.9	0.5
1	Ca-rich dolomite	NR1003-216-26	analcime smbr	210.8	19.5	0.3	2210	35.1	0.1	0.14	1.7	0.2	56.3	43.5	0.2
1	Ca-rich dolomite	NR1003-216-27	analcime smbr	210.8	14.9	0.2	1607	29.3	0.1	1.76	3.1	0.3	57.0	40.3	2.7
1	Ca-rich dolomite	NR1003-216-29	analcime smbr	210.8	13.5	0.2	1598	38.7	0.1	0.24	0.8	0.2	67.1	32.5	0.3
1	Ca-rich dolomite	NR1003-216-31	analcime smbr	210.8	16.7	0.2	1672	33.0	0.1	1.09	0.4	0.1	57.8	40.6	1.5
1	Ca-rich dolomite	NR1003-216-34	analcime smbr	210.8	18.3	0.2	1703	32.8	0.0	0.28	0.5	0.1	56.1	43.5	0.4
1	Ca-rich dolomite	NR1003-216-38	analcime smbr	210.8	19.4	0.2	1978	34.3	0.1	0.08	0.1	0.1	55.8	43.9	0.1

1	Ca-rich dolomite	NR1003-216-39	analcime smbr	210.8	18.7	0.1	849	33.3	0.0	0.65	1.8	0.3	55.7	43.4	0.8
1	Ca-rich dolomite	NR1003-216-40	analcime smbr	210.8	18.8	0.2	1598	33.0	0.1	0.21	0.4	0.0	55.5	44.1	0.3
1	Ca-rich dolomite	NR1003-216-42	analcime smbr	210.8	19.0	0.2	2033	34.4	0.1	0.18	0.1	0.0	56.3	43.3	0.2
1	Ca-rich dolomite	NR1003-216-43	analcime smbr	210.8	17.3	0.2	1489	32.2	0.2	0.70	0.8	0.1	56.5	42.3	1.0
1	Ca-rich dolomite	NR1003-216-44	analcime smbr	210.8	17.0	0.1	754	33.6	0.2	0.85	0.4	0.1	57.8	40.7	1.1
1	Ca-rich dolomite	NR1003-216-45	analcime smbr	210.8	18.3	0.2	1967	33.6	0.0	0.43	0.2	0.0	56.6	42.8	0.6
1	Ca-rich dolomite	NR1003-216-46	analcime smbr	210.8	15.9	0.1	686	33.7	0.2	0.93	0.8	0.1	59.4	39.0	1.3
1	Ca-rich dolomite	NR1003-216-47	analcime smbr	210.8	18.9	0.2	1633	34.3	0.0	0.22	0.4	0.0	56.4	43.3	0.3
1	Ca-rich dolomite	NR1003-216-48	analcime smbr	210.8	14.7	0.2	1334	28.2	0.1	1.29	2.7	0.3	56.7	41.1	2.0
1	Ca-rich dolomite	NR1003-216-49	analcime smbr	210.8	18.8	0.2	1344	33.1	0.2	0.48	0.4	0.1	55.4	43.8	0.6
1	Ca-rich dolomite	NR1003-216-50	analcime smbr	210.8	17.5	0.2	1678	32.4	0.1	0.62	1.1	0.1	56.6	42.5	0.8
1	Ca-rich dolomite	NR1003-216-52	analcime smbr	210.8	17.0	0.2	1951	32.5	0.1	0.53	1.2	0.2	57.4	41.8	0.7
1	Ca-rich dolomite	NR1003-216-55	analcime smbr	210.8	19.0	0.2	1763	34.7	0.0	0.33	1.8	0.3	56.5	43.1	0.4
1	Ca-rich dolomite	NR1003-216-03	analcime smbr	210.8	18.0	0.2	1764	33.8	0.0	0.57	4.4	0.6	57.0	42.2	0.8
1	Ca-rich dolomite	NR1003-216-18	analcime smbr	210.8	15.7	0.2	1823	30.5	0.1	0.94	3.6	0.5	57.4	41.1	1.4
1	Ca-rich dolomite	NR1003-216-20	analcime smbr	210.8	17.2	0.2	1900	30.6	0.1	0.25	3.0	0.3	55.8	43.8	0.4
1	Ca-rich dolomite	NR1003-216-21	analcime smbr	210.8	18.1	0.2	1807	34.1	0.1	0.18	3.3	0.4	57.3	42.4	0.2
1	Ca-rich dolomite	NR1003-216-33	analcime smbr	210.8	17.2	0.2	1575	30.7	0.0	0.48	3.2	0.3	55.7	43.6	0.7

5	dolomite (nearly stoichiometric)	NR1003-230-1	clinoptilolite smbr	223	22.7	0.2	1644	29.4	0.0	<0.024	<0.028	<0.028	48.1	51.8	0.0
5	dolomite (nearly stoichiometric)	NR1003-230-2	clinoptilolite smbr	223	21.6	0.2	1840	29.0	0.0	0.55	0.6	0.1	48.8	50.4	0.7
5	dolomite (nearly stoichiometric)	NR1003-230-3	clinoptilolite smbr	223	20.7	0.2	1892	29.8	0.0	0.08	0.9	0.1	50.8	49.0	0.1
5	dolomite (nearly stoichiometric)	NR1003-230-4	clinoptilolite smbr	223	21.3	0.3	2633	29.5	<0.034	<0.025	<0.030	<0.027	49.8	50.2	0.0
5	dolomite (nearly stoichiometric)	NR1003-230-5	clinoptilolite smbr	223	21.1	0.2	1902	28.7	<0.032	0.10	1.7	0.2	49.4	50.5	0.1
5	dolomite (nearly stoichiometric)	NR1003-230-8	clinoptilolite smbr	223	22.1	0.2	1982	29.8	<0.032	0.05	0.6	0.1	49.1	50.8	0.1
5	dolomite (nearly stoichiometric)	NR1003-230-9	clinoptilolite smbr	223	19.0	0.2	1753	27.0	<0.033	0.27	2.4	0.2	50.4	49.3	0.4
5	dolomite (nearly stoichiometric)	NR1003-230-10	clinoptilolite smbr	223	18.8	0.2	1901	26.1	<0.034	2.16	3.1	0.3	48.4	48.5	3.1
2	dolomite (nearly stoichiometric)	NR1003-230-11	clinoptilolite smbr	223	21.7	0.2	1808	29.1	<0.032	0.11	0.8	0.1	48.9	50.9	0.1

226

2	dolomite (nearly stoichiometric)	NR1003-230-12	clinoptilolite smbr	223	21.2	0.2	1643	27.7	<0.032	<0.025	<0.029	<0.029	48.4	51.6	0.0
2	dolomite (nearly stoichiometric)	NR1003-230-13	clinoptilolite smbr	223	21.9	0.2	1924	29.9	<0.032	0.04	0.1	<0.028	49.5	50.5	0.1
2	dolomite (nearly stoichiometric)	NR1003-230-14	clinoptilolite smbr	223	21.8	0.2	1754	29.3	<0.032	0.06	0.5	0.1	49.2	50.8	0.1
2	dolomite (nearly stoichiometric)	NR1003-230-15	clinoptilolite smbr	223	22.0	0.2	1853	29.9	0.0	0.04	0.1	<0.025	49.3	50.6	0.1
2	dolomite (nearly stoichiometric)	NR1003-230-16	clinoptilolite smbr	223	20.6	0.2	1974	30.4	0.0	0.04	0.3	0.0	51.5	48.4	0.0
2	dolomite (nearly stoichiometric)	NR1003-230-17	clinoptilolite smbr	223	22.3	0.2	1964	28.4	<0.032	0.12	0.6	0.1	47.6	52.2	0.2
2	dolomite (nearly stoichiometric)	NR1003-230-18	clinoptilolite smbr	223	22.1	0.2	2002	28.7	<0.032	0.05	0.8	0.1	48.3	51.7	0.1
2	dolomite (nearly stoichiometric)	NR1003-230-19	clinoptilolite smbr	223	21.8	0.2	1710	29.2	<0.033	0.05	0.8	0.1	49.0	50.9	0.1
2	dolomite (nearly stoichiometric)	NR1003-230-20	clinoptilolite smbr	223	21.4	0.2	1887	29.5	<0.034	0.04	0.4	<0.030	49.8	50.2	0.1

2	dolomite (nearly stoichiometric)	NR1003-230-21	clinoptilolite smbr	223	20.7	0.2	1963	29.3	<0.033	0.05	0.7	0.1	50.4	49.5	0.1
2	dolomite (nearly stoichiometric)	NR1003-230-22	clinoptilolite smbr	223	22.0	0.2	1556	28.7	<0.033	0.07	0.6	0.1	48.4	51.5	0.1
2	dolomite (nearly stoichiometric)	NR1003-230-23	clinoptilolite smbr	223	22.2	0.2	1942	29.5	0.0	0.04	0.2	<0.029	48.9	51.0	0.0
2	dolomite (nearly stoichiometric)	NR1003-230-24	clinoptilolite smbr	223	21.9	0.2	2060	29.0	<0.034	0.03	0.5	0.0	48.7	51.3	0.0
2	dolomite (nearly stoichiometric)	NR1003-230-26	clinoptilolite smbr	223	21.8	0.2	1794	28.0	<0.032	0.08	0.9	0.1	48.0	51.9	0.1
2	dolomite (nearly stoichiometric)	NR1003-230-27	clinoptilolite smbr	223	20.7	0.2	2113	28.9	<0.033	0.17	2.4	0.2	50.0	49.8	0.2
2	dolomite (nearly stoichiometric)	NR1003-230-29	clinoptilolite smbr	223	21.9	0.2	1675	28.1	<0.033	0.17	1.5	0.1	47.8	51.9	0.2
2	dolomite (nearly stoichiometric)	NR1003-230-30	clinoptilolite smbr	223	21.2	0.2	1652	29.2	<0.033	0.11	1.2	0.1	49.7	50.2	0.1
1	dolomite (nearly stoichiometric)	NR1003-230-31	clinoptilolite smbr	223	21.1	0.2	1966	29.9	<0.034	0.07	0.6	<0.028	50.4	49.5	0.1

1	dolomite (nearly stoichiometric)	NR1003-230-32	clinoptilolite smbr	223	20.7	0.3	2155	31.5	<0.034	<0.025	<0.030	<0.027	52.3	47.7	0.0
1	dolomite (nearly stoichiometric)	NR1003-230-33	clinoptilolite smbr	223	22.3	0.3	2165	31.1	<0.033	<0.025	0.1	<0.027	50.0	50.0	0.0
1	dolomite (nearly stoichiometric)	NR1003-230-34	clinoptilolite smbr	223	20.3	0.2	1919	29.3	<0.034	0.14	1.4	0.1	50.8	49.1	0.2
1	dolomite (nearly stoichiometric)	NR1003-230-35	clinoptilolite smbr	223	21.8	0.2	1798	28.5	<0.033	0.09	1.0	0.1	48.4	51.5	0.1
1	dolomite (nearly stoichiometric)	NR1003-230-36	clinoptilolite smbr	223	20.9	0.2	2060	29.5	<0.033	<0.026	0.3	<0.025	50.4	49.6	0.0
1	dolomite (nearly stoichiometric)	NR1003-230-37	clinoptilolite smbr	223	21.9	0.2	2042	31.2	<0.033	0.04	0.2	0.0	50.6	49.4	0.0
1	dolomite (nearly stoichiometric)	NR1003-230-38	clinoptilolite smbr	223	21.1	0.2	1818	29.4	<0.033	0.07	0.9	0.1	49.9	50.0	0.1
1	dolomite (nearly stoichiometric)	NR1003-230-39	clinoptilolite smbr	223	18.8	0.3	2177	28.3	<0.033	0.30	3.2	0.3	51.7	47.9	0.4
1	dolomite (nearly stoichiometric)	NR1003-230-40	clinoptilolite smbr	223	23.0	0.2	1760	30.4	0.0	<0.024	0.1	<0.024	48.7	51.2	0.0

1	dolomite (nearly stoichiometric)	NR1003-230-41	clinoptilolite smbr	223	22.3	0.2	1743	32.3	<0.032	0.06	0.5	0.0	50.9	49.0	0.1
1	dolomite (nearly stoichiometric)	NR1003-230-42	clinoptilolite smbr	223	22.8	0.2	1898	29.3	0.1	0.07	0.3	0.0	47.9	51.9	0.1
1	dolomite (nearly stoichiometric)	NR1003-230-43	clinoptilolite smbr	223	23.2	0.2	1926	30.2	0.0	0.11	1.6	0.1	48.2	51.6	0.1
1	dolomite (nearly stoichiometric)	NR1003-230-44	clinoptilolite smbr	223	21.6	0.3	2183	31.5	0.0	<0.025	0.3	<0.026	51.1	48.8	0.0
1	dolomite (nearly stoichiometric)	NR1003-230-45	clinoptilolite smbr	223	23.2	0.2	1788	30.1	<0.033	0.03	0.8	<0.027	48.2	51.7	0.0
1	dolomite (nearly stoichiometric)	NR1003-230-46	clinoptilolite smbr	223	21.6	0.3	2385	29.1	<0.034	0.05	0.8	0.1	49.1	50.8	0.1
1	dolomite (nearly stoichiometric)	NR1003-230-47	clinoptilolite smbr	223	21.3	0.2	1924	30.6	<0.033	0.09	1.1	0.1	50.7	49.2	0.1
1	dolomite (nearly stoichiometric)	NR1003-230-48	clinoptilolite smbr	223	21.6	0.2	1838	29.2	<0.033	0.09	0.4	<0.027	49.3	50.6	0.1
1	dolomite (nearly stoichiometric)	NR1003-230-49	clinoptilolite smbr	223	23.0	0.2	1917	29.2	<0.033	0.10	1.7	0.2	47.7	52.2	0.1

1	dolomite (nearly stoichiometric)	NR1003-230-50	clinoptilolite smbr	223	22.7	0.2	2003	29.7	<0.032	0.07	2.8	0.0	48.4	51.5	0.1
1	dolomite (nearly stoichiometric)	NR1003-230-51	clinoptilolite smbr	223	22.1	0.2	1782	31.7	<0.032	0.03	0.2	0.1	50.7	49.3	0.0
1	dolomite (nearly stoichiometric)	NR1003-230-52	clinoptilolite smbr	223	22.5	0.2	2093	29.7	0.0	0.09	0.7	<0.030	48.5	51.3	0.1
1	dolomite (nearly stoichiometric)	NR1003-230-53	clinoptilolite smbr	223	21.9	0.2	1963	31.3	<0.032	0.08	0.6	0.0	50.5	49.4	0.1
1	dolomite (nearly stoichiometric)	NR1003-230-54	clinoptilolite smbr	223	23.3	0.3	2234	31.0	<0.034	<0.026	0.1	0.0	48.9	51.1	0.0
1	dolomite (nearly stoichiometric)	NR1003-230-55	clinoptilolite smbr	223	22.5	0.2	1900	30.1	0.1	0.08	1.2	0.0	48.9	50.9	0.1

Table A.8 Statistics of the stable isotope results by different lithographic/isotopic members and mineral phases.

	Number of samples	δ13C Max	δ13C Min	δ13C Mean	δ13C SD	δ18O (corrected) Max	δ18O (corrected) Min	δ18O (corrected) Mean	δ18O (corrected) SD	δ13C-δ18O r value	test size	δ13C-δ18O p value
NR1003 all Samples	204	20.93	-10.13	3.67	6.62	5.28	-11.67	0.42	3.12	0.48	7.79	0.00
from 225.9 to 159.4 m depth, all samples	55	6.12	-10.13	0.62	3.66	5.28	-11.67	1.63	2.54	0.27	2.08	0.04
from 225.9 to 159.4 m depth, dolomite & dolomite dominated samples	53	6.12	-10.13	-0.10	3.88	5.28	-11.67	0.93	3.24	0.27	2.03	0.05
high δ13C interval all samples	71	20.93	3.47	10.88	4.43	4.80	-8.55	1.98	1.93	0.59	6.08	0.00
high δ13C interval calcite & calcite dominated samples (exclude one outlier NR1003-128)	10	13.62	4.28	6.92	2.83	4.38	-8.55	0.01	3.23	0.93	7.16	0.00
high δ13C dolomite & dolomite dominated samples	60	20.93	3.47	11.60	4.30	4.80	-0.73	2.33	1.35	0.58	5.40	0.00
Calcite samples (NR1003, exclude those from clay member and one outlier NR1003-128)	40	13.62	-6.82	1.12	4.79	4.38	-9.78	-2.69	3.47	0.88	11.26	0.00
Calcite samples before clay member (Nördlingen 1973)	17	10.50	-6.70	0.55	4.99	2.40	-10.40	-2.34	3.96	0.82	5.55	0.00

Table A.9 Stable isotope data of the reference Miocene freshwater carbonates from Ries surrounding areas

sample number	location	stratigraphic age	lithofacies association	sample description	analysed material	δ13C (‰ V-PDB)	δ18O (‰ V-PDB)
Miocene floodplain carbonates (Zeng et al., 2021)							
PF10	Pleinfeld, Franconian Alb, Germany	Karpatian	whitegrey limestone with root voids (LFT 9)	5.7 m core depth:	microcrystalline calcite	0.65	-4.97
PF10	Pleinfeld, Franconian Alb, Germany	Karpatian	whitegrey limestone with root voids (LFT 9)	5.7 m core depth:	microcrystalline calcite	0.45	-5.24
PF15	Pleinfeld, Franconian Alb, Germany	Karpatian	whitegrey limestone with root voids (LFT 9)	7.5 m core depth:	microcrystalline calcite	1.99	-4.73
PF16	Pleinfeld, Franconian Alb, Germany	Karpatian	whitegrey limestone with root voids (LFT 9)	7.95 m core depth:	microcrystalline calcite	0.97	-5.25
PF12	Pleinfeld, Franconian Alb, Germany	Karpatian	whitegrey calcareous marl with root voids (LFT 8)	6.7 m core depth:	microcrystalline calcite	1.34	-4.74

PF12	Pleinfeld, Franconian Alb, Germany	Karpatian	whitegrey calcareous marl with root voids (LFT 8)	6.7 m core depth:	microcrystalline calcite	1.51	-4.87
PF25	Pleinfeld, Franconian Alb, Germany	Karpatian	whitegrey calcareous marl with root voids (LFT 8)	12.4 m core depth:	microcrystalline calcite	-0.48	-5.06
PF27	Pleinfeld, Franconian Alb, Germany	Karpatian	whitegrey calcareous marl with root voids (LFT 8)	14.5 m core depth:	microcrystalline calcite	-2.25	-4.84
PF37	Pleinfeld, Franconian Alb, Germany	Karpatian	redbrown mottled marl (LFT 7b)	20.05 m core depth:	microcrystalline calcite	-0.68	-5.19
PF37	Pleinfeld, Franconian Alb, Germany	Karpatian	redbrown mottled marl (LFT 7b)	20.05 m core depth:	microcrystalline calcite	-0.51	-5.22
PF40	Pleinfeld, Franconian Alb, Germany	Karpatian	redbrown mottled marl (LFT 7b)	22.1 m core depth:	microcrystalline calcite	-1.81	-5.28
PF41	Pleinfeld, Franconian Alb, Germany	Karpatian	redbrown mottled marl (LFT 7b)	23.25 m core depth:	microcrystalline calcite	-3.50	-5.31
PF43	Pleinfeld, Franconian Alb, Germany	Karpatian	redbrown mottled marl (LFT 7b)	25.3 m core depth:	microcrystalline calcite	-4.58	-4.55
PF43	Pleinfeld, Franconian Alb, Germany	Karpatian	redbrown mottled marl (LFT 7b)	25.3 m core depth:	microcrystalline calcite	-3.71	-5.16
PF45	Pleinfeld, Franconian Alb, Germany	Karpatian	redbrown mottled marl (LFT 7b)	27.2 m core depth:	microcrystalline calcite	-3.94	-5.26
PF52	Pleinfeld, Franconian Alb, Germany	Karpatian	redbrown mottled marl (LFT 7b)	32.15 m core depth:	microcrystalline calcite	-6.42	-4.16
PF54	Pleinfeld, Franconian Alb, Germany	Karpatian	redbrown mottled marl (LFT 7b)	33.1 m core depth:	microcrystalline calcite	-0.22	-4.77
PF56	Pleinfeld, Franconian Alb, Germany	Karpatian	redbrown mottled marl (LFT 7b)	35.07 m core depth:	microcrystalline calcite	-0.03	-5.02
PF58	Pleinfeld, Franconian Alb, Germany	Karpatian	redbrown mottled marl (LFT 7b)	37.08 m core depth:	microcrystalline calcite	-3.41	-4.58
PF58	Pleinfeld, Franconian Alb, Germany	Karpatian	redbrown mottled marl (LFT 7b)	37.08 m core depth:	microcrystalline calcite	-6.90	-4.56
PF58	Pleinfeld, Franconian Alb, Germany	Karpatian	redbrown mottled marl (LFT 7b)	37.08 m core depth:	microcrystalline calcite	-7.38	-4.67
PF58	Pleinfeld, Franconian Alb, Germany	Karpatian	redbrown mottled marl (LFT 7b)	37.08 m core depth:	microcrystalline calcite	-0.30	-5.16
PF58	Pleinfeld, Franconian Alb, Germany	Karpatian	redbrown mottled marl (LFT 7b)	37.08 m core depth:	microcrystalline calcite	-0.37	-5.08

Table A.10 Stable isotope data of the Nördlingen 1973 drilling (Rothe and Hoefs, 1977).
Note that samples with No. 65 and 146 have high δ¹³C values.

	Sample number	depth [m]	CaCO₃ [%]	dolomite [wt %]	dolomite [mole %]	calcite [wt %]	calcite [mole %]	$\delta^{13}C$ [‰ PDB]	$\delta^{18}O$ [‰ PDB]	$\delta^{18}O$ corrected [‰ PDB]	remarks
Clay member	2	9.34	84	0	0	84	100	-3.2	-5.3	-5.30	meteoric diagenesis?
Clay member	6	12.75	83	0	0	83	100	-3.6	4.7	4.70	
Clay member	13	24.47	50	50	100	0	0	-2.5	4.3	2.66	**Dolomite**
Clay member	15	26.81	72	0	0	72	100	-0.9	-1.5	-1.50	
Clay member	25	36.67	74	3	4	71	96	3	-1.1	-1.17	
Clay member	29	39.57	58	0	0	58	100	3.4	0.4	0.40	
Clay member	30	43.4	87	82	94	5	6	1.6	-1.7	-3.24	**Dolomite**
Clay member	33	45.5	19	0	0	19	100	0.7	-3.4	-3.40	
Clay member	36	47.97	79	0	0	79	100	-11.5	0.4	0.40	
Marl member	41	53.02	80	80	100	0	0	3.7	2.4	0.76	**Dolomite**
Marl member	43	55	40	18	45	22	55	1.5	0.3	-0.43	
Marl member	45	57.06	55	38	69	17	31	1.7	1.5	0.37	
Marl member	48	59.92	25	15	60	10	40	0.7	-0.3	-1.28	
Marl member	50	61.98	38	25	66	13	34	1.9	2.2	1.12	
Marl member	53	65.44	27	18	67	9	33	0.1	2.3	1.21	
Marl member	55	66.75	46	33	72	13	28	1.9	2.4	1.23	
Marl member	56	72.26	55	38	69	17	31	3.2	1.7	0.57	
Marl member	58	77.76	68	68	100	0	0	**-2.4**	3.8	2.16	**Dolomite**
Marl member	60	79.79	42	24	57	18	43	1.6	0.1	-0.83	
Marl member	62	85.75	26	0	0	26	100	1.7	-1.7	-1.70	
Marl member	65	90.4	100	100	100	0	0	11.1	3.7	2.06	**Dolomite**
Marl member	68	93.56	32	23	72	9	28	1	0.9	-0.27	
Marl member	70	95.37	30	16	53	14	47	3.5	1.1	0.23	
Marl member	74	99.11	32	0	0	32	100	3.4	-2.7	-2.70	
Marl member	76	101.65	59	46	78	13	22	7.3	-0.4	-1.67	
Marl member	77	104.46	84	84	100	0	0	9.5	1.8	0.17	**Dolomite**
Marl member	82	109.42	41	0	0	41	100	1.9	-2.8	-2.80	

Laminite member	90	117.65	29	0	0	29	100	4.7	1	1.00	
Laminite member	101	127.48	64	64	100	0	0	7.7	3.2	1.56	**Dolomite**
Laminite member	113	138.78	49	49	100	0	0	7.2	6.4	4.76	**Dolomite**
Laminite member	117	142.18	48	42	88	6	13	7.2	3.5	2.07	**Dolomite**
Laminite member	121	146.12	24	13	54	11	46	3.8	1.3	0.42	Mg-Calcite (10-17 Mol% $MgCO_3$)
Laminite member	127	152.31	22	4	18	18	82	6.3	2.4	2.10	Mg-Calcite (10-17 Mol% $MgCO_3$)
Laminite member	133	158.19	25	15	60	10	40	4.3	1.5	0.52	Mg-Calcite (10-17 Mol% $MgCO_3$)
Laminite member	136	161.75	37	27	73	10	27	7.6	1.9	0.71	Mg-Calcite (10-17 Mol% $MgCO_3$)
Laminite member	142	167.16	38	31	82	7	18	6.2	2	0.67	Mg-Calcite (10-17 Mol% $MgCO_3$)
Laminite member	146	171.64	32	8	25	24	75	10.5	1.1	0.69	Mg-Calcite (10-17 Mol% $MgCO_3$)
Laminite member	156	181.22	29	20	69	9	31	6.2	1.1	-0.03	Mg-Calcite (10-17 Mol% $MgCO_3$)
Laminite member	160	185.5	37	29	78	8	22	7.8	1.9	0.62	Mg-Calcite (10-17 Mol% $MgCO_3$)
Laminite member	162	187.65	58	42	72	16	28	7.2	3.2	2.01	Mg-Calcite (6-20 Mol% $MgCO_3$)
Laminite member	163	188.53	40	19	48	21	53	5.3	1.1	0.32	Mg-Calcite (6-20 Mol% $MgCO_3$)
Laminite member	164	189	37	19	51	18	49	5.9	2.3	1.46	Mg-Calcite (6-20 Mol% $MgCO_3$)
Laminite member	170	195.32	27	20	74	7	26	8.1	3.5	2.29	Mg-Calcite (6-20 Mol% $MgCO_3$)
Laminite member	174	198.6	28	20	71	8	29	5.1	0.5	-0.67	
Laminite member	180	204.53	33	10	30	23	70	2.5	0.8	0.31	
Laminite member	187	211.87	23	18	78	5	22	1	1.7	0.42	

Laminite member	196	220.51	30	23	77	4	23	1.8	2	0.75	
Laminite member	205	228.08	50	45	90	5	10	2.8	2.5	1.03	**Dolomite**
Laminite member	208	231.25	45	37	82	5	18	4.7	1.4	0.06	
Laminite member	214	237.58	40	27	68	3	33	4.7	1.7	0.60	
Laminite member	222	244.14	72	0	0	72	100	-2.7	-4.9	-4.90	
Laminite member	228	250.82	63	60	95	0	5	1.3	4.8	3.24	**Dolomite**
Laminite member	230	252.45	30	10	33	0	67	3.9	1.5	0.96	
Basal member	239	260.6	90	70	78	20	22	-1.3	-1.5	-2.77	
Basal member	251	272.56	70	22	31	48	69	-3.5	-4.3	-4.81	
Basal member	252	273.37	69	5	7	64	93	-3.8	0.9	0.78	
Basal member	262	283.82	34	15	44	19	56	-4.9	-7.8	-8.51	
Basal member	264	285.39	42	0	0	42	100	-5	-7.4	-7.40	
Basal member	274	295.75	30	5	17	25	83	-5.8	-6.8	-7.07	
Basal member	298	319.42	22	10	45	12	55	-6.7	-10.4	-11.13	

Table A.11 C_{org}, C_{carb}, $CaCO_3$, d_{104} values and stable isotope data of the dolomite samples in the high $\delta^{13}C$ interval

sample number	depth (plot) [m.b.s.]	lithostratigraphic member	mineralogy	$\delta^{13}C$ ‰, VPDB	$\delta^{18}O$ (corrected) ‰, VPDB	C_{carb} [wt%]	$CaMg(CO_3)_2$ [wt%]	d_{104}-spacing
NR 1003-3	-74.4	varicolored marl smbr.	dolomicrite	6.99	1.38	10.3	78.8	2.901
NR 1003-124	-74.7	varicolored marl smbr.	dolomicrite	7.22	2.63	8.9	68.3	2.901
NR 1003-125	-75.7	varicolored marl smbr.	dolomicrite	5.61	3.49	7.6	58.5	2.895
NR 1003-126	-75.8	varicolored marl smbr.	dolomicrite	8.35	2.81	9.0	68.8	2.894
NR 1003-127	-76.2	varicolored marl smbr.	dolomicrite	8.04	2.45	9.0	69.1	2.904
NR 1003-129	-78.3	varicolored marl smbr.	dolomicrite	9.43	2.37	10.4	79.9	2.898
NR 1003-130	-79.5	varicolored marl smbr.	dolomicrite	11.13	2.94	9.8	75.0	2.900
NR 1003-131	-80.3	varicolored marl smbr.	dolomicrite	9.92	2.76	9.9	75.9	2.894
NR 1003-132	-82	varicolored marl smbr.	dolomicrite	9.92	4.28	9.0	69.4	2.895
NR 1003-133	-83.7	varicolored marl smbr.	dolomicrite	11.39	2.57	10.8	83.2	2.889
NR 1003-134	-84.9	varicolored marl smbr.	dolomicrite	16.07	3.28	7.8	60.0	2.895
NR 1003-4	-85.4	varicolored marl smbr.	dolomicrite	13.87	1.69	10.7	82.4	2.891
NR 1003-135	-85.9	varicolored marl smbr.	dolomicrite	12.17	3.90	10.6	81.2	2.895
NR 1003-136	-86.7	varicolored marl smbr.	dolomicrite	14.41	3.63	8.9	68.1	2.900
NR 1003-137	-87.7	diatom smbr.	dolomicrite	13.74	3.39	7.4	57.0	2.899
NR 1003-138	-89.2	diatom smbr.	dolomicrite	6.19	1.10	4.3	33.3	2.908

NR 1003-139	-93.1	diatom smbr.	dolomicrite predominated mixture	3.97	-0.23	3.5	27.1	2.910
NR 1003-140	-93.4	diatom smbr.	dolomicrite	8.06	0.00	6.0	45.8	2.908
NR 1003-141	-94.2	diatom smbr.	dolomicrite	11.46	1.43	9.1	70.0	2.906
NR 1003-142	-94.8	diatom smbr.	dolomicrite	12.43	2.37	8.4	64.2	2.905
NR 1003-143	-95.1	diatom smbr.	dolomicrite	12.16	0.42	10.3	78.8	2.895
NR 1003-5	-98.1	diatom smbr.	dolomicrite	16.40	0.28	12.0	91.7	2.888
NR 1003-146	-103.3	diatom smbr.	dolomicrite	18.72	2.33	8.7	67.0	2.890
NR 1003-147	-105.3	diatom smbr.	dolomicrite	19.72	3.13	10.7	81.9	2.894
NR 1003-6	-105.3	diatom smbr.	dolomicrite	20.93	2.00	11.8	90.7	2.894
NR 1003-148	-107.1	diatom smbr.	dolomicrite	19.74	3.86	9.6	73.6	2.901
NR 1003-149	-109	diatom smbr.	dolomicrite	10.97	0.55	4.7	35.7	2.905
NR 1003-150	-111.1	diatom smbr.	allochtounous calcite/dolomite clast	7.47	2.25	5.9	45.2	2.904
NR 1003-153	-113.5	diatom smbr.	dolomicrite	9.60	1.49	3.7	28.2	2.902
NR 1003-154	-114.6	diatom smbr.	dolomicrite	10.05	2.26	3.6	27.8	2.905
NR 1003-155	-116.5	diatom smbr.	dolomicrite	17.54	4.45	6.8	52.1	2.901
NR 1003-156	-116.7	diatom smbr.	dolomicrite	18.52	4.80	10.1	77.2	2.898
NR 1003-158	-119.9	diatom smbr.	dolomicrite predominated mixture	5.75	0.62	4.0	30.3	2.909
NR 1003-159	-121.6	diatom smbr.	dolomicrite	17.04	3.78	6.7	51.7	2.901
NR 1003-8	-121.6	diatom smbr.	dolomicrite	17.03	2.12	9.2	70.9	2.901
NR 1003-9	-123.6	diatom smbr.	dolomicrite	14.52	1.29	6.1	47.1	2.894
NR 1003-160	-123.8	diatom smbr.	dolomicrite	18.11	4.14	8.9	67.9	2.892

NR 1003-162	-128.7	bituminous smbr.	dolomicrite	16.34	3.21	6.0	46.1	2.900
NR 1003-163	-129.6	bituminous smbr.	dolomicrite predominated mixture	7.66	-0.08	4.1	31.7	2.909
NR 1003-164	-131.6	bituminous smbr.	dolomicrite predominated mixture	6.97	0.32	4.0	31.0	2.912
NR 1003-165	-133.6	bituminous smbr.	dolomicrite predominated mixture	6.25	-0.04	2.6	20.3	2.919
NR 1003-166	-135.9	bituminous smbr.	dolomicrite	17.49	4.30	6.5	49.8	2.903
NR 1003-167	-137.5	bituminous smbr.	dolomicrite	10.05	1.64	4.5	34.7	2.900
NR 1003-168	-138.6	bituminous smbr.	dolomicrite	14.74	3.61	4.9	37.9	2.896
NR 1003-169	-140	bituminous smbr.	dolomicrite predominated mixture	8.40	1.61	3.6	27.6	2.904
NR 1003-170-1	-142.8	bituminous smbr.	dolomicrite	12.73	3.10	9.7	74.6	2.899
NR 1003-170-2	-142.8	bituminous smbr.	dolomicrite	12.73	3.27	9.7	74.6	2.899
NR 1003-171	-143.2	bituminous smbr.	dolomicrite	11.46	3.43	8.8	67.2	2.903
NR 1003-172	-146.3	bituminous smbr.	dolomicrite	9.56	2.38	5.9	45.2	2.905
NR 1003-173	-147.8	bituminous smbr.	dolomicrite	12.94	3.88	7.6	58.2	2.901
NR 1003-174	-148.5	bituminous smbr.	dolomicrite	9.49	2.53	6.2	47.4	2.901
NR 1003-175	-149.3	bituminous smbr.	dolomicrite predominated mixture	5.51	0.66	4.3	32.9	2.908
NR 1003-176	-150.4	bituminous smbr.	dolomicrite	3.47	-0.73	5.4	41.1	2.919
NR 1003-177	-152.5	bituminous smbr.	dolomicrite	13.82	3.45	5.3	40.8	2.901
NR 1003-178	-152.6	bituminous smbr.	dolomicrite	10.79	2.31	3.8	28.9	2.902
NR 1003-179	-153.5	bituminous smbr.	dolomicrite	12.80	3.50	4.1	31.2	2.901

NR 1003-180	-155.1	bituminous smbr.	dolomicrite	10.93	2.71	3.7	28.6	2.904
NR 1003-181	-155.7	bituminous smbr.	dolomicrite	10.57	2.76	4.4	33.9	2.905
NR 1003-182	-156.2	bituminous smbr.	dolomicrite	10.05	2.85	2.5	18.9	2.905
NR 1003-183	-157.2	bituminous smbr.	dolomicrite	6.81	1.39	3.0	23.1	2.901

Table A.12 Hydrochemical data of waters in Ries basin.

Source of data	sample number	type of sampe	region	aquifer	T °C	pH	Na⁺ mg/L	K⁺ mg/L	Ca²⁺ mg/L	Mg²⁺ mg/L	Sr²⁺ mg/L	Fe²⁺/Fe³⁺ mg/L	Mn²⁺/Mn⁴⁺ µg/L	Cl⁻ mg/L	SO₄²⁻ mg/L	NO₃⁻ mg/L	HCO₃⁻ mg/L
Winkler 1972	A74	Spring discharge	Ries margin	Braunjura	7.4	7.3	1.7	1.4	59	7.3	0.072	0.07	-	10.1	14.5	15.5	166
Winkler 1972	A97	Spring site	Ries margin	Braunjura	9.4	7.1	3.2	1.5	88	1.8	0.068	n.a.	2.8	18.1	25	21.6	206
Winkler 1972	A98	Spring site	Ries margin	Braunjura	9	7.1	3.9	1.8	96.8	2.4	0.088	0.04	-	21.1	27.4	2.8	237
Winkler 1972	A65	Spring discharge	Ries margin	Schwarzjura	6.6	7.3	4.2	1.1	130.2	3	0.295	0.04	4.3	25	47	53.5	269
Winkler 1972	A66	Spring	Ries margin	Schwarzjura	6.8	7.4	5.9	1.1	154	4.2	-	0	-	39.1	80	34.5	306
Winkler 1972	A99	Spring discharge	Ries margin	Schwarzjura	8.8	7.3	6.2	1.5	142.5	13.3	0.185	n.a.	2.5	17.2	134	45.3	275
Winkler 1972	A68	Spring	Ries margin	Keuper	6.4	6.6	9.3	3.5	38	9.7	0.565	n.a.	-	6.1	34	2.9	142
Winkler 1972	A18/1	Drill well	Ries margin	bunte breccia	12.1	7.4	4.4	2.8	83	32.8	1.5	0.27	11	5.6	41.3		372
Winkler 1972	A18/2	Drill well	Ries margin	bunte breccia	10.5	7.3	5.1	4.2	79	37	1.5	0.33	11	7.6	46.5		376
Winkler 1972	A18/3	Drill well	Ries margin	bunte breccia	10.9	7.8	4	3.5	83	36.5	1.5	0.19	11	7	41.6		376
Winkler 1972	A18/4	Drill well	Ries margin	bunte breccia	11.6	7.3	3.9	3.3	82	34.6	1.5	0.32	11	8	47.2		376
Winkler 1972	A43	Drill well	Ries margin	bunte breccia	8.5	7.8	11.5	2.6	79	12.2	0.66	0.04	1.6	15.6	36	29	236
Winkler 1972	A44/3	Drill well	Ries margin	bunte breccia	8.5	8.1	9.8	11.5	102.1	18.8	0.495	0.17	300	21	68	13.5	323
Winkler 1972	A49	Spring site	Ries margin	bunte breccia	9.2	7.9	2.6	2.2	96	3.6	-	0.05	-	7	31	3.6	262
Winkler 1972	A50	Spring discharge	Ries margin	bunte breccia	9.6	6.9	2.7	0.8	116.1	1.3	-	0.04	-	22	22.8	26.3	272
Winkler 1972	A51	Spring site	Ries margin	bunte breccia	8.9	7	1.9	0.8	124	2.4	-	0.02	-	12.5	17.2	18.8	337

Source	ID	Type	Location	Rock													
Winkler 1972	A52	Spring discharge	Ries margin	bunte breccia	9.6	6.9	2.4	1.4	113.1	1.3	-	0.06	-	13.5	20	10.8	305
Winkler 1972	A53	Spring discharge	Ries margin	bunte breccia	9.7	7	6.2	2.9	130.1	3.1	-	0.05	-	17	18	12.8	372
Winkler 1972	A54	Spring site	Ries margin	bunte breccia	8.8	7	2.3	1.1	147.2		-	0.02	-	13.5	13.2	17.6	403
Winkler 1972	A55	Spring discharge	Ries margin	bunte breccia	9.9	7.3	2.9	1.3	132	4.3	-	0.07	-	13	19.6	25.5	359
Winkler 1972	A56	Spring site	Ries margin	bunte breccia	10.3	7.3	2.8	1.4	114.1	3.6	-	0.03	-	18	24.6	22.7	298
Winkler 1972	A57	Spring site	Ries margin	bunte breccia	10	7.1	3.7	1.6	120	2.4	-	0.03	-	27	43	68	228
Winkler 1972	A71	Spring discharge	Ries margin	bunte breccia	7.2	7.1	5.6	5.2	130.6	6.1	0.28	0.05	-	29.1	42.5	31	315
Winkler 1972	A73	Spring discharge	Ries margin	bunte breccia	7.6	7.3	4.2	2.5	140	8.5	0.345	0.03	-	18.5	53	39.6	342
Winkler 1972	A75	Spring discharge	Ries margin	bunte breccia	9.4	7.4	2.6	1.9	131	4.2	0.235	0.03	-	20.9	19.5	41.5	323
Winkler 1972	A79	Spring site	Ries margin	bunte breccia	7	7.3	4	1	123.1	5.5	0.145	0.06	-	13.8	32	14.5	337
Winkler 1972	A80	Spring discharge	Ries margin	bunte breccia	7.8	7.3	3.1	2.6	131	7.3	0.29	0.03	-	20.9	24	37.5	343
Winkler 1972	A93	Drill well	Ries margin	bunte breccia	7.9	7.1	9.6	2.6	135	11.5	0.41	-	24	21.3	59.2	36.5	352
Winkler 1972	A94	Drill well	Ries margin	bunte breccia	7.9	7	13	3.5	138.1	14.6	-	0.45	-	28.7	78	34.5	365
this study	OTT 01	Surface water	Central basin	suevite	13.9	7.6	6.3	3.2	82.9	9.9	0.2	0.0	13.3	14.5	9.3	10.4	276
this study	OTT 02	Surface water	Central basin	suevite	11.2	7.5	6.0	3.4	76.7	8.7	0.2	0.0	107.5	14.7	5.8	0.5	264
Winkler 1972	C1/3	Drill well	Crystalline wall spring /well	Crystalline rock	-	7.1	50.6	-	136	63.3	-	0.5	-	76	148	152	415

Winkler 1972	C2/1	Drill well	Crystalline wall spring /well	Crystalline rock	-	-	26	-	324	110	-	1.5	-	109	799	10	396
Winkler 1972	C2/5	Drill well	Crystalline wall spring/ well	Crystalline rock	-	7.4	44.5	11.5	234	94.8	-	-	-	95.5	605.8	3.8	382
Winkler 1972	C3/2	Drill well	Crystalline wall spring /well	Crystalline rock	18.2	7.8	192	10	15	9.1	0.195	0.1	37	19	82	0	471
Winkler 1972	C4/2	Drill well	Crystalline wall spring /well	Crystalline rock	11.3	8.1	83.2	7.8	33.1	17.6	0.4	0	75	3.7	41.6	12.5	359
Braunjura (mean)					8.6	7.2	2.9	1.6	81.3	3.8	0.1	0.1	2.8	16.4	22.3	13.3	203
Schwarzjura (mean)					7.4	7.3	5.4	1.2	142.2	6.8	0.2	0.0	3.4	27.1	87.0	44.4	283
Braunjura+Schwarzjura (mean)					8.0	7.3	4.2	1.4	111.8	5.3	0.1	0.0	3.2	21.8	54.7	28.9	243
Keuper (mean)					6.4	6.6	9.3	3.5	38.0	9.7	0.6	n.a.	n.a.	6.1	34.0	2.9	142
Bunte breccia (mean)					9.2	7.3	4.9	2.8	115.0	12.0	0.7	0.1	52.8	16.4	36.3	26.9	330
suevite (mean)					12.6	7.6	6.2	3.3	79.8	9.3	0.2	0.0	60.4	14.6	7.6	5.5	270
Crystalline rock (mean)					14.8	7.6	79.3	9.8	148.4	59.0	0.3	0.5	56.0	60.6	335.3	35.7	404

Appendix B

Supplementary Text

Sampling
Miocene lacustrine sedimentary rocks of the Ries crater lake were collected from the drill core NR1003, owned by Exxon Mobil GmbH (core facility at Nienhagen, Germany), by three campaigns during 11/2015 and 11/2018. Carbonate-rich beds were preferentially sampled (Zeng et al., submitted).

Pre-impact rocks (**Table B.2**) from the target area were sampled on 09/2020, including 7 drill cores hosted at Bavarian Geological Survey in Hof (Germany), covering the terrestrial Triassic rocks (Buntsandstein Group, Muschelkalk Group and Keuper Group, Freudenberger et al., 2000) (Freudenberger et al., 2000), Jurassic marine rocks (Schwarzjura Group, Braunjura Group and Weißjura Group, Groiss et al., 2000; Hüttner and Schmidt-Kaler, 1999) and the Miocene relic sedimentary rocks ("Albüberdeckung", Müller, 1969). In addition, 8 Keuper claystone and sandstone samples from outcrops inside the Ries basin were collected in the field at the localities of Fremdingen, Unterwillflingen and Dennenlohe. Samples for impact ejecta formations covered the **suevite** (impact-melt breccia) from quarries inside or in the vicinity of the Ries (Otting and Polsingen) and **crystalline basement rocks** from Erbisberg drilling (Arp et al., 2019a) and temporarily exposed outcrop on pipe trench at the Grosselfingen locality. The heterogeneity of Bunte Breccia (successive ejecta blanket) makes the representative sampling very difficult.

Leaching experiment
Elemental compositions, including Sr, of the bulk samples from the target formations and the impact ejecta formations above were dried and analysed by a Bruker M4 Tornado micro X-ray fluorescence analyser (**Table B.2**). Due to the "impact pre-processing" effect and to simulate the highly erodible rocks around the Ries catchment (Arp et al., 2019b), rock powders instead of chips are preferred in the leaching experiments. Nearly 8 g bulk powders of each formation were leached by 40 mL 1 M acetic acid for 2, 4 and 8 weeks, or by equivalent triple distilled water (Milli-Q) for 8 weeks in sealed Falcon tubes (**Table B.2**). During the leaching process, the reactants were shaken by an electronic shaker (GFL Type 3016, Hannover-Vinnhorst, Germany) at 50 Hz to unsettle the mixture of water and sediments.

The solutions were then centrifugated and separated into several aliquots for hydrochemistry analysis (**Table B.3**). The pH and redox potential of leachate and field water samples were measured with a WTW 340i pH meter (Xylem, NY, USA) equipped with an Inlab Solids Pro pH-electrode (Mettler Toledo, Columbus, OH, USA) or a Pt 5900 A redox electrode (SI Analytics, Mainz, Germany). Calibration of pH was performed against standard pH buffers 4.010, 7.010 and 10.010 (HI6004, HI6007, HI6010, Hanna Instruments, RI, USA). Concentrations of main cations (Ca^{2+}, Mg^{2+}, Na^+, K^+) and anions (Cl^-, F^-, Br^-, SO_4^{2-}, NO_3^-) were analysed by ion chromatography with non-suppressed and suppressed conductivity detection, respectively (Metrohm 820 IC, Metrohm 883 Basic IC; Metrohm, Herisau, Switzerland). Inductively coupled plasma optical emission spectrometry (ICP-OES; Agilent 5100 VDV) was used to determine minor and trace element concentrations. One aliquot was evaporated and concentrated, then subsequently pipetted through the Sr-spec crown ether for Sr isotope analysis.

Sr isotopes of lacustrine rocks and target rock leachates

Strontium isotope measurements were carried out at the Impact Science Center for Ries Crater, Nördlingen (ZERIN), Germany. Depending on the carbonate contents, 10-20 mg of pulverized lacustrine marlstone (NR1003) samples were pre-leached by 0.3 mL 1M ammonium acetate then centrifugated and disposed the supernatants. By this pre-leach step, labile Sr absorbed on the surface of clay minerals were removed (e.g. Doebbert et al., 2014; Zeng et al., 2021). To dissolve enough carbonate minerals, especially dolomites, the pre-leached sediments were subsequently reacted with 0.3 mL 2N HCL under warm ultrasonic bath (60 Celsius degree, 3 minutes). A comparison between 1N acetic acid and 2N HCL digestion was also tested with 6 samples. The reacted supernatants were extracted for column separation of strontium.

The Sr-spec crown ether resin was used for column separation to remove interferential cations such as Rb and Fe for both lacustrine samples and concentrated leachates. Column separated Sr was then evaporated and loaded in Birck's solution (Birck, 1986), mainly comprising a mixture of aggressive acids, onto single-band tungsten filaments. $^{87}Sr/^{86}Sr$ ratios were measured by a thermal ionization mass spectrometer [Thermo Finnigan MAT 261 modified by Spectromat GmbH (Bremen, Germany)]. The measured isotope ratios (**Table B.3 and B.4**) were normalized and corrected for mass fractionation using the invariant, natural $^{88}Sr/^{86}Sr$ ratio of 8.37521 and exponential fractionation law.

Volume estimation of the impact formations

The volume of suevite, Bunte Breccia and crystalline breccia were calculated geometrically using a bowl-shaped simple hemisphere segment (**Table B.5 and Table B.6, Figure B.1**). Radius and depth of the transient crater are set to 5.5 and 4 km, while the melting and excavation depth are 1738 and 1500 m, within the reported range (Artemieva et al., 2013; Stöffler et al., 2013; Wünnemann et al., 2005). Average thicknesses of each pre-impact sedimentary formation are taken: Triassic terrestrial rocks (Buntsandstein Group, Muschelkalk Group and Keuper Group, Freudenberger et al., 2000), Jurassic marine rocks (Schwarzjura Group, Braunjura Group and Weißjura Group, Groiss et al., 2000; Hüttner and Schmidt-Kaler, 1999; Müller, 1969).

The true radius of the hemisphere (R_0) in this model can be expressed as

$$R_0^2 = R_{tc}^2 + (R_0 - D_{tc})^2$$

whereas R_{tc} is the radius of transient crater and D_{tc} is the depth of transient crater.

Volume of the melted formations can be calculated as incremental hemisphere segment

$$V_{crystalline} = \frac{1}{3} \times \pi \times h_1^2 \times (3D_{melt} - h_1)$$

$$V_{Triassic} = \frac{1}{3} \times \pi \times h_2^2 \times (3D_{melt} - h_2) - V_{crystalline}$$

…

D_{melt} is the depth of the melting zone.

The volume of suevite is therefore expressed as total melted volume from crystalline basement to upper Jurassic rocks

$$V_{suevite} = V_{crystalline} + V_{Triassic} + V_{Jurassic}$$

The volume of the crystalline breccia is expressed as

$$V'_{Crystalline} = \frac{1}{3} \times \pi \times (h'_1)^2 \times (3 \times R_0 - h'_1) - \frac{1}{3} \times \pi \times (h'_0)^2 \times (3 \times R_0 - h'_0)$$
$$- \left\{ \frac{1}{3} \times \pi \times h_1^2 \times (3D_{melt} - h_1) - \frac{1}{3} \times \pi \times (h_0)^2 \times (3D_{melt} - h_0) \right\}$$

Likewise, the volume of the ejected formations is

$$V'_{Triassic} = \frac{1}{3} \times \pi \times (h'_2)^2 \times (3 \times R_0 - h'_2) - \frac{1}{3} \times \pi \times (h'_1)^2 \times (3 \times R_0 - h'_1)$$
$$- \left\{ \frac{1}{3} \times \pi \times h_2^2 \times (3D_{melt} - h_2) - \frac{1}{3} \times \pi \times (h_1)^2 \times (3D_{melt} - h_1) \right\}$$

…

and volume of Bunte Breccia as:

$$V_{Bunte\ Breccia} = V'_{Triassic} + V'_{Jurassic}$$

The melted and ejected mass of each formation is calculated using the volume from previous steps after a rock density correction based on different lithologies. The lithologies of sedimentary formations are simplified as limestones (including dolomites and marlstones, on average 2.5 g/cm^3, Manger, 1963), claystones (2.365 g/cm^3, Johnson and Olhoeft, 1984) and sandstones (the whole Keuper is simplified as sandstones, on average 2.22 g/cm^3, Johnson and Olhoeft, 1984). It is worth to mention that the crystalline basement of Ries crater comprises spatially heterogeneous rock, i.e. crystalline basement of the western side differs from the eastern. As a result, this heterogeneity leads to spatially different suevite (Siegert et al., 2017; Siegert and Hecht, 2019). For the reason that the lacustrine samples from NR1003 drill core are located at the western half of the Ries crater, the average of western crystalline basement is taken into account in our calculation (0.28mafic/0.31granite/0.38 gneiss, Siegert and Hecht, 2019), resulting in density of 2.721 g/cm^3 on average (Iturrino et al., 1991; Johnson and Olhoeft, 1984).

Volume and leachate Sr isotopes of impact ejecta formations

Volume
The calculated crater suevite volume is 11.0 km^3, similar to the estimation by Stöffler et al. (2013), 12.9 km^3 for crater suevite. The total volume of the primarily excavated rocks (including crystalline rocks) is calculated to be 137.9 km^3 whereas 128-136 km^3 was given by Stöffler et al. (2013). Calculated volume for the excavated sedimentary rocks is 62.4 km^3, approximately fit to 67 km^3 given in Artemieva et al. (2013) and 70 km^3 given in Stöffler et al. (2013).

Sedimentological constraints of the lake stages
1) Basal member
For the earliest lake stage, the sedimentological evidence clearly points to rework of crystalline basement rocks (e.g. granite and amphibolite pebbles in the conglomerates, Zeng et al., submitted) and suevites (Arp et al., 2019a). The extensive fluid-escape structures (**Figure B.2A**) within the laminated carbonate beds are interpreted as percolating hydrothermal waters from the fractured crystalline basement. Similar fluid escape structures are also shown in the suevite (Caudill et al., 2021), overlain by the basal member. Successively decreasing $\delta^{18}O$ values of the carbonates are evident from the underlying suevite to the basal member, supporting the stepwise cooling of the crater floor (Rothe and Hoefs, 1977; Zeng et al., submitted). Indeed, most lacustrine samples in the basal member show $^{87}Sr/^{86}Sr > 0.7130$ and confirm that most of the water raise from either the crystalline basement rock or Triassic Keuper aquifers. However, the leachate average $^{87}Sr/^{86}Sr$ ratio of the latter is 0.7135, slightly lower that the highest $^{87}Sr/^{86}Sr$ observed in the lacustrine carbonate while the most of the Triassics are typical of higher $^{87}Sr/^{86}Sr$ (0.7141 to 0.7172 except Feuerletten Fm. and Burgsandstein Fm.). More importantly, the groundwater from the Triassic aquifer is low in both pH and dissolved inorganic carbon (Winkler, 1972). Assuming discharges from the Triassic aquifers are the major source for the earliest lake stage, is incompatible with the early alkaline lake condition (Arp et al., 2013a; Stüeken et al., 2020). The cyclic fluvial-delta-shallow lake facies associations also clearly indicate that the lake level at the time of basal member is low. Proximal to inner ring, the basal member transected from the Enkingen SUBO 18 drill core is only less than 5 meter thick (Arp et al., 2013a); whereas at inner ring (Erbisberg 2011 drilling), the corresponding lithofacies of basal member is not distinguishable (Arp et al., 2019a). Furthermore, the $^{87}Sr/^{86}Sr$ values of the lacustrine carbonate facies from Erbisberg drilling are not higher than 0.7120. Thereby most possibly, the lake catchment during the deposition of basal member is restrictedly within the inner ring. Episodically increasing surface runoffs may indeed lead to rework of suevite and

as a result, decreasing $^{87}Sr/^{86}Sr$ signals in the carbonates. At the top part of basal member, the lacustrine facies show typical features of subaerial exposure, including in-situ brecciation and mud cracks, again pointing to temporary dry-out. Pseudomorphs after evaporite minerals, most likely gypsum pseudomorph, were also reported (Jankowski, 1981) thereby suggest highly evaporative setting. Sedimentological and isotopic evidence indicates that the heat generated by the impact event, released from the hot crater floor, is the most direct explanation.

2) clinoptilolite smbr

Overlying the basal member is the remarkable lithofacies change by the thick laminated marlstone and bituminous shale facies (**Figure 4.3**), indicating the onset of permanently stratified lake stage. Here, the $^{87}Sr/^{86}Sr$ trend of lacustrine carbonates shows a steep decrease and clearly suggests a quick transgression and change in solute provenance of the lake water. The decreasing $^{87}Sr/^{86}Sr$ trend from 0.7130 to 0.7110 indicates less significant influx from both crystalline basement and suevite, and increasingly important influx leaching the Bunte Breccia endmember. The lateral facies extension, i.e. the lake area of clinoptilolite smbr is also possibly restricted within the inner ring, as indicated by its furthermost detection at a drill core nearby the inner ring (NR-40, Rullkötter et al., 1990, in their Fig. 1) and the marginal carbonate travertine mound directly on top of the crystalline basement rock at inner ring (e.g. the Erbisberg mound, Arp et al., 2013b). Alternatively, a two-endmember mixing between crystalline basement water and Jurassic waters seems numerically resolving the $^{87}Sr/^{86}Sr$ of the lacustrine carbonate, however, not capable of producing the authigenic silicates (clinoptilolites) as well as the 660 °C montmorillonite (Salger, 1977).

The mesohaline to hypersaline lake condition revealed by the biomarkers (Barakat and Rullkötter, 1997) rather suggests that the clinoptilolite smbr was deposited under a highly evaporative and shallow setting. Here, the hydrothermal convection may still lead to a warm lake temperature and facilitate evaporation despite of increasing lake volume. For instance, the travertine carbonate mound itself provides convincing evidence for hydrothermal events (Arp et al., 2013b; 2019a). Some rare carbonates also show very negative $\delta^{18}O$ values (low as ca. -10 ‰, Zeng et al., submitted), in such an evaporative setting (typically positive $\delta^{18}O$ in carbonates), arguing for elevated ambient water temperature.

3) from analcime smbr to marl member

In the subsequent analcime smbr, successively decreasing $\delta^{18}O$ values (from ca. +5 to 0 ‰) of the Ca-rich dolomite poses a strong salinity contrast to the stoichiometric dolomite with high $\delta^{18}O$ in the clinoptilolite smbr (Zeng et al., submitted). To the upper part of the smbr, the $\delta^{18}O$ values only show minor variations around 0‰. While the carbonate content also decreases to <50 wt% as well as the most extensive soft deformation (slumping, **Figure 4.3**) exists, analcime smbr is interpreted to reach a maximum lake level. This interpretation is in accordance with the low-salinity indicative diatom species (Schauderna, 1983). Furthermore, the lake volume increase is supported by the decline of carbonate $^{87}Sr/^{86}Sr$ ranging from 0.7111 to 0.7107, indicating the increasing lake recharge by a low $^{87}Sr/^{86}Sr$ endmember, i.e. Bunte Breccia water. On the other hand, strong sulfate reduction in a redox-stratified lake stage analcime smbr (Zeng et al., submitted) meanwhile leads to increase in alkalinity (Kempe and Kazmierczak, 1994), to reach the highest pH along the lake history (Arp et al., 2013a; Stüeken et al., 2020).

The $^{87}Sr/^{86}Sr$ of lacustrine carbonate stabilized around 0.7105 (0.7103 to 0.7107) from the top part of analcime smbr to the top of dolomite-marl smbr. No systematic trend can be derived from $^{87}Sr/^{86}Sr$ of the lacustrine carbonate, nor a correlation between $^{87}Sr/^{86}Sr$ and $\delta^{18}O$ exists. Minor change in $^{87}Sr/^{86}Sr$ may indeed suggest the geochemical heterogeneity of Bunte Breccia or sporadic suevite influxes. There are several important sedimentological, stable carbon-oxygen isotopic and biogeochemical trends during this interval:

1) the slumping beds, most extensive in analcime smbr, faded and replaced by syn-sedimentary microfaults and gentler soft-sediment deformation structures (This study, **Figure 4.3**);

2) since the establishment of permanent lake, evidence for bioturbation and allochthonous clasts is only clear in diatom smbr for the first time (**Figure 4.3**);

3) the extremely ^{13}C-enriched dolomite and related biomarkers point to methanogenesis and temporary sulfate-depletion during the high δ^{13}C interval (bituminous to varicolored-marl smbr, Zeng et al., submitted, his Fig. 2);

4) the bifurcated trends of δ^{13}C and δ^{18}O indicate short-term variations in lake level and accompanied temporary sulfate change, resulting in systematic change in salinity and the strength of methanogenesis in lake water (Zeng et al., submitted). Indeed, temporary sulfate increase in the lake can only be introduced by surface runoff whereas the groundwaters are already depleted in sulfate. This suggests growing dominance of surface water for the lake hydrology than from the groundwaters in the previous analcime and clinoptilolite smbr;

5) At varicolored-marl and dolomite smbrs, bioturbations and indicators of subaerial exposures are more common. Onset of aerobic methanotrophy indicates complete lake mixing and oxygenation at the lake bottom. Shallow and highly evaporative condition is supported δ^{18}O values of the dolomites.

These trends suggest a decline in the extent of soft sediment deformation as well as in lake level, towards a less stratified, shallower and more evaporative setting.

4) clay member

At the base of the clay member (^{87}Sr/^{86}Sr: ca. 0.7105), the occurrence of magnesian calcite (Zeng et al., submitted, his Table S4) indicates that the lake water was possibly less saline than the previously dolomite-dominated stages (Müller et al., 1972). Low δ^{18}O values of the magnesian calcites also support an increasing freshwater influx (Zeng et al., submitted). However, at the upper part of the clay member (^{87}Sr/^{86}Sr: ca. 0.7109), a variety of shallow lake features are shown, including mud cracks, pedogenic slickensides, in addition to several gypsum pseudomorph-bearing beds even pointing to temporarily hypersaline condition (Arp et al., 2017; Jankowski, 1981). As pointed out by Arp et al. (2017), the cyclic sequences at comprising lignite, diatomite, claystone, marl- to limestone indicate not a simple shallow and evaporative, but a cyclic flooding-evaporative environment.

The change from analcime-rich dolomitic marlstone (dolomite-marl smbr) to flooding-evaporative cyclic facies at clay member, clearly indicates a major change in provenance and hydrology (Arp et al., 2017). Ubiquitous pyrite in the allochthonous lignite as well as in the marlstone beds indicates that significant Fe and SO_4 are required in the influxes (Zeng et al., submitted). Indeed, the Lower-Middle Jurassic marine claystone formations could easily produce such leachates (**Table B.7**). Among the Lower to Middle Jurassics, the Opalinuston Fm. is the only formation further producing a ^{87}Sr/^{86}Sr signal of 0.7110 in the leachates (**Table B.7**). North-eastern outside the crater rim, Opalinuston Fm. is exposed at 490-550 m a.s.l., which is thereby topographically high enough for inflows, to the area where the clay member is exposed at marginal crater area (490-550 m a.s.l., Arp et al., 2021, in his Fig. 6). Own mapping result shows that the fine-grained quartz sand mixed with calcareous oolites and *Hydrobia* (nearby the locality of Wornfeld), also suggests possible inflow from NE outside the crater rim. The disappearance of analcime also confirms a decrease in contributions of suevite and Bunte Breccia influxes in the catchment.

Hydrochemical modelling by PHREEQC program

Combined with sedimentological evidence, the relative fluid proportions were determined by their Sr concentration and ^{87}Sr/^{86}Sr ratios. Groundwater, surface water or lab leachate samples were then quantitatively mixed and reacted in the PHREEQC program (Appelo and Postma, 2005). For a better ion balance and pH control, the water leachates were used for modelling and run with the *phreeqc.dat* database. A ten-fold calcite supersaturation (SI_{Cc} = 1) was applied to simulate calcite precipitation. Dolomite (stoichiometric) precipitation was simulated by introducing a higher SI = 4. SI_{dol} values between 3 and 4 were taken as Ca-rich

dolomite. An ambient atmospheric pCO_2 similar to today (-3.5) was assumed. The results are shown in **Table B.8.**

In the first step, 0.465 volume crystalline basement water (Busse C3/2, Winkler, 1972) was mixed with 0.535 volume suevite water (Ott 1/2wr, **Table B.7**) to reach $^{87}Sr/^{86}Sr$ = 0.7125, reacted under 60 °C (lower part of basal member, solution 1a). The pCO_2 of the mixed solution was equilibrated to -2.8 in analogy to the modern hydrothermal **Lake Landbrot** (Owen et al., 2008).

At the top part of the basal member, a mixing ratio between crystalline rock:suevite = 0.86: 0.14 was considered (resulting $^{87}Sr/^{86}Sr$ =0.7135), based on the higher $^{87}Sr/^{86}Sr$ in the lacustrine carbonates (**Figure 4.3**). This solution was subsequently evaporated to reach an oligohaline salinity (solution 1b), with a total dissolved solids (TDS) of 4900 mg/L. A supersaturation index for strontianite (SI=0.5) was introduced to simulate Sr removal by co-precipitation with carbonate minerals.

In the next step, solution 1b (0.1 volume after evaporation) was mixed 0.175 volume Bunte Breccia water at 40 °C, resulting $^{87}Sr/^{86}Sr$ = 0.7115. Subsequent evaporation leads to a hypersaline water (solution 2, TDS = 52300 mg/L). To simulate a low-redox condition, oxygen was removed from the solution (pe = -5). Supersaturation indexes of calcite (SI=1), stoichiometric dolomite (SI=4) and strontianite (SI=0.5) were input during equilibrium phase. The solution 2 is analogous to the modern **Lake Bogoria**, a high pH (9.5-10.9) soda lake with hydrothermal springs, authigenic zeolite formations within the laminites, including analcime and minor clinoptilolite as well as anoxic bottom water (Renaut et al., 1986; Renaut and Tiercelin, 1993).

To reach $^{87}Sr/^{86}Sr$ = 0.7110 in the lake water of analcime smbr, 0.006 L Bunte Breccia water (Kirchheim A71, Winkler, 1972) was further added to solution 2 and mixed under 15 °C. Evaporation leads to salinity of 40600 mg/L under a normal pCO_2 (-3.5). The redox condition is set to be extremely low, 0.001 mol simple organic compound (CH_2O) was added to simulate sulfate reduction. thereby converting sulfate into hydrogen sulfide alkalinity to reach the highest pH (solution 3). The solution 3 is similar to the hydrochemistry of **Lake Van**, also a soda lake with a deep waterbody, monotonous laminites and sublacustrine spring mounds reported (Reimer et al., 2009).

The subsequent step, bituminous smbr to varicolored-marl smbr, is characterised by $^{87}Sr/^{86}Sr$ = 0.7105 in the lake water. The mix starts adding 0.005 volume Bunte Breccia water to solution 3 and the mixture was then evaporated to reach a TDS around 33300 to 38700 mg/L. pCO_2 was set to -3 for a deep, stratified water column. Another 0.001 mol CH_2O was added in this anoxic solution to simulate methanogenesis (SI_{CH4} between 3 and 4, solution 4a and 4b). They are analogous to the **Lake Satonda** (Arp et al., 2003; Huber et al., 1991) or **Lake Untersee** (Antarctica, Wand et al., 1997; 2006) with respect to extensive methanogenesis in the water columns. To mimic the water of varicolored-marl smbr, solution 4b was further evaporated (to TDS = 43200 mg/L, solution 5a). A parallelly stronger evaporation and higher pe were introduced to suppress methanogenesis in an alternative scenario (TDS = 46700, solution 5b).

A group of the lowest $^{87}Sr/^{86}Sr$ values of lacustrine carbonates (0.7103) was shown in dolomite-marl smbr. A further 0.008 volume Bunte Breccia water was thereby added to solution 5b to represent the less saline scenario of the dolomite-marl smbr (solution 6a, TDS = 26100 mg/L). Whereas in a more evaporative scenario, the solution 6a was evaporated to a TDS of 51400 mg/L (solution 6b). The less saline scenario is similar to the lake waters of modern **Lake Van**, despite of a much more shallower water depth, whereas the more saline scenario is similar to the **Hot Lake** (Lindemann et al., 2013).

The earlier accumulated dissolved solids were considered remaining in the lake during early stage of the clay member. To reach a $^{87}Sr/^{86}Sr$ = 0.7108 in the lake water, either 0.225 L field water (TFQ 01, **Table B.7**) or 0.006 volume leachate (TP39-1, **Table B.7**) from Opalinuston Fm. is required for mixing with solution 6b. The former results in a TDS of 2100 mg/L (solution 7a) whereas 30300 mg/L for the latter (solution 7b). In any case, both field and leachate water easily precipitate gypsum upon evaporation without mixing with previous solutions. Solution 7b is analogous to the **Lake Thetis** (Arp et al., 2013a). While new

tributary started outside the crater rim at the clay member, the change in hydrology indicates the few, remaining fluids from previous lake stages may be not important anymore. To fit with the successive pH decline (Arp et al., 2013a; Stüeken et al., 2020) and a replacement of the lake water (this study), we simulate the hydrochemical modelling by the following steps: 1) mixed solution 6b with 0.006 L Opalinuston Fm. water (solution 7b, $^{87}Sr/^{86}Sr = 0.7108$); 2) mixed solution 7b with 0.035 volume, 1 volume and 14.87 volume Opalinuston Fm. water, thereby replacing the lake with Opalinuston water by 75% (solution 7c), 98.5% (solution 7d) and 99.9%. The 99.9% Opalinuston water lake was then evaporated to test gypsum precipitation ($SI_{gyp}>0$, solution 7e).

Supplementary Figures
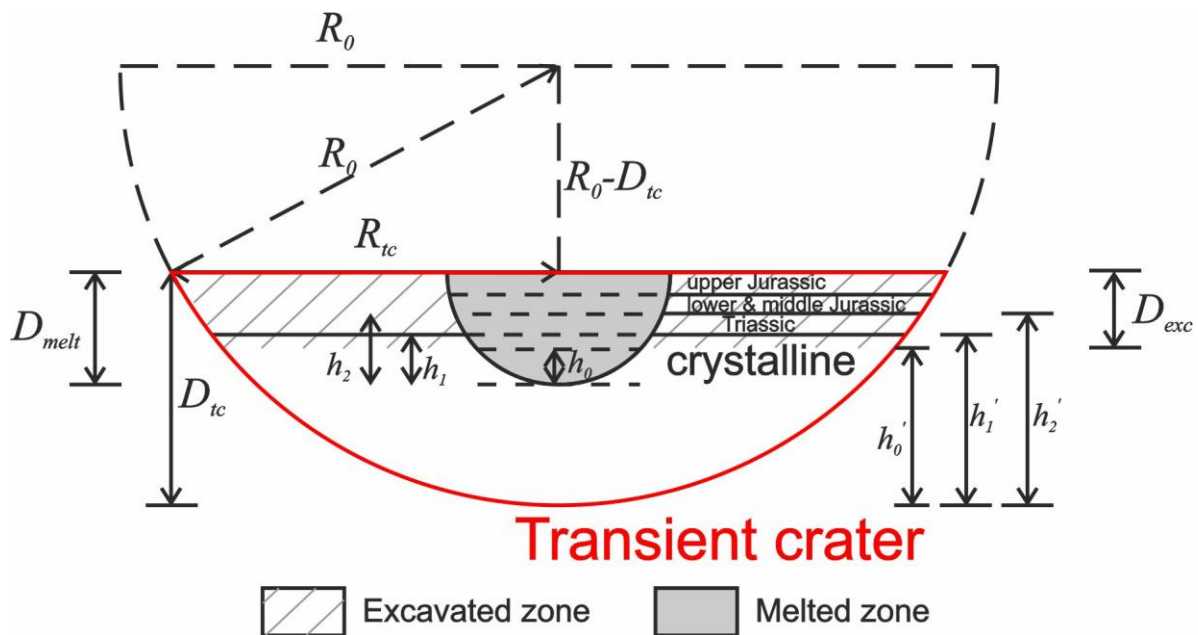
Figure B.1 Simple schematic concept of the transient crater, including the excavated zone and melted zone.
The former forms Bunte Breccia whereas the latter as suevite. Note that the thicknesses of Jurassic, Triassic and crystalline formations are not in scale. See text for the meaning of symbols.
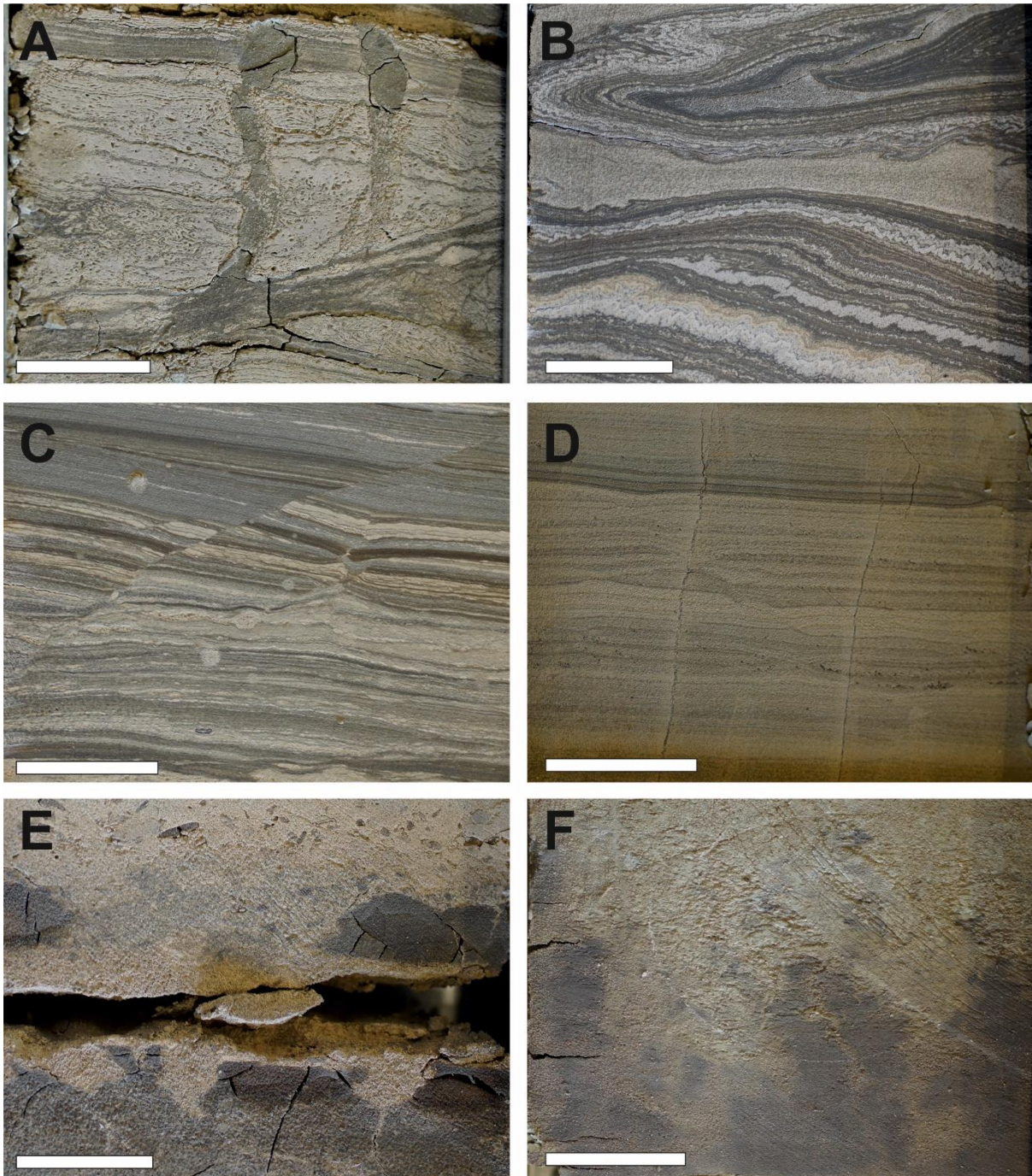
Figure B.2 sedimentary features of the drill core samples in NR1003.
A) Fluid escape structures in the basal member (243.2 to 243.3 m core depth), note the cm-sized chamber structure, possibly related to trapped fluid; B) slumped and deformed laminites in smbr (222.4 to 222.5 m core depth); C) microfault in smbr (218.0 to 218.1 m core depth); D) loop bedding (a sign for weak deformation, see Rodríguez-Pascua et al., 2000) and weak microfault in smbr (128.7 to 128.8 m core depth); E) bioturbation and mud crack in (80.4 to 80.5 m core depth); F) bioturbation in marl member (39.7 to 39.8 m core depth); in-situ brecciation in member (34.7 to 34.8 m core depth). Length of the bar: 2 cm.

Supplementary Tables

Table B.1 statistics of the sedimentary structures related to deformation and turbation in 5 catagories, including slumping, microfaults, gentler turbation, bioturbation and pedogenic structures.
The thickness of the affected beds was recorded every meter. *unclear weak turbation: slightly turbated, slightly inclined or deformed (e.g. loop bedding bedding).

core length [cm]	core top [m]	core end [m]	structure/intepretation	thickness of the turbated beds [cm]					relative percentage of the analysed structure					
				slum ping	micro faults	unclear weak turbation*	bioturbat ion	pedog enic	slumpi ng	microfa ults	unclear weak turbation	bioturba tion	pedog enic	unturba ted
90	-252.7	-253.6	massive beds						0.00	0.00	0.00	0.00	0.00	1.00
100	-251.7	-252.7	massive beds						0.00	0.00	0.00	0.00	0.00	1.00
70	-251	-251.7	massive beds					10	0.00	0.00	0.00	0.00	0.14	0.86
100	-248.5	-249.5	disturbed beds, cannot be discerned			5			0.00	0.00	0.05	0.00	0.00	0.95
100	-247.5	-248.5	disturbed beds cannot be discerned			12			0.00	0.00	0.12	0.00	0.00	0.88
100	-246.5	-247.5	disturbed beds cannot be discerned and mottled			24		13	0.00	0.00	0.24	0.00	0.13	0.63
100	-245.5	-246.5	disturbed beds, partly bioturbated (not fully convincing bioturbation)			10	38		0.00	0.00	0.10	0.38	0.00	0.52
50	-245	-245.5	disturbed beds, partly bioturbated (not fully convincing bioturbation)	6	9		16		0.12	0.18	0.00	0.32	0.00	0.38
90	-242.8	-243.7	disturbed beds related to fluid escape structure (FES), slumped and brecciated beds, partly bioturbated (not fully convincing bioturbation); at 245.19 m, intruded and fractured gravel (9cm)				12		0.00	0.00	0.00	0.13	0.00	0.87
80	-242	-242.8	disturbed beds related to fluid escape structure (FES), slumped and brecciated beds and mottled, at -243.48 m			16		4	0.00	0.00	0.20	0.00	0.05	0.75

			disturbed beds (15cm), including 1cm thick pillow cast										
100	-238.4	-239.4	disturbed beds, discontinuous bedding/lamination and mottled			5	6	0.00	0.00	0.05	0.00	0.06	0.89
100	-237.4	-238.4	mottled				43	0.00	0.00	0.00	0.00	0.43	0.57
100	-236.4	-237.4	disturbed beds, discontinuous bedding/lamination and mottled			20	9	0.00	0.00	0.20	0.00	0.09	0.71
40	-236	-236.4	mottled				14	0.00	0.00	0.00	0.00	0.35	0.65
100	-234	-235	mottled				15	0.00	0.00	0.00	0.00	0.15	0.85
100	-233	-234	mottled				5	0.00	0.00	0.00	0.00	0.05	0.95
100	-232	-233	mottled				12	0.00	0.00	0.00	0.00	0.12	0.88
100	-231	-232	disturbed beds, discontinuous bedding/lamination			18		0.00	0.00	0.18	0.00	0.00	0.82
100	-230	-231	disturbed beds, discontinuous bedding/lamination and mottled			9	36	0.00	0.00	0.09	0.00	0.36	0.55
100	-229	-230	disturbed beds, discontinuous bedding/lamination and mottled			30	6	0.00	0.00	0.30	0.00	0.06	0.64
100	-228	-229	disturbed beds, discontinuous bedding/lamination		7	49		0.00	0.07	0.49	0.00	0.00	0.44
100	-227	-228	disturbed beds related to fluid escape structure (FES), slumped and brecciated beds, partly bioturbated	5		6		0.05	0.00	0.06	0.00	0.00	0.89
100	-226	-227	disturbed beds related to fluid escape structure (FES), slumped and brecciated beds, pedogenic brecciation with sand dike and allochthonous caliche black pebbles				59	0.00	0.00	0.00	0.00	0.59	0.41
100	-225	-226	disturbed beds, discontinuous bedding/lamination			18		0.00	0.00	0.18	0.00	0.00	0.82

100	-224	-225	disturbed beds, discontinuous bedding/lamination, partly slumped	7		20	0.07	0.00	0.20	0.00	0.00	0.73
100	-223	-224	slumped beds, including ball and pillow structure (6-10 cm in size at least), partly concaved-up with solid lamination, partly brecciated	62		1	0.62	0.00	0.01	0.00	0.00	0.37
100	-222	-223	slumped beds, including ball and pillow structure (5 cm in size at least), partly brecciated	71		8	0.71	0.00	0.08	0.00	0.00	0.21
100	-221	-222	convoluted laminites, partly disturbed			10	0.00	0.00	0.10	0.00	0.00	0.90
100	-220	-221	slumped laminites, including ball and pillow structure (5 cm in size at least), partly brecciated	48			0.48	0.00	0.00	0.00	0.00	0.52
100	-219	-220	slumped laminites, partly highly liquefied, with disturbed beds	38		20	0.38	0.00	0.20	0.00	0.00	0.42
100	-217.6	-218.6	slumped laminites, partly highly liquefied, with disturbed beds	15		26	0.15	0.00	0.26	0.00	0.00	0.59
100	-216.6	-217.6	slumped laminites, partly highly liquefied, with disturbed beds	85		10	0.85	0.00	0.10	0.00	0.00	0.05
100	-215.6	-216.6	disturbed laminites with loop bedding and partly liquefied, slumped laminites	5		12	0.05	0.00	0.12	0.00	0.00	0.83
85	-214.75	-215.6	disturbed laminites, partly convoluted and contorted		2	19	0.00	0.02	0.22	0.00	0.00	0.75
90	-213.85	-214.75	disturbed laminites			12	0.00	0.00	0.13	0.00	0.00	0.87
85	-213	-213.85	disturbed laminites, partly convoluted and contorted, showing lobe structure related to subsidence , slightly slumped	12	15	36	0.14	0.18	0.42	0.00	0.00	0.26

							0.08	0.07	0.00	0.00	0.00	0.85
100	-212	-213	slumped laminites, partly with microfault	8	7		0.08	0.07	0.00	0.00	0.00	0.85
100	-211	-212	disturbed laminites, partly convoluted and contorted, partly highly liquefied, showing lobe structure related to subsidence , slightly slumped	57			0.57	0.00	0.00	0.00	0.00	0.43
100	-210	-211	disturbed laminites, partly convoluted and contorted, partly highly liquefied, showing lobe structure related to subsidence , slightly slumped	41		7	0.41	0.00	0.07	0.00	0.00	0.52
100	-209	-210	microfault				0.00	0.00	0.00	0.00	0.00	1.00
100	-208	-209	inclined slumped laminites, irregular convolution and microfaults				0.00	0.00	0.00	0.00	0.00	1.00
100	-207	-208	slumped bed (15) and microfaults (10cm)				0.00	0.00	0.00	0.00	0.00	1.00
100	-206	-207	disturbed laminites,with irregular slumping, convolutions, microfaults	6	15		0.06	0.15	0.00	0.00	0.00	0.79
100	-205	-206	disturbed laminites,with irregular slumping, convolutions, microfaults	82	6		0.82	0.06	0.00	0.00	0.00	0.12
100	-204	-205	disturbed laminites,with irregular slumping, convolutions, microfaults	28	13		0.28	0.13	0.00	0.00	0.00	0.59
100	-203	-204	disturbed laminites,with irregular slumpings and microfaults, partly brecciated	27	7		0.27	0.07	0.00	0.00	0.00	0.66
100	-202	-203	no soft sediment deformation				0.00	0.00	0.00	0.00	0.00	1.00
100	-201	-202	disturbed laminites with loop bedding and small and weak slumping	7	4		0.07	0.04	0.00	0.00	0.00	0.89

100	-200	-201	slumped beds, including ball and pillow structure (>30 cm in size for the largest) and brecciated beds	67			0.67	0.00	0.00	0.00	0.00	0.33
100	-199	-200	highly liquefied laminites with irregular convolution	33			0.33	0.00	0.00	0.00	0.00	0.67
100	-198	-199	slumped laminites, including ball and pillow structure (>3cm in size for the largest) and brecciated beds	24	9		0.24	0.09	0.00	0.00	0.00	0.67
100	-197	-198	slumped laminites, including ball and pillow structure (>16cm in size for the largest)	51	2		0.51	0.02	0.00	0.00	0.00	0.47
100	-196	-197	slumped laminites, including ball and pillow structure (>3cm in size for the largest) and brecciated beds	71	7		0.71	0.07	0.00	0.00	0.00	0.22
100	-195	-196	slumped laminites, including ball and pillow structure (>3cm in size for the largest) and brecciated beds	53	10		0.53	0.10	0.00	0.00	0.00	0.37
100	-194	-195	highly liquefied laminites with irregular convolution			42	0.00	0.00	0.42	0.00	0.00	0.58
100	-193	-194	slumped laminites, including ball and pillow structure (>3cm in size for the largest)	22	2		0.22	0.02	0.00	0.00	0.00	0.76
100	-192	-193	slumped laminites, including ball and pillow structure (>3cm in size for the largest)	35			0.35	0.00	0.00	0.00	0.00	0.65
100	-191	-192	slumped, highly liquefied laminites with irregular convolution	71			0.71	0.00	0.00	0.00	0.00	0.29
100	-190	-191	slumped laminites, including ball and pillow structure (1cm in size for the largest)	28			0.28	0.00	0.00	0.00	0.00	0.72

100	-189	-190	slumped laminites, including ball and pillow structure (1cm in size for the largest)	7			0.07	0.00	0.00	0.00	0.00	0.93
100	-188	-189	slumped laminites, including ball and pillow structure , brecciated beds and microfaults	87	10		0.87	0.10	0.00	0.00	0.00	0.03
100	-187	-188	slumped, highly liquefied laminites with irregular convolution	67	7		0.67	0.07	0.00	0.00	0.00	0.26
100	-186	-187	slumped beds, including ball and pillow structure (>2 cm in size for the largest) and brecciated beds	37	11		0.37	0.11	0.00	0.00	0.00	0.52
100	-185	-186	disturbed laminites, weakly slumped, with microfaults		15	52	0.00	0.15	0.52	0.00	0.00	0.33
100	-184	-185	disturbed laminites, weakly slumped, with microfaults:	60	17	80	0.60	0.17	0.80	0.00	0.00	0.00
70	-183.3	-184	disturbed laminites, weakly slumped, with microfaults	13		100	0.19	0.00	1.43	0.00	0.00	0.00
80	-182.5	-183.3	disturbed laminites, weakly slumped, with microfaults	17		80	0.21	0.00	1.00	0.00	0.00	0.00
120	-181.3	-182.5	slumped, highly liquefied laminites with irregular convolution	51	11		0.43	0.09	0.00	0.00	0.00	0.48
90	-180.4	-181.3	slumped, highly liquefied laminites with irregular convolution	90	25		1.00	0.28	0.00	0.00	0.00	0.00
90	-179.5	-180.4	disturbed laminites, with microfaults:	3	82		0.03	0.91	0.00	0.00	0.00	0.06
100	-178.5	-179.5	disturbed laminites, weakly slumped, with microfaults and brecciated beds	36	27		0.36	0.27	0.00	0.00	0.00	0.37
100	-177.5	-178.5	inclined (30-40 degree) and disturbed laminites, slumped resembling cross bedding, with microfaults	53			0.53	0.00	0.00	0.00	0.00	0.47

100	-176.5	-177.5	disturbed laminiates, faulted	9	30			0.09	0.30	0.00	0.00	0.00	0.61
100	-175.5	-176.5	disturbed laminites, weakly slumped, with microfaults resembling cross bedding	3	22			0.03	0.22	0.00	0.00	0.00	0.75
100	-174.5	-175.5	disturbed laminites, weakly slumped, with microfaults and loop bedding, resembling cross bedding	22	10	70		0.22	0.10	0.70	0.00	0.00	0.00
50	-174	-174.5	disturbed laminites, weakly slumped ,with microfaults and loop bedding, resembling cross bedding	3	12	50		0.06	0.24	1.00	0.00	0.00	0.00
100	-173	-174	disturbed laminites, weakly slumped, with microfaults and loop bedding, resembling cross bedding	14	26			0.14	0.26	0.00	0.00	0.00	0.60
100	-172	-173	slumped laminites, including ball and pillow structure (>20cm in size for the largest) and microfaults	25	20			0.25	0.20	0.00	0.00	0.00	0.55
100	-171	-172	slumped laminites, including ball and pillow structure (>30cm in size for the largest) and microfaults	69	2			0.69	0.02	0.00	0.00	0.00	0.29
100	-170	-171	highly liquefied disturbed laminites with slumping, brecciated bed and microfaults	24	27			0.24	0.27	0.00	0.00	0.00	0.49
100	-169	-170	slightly disturbed laminites with microfaults		29			0.00	0.29	0.00	0.00	0.00	0.71
100	-168	-169	slightly disturbed laminites with microfaults			5		0.00	0.00	0.05	0.00	0.00	0.95
115	-166.85	-168	highly liquefied disturbed laminites with slumping, brecciated bed, loop bedding (17)	75		17		0.65	0.00	0.15	0.00	0.00	0.20

100	-165.85	-166.85	disturbed laminites, including slumped ball and pillow structure, loop bedding, microfaults	36	6	40	0.36	0.06	0.40	0.00	0.00	0.18
100	-164.85	-165.85	slumped and brecciated laminites	100			1.00	0.00	0.00	0.00	0.00	0.00
100	-163.85	-164.85	disturbed laminites, weakly slumped mainly loop bedding	5	5	40	0.05	0.05	0.40	0.00	0.00	0.50
85	-163	-163.85	disturbed laminites, weakly slumped mainly loop bedding	10	10		0.12	0.12	0.00	0.00	0.00	0.76
100	-162	-163	disturbed laminites, weakly slumped, partly brecciated	19	15	79	0.19	0.15	0.79	0.00	0.00	0.00
100	-161	-162	disturbed laminites, weakly slumped, partly brecciated	30	10		0.30	0.10	0.00	0.00	0.00	0.60
100	-160	-161	disturbed laminites, weakly slumped, loop bedding and microfaults	6	5	44	0.06	0.05	0.44	0.00	0.00	0.45
100	-159	-160	disturbed laminites, weakly slumped, loop bedding and microfaults	15	19		0.15	0.19	0.00	0.00	0.00	0.66
100	-158	-159	disturbed laminites, weakly slumped, loop bedding and microfaults	7	48		0.07	0.48	0.00	0.00	0.00	0.45
100	-157	-158	disturbed laminites, weakly slumped, partly liquefied, loop bedding and microfaults	22	38	52	0.22	0.38	0.52	0.00	0.00	0.00
100	-156	-157	disturbed laminites, weakly slumped, highly liquefied and convoluted, loop bedding and microfaults	15	8	73	0.15	0.08	0.73	0.00	0.00	0.04
100	-155	-156	disturbed laminites, weakly slumped, highly liquefied and convoluted, loop bedding and microfaults	5	13	95	0.05	0.13	0.95	0.00	0.00	0.00
100	-154	-155	disturbed laminites, loop bedding and microfaults	8		92	0.08	0.00	0.92	0.00	0.00	0.00

100	-153	-154	disturbed laminites, weakly slumped, highly liquefied and convoluted, loop bedding and microfaults	34	15	63		0.34	0.15	0.63	0.00	0.00	0.00
100	-152	-153	disturbed laminites, weakly slumped, highly liquefied and convoluted, loop bedding and microfaults	31	20	64		0.31	0.20	0.64	0.00	0.00	0.00
100	-151	-152	disturbed laminites, weakly slumped, highly liquefied and convoluted, loop bedding and microfaults	17	7	66		0.17	0.07	0.66	0.00	0.00	0.10
100	-150	-151	disturbed laminites, and convoluted, loop bedding and microfaults		3	86		0.00	0.03	0.86	0.00	0.00	0.11
100	-149	-150	disturbed laminites, and convoluted, loop bedding and microfaults	2	3	93		0.02	0.03	0.93	0.00	0.00	0.02
100	-148	-149	disturbed laminites, and convoluted, loop bedding and microfaults		12	60		0.00	0.12	0.60	0.00	0.00	0.28
100	-147	-148	disturbed laminites, and convoluted, loop bedding and microfaults	3	44	93		0.03	0.44	0.93	0.00	0.00	0.00
100	-146	-147	disturbed laminites, and convoluted, loop bedding and microfaults		76	95		0.00	0.76	0.95	0.00	0.00	0.00
100	-145	-146	disturbed laminites, and convoluted, loop bedding and microfaults		75	91		0.00	0.75	0.91	0.00	0.00	0.00
100	-144	-145	disturbed laminites, weakly slumped and convoluted, brecciated, loop bedding and microfaults	23	51	51		0.23	0.51	0.51	0.00	0.00	0.00
100	-143	-144	disturbed laminites, weakly slumped and convoluted, brecciated, loop bedding and microfaults	12	18	88		0.12	0.18	0.88	0.00	0.00	0.00

100	-142	-143	disturbed laminites, liquefied and weakly slumped, convoluted, brecciated, loop bedding and microfaults		19	93		0.00	0.19	0.93	0.00	0.00	0.00
100	-141	-142	disturbed laminites, and convoluted, loop bedding and microfaults		5	80		0.00	0.05	0.80	0.00	0.00	0.15
100	-140	-141	disturbed laminites, and convoluted, loop bedding and microfaults		3	22		0.00	0.03	0.22	0.00	0.00	0.75
100	-139	-140	disturbed laminites, weakly slumped and convoluted, brecciated, loop bedding and microfaults	11	5	35		0.11	0.05	0.35	0.00	0.00	0.49
100	-138	-139	disturbed laminites, weakly slumped and convoluted, brecciated, loop bedding and microfaults		5	67		0.00	0.05	0.67	0.00	0.00	0.28
100	-137	-138	disturbed laminites, weakly slumped and convoluted, brecciated, loop bedding and microfaults		3	39		0.00	0.03	0.39	0.00	0.00	0.58
100	-136	-137	disturbed laminites, and convoluted, loop bedding and microfaults		2	33		0.00	0.02	0.33	0.00	0.00	0.65
100	-135	-136	disturbed laminites, and convoluted, loop bedding and microfaults			40		0.00	0.00	0.40	0.00	0.00	0.60
100	-134	-135	disturbed laminites, partly liquefied and convoluted, resembling cross bedding, loop bedding and microfaults		2	74		0.00	0.02	0.74	0.00	0.00	0.24
100	-133	-134	disturbed laminites, partly liquefied and convoluted, resembling cross bedding, loop bedding and microfaults			59		0.00	0.00	0.59	0.00	0.00	0.41

100	-132	-133	disturbed laminites, partly liquefied and convoluted, resembling cross bedding, loop bedding and microfaults	1	62		0.00	0.01	0.62	0.00	0.00	0.37
100	-131	-132	disturbed laminites, convoluted, resembling cross bedding, loop bedding and microfaults	5	93		0.00	0.05	0.93	0.00	0.00	0.02
100	-130	-131	disturbed laminites, weakly slumped, convoluted, resembling cross bedding, loop bedding and microfaults	2	81		0.02	0.00	0.81	0.00	0.00	0.17
100	-129	-130	disturbed laminites, and convoluted, loop bedding and microfaults	9	78		0.00	0.09	0.78	0.00	0.00	0.13
100	-128	-129	disturbed laminites, and convoluted, loop bedding and microfaults	7	39	3	0.00	0.07	0.39	0.03	0.00	0.51
100	-127	-128	disturbed laminites, and convoluted, loop bedding and microfaults	10	89		0.00	0.10	0.89	0.00	0.00	0.01
100	-126	-127	disturbed laminites, and convoluted, loop bedding and microfaults	2	38		0.00	0.02	0.38	0.00	0.00	0.60
100	-125	-126	disturbed laminites, and convoluted, loop bedding and microfaults		32		0.00	0.00	0.32	0.00	0.00	0.68
100	-124	-125	disturbed laminites, partly liquefied and convoluted, resembling cross bedding, loop bedding and microfaults	5	46		0.00	0.05	0.46	0.00	0.00	0.49
100	-123	-124	disturbed laminites, partly liquefied and convoluted, resembling cross bedding, loop bedding and microfaults	10	52		0.00	0.10	0.52	0.00	0.00	0.38
100	-122	-123	disturbed laminites, loop bedding and microfaults	2	9		0.00	0.02	0.09	0.00	0.00	0.89

100	-121	-122	disturbed laminites, loop bedding and microfaults		6	21		0.00	0.06	0.21	0.00	0.00	0.73
100	-120	-121	disturbed laminites, loop bedding and microfaults			34		0.00	0.00	0.34	0.00	0.00	0.66
100	-119	-120	disturbed laminites, loop bedding and microfaults			11		0.00	0.00	0.11	0.00	0.00	0.89
100	-118	-119	disturbed laminites, loop bedding and microfaults			15		0.00	0.00	0.15	0.00	0.00	0.85
100	-117	-118	disturbed laminites, loop bedding and microfaults			11		0.00	0.00	0.11	0.00	0.00	0.89
100	-116	-117	disturbed laminites, partly liquefied and convoluted, resembling cross bedding, loop bedding and microfaults	1	5	29		0.01	0.05	0.29	0.00	0.00	0.65
100	-115	-116	disturbed laminites, loop bedding and microfaults			13		0.00	0.00	0.13	0.00	0.00	0.87
100	-114	-115	disturbed laminites, loop bedding and microfaults			6		0.00	0.00	0.06	0.00	0.00	0.94
115	-112.85	-114	disturbed laminites, partly liquefied and convoluted, resembling cross bedding, loop bedding and microfaults	4		30		0.03	0.00	0.26	0.00	0.00	0.70
100	-111.85	-112.85	disturbed laminites, partly liquefied and convoluted, resembling cross bedding, loop bedding and microfaults		12	38		0.00	0.12	0.38	0.00	0.00	0.50
85	-111	-111.85	disturbed laminites, partly liquefied and convoluted, resembling cross bedding, loop bedding and microfaults	3		48		0.04	0.00	0.56	0.00	0.00	0.40

130	-109.7	-111	disturbed laminites, partly liquefied and convoluted, resembling cross bedding, loop bedding and microfaults	2	3	50	0.02	0.02	0.38	0.00	0.00	0.58
94	-108.76	-109.7	disturbed laminites, partly liquefied and convoluted, resembling cross bedding, loop bedding and microfaults			51	0.00	0.00	0.54	0.00	0.00	0.46
76	-108	-108.76	disturbed laminites, partly liquefied and convoluted, resembling cross bedding, loop bedding and microfaults			41	0.00	0.00	0.54	0.00	0.00	0.46
100	-107	-108	disturbed laminites, partly liquefied and convoluted, resembling cross bedding, loop bedding and microfaults		4	38	0.00	0.04	0.38	0.00	0.00	0.58
100	-106	-107	disturbed laminites, partly liquefied and convoluted, resembling cross bedding, loop bedding and microfaults		2	7	0.00	0.02	0.07	0.00	0.00	0.91
100	-105	-106	disturbed laminites, partly liquefied and convoluted, resembling cross bedding, loop bedding and microfaults		1	42	0.00	0.01	0.42	0.00	0.00	0.57
100	-104	-105	disturbed laminites, partly liquefied and convoluted, resembling cross bedding, loop bedding and microfaults		7	44	0.00	0.07	0.44	0.00	0.00	0.49
100	-103	-104	disturbed laminites, partly liquefied and convoluted, resembling cross bedding, loop bedding and microfaults			20	0.00	0.00	0.20	0.00	0.00	0.80

100	-102	-103	disturbed laminites, partly liquefied and convoluted, resembling cross bedding, loop bedding and microfaults	48		0.00	0.00	0.48	0.00	0.00	0.52
120	-100.8	-102	disturbed laminites, partly liquefied and convoluted, resembling cross bedding, loop bedding and microfaults	41		0.00	0.00	0.34	0.00	0.00	0.66
80	-100	-100.8	disturbed laminites, partly liquefied and convoluted, resembling cross bedding, loop bedding and microfaults	30		0.00	0.00	0.38	0.00	0.00	0.62
150	-98.5	-100	disturbed laminites, partly liquefied and convoluted, resembling cross bedding, loop bedding and microfaults	26		0.00	0.00	0.17	0.00	0.00	0.83
50	-98	-98.5	disturbed laminite/marl beds partly resembling bioturbation, partly liquefied and convoluted, resembling cross bedding, loop bedding and microfaults. clear salt precipitation at the surface of the core, possbily from the pore water.	7	2	0.00	0.00	0.14	0.04	0.00	0.82
200	-96	-98	disturbed laminite/marl beds partly resembling bioturbation, partly liquefied and convoluted, resembling cross bedding, loop bedding and microfaults	5	8	0.00	0.00	0.03	0.04	0.00	0.94

100	-95	-96	disturbed laminite/marl beds partly resembling bioturbation, partly liquefied and convoluted, resembling cross bedding, loop bedding and microfaults		5	12	0.00	0.00	0.05	0.12	0.00	0.83
100	-94	-95	disturbed laminite/marl beds partly resembling bioturbation, partly liquefied and convoluted, resembling cross bedding, loop bedding and microfaults		10	2	0.00	0.00	0.10	0.02	0.00	0.88
100	-93	-94	disturbed laminites, partly liquefied and convoluted, resembling cross bedding, loop bedding and microfaults	1	12		0.00	0.01	0.12	0.00	0.00	0.87
100	-92	-93	disturbed laminite/marl beds partly resembling bioturbation, partly liquefied and convoluted, resembling cross bedding, loop bedding and microfaults		2	2	0.00	0.00	0.02	0.02	0.00	0.96
100	-91	-92	disturbed laminite/marl beds partly resembling bioturbation, partly liquefied and convoluted, resembling cross bedding, loop bedding and microfaults		5	4	0.00	0.00	0.05	0.04	0.00	0.91
100	-90	-91	disturbed laminites, partly liquefied and convoluted, resembling cross bedding, loop bedding and microfaults	3	12		0.00	0.03	0.12	0.00	0.00	0.85
100	-89	-90	disturbed laminites, partly liquefied and convoluted, resembling cross bedding, brecciated, loop bedding and microfaults	3	13		0.00	0.03	0.13	0.00	0.00	0.84

100	-88	-89	disturbed laminites, partly liquefied and convoluted, resembling cross bedding, loop bedding and microfaults	1	2		0.00	0.01	0.02	0.00	0.00	0.97
100	-87	-88	disturbed laminite/marl beds partly resembling bioturbation, partly liquefied and convoluted, resembling cross bedding, loop bedding and microfaults	3	15	3	0.00	0.03	0.15	0.03	0.00	0.79
100	-86	-87	disturbed laminite/marl beds partly resembling bioturbation, partly liquefied and convoluted, resembling cross bedding, loop bedding and microfaults	2	5	23	0.00	0.02	0.05	0.23	0.00	0.70
100	-85	-86	disturbed laminite/marl beds partly resembling bioturbation, partly liquefied and convoluted, resembling cross bedding, loop bedding and microfaults		21	20	0.00	0.00	0.21	0.20	0.00	0.59
100	-84	-85	disturbed laminite/marl beds partly resembling bioturbation, partly liquefied and convoluted, resembling cross bedding, loop bedding and microfaults	4	17	23	0.00	0.04	0.17	0.23	0.00	0.56
100	-83	-84	disturbed laminite/marl beds partly resembling bioturbation, resembling cross bedding, loop bedding and microfaults. clear salt precipitation at the surface of the core, possbily from the pore water		7	12	0.00	0.00	0.07	0.12	0.00	0.81
100	-82	-83	disturbed laminite/marl beds resembling bioturbation,		10	27	0.00	0.00	0.10	0.27	0.00	0.63

100	-81	-82	disturbed laminite/marl beds resembling bioturbation,			66	0.00	0.00	0.00	0.66	0.00	0.34
100	-80	-81	disturbed laminite/marl beds resembling bioturbation,partly loop bedding and faulted. mud crack at -80.5 m,	10	16	28	0.00	0.10	0.16	0.28	0.00	0.46
100	-79	-80	disturbed laminite/marl beds resembling bioturbation,partly liquefied, loop bedding and faulted	3	11	33	0.00	0.03	0.11	0.33	0.00	0.53
100	-78	-79	disturbed laminite/marl beds resembling bioturbation,partly liquefied, loop bedding and faulted	3	14	10	0.00	0.03	0.14	0.10	0.00	0.73
200	-76	-78	disturbed laminite/marl beds resembling bioturbation,partly liquefied, loop bedding and faulted. mud crack at -76.36 m, -76.47m, a sand dike (10cm) structure at -76.67m		12	33	0.00	0.00	0.06	0.17	0.00	0.78
100	-75	-76	disturbed laminite/marl beds resembling bioturbation,partly liquefied, loop bedding and faulted. a small sand dike at -75.87m		8	7	0.00	0.00	0.08	0.07	0.00	0.85
100	-74	-75	disturbed laminite/marl beds resembling bioturbation,partly liquefied, loop bedding and faulted	4	15	6	0.00	0.04	0.15	0.06	0.00	0.75
100	-73	-74	disturbed laminite/marl beds resembling bioturbation,partly liquefied, loop bedding and faulted. salt precipitation at the surface of the core, possbily from the pore water		13	22	0.00	0.00	0.13	0.22	0.00	0.65
100	-72	-73	bioturbated beds			43	0.00	0.00	0.00	0.43	0.00	0.57

100	-71	-72	disturbed laminite/marl beds resembling bioturbation,partly liquefied, loop bedding and faulted. mud crack at -71.74 m	5	45	0.00	0.00	0.05	0.45	0.00	0.50
100	-70	-71	bioturbated beds		20	0.00	0.00	0.00	0.20	0.00	0.80
100	-69	-70	bioturbated beds		24	0.00	0.00	0.00	0.24	0.00	0.76
100	-68	-69	bioturbated beds		31	0.00	0.00	0.00	0.31	0.00	0.69
100	-67	-68	bioturbated beds	2	32	0.00	0.00	0.02	0.32	0.00	0.66
100	-66	-67	bioturbated beds		23	0.00	0.00	0.00	0.23	0.00	0.77
100	-65	-66	bioturbated beds		25	0.00	0.00	0.00	0.25	0.00	0.75
100	-64	-65	bioturbated beds		32	0.00	0.00	0.00	0.32	0.00	0.68
100	-63	-64	bioturbated beds		34	0.00	0.00	0.00	0.34	0.00	0.66
100	-62	-63	bioturbated beds, mud crack at -62.10		38	0.00	0.00	0.00	0.38	0.00	0.62
100	-61	-62	bioturbated beds,mud crack at -61.98		38	0.00	0.00	0.00	0.38	0.00	0.62
100	-60	-61	bioturbated beds, mud crack at -60.5		55	0.00	0.00	0.00	0.55	0.00	0.45
100	-59	-60	bioturbated beds, mud crack at -59.40, -59.90		25	0.00	0.00	0.00	0.25	0.00	0.75
100	-58	-59	bioturbated beds		48	0.00	0.00	0.00	0.48	0.00	0.52
100	-57	-58	bioturbated beds		9	0.00	0.00	0.00	0.09	0.00	0.91
100	-56	-57	bioturbated beds		9	0.00	0.00	0.00	0.09	0.00	0.91
100	-55	-56	bioturbated beds		73	0.00	0.00	0.00	0.73	0.00	0.27
100	-54	-55	bioturbated beds, mud crack at -54.2, -54.3		92	0.00	0.00	0.00	0.92	0.00	0.08
100	-53	-54	bioturbated beds, mud crack at -53.27		80	0.00	0.00	0.00	0.80	0.00	0.20
100	-52	-53	disturbed laminite/marl beds partly resembling bioturbation, partly liquefied and convoluted, resembling cross bedding, loop bedding and microfaults	41	47	0.00	0.00	0.41	0.47	0.00	0.12
100	-51	-52	bioturbated beds		30	0.00	0.00	0.00	0.30	0.00	0.70

100	-50	-51	bioturbated beds		34		0.00	0.00	0.00	0.34	0.00	0.66
100	-49	-50	bioturbated beds		84		0.00	0.00	0.00	0.84	0.00	0.16
100	-48	-49	bioturbated beds		70		0.00	0.00	0.00	0.70	0.00	0.30
100	-47	-48	bioturbated beds		43		0.00	0.00	0.00	0.43	0.00	0.57
100	-46	-47	bioturbated beds		53		0.00	0.00	0.00	0.53	0.00	0.47
100	-45	-46	bioturbated beds		31		0.00	0.00	0.00	0.31	0.00	0.69
100	-44	-45	bioturbated beds		35		0.00	0.00	0.00	0.35	0.00	0.65
100	-43	-44	bioturbated beds		42		0.00	0.00	0.00	0.42	0.00	0.58
100	-42	-43	bioturbated beds		70		0.00	0.00	0.00	0.70	0.00	0.30
150	-40.5	-42	bioturbated beds		100		0.00	0.00	0.00	0.67	0.00	0.33
80	-39.7	-40.5	bioturbated beds		48		0.00	0.00	0.00	0.60	0.00	0.40
70	-39	-39.7	bioturbated beds		24	14	0.00	0.00	0.00	0.34	0.20	0.46
100	-38	-39	bioturbated beds		24	8	0.00	0.00	0.00	0.24	0.08	0.68
100	-37	-38	bioturbated beds		23		0.00	0.00	0.00	0.23	0.00	0.77
100	-36	-37	pedogenic beds			56	0.00	0.00	0.00	0.00	0.56	0.44
100	-35	-36	bioturbated beds		19		0.00	0.00	0.00	0.19	0.00	0.81
100	-34	-35	bioturbated beds		24		0.00	0.00	0.00	0.24	0.00	0.76
140	-32.6	-34	bioturbated beds		8		0.00	0.00	0.00	0.06	0.00	0.94
100	-31.6	-32.6	bioturbated beds		28	12	0.00	0.00	0.00	0.28	0.12	0.60
60	-31	-31.6	bioturbated beds	4	5	9	0.00	0.07	0.00	0.08	0.15	0.70
100	-30	-31	bioturbated beds		16	19	0.00	0.00	0.00	0.16	0.19	0.65
100	-29	-30	bioturbated beds		13	49	0.00	0.00	0.00	0.13	0.49	0.38
50	-28.5	-29	pedogenic beds			50	0.00	0.00	0.00	0.00	1.00	0.00
250	-26	-28.5	pedogenic beds			100	0.00	0.00	0.00	0.00	0.40	0.60
100	-25	-26	pedogenic beds			100	0.00	0.00	0.00	0.00	1.00	0.00
100	-24	-25	bioturbated beds		23		0.00	0.00	0.00	0.23	0.00	0.77
100	-23	-24	bioturbated beds		7		0.00	0.00	0.00	0.07	0.00	0.93
100	-22	-23	pedogenic beds			100	0.00	0.00	0.00	0.00	1.00	0.00
200	-20	-22	bioturbated beds		25		0.00	0.00	0.00	0.13	0.00	0.88
200	-18	-20	pedogenic beds			70	0.00	0.00	0.00	0.00	0.35	0.65
100	-17	-18	bioturbated beds		13	30	0.00	0.00	0.00	0.13	0.30	0.57
100	-16	-17	bioturbated beds		6	35	0.00	0.00	0.00	0.06	0.35	0.59

| 100 | -15 | -16 | bioturbated beds | 35 | 0.00 | 0.00 | 0.00 | 0.35 | 0.00 | 0.65 |
| 100 | -14 | -15 | bioturbated beds | 34 | 0.00 | 0.00 | 0.00 | 0.34 | 0.00 | 0.66 |

Table B.2 Bulk geochemistry data of the leaching materials of the pre-impact formations from drill cores and outcrop samples. mXRF data: major elements as oxides and trace elements as simple substance

sample	Drill core/locality	Formation	lithology	CaO wt %	MgO wt %	Na_2O wt %	K_2O wt %	Al_2O_3 wt %	Fe_2O_3 wt %	SiO_2 wt %	SO_4 wt %	Sr wt %	Rb wt %
Eic 1	Bohrung Eichstätt-Lüften	Tertiary limnic sediments ("Albüberdeckung", Terra Rossa)	intense redbrown clay with coarse quartz grains and pebbles, massive, carbonate-free	0.6	0.2	-	-	23.9	7.2	50.3	-	0.004	0.002
Fra 1	Bohrung Frauenberg SPZ Solnhofen	Weißjura Group, Solnhofen Subformation	white-grey micritic limestone ("Plattenkalk"), inclined bedding	45.5	17.0	-	-	2.0	0.7	3.9	0.2	0.024	0.003
Fra 2	Bohrung Frauenberg SPZ Solnhofen	Weißjura Group, Frankenalb-Formation (dolomitized Weißjura)	light-grey crystalline dolomite with minor spar patches, massive	47.3	17.9	0.2	-	0.4	0.2	0.9	0.2	0.019	0.001
Fra 3	Bohrung Frauenberg SPZ Solnhofen	Weißjura Group, Treuchtlingen Formation (Weißjura δ)	white-grey micritic limestone with sponge layers and spar-cemented voids, bedded	69.1	2.1	-	-	0.7	0.3	3.9	0.1	0.029	0.002
Fra 4	Bohrung Frauenberg SPZ Solnhofen	Weißjura Group, Arzberg Formation (Weißjura γ)	white-grey argillaceous micritic limestone, bedded, with one ammonite cast and very minor iron sulfide patches	75.0	0.7	0.1	-	0.5	0.3	1.2	0.2	0.057	0.002
Urs 1	Bohrung Ursheim 2012	Weißjura Group, Dietfurt Formation (upper part, Weißjura β)	white-grey micritic limestone, 5-cm-bed	71.5	0.4	0.0	-	0.8	0.6	1.9	0.1	0.045	0.001
Urs 2	Bohrung Ursheim 2012	Weißjura Group, Dietfurt Formation (lower part, Weißjura α)	medium-grey calcareous marl with bioclasts, faint irregular stratification	61.5	1.0	0.1	-	4.0	1.5	9.3	0.5	0.079	0.005
Urs 3	Bohrung Ursheim 2012	Braunjura Group, Ornatenton Subformation (Braunjura ζ)	dark-grey marlstone, with abundant mica, disseminated iron sulfides and quartz silt, stratified	10.6	2.1	-	2.3	16.1	4.6	48.0	0.8	0.027	0.013
Urs 4	Bohrung Ursheim 2012	Braunjura Group, Sengenthal Formation (Braunjura γ-ε)	medium-grey to redbrown mottled, iron-oolitic argillaceous limestone, bioturbated, with calcitic shells (ammonites, brachiopods, bivalves)	33.6	1.2	-	-	7.1	27.8	10.0	0.5	0.044	0.002

Sample	Location	Formation	Description										
Urs 5	Bohrung Ursheim 2012	Braunjura Group, Eisensandstein Formation (Braunjura β)	intense redbrown fine-grained sandstone with hematite-coated quartz grains and hematite oolite layers, carbonate-free	0.2	0.4	0.0	0.2	4.3	11.7	48.5	-	0.005	0.001
Urs 6	Bohrung Ursheim 2012	Braunjura Group, Opalinuston Formation (Braunjura α, upper part)	medium-grey wavy bedded silt with clay layers, with minor mica, siderite patches and minor shell debris, belemnites	1.1	1.8	-	3.0	22.9	4.0	52.6	3.1	0.013	0.011
TP39-1	Bohrung Pilsach TP39 2019	Braunjura Group, Opalinuston Formation (Braunjura α, middle part)	medium grey calcareous claystone, bedded, minor disseminated iron sulfides; minor shell fragments	4.2	2.2	-	3.0	24.0	5.6	50.6	1.8	0.026	0.019
Auf 1	Bohrung Aufkirchen P1 1971	Schwarzjura Group, Posidonienschiefer Formation (Schwarzjura ε)	darkgrey bituminous laminated marlstone (with aragonitic shell debris: bivalves, compressed ammonites)	30.9	1.7	-	-	10.3	3.9	29.3	3.3	0.597	0.010
Wac 1	Bohrung Wachfeld 2018	Schwarzjura Group, Amaltheenton Formation (Schwarzjura δ)	medium grey calcareous claystone, bedded, minor disseminated iron sulfides	3.3	2.3	-	2.4	24.7	4.4	51.2	0.5	0.023	0.014
Wac 2	Bohrung Wachfeld 2018	Schwarzjura Group, Numismalismergel Formation (Schwarzjura γ)	light-grey argillaceous limestone, massive (bioturbated)	64.7	0.8	0.1	-	2.2	1.3	4.6	0.2	0.091	0.003
Wac 3	Bohrung Wachfeld 2018	Schwarzjura Group, Gryphaeensandstein Formation (Schwarzjura α3+β, "Arietensandstein")	light-grey coarse-grained to fine-conglomeratic, calcareous quartz sandstone, massive	41.6	3.0	0.1	-	1.8	2.6	26.5	0.2	0.024	0.002
Wac 4	Bohrung Wachfeld 2018	Schwarzjura Group, Angulatensandstein Formation (Schwarzjura α2)	medium grey clayey siltstone, slightly calcareous, bioturbated, poorly bedded	0.3	1.7	-	3.0	25.7	2.9	59.0	1.3	0.017	0.016
Fre 1	Bohrung Fremdingen	Schwarzjura Group, Angulatensandstein Formation (Schwarzjura α2)	yellow-brown fine-grained quartz sandstone with mica	0.1	0.4	0.0	0.6	6.8	1.1	69.5	-	0.004	0.003
Fre 2	Bohrung Fremdingen	Keuper Group, Trossingen Formation ("Feuerletten")	redbrown silty claystone with minor mica; carbonate-free	1.1	2.9	-	3.1	20.4	8.8	51.6	-	0.030	0.021
Fre 3	Bohrung Fremdingen	Keuper Group, Löwenstein Formation ("Burgsandstein")	light-grey coarse-grained to fine-conglomeratic arkose (with kaolinized feldspar grains)	0.1	0.6	0.1	4.7	11.4	0.3	74.5	0.0	0.017	0.010
Esc 1	Bohrung Eschertshofen 1981	Keuper Group, Hassberge Formation ("Coburger Sandstein")	light-grey coarse-grained to fine-conglomeratic arkose (with kaolinized feldspar grains)	0.6	0.2	0.0	5.1	22.7	0.4	68.8	0.0	0.016	0.011
Esc 2	Bohrung Eschertshofen 1981	Keuper Group, Hassberge Formation ("Blasensandstein")	medium-grey fine- to medium-grained sandstone, with some clay and mica, well bedded (shallow cross stratification?)	0.6	2.0	0.2	5.3	20.5	2.8	62.0	1.2	0.014	0.023

Sample	Location	Formation	Description										
Esc 3	Bohrung Eschertshofen 1981	Keuper Group, Steigerwald Formation ("Lehrbergschichten")	greenish-grey and violet mottled clayey coarse-grained arkose (with kaolinized feldspar grains)	0.2	1.2	0.0	4.4	18.0	2.1	70.5	0.0	0.019	0.019
Esc 4	Bohrung Eschertshofen 1981	Keuper Group, Benk Formation ("Benker Sandstein")	violett-redbrown siltstone to fine-grained sandstone with mica, faint stratification	1.3	1.4	-	3.4	24.2	5.3	54.1	-	0.016	0.027
Esc 5	Bohrung Eschertshofen 1981	Keuper Group, Grafenwöhr Formation ("Lettenkohlenkeuper")	redbrown coarse-grained quartz sandstone with some feldspar, minor clay content	0.1	0.5	0.0	2.8	13.5	2.3	74.2	0.1	0.014	0.010
Esc 6	Bohrung Eschertshofen 1981	Muschelkalk Group, Grafenwöhr Formation ("Muschelsandstein")	whitegrey to violett siltstone to medium/coarse grained sandstone with kaolinized feldspar, cross-stratification	0.6	1.4	0.1	4.9	21.3	3.0	60.0	-	0.015	0.024
Esc 7	Bohrung Eschertshofen 1981	Benk Formation (Benker Sandstein, including Estherien Beds)	dark redbrown siltstone to fine-grained sandstone, with mica, cross-stratified	0.2	2.3	-	5.9	24.3	5.1	49.9	-	0.017	0.030
Erb 104	Bohrung Erbisberg	Inner Ring, allochthonous crystalline block	Hornblende-Gneiss	3.0	3.5	0.4	1.2	15.9	5.7	55.0	-	0.048	0.011
Ott 1/2wr	Steinbruch Otting	suevite	grey suevite with carbonate in matrix and glass	7.4	1.8	1.7	2.0	12.6	5.0	51.7	-	0.071	0.018
Ott 1/2gb	Steinbruch Otting	suevite	glass bomb within suevite, with carbonate in gas bubbles	2.9	0.4	2.4	4.6	19.5	4.0	60.2	-	0.071	0.020
Pol 1	Steinbruch Polsingen	suevite	red melt agglomerate	8.2	4.1	1.9	0.8	15.6	6.7	44.5	1.4	0.202	0.009
Gro 4b	pipe trench Grosselfingen	Inner Ring, allochthonous crystalline block	light-grey brecciated granite, rich in white-grey feldspar	3.0	2.3	3.5	1.3	18.8	3.1	51.3	-	0.106	0.016
Unt 1	Unterwillfingen quarry	Keuper clast in Bunte Breccia, outcrop samples in Ries; ex situ from basis of outcrop wall	pinkish white-grey and yellowish grey mottled, fine-grained pebbly arkose clast	28.6	0.3	0.5	3.3	7.2	0.9	40.4	0.0	0.038	0.013
Unt 2	Unterwillfingen quarry	Keuper clast in Bunte Breccia, outcrop samples in Ries; ex situ from basis of outcrop wall	mixed material between Keuper arkose and Bunte breccia: pinky reddish medium to fine-grained arkose with olivine-grey mottled Bunte breccia matrixes	37.4	0.9	0.2	2.8	7.4	1.8	31.4	0.0	0.019	0.015
Unt 3	Unterwillfingen quarry	Keuper clast in Bunte Breccia, outcrop samples in Ries; from contact Keuper-suevite	white-grey fine-grained sanstone clast	18.4	0.5	1.1	3.7	11.4	0.7	51.2	0.0	0.026	0.014
Freq 1	Fremdingen road cut , Ries	Keuper group, outcrop samples in Ries, road cutting B25 (western slope)	white-grey coarse-grained quartz sandstone	0.1	-	0.7	3.1	8.7	0.2	82.5	0.3	0.010	0.009
Freq 2	Fremdingen road cut , Ries	Keuper group, outcrop samples in Ries, road cutting B25 (western slope)	ochre red claystone with mica	0.7	2.1	0.1	4.4	20.1	7.8	52.1	0.0	0.016	0.023

Freq 3	Fremdingen road cut , Ries	Keuper group, outcrop samples in Ries, road cutting B25 (western slope)	ochre red and yellowish-white mottled coarse-grained quartz sandstones with mica	0.1	0.3	0.8	3.5	10.6	0.5	77.3	0.0	0.012	0.010
Freq 4	Fremdingen road cut , Ries	Keuper group, outcrop samples in Ries, road cutting B25 (western slope)	ochre red, violet and white mottled claystone with mica	0.4	2.0	0.1	4.4	24.1	4.9	53.4	0.0	0.018	0.023
Den-1	Dennenlohe outcrop	Bayreuth Fm., Keuper group, outcrop sample 55 km NW' Ries	white grey coarse-grained quartz sandstone with muscovites	-	-	-	-	-	-	-	-	-	-

Table B.3 Hydrochemistry analysis of the field water and leachate samples.

Sample ID	lab ID	pH	T_{pH}	$^{87}Sr/^{86}Sr$	weight powder	Ca	Mg	Na	K	Sr	TA	Cl	SO_4	Acetat
			°C		gram	mg L^{-1}	mg L^{-1}	mg L^{-1}	mg L^{-1}	mg L^{-1}	meq L^{-1}	mg L^{-1}	mg L^{-1}	mg L^{-1}
15 days leaching with acetic acid:														
Eic 1	R15-01	5.29	21.5	0.70949	8.0201	86.6	1.27	3.90	0.71	0.027	2.28	1.7	1.4	306.6
Fra 1	R15-02	7.66	21.5	0.71176	8.018	180.3	73.26	3.43	6.39	0.079	10.60	2.5	4.4	544.9
Fra 2	R15-03	7.67	21.5	0.70769	8.0206	137.8	113.99	7.65	1.61	0.100	11.20	14.3	9.2	559.2
Fra 3	R15-04	7.41	21.4	0.70744	8.0092	238.3	33.26	4.30	3.20	0.448	9.20	8.6	6.1	571.5
Fra 4	R15-05	7.32	21.3	0.70750	8.0267	264.2	18.13	3.75	3.39	1.019	9.04	3.4	20.7	521.2
Urs 1	R15-06	7.29	21.3	0.70810	7.9773	268.4	7.15	3.39	5.25	0.430	8.72	2.0	4.1	465.6
Urs 2	R15-07	7.30	21.2	0.70845	8.0206	265.3	19.07	4.24	24.25	0.695	9.00	2.1	78.3	430.4
Urs 3	R15-08	7.43	21.7	0.70909	8.0117	302.6	34.51	5.25	63.03	1.813	9.36	1.6	248.9	558.5
Urs 4	R15-09	7.42	21.3	0.70865	8.0267	350.3	33.26	4.96	31.19	1.047	10.20	2.9	280.1	572.5
Urs 5	R15-10	5.54	21.4	0.71030	8.0347	122.3	27.36	3.99	8.23	0.205	2.70	2.1	8.6	575.5
Urs 6	R15-11	7.30	21.4	0.70951	7.9822	895.7	64.25	14.20	37.62	2.155	9.24	2.4	1546.9	578.4
TP39-1	R15-12	7.49	21.3	0.71075	8.0133	249.7	46.42	5.74	56.37	2.373	10.00	1.7	276.8	331.9
Auf 1	R15-13	7.50	21.3	0.70785	8.0389	544.0	77.93	9.13	35.65	8.117	10.20	2.4	924.3	470.4
Wac 1	R15-14	7.55	21.4	0.70939	8.0088	293.3	57.72	5.94	52.85	3.275	8.68	2.0	342.5	393.3
Wac 2	R15-15	7.28	21.3	0.70846	8.0293	269.4	15.75	6.91	17.72	1.306	8.94	4.5	40.8	510.5
Wac 3	R15-16	7.41	21.2	0.70913	8.0253	285.0	17.41	8.82	5.93	0.390	10.12	16.4	12.4	526.8
Wac 4	R15-17	3.20	21.2	0.70951	8.0282	213.5	89.53	6.00	33.47	3.720	0.00	1.8	1831.9	554.1
Fre 1	R15-18	4.34	21.3	0.71845	8.0154	37.3	1.28	3.53	4.47	0.026	0.60	2.3	2.5	369.2
Fre 2	R15-19	7.74	21.2	0.70914	7.9931	163.7	66.84	4.25	28.91	3.389	10.40	1.2	20.1	425.7
Fre 3	R15-20	4.31	21.4	0.71053	8.0261	31.5	8.31	4.60	13.99	0.376	0.60	4.4	6.5	438.5

Esc 1	R15-21	7.29	21.6	0.71532	8.0074	117.1	46.94	6.16	10.27	0.179	7.68	4.6	22.4	409.9
Esc 2	R15-22	3.29	21.3	0.71535	7.9925	217.6	36.06	14.61	44.04	0.483	0.00	2.3	850.4	598.9
Esc 3	R15-23	4.59	21.4	0.71313	7.9925	42.3	9.49	14.51	37.20	0.322	0.70	2.5	11.3	500.2
Esc 4	R15-24	7.52	21.3	0.71676	8.0032	126.4	51.40	20.00	33.47	0.533	6.92	5.1	1.8	563.5
Esc 5	R15-25	4.29	21.3	0.71560	7.999	27.0	8.69	20.73	16.48	0.205	0.60	15.7	4.2	522.8
Esc 6	R15-26	7.15	21.5	0.71646	7.997	122.3	52.54	17.51	28.50	0.448	8.60	8.1	4.6	651.8
Esc 7	R15-27	4.64	21.4	0.71552	7.995	38.2	11.81	22.38	36.17	0.437	1.40	11.1	1.7	506.9
Erb 104	R15-28	7.46	21.6	0.71144	7.9962	325.4	56.58	10.00	21.35	4.363	9.68	2.6	222.8	536.0
Ott 1/2wr	R15-29	5.25	21.6	0.71187	8.0062	191.7	36.06	7.16	18.55	0.753	2.40	2.4	2.2	763.0
Ott 1/2gb	R15-30	7.38	21.5	0.71160	8.0274	264.2	14.20	8.82	6.28	0.420	9.16	1.5	0.3	402.8
Pol 1	R15-31	4.78	21.5	0.71198	8.023	123.3	4.47	12.54	21.55	0.827	2.50	2.1	1.8	647.1
Gro 4b	R15-32	4.81	21.4	0.71426	7.9987	86.3	14.30	15.65	5.54	0.605	1.84	2.8	0.8	596.9
Unt 1	R14-33	7.43	21.4	0.71208		290.2	8.88	4.46	12.02	0.236	10.96	2.2	1.3	525.3
Unt 2	R14-34	7.48	21.3	0.71469		246.6	27.56	4.20	17.82	0.223	10.36	1.6	1.0	515.7
Unt 3	R14-35	4.53	21.4	0.71398		280.8	14.82	4.52	12.44	0.181	10.72	1.9	0.8	539.9
Freq 1	R14-36	4.35	21.3	0.71390		30.3	4.94	10.57	24.14	0.280	0.48	4.7	1.2	584.4
Freq 2	R14-37	4.71	21.4	0.71306		62.4	7.13	11.30	12.75	0.159	1.64	1.8	0.2	487.4
Freq 3	R14-38	4.35	21.3	0.71630		35.6	5.76	9.21	13.68	0.171	0.34	3.8	4.2	570.1
Freq 4	R14-39	4.45	21.2	0.71776		36.0	8.53	7.10	11.30	0.138	0.50	2.0	8.8	440.9
Den 1	R14-40	3.88	21.4	0.71709		1.8	0.50	4.56	10.17	0.076	0.00	5.2	0.4	583.3
Freq 2	R14-37	4.83	20.7	n.a.		26.4	3.11	11.38	5.62	0.000	1.64	1.5	0.1	219.6
Freq 3	R14-38	4.37	20.7	n.a.		35.7	5.71	11.01	14.13	0.000	0.50	3.7	4.7	558.7
Freq 4	R14-39	4.46	21.2	n.a.		35.0	8.35	10.36	10.40	0.000	1.78	2.1	8.7	422.8
Den 1	R14-40	3.96	20.5	n.a.		2.4	0.52	7.67	10.07	0.000	0.00	4.9	0.6	556.4

28 days leaching with acetic acid:

Eic 1	R28-01	5.52	20.2	0.70967	8.0241	79.4	1.12	2.29	0.74	0.024	2.56	1.2	1.4	251.9
Fra 1	R28-02	7.52	20.3	0.71211	7.9918	192.7	64.66	1.34	7.19	0.081	10.72	2.0	4.3	555.6
Fra 2	R28-03	7.79	20.2	0.70782	8.0086	142.0	110.88	5.77	2.01	0.111	11.20	13.7	10.5	580.1
Fra 3	R28-04	7.58	20.2	0.70747	8.0186	222.8	38.03	2.29	3.33	0.494	9.20	7.6	6.3	574.7
Fra 4	R28-05	7.40	20.3	0.70756	8.0113	247.7	22.69	1.93	4.33	1.275	8.96	3.2	24.6	492.1
Urs 1	R28-06	7.38	20.3	0.70823	8.0367	246.6	7.06	1.22	5.15	0.426	8.00	1.8	3.8	414.3
Urs 2	R28-07	7.41	20.3	0.70860	8.0479	241.4	21.76	3.06	30.88	0.804	7.68	2.1	77.6	376.7
Urs 3	R28-08	7.39	20.2	0.70919	8.0406	294.3	35.13	3.17	65.18	1.793	9.12	1.4	224.4	492.8
Urs 4	R28-09	7.47	20.5	0.70874	8.0194	298.4	33.99	3.03	32.85	1.057	7.76	2.3	261.0	384.3
Urs 5	R28-10	7.82	20.8	0.71078	8.0014	166.8	40.52	1.74	10.31	0.195	9.12	1.8	11.3	533.1
Urs 6	R28-11	7.81	20.2	0.70953	8.0287	866.1	68.39	13.26	40.21	2.218	11.44	1.8	1609.3	601.2
TP39-1	R28-12	7.79	20.3	0.71085	8.0377	244.6	46.63	3.91	60.10	2.363	10.00	1.2	152.5	421.3
Auf 1	R28-13	7.56	20.4	0.70794	8.0223	470.1	76.48	7.45	31.92	7.034	9.76	1.5	850.0	320.1

275

Wac 1	R28-14	7.57	20.2	0.70948	7.9946	285.0	59.27	3.52	55.96	3.294	9.20	1.0	323.5	406.5
Wac 2	R28-15	7.46	20.4	0.70860	8.0047	263.2	17.93	5.20	19.59	1.389	8.72	3.9	44.6	530.7
Wac 3	R28-16	7.52	20.4	0.70925	8.0047	278.8	21.76	6.99	6.70	0.429	9.44	15.8	18.6	554.7
Wac 4	R28-17	3.33	20.7	0.70961	8.0039	187.6	82.59	3.68	32.23	3.249	0.00	1.1	885.6	584.4
Fre 1	R28-18	4.46	20.8	0.71883	8.0142	41.1	1.39	1.42	5.23	0.027	0.80	1.4	2.5	351.6
Fre 2	R28-19	7.73	20.6	0.70923	8.0108	164.8	64.97	2.12	29.12	3.351	9.44	0.6	18.7	365.2
Fre 3	R28-20	4.48	20.6	0.71046	8.0241	30.8	8.10	2.28	14.40	0.361	0.50	2.4	6.0	358.2
Esc 1	R28-21	7.87	20.6	0.71531	8.0136	134.7	53.06	4.45	10.98	0.191	8.84	4.6	29.1	399.0
Esc 2	R28-22	3.32	20.7	0.71531	8.0141	221.8	36.79	12.85	46.01	0.503	0.00	1.2	862.9	591.4
Esc 3	R28-23	4.79	20.5	0.71322	8.0344	46.5	10.57	12.23	39.07	0.347	1.44	2.1	18.7	392.2
Esc 4	R28-24	7.87	20.5	0.71733	8.0332	125.4	50.36	18.45	36.48	0.535	9.92	4.7	2.2	394.3
Esc 5	R28-25	4.47	20.7	0.71582	8.0328	28.4	9.01	19.59	19.07	0.218	0.80	15.5	4.7	426.3
Esc 6	R28-26	7.79	20.6	0.71682	7.9998	128.5	53.89	14.92	30.88	0.442	8.48	7.7	4.6	630.1
Esc 7	R28-27	4.60	20.6	0.71542	8.0133	42.5	13.06	20.62	38.96	0.492	1.92	10.0	1.8	606.9
Erb 104	R28-28	7.55	20.5	0.71144	8.0295	312.9	60.52	8.62	24.77	4.573	9.20	1.7	215.4	500.6
Ott 1/2wr	R28-29	5.46	20.6	0.71183	8.0302	211.4	40.00	5.44	20.10	0.835	4.60	1.8	4.4	764.1
Ott 1/2gb	R28-30	7.41	20.5	0.71168	8.024	266.3	15.13	6.23	7.78	0.451	9.28	0.8	0.6	491.1
Pol 1	R28-31	4.85	20.6	0.71200	8.0078	126.4	4.63	11.40	23.21	0.857	3.30	1.6	1.4	634.4
Gro 4b	R28-32	4.84	20.5	0.71421	8.0142	86.9	15.03	10.78	5.70	0.651	3.15	1.5	0.6	675.5
77 days leaching with acetic acid:														
Eic 1	R77-01	7.78	21.5	0.70965	8.0129	53.7	0.73	3.95	0.37	0.016	2.48	1.3	5.2	74.3
Fra 1	R77-02	7.68	20.8	0.71153	8.0074	155.4	67.67	2.85	5.37	0.074	10.96	2.2	4.2	530.5
Fra 2	R77-03	7.89	20.6	0.70781	8.0156	113.0	109.84	7.25	1.85	0.102	11.64	13.2	11.4	534.8
Fra 3	R77-04	7.68	20.5	0.70741	7.9919	181.3	44.35	4.27	3.03	0.525	9.92	8.0	6.8	574.3
Fra 4	R77-05	7.48	20.5	0.70754	7.9913	207.3	20.93	3.60	3.59	1.098	8.64	2.9	26.4	444.1
Urs 1	R77-06	7.35	20.3	0.70816	8.0372	200.0	7.45	3.15	5.45	0.433	7.04	1.7	4.1	355.7
Urs 2	R77-07	7.29	20.6	0.70849	8.0172	204.1	21.14	4.24	24.04	0.630	6.96	1.9	99.5	239.6
Urs 3	R77-08	7.57	20.8	0.70922	8.0151	212.4	29.74	5.02	59.62	1.483	5.92	1.5	249.0	175.7
Urs 4	R77-09	7.44	20.5	0.70866	7.983	277.7	37.72	5.05	30.36	1.016	7.76	2.6	337.1	253.9
Urs 5	R77-10	6.68	20.7	0.71071	8.0376	138.9	34.30	4.00	10.36	0.222	8.28	2.2	13.5	604.2
Urs 6	R77-11	7.70	21.2	0.70947	8.0301	917.4	65.59	15.23	39.58	2.145	11.08	2.1	1626.4	603.6
TP39-1	R77-12	7.49	20.8	0.71084	7.9956	202.1	41.97	5.58	53.00	2.099	7.04	1.1	175.2	231.8
Auf 1	R77-13	7.58	20.7	0.70797	7.9992	469.9	75.23	9.46	35.13	7.117	7.92	1.9	913.3	245.9
Wac 1	R77-14	7.64	20.6		8.0094	225.9	51.29	5.55	50.88	2.807	6.00	1.2	383.4	109.6
Wac 2	R77-15	7.42	20.7	0.70861	8.0343	228.0	18.65	6.60	17.62	1.363	9.04	4.2	58.6	470.9
Wac 3	R77-16	7.37	20.7	0.70917	8.0018	241.4	26.01	8.74	6.31	0.426	10.08	15.9	22.8	545.0
Wac 4	R77-17	3.59	20.9		8.0274	178.2	80.21	5.85	30.78	3.089	0.00	1.1	889.4	236.7
Fre 1	R77-18	4.97	20.8	0.71884	8.0106	29.3	1.10	3.31	4.09	0.020	1.36	2.3	2.6	144.4

Fre 2	R77-19	7.70	20.8	0.70919	8.0073	133.7	55.85	3.98	27.77	2.882	7.84	1.4	19.3	174.2
Fre 3	R77-20	4.83	21	0.71045	8.0363	25.6	7.01	4.15	14.40	0.311	1.44	2.4	5.9	225.6
Esc 1	R77-21	7.96	21.1	0.71555	8.0261	139.9	55.65	6.71	12.12	0.195	8.96	4.8	33.3	604.6
Esc 2	R77-22	3.36	20.9	0.71567	8.0081	228.0	37.51	15.13	50.47	0.532	0.00	2.9	919.0	593.1
Esc 3	R77-23	7.32	21.2	0.71318	8.0232	31.6	7.40	14.20	32.64	0.246	2.60	2.3	10.4	106.4
Esc 4	R77-24	8.19	20.9	0.71685	8.0319	123.3	49.43	20.62	34.82	0.539	10.56	4.9	1.7	538.0
Esc 5	R77-25	4.31	20.8	0.71570	7.9969	28.8	9.39	20.83	18.45	0.227	1.28	15.2	4.1	628.0
Esc 6	R77-26	8.18	21	0.71687	8.0018	125.4	53.06	16.89	30.26	0.446	10.08	8.1	4.7	636.2
Esc 7	R77-27	7.02	21.1	0.71559	8.0132	29.9	9.54	22.28	34.09	0.349	3.20	11.2	2.5	195.6
Erb 104	R77-28	7.59	21	0.71144	8.0302	260.1	54.30	12.44	25.08	4.070	7.52	2.4	235.9	298.3
Ott 1/2wr	R77-29	7.92	21.3	0.71191	8.0071	149.2	28.70	7.19	14.71	0.597	9.44	2.3	1.9	412.5
Ott 1/2gb	R77-30	7.45	21.1	0.71168	8.0158	177.2	12.64	8.96	6.95	0.365	5.76	1.2	0.0	134.8
Pol 1	R77-31	4.87	21	0.71200	7.9918	125.4	4.68	13.57	22.59	0.865	5.56	2.0	1.6	637.9
Gro 4b	R77-32	4.95	21.2	0.71444	7.9915	91.2	14.82	15.65	6.63	0.656	4.68	1.8	1.0	589.4
78 days leaching with pure water:														
Eic 1	R78-01	7.89	21.1	0.70966	8.0313	17.7	0.16	3.03	0.19	0.005	0.69	1.8	10.2	0.0
Fra 1	R78-02	8.56	21.2	0.71306	8.0029	9.3	8.83	2.85	3.03	0.013	0.78	2.2	4.0	0.0
Fra 2	R78-03	9.16	20.9	0.70801	8.0264	5.1	20.37	6.38	1.47	0.012	1.12	13.7	9.4	0.1
Fra 3	R78-04	8.54	21.2	0.70753	8.0253	12.9	5.33	4.01	2.23	0.090	0.68	8.7	6.9	0.0
Fra 4	R78-05	8.33	21.2	0.70754	8.0204	29.3	7.16	3.68	3.33	0.379	1.08	3.8	33.5	0.0
Urs 1	R78-06	8.54	20.9	0.70808	8.0017	16.3	1.60	2.96	3.36	0.087	0.74	1.8	5.0	10.5
Urs 2	R78-07	8.10	21	0.70840	8.0374	60.1	14.62	4.90	23.43	0.409	1.79	2.6	130.6	0.0
Urs 3	R78-08	7.97	21.1	0.70932	7.9853	98.2	17.97	4.65	48.64	0.870	1.99	1.4	253.3	0.0
Urs 4	R78-09	7.92	20.8	0.70864	8.0387	126.8	27.72	5.59	27.87	0.717	2.54	2.9	330.2	0.0
Urs 5	R78-10	8.29	21.2	0.71079	8.031	40.7	5.55	3.63	6.44	0.057	2.78	2.2	9.6	0.0
Urs 6	R78-11	7.56	20.9	0.70966	7.9934	706.8	60.92	12.64	31.11	1.419	2.88	2.4	1851.0	1.5
TP39-1	R78-12	7.78	21.1	0.71101	8.0271	150.6	39.51	6.39	52.87	1.767	3.32	1.7	411.6	0.0
Auf 1	R78-13	7.85	21.1	0.70804	8.0269	384.2	76.40	10.09	33.78	5.881	3.35	2.3	1114.2	0.2
Wac 1	R78-14	8.22	21.4	0.70950	8	107.4	36.48	4.54	43.61	1.824	2.25	2.0	350.1	0.0
Wac 2	R78-15	8.35	21.1	0.70861	7.9845	27.7	7.39	7.20	13.16	0.431	1.53	4.5	48.2	0.0
Wac 3	R78-16	8.54	20.9	0.70939	8.0004	15.5	14.52	9.49	4.86	0.130	1.63	17.3	16.5	0.0
Wac 4	R78-17	3.36	20.9	0.70961	8.0005	246.6	103.11	7.28	34.92	3.143	0.00	1.6	1164.2	0.2
Fre 1	R78-18	7.90	21.3	0.71641	8.0205	5.5	0.33	6.50	1.31	0.012	0.40	4.0	3.4	0.1
Fre 2	R78-19	9.04	20.9	0.70918	7.9999	12.9	6.28	6.45	9.26	0.331	1.10	2.1	19.0	0.0
Fre 3	R78-20	8.24	21.4	0.71075	8.0335	7.2	2.38	4.73	7.50	0.086	0.67	5.0	6.5	0.0
Esc 1	R78-21	8.31	21.2	0.71572	8.0206	21.8	6.21	6.73	9.34	0.102	1.07	5.5	34.0	0.0
Esc 2	R78-22	3.42	21	0.71563	7.982	240.4	39.75	15.75	50.78	0.556	0.00	2.7	952.5	7.1
Esc 3	R78-23	8.94	21.3	0.71405	7.9947	15.8	3.71	19.93	27.02	0.141	1.91	7.5	9.8	0.5

277

Esc 4	R78-24	8.41	21	0.71631	8.023	11.3	3.63	18.41	16.30	0.086	1.46	5.4	1.6	0.0
Esc 5	R78-25	8.21	21.2	0.71680	7.9743	8.1	2.76	19.95	12.08	0.081	1.03	19.8	7.3	0.2
Esc 6	R78-26	8.43	20.7	0.71718	7.9959	11.5	3.31	15.72	18.20	0.091	1.41	7.9	6.6	0.5
Esc 7	R78-27	8.29	21.1	0.71672	7.9934	9.5	3.42	21.94	20.76	0.137	1.24	20.4	3.0	1.0
Erb 104	R78-28	7.76	21.2	0.71143	8.032	161.5	41.38	11.63	20.35	2.586	3.69	2.9	352.8	0.0
Ott 1/2wr	R78-29	8.10	21	0.71186	8.0276	87.1	15.96	6.54	11.61	0.362	6.25	2.8	1.3	0.9
Ott 1/2gb	R78-30	8.33	21	0.71179	8.0037	30.7	3.69	6.94	5.06	0.102	2.01	1.7	0.3	0.2
Pol 1	R78-31	8.00	21.1	0.71198	7.996	45.1	1.46	11.40	13.06	0.303	3.54	2.7	2.1	0.5
Gro 4b	R78-32	8.17	21.5	0.71491	8.0164	8.6	1.76	11.12	1.47	0.050	0.86	2.8	1.8	0.0
15 days leaching with pure water:														
Unt 1	R15-33	8.14	21.7	0.71231		16.2	1.81	4.28	7.60	0.046	4.45	2.3	1.5	0.0
Unt 2	R15-34	8.02	21.5	0.71477		16.2	5.39	4.24	11.50	0.034	1.28	2.8	1.3	0.0
Unt 3	R15-35	8.46	21.5	0.71435		11.7	3.17	4.99	9.87	0.025	3.80	2.4	1.0	0.0
Freq 1	R15-36	7.54	21.6	0.71352		1.4	0.26	8.54	7.38	0.011	0.75	4.9	12.2	0.0
Freq 2	R15-37	7.25	21.2	0.70918		5.7	0.69	17.25	10.59	0.043	0.60	11.2	7.4	0.0
Freq 3	R15-38	7.23	21.3	0.71547		3.5	0.57	15.30	4.77	0.013	0.80	5.9	6.1	0.0
Freq 4	R15-39	5.38	21.1	0.71415		2.5	0.56	12.66	3.14	0.006	0.20	4.3	18.1	0.0
Den 1	R15-40	6.60	20.7	no signal		0.9	0.18	8.90	5.03	0.001	0.32	5.1	1.6	0.0
78 days leached from the R78 series														
Erb 104	R78-28*	7.85	23.8	0.71190	-	-	-	-	-	-	-	-	-	-
Ott 1/2 (whole rock)	R78-29*	8.59	23.8	0.71178	-	-	-	-	-	-	-	-	-	-
Ott 1/2 (glass bomb)	R78-30*	7.86	23.7	0.71204	-	-	-	-	-	-	-	-	-	-
Pol 1	R78-31*	7.84	23.7	0.71150	-	-	-	-	-	-	-	-	-	-
Gro 4b	R78-32*	7.59	23.7	0.71526	-	-	-	-	-	-	-	-	-	-
Unt 1	R78-33*	8.39	23.7	0.71177	-	-	-	-	-	-	-	-	-	-
Unt 2	R78-34*	8.55	23.7	0.71524	-	-	-	-	-	-	-	-	-	-
Unt 3	R78-35*	8.57	23.7		-	-	-	-	-	-	-	-	-	-
Freq 1	R78-36*	7.54	23.7	0.71375	-	-	-	-	-	-	-	-	-	-
Freq 2	R78-37*	7.42	23.7	0.71262	-	-	-	-	-	-	-	-	-	-
Freq 3	R78-38*	7.32	23.7		-	-	-	-	-	-	-	-	-	-
Freq 4	R78-39*	5.59	23.6	0.71604	-	-	-	-	-	-	-	-	-	-
Den 1	R78-40*	6.79	23.6		-	-	-	-	-	-	-	-	-	-

Table B.4 Strontium isotope results of the Ries lacustrine carbonates.
The stable oxygen and carbon isotopes are reported in Zeng et al., submitted. Note: * leachated with 1N acetic acid

Lithostratigraphic member	sample	sample description	depth[m.b.s.]	CaMg(CO$_3$)$_2$wt%	^{87}Sr/^{86}Sr	2SE (Mean)	δ^{13}C	δ^{18}O
clay member	NR1003-1	whitegrey micrite	-14.3	71.99	0.710836	0.000023	-5.37	-3.26
	NR1003-20	white grey micrite	-15.9	76.44	0.710823	0.000023	-0.75	-3.43
	NR1003-23	light whitegrey micrite	-16.5	67.54	0.710850	0.000034	-5.09	-2.68
	NR1003-28	medium grey argillaceous clay	-18	-	0.710851	0.000017	-	-
	NR1003-36	white grey micrite	-23.2	77.97	0.710899	0.000019	-1.45	-0.12
	NR1003-45	medium grey marly micrite	-30	59.65	0.710790	0.000021	0.21	-1.98
	NR1003-59	light grey micrite	-33.3	81.57	0.710791	0.000019	0.94	-0.30
	NR1003-69	yellowish-light grey marly micrite	-36.05	68.23	0.710847	0.000012	0.78	-0.39
	NR1003-101	white grey marly micrite, homogeneous	-38.7	61.33	0.710501	0.000013	1.79	2.12
dolomite marl smbr	NR1003-102	white grey marly micrite, homogeneous	-39.7	70.53	0.710616	0.000016	1.83	0.71
	NR1003-103	white grey marly micrite, homogeneous	-42.5	30.90	0.710515	0.000021	1.18	0.62
	NR1003-104	white grey marly micrite, homogeneous	-44.4	36.72	0.710384	0.000016	1.19	2.02
	NR1003-105-3	white grey marly micrite, homogeneous	-46.3	41.48	0.710384	0.000023	2.33	1.84
	NR1003-107	white grey marly micrite, homogeneous	-48.3	60.80	0.710755	0.000017	3.13	0.96
	NR1003-2	white grey marly micrite, homogeneous	-52.2	71.99	0.710418	0.000018	-0.20	3.64
	NR1003-110	white grey marly micrite, homogeneous	-53.1	57.65	0.710616	0.000018	1.27	1.22
	NR1003-111	white grey marly micrite, homogeneous	-54.1	39.02	0.710752	0.000028	-0.22	1.11
	NR1003-114	white grey marly micrite, homogeneous	-59.7	51.52	0.710734	0.000017	8.43	1.67
	NR1003-115	white grey marly micrite, homogeneous	-62	78.35	0.710530	0.000017	6.90	1.28
	NR1003-116*	white grey marly micrite, homogeneous	-63	93.61	0.710480	0.000015	6.94	0.55
	NR1003-116	white grey marly micrite, homogeneous	-63	93.61	0.710464	0.000016	6.94	0.55
	NR1003-119	white grey marly micrite, homogeneous	-66.6	79.20	0.710477	0.000017	3.99	-0.58
	NR1003-121	medium grey marly micrite, homogeneous	-68.7	56.58	0.710441	0.000014	3.84	0.40
	NR1003-122	medium grey marly micrite, homogeneous	-70.5	31.74	0.710298	0.000022	1.76	-2.11
varicolored-marl smbr	NR1003-3	yellow grey marly micrite	-74.4	78.74	0.710622	0.000024	6.99	1.38
	NR1003-126	white grey marly micrite, homogeneous	-75.8	68.69	0.710634	0.000016	8.35	2.81
	NR1003-128	white grey marly micrite, homogeneous	-76.6	74.75	0.710727	0.000013	5.25	-8.55

	Sample	Description						
	NR1003-129	white grey marly micrite, homogeneous	-78.3	79.81	0.710373	0.000022	9.43	2.37
	NR1003-131	white grey marly micrite, homogeneous	-80.3	75.82	0.710492	0.000023	9.92	2.76
	NR1003-132	white grey marly micrite, homogeneous	-82	69.31	0.710520	0.000015	9.92	4.28
	NR1003-4	white grey marly micrite, homogeneous	-85.4	82.26	0.710427	0.000017	13.87	1.69
	NR1003-136	white grey marly micrite, homogeneous	-86.7	68.00	0.710615	0.00002	14.41	3.63
diatom smbr	NR1003-137	white grey marly micrite, homogeneous	-87.7	56.96	0.710714	0.000016	13.74	3.39
	NR1003-138	white grey marly micrite, homogeneous	-89.2	33.27	0.710599	0.000025	6.19	1.10
	NR1003-140	white grey marly micrite, homogeneous	-93.4	45.69	0.710496	0.000019	8.06	0.00
	NR1003-140	white grey marly micrite, homogeneous	-93.4	45.69	0.710524	0.000017	8.06	0.00
	NR1003-143	white grey marly micrite, homogeneous	-95.1	78.66	0.710501	0.000016	12.16	0.42
	NR1003-5	light grey micrite	-98.1	91.62	0.710405	0.000034	16.40	0.28
	NR1003-146	white grey marly micrite, homogeneous	-103.3	66.93	0.710375	0.000014	18.72	2.33
	NR1003-6	yellow grey, light yellowish micrite	-105.3	90.54	0.710391	0.000033	20.93	2.00
	NR1003-148	white grey marly micrite, homogeneous	-107.1	73.52	0.710357	0.000024	19.74	3.86
	NR1003-150	carbonate pebble micrite	-111.1	45.16	0.710630	0.00002	7.47	2.25
	NR1003-152-2	pinkish white grey layer, micrite, homogeneous	-112.6	40.94	0.710373	0.000014	10.82	3.27
	NR1003-156	white grey marly micrite, homogeneous	-116.7	77.13	0.710442	0.000013	18.52	4.80
	NR1003-8	whitegrey, light yellowish marly micrite	-121.6	70.84	0.710419	0.000028	17.03	2.12
	NR1003-9	whitegrey, light yellowish marly micrite	-123.6	47.00	0.710401	0.000025	14.52	1.29
	NR1003-160	white grey marly micrite, homogeneous	-123.8	67.85	0.710400	0.000019	18.11	4.14
bituminous smbr	NR1003-162	white grey marly micrite, homogeneous	-128.7	46.00	0.710366	0.000013	16.34	3.21
	NR1003-164	white grey marly micrite, homogeneous	-131.6	30.97	0.710289	0.000013	6.97	0.32
	NR1003-166	white grey marly micrite, homogeneous	-135.9	49.76	0.710701	0.000021	17.49	4.30
	NR1003-168	white grey marly micrite, homogeneous	-138.6	37.87	0.710735	0.000017	14.74	3.61
	NR1003-170-2	white grey marly micrite, homogeneous	-142.8	74.52	0.710622	0.00002	12.73	3.27
	NR1003-171	white grey marly micrite, homogeneous	-143.2	67.16	0.710691	0.000025	11.46	3.43
	NR1003-173	white grey marly micrite, homogeneous	-147.8	58.11	0.710548	0.000013	12.94	3.88
	NR1003-176	medium grey marly micrite, homogeneous	-150.4	41.09	0.710424	0.000013	3.47	-0.73
	NR1003-177	white grey marly micrite, homogeneous	-152.5	40.71	0.710586	0.000014	13.82	3.45
	NR1003-181	white grey marly micrite, homogeneous	-155.7	33.89	0.710497	0.000016	10.57	2.76
	NR1003-185*	white grey marly micrite, homogeneous	-161.2	20.09	0.710531	0.000012	3.18	1.33
	NR1003-185	white grey marly micrite, homogeneous	-161.2	20.09	0.710572	0.000024	3.18	1.33

	NR1003-186	white grey marly micrite, homogeneous	-164.8	36.34	0.710431	0.000022	4.55	0.49
	NR1003-187	white grey marly micrite, homogeneous	-166	47.69	0.710470	0.000019	5.90	-0.80
	NR1003-189	white grey marly micrite, homogeneous	-168.3	42.70	0.710380	0.000016	1.34	1.80
analcime smbr	NR1003-191	white grey laminae, marly micrite, homogeneous	-171.6	24.69	0.710658	0.000014	3.22	1.62
	NR1003-193	medium grey marly micrite	-175.9	25.30	0.710522	0.000009	1.89	2.27
	NR1003-195	white grey marly micrite	-178	51.14	0.710564	0.000017	0.86	3.57
	NR1003-197	white grey lamina, micrite, homogeneous	-181.9	39.25	0.710926	0.000018	2.82	1.58
	NR1003-198	white grey micrite, homogeneous	-183.6	35.19	0.710925	0.000016	2.96	0.69
	NR1003-200*	pinkish white grey marly micrite, homogeneous	-187.4	27.45	0.710872	0.000023	1.80	2.25
	NR1003-203	white grey marly micrite	-191.5	44.31	0.710933	0.000027	-0.94	1.63
	NR1003-204	medium grey marly micrite	-193.8	31.36	0.710890	0.000017	2.73	0.58
	NR1003-205	white grey marly micrite	-194.4	34.35	0.710886	0.000022	2.31	0.99
	NR1003-209	white grey marly micrite	-200.2	30.21	0.711003	0.000018	3.28	1.09
	NR1003-210	white grey marly micrite	-202.7	31.05	0.711042	0.000018	2.86	1.41
	NR1003-214	white grey marly micrite, homogeneous	-207.4	41.63	0.711046	0.000019	6.05	-0.48
	NR1003-216	yellowish grey marly micrite	-210.8	56.66	0.710736	0.000012	0.77	2.20
	NR1003-218-1	white grey marly micrite, homogeneous	-212.7	42.24	0.710974	0.000014	1.72	2.64
	NR1003-219	yellowish grey marly micrite	-213.2	54.97	0.711016	0.000011	-2.56	4.34
	NR1003-220	medium grey marly micrite, homogeneous	-214.6	42.63	0.711126	0.000013	0.90	1.77
clinoptilolite smbr	NR1003-223	weathered material, white grey and medium grey micrite	-215.9	69.31	0.711098	0.000013	-8.75	4.19
	NR1003-226*	white grey marly micrite	-219.9	84.87	0.711169	0.000014	-5.11	4.61
	NR1003-228-1	white grey marly micrite	-220.6	78.20	0.711107	0.000019	-4.69	3.95
	NR1003-229-1	dark grey lamina, micrite	-221.6	72.68	0.711505	0.00002	-4.06	3.76
	NR1003-231-2	white grey lamina, micrite, homogeneous	-223.3	84.03	0.711722	0.000012	-6.08	2.13
	NR1003-234	white grey micrite	-225.9	56.89	0.712509	0.000014	0.62	-0.96
basal member	NR1003-235-1	white grey micrite	-226.1	72.60	0.712838	0.000019	-3.67	-4.93
	NR1003-235-1*	white grey micrite	-226.1	72.60	0.712790	0.000012	-3.67	-4.93
	NR1003-235-1	white grey micrite	-226.1	72.60	0.712777	0.000029	-3.67	-4.93
	NR1003-237-2	white grey micrite, homogeneous	-226.8	90.62	0.713669	0.000015	-8.38	2.96
	NR1003-238B	dark grey lamina, micrite	-227.6	81.88	0.713253	0.000016	-2.11	-4.65
	NR1003-239*	white grey marly micrite	-228.3	65.86	0.712555	0.000019	-0.48	-0.91

	NR1003-242*	calcareous sand matrix	-233.6	14.57	0.712946	0.000014	-2.77	-6.69
	NR1003-242	calcareous sand matrix	-233.6	14.57	0.712877	0.000019	-2.77	-6.69
	NR1003-243	calcareous silt matrix	-236.5	18.40	0.713333	0.000011	-3.36	-3.31
	NR1003-244	calcareous sand matrix	-238.6	5.90	0.713769	0.000019	-5.93	-2.87
	NR1003-247*	white grey micrite, homogeneous	-242.9	75.52	0.713414	0.00002	-3.25	-5.10
	NR1003-10	white grey to light grey micrite	-243.4	73.75	0.713197	0.000031	-2.92	-8.52
	NR1003-11	white grey micrite	-245.2	-	0.713809	0.000024	-	-
	NR1003-250*	white grey marly micrite, homogeneous	-245.5	55.12	0.713602	0.000017	-3.02	-3.18
	NR1003-250	white grey marly micrite, homogeneous	-245.5	55.12	0.713492	0.00002	-3.02	-3.18
	NR1003-251	white grey marly micrite, homogeneous	-245.5	35.96	0.713178	0.000018	-3.16	-4.31
	NR1003-252-1*	white grey marly micrite, homogeneous	-246.1	33.50	0.713645	0.000017	-2.96	-5.89
	NR1003-252-1	white grey marly micrite, homogeneous	-246.1	33.50	0.713502	0.000016	-2.96	-5.89
standard	NBS987				0.7102109	0.000025		
					0.7102093	0.000018		
					0.7102167	0.000021		
					0.7102414	0.000017		
					0.7102242	0.000027		
					0.7102662	0.000025		
					0.710233	0.000018		
					0.7102207	0.000024		

Table B.5 Geometrical calculation of melted volumes (suevite).
Sr leachate: Data Table B.3; Sr bulk: Data Table B.2. Note that "*" represents the dolomitized part of the Weißjura Group (Solnhofen Subformation), estimated to comprise 50 % of Treuchtlingen Formation and Frankenalb Formation (**).

Lithostratigraphic units	thickness	reference	thickness	top	bot	h	sphere cap in suevite	Volume in suevite	Volume (after dolomitized correction)	volume in suevite	volume in suevite	density bulk	weight in suevite	Bulk weight (leaching experiment)	Sr leachate	Sr bulk
	[m]		[m]	a	b	[m]	[m³]	[m³]	[m³]	[km³]	[%]	[g/cm³]	[g]	[g]	[mg/L]	[wt%]
Tertiary limnic sediments ("Albüberdeckung", Terra Rossa)	0-25	Müller et al. 1969														
Weißjura Group, Solnhofen Subformation	variable	Hüttner and Schmidt-Kaler 1999							5.4E+08 *	0.54	5.0	2.5	1.4E+08	8.0264	0.012	0.019
Weißjura Group, Frankenalb-Formation (dolomitized Weißjura)	70-100	Hüttner and Schmidt-Kaler 1999	85	4281	4366	1738	1.1E+10	8.1E+08	4.0E+08 **	0.40	3.7	2.5	1.0E+08	8.0253	0.090	0.029
Weißjura Group, Treuchtlingen Formation (Weißjura δ)	30	Hüttner and Schmidt-Kaler 1999	30	4366	4396	1653	1.0E+10	2.8E+08	1.4E+08 **	0.14	1.3	2.5	3.5E+07	8.0204	0.379	0.057
Weißjura Group, Arzberg Formation (Weißjura γ)	20	Hüttner and Schmidt-Kaler 1999	20	4396	4416	1623	9.9E+09	1.9E+08	1.9E+08	0.19	1.7	2.5	4.7E+07	8.0017	0.087	0.045
Weißjura Group, Dietfurt Formation (upper part, Weißjura β)	40-50	Hüttner and Schmidt-Kaler 1999	45	4416	4461	1603	9.7E+09	4.2E+08	4.2E+08	0.42	3.9	2.5	1.1E+08	8.0374	0.409	0.079
Weißjura Group, Dietfurt Formation	2	Hüttner and Schmidt-Kaler	2	4461	4463	1558	9.3E+09	1.9E+07	1.9E+07	0.02	0.2	2.4	4.4E+06	7.9853	0.870	0.027

(lower part, Weißjura α)

Formation	Thickness	Reference														
Braunjura Group, Ornatenton Subformation (Braunjura ζ)	8	1999; Groiss et al. 2000 Hüttner and Schmidt-Kaler 1999; Groiss et al. 2000	8	4463	4471	1556	9.3E+09	7.5E+07	7.5E+07	0.08	0.7	2.5	1.9E+07	8.0387	0.717	0.044
Braunjura Group, Sengenthal Formation (Braunjura γ-ε)	40	Hüttner and Schmidt-Kaler 1999; Groiss et al. 2000	40	4471	4511	1548	9.2E+09	3.7E+08	3.7E+08	0.37	3.4	2.2	8.3E+07	8.031	0.057	0.005
Braunjura Group, Eisensandstein Formation (Braunjura β)	90-100	Hüttner and Schmidt-Kaler 1999; Groiss et al. 2000	95	4511	4606	1508	8.8E+09	8.8E+08	8.8E+08	0.88	8.0	2.4	2.1E+08	8.01025	1.593	0.020
Braunjura Group, Opalinuston Formation (Braunjura α, upper part)	3-16	Groiss et al. 2000; Müller 1969	10	4606	4616	1413	7.9E+09	9.1E+07	9.1E+07	0.09	0.8	2.4	2.2E+07	8	5.881	0.597
Braunjura Group, Opalinuston Formation (Braunjura α, middle part)	(0)-30-35	Groiss et al. 2000; Müller 1969	32.5	4616	4649	1403	7.9E+09	3.0E+08	3.0E+08	0.30	2.7	2.4	7.0E+07	8.0269	1.824	0.023

Schwarzjura Group, Posidonienschiefer Formation (Schwarzjura ε)	1-2	Groiss et al. 2000; own data (drill core Wachfeld 2018)	1	4649	4650	1370.5	7.6E+09	9.1E+06	9.1E+06	0.01	0.1	2.5	2.3E+06	7.9845	0.431	0.091
Schwarzjura Group, Amaltheenton Formation (Schwarzjura δ)	2	Groiss et al. 2000; own data (drill core Wachfeld 2018)	2	4650	4652	1369.5	7.6E+09	1.8E+07	1.8E+07	0.02	0.2	2.2	4.0E+06	8.0004	0.130	0.024
Schwarzjura Group, Numismalismergel Formation (Schwarzjura γ)	0-10	Groiss et al. 2000; own data (drill core Wachfeld 2018)	1	4652	4653	1367.5	7.5E+09	9.1E+06	9.1E+06	0.01	0.1	2.2	2.0E+06	8.0105	1.577	0.010
Trossingen Formation (Feuerletten)	20	Freudenberger et al. 2000	20	4653	4673	1366.5	7.5E+09	1.8E+08	1.8E+08	0.18	1.6	2.4	4.3E+07	7.9999	0.331	0.030
Löwenstein Formation (Burgsandstein)	85	Freudenberger et al. 2000	85	4673	4758	1346.5	7.3E+09	7.6E+08	7.6E+08	0.76	6.9	2.2	1.7E+08	8.0335	0.086	0.017
Hassberge Formation (Blasensandstein)	27	Freudenberger et al. 2000	27	4758	4785	1261.5	6.6E+09	2.4E+08	2.4E+08	0.24	2.1	2.2	5.2E+07	7.982	0.329	0.016
Steigerwald Formation (Lehrberg Beds)	16	Freudenberger et al. 2000	16	4785	4801	1234.5	6.4E+09	1.4E+08	1.4E+08	0.14	1.3	2.2	3.1E+07	7.9947	0.141	0.019

Benk Formation (Benker Sandstein, incl. Estherien Beds)	67+13	Freudenberger et al. 2000	80	4801	4881	1218.5	6.2E+09	6.8E+08	6.8E+08	0.68	6.2	2.2	1.5E+08	8.023	0.086	0.016
Grafenwöhr-Formation (Lettenkohlenkeuper + Muschelsandstein)	54	Freudenberger et al. 2000	54	4881	4935	1138.5	5.5E+09	4.5E+08	4.5E+08	0.45	4.1	2.2	9.9E+07	7.9743	0.086	0.015
Variscan Basement	-		846.5	4935	5781	1084.5	5.1E+09	5.1E+09	5.1E+09	5.09	46.3	2.7	1.4E+09	8.0242	1.318	0.054

Table B.6 Geometrical calculation of primary ejecta volumes (Bunte Breccia, exclusive of those produced by secondary cratering).

Lithostratigraphic units	sphere cap	Volume	Volume	Volume	volume (after dolomitized correction)	volume	volume	weight	leachate	$^{87}Sr/^{86}Sr$
	h	suevite+ejecta	suevite+ejecta	in ejecta		in ejecta	in ejecta	in ejecta	sample	leachate
	[m]	[m3]	[m3]	[m3]	[m³]	[km³]	[%]	[g]		
Tertiary limnic sediments									n.a.	n.a.
Weißjura Group, Solnhofen Subformation					5.5E+09	5.5	4.0	1.4E+18	Fra 2	0.7078
Weißjura Group, Frankenalb-Formation (dolomitized Weißjura)	5781	4.0E+11	8.9E+09	8.1E+09	4.1E+09	4.1	2.9	1.0E+18	Fra 3	0.7075
Weißjura Group, Treuchtlingen Formation (Weißjura δ)	5696	4.0E+11	3.1E+09	2.9E+09	1.4E+09	1.4	1.0	3.6E+17	Fra 4	0.7075
Weißjura Group, Arzberg Formation (Weißjura γ)	5666	3.9E+11	2.1E+09	1.9E+09	1.9E+09	1.9	1.4	4.8E+17	Urs 1	0.7081
Weißjura Group, Dietfurt Formation (upper part, Weißjura β)	5646	3.9E+11	4.7E+09	4.3E+09	4.3E+09	4.3	3.1	1.1E+18	Urs 2	0.7085
Weißjura Group, Dietfurt Formation (lower part, Weißjura α)	5601	3.9E+11	2.1E+08	1.9E+08	1.9E+08	0.2	0.1	4.5E+16	Urs 3	0.7092
Braunjura Group, Ornatenton Subformation (Braunjura ζ)	5599	3.9E+11	8.4E+08	7.6E+08	7.6E+08	0.8	0.6	1.9E+17	Urs 4	0.7087
Braunjura Group, Sengenthal Formation (Braunjura γ-ε)	5591	3.8E+11	4.2E+09	3.8E+09	3.8E+09	3.8	2.8	8.5E+17	Urs 5	0.7106
Braunjura Group, Eisensandstein Formation (Braunjura β)	5551	3.8E+11	1.0E+10	9.1E+09	9.1E+09	9.1	6.6	2.1E+18	TP39-1	0.7109
Braunjura Group, Opalinuston Formation (Braunjura α, upper part)	5456	3.7E+11	1.0E+09	9.6E+08	9.6E+08	1.0	0.7	2.3E+17	Auf 1	0.7079
Braunjura Group, Opalinuston Formation (Braunjura α, middle part)	5446	3.7E+11	3.4E+09	3.1E+09	3.1E+09	3.1	2.3	7.3E+17	Wac 1	0.7095
Schwarzjura Group, Posidonienschiefer Formation (Schwarzjura ε)	5414	3.7E+11	1.0E+08	9.6E+07	9.6E+07	0.1	0.1	2.4E+16	Wac 2	0.7086
Schwarzjura Group, Amaltheenton Formation (Schwarzjura δ)	5413	3.7E+11	2.1E+08	1.9E+08	1.9E+08	0.2	0.1	4.2E+16	Wac 3	0.7092

Schwarzjura Group, Numismalismergel Formation (Schwarzjura γ)	5411	3.7E+11	1.0E+08	9.6E+07	9.6E+07	0.1	0.1	2.1E+16	Wac 4; Fre 1	0.7139
Trossingen Formation (Feuerletten)	5410	3.7E+11	2.1E+09	1.9E+09	1.9E+09	1.9	1.4	4.5E+17	Fre 2	0.7092
Löwenstein Formation (Burgsandstein)	5390	3.6E+11	8.9E+09	8.1E+09	8.1E+09	8.1	5.9	1.8E+18	Fre 3	0.7105
Hassberge Formation (Blasensandstein)	5305	3.5E+11	2.8E+09	2.6E+09	2.6E+09	2.6	1.9	5.7E+17	Esc 1; Esc 2	0.7155
Steigerwald Formation (Lehrberg Beds)	5278	3.5E+11	1.7E+09	1.5E+09	1.5E+09	1.5	1.1	3.4E+17	Esc 3	0.7134
Benk Formation (Benker Sandstein, incl. Estherien Beds)	5262	3.5E+11	8.3E+09	7.6E+09	7.6E+09	7.6	5.5	1.7E+18	Esc 4	0.7168
Grafenwöhr-Formation (Lettenkohlenkeuper + Muschelsandstein)	5182	3.4E+11	5.6E+09	5.2E+09	5.2E+09	5.2	3.7	1.1E+18	Esc 5; Esc 6	0.7164
excavated+melted+unexcavated	5128	3.4E+11	8.1E+10	7.5E+10	7.5E+10	75.5	54.7	2.1E+19	Gro 4b; Erb-104	0.7141

Table B.7 Geometrical calculation of primary ejecta volumes (Bunte Breccia, exclusive of those produced by secondary cratering).

sample	Drill core/locality	Formation	lithology	pH	T_{pH} °C	$^{87}Sr/^{86}Sr$ (TIMS)	Ca mg/L	Mg mg/L	Sr mg/L	Na mg/L	K mg/L	Cl mg/L	SO$_4$ mg/L	TA meq/L
leachates														
Eic 1	Bohrung Eichstätt-Lüften	Tertiary limnic sediments ("Albüberdeckung", Terra Rossa)	intense redbrown clay with coarse quartz grains and pebbles, massive, carbonate-free	7.89	21.1	0.7097	17.7	0.16	0.005	3.03	0.19	1.8	10.2	0.69
Fra 1	Bohrung Frauenberg SPZ Solnhofen	Weißjura Group, Solnhofen Subformation	white-grey micritic limestone ("Plattenkalk"), inclined bedding	8.56	21.2	0.7131	9.3	8.83	0.013	2.85	3.03	2.2	4.0	0.78
Fra 2	Bohrung Frauenberg SPZ Solnhofen	Weißjura Group, Frankenalb-Formation (dolomitized Weißjura)	light-grey crystalline dolomite with minor spar patches, massive	9.16	20.9	0.7080	5.1	20.37	0.012	6.38	1.47	13.7	9.4	1.12
Fra 3	Bohrung Frauenberg SPZ Solnhofen	Weißjura Group, Treuchtlingen Formation (Weißjura δ)	white-grey micritic limestone with sponge layers and spar-cemented voids, bedded	8.54	21.2	0.7075	12.9	5.33	0.090	4.01	2.23	8.7	6.9	0.68
Fra 4	Bohrung Frauenberg SPZ Solnhofen	Weißjura Group, Arzberg Formation (Weißjura γ)	white-grey argillaceous micritic limestone, bedded, with one ammonite cast and very minor iron sulfide patches	8.33	21.2	0.7075	29.3	7.16	0.379	3.68	3.33	3.8	33.5	1.08
Urs 1	Bohrung Ursheim 2012	Weißjura Group, Dietfurt Formation (upper part, Weißjura β)	white-grey micritic limestone, 5-cm-bed	8.54	20.9	0.7081	16.3	1.60	0.087	2.96	3.36	1.8	5.0	0.74
Urs 2	Bohrung Ursheim 2012	Weißjura Group, Dietfurt Formation (lower part, Weißjura α)	medium-grey calcareous marl with bioclasts, faint irregular stratification	8.1	21	0.7084	60.1	14.62	0.409	4.90	23.43	2.6	130.6	1.79
Urs 3	Bohrung Ursheim 2012	Braunjura Group, Ornatenton Subformation (Braunjura ζ)	dark-grey marlstone, with abundant mica, disseminated irson sulfides and quartz silt, stratified	7.97	21.1	0.7093	98.2	17.97	0.870	4.65	48.64	1.4	253.3	1.99
Urs 4	Bohrung Ursheim 2012	Braunjura Group, Sengenthal Formation (Braunjura γ-ε)	medium-grey to redbrown mottled, iron-oolitic argillaceous limestone, bioturbated, with calcitic shells (ammonites, brachiopods, bivalves)	7.92	20.8	0.7086	126.8	27.72	0.717	5.59	27.87	2.9	330.2	2.54

Urs 5	Bohrung Ursheim 2012	Braunjura Group, Eisensandstein Formation (Braunjura β)	intense redbrown fine-grained sandstone with hematite-coated quartz grains and hematite oolite layers, carbonate-free	8.29	21.2	0.7108	40.7	5.55	0.057	3.63	6.44	2.2	9.6	2.78
Urs 6	Bohrung Ursheim 2012	Braunjura Group, Opalinuston Formation (Braunjura α, upper part)	medium-grey wavy bedded silt with clay layers, with minor mica, siderite patches and minor shell debris, belemnites	7.56	20.9	0.7097	706.8	60.92	1.419	12.64	31.11	2.4	1851.0	2.88
TP39-1	Bohrung Pilsach TP39 2019	Braunjura Group, Opalinuston Formation (Braunjura α, middle part)	medium grey calcareous claystone, bedded, minor disseminated iron sulfides; minor shell fragments	7.78	21.1	0.7110	150.6	39.51	1.767	6.39	52.87	1.7	411.6	3.32
Auf 1	Bohrung Aufkirchen P1 1971	Schwarzjura Group, Posidonienschiefer Formation (Schwarzjura ε)	darkgrey bituminous laminated marlstone (with aragonitic shell debris: bivalves, compressed ammonites)	7.85	21.1	0.7080	384.2	76.40	5.881	10.09	33.78	2.3	1114.2	3.35
Wac 1	Bohrung Wachfeld 2018	Schwarzjura Group, Amaltheenton Formation (Schwarzjura δ)	medium grey calcareous claystone, bedded, minor disseminated iron sulfides	8.22	21.4	0.7095	107.4	36.48	1.824	4.54	43.61	2.0	350.1	2.25
Wac 2	Bohrung Wachfeld 2018	Schwarzjura Group, Numismalismergel Formation (Schwarzjura γ)	light-grey argillaceous limestone, massive (bioturbated)	8.35	21.1	0.7086	27.7	7.39	0.431	7.20	13.16	4.5	48.2	1.53
Wac 3	Bohrung Wachfeld 2018	Schwarzjura Group, Gryphaeensandstein Formation (Schwarzjura α3+β, "Arietensandstein")	light-grey coarse-grained to fine-conglomeratic, calcareous quartz sandstone, massive	8.54	20.9	0.7094	15.5	14.52	0.130	9.49	4.86	17.3	16.5	1.63
Wac 4	Bohrung Wachfeld 2018	Schwarzjura Group, Angulatensandstein Formation (Schwarzjura α2)	medium grey clayey siltstone, slightly calcareous, bioturbated, poorly bedded	3.36	20.9	0.7096	246.6	103.11	3.143	7.28	34.92	1.6	1164.2	0.00
Fre 1	Bohrung Fremdingen	Schwarzjura Group, Angulatensandstein Formation (Schwarzjura α2)	yellow-brown fine-grained quartz sandstone with mica	7.9	21.3	0.7164	5.5	0.33	0.012	6.50	1.31	4.0	3.4	0.40
Fre 2	Bohrung Fremdingen	Keuper Group, Trossingen Formation ("Feuerletten")	redbrown silty claystone with minor mica; carbonate-free	9.04	20.9	0.7092	12.9	6.28	0.331	6.45	9.26	2.1	19.0	1.10
Fre 3	Bohrung Fremdingen	Keuper Group, Löwenstein Formation ("Burgsandstein")	light-grey coarse-grained to fine-conglomeratic arkose (with kaolinized feldspar grains)	8.24	21.4	0.7108	7.2	2.38	0.086	4.73	7.50	5.0	6.5	0.67

Sample	Location	Formation	Description											
Esc 1	Bohrung Eschertshofen 1981	Keuper Group, Hassberge Formation ("Coburger Sandstein")	light-grey coarse-grained to fine-conglomeratic arkose (with kaolinized feldspar grains)	8.31	21.2	0.7157	21.8	6.21	0.102	6.73	9.34	5.5	34.0	1.07
Esc 2	Bohrung Eschertshofen 1981	Keuper Group, Hassberge Formation ("Blasensandstein")	medium-grey fine- to medium-grained sandstone, with some clay and mica, well bedded (shallow cross stratification?)	3.42	21	0.7156	240.4	39.75	0.556	15.75	50.78	2.7	952.5	0.00
Esc 3	Bohrung Eschertshofen 1981	Keuper Group, Steigerwald Formation ("Lehrbergschichten")	greenish-grey and violet mottled clayey coarse-grained arkose (with kaolinized feldspar grains)	8.94	21.3	0.7141	15.8	3.71	0.141	19.93	27.02	7.5	9.8	1.91
Esc 4	Bohrung Eschertshofen 1981	Keuper Group, Benk Formation ("Benker Sandstein")	violett-redbrown siltstone to finegrained sandstone with mica, faint stratification	8.41	21	0.7163	11.3	3.63	0.086	18.41	16.30	5.4	1.6	1.46
Esc 5	Bohrung Eschertshofen 1981	Keuper Group, Grafenwöhr Formation ("Lettenkohlenkeuper")	redbrown coarse-grained quartz sandstone with some feldspar, minor clay content	8.21	21.2	0.7168	8.1	2.76	0.081	19.95	12.08	19.8	7.3	1.03
Esc 6	Bohrung Eschertshofen 1981	Muschelkalk Group, Grafenwöhr Formation ("Muschelsandstein")	whitegrey to violett siltstone to medium/coarse grained sandstone with kaolinized feldspar, cross-stratification	8.43	20.7	0.7172	11.5	3.31	0.091	15.72	18.20	7.9	6.6	1.41
Esc 7	Bohrung Eschertshofen 1981	Benk Formation (Benker Sandstein, including Estherien Beds)	dark redbrown siltstone to fine-grained sandstone, with mica, cross-stratified	8.29	21.1	0.7167	9.5	3.42	0.137	21.94	20.76	20.4	3.0	1.24
Erb 104	Bohrung Erbisberg	Inner Ring, allochthonous crystalline block	Hornblende-Gneiss	7.76	21.2	0.7114	161.5	41.38	2.586	11.63	20.35	2.9	352.8	3.69
Ott 1/2wr	Steinbruch Otting	suevite	grey suevite with carbonate in matrix and glass	8.1	21	0.7119	87.1	15.96	0.362	6.54	11.61	2.8	1.3	6.25
Ott 1/2gb	Steinbruch Otting	suevite	glass bomb within suevite, with carbonate in gas bubbles	8.33	21	0.7118	30.7	3.69	0.102	6.94	5.06	1.7	0.3	2.01
Pol 1	Steinbruch Polsingen	suevite	red melt agglomerate	8	21.1	0.7120	45.1	1.46	0.303	11.40	13.06	2.7	2.1	3.54
Gro 4b	pipe trench Grosselfingen	Inner Ring, allochthonous crystalline block	light-grey brecciated granite, rich in white-grey feldspar	8.17	21.5	0.7149	8.6	1.76	0.050	11.12	1.47	2.8	1.8	0.86

291

Unt 1	Unterwillfingen quarry	Keuper clast in Bunte Breccia, outcrop samples in Ries; ex situ from basis of outcrop wall	pinkish white-grey and yellowish grey mottled, fine-grained pebbly arkose clast	8.14	21.7	0.7123	16.2	1.81	0.046	4.28	7.60	2.3	1.5	4.45
Unt 2	Unterwillfingen quarry	Keuper clast in Bunte Breccia, outcrop samples in Ries; ex situ from basis of outcrop wall	mixed material between Keuper arkose and Bunte breccia: pinky reddish medium to fine-grained arkose with olivine-grey mottled Bunte breccia matrixes	8.02	21.5	0.7148	16.2	5.39	0.034	4.24	11.50	2.8	1.3	1.28
Unt 3	Unterwillfingen quarry	Keuper clast in Bunte Breccia, outcrop samples in Ries; from contact Keuper-suevite	white-grey fine-grained sanstone clast	8.46	21.5	0.7144	11.7	3.17	0.025	4.99	9.87	2.4	1.0	3.80
Freq 1	Fremdingen road cut , Ries	Keuper group, outcrop samples in Ries, road cutting B25 (western slope)	white-grey coarse-grained quartz sandstone	7.54	21.6	0.7135	1.4	0.26	0.011	8.54	7.38	4.9	12.2	0.75
Freq 2	Fremdingen road cut , Ries	Keuper group, outcrop samples in Ries, road cutting B25 (western slope)	ochre red claystone with mica	7.25	21.2	0.7092	5.7	0.69	0.043	17.25	10.59	11.2	7.4	0.60
Freq 3	Fremdingen road cut , Ries	Keuper group, outcrop samples in Ries, road cutting B25 (western slope)	ochre red and yellowish-white mottled coarse-grained quartz sandstones with mica	7.23	21.3	0.7155	3.5	0.57	0.013	15.30	4.77	5.9	6.1	0.80
Freq 4	Fremdingen road cut , Ries	Keuper group, outcrop samples in Ries, road cutting B25 (western slope)	ochre red, violet and white mottled claystone with mica	5.38	21.1	0.7142	2.5	0.56	0.006	12.66	3.14	4.3	18.1	0.20
Den-1	Dennenlohe outcrop	Bayreuth Fm., Keuper group, outcrop sample 55 km NW' Ries	white grey coarse-grained quartz sandstone with muscovites	6.6	20.7	no result	0.9	0.18	0.001	8.90	5.03	5.1	1.6	0.32
surface water														
OTT 01	Ottingen Suevite Quarry 1			7.65	13.9	no result	82.9	9.86	0.238	6.33	3.24	14.5	9.3	4.53
OTT 02	Ottingen Suevite Quarry 2			7.53	11.2	no result	76.7	8.66	0.193	6.04	3.42	14.7	5.8	4.32
DOO 01	Wemding Doos spring, Upper Jurassic carbonate megablock within ejecta			7.15	8.5	no result	124.7	3.35	0.123	6.77	1.28	18.3	23.1	5.28

HUQ	Hohenaltheim Spring, parautochthonous/autochthonous Upper Jurassic carbonates (southern crater rim)	7.39	8.7	no result	109.4	18.01	0.073	6.09	0.82	15.7	17.5	6.14
TFQ 01	Trochtelfingen Spring, Eisensandstein/Opalinuston boundary	6.94	8.8	no result	21.0	3.18	0.042	2.70	0.74	6.7	6.6	0.82
reference data (Winkler 1972)												
C3/2	Nördlingen Drilling Busse, groundwater from crystalline ring	7.80	18.2	no result	15.0	9.10	0.195	192.0	10.00	19.0	82.0	0.00
A71	Drilling Kirchheim, groundwater from Bunte Breccia	7.10	7.2	no result	130.6	6.10	0.280	5.60	5.20	29.1	42.5	5.17

Table B.8 Results of hydrochemical modelling calculations (PHREEQC) for different lake stages of the Ries Crater lake, in comparison with potential present-day analogues.

	pH	T °C	Ca²⁺ mM	Mg²⁺ mM	Sr²⁺ mM	Na²⁺ mM	K²⁺ mM	Cl⁻ mM	SO₄²⁻ mM	Alk mM	TDS mg/L	pCO₂	SI$_{Cc}$	SI$_{Dol}$	SI$_{Gyp}$	SI$_{Str}$	⁸⁷Sr/⁸⁶Sr	Methane
Step 1a: basal member																		
solution 1a	8.56	60	0.30	0.51	0.0031	4.6	0.3	0.3	0.5	6.1	456	-2.80	1	2.58	-2.76	-0.27	0.7125	no
Lake Landbrot LDB4(ILd7)	8.29	54	0.52	0.04	-	6.8	0.1	3.2	0.6	3.3	556	-2.82	0.74	0.67	-2.31	-	-	
Step 1b: basal member (top)																		
solution 1b	9.35	60	0.10	2.61	0.0036	72.8	2.6	4.8	7.4	74.7	4908	-3.00	1	4	-3.23	0.50	0.7135	no
Step 2, clinoptilolite smbr																		
solution 2	9.61	40	0.07	2.41	0.0024	556.4	21.8	47.2	62.3	507.0	52298	-3.00	1	4	-3.14	0.5	0.7115	no
Lake Bogoria, BW2, surface water	9.95	27	0.30	0.04	-	1070.0	11.1	160.2	3.4	683.8	72782	-3.57	1.72	2.92	-3.87	-	-	
Step 3, analcime smbr																		
solution 3 Lake Alchichica, average of 52 measurements	10.07	15	0.05	3.25	0.0010	716.5	28.2	61.2	31.6	749.6	40631	-3.50	1	3.99	-3.74	0.5	0.7110	no
	9.00	20	0.15	6.81	-	87.2	5.6	85.2	5.3	20.9	7201	-3.15	0.73	3.23	-2.66			-
Lake Van, 1989, 5m	9.73	20	0.11	4.40	0.0079	338.0	10.8	160.0	24.5	151.0	25544	-3.48	1.15	4.14	-2.91	-	-	
Step 4, high δ¹³C interval																		
solution 4a	9.81	25	0.06	2.53	0.0014	719.9	28.4	61.9	0.002	814.6	38680	-3.00	1	4	-8.26	0.5	0.7105	yes
solution 4b	9.76	25	0.06	2.63	0.0014	611.0	24.1	52.6	0.003	692.4	33258	-3.00	1	4	-7.83	0.5	0.7105	yes

Step 5, varicoloured-marl smbr

solution 5a	9.70	25	0.06	2.56	0.0014	790.7	31.2	68.0	2.0	890.4	43171	-2.90	1	4	-4.92	0.5	0.7105	yes
solution 5b	9.68	25	0.06	2.72	0.0015	789.7	31.1	67.9	51.2	791.0	46667	-3.00	1	4	-3.47	0.5	0.7105	no

Step 6, dolomite-marl smbr

solution 6a	9.65	25	0.07	1.53	0.0018	408.8	16.2	35.5	46.2	369.7	26106	-3.01	1	3.68	-3.18	0.5	0.7103	yes
solution 6b	9.73	25	0.06	2.78	0.0015	827.9	32.7	72.0	93.7	748.0	51362	-3.00	1	4	-3.22	0.5	0.7103	

Step 7, clay member

solution 7a	9.13	25	0.11	0.23	0.0018	31.3	1.3	2.9	0.0	34.6	2098	-3.00	1	2.54	-6.16	-0.4	0.7108	yes
solution 7b	9.43	25	0.10	0.22	0.0006	27.2	1.1	2.5	3.1	23.6	2509	-3.50	1	2.56	-2.94	-0.32	0.7108	no
solution 7c	8.92	25	0.39	0.22	0.0007	6.0	0.3	0.8	0.8	5.1	579	-3.50	1	1.76	-2.4	-0.91	0.7108	no
solution 7d	8.59	25	1.43	0.15	0.0008	0.6	0.1	0.3	0.2	2.2	239	-3.50	1	1.14	-2.4	0.2	0.7108	no
solution 7e	7.84	25	33.62	15.02	0.0800	63.3	5.2	31.0	16.9	1.8	6208	3.50	1	1.78	0.02	-0.84	0.7108	no

Acknowledgements

Curriculum Vitae

Lingqi Zeng

Date of birth: 18.04.1993

Place of birth: Leshan, China

Education

2017 — present **Doctoral student** Geosciences (GAUSS program), Division of Geobiology, Geoscience Center, University of Göttingen, Göttingen, Germany

2014 — 2017 **Graduate student** (M. Eng.) Geological Engineering (Sedimentology), Institute of Sedimentary Geology, Chengdu University of Technology, Chengdu, China. Title of the thesis: ***Paleoclimate and paleoenvironment significance research of lacustrine and marine stromatolites***

2010 — 2014 **Undergraduate student** (B. Eng.) Resources Exploration Engineering (Ore deposits), College of Earth Science, Chengdu University of Technology, Chengdu, China.

Grants and scholarships

2016   Guest Student Scholarship (1 year, Chengdu University of Technology)

2017   PhD scholarship (4 years, China Scholarship Council)

2018   Travel Grant (Freunde des Rieskratermuseums)

Publications

Zeng, L., Ruge, D.B., Berger, G., Heck, K., Hölzl, S., Reimer, A., Jung, D. and Arp, G. (2021) Sedimentological and carbonate isotope signatures to identify fluvial processes and catchment changes in a supposed impact ejecta-dammed lake (Miocene, Germany). Sedimentology 68, 2965-2995.

Arp, G., Dunkl, I., Jung, D., Karius, V., Lukács, R., Zeng, L., Reimer, A. and Head III, J.W. (2021) A Volcanic Ash Layer in the Nördlinger Ries Impact Structure (Miocene, Germany): Indication of Crater Fill Geometry and Origins of Long-Term Crater Floor Sagging. Journal of Geophysical Research: Planets 126, e2020JE006764.

Zeng, L.-Q., Yi, H.-S., Xia, G.-Q., Simon, K., Heim, C. and Arp, G. (2019) Palaeoenvironmental setting of lacustrine stromatolites in the Miocene Wudaoliang Group, northern Tibetan Plateau. Journal of Palaeogeography 8, 18.

Zeng, L., Yi, H., Xia, G., Yuan, T. (2017) Sedimentary sequences and implications for paleoenvironment of Cenozoic lacustrine stromatolites, Qaidam Basin. Geosciences 31, 1251-1260. (In Chinese with English abstract)